UNIVERSITY OF SOUTHAMPTON

NUMERICAL MODELLING OF CHANNEL ADJUSTMENT IN ALLUVIAL MEANDERING RIVERS WITH RIPARIAN VEGETATION

Marco Johan Van De Wiel

A thesis submitted for the degree of Doctor of Philosophy

Faculty of Science

Department of Geography

July 2003

UNIVERSITY OF SOUTHAMPTON

ABSTRACT

FACULTY OF SCIENCE

DEPARTMENT OF GEOGRAPHY

Doctor of Philosophy

NUMERICAL MODELLING OF CHANNEL ADJUSTMENT IN ALLUVIAL MEANDERING RIVERS WITH RIPARIAN VEGETATION

by Marco Johan Van De Wiel

It is generally acknowledged that riparian vegetation influences the geomorphological dynamics of rivers. However, the precise nature of the impact depends on a wide range of ecological and geomorphological processes, making it difficult to study the effects of specific individual factors in a field or laboratory setting. As a result, there are many uncertainties concerning the effects of riparian vegetation on channel morphology, riverbank erosion and meander migration. However, riparian vegetation is increasingly seen as an effective and environmentally acceptable tool in river management and river engineering, which necessitates a better understanding of the geomorphological impact of vegetation. This study examines the potential of a computational approach to address these issues, based on undertaking controlled experiments using a newly developed numerical model. The new model, MRIPA, combines an existing two-dimensional flow and sediment transport model with a geotechnical bank-stability analysis, and is further extended to account for the hydraulic and geotechnical effects of riparian vegetation. This coupled fluvial-geotechnical model is then calibrated and evaluated, before being applied to simulate a range of vegetation scenarios to investigate the influence of vegetation density and biophysical characteristics of vegetation on geomorphological change in single-thread alluvial, meandering river channels. Results show that riparian vegetation can have a considerable impact on the morphological evolution of such rivers. The most pronounced effect is on channel planform evolution, with up to 60% reduction in floodplain area loss, depending on the species and density of the simulated vegetation. Bed topography is also affected, albeit to a lesser extent. Throughout the scenarios investigated herein, the impact of simulated woody species on bed topography change and bank retreat is consistently higher than the impact of simulated herbaceous species. Finally, and critically, it is found that the impact of vegetation is spatially variable, as the local effects of vegetation can propagate downstream due to the interactions between channel planform, flow and bed response. This spatial variability of the effects of vegetation highlights the complexity and intricacy of fluvial systems.

Table of Contents

Abstract i
Table of Contents ii
List of Figures v
List of Tables ix
Notation xi
Acknowledgements xvi

Chapter 1 : Introduction 1
1.1. Aim and objectives 1
1.2. Background 1
1.3. A new model? 3
1.4. Structure of the text 4

Chapter 2 : Literature Review 6
2.1. Introduction 6
2.2. Numerical modelling 6
2.3. Meandering 11
2.3.1. Meander morphology and geometry 12
2.3.2. Flow processes in meander bends 16
2.3.3. Sediment related processes in meander bends 23
2.3.4. Meander morphogenesis 26
2.3.5. Planform change modelling 31
2.4. Bank erosion 33
2.4.1. Processes of bank erosion 33
2.4.2. Rates of bank erosion and process dominance 43
2.5. Bank accretion 44
2.5.1. Bank accretion processes 46
2.5.2. Rates of bank accretion processes 49
2.5.3. Relation to bank erosion processes 50
2.6. Riparian vegetation 51
2.6.1. Effects of vegetation on hydraulics 52
2.6.2. Geotechnical effects of vegetation on bank stability 59
2.6.3. Other aspects of riparian vegetation 62
2.7. Conclusion 64

Chapter 3 : Model Development 66
3.1. Introduction 66
3.2. Coordinate system 68

3.3. Flow submodel 72
3.3.1. Flow equations for orthogonal coordinate systems 72
3.3.2. Flow equations for non-orthogonal coordinate systems 76
3.3.3. Numerical implementation 79
3.3.4. Effects of vegetation on flow 83
3.4. Sediment transport submodel 91
3.4.1. Magnitude of sediment transport 91
3.4.2. Direction of sediment transport 94
3.4.3. Bed topography change 96
3.4.4. Hydraulic bank erosion 97
3.4.5. Effects of vegetation on sediment transport 98
3.5. Geotechnical bank erosion submodel 101
3.5.1. Definitions, concepts and parameters 101
3.5.2. Factor of safety 104
3.5.3. Failure plane angle 111
3.5.4. Effects of vegetation on bank stability 118
3.6. Model structure 126
3.6.1. Overall model structure 127
3.6.2. Submodel interactions 127
3.6.3. Assumptions and limitations 134
3.7. Conclusion 134

Chapter 4 : Model Calibration and Validation 136
4.1. Introduction 136
4.2. Parameter sensitivity analysis 136
4.2.1. Parameters 137
4.2.2. Sample channel 138
4.2.3. Definition of the sensitivity index 138
4.2.4. Parameter sensitivity 142
4.2.5. Limitations of the sensitivity analysis 150
4.3. Calibration 152
4.3.1. Calibration method 152
4.3.2. Calibration of flow and sediment transport parameters 154
4.3.3. Calibration of bank erosion parameters 176
4.4. Validation 180
4.4.1. Site description 180
4.4.2. Numerical representation 183
4.4.3. Results 185
4.4.4. Discussion 188
4.5. Conclusion 189

Chapter 5 : Analysis of Vegetation Effects 190
5.1. Introduction 190

5.2. Parameterization of vegetation properties 190
5.2.1. Selection of species 191
5.2.2. Parameterization 192
5.2.3. Overview 202
5.3. Geotechnical bank stability analysis with vegetation 203
5.3.1. Setup of the analysis 203
5.3.2. Results with a single vegetation element 206
5.3.3. Results with multiple vegetation elements 218
5.3.4. Sensitivity of species parameterization 232
5.3.5. Discussion 240
5.4. Effects of vegetation in MRIPA 243
5.4.1. Setup of the analysis 244
5.4.2. Quantitative indicators 248
5.4.3. Reference scenario without vegetation 250
5.4.4. Effects of species variation 260
5.4.5. Effects of density variation 266
5.4.6. Discussion 280
5.5. Conclusion 285

Chapter 6 : Model Application 287
6.1. Introduction 287
6.2. Experiment setup 287
6.3. Results 291
6.3.1. Bed topography change 293
6.3.2. Planform change 303
6.4. Discussion 308
6.5. Conclusion 311

Chapter 7 : Conclusion 312
7.1. Introduction 312
7.2. The MRIPA model 312
7.3. Impact of vegetation on channel morphology 314
7.4. Scope for further research 317

Appendix 1 : Rates of Bank Adjustment 319
A1.1. Bank erosion rates 319
A1.2. Bank accretion rates 319
Appendix 2 : Expression for Failure Plane Angle under Simplified Conditions 328
Appendix 3 : Grid Sensitivity Analysis 330
Appendix 4 : Mass Conservation 330
A4.1. Conservation of water 336
A1.2. Conservation of sediment 338
Bibliography 339

List of Figures

Figure 1.1: Relations between flow, sediment, vegetation and river geometry. 5
Figure 2.1: Generalized view of meander bend morphology. 14
Figure 2.2: Generalized sketch of meander geometry. 14
Figure 2.3: Vertical velocity profile. 18
Figure 2.4: Planform distribution of downstream surface velocity in a flume bend. 18
Figure 2.5: Helicoidal flow. 20
Figure 2.6: Generalized secondary flow pattern in cross-section of a meander bend. 20
Figure 2.7: Generalized scheme of meander evolution. 28
Figure 2.8: Relation between meander migration rate and bend curvature. 30
Figure 2.9: Simulated long term meander evolution of a initially nearly straight river. 30
Figure 2.10: Relations between bank erosion processes. 34
Figure 2.11: Types of bank failure. 39
Figure 2.12: Resisting and driving forces for simple planar failure. 41
Figure 2.13: Sediment fluxes at the bank basal zone. 41
Figure 2.14: Bank erosion rates as a function of drainage area. 45
Figure 2.15: Sediment movement in a meander bend. 48
Figure 2.16: Location and planform of two concave-bank benches. 49
Figure 2.17: Mutual dependency of flow velocity and vegetation roughness. 54
Figure 2.18: Vertical velocity profiles for flow through species of vegetation. 56
Figure 3.1: Genealogy of the MRIPA model. 67
Figure 3.2: Channel representation on different grids. 69
Figure 3.3: Directions of axes in orthogonal and non-orthogonal coordinate systems. 71
Figure 3.4: Components of a vector in an orthogonal and a non-orthogonal system. 71
Figure 3.5: Spacing in a curvilinear grid does not have to be constant in space. 80
Figure 3.6: Example of curvilinear grid where all n-axes are parallel to the y-axis. 80
Figure 3.7: Schematic representation of the flow field calculation procedure. 82
Figure 3.8: Cross-channel distribution of the reduction coefficient 84
Figure 3.9: Effects of bending on the projected height of submerged vegetation. 87
Figure 3.10: Schematic representation of procedure for calculating vegetation roughness and flow velocity for submerged flexible vegetation. 89
Figure 3.11: Possible relations between the bank shear proportionality coefficient and bank angle. 99
Figure 3.12: Shear stress distribution over the periphery of a trapezoidal channel. 99
Figure 3.13: Possible ways to account for lateral erosion. 100
Figure 3.14: Definition sketch of basic parameters for the bank stability analysis. 103
Figure 3.15: Definition sketch of basic forces in bank stability analysis. 105
Figure 3.16: Definition sketch of unsaturated and saturated parts of the bank. 105
Figure 3.17: Definition sketch of hydrostatic confining pressure. 109

Figure 3.18: Schematic representation of bank stability calculations. 117
Figure 3.19: Dependency of bracketed term of equation 3.106 on shear distortion angle and internal friction angle. 119
Figure 3.20: Different root cone shapes as determined through the root parameters. 122
Figure 3.21: Definition sketch of root regions. 122
Figure 3.22: Possibilities of failure plane intersection with the root cone. 125
Figure 3.23: Schematic representation of the structure of the MRIPA model. 128
Figure 3.24: Interactions between the submodels. 129
Figure 3.25: Definition sketch for calculating near-toe lateral erosion. 131
Figure 3.26: Distribution of failed material. 131
Figure 4.1: Layout-sketch of the sample channel. 139
Figure 4.2: Numerical grid for the sample channel. 139
Figure 4.3: Predicted flow velocity in the sample channel. 140
Figure 4.4: Predicted bed topography in the sample channel. 140
Figure 4.6: Sensitivity plot of the exponent in the power law for sediment transport. ... 145
Figure 4.7: Sensitivity plot of the coefficient in the power law for sediment transport. .. 146
Figure 4.8: Sensitivity plot of the weighing coefficient for secondary flow intensity. ... 147
Figure 4.9: Sensitivity plot of the Chezy roughness coefficient. 148
Figure 4.10: Sensitivity plot of the coefficient in the transverse slope model. 149
Figure 4.11: Example of parameter space sampling strategies 151
Figure 4.12: Relation between the secondary flow convection factor and the Chezy roughness coefficient. 156
Figure 4.13: IIHR laboratory flume layout. 157
Figure 4.14: UCB flume layout. 158
Figure 4.15: Grid used for IIHR simulations. 158
Figure 4.16: Grid used for UCB simulations. 159
Figure 4.17: Differences in bed-level erosion at a boundary point in the IIHR laboratory experiment and in the numerical model. 161
Figure 4.18: Comparison between observed and modelled bed-topography. 163
Figure 4.19: Observed and modelled flow depths at selected cross-sections. 164
Figure 4.20: Observed and modelled flow depths at longitudinal profiles. 166
Figure 4.21: Distribution of differences in flow depth. 166
Figure 4.22: Comparison between observed and modelled bed-topography. 168
Figure 4.23: Observed and modelled flow depths at selected cross-sections. 169
Figure 4.24: Distribution of differences in flow depth. 171
Figure 4.25: Observed and modelled flow depths at longitudinal profiles. 171
Figure 4.26: Modelled and observed bank erosion in the UCB2-flume. 179
Figure 4.27: Location of the Goodwin Creek basin. 181
Figure 4.28: Goodwin Creek study reach. 182
Figure 4.29: Final simulated planform and flow depth for the study reach. 186
Figure 4.30: Observed and simulated cross-section topography for May 1988. 186
Figure 4.31: Modelled and observed bank retreat in the study reach for May 1988. 187
Figure 5.1: Root tensile strength as function of root diameter for different tree species. . 197

Figure 5.2: The "standard" river bank for geotechnical analyses. 204
Figure 5.3: Vegetation positioning. 205
Figure 5.4: Spatial distribution of root-area-ratio and root cohesion for a single "*Populus*" tree. 207
Figure 5.5: Spatial distribution of root cohesion for different tree species. 208
Figure 5.6: Distribution of root cohesion along the failure plane for individual trees. . . . 209
Figure 5.7: Distribution of root cohesion along the incipient failure plane for individual "*Populus*" trees located at different lateral positions. 211
Figure 5.8: Distribution of root cohesion along the incipient failure plane for individual "*Salix*" trees located at different lateral positions. 212
Figure 5.9: Distribution of root cohesion along the incipient failure plane for individual "*Betula*" trees located at different lateral positions. 213
Figure 5.10: Average root cohesion as a function of tree position. 214
Figure 5.11: Vegetation surcharge as function of tree position. 216
Figure 5.12: Factor of safety as function of tree position. 216
Figure 5.13: Effect of vegetation ground cover on vegetation forces and factor of safety. 220
Figure 5.14: Effect of bank slope on bank stability and vegetation impact. 222
Figure 5.15: Effect of bank height on bank stability and vegetation impact. 224
Figure 5.16: Effect of tension crack depth on bank stability and vegetation impact. 226
Figure 5.17: Effect of soil cohesion on bank stability and vegetation impact. 227
Figure 5.18: Effect of internal friction angle on bank stability and vegetation impact. . . 229
Figure 5.19: Effect of bank hydrology on bank stability and vegetation impact. 231
Figure 5.20: Sensitivity of root depth parameterization. 234
Figure 5.21: Sensitivity of root extent parameterization. 234
Figure 5.22: Sensitivity of root tensile strength parameterization. 236
Figure 5.23: Sensitivity of tree height parameterization. 236
Figure 5.24: Sensitivity of stem base diameter parameterization. 238
Figure 5.25: Sensitivity of stem top diameter parameterization. 238
Figure 5.26: Sensitivity of mass density parameterization. 239
Figure 5.27: Impact of vegetation cover on the factor of safety of the standard bank . . . 242
Figure 5.28: Channel geometry of idealized reach. 245
Figure 5.29: Numerical grid for the idealized reach. 247
Figure 5.30: Flow pattern for the unvegetated reference scenario. 251
Figure 5.31: Final bed topography for the unvegetated reference scenario. 252
Figure 5.32: Phase shift between planform shape and morphological change. 254
Figure 5.33: Spatial occurrence of bank retreat in the unvegetated scenario. 255
Figure 5.34: Temporal evolution of factor of safety for selected cross-sections. 256
Figure 5.35: Cross-sectional change over the simulation period. 257
Figure 5.36: Cross-sectional velocity profiles. 259
Figure 5.37: Spatial distribution of bank retreat for different vegetation species. 262
Figure 5.38: Final bed topography for a stand of "*Populus*", at 30% ground cover. 264
Figure 5.39: Difference in final bed topography between unvegetated scenario and a stand of "*Populus*" at 30% ground cover. 265

Figure 5.40: Frequency distribution of change in channel bed elevation for each of the vegetation scenarios. 267
Figure 5.41: Difference in final bed topography between unvegetated scenario and a stand of "*Convolvulvus*" at 30% ground cover. 268
Figure 5.42: Selected cross-sectional profiles along the reach. 269
Figure 5.43: Effect of species density on floodplain area loss. 271
Figure 5.44: Spatial distribution of bank retreat for different species and densities. 273
Figure 5.45: Effect of vegetation density on simulated spatial extent of bed erosion and bed deposition. 275
Figure 5.46: Effect of vegetation density on total erosion and total deposition volumes. 276
Figure 5.47: Effect of vegetation density on maximal channel incision and maximal channel aggradation. 278
Figure 5.48: Changes in bed undulation for three different vegetation densities 279
Figure 5.49: Effect of vegetation density on the magnitude of the phase shift between channel planform shape and bed topography undulation. 279
Figure 6.1: Goodwin Creek study reach. 288
Figure 6.2: Modelled bank retreat in the unvegetated control scenario and the validation exercise 290
Figure 6.3: Effect of vegetation density on maximal bed erosion and maximal bed deposition. 294
Figure 6.4: Effect of vegetation density on average bed erosion and average bed deposition. 295
Figure 6.5: Effect of vegetation density on spatial extent of bed erosion and bed deposition. 296
Figure 6.6: Effect of vegetation density on total erosion and total deposition volumes. . 297
Figure 6.7: Modelled channel morphology for scenario B1 (low density "*Betula*"). 299
Figure 6.8: Modelled channel morphology for scenario B2 (high density "*Betula*"). . . . 299
Figure 6.9: Modelled channel morphology for scenario S1 (low density "*Salix*"). 300
Figure 6.10: Modelled channel morphology for scenario S2 (high density "*Salix*"). 300
Figure 6.11: Modelled channel morphology for scenario P1 (low density "*Populus*"). . . 301
Figure 6.12: Modelled channel morphology for scenario P2 (low density "*Populus*"). . . 301
Figure 6.13: Influence of vegetation density on bank retreat. 304
Figure 6.14: Temporal change in the simulated factor of safety at the point of maximal bank retreat. 306
Figure 6.15: Spatial distribution of bank retreat along the left bank of Goodwin Creek for selected vegetation scenarios. 307
Figure A3.1: Sensitivity of maximum flow velocity to grid cell dimensions. 332
Figure A3.2: Sensitivity of average bed erosion to grid cell dimensions. 333
Figure A3.3: Sensitivity of average bed deposition to grid cell dimensions. 333
Figure A3.4: Sensitivity of total erosion volume to grid cell dimensions. 334
Figure A3.5: Sensitivity of total deposition volume to grid cell dimensions. 334
Figure A4.1: Deviation in cross-sectional discharge throughout the channel. 332

List of Tables

Table 2.1: Model representation of the real world 7
Table 2.2: Examples of statistical relations of meander wavelength 13
Table 2.3: Relative importance of bank erosion processes to sediment supply. 43
Table 2.4: Processes selected for model representation. 65
Table 3.1: Assumptions made in the mRIPA model. 135
Table 4.1: Parameters used in the sensitivity analysis. 137
Table 4.2: Setup of the parameter sensitivity analysis. 142
Table 4.3: Global sensitivity index of MRIPA parameters. 144
Table 4.4: Flume experiment details. 156
Table 4.5: Grid details. 160
Table 4.6: Descriptive statistics of differences in flow depth. 167
Table 4.7: Descriptive statistics of differences in flow depth. 172
Table 4.8: Comparison of calibrated parameter values with published values. 175
Table 4.9: Physical characteristics of the UCB and UCB2 experiments. 177
Table 4.10: Grid details. 182
Table 4.11: Characteristics of the Goodwin Creek reach. 184
Table 4.12: Values for the calibration parameters. 184
Table 5.1: Biophysical properties selected for parameterization. 191
Table 5.2: The origin of species. 192
Table 5.3: Typical above-ground dimensions for mature trees of various species. 193
Table 5.4: Parameterization of above-ground properties. 193
Table 5.5: Qualitative description of the root structure for various plant species. 195
Table 5.6: Parameterization of root geometry. 195
Table 5.7: Root tensile strength for various plant species. 198
Table 5.8: Parameterization of tensile strength. 199
Table 5.9: Wood mass densities for various tree species. 199
Table 5.10: Wood mass density for the modelled species. 199
Table 5.11: Parameterization of modus of elasticity. 199
Table 5.12: Modi of elasticity for various species. 200
Table 5.13: Parameterization of drag coefficient 201
Table 5.14: Parameterization of the shear strength modifier. 202
Table 5.15: Vegetation parameters used in the mRIPA model. 202
Table 5.16: Properties of the "standard" riverbank. 204
Table 5.17: Failure variables of the "standard" riverbank 204
Table 5.18: Maximal values of local and average root cohesion. 214
Table 5.19: Sensitivity of vegetation parameters. 239
Table 5.20: Properties of the idealized channel. 246
Table 5.21: Values for the calibration parameters. 246

Table 5.22: Summary of channel change for the unvegetated scenario. 260
Table 5.23: Floodplain area loss for the vegetation scenarios. 261
Table 5.24: Bed topography change in the vegetation scenarios. 263
Table 5.25: Setup of vegetation density scenarios. 270
Table 6.1: Redefined setup parameters. 290
Table 6.2: setup of vegetation density scenarios. 291
Table 6.3: Overview of results. 292
Table 6.4: Scenarios selected for spatial analysis. 298
Table 6.5: Scenarios selected for spatial analysis. 306
Table 6.6: Comparison of vegetation effects in an idealized meandering channel and a natural channel. 309
Table A1.1: Overview of published bank erosion rates. 320
Table A1.2: Overview of published accretion rates. 327
Table A3.1: Overview of grid sensitivity simulations. 331
Table A3.2: Descriptive statistics of grid sensitivity simulations. 332
Table A4.1: Water conservation data 337

Notation

symbol	description	value	units
a_0	coefficient in root distribution function		-
a_1	coefficient in root distribution function		-
a_2	coefficient in root distribution function		-
c	effective soil cohesion		$N\ m^{-2}$
c_a	apparent soil cohesion		$N\ m^{-2}$
c_1	coefficient in root-area-ratio function		-
c_2	coefficient in root-area-ratio function		-
c_3	coefficient in root-area-ratio function		-
c_4	coefficient in root-area-ratio function		-
d	flow depth		m
d_v	vegetation stem diameter		m
d_{vb}	vegetation stem diameter at base		m
d_{vt}	vegetation stem diameter at top		m
f_s	sediment transport rate		$m^2\ s^{-1}$
g	gravitational acceleration	9.81	$m\ s^{-2}$
h	flow depth		m
i_s	intensity of the secondary flow		$m\ s^{-1}$
k_B	erodibility of bank material		-
k_{ls}	weighting coefficient for the longitudinal bed slope		-
k_s	coefficient in power-law for sediment transport		-
k_{si}	coefficient to adjust secondary flow intensity		-
k_{sn}	secondary flow convection factor		-
k_{tm}	coefficient in transverse slope model		-
k_{ts}	weighting coefficient for the transverse bed slope		-
k_τ	proportionality coefficient for τ_B		-
$k_{\tau,veg}$	shear stress modification factor		-
n	Manning's n roughness coefficient		-
n_{dep}	number of grid cells with bed erosion		-
n_{ero}	number of grid cells with bed deposition		-
n_L	distance to channel centre line		m
p_B	exponent in hydraulic bank erosion formula		-
p_s	exponent in power-law for sediment transport		-
p_{tm}	exponent in transverse slope model		-
q	exponent of artifice		-
r_c	radius of curvature		m
r_c^*	effective radius of curvature		m
s	shear strength		$N\ m^{-2}$

symbol	description	value	units
s_b	silt and clay ratio of bed material		-
s_c	silt and clay ratio of bank material		-
s_R	root shear strength		N m^{-2}
x_v	lateral distance of vegetation element to bank toe		m
z_b	bed elevation		m
z_w	water surface elevation		m
A	drainage basin area		km^2
A_{dep}	areal extent of bed deposition		m^2
A_{ero}	areal extent of bed erosion		m^2
A_{fpl}	floodplain-area-loss		m^2
A_{gv}	vegetation ground cover		-
A_m	meander amplitude		m
A_R	root area ratio		-
A_v	projected vegetational area		m^2
C	Chezy conveyance factor (roughness coefficient)		-
C_d	drag coefficient		-
C_δ	proportionality constant in calculation of δ		-
D	sediment size		m
D_{50}	median sediment size		m
E	erosion rate		m yr^{-1}
E	modulus of elasticity		N m^{-2}
E_r	bank erosion coefficient		-
F_α	force applied on vegetation		N
F_{cp}	hydrostatic confining pressure		N
F_d	drag force		N
F_D	total driving force		N
F_{ms}	matric suction		N
F_{pp}	pore pressure		N
F_R	total resisting force		N
H_b	bank height		m
H_c	height of vertical cliff at banktop		m
H_{cb}	height of cutbank at banktoe		m
H_g	groundwater level		m
H_t	tension crack depth		m
H_v	vegetation height		m
H_v^*	projected height of the plant		m
H_w	surface water level		m
I	second moment of inertia		m^4
K_R	ripple factor in Meyer-Peter-Müller formula		-
L	reach length		m

symbol	description	value	units
L_f	length of failure plane		m
L_{rH}	horizontal root extent		m
L_{rV}	vertical root depth		m
L_{xH}	horizontal distance to centre of roots		m
L_{xV}	vertical distance to top of roots		m
M_s	silt-clay ratio		-
N_A	term in rearranged momentum equation		-
N_B	term in rearranged momentum equation		$m\ s^{-2}$
N_C	term in rearranged momentum equation		-
N_D	term in rearranged momentum equation		$m\ s^{-2}$
N_{FS}	factor of safety		-
N_{Sl}	sensitivity index		-
N_{Slv}	sensitivity index of vegetation parameter		-
N_P	number of parameter simulations		-
N_1	term in rearranged momentum equation		-
N_2	term in rearranged momentum equation		-
P	parameter value		variable
R_f	radius of curvature of the flow line		m
R_n	radius of curvature for transverse coordinate lines		m
R_s	radius of curvature for streamwise coordinate lines		m
R_r	radius of curvature for non-orthogonal streamwise coordinate lines		m
Q	discharge		$m^3\ s^{-1}$
Q_b	bankfull discharge		$m^3\ s^{-1}$
Q_{ma}	mean annual discharge		$m^3\ s^{-1}$
S	sediment transport vector		$m^2\ s^{-1}$
S	sediment transport flux		$m^2\ s^{-1}$
S_m	sinuosity		-
S_n	transverse sediment transport flux		$m^2\ s^{-1}$
S_s	streamwise sediment transport flux		$m^2\ s^{-1}$
S_x	downstream slope of water surface		-
T_R	root tensile strength		$N\ m^{-2}$
U	flow vector		$m\ s^{-1}$
U	flow velocity		$m\ s^{-1}$
U_n	transverse flow velocity		$m\ s^{-1}$
$\tilde{U}_n$	local orthogonal transverse flow velocity		$m\ s^{-1}$
U_{nb}	near-bank flow velocity		$m\ s^{-1}$
U_s	streamwise flow velocity		$m\ s^{-1}$
$\tilde{U}_s$	local orthogonal streamwise flow velocity		$m\ s^{-1}$
V_{dep}	volume of bed deposition		m^3

symbol	description	value	units
V_{ero}	volume of eroded bed material		m^3
V_f	volume of the failure block		m^3
V_h	volume of entrained bank sediment		m^3
V_v	volume of vegetation element		m^3
W	channel width		m
W_f	weight of the failure block		N
W_v	weight of vegetation		N
ΔZ_{dep}	vertical height of bed deposition		m
ΔZ_{ero}	vertical height of bed erosion		m
α_{cp}	angle between ω_{cp} and the normal to β_f		°
α_v	degree of vegetation bending		°
β_b	slope of bank face		°
β_f	slope of failure plane		°
γ	unit weight of water	9810	$N\ m^{-3}$
γ_s	unit weight of soil		$N\ m^{-3}$
δ	angle between near-bed and depth-averaged flow directions		°
$\delta(n)$	lateral distribution function for bank sediment		-
ε	grid skewness		-
ε^*	degree of orthogonality		-
θ_s	angle of shear distortion at bank failure		-
θ_s	shields parameter		-
$\theta_{s,c}$	critical Shields parameter		-
θ_R	root inclination angle		°
κ	Von Kármán constant	0.4	-
λ_m	meander wavelength		m
λ_r	adaptation length of secondary flow		m
μ	dynamic viscosity of water	$1.31\ 10^{-3}$	$kg\ m^{-1}\ s^{-1}$
ν	turbulent eddy viscosity		$kg\ m^{-1}\ s^{-1}$
ρ	density of water	1000	$kg\ m^{-3}$
ρ_{rel}	relative density of sediment		-
ρ_s	density of sediment	2650	$kg\ m^{-3}$
ρ_v	wood mass density		$kg\ m^{-3}$
σ_n	normal stress of the soil weight		$N\ m^{-2}$
σ_v	lateral spacing of vegetation		-
τ	shear stress		$N\ m^{-2}$
τ_{bn}	transverse bed shear stress		$N\ m^{-2}$
τ_{bs}	streamwise bed shear stress		$N\ m^{-2}$
τ_B	bank shear stress		$N\ m^{-2}$
$\tau_{B,c}$	critical shear stress for entrainment of bank material		$N\ m^{-2}$
τ_c	critical shear stress for entrainment of bed sediment		$N\ m^{-2}$

symbol	description	value	units
τ_f	available soil shear stress at failure		N m^{-2}
τ_0	boundary shear stress		N m^{-2}
ϕ	internal friction angle of soil		°
ϕ^b	matric suction angle		°
ϕ_s	dimensionless sediment transport parameter		-
φ_{sn}	angle of deviation from orthogonality		°
φ_U	direction of flow vector		°
ψ_S	direction of sediment transport vector		°
ψ_τ	direction of bed shear stress		°
ω_{cp}	direction of resultant confining pressure		°
ω_{f1}	fraction of fine cohesive failed bank sediment		-
ω_{f2}	fraction of small granular failed bank sediment		-
ω_{f3}	fraction of coarse granular failed bank sediment		-
ω_{h1}	fraction of fine cohesive entrained bank sediment		-
ω_{h2}	fraction of granular entrained bank sediment		-

Acknowledgements

Many thanks to Dr. Steve Darby, whose encouragement, advice and editorial comments are greatly appreciated, and whose continual optimism and belief in this project have certainly contributed to its completion. The project has further benefited from the support of Dr. Erik Mosselman (Delft Hydraulics), who generously provided the original RIPA code, and from the involvement of Prof. Andrei Alabyan (Moscow State University), who contributed to the development of the linkage between the flow model and the bank erosion algorithms. Dr. Peter Whiting (Case Western Reserve University) kindly provided the laboratory notes from his flume experiments.

I gratefully acknowledge the support of a High Performance Computing bursary from the University of Southampton, without which I would not have been able to undertake this research. Furthermore, I like to thank Dr. Tom Coulthard and Prof. Mark Macklin (both University of Wales, Aberystwyth) for providing a flexible working environment, in which I could finalize the latter parts of this thesis.

During this research I have enjoyed the company of many people, at the Department of Geography and elsewhere. Particular thanks to Richard Jeffries and Nick Odoni for various discussions on rivers and the merits of modelling them; to Antony Blundell for letting me win our snooker games; to Jenny Schulz , Ilse Steyl and all the others for their friendship; and, of course, to Laurence Ghaye and Jana Fried for being who they are.

Finally, I would like thank my parents, Wim and Diny Van De Wiel, for their love, support and encouragement. I love you both.

Marco J. Van De Wiel
Southampton, July 26th, 2003.

Chapter 1
Introduction

1.1. Aim and objectives

The research described herein explores the development, evaluation and application of a new numerical model for predicting planform adjustment in single-thread alluvial meandering rivers with riparian vegetation. The model aims to improve the understanding of the impact, on a reach scale, of vegetation on fluvial geomorphological processes, with the added possibility of evaluating the potential of using riparian vegetation as a tool in river management. Within this generic framework several specific research questions can be defined: How do the geomorphological processes of river bank erosion, bed scour, bed deposition and bar formation interact to define the morphological evolution of an alluvial meandering river reach? To what extent does the presence of riparian vegetation affect these processes and their interaction? Is there a significant difference between the impacts of various species of riparian vegetation? Which aspects of the riparian vegetation (e.g. vegetation density, hydraulic roughness, rooting properties, ...) are the most influential in affecting the morphological evolution of a river reach? These questions, and related issues, are explored herein, within the specific context of single-thread alluvial meandering rivers with erodible banks. The research is mainly concerned with intermediate spatial scales which are of relevance in river management, *i.e.* with river reaches, comprising a few consecutive meander bends (*ca.* 300 m to 3000 m), and with medium timescales (*ca.* 0.1 yrs to 10 yrs).

1.2. Background

Rivers have fascinated humankind for millennia. The intrinsic beauty of rivers and their bankside flora and fauna have been a source of inspiration for artists, writers and poets throughout history. Not only is the dynamic riverine environment a source of inspiration, it also is a source of life and economic prosperity. As such, rivers have been a basis for biological and human activity, and scientific research, as well as political and military conflict, dispute and natural catastrophe.

Rivers are dynamic landscape features, in which erosion, transport and deposition take place over a wide range of spatial and temporal scales. The lateral changes in the river geometry, denoted by processes like bank erosion, point bar growth and meander migration, can have a particularly significant impact on the landscape. The geomorphological processes along a river are closely linked to a unique, dynamic ecosystem. The riparian zone, which is made up of the river banks and their immediate surroundings, forms a rich ecological habitat for many species of plants and animals, where the sequences of erosion and sedimentation continually rework the landscape and the composition of life thereupon. This ever-repeating cycle of colonization, destruction and re-colonization lies at the heart of the very uniqueness of the riparian ecosystem.

The dynamic nature of river systems is, however, often in conflict with economic interests. River floodplain areas, because of their rich natural resources, attract human activities. These activities depend on the land adjacent to rivers and on the infrastructure built thereupon. Consequently, lateral migration of rivers poses a threat to these activities, resulting in agricultural or recreational land loss, damage to roads, bridges and other infrastructure, sometimes even leading to the destruction of entire villages. So, from an economic viewpoint, a less dynamic, nearly stable river would be far more desirable.

Despite its long history, the conflict between river dynamics and human activity is far from resolved. In order to protect economic interests, humans have tried to control rivers and their damaging effects for thousands of years, with an increasing intensity over the last century. Various projects of bank protection, bank stabilization and river channelization have been implemented, with varying degrees of success and almost universally without regard to environmental consequences. Only recently has an increased awareness of the ecological value of riparian habitats emerged. It has now become clear that sustainable management of river resources and responsible river engineering must achieve a delicate balance between the need to preserve geomorphological dynamism and habitat quality, while minimizing the occurrence of accelerated erosion and sedimentation. Consequently, more environmentally friendly management options are seriously being considered, one of which is the use of riparian vegetation as an engineering tool. Application of this approach is limited at present, because of the many uncertainties about the various impacts of vegetation on channel conveyance and bank stability in different specific settings.

Past experiences have shown that ideas which have promising potential when being designed, frequently turn out to have negative consequences or sometimes even completely adverse impact after being implemented. This can be ascribed to a lack of scientific understanding about the complex dynamics of river systems, as well as to a public eagerness to implement engineering works as soon as possible, without due consideration. Currently, however, river-engineers and river-managers are more aware of the fact that even local, minor changes can have major impacts throughout whole river reaches. There is, therefore, a general recognition of a need for improved predictive abilities in fluvial engineering.

1.3. A new model?

In this study a numerical modelling approach has been chosen to investigate the impact of riparian vegetation on the morphological evolution of meandering, alluvial rivers. Numerical modelling has, over the last two decades, established itself as useful research tool in fluvial geomorphology and fluvial engineering, and offers several advantages over the more traditional approaches in fluvial geomorphology (*i.e.* field studies and laboratory experiments): an unprecedented control over the parameters involved in the study; potential of "what-if" scenario modelling, in which virtual scenarios can be explored; extension of spatial and temporal scales of study beyond those practical in physically based studies; perfect repeatability of the experiments - at least if no probabilistic or other random assumptions are made during the simulations. Notwithstanding these advantages, numerical modelling is strongly reliant on physically based studies. Numerical modelling is pointless without empirical data, which is required for application as well as for verification of the model, or without a sound understanding of the processes to be modelled. Both of these are derived from field studies and laboratory experiments. As such, numerical modelling is not an alternative, but rather a complementary technique, to those traditional approaches to fluvial geomorphology.

An improved understanding of the geomorphological processes in riverine ecosystems during the last few decades, coupled with advances in computational hardware and techniques, has led to the development of a whole range of numerical models as tools to aid scientists, managers and engineers. Using such numerical models, the key processes in fluvial geomorphology can be studied, future channel changes can be predicted and different scenarios can be evaluated; all within the limitations of the model being used. However,

most of the existing models are focussed on flow properties or bed topography, and only a few account for width adjustments. Even fewer attempt to include interactions between vegetation, flow and sediment (figure 1.1). This study seeks to address these gaps by developing a new numerical model, which allows prediction of planform changes in vegetated alluvial river channels. The model is then used to undertake "what-if scenarios", in which the impacts of different assemblages of riparian vegetation on bank stability can be assessed, at least within the limits of the predictive ability and scope of the developed model.

1.4. Structure of the text

Any attempt to describe the interaction between water flow, sediment and vegetation draws upon a wide scientific background, involving elements of geomorphology, geology, mathematics, physics, flow hydraulics, hydrology, ecology and biology. Chapter 2 gives an overview of the relevant literature in these fields of research and application, with an emphasis on the relevant geomorphological processes. The following chapters deal with the development, evaluation and application of the numerical model. Starting from an existing two-dimensional model for flow and sediment transport, a new model is constructed through gradual expansion of the model's functionality. Specifically, submodels to account for bank erosion processes and vegetation interaction have been added. The development of the numerical model is described in chapter 3, with detailed explanation of the mathematical foundations and assumptions made. In chapter 4, the calibration and evaluation of the model is discussed, based on a comparison of model predictions with observations from flume experiments and a natural river channel, both without vegetation. Chapter 5 describes the assessment of the vegetation components of the model, based on comparative analysis of different scenarios in an idealized river channel. The model's potential for practical application is illustrated in chapter 6, which investigates the evolution of a natural river reach under several scenarios involving different vegetation covers. A general conclusion, in which all of the findings are combined and summarized, is presented in chapter 7.

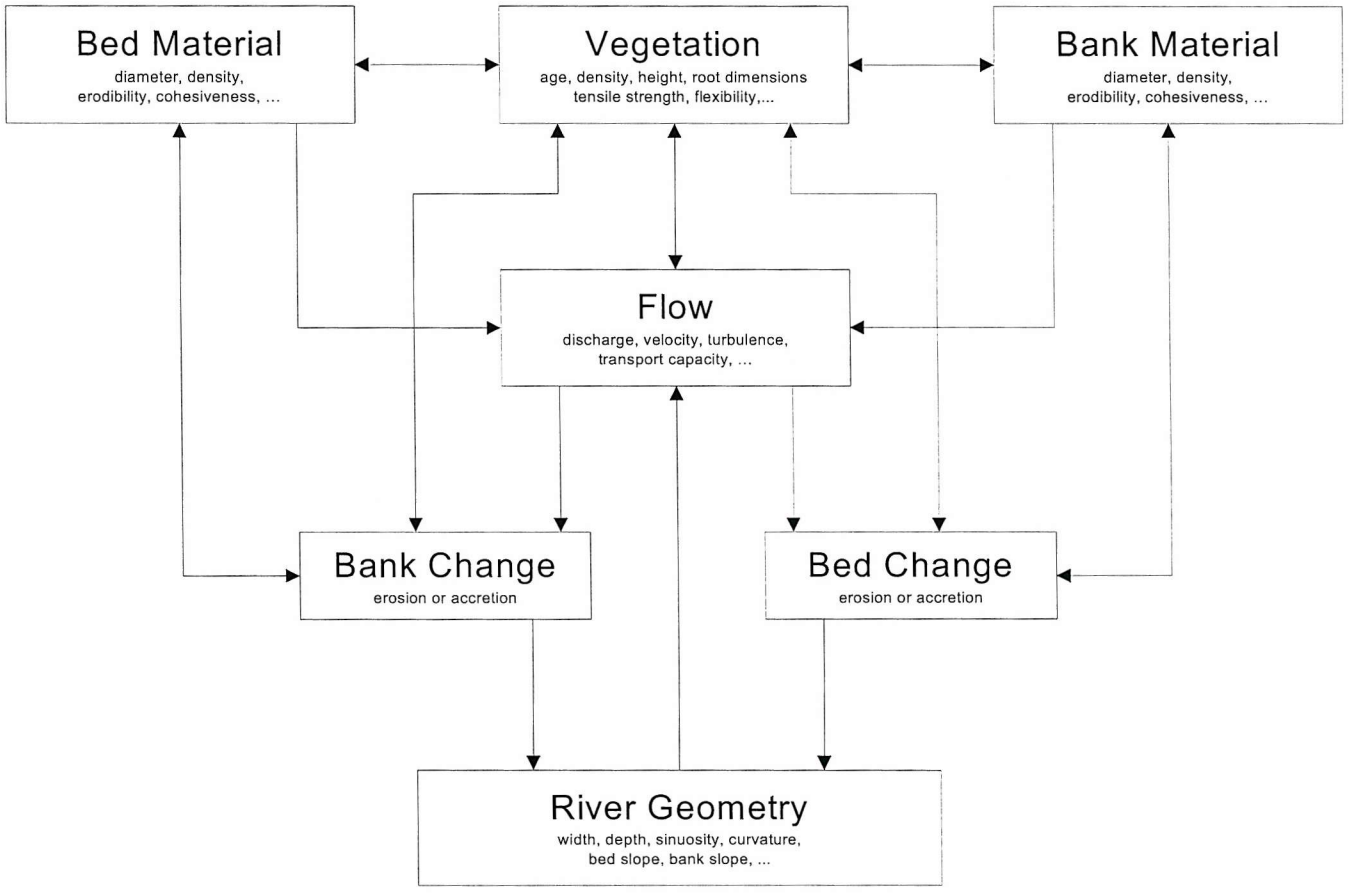

Figure 1.1: Relations between flow, sediment, vegetation and river geometry.

Chapter 2
Literature Review

2.1. Introduction

This chapter presents an overview of literature relating to the physical interactions between flow, sediment and vegetation in meandering alluvial rivers, and to the modelling thereof. The aim of this review is to provide a context for the ideas and discussions presented in the following chapters. The overview is organized in five major topics: numerical modelling (section 2.2), river meandering (section 2.3), bank erosion (section 2.4), bank accretion (section 2.5) and riparian vegetation (section 2.6). The first topic introduces general concepts relating to numerical modelling techniques, the latter four topics explore the processes and agents governing geomorphological change in meandering, alluvial rivers. A general conclusion summarizes the main findings (section 2.7). Both the study of these topics and their application is highly interdisciplinary, involving elements of geomorphology, geology, soil science, hydraulics, geotechnical and environmental engineering, mathematics, physics, hydrology, ecology, biology and environmental management. The current review mainly focusses on the geomorphological relations between flow, sediment and vegetation, although the other aspects are briefly touched on as well. Emphasis is placed on the current understanding of geomorphological processes, both qualitative and quantitative.

2.2. Numerical Modelling

Numerical models differ from their conceptual, empirical and analytical counterparts in that they are multidimensional, capable of dealing both with spatial and temporal dimensions. In a numerical model, physical space is represented by a grid or mesh consisting of a finite number of points. Spatial physical properties or characteristics (e.g. elevation, water depth, flow velocity, roughness, sediment concentration, *etc.*) are represented on this grid by a set of discrete values. The time dimension is also discretized into time steps, and temporal change or evolution of the physical properties is represented by changes in the

values on the grid (see table 2.1). Representation of the physical processes relevant to a particular problem is achieved in three steps. First, the relevant processes are identified. Second, a mathematical representation of these processes is derived (*i.e.* a set of governing process equations is formulated). Third, a numerical algorithm is developed in order to solve or approximate the governing equations over the discretized grid. In this section, a short overview is given (largely based on Darby and Van De Wiel, 2003) of general concepts and issues relating to numerical modelling as a tool in fluvial geomorphology. In the subsequent sections the relevant geomorphological processes in meandering alluvial rivers with riparian vegetation are identified, while the mathematical and numerical 'translation' of these processes are described in chapter 3.

Table 2.1: Model representation of the real world.

real world	model representation
space	grid (discretization)
time	time steps (discretization)
physical properties	discrete values on grid
physical processes	algorithm
evolution	change of values on grid

The use of numerical models in fluvial geomorphology has rapidly increased during the last twenty years. Numerous models have been developed for various applications. The models developed can be broadly categorized in four groups: flow models, solute transport models, sediment transport models and planform change models. Flow models are used to simulate flow pattern and flow velocity in a wide range of settings, including the simulation of flow fields through meander bends (e.g. De Vriend and Geldof, 1983; Smith and McLean, 1984; Hodskinson and Ferguson, 1998; Lien *et al.*, 1999), in channel confluences and divergences (e.g. Bradbrook *et al.*, 1998; Lane and Richards, 1998), in estuaries (e.g. Clarke and Elliot, 1998; Tattersall *et al.*, 2003), and over floodplains (e.g. Gee *et al.*, 1990; Thomas and Williams, 1995; Bates *et al.*, 1992; 1997; 1998; Beffa and Connell, 2001; Nicholas and Mitchell, 2003). Solute transport models use the predictions from flow models to drive a submodel for the movement of sediments and pollutants, and are mainly used in contamination studies (e.g. Wu and Tsanis, 1994; Steward *et al.*, 1998; Moulin and Ben Slama, 1998). Erosion and sedimentation models contain additional sediment entrainment and deposition routines, which permits prediction of bed change and, hence, of

morphological evolution of the channel bed (e.g. Olesen, 1987; Hardy *et al.*, 2000; Wu *et al.*, 2000; Niño *et al.*, 2002). Lastly, planform change models include routines to predict lateral changes in the river form (e.g. Mosselman, 1992; Darby *et al.*, 1996; Nagata *et al.*, 2000). These applications cover a whole range of spatial and temporal scales, varying from detailed predictions of flow field in just a few metres of a channel reach to the evolution of several kilometres of floodplain over several tens or hundreds of years. The examples cited above also trace a historical change in numerical modelling. Early models were predominantly restricted to one spatial dimension, and although one-dimensional models are still being used and developed, advances in computational hardware now provide the capability of dealing with two or three dimensions. It is these advances that are now unlocking the real potential of numerical modelling for fluvial geomorphology.

Irrespective of the exact application, representing fluid motion is one of the inherent challenges of all numerical models in fluvial geomorphology. The basic laws governing the motion of fluids are the "conservation of mass" and the "conservation of momentum". The former states that during motion no fluid is created nor destroyed, while the latter essentially is Newton's second law applied to fluids. Mathematically these laws are expressed by a set of non-linear differential equations (Tritton, 1988):

$$\frac{\partial \rho}{\partial t} + \nabla \cdot (\rho U) = 0 \tag{2.1}$$

$$\rho \frac{D(U)}{Dt} = -\nabla p + \mu \nabla^2 U + F \tag{2.2}$$

where U denotes the flow velocity vector, t represents time, ρ is the fluid density, p denotes pressure, μ is the viscosity coefficient, and F represents the sum of all external forces (including friction). In their general form, applying to all fluid motion, these equations are called the Navier-Stokes equations. Nearly all numerical flow models of rely on solving these equations in one form or another (though see Murray and Paola (1997), Bates and De Roo (2000), Coulthard *et al.* (2002), Thomas and Nicholas (2002) for an alternative approach based on cellular automata). Theoretically, the Navier-Stokes equations cannot be solved exactly, but they can be approximated using numerical techniques. Most commonly these involve finite difference, finite volume or finite element discretization techniques (Sewell, 1988; Anderson, 1995; Versteeg and Malalasekera, 1995). These solving techniques

mainly differ in their ease of implementation, computational efficiency and conservation properties, although they can also cause minor variations in model output (Bates *et al.*, 1996). In general, finite difference techniques are easier to implement in a model, while finite element techniques tend to use less computing time, and allow more freedom in assembling the computational grids, which is convenient when dealing with highly irregular geometries (Rice, 1983; Sewell, 1988).

Each of the solving techniques requires the spatial discretization of the Navier-Stokes equations on a numerical grid. Numerical grids can differ in many ways: coordinate system (Cartesian, cylindrical, curvilinear), dimension (1, 2 or 3), shape of the elements (triangular, quadragonal, hexagonal). These grid attributes are generally determined by the numerical techniques used for solving the mathematical equations and, given a certain model, cannot be influenced by the user. However, the user is usually faced with constructing a grid which represents the physical world with a sufficient accuracy. The resolution of the grid affects the internal working of the model and its output (Olsen and Kjellesvig, 1998; Hardy *et al.*, 1999). It is often thought that the accuracy of a model prediction will increase with increasing grid resolution. This hypothesis is powered by the idea that a finer grid results in a better representation of the physical world and improved stability of the numerical algorithm (Hardy *et al.*, 1999). According to this reasoning, any predictive accuracy can be achieved, if only the necessary computational resources are invested. However, recent research suggests that the hypothesis only holds true up to a certain level and that there is an upper limit, beyond which further increases in spatial resolution will not result in a significant improvement of predictive accuracy (Farajalla and Vieux, 1995; Bates *et al.*, 1996; Hardy *et al.*, 1999). At that stage further improvement can only be made by explicitly modelling the subgrid-scale processes. However, this is often computationally unachievable, as has been shown for the explicit modelling of turbulence (Hervouet and Van Haren, 1996; Lane, 1998). As long as the optimal resolution has not been reached (which, due to computational restrictions, is usually the case), model output can be sensitive to changes in grid density. It is therefore suggested that numerical models are run on different spatial resolutions to determine an envelope of response (Hardy *et al.*, 1999).

All numerical models require input data. In the case of fluvial models these usually include topography, discharge and bed roughness. Additional input requirements are dependent on the application and can involve elements like bank and floodplain roughness, vegetation, infiltration rate, and so on. It seems trivial to note that the accuracy of the input

data influences the output of the model. Nonetheless, this is a point of importance as some data may be difficult or expensive to obtain accurately. Nearly all field data which are used as input are obtained from a relatively sparse collection of point measurements. Spreading these values over the spatial grid requires assumptions about their spatial (and sometimes temporal) distribution and usually involves some sort of interpolation routine, which introduces yet another source of uncertainty.

Frequently a model uses numerical parameters which can only be guessed at within a certain range. When running the model using a known data set, these parameters are adjusted until an acceptable agreement between model prediction and observed data is found. This process is known as calibration. The parameter values used to obtain the optimal result are then recommended to be used in other applications of the model. This calibration process is not undisputed (Beven and Binley, 1992; Bates *et al.*, 1998; Odoni and Darby, 2002). When several parameters are adjusted during calibration, the uniqueness of an optimal setting is not guaranteed. There might be other combinations of calibration parameters which provide equally acceptable predictions, a condition known as "model equifinality" (Beven, 1996). Furthermore, the obtained calibrated parameters may mask systematic errors in model predictions. Alternative calibration schemes which partially address these problems have been proposed (Beven and Binley, 1992; Bates *et al.*, 1998; Hankin and Beven, 1998; Campbell *et al.*, 1999). It should be noted, however, that the influence of the calibration parameters on the model results can be outweighed by other sources of uncertainty, such as grid construction (Hardy *et al.*, 1999) or the limited accuracy of input data. Once calibrated, a model is usually validated by running it against another known data set and checking the predicted results versus observed data. If this comparison is satisfactory, the model is said to perform well; if not, the model will be checked for errors and re-calibrated. Both calibration and validation require complete data sets, in which some entity, for which predictions can be made, is known. The existence of, or access to, such data sets for natural fluvial systems is not always guaranteed (Bates *et al.*, 1997). Very often, therefore, models are calibrated and validated on laboratory data, which may undermine their applicability in natural systems (ASCE Task Committee, 1998).

Recent numerical models generally provide a graphical user-interface (GUI) which enhances the ease-of-use. Numerical models provide a vast amount of data as output, which can be summarized in tables, analysed statistically or visualized graphically. This often very detailed output can be overwhelming and can easily inspire unjustified faith in its accuracy.

For this reason it is important that the user, when interpreting model results, is made aware of the underlying assumptions and inherent limitations of a model. Although limitations may arise from practical problems, such as difficulties in data collection and availability of computational resources, most of the pitfalls of numerical modelling relate to the representation of physical processes within a model. Numerical modelling is inherently dependent on an adequate representation of the physical world. As mentioned in the beginning of this chapter, this involves selecting of the relevant processes that govern the problem under consideration, an accurate translation in mathematical form thereof, and an appropriate numerical discretization of the mathematical equations. In the next sections, the relevant geomorphological processes in meandering alluvial rivers with riparian vegetation are identified, while the mathematical and numerical development of the model is described in chapter 3.

2.3. Meandering

Meandering rivers appeal to people. There is an intrinsic beauty to the remarkable pattern of their windings, which is simultaneously perceived as regular and chaotic. The dynamical, ever-changing nature of those meandering patterns only enhances the effect. It is therefore no surprise that, throughout history, meandering rivers have been a source of inspiration for many - poets, painters, philosophers, travellers and scientists alike.

Apart form being visually appealing, meandering rivers are features of interest from various other perspectives. The combination of lateral erosion and deposition processes results in a continual reworking of riparian landforms. This dynamism, which from a geomorphological point of view is interesting in its own right, is of prime importance for the existence and diversity of riparian ecosystems. It is also responsible for the creation of an environment which is rich in natural resources. Thus, the dynamic environment of meandering rivers and their floodplains is a source of life and economic prosperity. The appeal of meandering rivers is therefore not restricted to aesthetic values, but also includes scientific, ecological and economic factors.

From a scientific point of view, river meandering poses two fundamental questions: "Why do rivers meander?" and "Is there a stable meandering form or shape?". The first of these problems is the oldest and has puzzled many throughout history. In spite of all this attention a definite answer is still lacking. The second question may be considered even more fundamental - even if it has not received as much attention from philosophers. When answered affirmatively it immediately generates two sub-questions: "What is that stable form?" and "Why?". In the following paragraphs an attempt is made to summarize current knowledge and hypotheses.

2.3.1. Meander morphology and geometry

The planform geometry of river channel patterns can take several forms: straight, meandering, anastomosing and braided, with a continuum of channel types in between each. The distinctions and similarities between each of these, and the various controls on their formation, have been a subject of study over many years (Leopold and Wolman, 1957; Parker, 1976; Fredsøe, 1978; Schumm, 1985; Van den Berg, 1995; Alabyan and Chalov, 1998; Millar, 2000; Lewin and Brewer, 2001). This review considers only meandering rivers. More particularly, it focuses on free meandering rivers that develop in alluvial sediments. Although meanders incised in bedrock or confined between valley walls are theoretically subject to similar morphological processes, their sedimentary environment inhibits or severely restricts widening and lateral movement.

Morphology of meander bends

A typical meander bend has an asymmetrical cross-section. Near the convex inner bank, the bed usually consists of a gently sloping point bar, while the thalweg of the channel is located near the concave outer bank (figure 2.1). Generally, the slope at the outer bank is steeper because of scour at the toe of the bank. The deeper part of the channel along the outer bank is often considered analogous to the pool in straight river pool-riffle sequences (Allen, 1984; Morisawa, 1985; Thompson, 1986). Similarly, the analogue of the riffle is found at the inflection point between successive meander bends, where the cross-section is generally shallower and more symmetrical. The description presented here is very generalized and merely serves as an introduction to the morphology of meander bends. The

actual morphology of a specific natural bend is likely to differ from the idealized scheme above. For example, depositional landforms can form along the concave bank (Hickin, 1979; Woodyer *et al.* 1979; Page and Nanson, 1982) or multiple pools may form in long elongated meanders (Thompson, 1986; Whiting and Dietrich, 1993b).

Planform geometry of meandering systems

A convenient way of defining meandering rivers mathematically is based on statistical procedures applied to meander geometry. In order to describe meander geometry statistically a whole range of variables are available: meander wavelength and amplitude, length across valley, length along river, meander arc length and arc angle, sinuosity and radius of curvature are among the most obvious (figure 2.2), although many others can be derived (Howard and Hemberger, 1991).

Based on observations in natural rivers and laboratory flumes, various empirical relations have been derived correlating these geometric meander variables with each other and with hydraulic variables. Most common are equations that link meander wavelength, λ_m, and amplitude, A_m, to river width, W, or to a measure of river discharge such as bankfull discharge, Q_b, or mean annual discharge, Q_{ma} (table 2.2). Other relations, using parameters like sinuosity, wetted perimeter and channel curvature have been developed, and more extensive reviews can be found elsewhere (Chitale, 1973; Williams, 1986).

Table 2.2: Examples of statistical relations of meander wavelength.

meander wavelength	reference
$\lambda_m = 75 Q_{ma}^{0.5}$	Jefferson, 1902
$\lambda_m = 7.5 Q_{ma}^{0.62}$	Leopold and Wolman, 1957
$\lambda_m = 106.1 Q_{ma}^{0.46}$	Carlston, 1965
$\lambda_m = 54.3 Q_b^{0.5}$	Dury, 1965
$\lambda_m = 8.2 Q_b^{0.62}$	Carlston, 1965
$\lambda_m = 6.6 W^{0.99}$	Inglis, 1949
$\lambda_m = 10.9 W^{1.01}$	Leopold and Wolman, 1957
$\lambda_w = 10 W^{1.03}$	Zeller, 1967
$\lambda_m = 12.34 W$	Richards, 1982

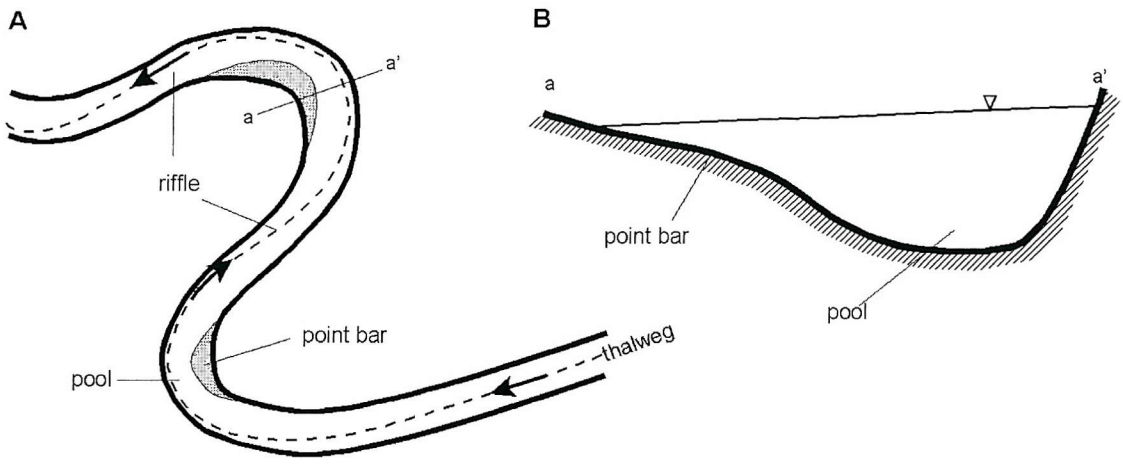

Figure 2.1: Generalized view of meander bend morphology. **A**: planform (after Allen, 1984). **B**: cross-section.

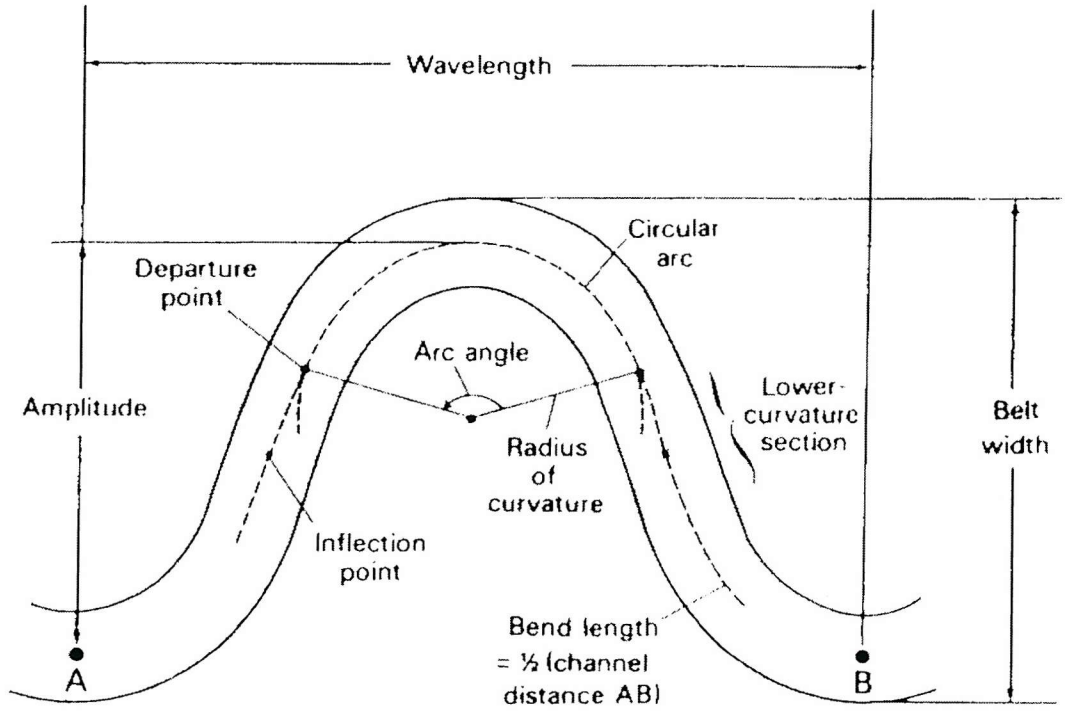

Figure 2.2: Generalized sketch of meander geometry (from Williams, 1986).

Several authors have made refinements to these statistical models to account for sediment properties (Schumm, 1960, 1969; Henderson, 1961; Ackers, 1982) and valley slope (Chitale, 1970). This is illustrated by Schumm's (1969) equation, which incorporates sediment properties of bed and bank:

$$\lambda_m = 618 Q_b^{0.43} M_s^{-0.74} \tag{2.3}$$

where:

$$M_s = \frac{s_b W + 2 s_c d}{W + 2d} \tag{2.4}$$

in which s_b and s_c denote the silt and clay fraction of bed and bank respectively, and d is the flow depth. Equation 2.3 is noteworthy in the context of the present study, in that it implies that as the channel banks get more cohesive, the meander wavelength, λ_m, decreases – a feature which has been observed in natural rivers (Schumm, 1960, 1963; Pickup and Warner, 1976) and also has been derived theoretically (Parker, 1976).

Remarkably, although these statistical equations have been derived for meanders in natural rivers and in laboratory flume experiments, in broad terms they seem to apply equally well to a whole range of meandering systems, from surface tension rivulets on a glass plate (Gorycki,1973; Davies and Tinker, 1984), to supraglacial meanders (Leopold *et al.*,1964) and submarine meanders (Flood and Damuth, 1987; Clark *et al.,* 1992), to the meanders in the Gulf Stream (Leopold *et al.,* 1964) and even meandering features on the surface of the Moon, Mars and Venus (Graf and Warlick, 1971; Davies and Sutherland, 1980; Komatsu and Baker, 1994).

The perceived consistency of these statistical relations over a wide range of scales and environments has led to the belief that meandering is inherent to the flow of fluids and that there indeed may be an ideal, stable geometry towards which meandering rivers evolve. Similar to the development of stable meander forms found in rivulets on a smooth plate (Tanner, 1960; Gorycki,1973; Davies and Tinker, 1984) and in laboratory flumes (Friedkin, 1945; Ackers and Charlton, 1970; Schumm and Khan, 1972), it is possible that natural rivers also tend to evolve towards a stable meandering pattern. However, the local variations in climate, catchment structure, discharge, sediment properties and environmental influences cause each meandering river to evolve towards a different stable form. Moreover, since most

of these variables may vary over time, it is possible that this stable form is never achieved and that the river is evolving towards a continuously changing goal (Stevens *et al.,* 1975; Lewin *et al.,* 1988).

Unsurprisingly, the perceived regularity of meandering channels has prompted several mathematical procedures for generating meandering curves. The properties of the circular arc model (Chitale, 1970), Fargue's spiral (Leliavsky, 1955), Von Schelling's curve (Von Schelling, 1951) and the sine-generated curve (Langbein and Leopold, 1966) were discussed by Ferguson (1973), while Chang (1984) added another method, partly based on physical properties of flow in meander bends. These mathematical models, and in particular the sine-generated curve, are widely used, although they have been criticized for not providing any insights in morphological processes in meanders (Ferguson, 1973) and for not representing observed asymmetries in meander planform (Carson and Lapointe, 1983; Carson, 1986). More recently, numerical models, based on physical processes, have been employed to simulate meander development and evolution (section 2.3.5).

This discussion has focussed on simple correlation analyses, which make up the bulk of the literature, but it must be recognized that more advanced statistical techniques like spectral analysis (Speight, 1965; Chang and Toebes, 1970; Ferguson, 1975), multivariate analysis (Howard and Hemberger, 1991) and fractal scaling (Stølum, 1998) have been employed as well. Although all these statistical analyses are useful for describing meander geometry, they do not go very far in terms of explaining the processes and mechanisms responsible for meander development. Consequently, over the last twenty years or so the focus of research has shifted from statistical description of meander geometry to developing a more fundamental understanding of geomorphological processes in meandering rivers. Particular interest has been given to the study of the properties and processes of flow and sediment transport in meander bends, as reviewed next (sections 2.3.2 and 2.3.3).

2.3.2. Flow processes in meander bends

In-channel flow is constrained by the channel boundaries. The main component of the flow is directed downstream and is termed "primary flow". Deviations from this main flow direction, termed "secondary flow", are smaller in magnitude, but have important geomorphological consequences.

Vertical distribution of primary flow

Because of friction near the bed there is typically a non-uniform vertical velocity distribution in natural rivers. In laminar flow, the velocity varies parabolically with height above the bed. In natural rivers, where flow is usually turbulent, laminar flow is restricted to a very thin boundary layer. In the turbulent region above this thin laminar flow layer, the effects of friction are often assumed to diminish logarithmically with height above the bed, although in the upper part of the flow the variation of flow with height is best described using a parabolic function (figure 2.3) (Rozovskii, 1957; Engelund, 1974; De Vriend, 1977; Brandt and Thornes, 1987). Actual velocity profiles in natural rivers may deviate from the generalized distribution. The differences may be induced by friction at the free surface, by transport of suspended sediment (Vanoni and Nomicos, 1959; Coleman, 1986), by overland flow during high stages (Sellin *et al.*, 1993), by secondary currents (see below), by large-scale morphological features (Allen, 1984), and by vegetation (section 2.6).

Planform distribution of primary flow

In a straight flat-bed channel with large width/depth ratio the lateral distribution of flow velocity is approximately uniform, except near the banks where boundary friction slows the flow. As such, when lateral uniform flow enters a flat-bed bend, the flow velocity might be expected to be highest along the inside bend because of conservation of momentum along a smaller radius of curvature. Similarly, flow along the outside bend might be expected to be slower, due to the larger radius of curvature. This is confirmed in several flume experiments (Robertson, 1944; Rozovskii, 1961; De Vriend, 1977). These flume experiments also indicate that as flow continues around the bend, the core of high velocity flow gradually shifts to the outer bank (figure 2.4), as a result of a centrifugal force acting on the water while flowing through a curved channel. In natural rivers, a similar outward shift in flow can be observed (Dietrich *et al.*, 1979; Bridge and Jarvis, 1982; Van Alphen *et al.*, 1984), albeit less pronounced. The shallow flow over the point bar at the inside of the bend suppresses the formation of a core of high velocity flow close to the inner bank. The downstream flow velocity in meander bends is highest along the thalweg of the channel, which is usually located along the outer bank. While the core of high velocity flow has not reached the outer bank, the flow is "developing". Once the outer bank position is occupied, the flow is said to be "developed" and approaches the condition of uniform flow (Bridge and Jarvis, 1982).

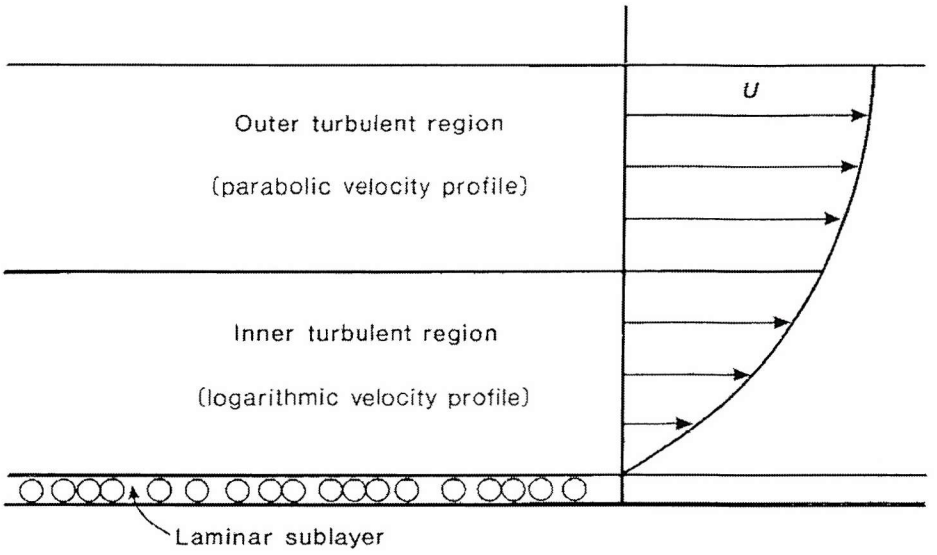

Figure 2.3: Vertical velocity profile (from Brandt and Thornes, 1987).

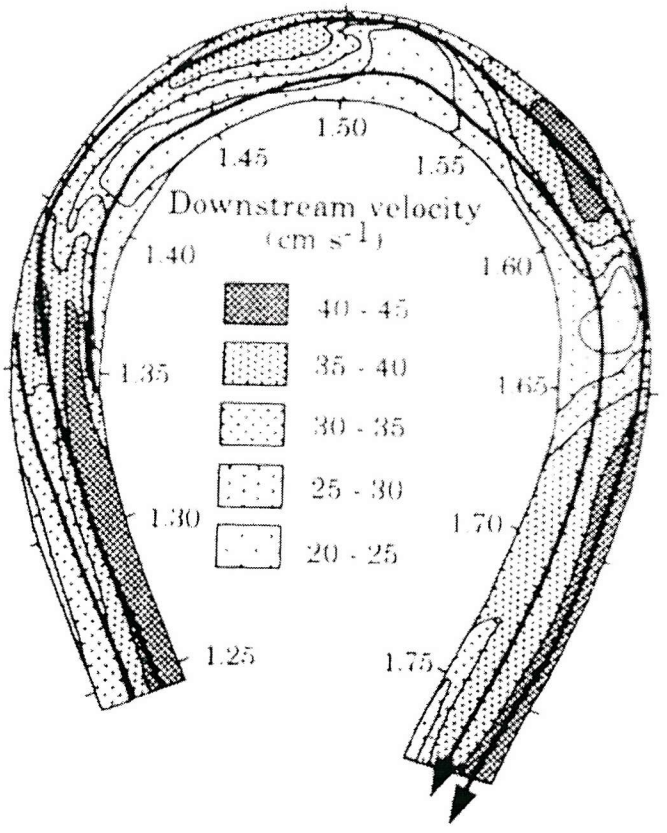

Figure 2.4: Planform distribution of downstream surface velocity in a flume bend (from Whiting and Dietrich, 1993b). Heavy lines indicate selected flow paths.

Secondary flow

Two types of secondary flow can be distinguished in natural river channels. The first is a skew-induced flow which results from non-uniformity in channel planform (Prandtl, 1952; Perkins, 1970; Markham, 1990) or bed form (Dietrich and Smith, 1983; Thompson, 1986; Whiting and Dietrich, 1993a). It is most pronounced in channel bends, where there is both a non-flat bed topography and notable planform curvature. The other type of secondary motion, stress-induced flow, results from the interaction between turbulent flow and the channel boundary (Prandtl, 1952; Einstein and Li, 1958; Einstein and Shen, 1964; Shen and Komura, 1968). This type of secondary flow is much weaker in magnitude than skew-induced flow, such that it can hardly be detected in natural channels (Bathurst, 1979; Bathurst *et al.*, 1979). Stress-induced secondary flow is not discussed here, but mention of its theoretical importance in meander initiation is made below (section 2.3.4).

Flow of water through a curved channel is subject to centrifugal forces, pushing the flow towards the outer bank. The outward flow causes a super-elevation of water near the outer bank and thus results in a lateral water surface slope. The increased pressure of the superelevated water generates a cross-stream pressure gradient force, which is equal and opposite to the depth-averaged centrifugal force. Consequently, an excess outward force exists near the water surface where the centrifugal force exceeds the pressure gradient force, while an excess inward force exists near the channel bed. The net result of this is a circular motion in the cross-channel dimension, which, when combined with the downstream primary flow, results in a spiralling or helicoidal motion through the channel (figure 2.5).

The concept of a force imbalance resulting in a helicoidal motion is long known (Thomson, 1876) and well established. For a long time it had been thought that it would apply to the whole river bend cross-section, but over the last few decades some enhancements have been made to account for observed anomalies near the channel banks. The secondary flow, as described above, applies only to the mid-channel region where it forms the main secondary flow cell (figure 2.6). The mid-channel region conveys about 90% of the flow (Markham, 1990), so this main cell is still the most prominent feature. Near the outer bank another, usually smaller, reverse cell can be observed (figure 2.6). This outer bank cell, which occurs only near steep banks, is thought to result from interaction of the main cell with the bank (Einstein and Harder, 1954; Hey and Thorne, 1975; Bathurst *et al.*, 1977; Thorne and Hey, 1979; Markham, 1990). The combination of the two cells results in a

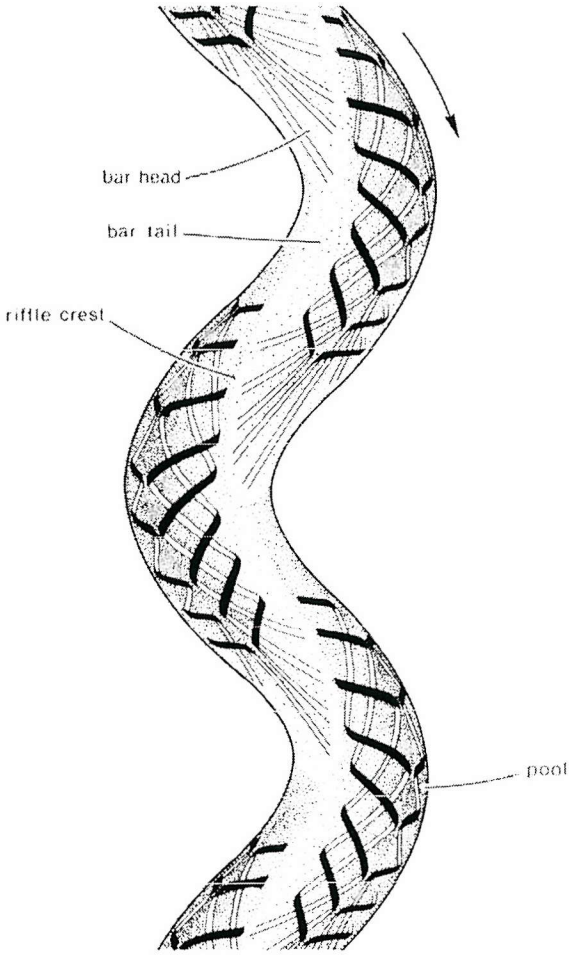

Figure 2.5: Helicoidal flow (from Thompson, 1986). Black lines indicate surface currents, white lines indicate near-bed flow. The pitch of the spiral motion is strongly exaggerated.

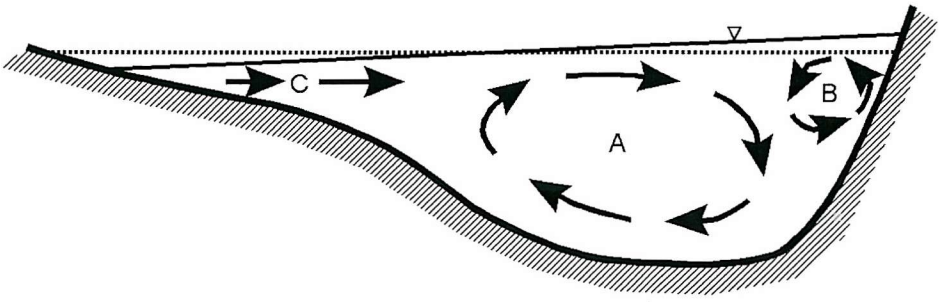

Figure 2.6: Generalized secondary flow pattern in cross-section of a meander bend. The dotted line indicates a hypothetical horizontal water surface. **A**: main flow cell. **B**: reverse outer bank cell. **C**: topography-induced shoaling.

zone of flow downwelling, which is located near the outer bank, but not against it. Flow at the inside bank can also deviate from the standard helical flow pattern, depending on the morphology of the bend (Dietrich and Smith, 1983; Bridge, 1984; Thorne *et al.*, 1985; Markham, 1990). When flow over the point bar is high, the main secondary flow cell extends over the bar, as expected. However, when flow over the point bar is shallow, the flow direction is observed to be radially outward (figure 2.6), as a result of flow continuity requirements, caused by the rising topography of the bar as the flow approaches from upstream. Effectively, the flow is forced around the point bar (Nelson and Smith, 1989a; Dietrich and Whiting, 1989). This topographic steering of the flow is usually described as "shoaling". Similar topography-induced shoaling of the flow may be observed over bars in straight channels with a meandering thalweg (Thompson, 1986).

Strength of secondary flow

Generally, the secondary flow velocities are about an order of magnitude less than the primary velocity. The strength of the helicoidal motion can be expressed by the angle, δ, by which the near bed flow velocity deviates from the local, depth-averaged streamwise flow direction. The angle of deviation, δ, has been shown to be proportional to the ratio between local flow depth, d, and radius of curvature, r_c (Van Bendegom, 1947; Rozovskii, 1957; Engelund, 1974; Zimmerman, 1977):

$$\tan\delta = C_\delta \frac{d}{r_c} \tag{2.5}$$

The value of the proportionality constant, C_δ, varies slightly with stage and roughness, but generally takes a value between 7 and 13 (Van Bendegom, 1947; Rozovskii, 1957; Engelund, 1974; Zimmerman, 1977; Bridge and Jarvis, 1982). Equation 2.5 is only applicable to the main secondary flow cell in fully developed flow. The effects of developing flow can be compensated for by using an effective radius of curvature, r_c^* (Struiksma and Crosato, 1989). However, the effects of overlapping flow cells and topography-induced shoaling are not be accounted for in this simple model.

Since vegetation can have a considerable impact on the flow distribution and boundary roughness (see section 2.6.1), it can be expected that in certain circumstances this may also be manifest in the behaviour of the secondary flow. This is supported by recent research, which suggests that vegetation may have a considerable influence on the secondary currents in river channels (Thorne and Furbish, 1995; Sand-Jensen and Mebus, 1996; Tsujimoto, 1996, 1999; Naot *et al.,* 1996). The additional roughness of vegetation inhibits outward directed flow from closely approaching the outer bank. Therefore, superelevation is suppressed and, consequently, the strength of the main secondary flow cell is as well. This has important implications for the resulting pattern of boundary shear stress and hence for the geomorphological development of vegetated bends.

Boundary shear stress

The change of flow velocity with depth generates momentum exchanges between fast and slow moving flow, thereby causing internal shear. In mid-channel regions, not influenced by friction from the channel banks, the shear stress, τ, is proportional to the vertical velocity gradient of the flow:

$$\tau = (\mu + \nu)\rho \frac{\partial U}{dz} \tag{2.6}$$

where μ is the dynamic viscosity of the fluid, ν is an apparent viscosity or eddy viscosity due to the turbulence of the flow, and U is the flow velocity. In turbulent flow the dynamic viscosity is usually small in relation to the eddy viscosity and can be neglected (Richards, 1982; Nelson and Smith, 1989a), so that the above equation reduces to :

$$\tau = \nu\rho \frac{\partial U}{dz} \tag{2.7}$$

The boundary shear stress, τ_0, is defined as the drag exerted on the bed and banks by the moving fluid and is, therefore, a significant factor in controlling sediment entrainment and transport. It is opposite and equal to the resistance offered by the boundary to the flow. As the boundary shear stress is dependent on the vertical velocity gradient above the bed, the

flow distribution across a bend has important consequences. In particular, the vertical velocity profile of the primary flow is distorted by secondary currents. Through its influence on the vertical velocity gradient the secondary flow alters the boundary shear stress distribution across the bend to a much greater extent than its small value relative to the primary flow would suggest. The highest boundary shear stress values are associated with the zone of maximum flow velocity and with the downwelling near steep outer banks (Bathurst, 1979). As the zone of maximum flow tends to be near the inner bank at the entrance of a bend and gradually shifts toward the outer bank throughout the bend, a similar pattern should be expected for the zone of maximum boundary shear stress. This has indeed been observed in flume channels (Ippen and Drinker, 1962; Hooke, 1975) as well as in natural rivers (Bathurst *et al.,* 1977; Bathurst, 1979; Dietrich *et al.,* 1979; Dietrich and Smith, 1984). When crossing the channel, the region of high boundary shear stress usually lags behind the zone of maximum flow velocity, due to interaction with the main secondary flow cell and because of the shoaling secondary flows (Bathurst, 1979).

Various methods for the measurement or calculation of the boundary shear stress exist, each with their own advantages and limitations (Dietrich and Whiting, 1989). A frequently used method to calculate the boundary shear stress at the bed is:

$$\tau_0 = \rho g d S_x \tag{2.8}$$

where d denotes the total flow depth, and S_x is the downstream slope of the water surface. This method is valid for steady uniform flow. It neglects the effects of shoaling secondary flows and thus represents a mean value for an entire cross-section.

2.3.3. Sediment related processes in meander bends

The previous discussion has highlighted the important role of secondary flows in determining the boundary shear stress, which in turn links flow conditions to sediment behaviour. The distribution of secondary flow and boundary shear stress across the bend thus have a pronounced influence on the geomorphological processes of sediment transport, as well as bank and bed erosion and deposition. This section provides a brief review of channel bed processes. However, the flow structure in meander bends also has a notable impact on

lateral processes and the morphology of the banks. Because of their importance in the context of the current study, the processes of bank erosion and bank accretion is discussed separately (sections 2.4 and 2.5).

Bed material scour and deposition

Bed scour occurs when sediments of the channel bed are entrained by the flow at a higher rate than they are replaced. The intensity of the entrainment is determined by the shear stress exerted by the flow on the bed and, hence, by the vertical velocity gradient (equation 2.7), and by the resistance to entrainment of the sediment particles, which, for non-cohesive bed-materials, depends on the weight of the grains and on the friction resulting from contact with other sediment particles (Komar and Li, 1986). Since the entrainment of particles is directly related to turbulent sweeps of the flow (Jackson, 1976b), particle entrainment could theoretically occur for any turbulent flow condition (Lavelle and Mofjeld, 1987), but in general a certain threshold of shear stress must be exceeded before any significant entrainment takes place. The resistance to entrainment is, therefore, usually expressed as a threshold of critical shear stress, τ_c. Several empirical and theoretical studies have been undertaken (e.g. Shields, 1936) to determine the critical shear stress of various sediments. This research has resulted in an abundance of statistical and physically-based relations, which are reviewed by Garde and Ranga Raju (1985) and Julien (1995), but is not discussed here. Most of the relations are applicable to granular material, where the grain resistance can be described in terms of sediment size, density and angle of repose (Komar and Li, 1986; Komar, 1996). For cohesive sediments, where biochemical and physicochemical bonds between particles cause the formation of aggregates, the situation becomes more complex and is less well understood. Berlamont *et al.* (1993) list 32 parameters necessary for the characterization of cohesive sediments.

Sedimentation occurs when eroded and transported particles settle out of the flow and are deposited on the bed. This is dependent on the balance between gravity, pulling the particle down and turbulent flow forces, allowing a particle to remain in transport. Generally, deposition occurs in areas of relatively slow flow, such as the inside of meander bends, recirculation zones and vegetated areas.

Sediment transport

Sediment can be transported either as bed load or as suspended load. The magnitude of the sediment transport is limited by either the transport capacity of the flow or by the availability of sediment. Many empirical and semi-theoretical equations have been developed to predict transport by bed load, suspended load or total load. Some of the most commonly used equations are the bed load transport formulae of Meyer-Peter and Müller (1948), Einstein (1950), Yalin (1963) and Yang (1973), and the total load formulae of Engelund and Hansen (1967) and Ackers and White (1973). Reviews of the capabilities and limitations of these and other transport formulae are given by Gomez and Church (1989), Yang and Wan (1991) and Reid *et al.* (1997). The sediment transport formulas which are used in the model developed herein are described in more detail in section 3.4.1.

The spatial routing of sediment within the channel is determined by the spatial distribution of the boundary shear stress, which is strongly influenced by secondary flow patterns (see above). In meander bends, the main secondary cell directs the near bed flow and the sediment transported as bed load towards the inner bank, *i.e.* away from the pool and up the point bar (Nelson and Smith, 1989b; Kisling-Møller, 1993; Booker *et al.*, 2001). The influence of the primary flow is generally sufficient to transport the sediments downstream and deposit the material at the next inside bank, so that sediments usually do not cross the stream (Friedkin, 1945; Thorne, 1978).

Basic considerations on conservation of mass imply that the amount of erosion or deposition at a particular area of the channel bed is equal to the difference between the amounts of sediment transported in to and out of that area. Application of this mass conservation principle to the spatial variations in sediment flow across a meander bend, has profound implications on the morphology of the bend. The deprivation of sediment influx along the outer bank and deposition of transported sediments along the inside bend are important elements in establishing the typical asymmetrical cross-sections of meander bends (section 2.5.1).

2.3.4. Meander morphogenesis

Meander development

The previous discussion indicates that meander development and bank erosion are intimately linked and, more precisely, that secondary flow is both a requirement for and a result of meandering. The so-called "bend-theory" of meander development (Ikeda *et al.*, 1981; Parker *et al.*, 1982; Parker, 1984; Parker and Andrews, 1986) states that, once an initial meandering pattern is established, the generation of secondary flow due to channel curvature means it is inevitable that channel bends will grow and migrate. Theoretical investigations of the evolution of nearly straight channels with erodible banks show that initial irregularities in channel planform will grow and expand until a meandering channel develops. However, the theory does not provide an explanation for the cause of the initial disturbance. The first fundamental question of river meandering, "Why do rivers meander?" is thus reduced to what is essentially a chicken-or-egg type question: "Does secondary flow precede channel planform deformation or vice-versa?".

The question may be provisionally answered through the distinction of the two types of secondary flow, as mentioned above. Even in homogeneous, straight, flat-bed channels there can be secondary flows, albeit very weak in magnitude. Throughout history these have been attributed to a variety of causes, such as the impact of Coriolis forces (Gilbert, 1884; Eakin, 1911; Einstein, 1926; Ludin, 1926) and differences in water temperature and density due to shading (Schauberger, 1930). Such theories have been criticized because of their weak explanatory power (Howard, 1941; Werner, 1951), although Coriolis forces may be a factor in wide rivers in high latitudes (Neu, 1967; Larsson, 1986). It is currently believed that the weak secondary currents result from stress differences due to the anisotropy of turbulence near the channel boundaries (Prandtl, 1952; Einstein and Li, 1958; Einstein and Shen, 1964; Shen and Komura, 1968). However, the exact causes of such anisotropy are not entirely clear (Markham, 1990; Raudkivi, 1990). In spite of their small magnitude, these stress-induced secondary motions do affect the flow of fluid and, hence, sediment transport. Subsequent preferential erosion and deposition on the channel bed may result in small irregularities in the channel bed topography.

Theoretical investigations of topographic instabilities on the channel bed (Hansen, 1967; Callander, 1969; Parker, 1976; Fredsøe, 1978; Columbini *et al.*, 1987; Seminara and

Tubino, 1989; Struiksma and Crosato, 1989; Tubino *et al.,* 1999) support the "bar-theory" of meander development. This theory essentially states that a small instability on the channel bed, which could be due to irregularities in the cross-sectional distribution of upstream sediment supply (Seminara, 2002 pers. comm.), will result in the formation of migrating alternate bars and pools. This pattern of alternating bars creates a meandering thalweg within the straight channel. Subsequent growth and fixation of these bars results in channel narrowing and produces a meandering channel. However, the theory is based entirely on in-channel processes and does not provide for bank erosion. Consequently, the development of a meandering channel is confined to the boundaries of the initial straight channel.

A unified "bar-bend-theory" combines the essential elements of both of the above theories. Stress-induced secondary flows may produce topographic instabilities on the channel bed that evolve in to an alternating bar topography (bar-theory). Stronger, topography-induced secondary flows over these bars and pools may be sufficient to cause erosion of the channel banks and, hence, disturbances in channel planform. Positive feedback between secondary flows caused by this planform deformation and further bank erosion will result in the development of fully meandering channels (bend-theory) with secondary flow cells and helicoidal motion as described above (section 2.3.2). Theoretical investigations of the "bar-bend-theory" show that there is a resonance between the wavelengths of the meanders predicted by the bar-theory and bend-theory (Blondeux and Seminara, 1985; Johannesson and Parker, 1989; Seminara and Tubino, 1989), indicating that the two theories indeed work together, rather than against each other. It must be emphasized that all the "theoretical investigations" mentioned in this section are analytical studies dependent on a correct mathematical description of the flow processes. Different assumptions in mathematical representations of the flow might lead to different interpretations of meandering theories.

The theoretical model outlined above seems to be supported by empirical models of meander evolution (Keller, 1972; Thompson, 1986; Hooke, 1995). A generalized meander evolution model starting from a straight river with alternating bar-pool sequences is illustrated in figure 2.7. Shoaling secondary flows produced by the bed topography (stage 1) cause lateral deformation (stage 2). This generates additional skew-induced secondary motions which accelerate the downstream and lateral migration (stage 3). As the sinuosity increases, lateral migration or growth becomes more important than downstream migration (stage 4). With increasing meander amplitude, more complex changes may occur, such as the

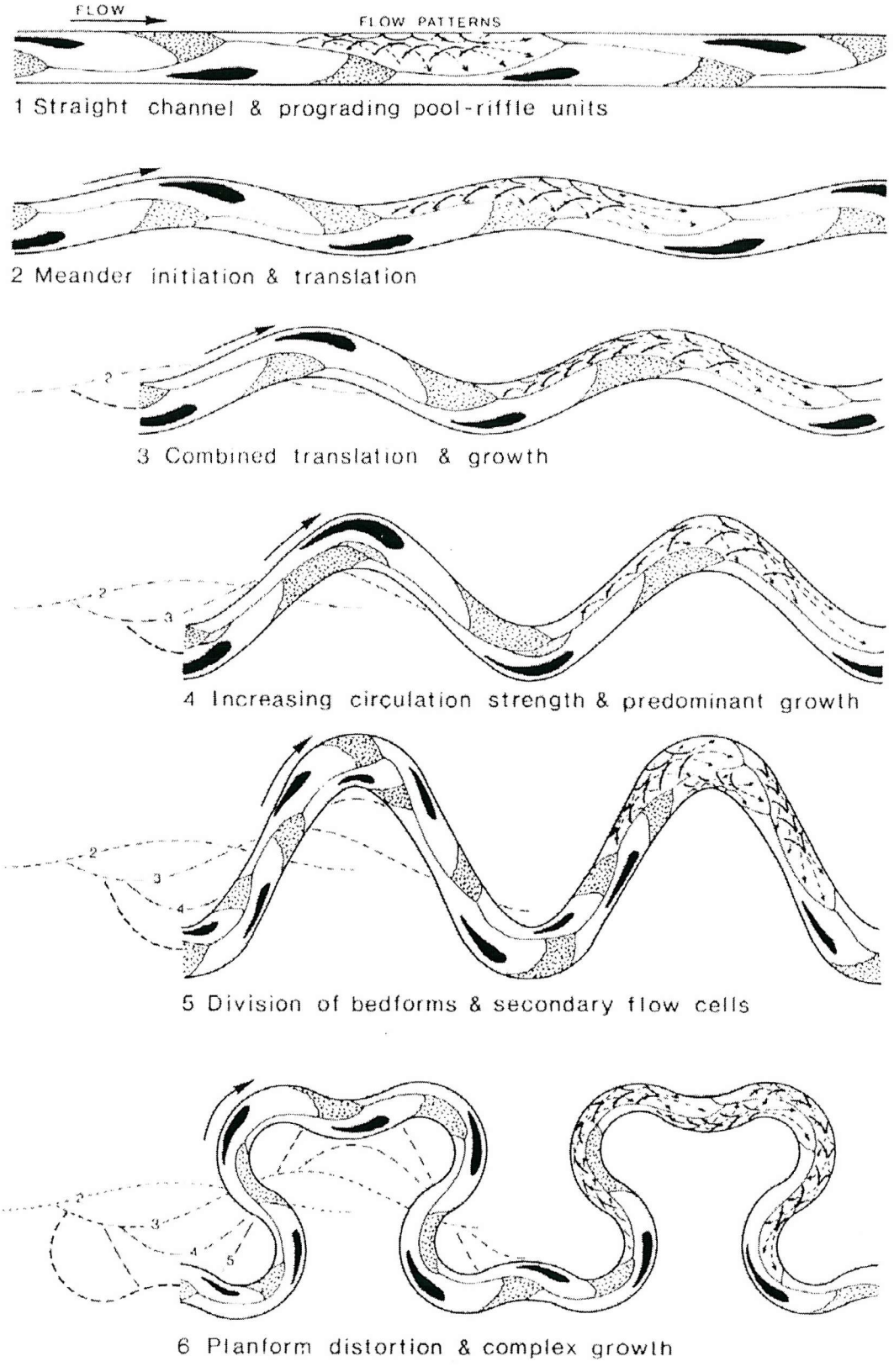

Figure 2.7: Generalized scheme of meander evolution (from Thompson, 1986). Pools are indicated in black; dotted areas indicate riffles and bars. Schematized flow patterns are illustrated with arrows.

development of additional pools and riffles (stage 5) or the development of new superimposed planform distortions (stage 6). Stages 5 and 6 are highly generalized and many variations are possible, including the development of meander cutoffs and the formation of oxbow lakes.

The bar-bend-theory is currently considered the most plausible cause of the initiation and evolution of meandering behaviour (Rhoads and Welford, 1991), although it is not uniformly accepted throughout the scientific community (Ikeda, 1989a). It is noteworthy that this theory implies that a tendency for meander development is inherent in all fluid motion, but that in natural channels sediment transport is required to amplify the weak secondary flows to an extent where bank erosion is possible.

Meander migration

It has been long recognized that meander development is influenced by many factors: flow discharge, sediment properties of the bed and bank material, slope, and the geometry of the channel itself (Matthes, 1941, Werner, 1951). However, due to the perceived importance of statistical relations, which indicate a close relation between a representative discharge and meander geometry, much emphasis has been placed on the role of discharge. Multivariate studies of meander migration recognize discharge as one of the prime variables explaining meander migration rates (Hickin and Nanson, 1984; Hooke, 1987). Yet these same studies also identify other variables as controlling factors: silt-clay content of bank material, erosion resistance, radius of curvature, width/depth ratio.

Since meander migration itself is influenced by many factors, so is the rate of meander migration. It has been suggested that maximal migration rates are possible when the ratio of radius of curvature over channel width is just below 3.0 (figure 2.8), where the bend is sufficiently abrupt to instigate flow separation at the outer bend (Hickin and Nanson, 1984; Biedenham *et al.,* 1989; Hooke, 1997, 2003). Actual meander migration rates and the influence of discharge and other variables will be further discussed in section 2.4.2 which deals with bank erosion rates in a more general context.

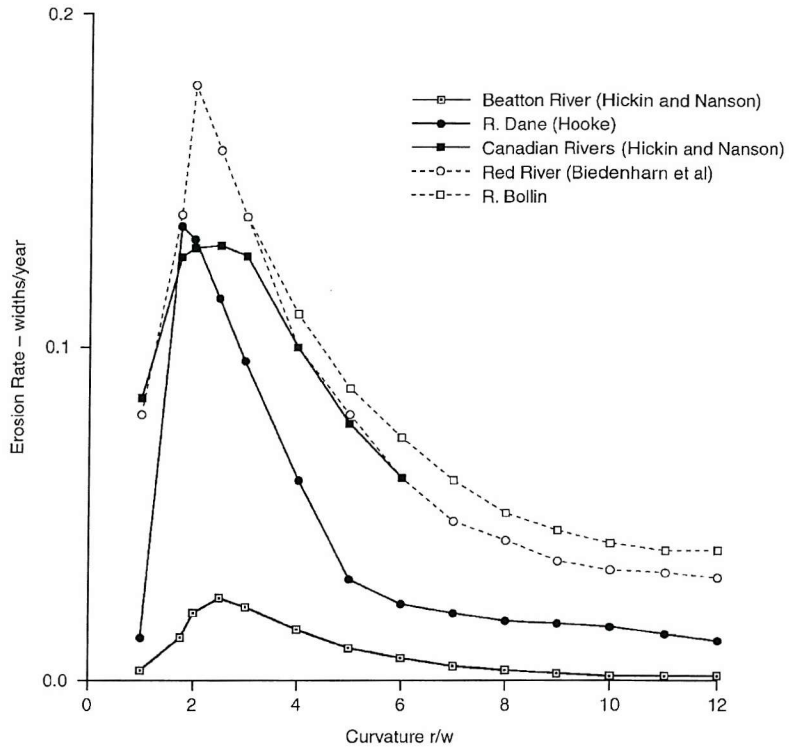

Figure 2.8: Relation between meander migration rate (erosion rate) and bend curvature, both scaled by river width (from Hooke, 2003).

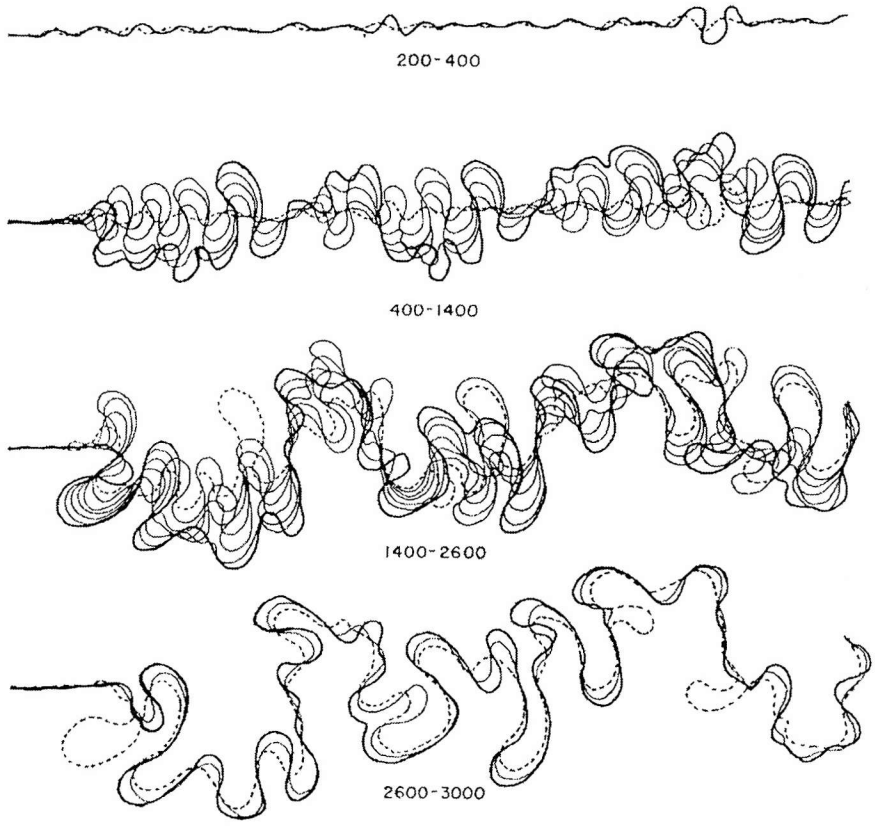

Figure 2.9: Simulated long term meander evolution of a initially nearly straight river (Howard and Knutson, 1984).

2.3.5. Planform change modelling

Numerical modelling of bank erosion and planform change is a relatively new research topic within geomorphology. While some work has been done in the 1980's, most advances in this area were made in the last decade. The report of the ASCE Task Committee (1998b) summarizes most of the current knowledge.

Hydraulic bank erosion models

According to the "bend-theory" of meander development (Ikeda *et al.,* 1981; Parker *et al.,* 1982), a small disturbance in channel planform will initiate meandering behaviour. In hydraulic bank erosion models, the lateral erosion is governed by a simple equation relating the bank erosion rate to an excess flow velocity in the near-bank area (Ikeda *et al.,* 1981):

$$E = E_r\left(U_{nb} - U\right) \tag{2.9}$$

in which E is the bank erosion rate, E_r is a bank erosion coefficient, U is the mean flow velocity and U_{nb} is the near-bank flow velocity. The bank erosion coefficient is dependent on both bank material properties and hydraulic properties (Hasegawa, 1989). A similar hydraulic technique has been applied to simulate meander evolution over much larger spatial and temporal scales. (Howard, 1984; Howard and Knutson, 1984; Crosato, 1990; Howard, 1992, 1996; Sun *et al.,* 1996, 2001; Stølum, 1998). In these simulations a long, initially nearly straight channel is allowed to develop freely, so that meanders may form, grow, migrate and bends can be cut-off (figure 2.9). In general, this type of modelling involves a series of simplifying assumptions (Stølum, 1998): channel width and average channel depth are assumed constant in both space and time; discharge is constant; there are no transient bed forms such as dunes, ripples and migrating bars; transverse variation in primary flow is linear; water surface superelevation is linear; there are no side-wall effects on the near-bank flow; downstream energy gradient is uniform; the surface gradient is constant and the channel is in equilibrium with the surface gradient; there is no downcutting or aggradation; cut-offs can occur, but there is no branching or anastomosing. Recent work includes studies on the effects of spatially heterogenous bank material characteristics (Sun *et al.,* 1996) and on the fractal geometry of meandering systems (Stølum, 1998).

Mosselman (1992) applied a similar technique, but related the bank erosion rate to relative excess shear strength near the banks:

$$E = E_r \left(\frac{\tau - \tau_c}{\tau_c} \right) \tag{2.10}$$

where τ is the shear stress exerted by the flow and τ_c is the critical shear stress versus entrainment for the bank material. The bank erosion coefficient, E_r, might take a different value in this relation.

Geotechnical bank erosion models

In addition to simulating particle entrainment, geotechnical models are capable of simulating bank mass failures. In quasi-geotechnical models (Mosselman, 1992, Nagata *et al.,* 2000) this is done by using a bank height failure criterion. Mosselman (1992) applies an excess bank height equation:

$$E = E_r \left(\frac{H - H_c}{H_c} \right) \tag{2.11}$$

where H is the bank height and H_c is the critical bank height. Again, the erosion coefficient, E_r, can take a different value from that in equations 2.9 and 2.10. In the model of Nagata *et al.* (2000), a more advanced equation is used which is based on both the bank freeboard height and the volume eroded by shear erosion (Hasegawa, 1981).

An entirely different type of model uses physically-based geotechnical bank stability analyses (Osman and Thorne, 1988; Simon *et al.,* 1991; Darby, 1994; Darby and Thorne, 1996a; Darby *et al.,* 1996; Casagli *et al.*, 1999; Rinaldi and Casagli, 1999). Although this approach provides a major conceptual improvement over the empirical models of equations 2.9 to 2.11, it has, until this study, not been integrated within curved channel flow and sediment transport models. The salient aspects of these geotechnical analyses are briefly discussed in section 2.4. A detailed mathematical description of the stability analysis applied in this study is given in the next chapter (section 3.5).

2.4. Bank erosion

Although it is a key mechanism in the lateral migration of meandering rivers, the processes of bank erosion have only received serious attention in the academic literature during the last two decades. Even though some illuminating case studies had been published previously (Wolman, 1959; Twidale, 1964; Stanley *et al.,* 1966; Hill, 1973; Knighton, 1973), rigorous investigation into the causes, controlling factors, processes and mechanics of bank erosion only began in the late seventies (Thorne, 1978, 1982; Hooke, 1979, 1980; Thorne and Tovey, 1981; Lawler, 1986, 1992; Osman and Thorne, 1988; Hagerty, 1991). Recently, an international panel of specialists reviewed, summarized and discussed the current knowledge of bank erosion processes (ASCE Task Committee, 1998a).

2.4.1. Processes of bank erosion

The term "bank erosion" is used to describe the geomorphic process by which sediment is (1) detached from its position on a river bank, and (2) taken up by the river flow and transported downstream. There are several mechanisms which can move sediment from the banks into the river channels. For clarity, the processes involved have been grouped into four categories: weakening processes, entrainment processes, bank failure mechanisms, and 'other' processes. It is stressed that this division is both artificial and arbitrary. In reality it is often impossible to attribute bank erosion to one single process of sediment detachment or removal (Hooke, 1979; Thorne, 1982; Lawler, 1992). Instead there is a complex relation between the various processes (figure 2.10), such that different mechanisms are likely to operate simultaneously, or trigger other erosional processes. The different mechanisms of bank erosion and the more common relationships between them are discussed next.

Weakening processes

Weathering and weakening of the soil can increase the erodibility of river bank material (ASCE Task Committee, 1998a). The most common weakening processes are wetting, drying, and frost heaving. Although some of these processes can transport sediment directly from the bank into the river channel, it is commonly accepted that they are more

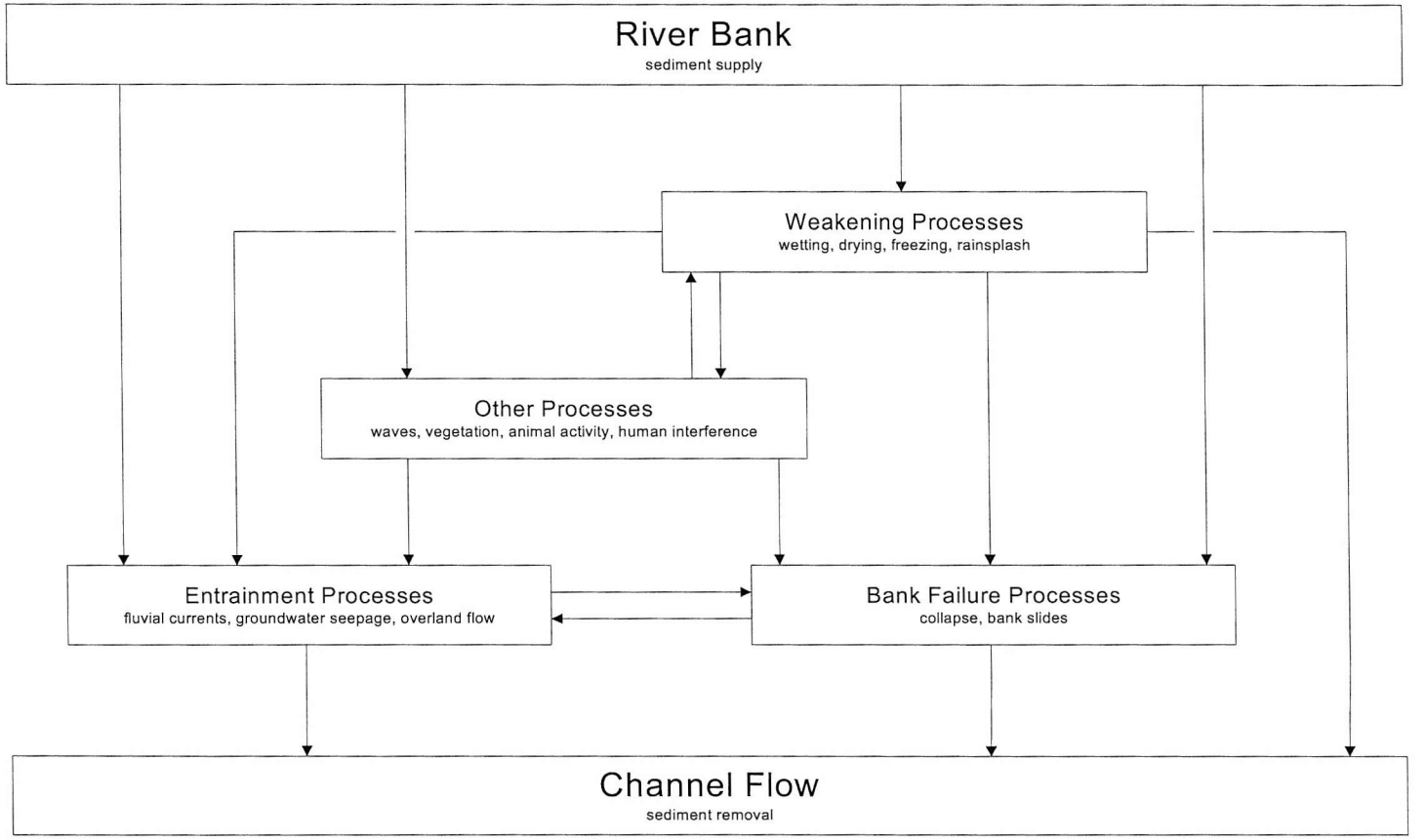

Figure 2.10: Relations between bank erosion processes.

important in preparing the bank material for erosion by other processes. The efficiency of entrainment and bank failure processes is largely influenced by this preparation (Wolman, 1959; Knighton, 1973; Hooke, 1979; Thorne, 1982; Lawler, 1986, 1992; ASCE Task Committee, 1998a).

Wetting of the bank primarily occurs because of three reasons: a rise in river stage, inflow of groundwater from the valley slopes, and/or heavy or prolonged precipitation. Wetting increases the weight of the bank and builds up positive pore pressures, both of which may reduce the bank's stability with respect to mass failure processes (Wolman, 1959; Coleman, 1969; Kesel and Baumann, 1981; Weigel and Hagerty, 1983; Darby and Thorne, 1996a; ASCE Task Committee, 1998a). At high flow stages, the increased pore pressures in the bank are at least partially compensated for by the confining pressure of the river water. During drawdown this confining pressure is removed, leaving a potentially unstable bank (Darby and Thorne, 1996a; Rinaldi and Casagli, 1999). Also, rapid wetting of a bank can dislodge particles and aggregates because of pressure build up of trapped air (ASCE Task Committee, 1998a).

Repeated cycles of freezing and thawing or wetting and drying lead to the formation of soil cracks and to disintegration of aggregates. Cracking of the soil can influence the flow of groundwater (Ullrich *et al.,* 1986) and aid in the formation of tension cracks, which seriously decrease bank stability with respect to bank failure. Disintegration of aggregates into smaller particles facilitates their entrainment (Wolman, 1959; Gardiner, 1983; Lawler, 1986, 1993). Although it is recognized that the intensity and duration of the frost period are important factors controlling the efficiency of freeze/thaw weathering (Lawler, 1993), it is also observed that the frequency of the freeze/thaw cycle also exercises control over the degree of bank preparation. It seems appropriate to extend this idea to wetting/drying cycles as well.

Formation of needle ice dislodges particles and aggregates and pushes them outward. Subsequent melting of the needle ice causes the dislodged sediment particles either to move down the bankslope into the river, thus contributing directly to bank erosion, or to remain on the bank slope as an easily erodible skin of loose material, which will be entrained at the earliest available opportunity (McGreal and Gardiner, 1977; Gardiner, 1983; Lawler, 1986, 1993).

Rainsplash can both disintegrate aggregates and move particles downslope. Surprisingly, there are only a few publications that mention rainsplash as a bank weakening process. This may be because of the limited access of raindrops on near vertical bank slopes, or because of an a priori assumption of relative unimportance. Duijsings (1987), however, noted that rainsplash can be an effective bank erosion mechanism, of the same importance as other weakening processes.

Entrainment processes

Entrainment of bank material is obviously an essential component of bank erosion. If no entrainment were to occur, sediments would remain in place, or simply accumulate at the bank toe because of gravitational forces. The detachment and removal of particles or aggregates of soil by flowing water clears the bank face and allows continued operation of weakening or bank failure processes.

The process of detachment and entrainment of soil particles or aggregates on the channel bank is similar to that of the entrainment of particles on the channel bed (section 2.3.3). It depends on the balance between the driving forces of drag and lift exerted by flowing water, and the resisting forces of gravity, friction and cohesion exerted by the bank material (Hasegawa, 1981, 1989; Thorne, 1982; ASCE Task Committee, 1998a). As long as the resisting forces are greater or equal to the driving forces, the particle will remain in place. The driving forces are a function of flow hydraulics, and the near-boundary velocity gradient in particular, while the resisting forces are largely determined by the bank material properties and antecedent bank weakening.

For non-cohesive soil material, particles are entrained individually. The essential resisting forces in this case are gravity and frictional effects due to particle interlocking. Entrainment of cohesive material is more complex, since the particles are bonded together to form small aggregates. Fluvial erosion of cohesive sediments is not fully understood, but appears to be related to the biochemical physicochemical bonding forces which form the aggregates (Grissinger, 1982; Berlamont *et al.,* 1993).

Entrainment of both cohesive and non-cohesive materials requires a flow of water over the sediments. Three sources of flowing water can be identified: river flow itself, outward seepage of groundwater and overland flow. Of these, river flow is the most obvious cause of particle entrainment. The process is similar to the scour of the river bed, and is often termed "lateral scour". The intensity of the process is directly related to the near bank flow velocity gradients. Consequently, lateral scouring is usually greater at the outer banks of river meanders or in areas of flow deflection or constriction. For cohesive sediments, the chemical properties of the water also may be important. Lateral scouring only affects the bank up to the height of the flow. The upper parts of a river bank are therefore affected only during relatively infrequent bankfull stages; the lower parts are more frequently subjected to entrainment. Even though the flow velocities are smaller during low stages, this usually leads to vertical zonation of erosional intensity. Very often this will result in either steepening of the bankslope or undercutting of the upper bank, both of which can trigger bank failures (Coleman, 1969, Knighton, 1973; Kesel and Bauman, 1981; Thorne and Tovey, 1981; Thorne, 1982; Duijsings, 1987).

When a river bank becomes saturated, seepage flow may occur if a sufficiently large hydraulic gradient builds up (Hagerty, 1991). Alternatively, in unsaturated banks, negative pore water pressure, or matric suction, causes an apparent cohesion of the soil sediment (Casagli *et al.*, 1999; Rinaldi and Casagli, 1999; Simon and Collison, 2001). In either case, the pore pressure forces the water inward or outward, often dislodging and removing bank particles (Simon and Collison, 2001). Where groundwater is concentrated because of bank stratigraphy, soil cracks or soil pipes, the velocity of the seepage flow is markedly intensified, and can therefore be a significant cause of bank undercutting and bank collapse (Henkel, 1967; Hagerty *et al.*, 1981; Ullrich *et al.*, 1986; Hagerty, 1991).

A final form in which flowing water can present itself on a bank slope is through overland flow (Thorne, 1982). The term "overland flow" is used here to describe all forms of surface water flow on the bank slope above the river level. Overland flow can be an efficient means of removing particles which were loosened by bank weakening processes and which are out of reach of river flow. In certain cases, overland flow can even lead to the formation of gullies on the bank slope (Duijsings, 1987; Vandekerckhove *et al.*, 2000).

Bank failure processes

Bank failure refers to the geotechnical process whereby relatively large blocks of sediment are detached from the bank and fall, slide or topple down the bank slope. Since this process can supply large amounts of sediment to the river and may cause considerable bank retreat, it has received a lot of attention in academic research. Several types of failures have been identified (figure 2.11). In non-cohesive sediments it usually consists of shear failure along shallow, planar slip surfaces (figure 2.11a,b,c) (Thorne, 1982); in cohesive materials deep seated rotational failures (figure 2.11d,f) (Thorne, 1982) are more likely to occur. Vertical differentiation of bank material properties, due to the presence of vegetation or because of bank stratigraphy, can lead to cantilever failures (figure 2.11g,h) (Thorne and Tovey, 1981; Abam, 1997) or complex composite failure forms (figure 2.11e) (Henkel, 1967; Thorne and Tovey, 1981; Okagbue and Abam, 1986; Abam, 1997).

Bank mass failure can be considered as a special category of slope failures in general. For more than a century, geotechnical engineers have derived methods for calculating the stability of hillslopes (Culmann, 1866; Fellenius 1927; Taylor, 1948; Bishop, 1955; Morgenstern and Price, 1965; Spencer, 1967; Sarma 1973, 1979; Chen and Morgenstern, 1983) and new, improved techniques for stability analysis are still part of engineering research (Leschinsky, 1990; Espinoza *et al.,* 1992; Michalowski, 1995; Kim *et al.*, 2002). Using the principles of geotechnical engineering, analytical expressions of bank stability have been developed. These expressions take the form of a "factor of safety"-number, N_{FS}, which is the ratio of the total resisting force (*i.e.* friction, cohesion and confining pressure) over the total driving force (*i.e.* gravity). When $N_{FS} \geq 1$, the total resisting force exceeds the total driving force and the bank is stable. Shifting the balance in favour of the driving forces until $N_{FS} < 1$, will cause the bank to become unstable and collapse. Generally this is achieved by oversteepening or undercutting of the bank due to sediment removal at the bank toe (Knighton, 1973; Hagerty 1991; Abam, 1997), by increasing the weight of the soil by bank wetting (Hooke, 1979), by reducing the length of the shear plane due to the formation of tension cracks (Springer *et al.,* 1985; Ullrich *et al.,* 1986; Darby and Thorne, 1994; ASCE Task Committee, 1998a), by increasing the pore water pressure (Simon and Collison, 2001), or by removing the hydrostatic confining pressure due to lowering of the river level (Abam, 1993; Darby and Thorne, 1996a; Rinaldi and Casagli, 1999; Simon *et al.,* 1999), or by a combination of any or all of the above.

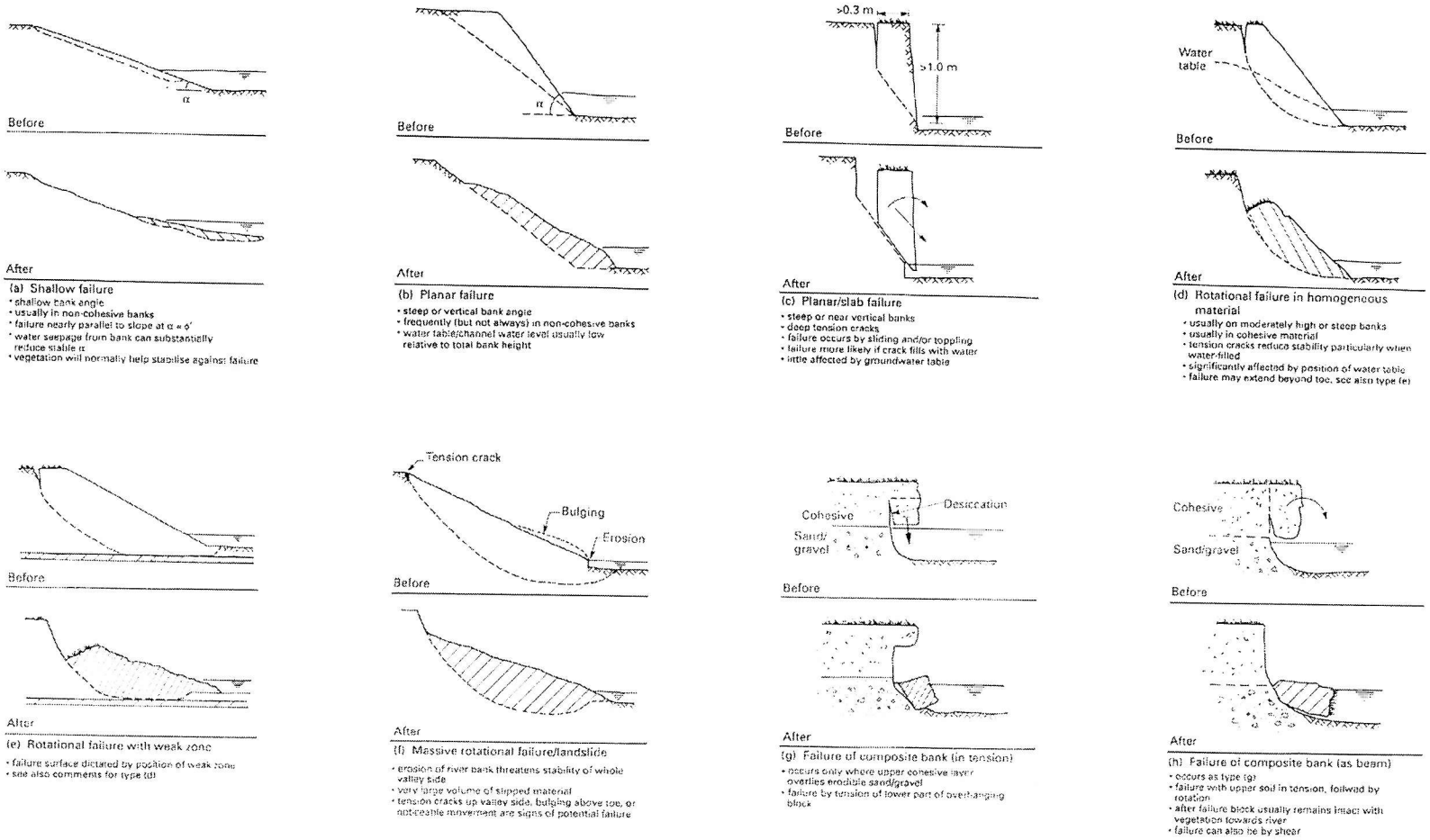

Figure 2.11: Types of bank failure (from Hemphill and Bramley, 1989).

The mathematical expression of both the driving and resisting forces depends on the shape of the bank, and on the type of failure. Expressions for factors of safety have been derived for various failure types, and various assumptions regarding hydrostatic confining pressures and pore pressures. Most analysis only consider planar failures, where the factor of safety is calculated by deriving expressions for the forces acting on a wedge of bank material (figure 2.12). Early analyses applied to simple geometries, without regard for hydrostatic confining pressures or soil moisture conditions (Thorne, 1982). Later more complex expressions, accounting for non-monoclinal bank slopes, tension cracks, soil moisture conditions and hydrostatic confining pressure were developed (Osman and Thorne, 1988; Simon *et al.,* 1991; Darby and Thorne, 1996b; Casagli *et al.*, 1999; Rinaldi and Casagli, 1999). An improved variant of these planar stability analysis, which incorporates effects of vegetation, is developed in section 3.5. For rotational and complex failures, an expression for N_{FS} can be derived by dividing the failure block in vertical segments and calculating the forces on each segment. Several variants of the segmentation method in geotechnical engineering are reviewed by Nash (1987). Thus, a different analysis exists for each of the failure types, each associated with a particular "factor of safety"-number. Bank failure will occur if one of these N_{FS} values indicates instability. Where the bank is unstable to several failure types, failure occurs according to the most unstable situation.

After failure, the failed material is deposited at the toe of the bank. This will - at least temporarily - stabilize the bank, because it reduces the bank angle and protects the toe against further scour. For bank failure processes to continue at a given site, evacuation of the failed material at the bank toe is essential (Carson and Kirkby, 1972; Hooke, 1975; Thorne, 1982; Lapointe and Carson, 1986; Richards and Lorriman, 1987; Thorne and Osman, 1988; ASCE Task Committee, 1998a). Thorne (1982) has termed this concept "basal endpoint control". It acknowledges the role of bank failure processes as sediment suppliers, but at the same time stresses the importance of hydraulic forces in evacuating the sediments (figure 2.13). If bank failure processes supply sediment at a higher rate than it is removed by the flow - a situation termed "impeded removal" - an accumulation of sediment at the toe of the bank will result, thus decreasing bank height and slope angle. Consequently, the bank becomes more stable and the rate of sediment supply will decrease. Alternatively, if the hydraulic forces evacuate sediments at a higher rate than they are supplied by bank failure processes - a situation known as "excess basal capacity" - the toe of the bank will scour, thus increasing bank height and slope angle. Therefore, the bank will become less stable and the rate of sediment supply will increase. Both the impeded removal situation and excess basal

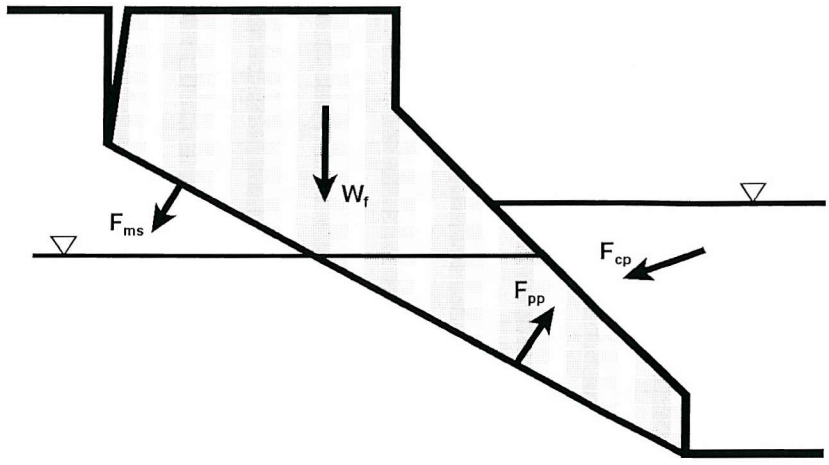

Figure 2.12: Resisting and driving forces for simple planar failure. W_f : weight of the failure block. F_{cp} : hydrostatic confining pressure. F_{pp} : positive pore pressure. F_{ms} : matric suction. See section 3.5.2 for full explanation.

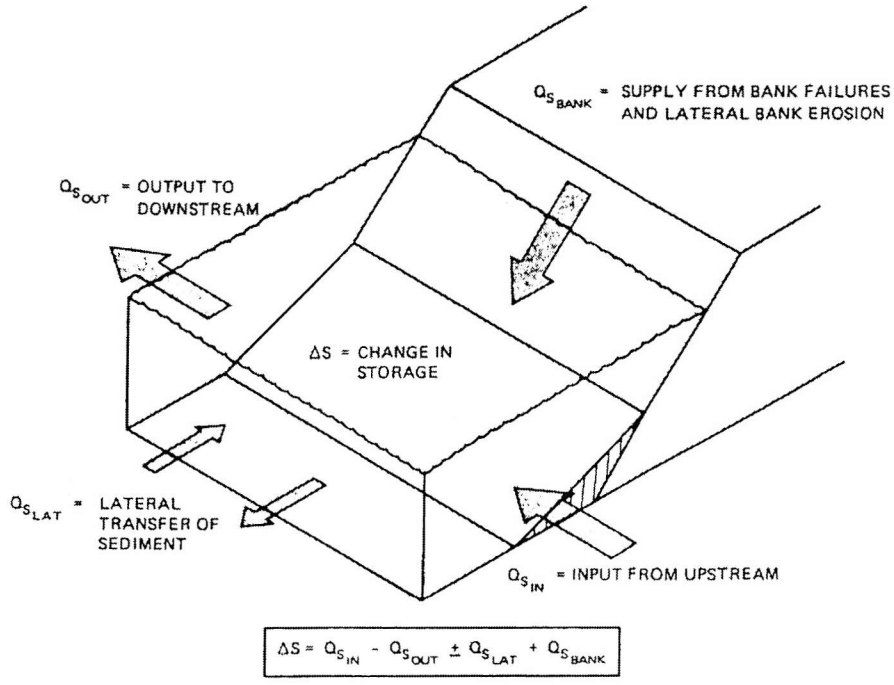

Figure 2.13: Sediment fluxes at the bank basal zone (from Thorne and Osman, 1988).

capacity situation will evolve towards an equilibrium in which the bank failure processes delivering sediment to the toe of the bank are in balance with the hydraulic processes removing it. In this situation - known as "unimpeded removal" - bank height and slope do not change, and the bank recedes by parallel retreat at a constant rate, determined by the hydraulic activity (Thorne, 1982; Thorne and Osman, 1988).

Other processes

The processes described in the preceding paragraphs are most frequently acknowledged as significant causes of bank erosion. There are, however, numerous other processes which contribute to river bank erosion, but which are not always recognized as such and receive relatively less attention in research studies. These other processes include such diverse elements as shearing by river debris (Parsons, 1960; Neill and Mollard, 1980; Walker *et al.,* 1987), washing of waves (Walker and Morgan, 1964; Walker *et al.,* 1987; Hagerty *et al.,* 1995; Williams *et al.,* 1979; Nanson *et al.,* 1994), trampling or tunnelling by animals (Meehan and Platts, 1978; Pierson, 1983; Trimble, 1994; Trimble and Mendel, 1995; Meentemeyer *et al.,* 1998), and sediment entrainment by wind (Twidale, 1964). Moreover, nearly all bank erosion processes are affected by human activities, both near the river and across the catchment: river management schemes, bank protection, river engineering, flow alteration, agricultural practices, land use, recreational activities, and many more.

The direct effects of growing vegetation on bank erosion are limited to windthrow of high vegetation, thus dislodging the sediment around the root system (Zimmerman *et al.,* 1967; Gregory and Gurnell, 1988). However, the indirect effects of vegetation are numerous and complex. It is generally accepted that vegetation tends to reduce erosion or enhance sedimentation by decreasing flow velocities, trapping fluvial and colluvial sediment, and anchoring bank sediment. Other effects of vegetation are often ignored, usually these are the ones that tend to enhance erosion: possible increased turbulence, increased bank weight due to the surcharge of tree biomass, flow pattern alteration due to large woody debris dams. The influence of vegetation on bank erosion will be discussed in more detail in section 2.6.

2.4.2. Rates of bank erosion and process dominance

Considering the numerous factors and processes involved, it should not be surprising that published rates of bank erosion are highly variable, both spatially and temporally, ranging from a few millimetres per year up to several hundreds of metres per year. A review of published erosion rates is given in appendix A1.

The temporal variability of bank erosion rates can partly be explained by the episodic nature of bank failure processes. At the time of bank failure, high erosion rates are recorded; during the period in which the failed sediment is removed from the toe of the bank by entrainment, retreat is much less intense. Short term erosion rates resulting from extreme flooding events can be overwhelming. Carey (1969) mentions a few examples where the river banks "*receded hundreds of feet ... in a matter of hours or minutes*". Furthermore, erosion rates often show a certain degree of seasonality, related to the climatic controls of the weakening processes. Higher erosion rates are generally found during the wet season, during snow melt or during periods of soil frost.

The spatial variability of bank erosion rates reflects a whole range of differences in controlling factors, such as hydraulic activity, channel geometry, engineering properties of the bank material, climate, geology, vegetation and human interference. An attempt to assess the relative importance of the different erosion processes in supplying sediment to the river varies with spatial scale is summarized in table 2.3. Generally, weakening processes are

Table 2.3: Relative importance of bank erosion processes to sediment supply.

erosion mechanism	catchment size		
	small	intermediate	large
weakening processes	++	+	-
bank failure processes	-	+	++
hydraulic processes	+	++	+
waves	-	++	+
vegetation effects	++	+	-
windthrow	+	-	-
animal activity	++	+	-
human interference	++	++	++

\- : low importance
\+ : medium importance
++ : high importance

more important in small catchments; bank failure processes are more important in large catchments, and hydraulic processes are more important in intermediate catchments (Lawler, 1992). It should be noted, however, that sediment supply only constitutes one part of the erosion process. The second part, sediment removal, is almost completely controlled by the hydraulic characteristics of the river flow. Consequently, one might expect river flow characteristics to be largely responsible for the rates of lateral erosion in the long term (Thorne, 1982). There is indeed a strong tendency for higher erosion rates with increasing hydraulic activity (figure 2.14, using basin drainage area as a proxy for hydraulic activity). Even though the correlation is fairly high ($r = 0.81$), the amount of scatter is still considerable - about one order of magnitude on either side of the regression curve. Some scatter might be expected, as erosion rates are frequently averaged over different scales of time and space. Nonetheless, most of the scatter should be interpreted as indications of the relative importance of other factors and processes. Multiple regression analysis (Hooke, 1980; 1987), confirms that drainage area is indeed the dominant variable in explaining mean erosion rates, but also acknowledges the importance of the textural composition of the material (silt-clay percentage), bank slope and curvature of channel bends (Hickin and Nanson, 1984). Variation in physical and geometrical properties along river channels implies that the rates of erosion may vary considerably, even within a single system (Hooke and Redmond, 1992). Gilvear *et al.* (2000) noted that bank erosion rates not only differ between bends, but also tend to increase steadily within a single bend.

2.5. Bank accretion

While bank erosion is responsible for the loss of floodplain lands, sediment accretion along river banks accounts for the rejuvenation of the floodplain. Especially along meandering rivers, bank accretion has long been recognized as an important process in the construction of alluvial floodplains, although other modes of floodplain formation are possible as well (Nanson and Young, 1981; Nanson and Croke, 1992).

Sediment deposition along river banks and floodplain formation have been studied for well over a century (e.g. Lyell, 1830). Extensive reviews of sedimentary processes and landforms in various fluvial environments are given in Allen (1965, 1984) and Miall (1996), while an overview of the physical principles involved is given by Hsü (1989).

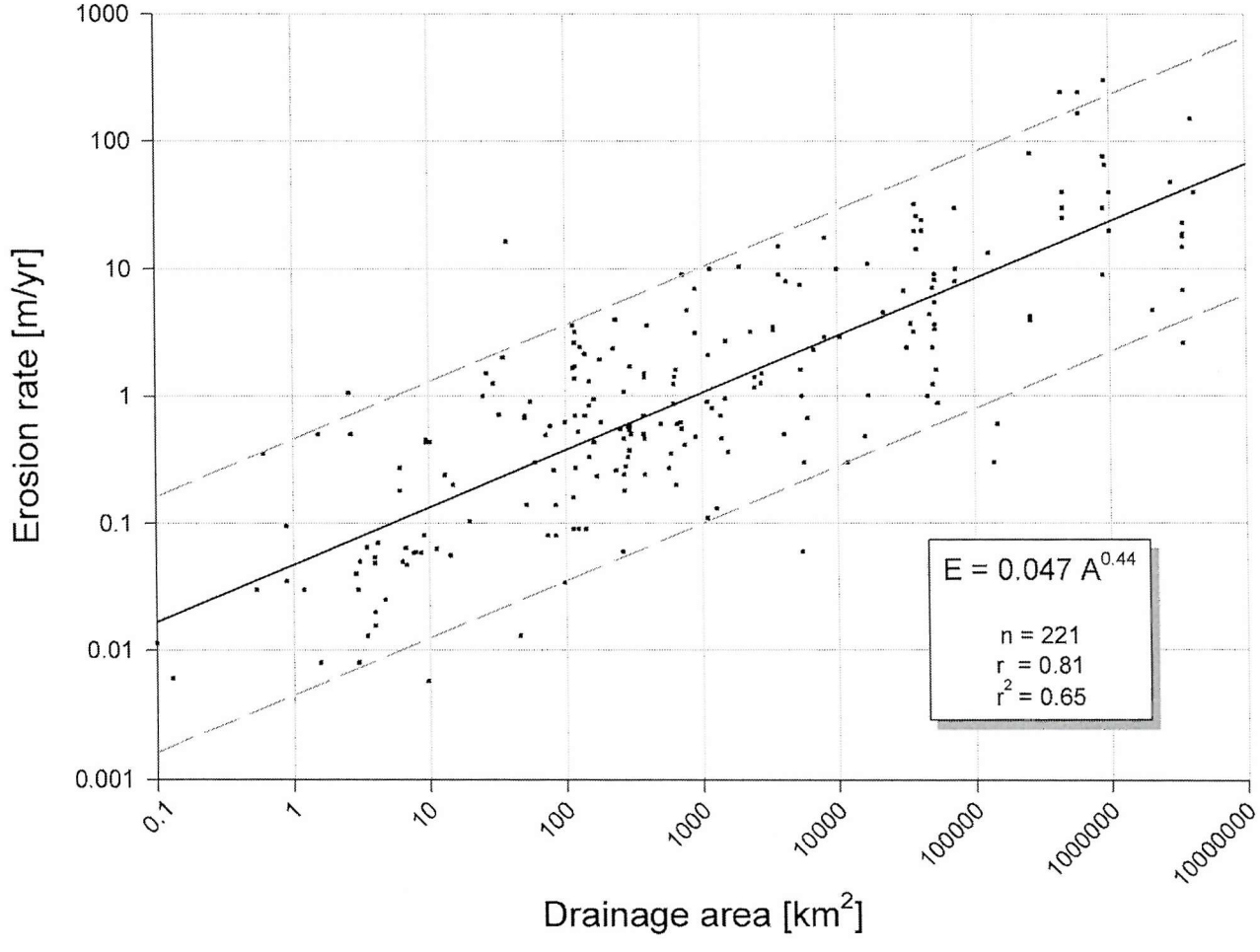

Figure 2.14: Bank erosion rates (E) as a function of drainage area (A). The black line represents the best fit by regression: $E = 0.047\ A^{0.44}$. The hashed lines above and below mark a boundary of an order of magnitude to either side. The data for all entries is given in appendix A1.

2.5.1. Bank accretion processes

Fluvial depositional structures and landforms in alluvial zones can be broadly classified in two categories: in-channel deposits and on-floodplain deposits. The first consists of structures like point bars, benches, pools, riffles, ripples, and deposits from bank failures, while the latter comprises levees, crevasse-splays, backswamps and oxbow-fills (Allen, 1965; Nanson and Croke, 1992; Miall, 1996). On-floodplain deposits are mainly due to particle settlement out of overbank flood flows, while in-channel deposits may form during lower discharges as well as during floods. Bank accretion, which spatially occurs on the contact point of floodplain and channel, involves processes from both groups: mass failure deposition, point bar accretion and bench formation, which account for lateral growth of the bank, and overbank deposition which accounts for vertical growth of the bank.

Mass failure deposition

Deposits of failed bank material strictly speaking do not contribute to bank accretion, since the sediment already formed part of the bank before failure. Nor is it a true fluvial deposition, although the failure is likely to be caused by bank steepening or undercutting due to hydraulic forces (section 2.4.1). However, mass failure deposits do alter the shape of the bank and may have a profound impact on its further evolution. After failure, part of the eroded material may remain deposited at the toe of the bank, thereby stabilising the bank (section 2.4.1). The failed material effectively forms a bench within the channel, over which the flow is more shallow, or which may not be submerged at all during lower flow. The altered flow regime over the bench may result in additional sedimentation. Benches of this form may also provide suitable areas for colonisation by pioneering vegetation species, which in turn may initiate further sedimentation (Hupp and Simon, 1991).

Point bar accretion

One of the most readily identifiable fluvial deposits is the point bar. Its appearance at the inner bank of a meander bend is due to the helical flow structure, directing near bed flow and bedload sediment towards the inner bank. The combination of deposition at the inside bank and scour at the outside bank (section 2.3.3) produces a point bar along the inner bank.

Point-bar deposition of heterogeneous sediments shows a gradual fining of the sediments along the bar slope, with the coarsest sediments near the pool and the finest sediments higher on the bar (Jackson, 1975; Dietrich *et al.,* 1979; Bridge and Jarvis, 1982; Van Alphen *et al.,* 1984). In fully developed secondary flow, sediment particles on the point bar are subject to two lateral forces: flow forces induced by the secondary flow cell, driving the sediments toward the inner bank, and gravitational pull along the bar face, driving them towards the outer bank (Allen, 1970). Selective sorting of grainsize occurs because the outward gravitational component of the force balance is proportional to the cube of the grain diameter, while the inward component is proportional to the square thereof (Allen, 1970; Parker and Andrews, 1985; Ikeda, 1989b). Modifications to this simple conceptual model have been made to account for the effects of topography-induced shoaling, such that the net balance should not be equal to zero (Dietrich and Smith, 1983, 1984; Dietrich and Whiting, 1989). Thus, cross-stream sediment discharge is possible, even on equilibrium bed forms (figure 2.15). The effects of sediment sorting can be seen by the crossing paths of fine and coarse sediment. As this conceptual model does not apply to areas where the flow is not fully developed, the sorting effect may be less pronounced or absent at the bend entrance (Miall, 1996). Hence, a secondary sorting effect may exist, in the streamwise direction, with deposition of coarser sediments at the upstream part of the point bar (Jackson, 1975; Bridge and Jarvis, 1982; Carson, 1986).

The point bar is a bed form which, by its nature, connects smoothly with the inside bank of the channel. Because of this, the distinction between bank and bed may not always be clear, especially in wide rivers, where the transverse slope of the deposits is generally small. Additionally, the surface of the point bar may be covered with other fluvial deposits such as ripples, dunes and scrollbars (Nanson, 1981; Gibling and Rust, 1993; Miall, 1996), enhancing the obscurity. As the point bars grow, they gradually merge with the floodplain, creating a new surface that can be invaded and colonized by vegetation. This incorporation of depositional surfaces into the floodplain is one of the key elements of river migration.

Bench formation

Sedimentation may also occur along the outside bank of a river bend (figurge 2.16; Woodyer, 1975; Hickin, 1979; Page and Nanson, 1982). This is most notable along abruptly curving bends, *i.e.* with a curvature over width ratio, r_0/w, of less than 3.0, where flow

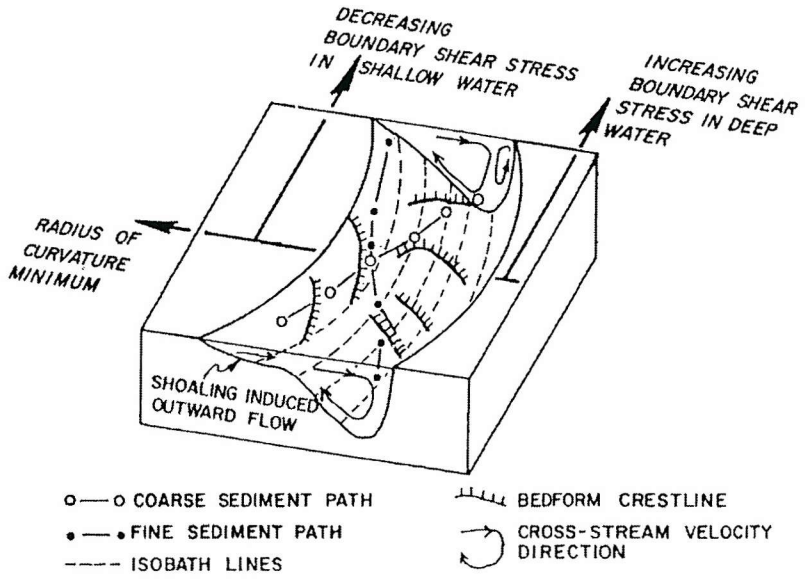

Figure 2.15:Sediment movement in a meander bend. Flow direction is from the lower end to the upper end of the figure (from Dietrich and Smith, 1984).

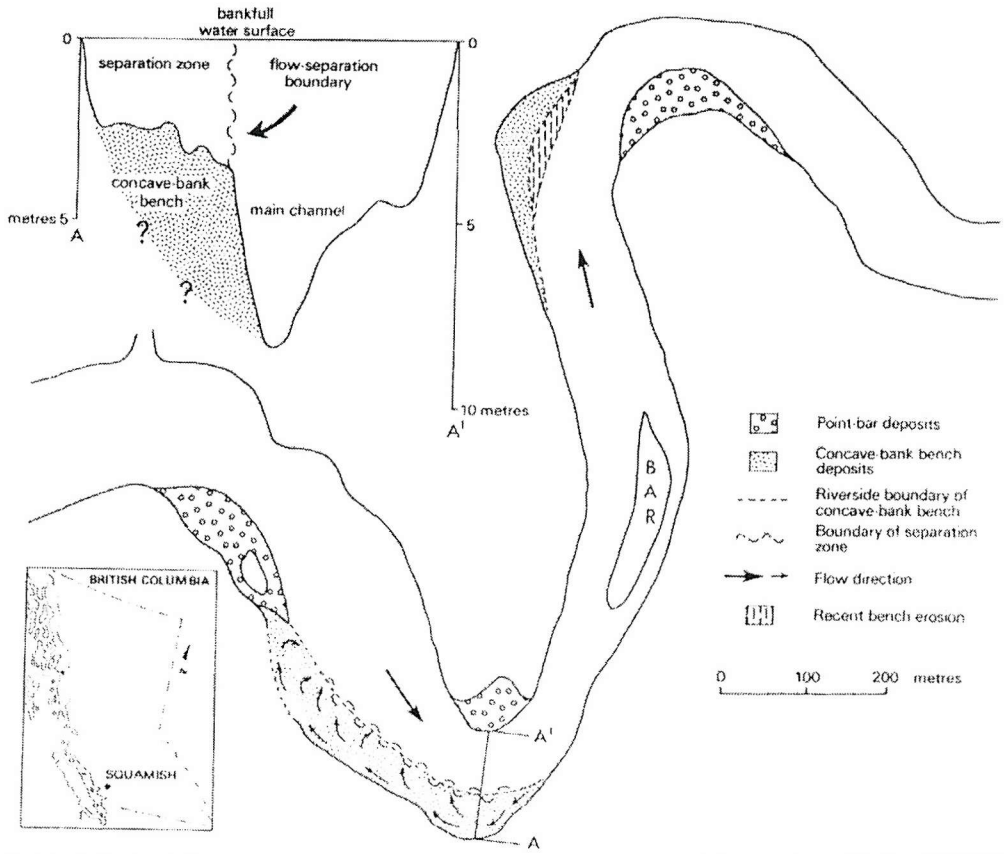

Figure 2.16: Location and planform of two concave-bank benches of the Squamish River, British Columbia (from Hickin, 1979).

separation and recirculation at the concave bank induce rapid sediment deposition (Hickin, 1979; Woodyer *et al.,* 1979; Page and Nanson, 1982). The deposits thus formed are termed "concave-bank benches". Usually a small channel exits between the incipient bench and the concave bank. As the bench grows, this channel becomes smaller and is gradually filled with sediment, thereby linking the bench with the bank (Page and Nanson, 1982). The sediment deposited in the recirculation zone is usually fine and while there usually is a coarsening of concave bench sediments in the downstream direction (Page and Nanson, 1982; Smith, 1990), the deposits are generally finer than point bar deposits in the same channel (Page and Nanson, 1982; Changxing *et al.,* 1999). The occurrence of flow separation and recirculation is not exclusively linked with abrupt channel bends. Downstream changes in channel width, *i.e.* channel constriction or expansion, may also result in flow reversal, in which case similar type bench formation may occur on straighter reaches as well (Smith, 1990).

Overbank deposition

The sediments deposited on the floodplain as a river overflows it banks contribute to the vertical growth of the floodplain, and hence of the channel banks. Overbank deposition is often ignored in studies of bank accretion, presumably because it does not contribute directly to planform change or possibly because of its perceived unimportance relative to lateral bank accretion. However, it is the main cause of vertical growth of river banks and in some cases may be the only form of floodplain growth (Nanson, 1986; Nanson and Croke, 1992). Overbank deposits generally show a lateral fining away from the channel (Morisawa, 1985; Guccione, 1993). Levees are the relatively coarse sediments formed by overbank flow of channel bedload and can be up to 10 metres thick (Miall, 1996). Finer sediments deposit further away from the channel form backswamps (Miall, 1996) and in-fills of cutoff meander bends (Shields and Abt, 1989).

2.5.2. Rates of bank accretion processes

In contrast with bank erosion rates, there are few published measurements of bank accretion rates. The lack of data on bank accretion rates has resulted in an often reoccurring hypothesis that bank accretion matches erosion on the opposite bank (Miall, 1996), effectively implying a constant river width. While this assumption may hold for rivers in

equilibrium, it may be invalid for channels not in equilibrium, which can be either widening or narrowing depending on the difference between lateral accretion and erosion rates. In a study of various Tennessee rivers, with different sizes and in different states of disequilibrium, Hupp (1992) found lateral bank accretion rates to be about one order of magnitude less than lateral erosion rates. Vertical accretion rates are usually much lower than lateral accretion rates (Appendix A1). It must be noted that measurement of accretion rates is dependent on the timescale of measurement, as well as on location, since the accretional deposits can be partly or wholly eroded during flood events. In addition, the sedimentary regime of a river is not constant through time or space. Changes in sedimentary regime can be induced by changes in climate (Hereford, 1984), by base-level change (Schumm, 1993), by changes in discharge-regime (Everitt, 1993), by changes in land-use (Wolman, 1967) and by changes in vegetation cover (section 2.6). Of these external controls, land-use and vegetation are most likely to exert their influence over shorter time scales.

The reduction of flow velocities through the presence of vegetation enhances depositional processes. Lateral growth of banks and the formation of benches in the wake of vegetation has been recognized by many (Woodyer *et al.,* 1979; Nanson, 1981; Hupp and Simon, 1991; Changxing *et al.,* 1999). Vegetation growth, and hence sediment trapping by vegetation (Abt *et al.,* 1994; Thornton *et al.,* 1997), is intensified as the bar or bench builds up above the low-flow water level. The impact of vegetation is discussed in more detail in section 2.6.

2.5.3. Relation to bank erosion processes

There is a complex relation between bank accretion and bank erosion. The balance between the two processes regulates channel geometry and, hence, the flow structure, which in turn exerts considerable influence on both accretional and depositional processes. Furthermore, erosion of river banks can act as a significant source of sediment to the flow and spatial differentiation of bank erosion may thus influence the local supply of material for deposition. The relation is complicated further by the fact that the continued migration of the channel may expose the preserved sedimentary structures along the cutbank (Bluck, 1971; Jackson, 1976a), which can result in spatially variable bank sediment properties and, hence, in localized spatial and temporal variability in bank erosion processes.

2.6. Riparian vegetation

The extent to which vegetation influences morphological processes is only gradually becoming clear. There is, at the moment, no accepted generalized theory which incorporates the mutual relationships between vegetation and the morphology of fluvial landforms. Several researchers have prompted the need for a better understanding of the role of vegetation in the fluvial environment (Hickin, 1984; Rhoads and Welford, 1991; ASCE Task Committee, 1998a). These requests have resulted in a growing number of case studies where various aspects of the vegetation-morphology interaction have been examined. As a result, knowledge and understanding of processes in vegetated river channels is gradually increasing.

This section provides an overview of the different aspects of vegetation in a fluvial environment. In the existing literature the relation between the fluvial system and its ecology is usually considered from one of two perspectives, largely depending on disciplinary background. Geomorphologists and engineers largely concentrate on the influence of vegetation on hydraulic and geomorphological variables, while ecologists focus on the influence of hydrogeomorphological variables in determining the spatial and temporal distribution of riparian vegetation (Hooper, 1992). Few studies consider both elements of the relationships.

Fluvial geomorphologists are generally aware of the existence of vegetation and acknowledge its potential for influencing geomorphological processes. However, vegetation is often ignored in fluvial geomorphology, because it is not readily quantifiable (Hickin, 1984). For many years vegetation was considered a nuisance, a disturbing element in research studies. Field experiments were more often than not set up at sites without vegetation or where vegetation was carefully removed, so that it could not interfere with the processes being studied. Where vegetation was considered as part of a field study, only general observations were made, at best resulting in empirical relations between vegetation and hydraulics. Until about twenty years ago few attempts had been made to systematically study the processes governing the relationships between riparian ecology and fluvial geomorphology. Since the late seventies however, a more critical consideration of the impacts and responses of vegetation in a riverine environment, from both an ecological and geomorphological viewpoint, resulted in an improved appreciation of the complexity,

subtleness and importance of the relationships between riparian vegetation and geomorphology (Hupp and Osterkamp, 1985; Gregory and Gurnell, 1988; Hupp, 1990; Spencer *et al.,* 1990; Thorne, 1990; Gurnell and Gregory, 1995; Gurnell, 1995).

The acknowledgement of the complex and subtle interactions between vegetation, flow and sediment is often lost in the generalized descriptions thereof (Thorne, 1990). A common perception of the effects of vegetation is that it will decrease bank erosion and induce sedimentation by protecting bank sediment and lowering flow velocities. While this may hold in several situations, it certainly is not a universal rule. The relationships between vegetation and fluvial geomorphology involve many elements and are sufficiently complex to preclude such general statements. In the following paragraphs, the various elements of the relationships are discussed separately, for ease of comprehension. It should be noted however that in natural rivers many or all of these elements operate simultaneously and it is often difficult or impossible to unequivocally link a specific observation with one individual process. Such complexity makes controlled empirical studies difficult and may lead to ambiguity in the interpretation of observations. The challenge in developing physically realistic models of riparian vegetation is all the greater.

2.6.1. Effects of vegetation on hydraulics

Much of the current understanding of the way in which vegetation effects flow hydraulics and sediment transport was first established in studies concerning air flow and the effects of vegetation on wind erosion, where the active processes can be more easily observed (Wilson and Shaw, 1977; Raupach *et al.,* 1980; De Bruin and Moore, 1985). There are indeed many similarities between the flow of air and the flow of water over vegetated surfaces. The main effects of vegetation on air flow - roughness increase, a general decrease in flow velocity within the vegetation, distortion of the velocity profile and changes in turbulence - are also observed in water flow, albeit in a quantitatively different form due to the diverse physical properties of the fluids. However, the main conceptual difference between the two fluids is the depth of the flow layer. Vegetation is always completely submerged in air flows, while this is not necessarily true for water flows, especially not when bank vegetation is being considered.

Vegetative roughness

Generally, vegetation is considered to be an element contributing to the hydraulic roughness of a channel. Analogous to the work of Einstein and Barbarossa (1952), the hydraulic roughness in vegetated channels can be conceptually divided into soil grain roughness, form roughness and vegetative roughness (Cowan, 1956; Wu *et al.,* 1999). Several case studies, comparing Manning's roughness coefficient for vegetated and unvegetated conditions at the same site, have shown that the presence of vegetation can increase the total channel roughness by more than an order of magnitude (Stephens *et al.*, 1963; Severn, 1982; Pitlo, 1982; Watson, 1987).

If all other variables remain constant, the increase in roughness can be translated directly to a decrease in flow velocity through Manning's formula or the Darcy-Weisbach formula. Unfortunately, the interaction between flow velocity and vegetation induced roughness is more complex, since an increase in roughness, and the subsequent decrease in flow velocity, will also affect flow depth and thus cross-sectional area and hydraulic radius. Moreover, there is a mutual dependency between flow velocity and vegetative roughness. The flow velocity in a channel is a function of channel roughness, which is dependent on the vegetative roughness. However, the vegetative roughness itself is dependent on the drag exerted by the flow, which together with the physical properties of the vegetation determines the degree of bending, and thus the effective roughness height and vegetative roughness (figure 2.17).

Early work dealing with vegetation induced roughness concentrated on establishing empirical relations between roughness and flow velocity (Cox and Palmer, 1948; Ree and Palmer, 1949). Alternatives have been developed since the early seventies, based on physical properties of flow and vegetation, such as flow strength, stem flexibility, vegetation drag coefficient and vegetation density, with different approaches for different vegetation types. For submerged, flexible vegetation, attention focussed on the degree of bending and the effective roughness height, as functions of stem stiffness (Kouwen *et al.,* 1969; Kouwen and Unny, 1973; Kouwen and Li, 1980; Kouwen *et al.,* 1981; Kouwen, 1988). For stiff, non-submerged vegetation, which is often simplified as rigid vertical cylinders, attention focussed on the fluid drag exerted on the vegetation and on the turbulence in the wakes of stems (Li and Shen, 1973; Klaassen and Van der Zwaard, 1973; Petryk and Bosmajian, 1975; Thompson and Roberson, 1976; Lindner, 1982; Pasche and Rouvé, 1985; Nuding,

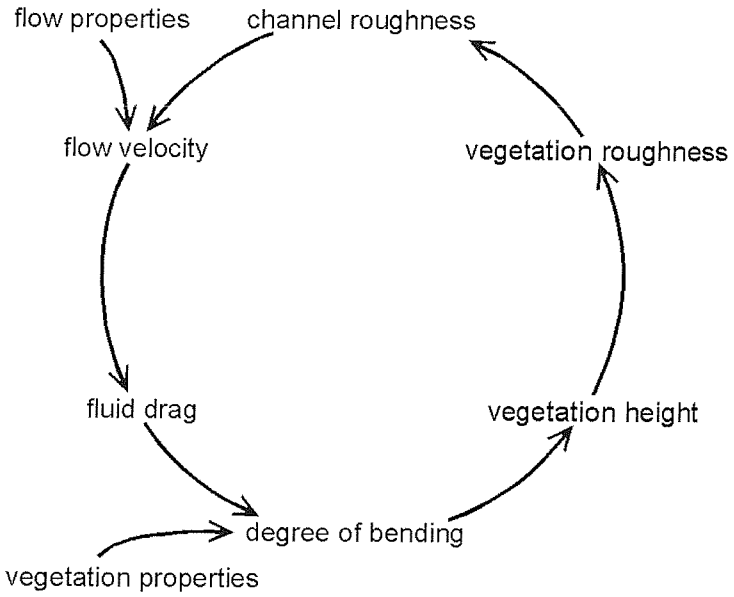

Figure 2.17: Mutual dependancy of flow velocity and vegetation roughness.

1994). More recent research studies have attempted to unify these approaches, either by applying the drag force method to submerged vegetation (Wu *et al.,* 1999; Fischer-Antze *et al.,* 2001) or by looking at flexible emergent vegetation (Fathi-Moghadam and Kouwen, 1997; Rahmeyer *et al.*, 1999; Kouwen and Fathi-Moghadam, 2000; Freeman *et al.*, 2000).

It is important to realize that although these semi-theoretical approaches are all based on relations between physical properties of flow and vegetation, they still have an explicit empirical component. Nearly all the equations rely on some sort of empirical coefficient or vegetation parameter - effective vegetation stiffness, drag coefficient, vegetative characteristic number, vegetation index - which can not always be easily determined and for which only rough guidelines are given, based on rather limited data.

Flow velocity

Since erect vegetation increases channel roughness, and since flow velocity is inversely proportional to the roughness, it is logical to expect the flow velocity to decrease within a vegetated part of the channel. This qualitative interpretation of the effect of vegetation on flow velocity generally holds true, although it has already been mentioned that the exact quantitative relationship between vegetative roughness and flow velocity is complex because of their mutual dependency (figure 2.17).

In natural channels, with turbulent flow, the vertical profile of the mean flow velocity approximates a logarithmic function of the distance above the bed (figure 2.3). It is widely established that, for submerged vegetation, the velocity profile above the vegetation follows a similar profile (Axelsson, 1967; Gourlay, 1970; Temple, 1986; Pethick *et al.,* 1990; Thorne, 1990; Fischer-Antze *et al.,* 2001). This is similar to the effects of vegetation in air flow, where it is suggested that the logarithmic profile works well down to twice the roughness height (Raupach *et al.,* 1980; Wolfe and Nickling, 1993). However, the vertical velocity profile within a vegetated zone or layer differs from this standard logarithmic profile (figure 2.18). Initially it was thought that the flow velocity within vegetation should also display a logarithmic profile (Kouwen and Unny, 1973; Thompson and Roberson, 1976) or be constant (Temple, 1986), while later research suggests a linear profile (Pethick *et al.,* 1990; Lopez and Garcia, 1997; Tsujimoto *et al.,* 1991). However, other recent experiments show that the vertical velocity profile within vegetation is much more erratic (figure 2.18)

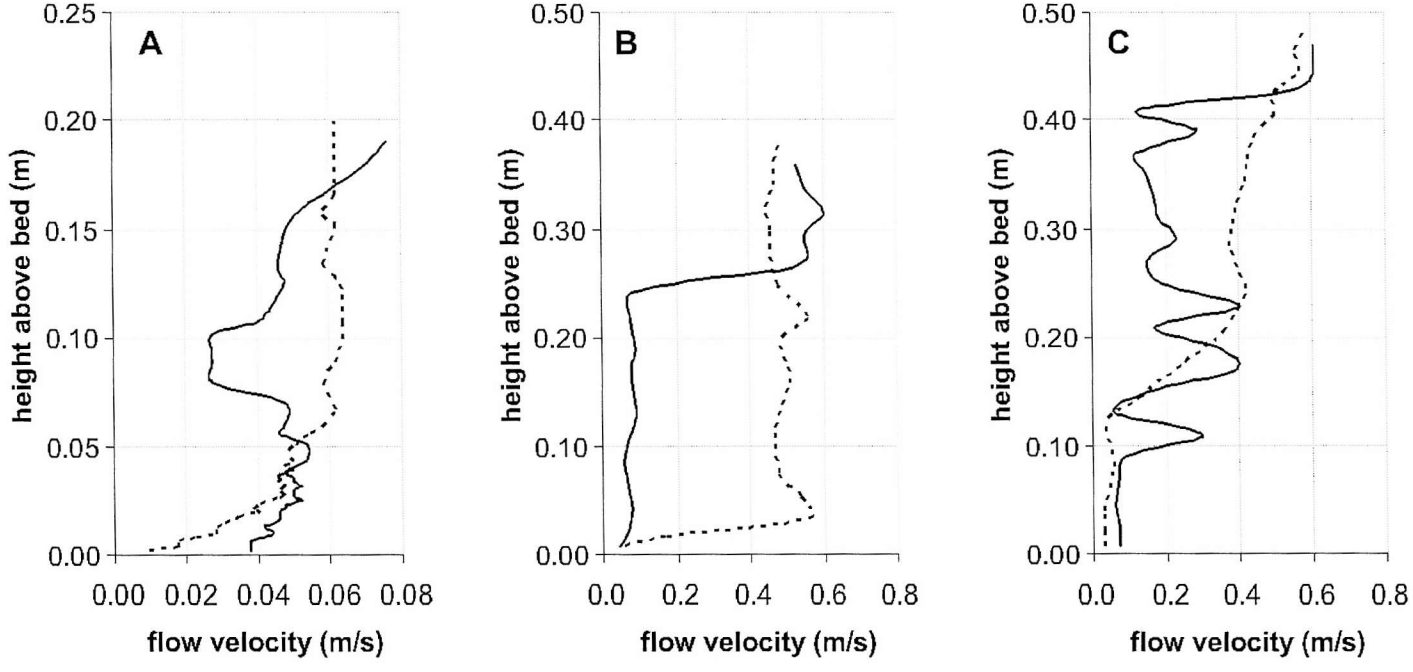

Figure 2.18: Vertical velocity profiles for flow through species of vegetation (solid lines). The velocity profile without vegetation (dashed lines) is taken 50 cm upstream from the vegetated zone. **A**: *Spartina anglica* - unsubmerged (based on Pethick *et al.,* 1990). **B**: *Callitriche cophocarpa* - submerged, vegetation height = 0.25m (based on Sand-Jensen, 1998). **C**: *Sparganium emersum* - submerged, vegetation height = 0.41m (based on Sand-Jensen, 1998). Note the different scales in figure **A**.

and highly dependent on the structure and density of the vegetation (Sand-Jensen and Mebus, 1996; Sand-Jensen, 1998). Similar observations have been made for the velocity profile of air flow through vegetation, which is dependent on height, width, shape, spacing and arrangement of the vegetation (Raupach and Shaw, 1982; Wolfe and Nickling, 1993). The velocity profile is also distorted for flow through emergent vegetation, where wakes of low flow velocity are created behind the plant stems. The wake velocity can be calculated directly for single plants or for groups of plants, by using the drag force method (Li and Shen, 1973; Thompson and Roberson, 1976). For a single stem, the wake velocity is a function of the approach velocity. For groupings of plants, the arrangement and spacing of the vegetation is important as well, as some stems may be located in the wake of upstream plants (Li and Shen, 1973; Thompson and Roberson, 1976).

Because of the reduction in flow velocity, vegetation has often been considered a factor responsible for retarding the flow and reducing the discharge capacity (Stephens *et al.*, 1963; Kouwen *et al.*, 1969; Gwinn and Ree, 1980; Temple, 1982). While river engineers and managers consider this effect beneficial in some cases because it may promote sediment stability, they usually find it undesirable because of an increase of flow depth and flood height. However, the reasoning behind this is based upon the application of increased roughness coefficients over the entire cross-section, while many natural channels only have vegetated banks and an unvegetated channel bed (Masterman and Thorne, 1992). When calculations are performed accounting for sediment beds and vegetated banks, changes in discharge capacity are often found to be negligible or sometimes even positive, especially in rivers with a large width/depth ratio where the banks only form a small part of the wetted perimeter (Darby and Thorne, 1996c; Darby *et al.*, 1997; Darby, 1999).

Turbulence

In general, vegetation acts to damp turbulence by absorbing energy from the flow, and by breaking down large eddies into smaller scale motions (Thorne, 1990; Wolfe and Nickling, 1993). Since the entrainment of particles is directly related to turbulent sweeps of the flow (Jackson, 1976b; Best, 1996), the presence of vegetation should help protect the bank or bed from scour by reducing these turbulent sweeps. Occasionally, however, vegetation may induce turbulence, rather than dampen it. This situation can occur with long flexible plants, which, when deflected, wave in the flow and thus create vortices and erosion

(Sand-Jensen, 1998). Although this effect of flexible vegetation can sometimes be significant, most vegetation induced turbulence is associated with tall, stiff vegetative elements, usually trees. There is considerable turbulence upstream of stiff vegetation elements, which can result in local scour of the bed or bank, especially around the trunk of the tree (Lindsey *et al.,* 1961; Raudkivi, 1990; Graeme and Dunkerley, 1993). Isolated tall, stiff plants may introduce additional turbulence in their wake, and thus become a source of bank erosion (Zimmerman, 1977; Thorne, 1990; Trimble, 1994). This effect is stage dependent, so that vegetation which dampens turbulence at low discharges, can become a cause of increased turbulence at high discharges (Trimble, 1994). The spacing of these tall, stiff vegetative elements thus becomes very important, as well as the frequency of high flow conditions. Dense accumulations of stiff vegetation will serve to protect a bank from flow scour, while sparse vegetation assemblies might achieve the opposite effect (Thorne, 1990).

Sediment transport

Vegetation affects both the entrainment and the transport of sediment. The former is due to the changes in flow velocity through the vegetation, which affect the boundary shear stress and, hence, the forces of fluid drag responsible for sediment entrainment. Furthermore, plants also cover the sediments in its immediate surroundings, thus providing a direct protection against sediment entrainment by channel and overland flow. This effect is further enhanced by soil binding due to the plant roots, which adds extra cohesion to the soil (Thorne, 1990). Apart from preventing sediment particles from being entrained, vegetation also affects the movement of particles already in transport. Plants influence the transport of sediment particles by water flow in two distinct ways. Firstly, the presence of vegetation may promote sedimentation by reducing the flow's capacity to transport sediment (Hupp and Simon, 1991; Hupp and Osterkamp, 1996 ; Sand-Jensen, 1998), although it also has been shown that in some circumstances the sedimentation rate within the vegetated areas can be lower than in the surrounding areas (Pethick *et al.,* 1990). A second, more direct effect of vegetation on sediment transport is the active trapping of sediments by the stem and leaves (Abt *et al.,* 1994; Thornton *et al.,* 1997).

2.6.2. Geotechnical effects of vegetation on bank stability

This domain of research is relatively well developed compared with all other aspects of vegetation effects. The potential of using vegetation as a tool in slope stability improvement has been long recognized by geotechnical engineers, and although there are some differences, much of the knowledge derived from hillslope stability studies can be applied to streambanks as well. The vegetation species may not always be adapted to riparian habitats or suitable for river management purposes, but most of the concepts and processes involved are still applicable to bank slopes. Much of the vast amount of information available has been compiled and several overviews of the impacts of vegetation on slope stability have been made (Lee, 1985; Greenway, 1987; Coppin and Richards, 1990; Gray 1995). The effects of vegetation can be grouped in four categories: root reinforcement, surcharge, impact on bank hydrology and transmission of wind forces. However, recent studies have highlighted several gaps and ambiguities in our understanding of the interactions between these processes in riparian settings (Abernethy and Rutherford, 2000a, 2000b; Simon and Collison, 2002).

Root reinforcement

Vegetation affects mass stability in several ways, but mainly by increasing the shear strength of the soil. Roots add tensile strength to the soil and distribute local stress build-ups over a wider area (Thorne, 1990). Assuming that the roots are elastic and that there is enough anchoring and adhesion so that the roots do not pull out of the soil, the increase in shear stress due to the root system, results in an apparent increase in soil cohesion (Wu *et al.*, 1979). The magnitude of this increase typically ranges between 1 and 20 kPa (Sidle *et al.*, 1985; Simon and Collison, 2002), mainly depending on the density and tensile strength of the roots. A new method to calculate root-induced soil cohesion is developed in section 3.5.4. It should be noted that the reinforcing effect of roots only extends down to the rooting depth, as the root system has to penetrate the failure plane in order to offer any protection versus mass failure (Thorne, 1990; Gray, 1995). When failure occurs along a deeper seated slip surface, the whole segment – including the vegetation – will collapse and slump towards the toe of the bank. However, the roots will continue to bind the failed segment together, and offer protection against shear erosion by the flow (Thorne, 1990).

Bank hydrology

Bank hydrology is an important factor in stability analysis, since it influences the bulk unit weight and the pore pressures within the soil (Simon *et al.,* 1999; Rinaldi and Casagli, 1999). Recent research suggests that the hydrological effects of vegetation can be as important as the mechanical effects (Simon and Collison, 2002). In general, vegetated banks are well drained, as vegetation influences the soil moisture conditions of its environment in several ways (Thorne, 1990). First, precipitation interception and evaporation by the canopy prevents part of the water from reaching the soil. Second, plants actively extract water from the soil, thus reducing soil moisture and increasing matric suction (Simon and Collison, 2002). Additionally, the more open structure of a vegetated soil increases the hydraulic conductivity, thereby lowering the pore pressures. Both these pore pressure changes are beneficial to bank stability (section 2.4.1). However, in some circumstances vegetation may have adverse effects on drainage that prove to be detrimental to bank stability (Simon and Collison, 2002). Excessive moisture extraction may result in the formation of shrinkage cracks, which can lead to increased infiltration and pore pressures, thereby destabilizing the bank with regard to mass failure (Greenway, 1987; Coppin and Richards, 1990). Furthermore, when the cracks are deep enough to penetrate the slip surface, they will shorten the length of the failure plane, which also has an adverse impact on bank stability (Darby and Thorne, 1994). The presence of relic root holes in the soil, after decay of the vegetation, has a similar effect on bank drainage. When growing, roots wedge their way through the soil, pushing sediment aside and opening up fissures in the substrate (Coppin and Richards, 1990). Relic root holes provide pathways for seepage, which may result in soil piping (Thorne, 1990; Hagerty, 1991).

Surcharge

The presence of vegetation can alter the bank weight by external loading of its biomass. The impact of surcharge on bank stability is negligible for herbaceous vegetation, and is usually considered to be more influential for woody vegetation (Greenway, 1987; Thorne, 1990; Gray, 1995). However, recent research suggests that tree surcharge has but a marginal effect on bank stability (Abernethy and Rutherfurd, 2000b). The uncertainty arises because the overall effect of tree surcharge can be both beneficial and detrimental to bank stability, as external loading changes both the downslope component of the bank weight,

which is a driving force in the bank failure mechanisms, and the normal component of bank weight, which is a stabilizing force. The way in which biomass affects the bank stability mainly depends on the angle of the failure plane, which determines the distribution of the additional load over the downslope and normal components of the gravitational force (Thorne, 1990). When considering planar failures, surcharge is beneficial to bank stability when groundwater level and internal friction angle are of high value, and when cohesion and failure angle are of low value (Gray and Megahan, 1981). For rotational failures the position of the trees, relative to the centre of the slip circle is also of importance (Coppin and Richards, 1990; Thorne, 1990).

Windthrow

Wind applies pressure on the vegetation canopy. This pressure is transferred to the root system and as such wind loading may become an additional shearing force. For normal wind speeds this does not have any significance, but winds speeds over 11 m/s (Beaufort scale 6 : strong breeze) may be sufficient to initiate bank slips (Coppin and Richards, 1990). Even if the slope itself is stable enough to avoid failure under wind loading, the trees on it may still be uprooted (Beaufort scale 10; wind speeds over 25 m/s). Apart from slope failures due to wind loading, five additional types of treefall can be recognized: tree leaning, where the fall of the tree is halted by other trees; windsnap, where the stem breaks at a weak point but where root and trunk remain; dead falls, where trees with dead or decaying root systems are uprooted and which involves little soil disturbance; root slab failure, in which a tree fails just below ground and disturbs the top sediment layer; and root ball failure, where a healthy tree is uprooted together with its entire root system and surrounding sediment (Mitchell, 1988). When the uprooting involves sediment disturbance, the process of windthrow can contribute directly to the erosion of the bank (Zimmerman *et al.,* 1967; Gregory and Gurnell, 1988). Treefall is controlled by wind direction and strength, the root pattern, soil moisture conditions, slope and aspect, and root structure (Falinski, 1977; Mitchell, 1988). Tall vegetation with shallow or weak root systems is most susceptible to uprooting (Greenway, 1987; Coppin and Richards, 1990).

2.6.3. Other aspects of riparian vegetation

The numerical model, as developed in the next chapter, focusses on the salient hydraulic and geomorphological impacts discussed in the preceding sections. However, there are many other aspects to riparian vegetation and its relation with the fluvial system. These mainly are related to the vegetation's dynamic life cycle and to its ecological functioning. Although no attempt is made to model these aspects in this study, they are discussed briefly because of their potential significance.

Vegetation dynamics

Vegetation is not static – it grows and changes, both on the level of individual plants and on the level of populations and communities. The dynamism of riparian vegetation communities is, therefore, apparent on various temporal and spatial scales. The continual disturbance, destruction and reconstruction of the riparian landscape, driven by fluvial geomorphic processes, puts existing vegetal communities under pressure and creates opportunity for renewed colonization by pioneering species. As new floodplain surface is created, through bank accretion or channel abandonment, it may be colonized by new vegetation. This process occurs in stages, as floodplain evolves while the river continues to migrate. Typical pioneering species include herbaceous plants, grasses and sedges, as well as various inundation-tolerant species of willow, poplar and alder. The later successional stages show a much wider variety of species, but generally consist of less grasses and more mosses, while woody vegetation tends to include more shade-tolerant species like oaks and elm (Fonda, 1974; Hupp, 1992). Not only the composition of vegetation communities changes through time; individual plants change as well: germinating, growing to maturity and dying. This small-scale dynamism is equally significant for vegetation modelling, as the biophysical properties of the vegetation are likely to change over time (*cf.* section 5.2).

Large woody debris

The model developed herein considers living vegetation only. However, dead woody vegetation which ends up in the river channel may still exert considerable influence on the channel geometry: either through shearing of the banks while in transport (Yanoski, 1982;

Biggs, 1996), or through the formation of debris jams which can influence flow velocity and flow direction (Abbe and Montgomery, 1996; Davis and Gregory, 1994), scour and sediment deposition (Abbe and Montgomery, 1996; Gurnell *et al.*, 2000), bank erosion or bank stabilisation (Keller and Swanson, 1979; Nakamura and Swanson, 1993; Davis and Gregory, 1994), floodplain development (Fetherston *et al.*, 1995; Piégay and Marston, 1998) and the colonisation patterns of vegetation species (Fetherston *et al.*, 1995).

Effects of flow on vegetation

The flow of water is a mixed blessing for riparian vegetation. It is essential to the plants for the supply of oxygen and matter, but it can also be the source of damage and destruction. Just like wind, the flow of water exerts a drag force, which when of sufficient magnitude can damage or destroy vegetation by breaking branches or stems or by uprooting the entire plant (Hupp, 1988; Thorne, 1990). Different species of vegetation have different thresholds to resist vegetation damage, and even within a specific species there can be differences according to age and health of the plants. However, for most species which naturally grow in the riparian zone the tolerance is relatively high, so that significant vegetation damage only occurs during large flood events (Haslam, 1978; Gurnell, 1995; Bendix, 1998). By their nature, many riparian species are adapted to withstand occasional flooding. Most species can withstand a certain level of strain, and damage is rarely fatal (Hooper, 1992). Flattened or bent vegetation will usually recover after the flood, while snapped or broken vegetation will also often continue to grow, except perhaps at the scarred location. Even uprooted trees can sprout new branches when covered with sediments (Everitt, 1968; Hupp, 1988). This ability of plants to recuperate from inflicted damages is, from an engineering point of view, a unique feature. No other construction or engineering material exhibits this level of self-maintenance (Sotir, 1995; Tobias, 1995).

Ecological impacts of vegetation

Riparian zones form the border between the aquatic and terrestrial ecosystems. The dynamic geomorphological, hydrological and ecological interactions that occur along this frontier make riverbanks and their adjacent floodplains some of the most diverse and complex biophysical habitats on the planet (Gregory *et al.*, 1991; Malanson, 1993; Naiman

and Décamps, 1997). The riparian landscape, in all its geomorphological dynamism, hosts an ecosystem with an abundant species richness. In an environment where flooding and erosion are norm rather than disturbance (Bayley, 1995), the hydraulic and geomorphological behaviour of the river can be considered the driving force behind the biodiversity of the ecosystem. Even simplified food-web models, with only few species and generalized assumptions, show a complex dependency on the hydraulics and geomorphology of the riverine environment (Power *et al.,* 1995a; 1995b). The ecological functionality of riparian vegetation can be grouped in a few broad categories: provision of food and shelter, influencing of microclimate, regulation of nutrient and sediment fluxes, and linking of ecosystems (Gregory *et al.,* 1991; Naiman and Décamps, 1997). Thus, vegetation appears to be the key element linking the ever-changing morphology of the riparian landscape to an equally diverse and dynamic ecosystem.

2.7. Conclusion

The alluvial floodplain can be considered as a fluvial landform, constructed and maintained by the river itself, although aeolian, colluvial and anthropogenic entities may be present. As the river meanders and migrates through the floodplain, it continually reworks the floodplain sediments, eroding them in one place and depositing them in another. Alluvial floodplains, and riparian zones in particular, thus are very dynamic geomorphological entities. Any attempt at numerical modelling of this dynamism should include, at a minimum, the salient processes governing the movement of sediment through this system.

Although bank erosion is most readily associated with the dynamic geomorphic behaviour of meandering alluvial rivers, the review in the preceding sections has identified several other processes, agents and controls that contribute to the morphological evolution of the riparian landscape. However, including each of these elements in a numerical model is both infeasible and inappropriate. Models, both numerical and otherwise, are simplified representations of a physical reality (Darby and Van De Wiel, 2003), where part of the simplification involves selecting which processes are relevant to the problem under consideration. For the current study, which focuses on the investigation of the impact of riparian vegetation on geomorphological processes in meandering alluvial rivers (*cf.* section 1.1), the essential elements to be included in the model are listed in table 2.4.

Table 2.4: Processes selected for model representation.

process	discussed in
flow propagation through the channel	section 2.2.2
presence of secondary flow in channel bends	section 2.2.2
fluvial entrainment of bed sediments	section 2.2.3
fluvial entrainment of bank sediments	section 2.3.1
transport of entrained sediments as bed load	section 2.2.3
deposition of entrained sediments	sections 2.2.3 and 2.4.1
geotechnical mass wasting along planar failures	section 2.3.1
basal endpoint control	section 2.3.1
effect of vegetation on flow pattern	section 2.5.1
effect of vegetation on sediment entrainment	section 2.5.1
vegetation surcharge	section 2.5.2
root reinforcement of bank material	section 2.5.2

It is recognized that the additional inclusion of other processes (e.g. rotational and cantilever bank failures, suspended sediment transport, overbank flow, vegetation population dynamics, ...) would be desirable for river engineering and river management purposes, as it would allow application of the model to a wider range of channels. However, inclusion of these processes would introduce many additional variables and potential uncertainties in the model. With respect to the specific investigative aims of this study (*cf.* section 1.1), it is, therefore, considered to be more beneficial to conduct the simulations in a highly simplified and restricted virtual environment, which facilitates the interpretation of the simulation results in terms of the input variables. However, care must be taken when the results and interpretations of such a restrictive model are extrapolated beyond the limited environment as defined by the processes included in the model.

Chapter 3
Model Development

3.1. Introduction

The previous chapter reviewed and identified the salient processes that govern the morphological evolution of alluvial, meandering rivers. This chapter describes the derivation of mathematical expressions for these processes and the development of a new numerical model for the solving them.

In this study, an existing numerical model for the simulation of flow and sediment transport is used as a base platform. Additional routines, accounting for geotechnical bank failure and vegetation effects, are added to this base model, such that all the relevant physical processes (*cf.* table 2.4) are incorporated in the newly developed model. Although several other models exist, the RIPA-model (Mosselman, 1992) is selected as base platform for the model developed herein, because of four specific characteristics that make it suitable to serve this purpose. First, RIPA is specifically designed for simulating flow and bedload sediment transport in meandering rivers. It is part of a long lineage of established flow models developed at Delft Hydraulics and the University of Delft (figure 3.1). In RIPA, the Navier-Stokes equations for flow (equation 2.1 and 2.2) are reduced to a two-dimensional, depth-averaged form, solved using an implicit finite-difference scheme, which explicitly accounts for the presence of secondary flow in meander bends. Second, RIPA discretizes the flow equations on a curvilinear, non-orthogonal, boundary-fitted coordinate system. The possibility of using non-orthogonal grids facilitates simulations involving moving lateral boundaries, which is an inherent aspect of simulations involving channel planform change. Third, RIPA includes a simple bank erosion routine. Although this routine is replaced by a more advanced geotechnical stability analysis in the new model, it does provide the basic infrastructure to do so. And fourth, Dr. Erik Mosselman, kindly agreed to donate the source code of the RIPA-model free of charge. Many commercially available models are prohibitively expensive, while even freely available models usually do not permit access the source code. However, availability of the source code is obviously useful, given the model's role as a base platform, to be expanded with additional or enhanced features and routines.

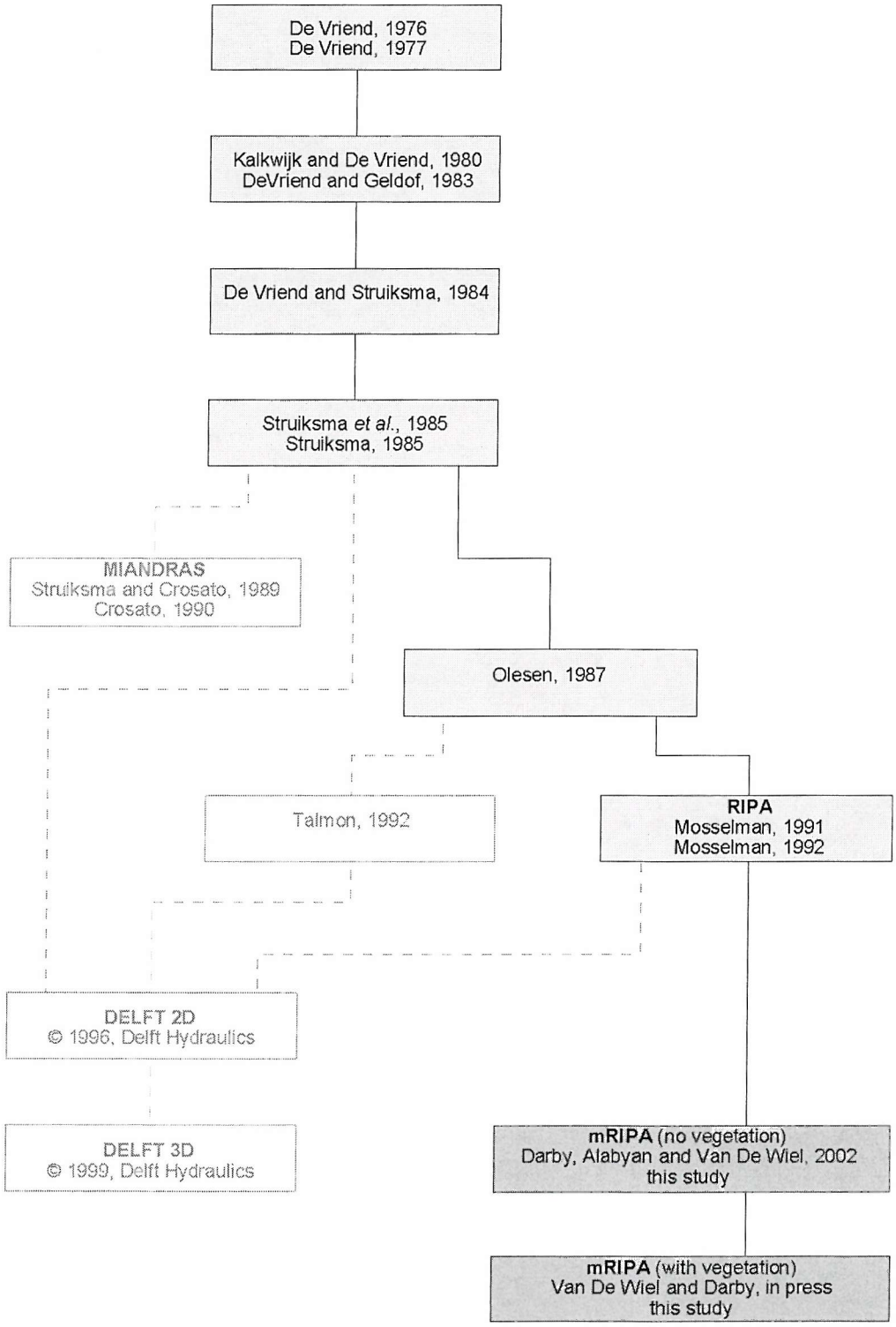

Figure 3.1: Genealogy of the MRIPA model.

For this study, the RIPA-model has been extended to incorporate geotechnical bank failures (Darby, Alabyan and Van De Wiel, 2002) and to account for the effects of riparian vegetation on the geomorphological evolution of the river bed and planform (Van De Wiel and Darby, in press). The new model is named MRIPA, meaning "modified RIPA", and consists of three major components or submodels, respectively addressing the simulation of flow pattern, sediment transport and bank stability. Sections 3.3 and 3.4 describe the flow submodel and the sediment transport submodel, respectively. These sections focus on the modifications made to these submodels to allow for lateral inputs of sediments from geotechnical bank failure and to account for the influence of riparian vegetation. The underlying flow and sediment transport submodels are described briefly, but are not elaborated in detail, as they are almost entirely inherited from RIPA. For a more in-depth analysis of the original flow and sediment transport submodels, the reader is referred to the reports by Olesen (1987) and Mosselman (1991; 1992). In section 3.5, an improved geotechnical bank-stability analysis is developed. This submodel constitutes the core part of MRIPA and will, therefore, be discussed in more detail. It contains a separate sub-section describing how the effects of riparian vegetation are accounted for in the stability analysis. Section 3.6 describes the overall model structure. Particular attention is paid to the links between each of the submodels, and to the assumptions and limitations of the model. However, before discussing any of these topics, a short overview of the essential properties of the model's non-orthogonal coordinate system is given.

3.2. Coordinate system

It is often difficult to represent the geometry of meandering rivers in a Cartesian grid to a sufficient degree of accuracy (figure 3.2A, B). Most approaches in computational fluid dynamics, therefore, use a curvilinear coordinate system (figure 3.2C), which is better suited to represent channel geometry, albeit at the expense of a more complex formulation of the flow equations. In the current study, channel planform is represented using a two-dimensional, non-orthogonal curvilinear coordinate system. The s-direction is taken to follow the streamwise direction of the river, approximately parallel to the streamlines and fitted along the banks. The n-direction is the transverse direction (figure 3.2C). In orthogonal coordinate systems, the n-direction would have to be normal to the s-direction. However, Mosselman (1991; 1992) introduced a technique to relax this condition, thus allowing for

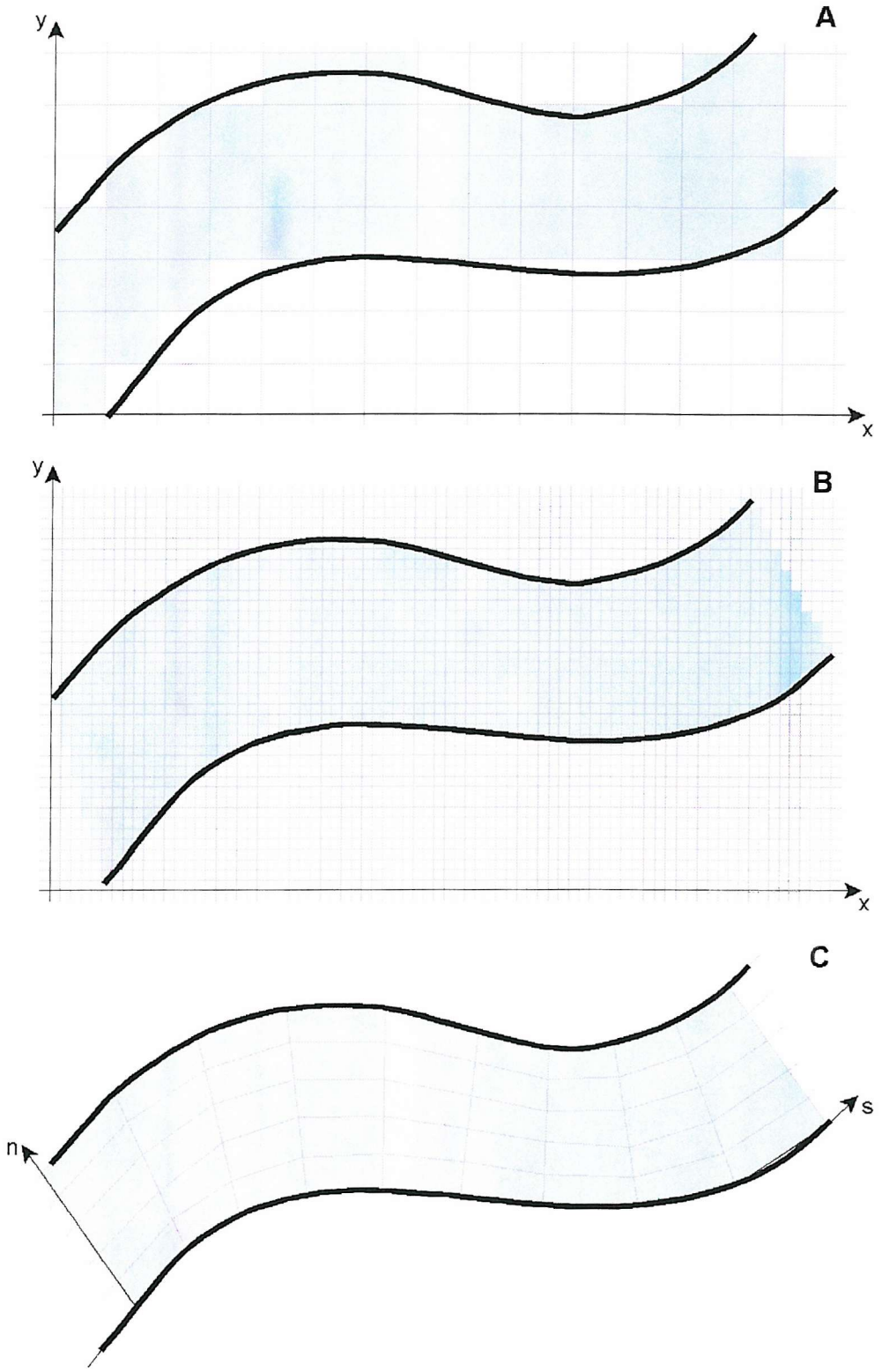

Figure 3.2: Channel representation on different grids. Thick black lines are planform channel boundaries; blue shading depicts how channel area is represented on the grids. **A**: low resolution Cartesian grid: poor accuracy, low computation cost; **B**: high resolution Cartesian grid: improved accuracy, high computation cost; **C**: low resolution curvilinear grid: further accuracy improvements, low computation cost. The Cartesian grids use conventional orthogonal axes (x,y). The curvilinear grid uses streamwise and transverse boundary-fitted axes (s,n).

non-orthogonal coordinate systems, where the n-direction is permitted to deviate from the normal to the s-direction (figure 3.3). The non-orthogonality can be quantified through either of two related quantities, the first being the skewness of the grid, ε, the second being the degree of orthogonality, ε^*. These quantities are defined as:

$$\varepsilon = \cos\varphi_{sn} \tag{3.1}$$

$$\varepsilon^* = \sin\varphi_{sn} = \sqrt{1-\varepsilon^2} \tag{3.2}$$

where φ_{sn} denotes the angle of deviation of orthogonality, *i.e.* the angle between the n-direction and the s-direction (figure 3.3).

In the general case, a river will not have a constant width or curvature. As a result, the coordinate lines are not parallel in a curvilinear coordinate system. The divergence of the coordinate lines can be expressed by the quantities $1/R_s$, denoting the divergence of the transverse coordinate lines (n-direction; note the reverse notation of the subscript), and $1/R_n$, denoting the divergence of the streamwise coordinate lines (s-direction). In orthogonal systems, R_s and R_n would denote the radii of curvature of the streamwise and transverse coordinates, respectively. In non-orthogonal systems this simple relationship does not hold, and no direct physical or geometrical interpretation can be attached to R_s and R_n themselves, other than being the reciprocals of the divergence of coordinate lines. General expressions for the quantities $1/R_n$ and $1/R_s$, in terms of the base-vectors of the coordinate system, are derived by Mosselman (1991; 1992). These expressions are not reproduced here to avoid a lengthy mathematical digression concerning the base-vectors of the coordinate system.

Even though the calculations are performed on a non-orthogonal grid, it is often more convenient to represent vectors in a local orthogonal system. For example, the flow velocity, U, can, in a non-orthogonal system, be split into streamwise and transverse components, U_s and U_n. These can be transformed into their respective local orthogonal counterparts, $\tilde{U}_s$ and $\tilde{U}_n$, using (figure 3.4):

$$\tilde{U}_s = U_s + \varepsilon U_n \tag{3.3}$$

$$\tilde{U}_n = \varepsilon^* U_n \tag{3.4}$$

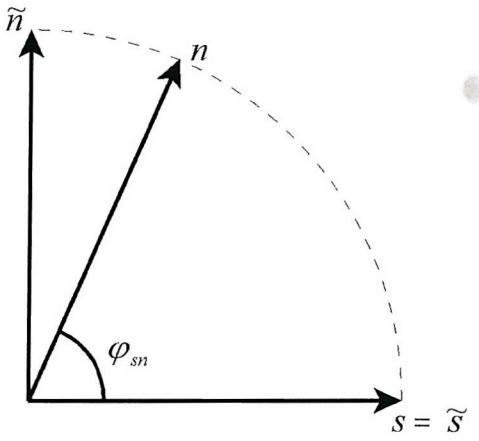

Figure 3.3: Directions of axes in an orthogonal and a non-orthogonal coordinate system (after Mosselman, 1992). Orthogonal axes are marked with a tilde. The angle φ_{sn} marks the orientation of the *n*-axis with respect to the *s*-axis. In orthogonal systems φ_{sn} is equal to 90 degrees.

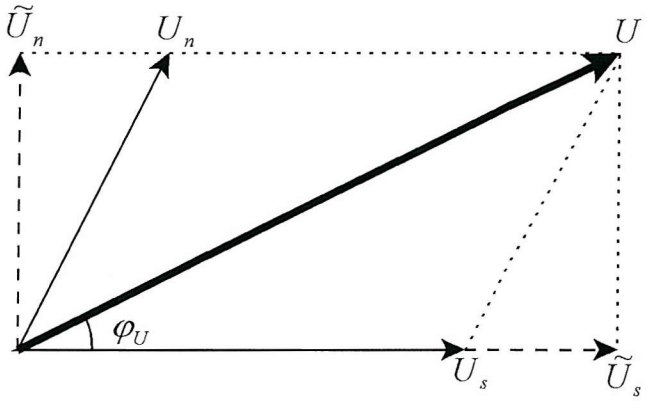

Figure 3.4: Components of a vector, *U*, in an orthogonal and a non-orthogonal system (after Mosselman, 1992). Orthogonal vector components are marked with a tilde. The angle φ_U defines the orientation of the vector with respect to the *s*-axis.

Using the local orthogonal system also facilitates the determination of the direction and magnitude of vectors. The direction of a vector is defined as an angle φ between the vector and the s-direction. Continuing form the previous example, the magnitude, $|U|$, and the direction, φ_U, of the flow velocity vector, U, are obtained as (figure 3.4):

$$|U| = \sqrt{\widetilde{U}_s^2 + \widetilde{U}_n^2} = \sqrt{U_s^2 + U_n^2 + 2\varepsilon U_s U_n} \tag{3.5}$$

$$\tan\varphi_U = \frac{\widetilde{U}_n}{\widetilde{U}_s} = \frac{\varepsilon^* U_n}{U_s + \varepsilon U_n} \tag{3.6}$$

Similar expressions can be obtained for other vectors that are used within the model.

3.3. Flow submodel

The flow submodel in MRIPA is, like most other computational fluid dynamic models, based on finding an approximate solution to the Navier-Stokes equations, which describe the motion of fluids (section 2.2). As mentioned in the previous section, a two-dimensional, non-orthogonal, curvilinear grid is used. The governing equations must, therefore, be adapted to fit this form. In this section a summary of the most relevant terms and equations is presented. First, the equations are described for orthogonal coordinate systems. Extensions for the more general non-orthogonal system are discussed next, followed by a short overview of the numerical implementation. Finally, the method for modelling the effects of vegetation on flow hydraulics is described. With the exception of this last topic, the contents of this section are largely based on the more extensive treatments by Olesen (1987), Mosselman (1992) and Darby, Alabyan and Van De Wiel (2002).

3.3.1. Flow equations for orthogonal coordinate systems

The flow equations are reduced to two-dimensional form by depth-averaging the full set of Navier-Stokes equations. In RIPA a self-similarity hypothesis is applied to facilitate the depth-averaging procedure. This hypothesis states that the vertical velocity profile of

primary and secondary flow are self-similar, an assumption which is said to holds for shallow, mildly curved channels[1] (De Vriend, 1981). Applying the self-similarity hypothesis, the continuity and momentum equations for a two-dimensional orthogonal, curvilinear coordinate system can be expressed as (Kalkwijk and De Vriend, 1980; Mosselman, 1992):

$$\frac{\partial(hU_s)}{\partial s} + \frac{\partial(hU_n)}{\partial n} + \frac{hU_s}{R_s} + \frac{hU_n}{R_n} = 0 \tag{3.7}$$

and

$$U_s \frac{\partial U_s}{\partial s} + U_n \frac{\partial U_s}{\partial n} + \frac{1}{\rho}\frac{\partial p}{\partial s} + \frac{U_s U_n}{R_s} - \frac{U_n}{R_n} + \frac{\tau_{bs}}{\rho h} = 0 \tag{3.8a}$$

$$U_s \frac{\partial U_n}{\partial n} + U_n \frac{\partial U_n}{\partial n} + \frac{1}{\rho}\frac{\partial p}{\partial n} + \frac{U_s U_n}{R_n} - \frac{U_s}{R_s} + \frac{\tau_{bn}}{\rho h} = 0 \tag{3.8b}$$

where s and n respectively are the streamwise and transverse directions, U_s and U_n are the corresponding components of the flow velocity, τ_{bs} and τ_{bn} are the corresponding components of the bed shear stress, $1/R_n$ denotes the divergence of the streamwise coordinate lines, $1/R_s$ represents the divergence of the transverse coordinate lines, p is pressure, h is flow depth, and ρ is the density of water.

Further expansion of the momentum equations (equations 3.8a and 3.8b) is obtained by elaborating the pressure and friction terms. Assuming hydrostatic water pressure, the following relation is obtained:

$$p = \rho g z_w = \rho g(z_b + h) = \rho g z_b + \rho g h \tag{3.9}$$

---

[1] The terms "shallow"and "mildly curved" are rather vague, and there does not appear to a consensus over their meaning. Kalkwijk and Booij (1986) provide some apparently arbitrary guidelines, suggesting $W/d > 10$ for shallow channels and $r_c/W > 5$ for mildly curved channels, where W denotes channel width, d is the flow depth and r_c is the radius of curvature of the channel centre line. However, Struiksma *et al.* (1985) and Olesen (1987) include simulations, using the same flow model as Kalkwijk and Booij (1986), where $r_c/W < 2.5$. In this study it is assumed that "sharply curved" is defined by $r_c/W < 2.5$, while "mildly curved" is defined by $r_c/W > 5.0$, with a fuzzy transition in between. It is worth noting that this fuzzy zone coincides with the bend curvatures that induce highest lateral erosion rates (*cf.* figure 2.8)

where z_w and z_b denote water level and bed level, respectively, and g is the gravitational acceleration. The bed shear stress components in the friction terms are defined as:

$$\tau_{bs} = \frac{\rho g|U|}{C^2} U_s \tag{3.10}$$

$$\tau_{bn} = \frac{\rho g|U|}{C^2} U_n \tag{3.11}$$

where C denotes the Chezy coefficient for hydraulic roughness. As a first approximation, the magnitude of the flow velocity vector, $|U|$, can be taken to be equal to the primary flow velocity, U_s (*i.e.* assuming $U_n \ll U_s$ and *cf.* equation 3.5). Applying this approximation, and inserting equations 3.9, 3.10 and 3.11 in equations 3.8a and 3.8b, the flow momentum equations can be rewritten as:

$$U_s \frac{\partial U_s}{\partial s} + U_n \frac{\partial U_s}{\partial n} + \frac{U_s U_n}{R_s} - \frac{U_n^2}{R_n} + g\frac{\partial z_b}{\partial s} + g\frac{\partial h}{\partial s} + \frac{gU_s^2}{hC^2} = 0 \tag{3.12a}$$

$$U_s \frac{\partial U_n}{\partial n} + U_n \frac{\partial U_n}{\partial n} + \frac{U_s U_n}{R_n} - \frac{U_s^2}{R_s} + g\frac{\partial z_b}{\partial n} + g\frac{\partial h}{\partial n} + \frac{gU_s U_n}{hC^2} = 0 \tag{3.12b}$$

When the transverse flow velocity, U_n, is not equal to zero, the flow streamlines deviate slightly from the streamwise coordinate lines. Hence, the flow streamline curvature, R_f, is, in general, similar but not necessarily equal to the curvature of the streamwise coordinate line, R_s. An expression for the relation between these two quantities was first proposed by De Vriend (1976), and later simplified by Olesen (1987):

$$\frac{1}{R_f} = \frac{1}{R_s} - \frac{1}{U_s}\frac{\partial U_n}{\partial s} \tag{3.13}$$

Curved streamlines induce secondary flow, which, in turn, deforms the horizontal distribution of the primary flow. The transverse exchange of momentum that follows from this redistribution of the primary flow can, in depth-averaged models, be represented by incorporating an additional acceleration or friction term, F_{sf}, to the streamwise momentum equation (De Vriend, 1976; Kalkwijk and De Vriend, 1980). The last term of equation 3.12a is then expanded as:

$$\frac{gU_s^2}{hC^2} \mapsto \frac{gU_s^2}{hC^2} + k_{sn}\frac{U_s^2}{h}\frac{\partial}{\partial n}\left(\frac{i_s h}{U_s}\right) \tag{3.14}$$

in which k_{sn} and i_s are two parameters describing the secondary flow: i_s represents the secondary flow intensity and k_{sn} denotes the secondary flow convection factor, which is treated as a calibration parameter (section 4.3). The development of the secondary flow intensity is described by (De Vriend, 1981; Struiksma *et al.*, 1985):

$$\lambda_r \frac{\partial i_s}{\partial s} + i_s = \frac{h|U|}{R_f} \approx \frac{h U_s}{R_f} \tag{3.15}$$

where λ_r denotes the adaptation length of the secondary flow. It is small compared to other length scales in the flow model and may be omitted from flow calculations (but not from sediment transport calculations, see below), *i.e.* secondary flow is assumed to adapt immediately to the channel geometry. Hence, the above relation may be reduced to:

$$i_s = \frac{h|U|}{R_f} \approx \frac{h U_s}{R_f} \tag{3.16}$$

Equation 3.14 formally applies to characteristics that do not coincide with the streamlines, but that gradually shift towards the concave bank (Kalkwijk and De Vriend, 1980). However, the error induced by applying the relation along the streamwise coordinate lines is negligible for mildly curved channels (Mosselman, 1992).

Using equations 3.14 and 3.16, the streamwise momentum equation (equation 3.12a) may now be rewritten as:

$$U_s \frac{\partial U_s}{\partial s} + U_n \frac{\partial U_s}{\partial s} + \frac{U_s U_n}{R_s} - \frac{U_n^2}{R_n} + g\frac{\partial z_b}{\partial s} + g\frac{\partial h}{\partial s} + \frac{U_s^2 g}{hC^2} + k_{sn}\frac{U_s^2}{h}\frac{\partial}{\partial n}\left(\frac{h^2}{R_f}\right) = 0 \qquad (3.17a)$$

3.3.2. Flow equations for non-orthogonal coordinate systems

The relations derived above (equations 3.7 to 3.17) hold for orthogonal curvilinear systems. In the MRIPA model the orthogonality condition is relaxed, and the equations are expanded to allow for non-orthogonal curvilinear coordinate systems (Mosselman, 1991; 1992). This is achieved by accounting for the skewness of the grid (equations 3.1 and 3.2), and mapping the orthogonal flow velocity components to their non-orthogonal counterparts (*cf.* equations 3.3 and 3.4):

$$U_s \quad \mapsto \quad U_s + \varepsilon U_n \qquad (3.18)$$

$$U_n \quad \mapsto \quad \varepsilon^* U_n \qquad (3.19)$$

The equations from section 3.3.1 can then be expanded into non-orthogonal form. Thus, equations 3.16 and 3.13 become:

$$i_s \approx \frac{h\left(U_s + \varepsilon U_n\right)}{R_f} \qquad (3.20)$$

$$\frac{1}{R_f} = \frac{1}{R_r} - \frac{1}{U_s + \varepsilon U_n}\frac{\partial\left(\varepsilon^* U_n\right)}{\partial s} \qquad (3.21)$$

in which R_r denotes the radius of curvature of the streamwise coordinate line, which, for non-orthogonal grids, does not correspond with R_s (Mosselman, 1991; 1992). Likewise, and again assuming $U_n \ll U_s$, the expressions for the components of the bed shear stress (equations 3.10 and 3.11) become:

$$\tau_{bs} = \frac{\rho g}{C^2}\left(U_s^2 + \varepsilon U_s U_n\right) \tag{3.22}$$

$$\tau_{bn} = \frac{\rho g}{C^2}\left(U_s U_n + \varepsilon U_n^2\right) \tag{3.23}$$

Using these relations, and applying a similar expansion of the flow velocity components, the flow equations are then expressed as (Mosselman, 1991; 1992):

$$\frac{\partial\left(hU_s\varepsilon^*\right)}{\partial s} + \frac{\partial\left(hU_n\varepsilon^*\right)}{\partial n} + \frac{hU_s\varepsilon^*}{R_n} + \frac{hU_n\varepsilon^*}{R_s} = 0 \tag{3.24}$$

$$\begin{aligned} U_s\frac{\partial U_s}{\partial s} + U_n\frac{\partial U_s}{\partial n} + \varepsilon U_s\frac{\partial U_n}{\partial s} + \varepsilon U_n\frac{\partial U_n}{\partial n} + \left(\frac{1}{R_s} - \frac{\varepsilon}{R_n}\right)U_sU_n - \left(\frac{\varepsilon}{R_s} - \frac{1}{R_n} + \frac{\partial\varepsilon}{\partial n}\right)U_n^2 \\ + g\frac{\partial z_b}{\partial s} + g\frac{\partial h}{\partial s} + \frac{g}{hC^2}\left(U_s^2 + \varepsilon U_sU_n\right) \\ + k_{sn}\frac{\left(U_s^2 + 2\varepsilon U_sU_n + \varepsilon^2U_n^2\right)}{h}\frac{\partial}{\partial\tilde{n}}\left(\frac{h^2}{R_f}\right) = 0 \end{aligned} \tag{3.25a}$$

$$\begin{aligned} \varepsilon U_s\frac{\partial U_s}{\partial s} + \varepsilon U_n\frac{\partial U_n}{\partial n} + U_s\frac{\partial U_n}{\partial s} + U_n\frac{\partial U_n}{\partial n} + \left(\frac{1}{R_n} - \frac{\varepsilon}{R_s}\right)U_sU_n - \left(\frac{\varepsilon}{R_n} - \frac{1}{R_s} + \frac{\partial\varepsilon}{\partial s}\right)U_s^2 \\ + g\frac{\partial z_b}{\partial n} + g\frac{\partial h}{\partial n} + \frac{g}{hC^2}\left(U_sU_n + \varepsilon U_n^2\right) = 0 \end{aligned} \tag{3.25b}$$

where $\tilde{n}$ denotes the n-direction in the local orthogonal system, *i.e.* the normal to the s-direction. Rearranging terms and using equation 3.21 to obtain $\partial U_n/\partial s$, the momentum equations can be rewritten as (Mosselman, 1991):

$$g\frac{\partial z_w}{\partial s} + \frac{1}{2}\frac{\partial U_s^2}{\partial s} + N_A U_s^2 + N_B = 0 \tag{3.26a}$$

$$g\frac{\partial z_w}{\partial n} + N_C U_s^2 + N_D = 0 \tag{3.26b}$$

where N_A, N_B, N_C, N_D are functions of U_s and U_n, defined as:

$$N_A = \varepsilon N_1 + N_2 \tag{3.27}$$

$$N_B = \left(\frac{\partial U_s}{\partial n} + \varepsilon\frac{\partial U_n}{\partial n}\right)U_n + \left(\varepsilon^2 N_2 + \frac{\varepsilon}{R_s} - \frac{1}{R_n} + \frac{\partial \varepsilon}{\partial n}\right)U_n^2$$
$$+ \left(\varepsilon^2 N_1 + 2\varepsilon N_2 + \frac{1}{R_s} - \frac{\varepsilon}{R_n} + \frac{\varepsilon^2}{\varepsilon^{*2}}\frac{\partial \varepsilon}{\partial s}\right)U_s U_n \tag{3.28}$$

$$N_C = N_1 + \varepsilon N_2 - \frac{1}{R_s} + \frac{\varepsilon}{R_n} + \frac{\partial \varepsilon}{\partial s} \tag{3.29}$$

$$N_D = \varepsilon U_s \frac{\partial U_s}{\partial s} + \left(\varepsilon\frac{\partial U_s}{\partial n} + \frac{\partial U_n}{\partial n}\right)U_n + \left(\varepsilon^3 N_2 + \frac{\varepsilon\varepsilon^{*2} g}{hC^2}\right)U_n^2$$
$$+ \left(\varepsilon N_1 + 2\varepsilon^2 N_2 + \frac{\varepsilon^{*2} g}{hC^2} - \frac{\varepsilon}{R_s} + \frac{1}{R_n} + \frac{\varepsilon^2}{\varepsilon^{*2}}\frac{\partial \varepsilon}{\partial s}\right)U_s U_n \tag{3.30}$$

in which the auxiliary functions, N_1 and N_2, are given as:

$$N_1 = \frac{1}{\varepsilon^{*2}}\left(\frac{1}{R_r} - \frac{1}{R_f}\right) \tag{3.31}$$

$$N_2 = \frac{g}{hC^2} + \frac{k_{sn}}{h}\frac{\partial}{\partial \tilde{n}}\left(\frac{h^2}{R_f}\right) \tag{3.32}$$

3.3.3. Numerical implementation

The river channel bed is discretized as a curvilinear grid of points. In the general case, neither the longitudinal spacing of grid points, Δs, nor the transverse spacing of points, Δn, are constant in space (figure 3.5). Representing a function $\partial f/\partial x$ on such a discretized curvilinear grid induces a truncation error, T_x (Thompson *et al.*, 1985). It is not possible to derive a generalized expression for this truncation error, due to the dependence of T_x on the directions of the coordinate lines with respect to the xy-directions of a Cartesian grid. However, using a simplified error analysis on a restricted curvilinear grid, where all n-axes are presumed to be parallel to the y-axis of a Cartesian grid (figure 3.6), Mosselman (1991; 1992) shows that T_x is determined as:

$$T_x = -\frac{1}{2}\Delta s\frac{\partial(\varepsilon^*\Delta s)}{\partial s}\frac{\partial^2 f}{\partial x} - \frac{1}{4}\Delta s\left(\frac{\varepsilon}{\varepsilon^*}\frac{\partial(\varepsilon^*\Delta s)}{\partial s}+\frac{\partial(\varepsilon\Delta s)}{\partial s}\right)\frac{\partial^2 f}{\partial x\partial y} + \frac{1}{2}\frac{\varepsilon}{\varepsilon^*}\left(\Delta n\frac{\partial\Delta n}{\partial n}-\Delta s\frac{\partial(\varepsilon\Delta s)}{\partial s}\right)\frac{\partial^2 f}{\partial y^2} + h.o.t. \qquad (3.33)$$

where Δs and Δn represent the longitudinal and transverse coordinate differences and *h.o.t.* is an abbreviation for 'higher order terms'. For orthogonal grids ($\varepsilon = 0$; $\varepsilon^* = 1$), the second and third terms are equal to zero, and the expression is reduced to:

$$T_x = -\frac{1}{2}\Delta s\frac{\partial(\Delta s)}{\partial s}\frac{\partial^2 f}{\partial x^2} + h.o.t. \qquad (3.34)$$

The term $\partial(\Delta s)/\partial s$ denotes the longitudinal gradient of grid point spacing, while $\partial^2 f/\partial x^2$ represents a numerical diffusion of the function $\partial f/\partial x$. Since this numerical diffusion term can also be negative, it can be destabilizing. The numerical grid, on which the flow equations are solved, should, therefore, be constructed in such a way that the truncation error is minimized.

The model employs a simple grid generator (Mosselman, 1991), based on algebraic interpolation. Grid generation requires, for each of the cross-sections, the coordinates for

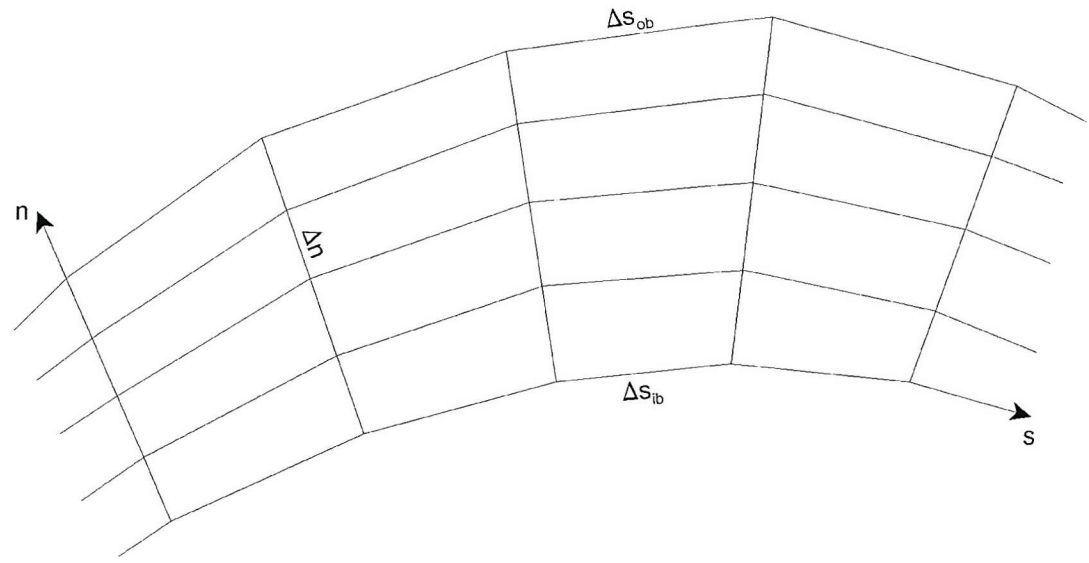

Figure 3.5: Spacing in a curvilinear grid does not have to be constant in space. The longitudinal distance between two consecutive grid points, Δs, will usually be smaller along the inside bend than on the outside bend: $\Delta s_{ib} < \Delta s_{ob}$. Similarly, the transverse spacing of grid points, Δn, may vary in widening or narrowing channels.

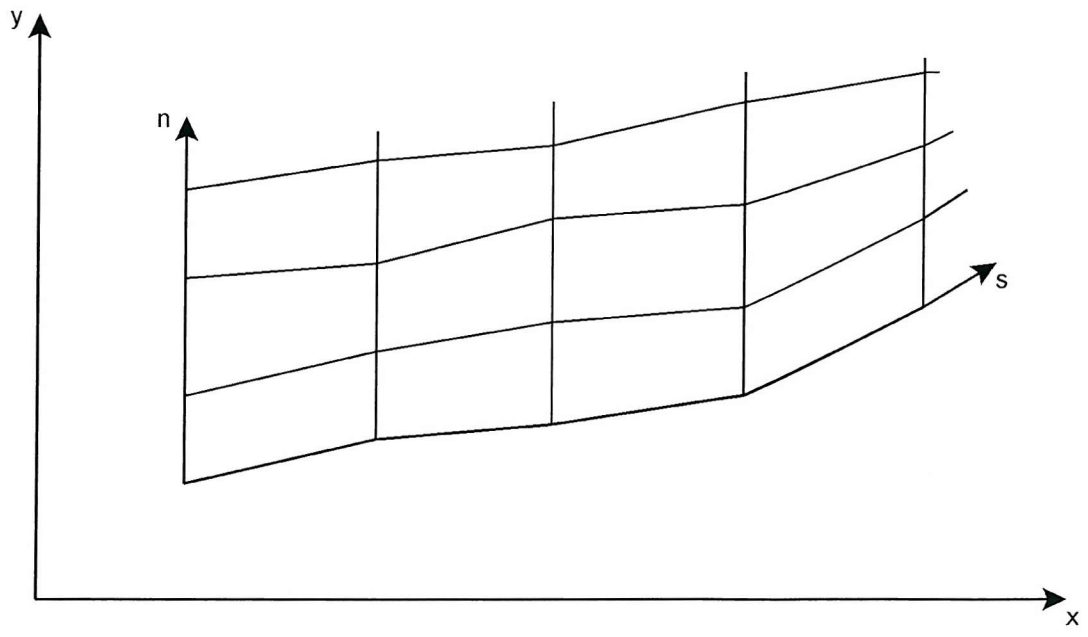

Figure 3.6: Example of curvilinear grid where all *n*-axes are parallel to the Cartesian *y*-axis.

points on the right and left bank. From equations 3.33 and 3.34 it follows that, in order to improve accuracy of the solution, the longitudinal gradient of point spacing should be minimized, *i.e.* the distribution of points along the bank should be smooth. Equation 3.33 also suggests that it is best to minimize the skewness of the grid. This implies that, although orthogonality of the grid is not required, it is recommended not to deviate too much from it. Using a cubic interpolation method, orthogonality can be imposed on the grid along the banks (Mosselman, 1992). The grid is constructed such that the curvilinear coordinate lines are more or less parallel to the stream lines and the banks. The automated grid generator is invoked several times during a simulation, to allow for planform changes induced by bank erosion (section 3.4.4). After bank erosion, bank points are moved perpendicular to the bank lines, not along the bank lines. Thus, repeated deformation of the grid may result in steeper gradients of grid point spacing and, hence, in instability. It may, therefore, be necessary to interrupt long simulations and manually adjust the bank point spacing.

Equations 3.24, 3.26a and 3.26b are solved over the numerical grid using a second order central difference scheme. The discretization procedure follows Kalkwijk and De Vriend (1980) and is fully explained by Mosselman (1991) and Darby, Alabyan and Van De Wiel (2002). The steady-state solution is obtained starting from an estimated initial state and using time as a natural iteration parameter (Struiksma, 1985). An iterative scheme is adopted (figure 3.7), in which, for each of the cross-sections in the reach, consecutive estimates of U_s^2 are improved until the total water flux through a cross-section equals the specified discharge. From U_s^2 the value for U_s can be obtained directly, while U_n is obtained using the continuity equation. These values are then inserted in equations 3.27 to 3.30, and are used to find a new estimate for U_s^2. Solving the equations in terms of U_s^2 implies that return flows ($U_s < 0$) cannot be detected. This, again, accentuates the restriction of the application domain to mildly curved channels ($R_c/W > 5.0$). In RIPA the initial estimates of U_s^2 are made along the right bank. For certain combinations of channel geometry and discharge, the iteration procedure converges to negative values of U_s^2, which is, by definition, not allowed. To improve on this issue, the MRIPA model also allows users to start estimates along the left bank or at the centre line. Where U_s^2 is still negative, in spite of the improvements, it is assumed that the magnitude of the flow velocity equals zero ($U_s = 0$; $U_n = 0$) and that the streamline curvature equals the local curvature of the coordinate line ($R_f = R_r$). The cross-sectional flux is obtained through a Simpson-integration, which theoretically is only valid for equidistant transverse point spacing, but which is of sufficient accuracy for small variations in point spacing (Mosselman, 1992).

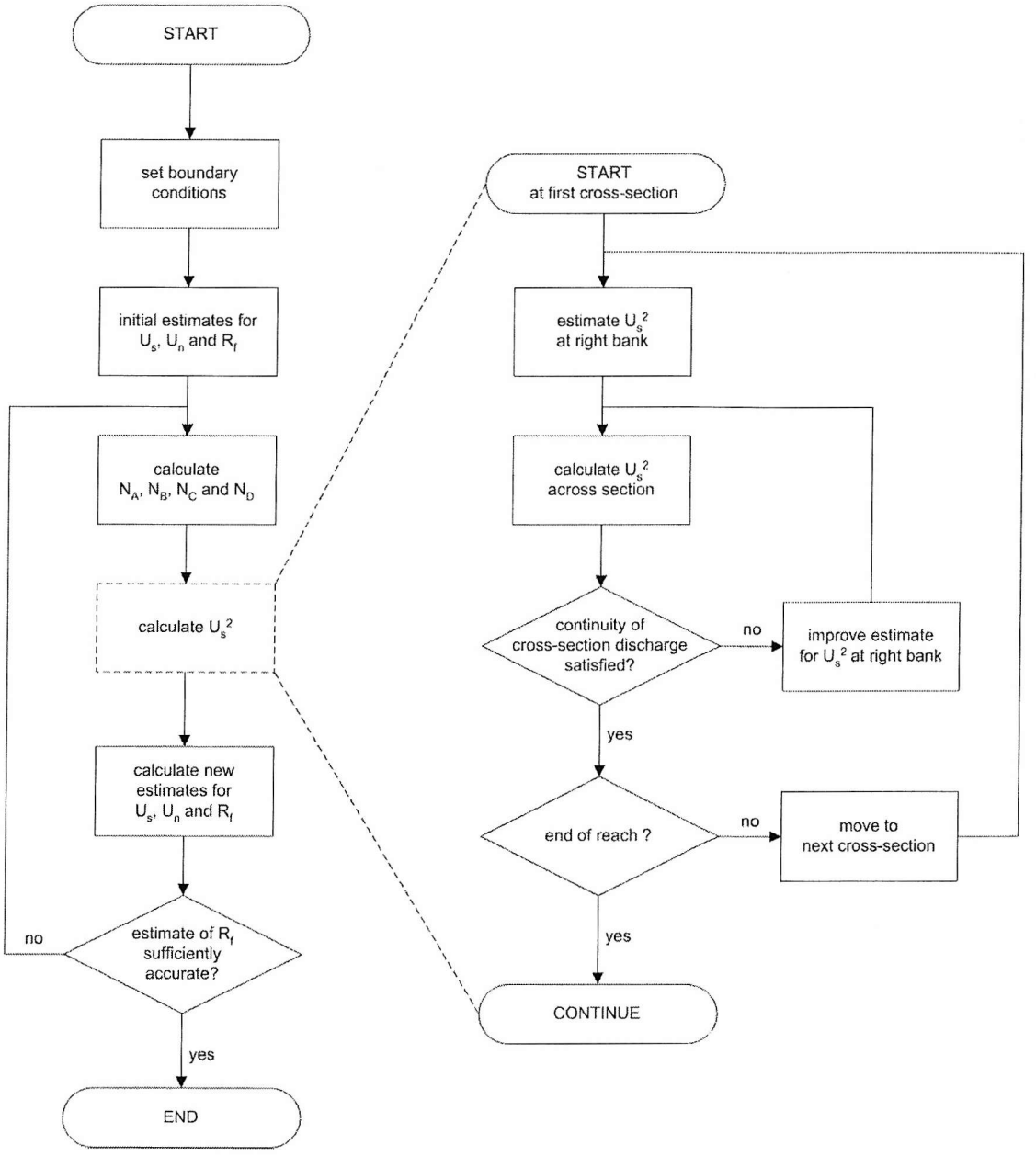

Figure 3.7: Schematic representation of the flow field calculation procedure.

Assuming that flow in the channel is subcritical and Froude numbers are small, a rigid lid approximation is applied at the water surface. Thus, bed topography can then be represented by the distribution of flow depths. At the banks, the secondary flow is assumed to be equal to zero. The depth-averaged model is not very accurate near steep banks, because lateral friction is ignored and because the self-similarity hypothesis, underlying the depth-averaging procedure, is not valid in the near-bank zone (Mosselman, 1992). The resulting unreliable growth of primary flow velocity near concave banks is suppressed through an artificial correction for the near bank decay of secondary flow intensity (Olesen, 1987). In effect, equation 3.16 is modified to:

$$i_s \approx \frac{hU_s}{R_f}\left(1-\left|\frac{2n_L}{B}\right|^q\right) \tag{3.35}$$

where n_L is the transverse distance to the centerline, B represents the channel width and q is an "exponent of artifice" (terminology by Olesen, 1987). The term $2n_L/B$ is a normalized transverse distance measure. The bracketed term is a reduction coefficient, such that the secondary flow intensity is maximized in the centre of the channel, and minimized along the banks (figure 3.8). Empirical values for q range from $q = 2$ for flumes (Olesen, 1987) to $q = 6$ for natural channels (Ananyan 1957; referenced by Olesen, 1987). However, it is found that numerical stability is improved for smaller values of q (Olesen, 1987). In the current study, q is taken equal to 2, in accordance with Olesen's recommendations.

3.3.4. Effects of vegetation on flow

Vegetation interacts with the flow in several ways. The main effects are a change in channel roughness and the associated change of flow velocities, redirection of flow, lateral exchange of momentum and the creation of turbulence (section 2.6.1). Obviously, these effects only occur when at least part of the vegetation is submerged by the flow.

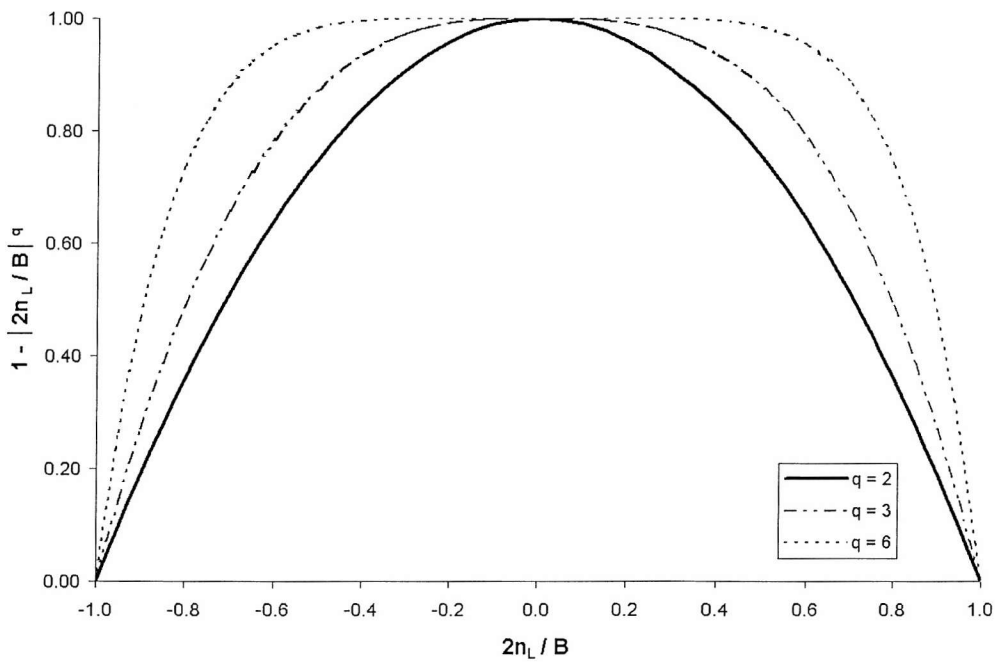

Figure 3.8: Cross-channel distribution of the reduction coefficient in equation 3.35, for different values of the exponent *q*. Values on the *X*-axis are normalized distances to the centre of the channel. The reduction coefficient equals unity (no reduction) in the centre of the channel and gradually diminishes towards the banks, where it equals zero (full reduction). (after Olesen, 1987)

Roughness and flow velocity

A change in total channel roughness affects the flow velocities, as is clear from the two-dimensional momentum equations (equations 3.25a and 3.25b). The total channel roughness is a function of both the channel's geomorphology and its vegetation (section 2.6.1). As the vegetation can be spatially variable, MRIPA differs from the original RIPA in that it allows for roughness to be specified locally (*i.e.* at each grid cell). Following the ideas mentioned in section 2.6.1, the total roughness at a point can be considered as a summation of the roughness of the unvegetated channel and the roughness of the vegetation at that point. The relation derived by Petryk and Bosmajian (1975) can be expressed, in terms of Manning's n, as:

$$n_{tot} = \sqrt{n_{bare}^2 + n_{veg}^2} \tag{3.36}$$

which, when expressed in terms of Chezy C, becomes:

$$C_{tot} = \frac{C_{bare}\, C_{veg}}{\sqrt{C_{bare}^2 + C_{veg}^2}} \tag{3.37}$$

where the subscripts $_{bare}$, $_{veg}$ and $_{tot}$ refer to unvegetated, vegetated and total roughness, respectively. The same relation can also be derived from the work of Lindner (1982). Where the vegetation roughness is very small, relative to the unvegetated channel roughness ($C_{veg} \gg C_{bare}$), equation 3.37 reduces to the trivial case $C_{tot} \approx C_{bare}$. Similarly, where the roughness induced by the vegetation is much larger than that of the unvegetated channel ($C_{veg} \ll C_{bare}$), the total roughness approximately corresponds to the vegetation roughness, so that $C_{tot} \approx C_{veg}$.

The vegetation roughness is commonly represented as a fixed value dependent on vegetation species only. In this respect, empirical values for n_{veg} or C_{veg} can be found in a few well-known publications (e.g. Chow, 1959; Barnes, 1967; Arcement and Schneider, 1989). This approach is very convenient – and easily implemented from a modelling point of view – but ignores some important elements: the variation of biophysical properties within a species, the effect of vegetation density, and the dependency of the roughness on flow

velocity (section 2.6.1). In the current work, therefore, vegetation roughness is determined from biophysical properties of both the plants and the flow. This alternative approach, as developed in the next paragraph, is more in line with recent research on the interactions between flow and vegetation (Fathi-Moghadam and Kouwen, 1997; Freeman *et al.*, 1998; Rahmeyer *et al.*, 1999). It is particularly relevant to submerged flexible vegetation, but is equally applicable to rigid or emergent vegetation.

The vegetation roughness can be determined from basic physical principles. Many researchers (Petryk and Bosmajian, 1975; Lindner, 1982; Rahmeyer *et al.*, 1999; Kouwen and Fathi-Moghadam, 2000) have expressed vegetation roughness in a form similar to:

$$C_{veg} = \sqrt{\frac{2g}{C_d}\frac{1}{A_v}} \tag{3.38}$$

where C_d is a species-dependent drag coefficient, and A_v is the projected area of the vegetation normal to the flow, which depends on both the density of the vegetation and the shape of the plants. The problem with the application of equation 3.38 is that, for flexible vegetation, A_v not only depends on vegetation properties, but also on the local flow velocities, which are themselves dependent on roughness (*cf.* figure 2.17). Applying the common assumption that the main contribution to the vegetation roughness is derived from the plant stem, and that the stem can be represented as a cylinder, the projected vegetation area can be calculated from:

$$A_v = \sigma_{v,n} d_v H_v^* \tag{3.39}$$

where $\sigma_{v,n}$ denotes the lateral spacing of vegetation elements, d_v is the stem diameter and H_v^* is the projected height of the plant. For emergent plants, H_v^* corresponds to the local flow depth. For submerged vegetation it can be calculated as:

$$H_v^* = H_v \cos\alpha_v \tag{3.40}$$

in which H_v is the vegetation height and α_v denotes the degree of bending of the plant (figure 3.9). For rigid submerged vegetation H_v^* is equal to H_v ($\alpha_v = 0$). For flexible submerged

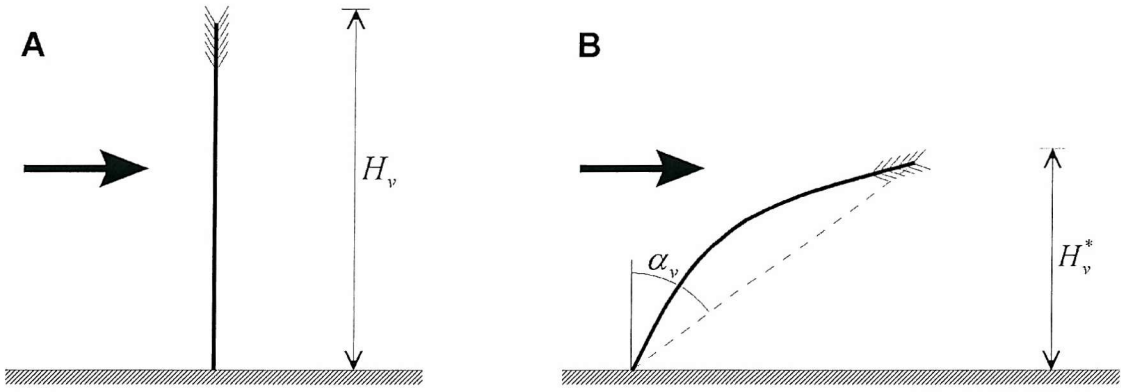

Figure 3.9: Effects of bending on the projected height, H_v^*, of submerged vegetation. The arrow indicates flow direction. The degree of bending is defined as the angle between the straight line, connecting the base of the plant with the top, and the vertical.

A Rigid vegetation : $H_v^* = H_v \cos 0° = H_v$.

B Flexible vegetation : $H_v^* = H_v \cos \alpha_v$.

vegetation, however, the angle α_v will depend on the applied force, F_α. Rahmeyer *et al.* (1999) expressed this dependence for the specific case where α_v equals 45 degrees. However, their relation can easily be generalized to:

$$F_\alpha = \frac{6EI}{H_v^2} \sin^2 \alpha_v \tag{3.41}$$

where the plant's modus of elasticity, E, and its moment of inertia, I, are obtained as:

$$E = 7.648 \times 10^6 \left(\frac{H}{d_{vb}}\right) + 2.174 \times 10^4 \left(\frac{H}{d_{vb}}\right)^2 + 1.809 \times 10^3 \left(\frac{H}{d_{vb}}\right)^3 \tag{3.42}$$

$$I = \frac{\pi d_v^4}{64} \tag{3.43}$$

in which d_{vb} is the diameter of the plant stem at the base. Equation 3.42 is an empirical relation, based on a range of laboratory and field experiments (Freeman *et al.*, 2000). Equation 3.43 is a theoretical equation, which assumes that the plant can be represented as a cylinder.

The force, F_α, applied on the vegetation is, by definition, equal to the drag force, F_d, exerted by the flow. Approximating the flow velocity with U_s, the drag force is calculated as:

$$F_d = \frac{C_d \gamma U_s^2 A_v}{2g} \tag{3.44}$$

As flow velocities increase, the drag force exerted on the plants increases, causing the plants to bend more and A_v to reduce. As a consequence, the vegetation roughness is reduced, resulting in a decrease in flow velocity. Hence, drag force becomes smaller and the plants will bend less, *etc.* In MRIPA, this cycle of adjustment is solved iteratively, using equations 3.38 to 3.44 (figure 3.10). The central idea of the entire procedure is the almost trivial assumption that the force applied on the vegetation must equal the force exerted by the flow: $F_\alpha = F_d$. Essentially this implies that the degree of bending of the plants will be such that the internal resistance to any further bending equals the drag force applied by the flow velocity, as predicted by the vegetation roughness derived from the current degree of bending.

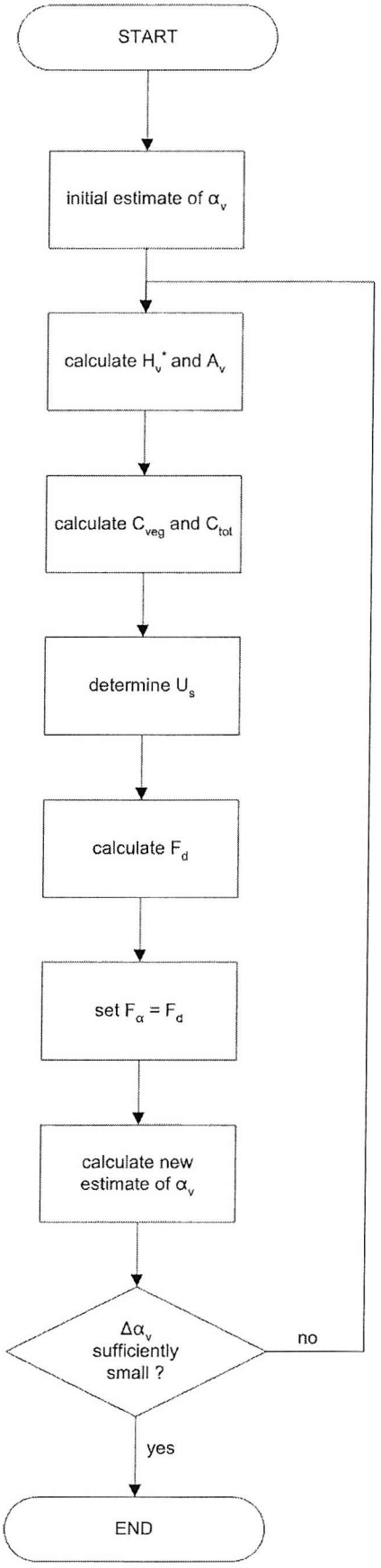

Figure 3.10: Schematic representation of procedure for calculating vegetation roughness and flow velocity for submerged flexible vegetation.

In view of the simplifications made in terms of the shape of the vegetation, and considering the availability and uncertainty of values for the parameters C_d and E (section 5.2), the advantage of using this physically-based procedure, rather than applying a simple fixed-value vegetation roughness coefficient, is probably very questionable. However, this is not a problem with the procedure itself, but a consequence of a current lack of empirical data. Hence, the procedure is applied nonetheless, on the basis that it at least attempts to incorporate the concept that roughness values of flexible vegetation are dependent on flow velocity, and in the hope that more accurate data will become available in the future.

Other vegetation effects

Although flow patterns and wake turbulence in the local neighbourhood of the plant pose interesting problems in small scale computational fluid dynamics, they are beyond the scope of the current model which looks at flow conveyance on a reach scale. This is because the grid cells are often simply too large to capture any of these small scale processes directly. However, the aggregate impacts of vegetation, such as larger scale flow redirection and momentum exchange, are modelled, albeit indirectly only - through the vegetation roughness.

As is clear from the momentum equations (equations 3.25a and 3.25b), the flow velocities are partly determined by the roughness. Increased roughness along the banks, due to the presence of vegetation, reduces the flow velocities locally. In order to satisfy the continuity for flow through the cross-section, this will result in higher flow velocities in the channel. The redirection of flow is thus not modelled explicitly, on a plant-by-plant basis, but rather follows indirectly from the aggregate vegetation roughness over a grid element.

The lateral dissipation of energy could, possibly, be incorporated directly in the model through a change in the exponent q in equation 3.35. However, this exponent already is a rather arbitrary 'fudge' of the theoretical equations, and the uncertainty of its value is likely to be greater than the change imposed on it by vegetation. In any case, it would be difficult, if not impossible, to find an acceptable relation between q and the properties of vegetation. It is decided, therefore, not to use the exponent q to represent the effects of vegetation. However, the effects of vegetation on lateral momentum exchange are already incorporated in equation 3.25a, again indirectly through the vegetation roughness. The secondary flow

convection parameter, k_{sn}, is a function of the Chezy roughness coefficient (*cf.* section 4.3). Any changes in C induced by the presence of vegetation are thus transferred to the momentum equations of flow.

3.4. Sediment transport submodel

The evolution of the channel bed is governed by spatial divergences in the sediment transport rate. In MRIPA, only bed load transport is considered; for suspended load transport reference is made to Talmon (1992). Sediment transport is represented by a sediment transport vector, S, the magnitude and direction of which are calculated separately. Change in bed topography is based on the principle of mass-conservation. Sections 3.4.1 to 3.4.3, which explain these elements, are largely based on the more detailed descriptions of Olesen (1987) and Mosselman (1991; 1992). Incorporation of the hydraulic entrainment of bank sediment is treated in section 3.4.4, while section 3.4.5 discusses the effects of vegetation on sediment transport.

3.4.1. Magnitude of sediment transport

The magnitude of the sediment transport vector is given by (Mosselman, 1992):

$$|S| = \left(1 - k_{ls}\frac{\partial z_b}{\partial s}\right) f_s(U, h, C, D_{50}) \tag{3.45}$$

where f_s is the sediment transport rate, as predicted by a transport formula, and where the first factor of the right hand side is a correction accounting for the influence of the streamwise bed slope, in which k_{ls} is a weighting coefficient to be calibrated (section 4.3). Most sediment transport formulas are expressed as a dimensionless transport parameter, ϕ_s, which is related to the sediment transport rate, f_s, by:

$$\phi_s = \frac{f_s}{\sqrt{\rho_{rel} g D_{50}^3}} \tag{3.46}$$

where ρ_{rel} is the relative density of the bed material ($\rho_{rel} = (\rho_s - \rho_w) / \rho_w$), g is the gravimetric constant, D_{50} is the median grain size. It should be noted that although MRIPA's sediment transport component assumes a homogenous bed material (*i.e.* sorting effects are excluded), it uses two parameters, D_{50} and D_{90}, to represent this. The latter is introduced later to calculate the "ripple factor" in the Meyer-Peter-Müller transport formula (see below). Usually, ϕ_s or f_s are expressed as a function of dimensionless shear stress or Shields parameter, θ_s, which is defined as:

$$\theta_s = \frac{\tau_b}{(\rho_s - \rho_w) g D_{50}} \approx \frac{U_s^2}{C^2 \rho_{rel} D_{50}} \tag{3.47}$$

The approximation is obtained by assuming that the total bed shear stress can be approximated by the streamwise bed shear stress ($\tau_b \approx \tau_{bs}$), and inserting equation 3.10.

Currently, MRIPA allows users to choose between three transport formulas from which ϕ_s and f_s may be calculated: the Meyer-Peter-Müller formula (Meyer-Peter and Müller, 1948), the Engelund-Hansen formula (Engelund and Hansen, 1967) and a generic power law. These three formulas can be applied in a wide range of situations, although it is not suggested that they are appropriate for use in all situations. However, the working of the model can be adequately illustrated without implementing any other transport formulas - even though this could easily be done.

Meyer-Peter-Müller formula

The Meyer-Peter-Müller transport equation is frequently used as a bed load transport predictor, and performs well for coarse sediments (Olesen, 1987). It may be written as:

$$\phi_s = 13.3 \left(K_R \theta_s - \theta_{s,c} \right)^{3/2} \tag{3.48}$$

where $\theta_{s,c}$ is the critical Shields parameter and K_R is a shear correction factor to account for the presence of bed form resistance (Meyer-Peter and Müller, 1948; Gomez and Church, 1989). The critical shear stress represents a threshold value below which no sediment

transport occurs, and is usually taken to equal 0.047. The correction factor, K_R, is referred to as a "ripple factor". It normally takes a value between 0.5 and 1, indicating a loss of available shear energy because of the bed form resistance (Raudkivi, 1990). The ripple factor can be calculated from (Van Rijn, 1984):

$$K_R = 18 \log\left(\frac{12R_b}{k_s}\right) \tag{3.49}$$

in which k_s is a roughness height of the bed. Van Rijn (1984) uses $k_s = 3D_{90}$, where D_{90} is the grain size such that 90% of all grains are smaller. Mosselman (1992) uses $k_s = D_{90}$. Inserting equations 3.48 and 3.47 in equation 3.46 and rearranging terms, the sediment transport rate can be written as:

$$f_s = 13.3\sqrt{\rho_{rel} g D_{50}^3}\left[\frac{K_R U_S^2}{C^2 \rho_{rel} D_{50}} - 0.047\right]^{3/2} \tag{3.50}$$

Engelund-Hansen formula

The Engelund-Hansen formula is a total load predictor. However, for low values of the Shields parameter it can be used to predict bed-load transport only (Olesen, 1987). In contrast to the Meyer-Peter-Müller formula, there is no critical value, and hence no zero-bedload. The formula is usually expressed as:

$$\phi_s = 0.084\frac{C^2}{g}\theta_s^{5/2} \tag{3.51}$$

Using equations 3.46 and 3.47, this can be related to the sediment transport rate as:

$$f_s = \frac{0.084\,U^5}{\sqrt{g}\,C^3\,\rho_{rel}^2\,D_{50}} \tag{3.52}$$

Generic power law

The generic power law is a simple, generalized transport equation. Like the Engelund-Hansen formula, it does not contain a critical value, and therefore will not predict zero-bedload. It is given as:

$$f_s = k_s U^{p_s} \tag{3.53}$$

where k_s and p_s are calibration parameters (section 4.3). It can be seen from equations 3.52 and 3.53 that the Engelund-Hansen formula is a special case of the power law, with $p_s = 5$, and k_s a function of C, ρ_s and D_{50}. Olesen (1987) showed that the Meyer-Peter-Müller formula can, under certain conditions, also be written in a power-law form, where:

$$p_s = \frac{3K_R\theta_s}{K_R\theta_s - \theta_{s,c}} \tag{3.54}$$

3.4.2. Direction of sediment transport

The direction of the bedload transport is defined as the angle, ψ_S, between the transport vector and the s-direction of the grid. Bed load transport is affected by the bed shear stress, acting along the near bed flow direction, and by gravity, acting along the slope of the bed. Taking these factors in account, the angle ψ_S can be determined as (Van Bendegom, 1947; De Vriend and Struiksma, 1984):

$$\tan\psi_S = \frac{\sin\psi_\tau - k_{ts}\dfrac{\partial z_b}{\partial n}}{\cos\psi_\tau - k_{ls}\dfrac{\partial z_b}{\partial s}} \tag{3.55}$$

where ψ_τ denotes the direction of the bed shear stress, $\partial z_b/\partial s$ and $\partial z_b/\partial n$ respectively represent the longitudinal and transverse bed slope, and k_{ts} and k_{ls} respectively are weighting coefficients for the influence of transverse and longitudinal slope. The two weighting

coefficients are treated as calibration parameters (section 4.3). The angle ψ_τ, appearing in equation 3.55, can be derived from the local near-bed flow properties (Struiksma *et al.*, 1985; Struiksma and Crosato, 1989):

$$\psi_\tau = \arctan\left(\frac{U_n}{U_s}\right) - \arctan\left(k_{si}\frac{i_s}{U_s}\right) \tag{3.56}$$

in which k_{si} is a coefficient to adjust the influence of the secondary flow intensity, which represents the effect of secondary flow on the bed shear stress. It is a function of hydraulic roughness and of the eddy viscosity model applied. In MRIPA, k_{si} is treated as a calibration parameter (section 4.3). The first term on the right hand side of equation 3.56 denotes the depth-averaged flow direction, and the second term is the deviation between the near-bed and depth-averaged flow directions, caused by the presence of the secondary circulation. Olesen (1987) recommends the secondary flow intensity, i_s, to be obtained using equation 3.15, rather than equation 3.20, because omission of the adaptation length, λ_r, may cause instability in the mathematical model. Assuming that the longitudinal slope is negligible ($\partial z_b/\partial s \approx 0$), recognizing that ψ_τ is generally small ($\cos \psi_\tau \approx 1$; $\sin \psi_\tau \approx \tan \psi_\tau$), and inserting equation 3.56 into equation 3.55, the following relation for the bed load transport direction, ψ_S, is obtained:

$$\psi_S = \frac{U_n}{U_s} - k_{si}\frac{i_s}{U_s} - k_{ts}\frac{\partial z_b}{\partial n} \tag{3.57}$$

The first two terms on the right hand side of equation 3.57 represent the effect of the flow on bed load transport direction, and the last term represents the effect of bed topography. The weighting coefficient, k_{ts}, is derived from a transverse bed slope model, defined by (Olesen, 1987):

$$k_{ts} = k_{tm}\,\theta_s^{-p_{tm}/2} \tag{3.58}$$

in which θ_s is the Shields parameter and k_{tm} and p_{tm} are two calibration parameters (section 4.3). Equation 3.57 is valid for orthogonal grids. Adjusting for grid skewness in non-orthogonal coordinate systems, the streamwise and transverse components of the sediment vector, denoted by S_s and S_n, respectively, are calculated as:

$$S_s = \frac{|S|}{\sqrt{1 + \frac{\tan\psi_S}{\varepsilon^* - \varepsilon\tan\psi_S}}} \tag{3.59}$$

and

$$S_n = \frac{\tan\psi_S}{\varepsilon^* - \varepsilon\tan\psi_S} S_s \tag{3.60}$$

These components satisfy the general properties of vector components on a non-orthogonal grid, similar to those expressed in equations 3.5 and 3.6:

$$|S| = \sqrt{S_s^2 + S_n^2 + 2\varepsilon S_s S_n} \tag{3.61}$$

and

$$\tan\psi_S = \frac{\varepsilon^* S_n}{S_s + \varepsilon S_n} \tag{3.62}$$

3.4.3. Bed topography change

As sediment is transported from one place to another, it will cause changes in bed topography by scouring the bed or depositing sediment. Changes in bed topography are modelled using the continuity equation for sediment movement, which for orthogonal grids reads (Olesen, 1987):

$$\frac{\partial z_b}{\partial t} + \frac{\partial S_s}{\partial s} + \frac{\partial S_n}{\partial n} + \frac{S_s}{R_n} + \frac{S_n}{R_s} = 0 \tag{3.63}$$

For non-orthogonal grids this can be reworked to (Mosselman, 1991; 1992):

$$\varepsilon^* \frac{\partial z_b}{\partial t} + \frac{\partial(\varepsilon^* S_s)}{\partial s} + \frac{\partial(\varepsilon^* S_n)}{\partial n} + \frac{\varepsilon^* S_s}{R_n} + \frac{\varepsilon^* S_n}{R_s} = 0 \tag{3.64}$$

The model assumes a rigid lid on the water surface. Hence, bed topography can be expressed by water depths, and, consequently, changes in bed topography by changes in water depth. The rigid assumption implies that $\partial h/\partial z_b = -1$ (Olesen, 1987), so that:

$$\varepsilon^* \frac{\partial h}{\partial t} = \frac{\partial(\varepsilon^* S_s)}{\partial s} + \frac{\partial(\varepsilon^* S_n)}{\partial n} + \frac{\varepsilon^* S_s}{R_n} + \frac{\varepsilon^* S_n}{R_s} \tag{3.65}$$

The numerical implementation of equation 3.65 employs a central difference scheme to solve the spatial derivatives, while the time derivative is approximated as a first order difference (Olesen, 1987). At the inflow boundary, a fixed bed level distribution is prescribed.

3.4.4. Hydraulic bank erosion

Interaction of the flow with sediment does not only occur on the channel bed. Sediment can also be entrained from the banks. Indeed, hydraulic erosion of bank material is one of the two main processes of bank retreat; the other one being geotechnical bank failure, which is discussed in section 3.5.

Lateral erosion of the bank by hydraulic forces depends on the shear exerted on the bank material, and may be expressed using a simple excess shear stress formula (Ariathurai and Arulanandan, 1978):

$$\left|\frac{\partial n_B}{\partial t}\right| = k_B \left(\frac{\tau_B - \tau_{B,c}}{\tau_B}\right)^{p_B} \qquad \text{if } \tau_B > \tau_{B,c} \tag{3.66a}$$

$$\left|\frac{\partial n_B}{\partial t}\right| = 0 \qquad \text{if } \tau_B \leq \tau_{B,c} \tag{3.66b}$$

where $\partial n_B/\partial t$ represents the rate of lateral retreat, τ_B is the shear stress applied on the bank, $\tau_{B,c}$ is the critical shear stress for bank sediment entrainment, k_B denotes the erodibility of the bank material, and p_B is an exponent, which is usually taken to equal unity. Formally,

hydraulic entrainment on the bank face is governed by the thee-dimensional flow field. However, for mildly curved channels it may be represented relatively well by the longitudinal shear stress, since the secondary flow components are driven by the streamwise flow and are small with respect to latter (Mosselman, 1992). The shear stress, τ_B, is then a simple function of the longitudinal shear stress applied on the bed, τ_{bs}:

$$\tau_B = k_\tau \tau_{bs} \tag{3.67}$$

where τ_{bs} is obtained from equation 3.22 and k_τ is a proportionality coefficient, which is normally taken to equal 0.75 (Lane, 1955). In practice, k_τ, is not a constant, but would vary with bank angle and vertical position along the bank. It might be possible to derive a semi-empirical function to relate k_τ to bank angle (figure 3.11), but this has not been implemented, since such a relation is untested at the moment. The vertical dependency of k_τ (figure 3.11) is less of a problem than it first appears, since lateral shear erosion is not applied over the whole bank face, but only near the toe of the bank (figure 3.13). Hence, the model assumes a constant value ($k_\tau = 0.75$), in accordance with Lane (1955). The sediment produced by lateral erosion is added to the sediment load of the channel. Details of this procedure are described in section 3.6.2.

3.4.5. Effects of vegetation on sediment transport

In this model, the effects of vegetation on sediments in transport are only indirectly accounted for, through the hydraulic influence of vegetation. The direct effect of sediment trapping by the stems and leaves of the vegetation is, therefore, not represented in the model. However, an attempt has been made to incorporate the effect of plants in covering sediment and binding the soil with their roots. This is achieved through a simple modification of the critical shear strength of the bank sediment (Collins *et al.*, 2001):

$$\tau_{c,tot} = k_{\tau,veg} \tau_c \tag{3.68}$$

where $\tau_{c,tot}$ denotes the total critical shear strength, τ_c is the critical shear strength for unvegetated soil, and $k_{\tau,veg}$ is a vegetation dependent shear modification factor (section 5.2).

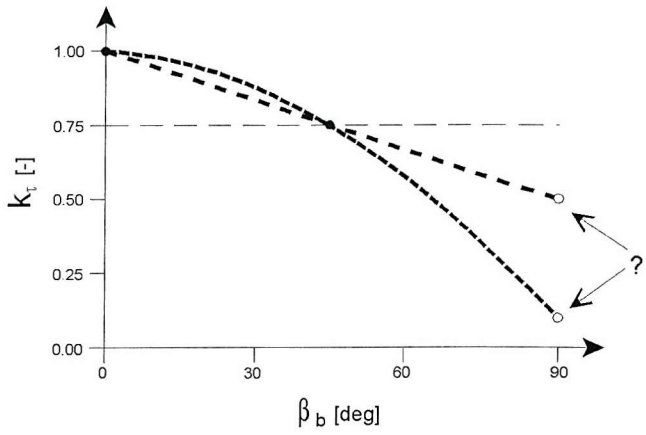

Figure 3.11: Possible relations between the bank shear proportionality coefficient, k_τ, and bank angle, β_b. For a bank angle of 45 degrees the coefficient equals 0.75 (Lane, 1955). When the bank angle equals 0 degrees (*i.e.* no bank), bank shear stress would equal bed shear stress: $\tau_B = \tau_{bs}$, and hence $k_\tau = 1.00$. Based on these two points, it seems reasonable to assume a continuous decline. However, to be able to derive a useful relationship, a third point is needed to obtain knowledge about the shape of the decline. Unfortunately, this is unknown and can only be guessed at. The illustration shows two possible relations, both in dashed lines: the first assumes $k_\tau = 0.10$ on vertical banks; the other assumes $k_\tau = 0.50$, resulting in a linear decline. Other values could be assumed and would lead to different curves. In view of the uncertainty, the model currently applies Lane's (1955) assumption to all bank angles, as illustrated by the thin full line. This seems to imply that bank shear stress will be underestimated on shallow banks ($\beta_b < 45°$), and overestimated on steep banks ($\beta_b > 45°$). However, this overestimation effect may partly be compensated for by acknowledging that bank shear stresses induced by secondary flows, which are not incorporated in the shear proportionality coefficient, are likely to be strongest near steep banks.

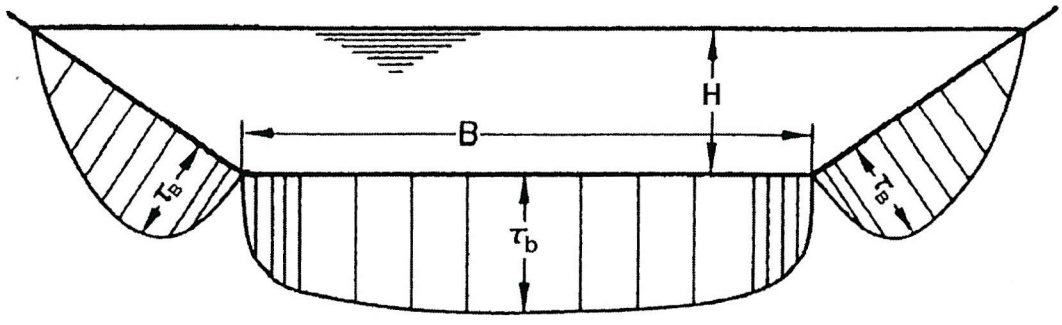

Figure 3.12: Shear stress distribution over the periphery of a trapezoidal channel (slightly modified from Raudkivi, 1990). The bank shear stress, τ_B, distribution varies with depth. It is maximal between 0.1 and 0.2 times the flow depth.

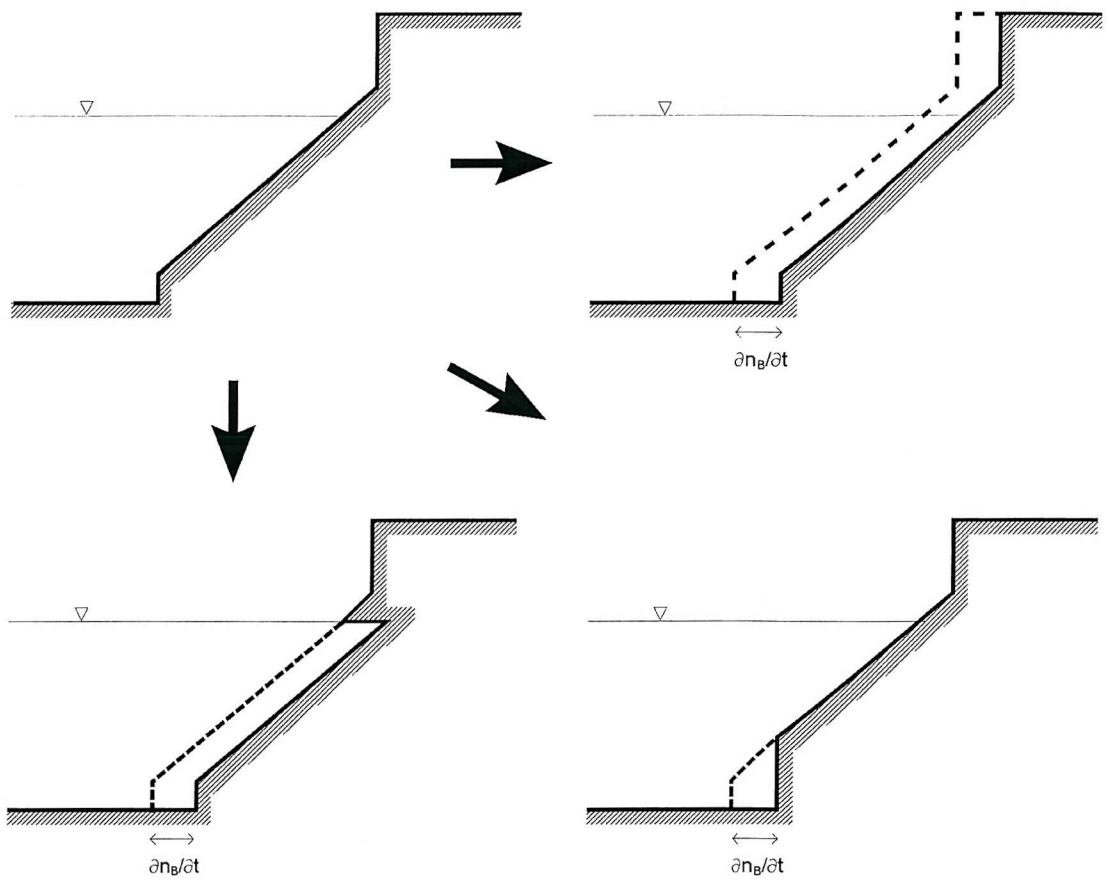

Figure 3.13: Possible ways to account for lateral erosion, $\partial n_B/\partial t$. The original profile is shown top left, and in dashed lines on the other profiles. In the top right, the erosion is applied over the entire bank profile. This method is very simple, but the implied parallel bank retreat is unrealistic for hydraulic erosion, as even sediments above the water level are entrained. Also, the fact that bank shear stress diminishes higher up the bank (figure 3.68) is ignored. Part of this problem would be solved using the method illustrated bottom left, where the erosion is applied up to the water level only. However, this still ignores the diminishing bank shear stress, and also would lead to complex bank geometries. As an alternative, the model uses the method shown bottom right. Here, lateral erosion is only applied near the toe of the bank. This will underestimate the entrainment from the bank face. However, most of the hydraulic activity occurs near the toe of the bank, and it is this factor which is of importance to geotechnical bank stability (Osman and Thorne, 1988). Additionally, this method does not lead to overly complex bank geometries.

Since the MRIPA model does not allow for in-channel vegetation, only sediment entrainment from the banks is affected by these impacts of vegetation, so that equations 3.66a and 3.66b are adjusted as:

$$\left|\frac{\partial n_B}{\partial t}\right| = k_B\left(\frac{\tau_B - \tau_{B,c,veg}}{\tau_B}\right)^{p_B} \qquad \text{if } \tau_B > \tau_{B,c,veg} \tag{3.69a}$$

$$\left|\frac{\partial n_B}{\partial t}\right| = 0 \qquad \text{if } \tau_B \leq \tau_{B,c,veg} \tag{3.69b}$$

It is worth pointing out that τ_B itself is also affected by the presence of vegetation, albeit indirectly, through a decrease in the Chezy conveyance factor, C, and corresponding changes in flow velocity (*cf.* equations 3.37, 3.25 and 3.22).

3.5. Geotechnical bank erosion submodel

In the following sections the geotechnical aspects of the bank erosion submodel are described. Sections 3.5.1 to 3.5.3 detail the basic bank stability analysis. Further extension of this stability model to include the effects of vegetation is discussed in section 3.5.4. The bank stability analysis is performed in the cross-sectional profile. As the flow and sediment transport model work in the planform dimension, interaction with the geotechnical bank erosion submodel requires some careful manipulation. This is detailed in section 3.6.

3.5.1. Definitions, concepts and parameters

Although there are many different failure types (*cf.* section 2.4.1), the bank stability analysis presented here is restricted to planar failures. It is based upon the analyses by Osman and Thorne (1988), Darby and Thorne (1996a), Rinaldi and Casagli (1999), and Simon *et al.* (2000). Similar to these bank-stability analyses, the approach described in this section uses a cross-sectional geometry. The third dimension is assumed implicitly by applying this cross-sectional analysis over a unit length of channel bank.

The geometry of the bank is defined through a set of basic parameters (figure 3.14A): total bank height, H_b, cutbank height, H_{cb}, height of the vertical cliff near the bank top, H_c, upper bank slope, β_b, and tension crack depth, H_t. Figure 3.14A further introduces the two hydrological parameters that are used in the stability analysis: water depth in the main channel, H_w, and ground water level, H_g. Another group of parameters defines the bank material properties: soil cohesion, c, soil unit weight, γ_s, internal friction angle, ϕ, and the rate of increase in soil strength relative to matric suction, as expressed by the angle of matric suction, ϕ^b.

Assuming an incipient planar failure through the toe of the bank, inclined at a failure plane angle β_f, the following relations hold for the failure block (figure 3.14B):

$$L_f = \frac{H_b - H_t}{\sin \beta_f} \tag{3.70}$$

$$V_f = \frac{H_b^2 - H_t^2}{2 \tan \beta_f} - \frac{\left(H_b - H_{cb}\right)^2 - H_c^2}{2 \tan \beta_b} \tag{3.71}$$

and

$$W_f = \gamma_s V_f \tag{3.72}$$

where L_f denotes the length of the incipient failure plane, V_f and W_f respectively represent the volume and weight of the failure block, and γ_s is the unit weight of the soil.

The only unknown in equations 3.70 to 3.72 is the slope of the failure plane, β_f. A key task of the bank stability analysis, therefore, is not only to indicate stability or instability of the riverbank, but also to provide a value for β_f from which the failure geometry can be determined. In practice, the calculations are performed in reverse order: first β_f is calculated to define the most probable geometry of a potential failure block, and from this the stability of the riverbank is evaluated.

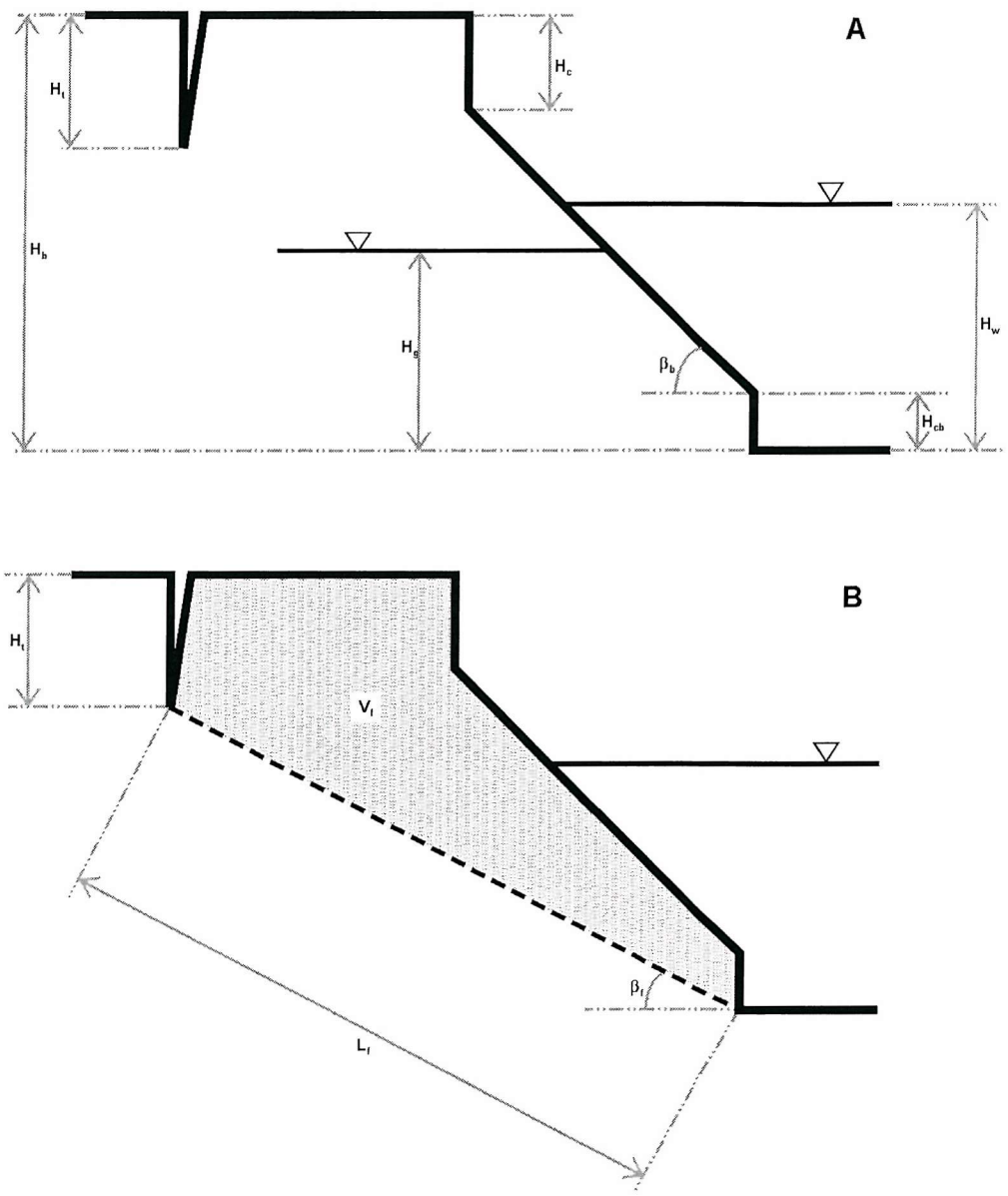

Figure 3.14: Definition sketch of basic parameters for the bank stability analysis.

A: Parameters describing initial bank geometry and hydrology. Thick line represents bank cross-sectional geometry, thin lines represent water surfaces: H_b = total bank height, H_{cb} = cutbank height, H_c = height of vertical cliff, β_b = angle of bank slope, H_t = depth of tension crack. Hydrological parameters: H_w = flow depth in channel, H_g = height of groundwater table.

B: Additional parameters needed to describe failure geometry. The dashed line represents an assumed incipient failure plane and the shaded area represents the incipient failure block: β_f = angle of assumed incipient failure plane, L_f = length of failure plane and V_f = volume of the failure block.

3.5.2. Factor of safety

The stability of a bank is usually expressed as a factor of safety, N_{FS}, describing the balance between the driving forces, F_D, and the resisting forces, F_R, acting upon an incipient failure block:

$$N_{FS} = \frac{F_R}{F_D} \tag{3.73}$$

As long as the factor of safety is above unity ($N_{FS} > 1$), the resisting forces outweigh the driving forces and the bank is stable. When the factor of safety drops below unity ($N_{FS} < 1$) the driving forces outweigh the resisting forces and the bank will fail. When N_{FS} equals 1, the bank is at a critical condition and failure is imminent. The driving and resisting forces are the resultants of several forces acting on the bank: gravity, cohesive forces within the soil, friction along the failure plane, pore pressure, confining pressure of channel water and soil matric suction (figure 3.15). The importance of these elements was highlighted in the previous chapter (section 2.4.1). Here, the relevant mathematical expressions will be developed.

Gravity

Assuming, for the moment, that the riverbank is free of external loading or surcharge, such as trees or buildings, the weight of the bank depends on the shape of the failure block, soil material density and porosity, and groundwater level. The total weight can then be calculated as the sum of the weights of the saturated and unsaturated parts of the failure block (figure 3.16):

$$W_f = \gamma_{s,sat} V_{f,sat} + \gamma_{s,uns} V_{f,uns} \tag{3.74}$$

in which W_f denotes the total weight of the incipient failure block, $\gamma_{s,sat}$ and $\gamma_{s,uns}$ respectively are the saturated and unsaturated soil unit weight, and $V_{f,sat}$ and $V_{f,uns}$ are the saturated and unsaturated volumes of the failure block. Assuming that the groundwater level is horizontal

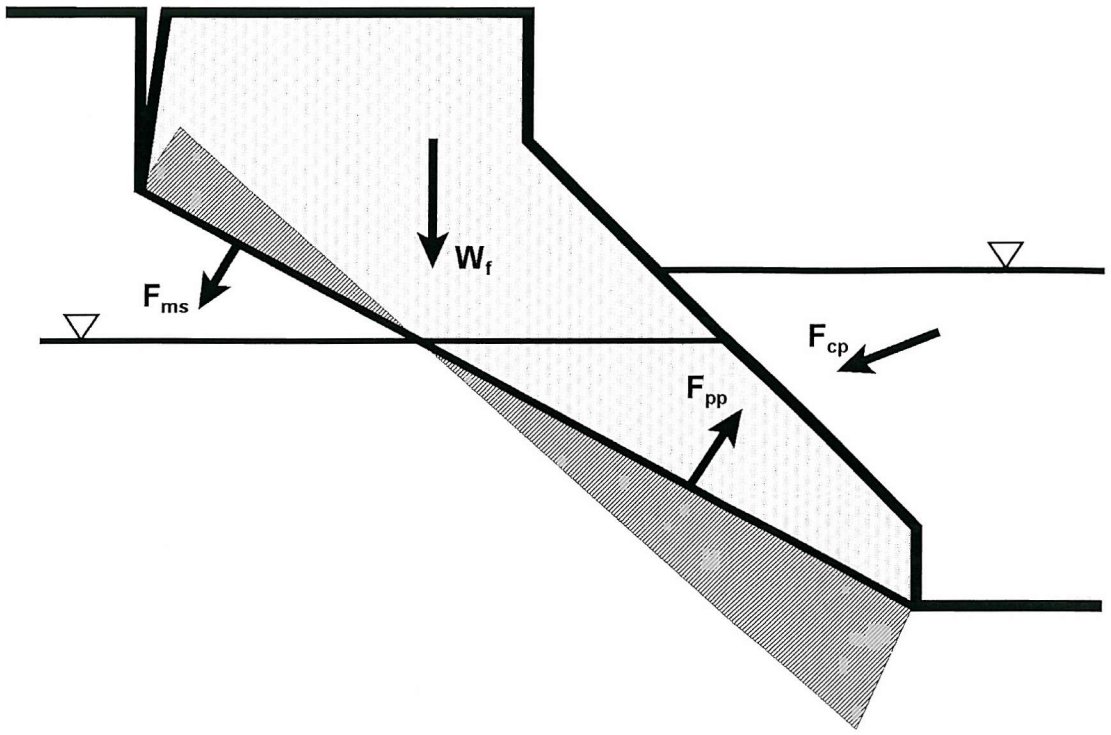

Figure 3.15: Definition sketch of basic forces in bank stability analysis. W_f denotes weight of the failure block, F_{cp} is the hydrostatic confining pressure of channel water, F_{pp} represents the pore pressure and F_{ms} is the matric suction force. Not depicted is soil cohesion, c, along the failure plane.

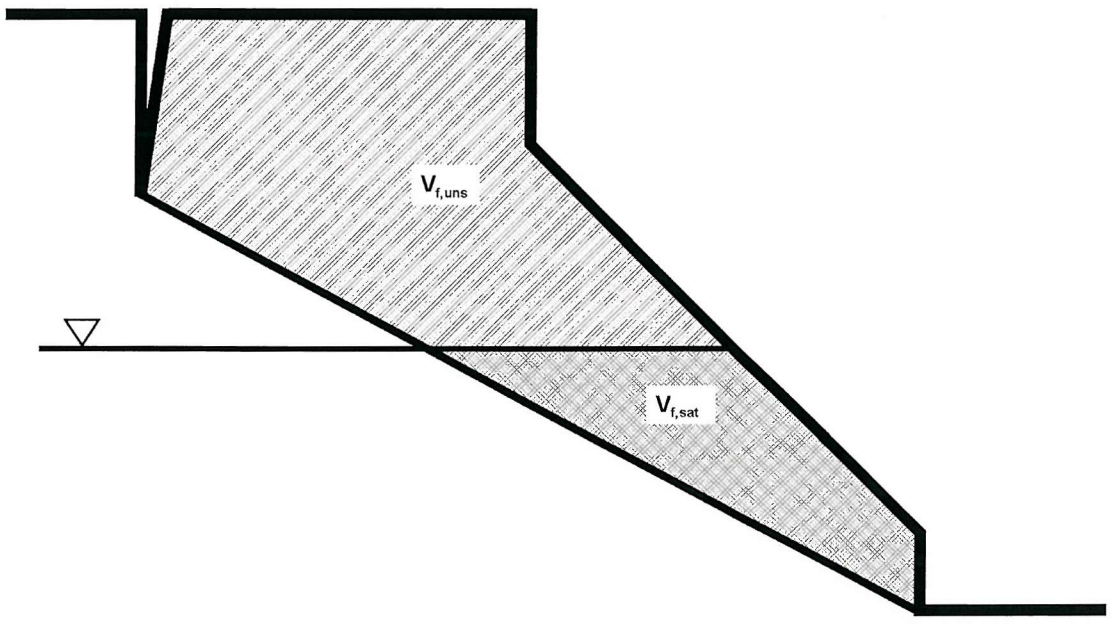

Figure 3.16: Definition sketch of unsaturated and saturated parts of the bank.

throughout the bank, $V_{f,sat}$ and $V_{f,uns}$ are calculated as (*cf.* figure 3.14):

$$V_{f,uns} = V_f - V_{f,sat} \tag{3.75a}$$

$$V_{f,sat} = V_{f1} - V_{f2} - V_{f3} + V_{f4} \tag{3.75b}$$

where

$$V_{f1} = \frac{H_g^2}{2\tan\beta_f} \tag{3.76a}$$

$$V_{f2} = \begin{cases} 0 & if\ H_g \le H_{cb} \\ \dfrac{\left(H_g - H_{cb}\right)^2}{2\tan\beta_b} & if\ H_g > H_{cb} \end{cases} \tag{3.76b}$$

$$V_{f3} = \begin{cases} 0 & if\ H_g \le H_b - H_t \\ \dfrac{\left(H_g - \left(H_b - H_t\right)\right)^2}{2\tan\beta_f} & if\ H_g > H_b - H_t \end{cases} \tag{3.76c}$$

$$V_{f4} = \begin{cases} 0 & if\ H_g \le H_b - H_c \\ \dfrac{\left(H_g - \left(H_b - H_c\right)\right)^2}{2\tan\beta_b} & if\ H_g > H_b - H_c \end{cases} \tag{3.76d}$$

The presence of vegetation induces an additional surcharge, which should be added where appropriate (section 3.5.4).

Pore pressure

The positive pore pressure at any point on the failure plane is determined by the groundwater level. Again assuming that the groundwater level is horizontal throughout the bank, an analytical expression for the pore-pressure can be derived from the geometry of the bank profile and the groundwater level. Since positive pore-pressures only occur in the saturated part of bank, the expression for F_{pp} is directly related to that of $V_{f,sat}$ in the paragraph above:

$$F_{pp} = \frac{\gamma_w}{\cos\beta_f} V_{f,sat} \tag{3.77}$$

Matric suction

Matric suction, or negative pore pressure, occurs in the unsaturated part of the soil. The matric suction force, F_{ms}, is calculated by integrating the negative head of the groundwater along the unsaturated part of the failure plane:

$$F_{ms} = \begin{cases} 0 & if\ H_g \geq H_b - H_t \\ \dfrac{\gamma_w}{2\sin\beta_f}\left(\left(H_b - H_t\right) - H_g\right)^2 & if\ H_g < H_b - H_t \end{cases} \tag{3.78}$$

The matric suction force interacts with the failure plane along a "suction angle", ϕ^b, which expresses the rate of increase in strength relative to the matric suction (Casagli *et al.*, 1999). The suction angle is always smaller or equal to the internal friction angle of the soil (Fredlund and Rahardjo, 1993), and can either be obtained from field measurements or as a simple function of the internal friction angle, the volumetric water content and the plasticity index of the soil (Vanapalli and Fredlund, 2000; Vanapalli, 2001).

Confining pressure

The hydrostatic confining pressure, F_{cp}, depends on the bank geometry and the flow depth in the near-bank zone (figure 3.17). It can easily be calculated from its horizontal and vertical components $F_{cp,x}$ and $F_{cp,y}$:

$$F_{cp} = \sqrt{F_{cp,x}^2 + F_{cp,y}^2} \tag{3.79}$$

where:

$$F_{cp,x} = \frac{\gamma_w}{2} H_w^2 \tag{3.80}$$

and $F_{cp,y}$ equals zero for vertical banks ($\beta_b = 90°$) or, for non-vertical banks:

$$F_{cp,y} = \begin{cases} \dfrac{\gamma_w \left(H_w - H_{cb}\right)^2}{2 \tan \beta_b} & \text{if } H_w \leq H_b - H_c \\ \dfrac{\gamma_w \left[\left(H_w - H_{cb}\right)^2 - \left(H_w - \left(H_b - H_c\right)\right)^2\right]}{2 \tan \beta_b} & \text{if } H_w > H_b - H_c \end{cases} \tag{3.81}$$

The direction of the confining pressure, ω_{cp}, is given by:

$$\omega_{cp} = \arctan \frac{F_{cp,y}}{F_{cp,x}} \tag{3.82}$$

For the stability analysis, the components of F_{cp} normal and parallel to the failure plane need to be used. The hydrostatic confining force is transmitted over the failure plane at an angle, α_{cp}, which is defined as the angle between ω_{cp} and the normal to β_f. This angle can be calculated as:

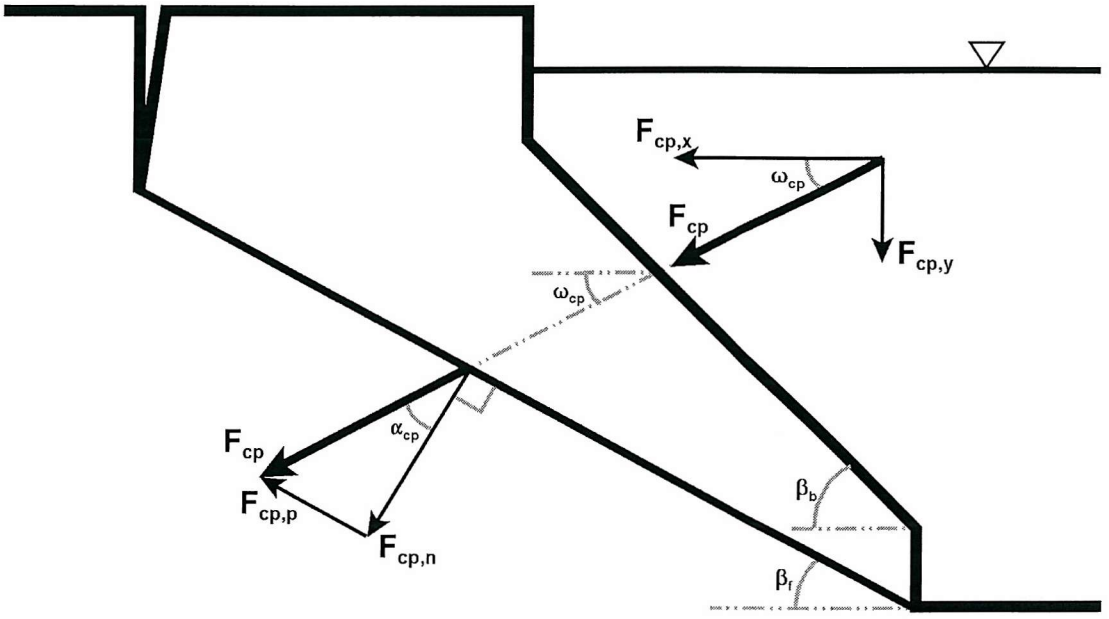

Figure 3.17: Definition sketch of hydrostatic confining pressure, F_{cp}. The angle of interaction with the bank face is defined through ω_{cp} and the angle of interaction with the failure plane is defined via α_{cp}. (after Darby and Thorne, 1996a)

$$\alpha_{cp} = \frac{\pi}{2} - \left(\beta_f + \omega_{cp}\right) \tag{3.83}$$

From this the components of F_{cp} normal and parallel to the failure plane can be derived:

$$F_{cp,n} = F_{cp} \cos\alpha_{cp} \tag{3.84}$$

$$F_{cp,p} = F_{cp} \sin\alpha_{cp} \tag{3.85}$$

Factor of safety for planar failures

The forces acting on the bank, as described above, can be combined in a total driving force and a total resisting force, from which a factor of safety is derived using equation 3.73. The resistance force, F_R, results from cohesion effects and friction along the failure plane and is usually derived from the Coulomb equation which describes the shear strength at a point on the failure plane (Selby, 1993):

$$\tau_f = c + \sigma_n \tan\phi \tag{3.86}$$

in which τ_f is the total available shear resistance or shear strength at the moment of failure, c is the effective cohesion of the soil, σ_n is the normal stress of the soil weight, and ϕ is the friction angle of the soil. Integrating this over the entire failure length results in the following expression for the resisting force:

$$F_R = cL_f + W_f \cos\beta_f \tan\phi \tag{3.87}$$

This expression can be extended to include the effects of matric suction, pore pressure and confining pressure. Matric suction in the unsaturated part of the soil physically results in a cohesion-like effect, and hence an apparent cohesion, c_a, can be calculated as:

$$c_a L_f = cL_f + F_{ms} \tan\phi^b \tag{3.88}$$

It is important to note the difference between the effective and apparent cohesion. The effective cohesion, c, depends on soil properties only, while the apparent – or total – cohesion, c_a, includes other cohesion-like effects, such as matric suction. In section 3.5.4, a further element will be added to account for the effects of vegetation roots. The pore pressure, F_{pp}, and hydrostatic confining pressure, F_{cp}, both affect the frictional force in equation 3.87. Pore pressure effects decrease friction along the failure plane, while the normal component of the confining pressure increases friction. Thus the expression for F_R can be expanded to account for pore pressure, confining pressure and matric suction, by incorporating equations 3.78 and 3.77, as well as equation 3.79:

$$F_R = cL_f + F_{ms} \tan\phi^b + \left(W_f \cos\beta_f - F_{pp} + F_{cp} \cos\alpha_{cp}\right) \tan\phi \tag{3.89}$$

The total driving force acting upon the incipient failure block, F_D, is the sum of the downslope component of the gravitational force and the downslope component of the confining pressure:

$$F_D = W_f \sin\beta_f - F_{cp} \sin\alpha_{cp} \tag{3.90}$$

Inserting equations 3.89 and 3.90 in equation 3.73 yields the following general expression for the factor of safety for planar failures:

$$N_{FS} = \frac{cL_f + F_{ms} \tan\phi^b + \left(W_f \cos\beta_f - F_{pp} + F_{cp} \cos\alpha_{cp}\right) \tan\phi}{W_f \sin\beta_f - F_{cp} \sin\alpha_{cp}} \tag{3.91}$$

3.5.3. Failure plane angle

The central unknown in equations 3.70 to 3.91 is the angle of the failure plane, β_f. Under critical conditions ($N_{FS} = 1$), the failure plane coincides with the plane of fully developed cohesion, *i.e.* where the cohesion, c, reaches a maximum with respect to the failure plane angle, β_f (Taylor, 1948). This condition is satisfied when:

$$\frac{\partial c}{\partial \beta_f} = 0 \tag{3.92}$$

Assuming critical conditions ($N_{FS} = 1$), and rearranging the terms of equation 3.91 in function of c, results in the following expression:

$$c = \frac{1}{L_f}\Big[W_f \sin\beta_f - F_{cp} \sin\alpha_{cp} - F_{ms} \tan\phi^b - \left(W_f \cos\beta_f - F_{pp} + F_{cp} \cos\alpha_{cp}\right) \tan\phi\Big] \tag{3.93}$$

Using equation 3.70, this can be written as

$$c = \frac{1}{H_b - H_t}\left(f_1 + f_2 + f_3 + f_4 + f_5 + f_6\right) \tag{3.94}$$

where

$$f_1 = f_1\left(\beta_f\right) = W_f \sin^2 \beta_f \tag{3.95a}$$

$$f_2 = f_2\left(\beta_f\right) = -F_{cp} \sin\alpha_{cp} \sin\beta_f \tag{3.95b}$$

$$f_3 = f_3\left(\beta_f\right) = -W_f \cos\beta_f \sin\beta_f \tan\phi \tag{3.95c}$$

$$f_4 = f_4\left(\beta_f\right) = F_{pp} \sin\beta_f \tan\phi \tag{3.95d}$$

$$f_5 = f_5\left(\beta_f\right) = -F_{cp} \cos\alpha_{cp} \sin\beta_f \tan\phi \tag{3.95e}$$

$$f_6 = f_6\left(\beta_f\right) = -F_{ms} \sin\beta_f \tan\phi^b \tag{3.95f}$$

Inserting equations 3.94 and 3.95a-f into equation 3.92 yields:

$$f' = f_1' + f_2' + f_3' + f_4' + f_5' + f_6' = 0 \tag{3.96}$$

where f'_i denotes the derivative of f_i with respect to β_f. These derivatives are given by:

$$f_1' = \frac{d(f_1)}{d\beta_f} = 2W_f \sin\beta_f \cos\beta_f - f_{aux2} \tag{3.97a}$$

$$f_2' = \frac{d(f_2)}{d\beta_f} = F_{cp}\left(\cos\alpha_{cp} \sin\beta_{f1} - \sin\alpha_{cp} \cos\beta_f\right) \tag{3.97b}$$

$$f_3' = \frac{d(f_3)}{d\beta_f} = \left[\frac{f_{aux2}}{\tan\beta_f} - W_f\left(\cos^2\beta_f - \sin^2\beta_f\right)\right]\tan\phi \tag{3.97c}$$

$$f_4' = \frac{d(f_4)}{d\beta_f} = \left(F_{pp}\sin\beta_f - f_{aux1}\right)\frac{\tan\phi}{\sin\beta_f \cos\beta_f} \tag{3.97d}$$

$$f_5' = \frac{d(f_5)}{d\beta_f} = -F_{cp}\left(\cos\alpha_{cp}\cos\beta_f + \sin\alpha_{cp}\sin\beta_f\right)\tan\phi \tag{3.97e}$$

$$f_6' = \frac{d(f_6)}{d\beta_f} = 0 \tag{3.97f}$$

in which the two auxiliary functions, f_{aux1} and f_{aux2}, are defined as:

$$f_{aux1} = \begin{cases} \dfrac{\gamma}{2}H_g^2 & \text{if } H_g \le H_b - H_t \\ \dfrac{\gamma}{2}\left[H_g^2 - \left(H_g - H_b + H_t\right)^2\right] & \text{if } H_g > H_b - H_t \end{cases} \tag{3.98a}$$

$$f_{aux2} = \frac{\gamma}{2}\left(H_b^2 - H_t^2\right) \tag{3.98b}$$

Part of the complexity of equation 3.96 is due to the fact that W_t, F_{pp}, F_{ms}, F_{cp} and α_{cp} are themselves functions of β_f. Theoretically, the angle of the failure plane can now be found by solving equation 3.96 for β_f. In the general case, however, it is very difficult or impossible to solve this equation analytically. A solution must, therefore, be found by other means (see below), although it is possible to derive an analytical expression for β_f under simplified conditions.

Solution for the simplified case

Equation 3.96 can be simplified by neglecting or ignoring some of the forces acting on the bank. Most commonly, the effects of matric suction, pore pressure and hydrostatic confining pressure are ignored ($F_{pp} = 0$, $F_{ms} = 0$ and $F_{cp} = 0$). This results in an analysis similar to those of Culmann (1886) and Osman and Thorne (1988), where equation 3.91 is reduced to:

$$N_{FS} = \frac{cL_f + W_f \cos\beta_f \tan\phi}{W_f \sin\beta_f} \tag{3.99}$$

In this simplified case β_f is a function only of the internal friction angle and the geometry of the bank (see appendix A2 for the derivation of this solution):

$$\beta_f = \frac{\gamma}{2}\left[\arctan\left(\frac{H_b^2 - H_t^2}{(H_b - H_{cb})^2 - H_c^2}\tan\beta_b\right) + \phi\right] \tag{3.100}$$

This solution differs from the Culmann and Osman-Thorne analyses only in the complexity of the bank geometry. In the special case where there is no vertical cliff near the bank top ($H_c = 0$), equation 3.100 is equivalent to the expression obtained by Osman and Thorne (1988):

$$\beta_f = \frac{1}{2}\left[\arctan\left(\frac{H_b^2 - H_t^2}{(H_b - H_{cb})^2}\tan\beta_b\right) + \phi\right] \tag{3.101a}$$

while in the special case where there is no vertical cliff near the bank top ($H_c = 0$), no tension crack ($H_t = 0$) and no cutbank ($H_{cb} = 0$), equation 3.100 reduces to the Culmann-expression for the failure plane angle (Culmann, 1886):

$$\beta_f = \frac{1}{2}(\beta_b + \phi) \tag{3.101b}$$

Solution for the general case

As mentioned above, it is not possible to solve equation 3.96 analytically for β_f in the general case where pore pressure, hydrostatic confining pressure and matric suction are taken into account. In this case, however, a solution can be found through an iterative scheme. An initial estimate of the angle of failure, $\beta_{f,0}$, to start off the iteration is obtained from equation 3.100. Subsequent estimates, $\beta_{f,i+1}$, are obtained through a Newton-Raphson iteration:

$$\beta_{f,i+1} = \beta_{f,i} - \frac{f'(\beta_{f,i})}{f''(\beta_{f,i})} \tag{3.102}$$

in which $f'(\beta_{f,i})$ and $f''(\beta_{f,i})$ respectively are the first and second derivative of the right-hand side of equation 3.94, using the i-th estimate of β_f. Using the notation of equations 3.95a-f, the derivatives can be obtained as:

$$f' = f_1' + f_2' + f_3' + f_4' + f_5' + f_6' \tag{3.103}$$

and

$$f'' = f_1'' + f_2'' + f_3'' + f_4'' + f_5'' + f_6'' \tag{3.104}$$

where $f'_1, f'_2, f'_3, f'_4, f'_5$, and f'_6, are given by equations 3.97a-f, and where:

$$f_1'' = \frac{d^2(f_1)}{d\beta_f^2} = 2W_f\left(\cos^2\beta_f - \sin^2\beta_f\right) - 2\frac{f_{aux2}}{\tan\beta_f} \tag{3.105a}$$

$$f_2'' = \frac{d^2(f_2)}{d\beta_f^2} = 2F_{cp}\left(\sin\alpha_{cp}\sin\beta_f + \cos\alpha_{cp}\cos\beta_f\right) \tag{3.105b}$$

$$f_3'' = \frac{d^2(f_3)}{d\beta_f^2} = \left(4W_f\sin\beta_f\cos\beta_f - 2f_{aux2}\right)\tan\phi \tag{3.105c}$$

$$f_4'' = \frac{d^2(f_4)}{d\beta_f^2} = 2\left(F_{pp}\sin\beta_f - f_{aux1}\right)\frac{\tan\phi}{\cos^2\beta_f} \tag{3.105d}$$

$$f_5'' = \frac{d^2(f_5)}{d\beta_f^2} = 2F_{cp}\left(\cos\alpha_{cp}\sin\beta_f - \sin\alpha_{cp}\cos\beta_f\right)\tan\phi \tag{3.105e}$$

$$f_6'' = \frac{d^2(f_6)}{d\beta_f^2} = 0 \tag{3.105f}$$

in which the auxiliary functions, f_{aux1} and f_{aux2}, are defined in equations 3.98a,b. The iteration, as defined in equation 3.102, is run until the difference between two successive estimates of β_f is sufficiently small. The Newton-Raphson iteration is known to converge rapidly in most conditions. If the iteration does not converge, MRIPA uses the initial estimate for β_f (equation 3.100).

When a value for the failure plane angle, β_f, has been found, it can be used to evaluate the stability of the bank (equation 3.91). The full procedure for determining geotechnical bank stability or instability is summarized in figure 3.18.

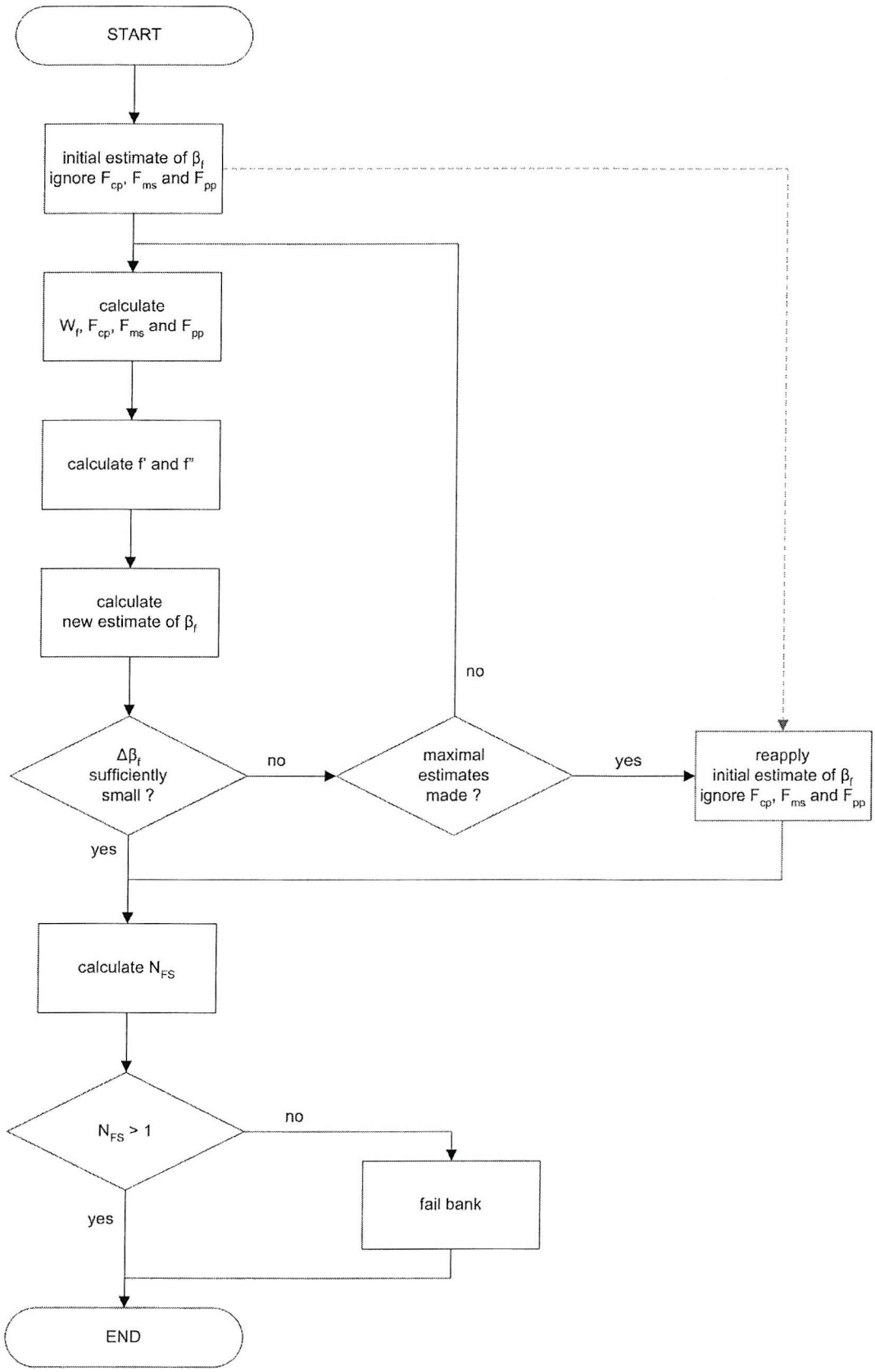

Figure 3.18: Schematic representation of bank stability calculations.

3.5.4. Effects of vegetation on bank stability

Vegetation affects several parameters in the preceding analysis. As outlined in section 2.6.2, the most important of these are: additional shear strength over the failure plane due to the reinforcing effect of roots, a surcharge on the bank, and modified bank drainage. In this section mathematical expressions of these vegetation effects will be derived and incorporated into the bank stability analysis.

Shear strength

Wu (1976) and Wu *et al.* (1979) have shown that, if it is assumed that the vegetation roots are perpendicular to the shear zone, the increase in soil shear strength, s_R, can be represented by the following relation:

$$s_R = A_{R,avg} T_R \left(\sin\theta_s + \cos\theta_s \tan\phi \right) \tag{3.106}$$

where $A_{R,avg}$ denotes the average root area ratio (a measure of root density - see below), T_R is the mean tensile strength of the plant's roots, ϕ is the internal friction angle of the soil, and θ_s is the angle of distortion of the shear zone at the moment of failure. Field observations and laboratory experiments indicate that θ_s is most likely to take a value between 40° and 70° (Wu *et al.*, 1979; Gray and Leiser, 1982). In this range of θ_s the bracketed term is relatively insensitive to changes in θ_s (figure 3.19). In this study a representative value $\theta_s = 55°$ is chosen, with only a small loss of accuracy. It is common to take the simplification even further by also neglecting the variation due to ϕ, in which case the bracketed term is usually equated to a value of 1.2 (Wu *et al.*, 1979; Greenway, 1987). In practice, the increase in shear strength can be treated as an increase in cohesion (Greenway, 1987), so that the expression for apparent cohesion (equation 3.88) can be extended as:

$$c_a L_f = cL_f + F_{ms} \tan\phi^b + c_v L_f \tag{3.107}$$

where c_v denotes the additional cohesion due to the vegetation roots ($c_v = s_R$).

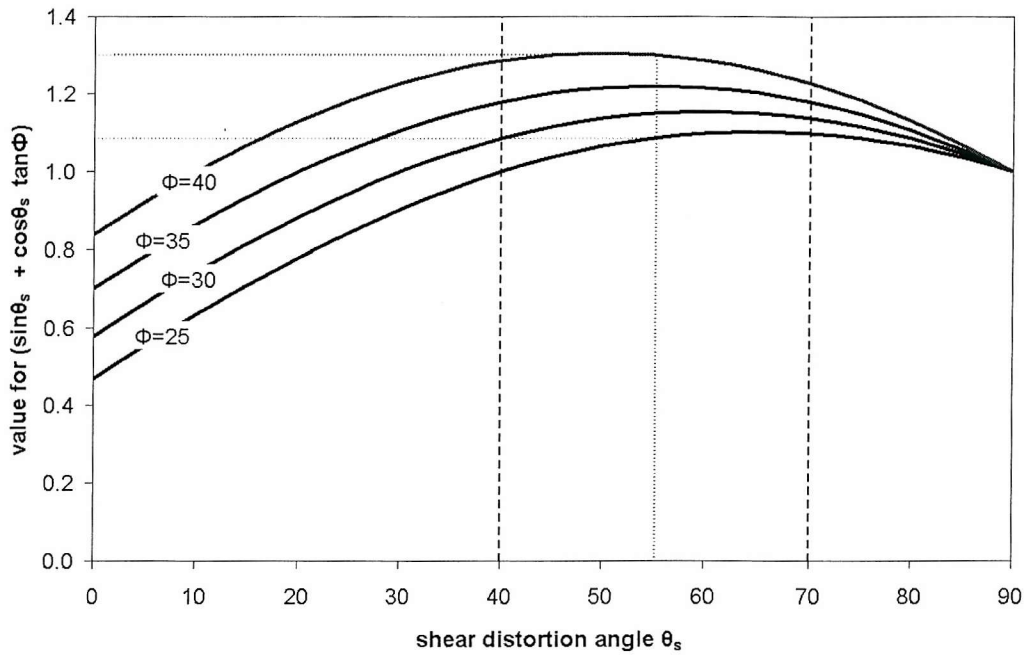

Figure 3.19: Dependency of bracketed term of equation 3.107 on shear distortion angle, θ_s, and internal friction angle, ϕ (after Greenway, 1987). For a given value of ϕ, the bracketed term is relatively insensitive to changes in θ_s when $\theta_s > 40°$ and $\theta_s < 70°$ (range is indicated by hashed lines). By selecting $\theta_s = 55°$ as a representative value, instead of the true value, a small error is introduced for the bracketed term (maximal relative error is less than 8 %, average error for all depicted friction angles is less than 2 %). For this representative value, the bracketed term will always take a value between 1.1 and 1.3.

The above analysis can be extended to include non-perpendicular roots that intersect the failure plane at a root-inclination angle, θ_R. In this case the bracketed term of equation 3.107 becomes a complex function of θ_R, θ_s, and ϕ (Gray and Leiser, 1982). In most practical cases, an a-priori knowledge of root orientation is not available. Nor is there, in the general case, reason to presume a systematic root inclination angle for all roots of a plant. Instead, it seems reasonable to assume that the roots are randomly oriented with respect to the failure plane. In laboratory experiments with randomly oriented fibres the aggregate reinforcing effect appears to be similar to that of the perpendicular-root model (Gray and Ohashi, 1983). For practical purposes, therefore, equation 3.107 can still be used, even for non-perpendicular root orientations (Greenway, 1987).

Using a fixed value for θ_s, equation 3.107 is a function of the soil friction angle, ϕ, and root properties, T_R and $A_{R,avg}$. Approximate values for the mean tensile strength of the roots, T_R, can be found in the literature (*cf.* table 5.8), or may be obtained experimentally (Collison *et al.*, 2001; Abernethy and Rutherfurd, 2001). The average root-area-ratio, $A_{R,avg}$, depends on the spatial distribution of root densities, which is relatively poorly documented (*cf.* section 5.2). In absence of sufficient direct data on the spatial distribution of root densities, a mathematical model is proposed to derive an approximation of $A_{R,avg}$ from other root geometry parameters, which are slightly more accessible: maximal root density, rooting depth, and lateral root extent. The average root-area-ratio, $A_{R,avg}$, is a measure of root density along the failure plane. At any point in the soil, the local root-area-ratio, A_R, is defined as the proportion of the soil area that is occupied by roots, for an arbitrary section of soil:

$$A_R = \frac{area\ of\ roots}{total\ area} \tag{3.108}$$

The root-area-ratio varies along the bank in all spatial dimensions, and depends on vegetation density and species rooting properties. For a single vegetation element, A_R is usually maximal directly underneath the plant's stem, and diminishes in both the lateral and vertical dimensions (Abernethy and Rutherfurd, 2001). Natural vegetation may be subject to preferential root growth in a particular direction, which may lead to a skewed root density distribution. For modelling purposes, however, and in absence of detailed empirical data, a generalized symmetrical distribution is assumed, defined by a rate of lateral decline and a

rate of vertical decline. Further assuming the decline is exponential (Abernethy and Rutherfurd, 2001), this can be represented mathematically as:

$$A_R = e^{a_0 + a_1 L_{xH} + a_2 L_{xV}} \tag{3.109a}$$

or

$$\ln A_R = a_0 + a_1 L_{xH} + a_2 L_{xV} \tag{3.109b}$$

where L_{xH} and L_{xV} are the horizontal and vertical distance to the plant stem, respectively, and a_0, a_1 and a_2 are non-positive coefficients describing the rate of decline. Physically, this function is incorrect, since it never reaches a value of zero, implying an infinite extent of the tree roots. It is, therefore, necessary to assume a critical value, $A_{R,min}$, below which the root-area-ratio can be neglected. Arbitrarily, a value of $A_{R,min} = 0.0001$ has been chosen for all species, indicating the presence of 1 mm^2 of roots in a 10 cm x 10 cm section of soil as the minimal density of roots to influence soil strength. The coefficients a_i can then be calculated as:

$$a_0 = \ln A_{R,\max} \tag{3.110}$$

$$a_1 = \frac{\ln A_{R,\min} - a_0}{L_{rH}} \tag{3.111}$$

$$a_2 = \frac{\ln A_{R,\min} - a_0}{L_{rV}} \tag{3.112}$$

where L_{rH}, L_{rV}, $A_{R,max}$ are three essential root parameters, respectively denoting maximum root extent, maximum root depth, and maximum root density (*i.e.* the root density just below the tree trunk). According to this model the root cluster underneath a single vegetation element is cone-shaped. The cone assumes different forms, ranging from narrow to wide and from shallow to deep (figure 3.20), depending on the root parameters (*cf.* section 5.2).

Using this simple rooting geometry model, the interaction of roots with the incipient failure block can now be explored. Let $P(x,y)$ be a point on the failure plane at a distance x from the toe of the bank. In the general case, where the failure plane intersects the root zone at points $P_1(x_{P1},y_{P1})$ and $P_2(x_{P2},y_{P2})$, four distinct regions can be identified (figure 3.21):

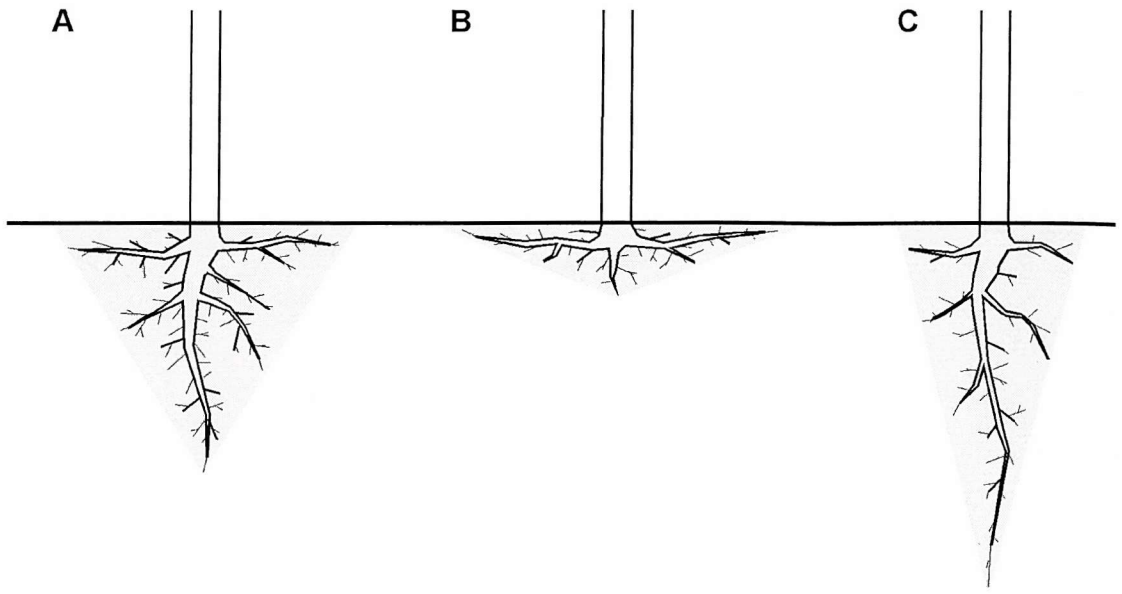

Figure 3.20: Different root cone shapes as determined through the parameters L_{rH} and L_{rV}.
A: $L_{rH} \approx L_{rV}$
B: $L_{rH} \gg L_{rV}$: shallow widespread roots
C: $L_{rH} \ll L_{rV}$: narrow root system with deep taproot

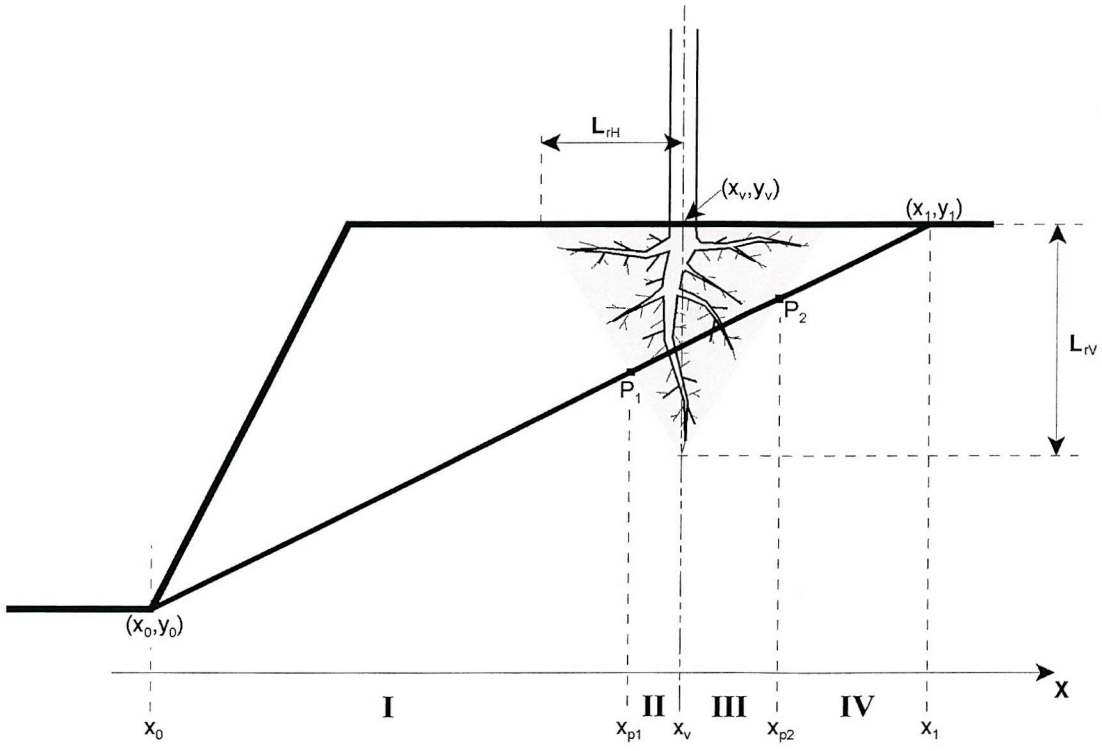

Figure 3.21: Definition sketch of root regions. The regions are determined by the X-coordinates of the vegetation element and the intersection points P_1 and P_2.

region I where $x \in [0,x_{P1}[$

region II where $x \in [x_{P1},x_v]$

region III where $x \in [x_v,x_{P2}]$

region IV where $x \in]x_{P2},x_1]$

The definition of these regions is important because clearly the local root area ratio, A_{Rx}, at a point $P(x,y)$ will depend on the region in which it is located. Regions I and IV are free from root intersection, while in regions II and III the local root area ratio can be calculated by inserting equations 3.110 to 3.112 in 3.109, so that:

$$A_{Rx}^{I} = 0 \tag{3.113a}$$

$$A_{Rx}^{II} = e^{c_1 - c_2 x} \tag{3.113b}$$

$$A_{Rx}^{III} = e^{c_3 - c_4 x} \tag{3.113c}$$

$$A_{Rx}^{IV} = 0 \tag{3.113d}$$

where

$$c_1 = a_0 + a_1 x_v + a_2 y_v - a_2 \tan\beta_f \tag{3.114a}$$

$$c_2 = a_2 \tan\beta_f + a_1 \tag{3.114b}$$

$$c_3 = a_0 - a_1 x_v + a_2 y_v - a_2 \tan\beta_f \tag{3.114c}$$

$$c_4 = a_2 \tan\beta_f - a_1 \tag{3.114d}$$

in which β_f is the failure plane angle as defined by equation 3.100 or 3.102, and a_0, a_1, and a_2 are the coefficients defined in equations 3.110 to 3.112. In region II, the local root area ratio will increase exponentially from $A_{R,min}$ to a local maximum as the failure plane penetrates the root zone. In region III, A_{Rx} will eventually decrease back to $A_{R,min}$, although it might reach a local maximum first, depending on the values of a_1 and a_2. The behaviour of the above root area ratio model is illustrated in section 5.3.2.

From equations 3.113a through 3.113d, the average root area ratio, $A_{R,avg}$, along the entire failure plane can be calculated as:

$$A_{R,avg} = \frac{\int_{x_0}^{x_1} A_{Rx}\,dx}{x_1 - x_0} = \frac{\int_{x_{P1}}^{x_v} A_{Rx}^{II}\,dx + \int_{x_v}^{x_{P2}} A_{Rx}^{III}\,dx}{x_1 - x_0} \tag{3.115}$$

or

$$A_{R,avg} = \frac{\frac{e^{c_1}}{c_2}\left(e^{-c_2 x_{P1}} - e^{-c_2 x_v}\right) + \frac{e^{c_3}}{c_4}\left(e^{-c_4 x_v} - e^{-c_4 x_{P2}}\right)}{x_1 - x_0} \tag{3.116}$$

The above analysis is based on the general situation, where each of the four regions exists (figure 3.22A). Other situations, where not all four regions are present, could also occur, depending on the position of the tree with respect to the failure plane. For example, there may be no intersection at all when the tree stands too far from the bank, or if the rooting depth is too shallow (figures 3.22B and 3.22C), in which case regions II and III do not exist. Alternatively, point $P_2(x_{P2},y_{P2})$ may not physically exist, if the tree is positioned such that the failure plane ends within the root zone (figures 3.22D and 3.22E). These situations differ only slightly in their analysis and are not explicitly described here, although they are, of course, accounted for in MRIPA.

Surcharge

For grasses, the surcharge effect is neglected. For brush and tree species, the plant weight, W_v, can be calculated relatively easily as:

$$W_v = \rho_v V_v \tag{3.117}$$

in which V_v denotes plant volume and ρ_v is wood mass density. Values for the latter can be found in the literature (section 5.2), while the former is estimated using the De Vries method, which treats stems as tapered cylinders and ignores the contribution of roots and branches to the biomass (De Vries, 1974):

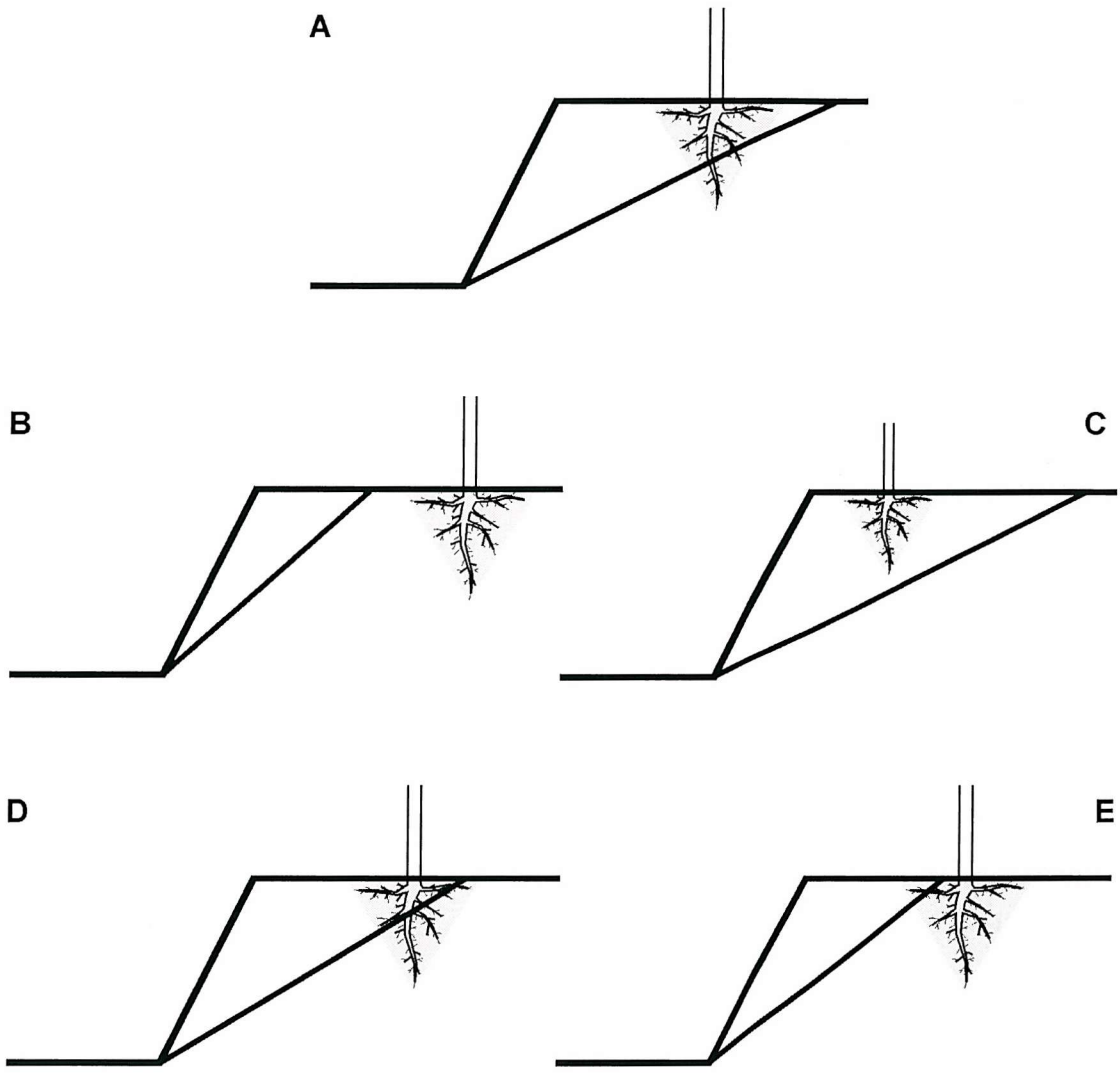

Figure 3.22: Possibilities of failure plane intersection with the root cone.
A full intersection
B, **C** no intersection
D, **E** partial intersection

$$V_v = \frac{\pi}{8} H_v \left(d_{vb}^2 + d_{vt}^2 \right) \tag{3.118}$$

where H_v represents the height of the plant, and d_{vb} and d_{vt} respectively denote the stem diameter at the base and the top. Distributing the weight over the near-surface root area and converting into a force, the surcharge, W_v, is determined as:

$$W_v = \frac{\rho_v g H_v \left(d_{vb}^2 + d_{vt}^2 \right)}{8 \, L_{rH}^2} \tag{3.119}$$

Factor of safety for vegetated banks

The general expression for the factor of safety (equation 3.91) can be expanded to incorporate these vegetation effects by inserting equations 3.107 and 3.119 as additional terms. The factor of safety for vegetated banks is then obtained as:

$$N_{FS} = \frac{\left(c + c_v \right) L_f + F_{ms} \tan \phi^b + \left[\left(W_f + W_v \right) \cos \beta_f - F_{pp} + F_{cp} \cos \alpha_{cp} \right] \tan \phi}{\left(W_f + W_v \right) \sin \beta_f - F_{cp} \sin \alpha_{cp}} \tag{3.120}$$

3.6. Model structure

As is clear from the previous sections, the model consists of three main submodels. Each of these deals with a specific physical process: the flow of water, the dynamics of sediment movement and the failure of riverbanks. In the past these elements have usually been treated in isolation, and it is one of the key features of MRIPA that all three submodels are combined in an integrated channel evolution model, which allows for interactions between each of them.

3.6.1. Overall model structure

The essential idea of the integrated model is that, although each of the submodels should interact with each other, the timescales of the different processes represented in the submodels are such that their calculations can be decoupled. This idea is translated as two assumptions in the model. First of all, flow is assumed to be quasi-steady. This means that flow discharge is considered constant during each timestep, and that variable discharges are represented by stepped hydrographs. The timescale at which the flow field responds to changes in the stepped hydrograph are, in general, much smaller than the timescale at which the bed topography responds. Hence, the bed topography calculations can be decoupled from the flow field computations. Second, it is assumed that planimetric changes of the river channel occur at a lower rate than bed topography changes. This allows bank erosion calculations to be decoupled from the bed computations. Both these assumptions are justifiable for mildly curved ($r_c/W > 5$), alluvial channels with cohesive banks.

Applying these assumptions results in a triple-nested computation procedure, which is summarized in figure 3.23. In the innermost loop the bank and bed are assumed to be fixed, and the flow field is calculated. Sediment transport rates are calculated simultaneously, but only applied at certain timesteps, corresponding to the second loop. At this point bed topography is adjusted, but bank topography is still kept fixed. A third loop cycles through the bank migration timesteps. In this loop, hydraulic bank erosion is applied and checks are made for geotechnical bank stability. The resulting changes in planform shape require the calculation of a new grid. The number of times each loop is activated depends on the total simulation time, the timestep for planform change and the timestep for bed level change, each of which is defined as an input parameter.

3.6.2. Submodel interactions

Although the computation of flow, bed level change and planform change may be decoupled, that does not mean there is no interaction between them. On the contrary, the capability to model the interaction between them is essential, and is what drives MRIPA as a channel evolution model. The interactions between the submodels are illustrated in figure 3.24. Interactions between the flow submodel and the bed topography submodel are fairly

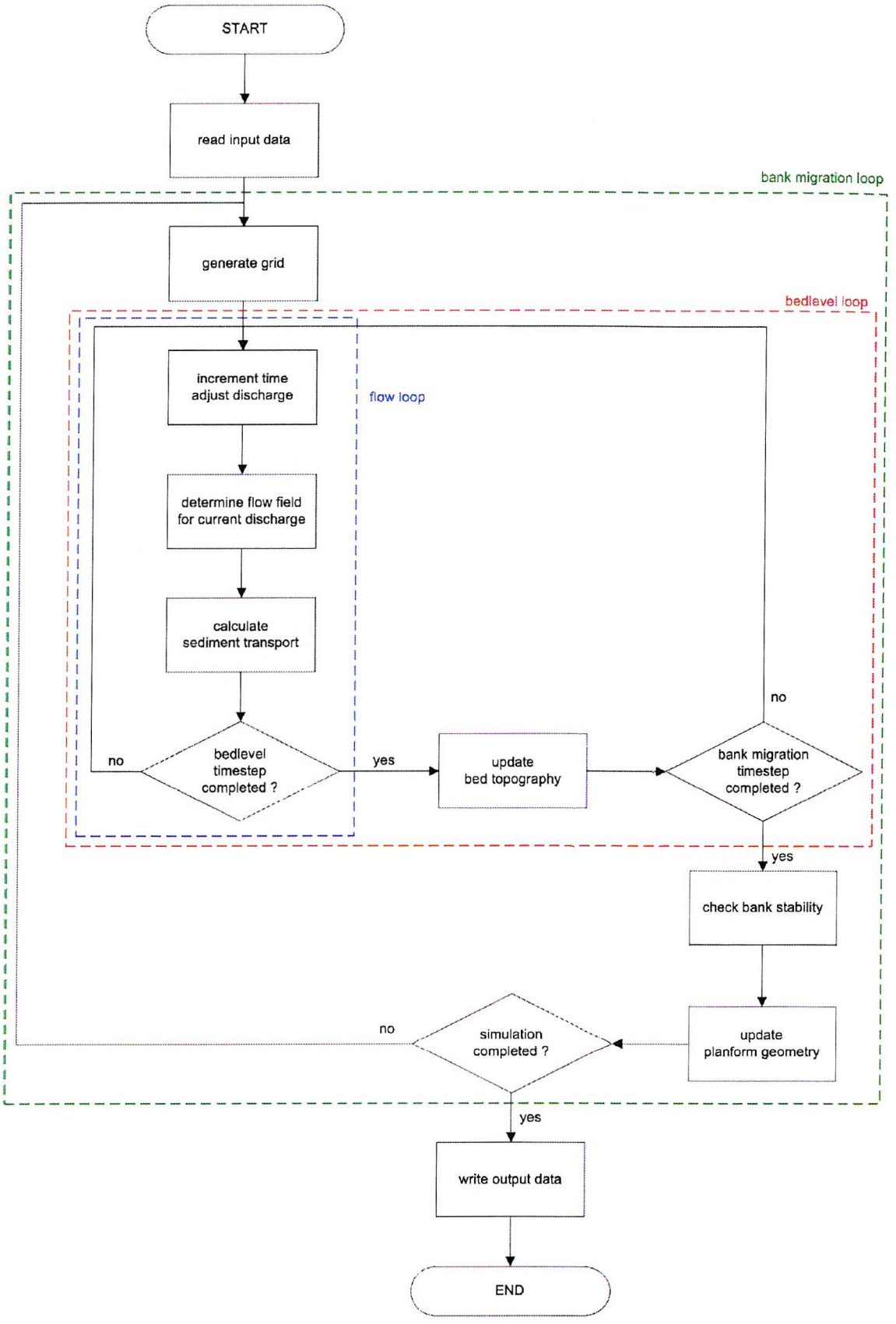

Figure 3.23: Schematic representation of the structure of the MRIPA model. The three nested loops, indicated by the coloured boxes, each focus on one of the three submodels.

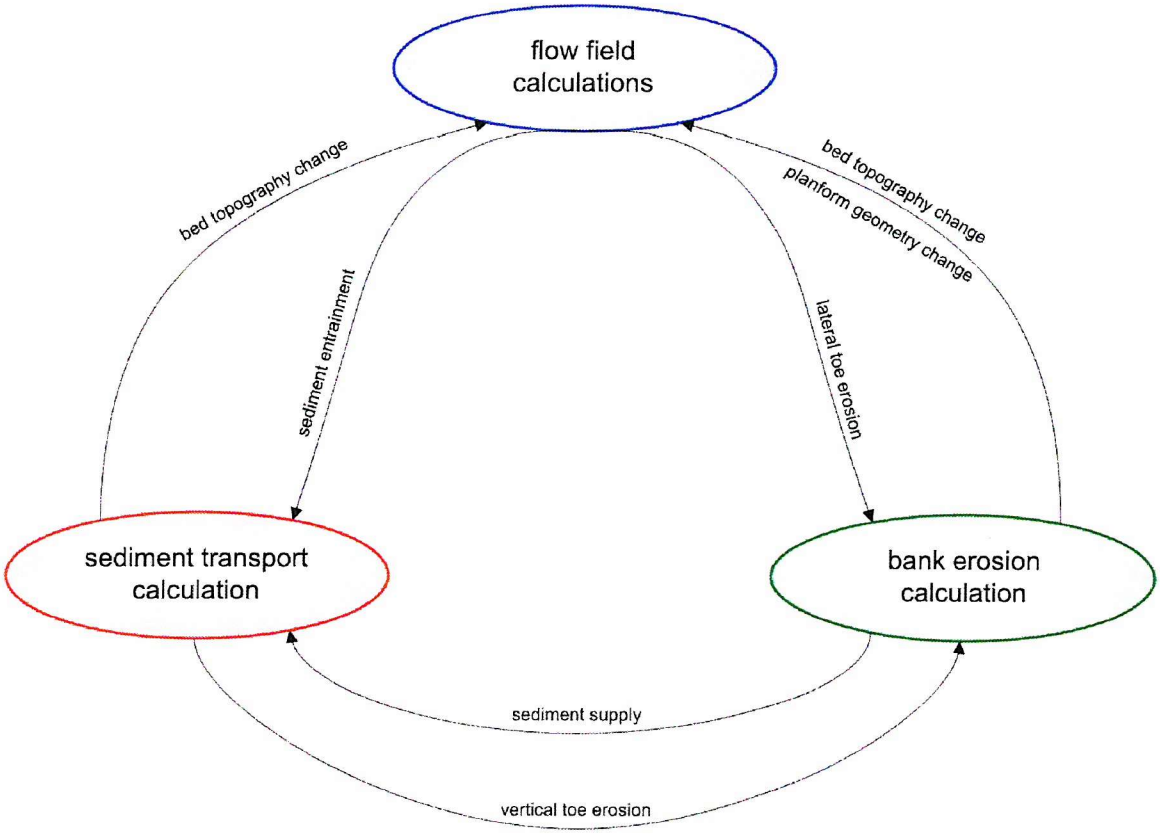

Figure 3.24: Interactions between the submodels.

straightforward. Flow provides a mechanism for sediment entrainment and sediment transport, which results in bed topography changes, which in turn affects the flow field. Both of these submodels operate in the horizontal *sn*-dimensions and on the same grid, which allows for relatively easy computational implementation of their interactions. The bank erosion submodel, on the other hand, works on a cross-profile *nz*-dimension. The interaction between the bank erosion submodel and either of the other two submodels, therefore, deserves some special attention.

It has already been stated that hydraulically driven lateral erosion is applied near the toe of the bank (*cf.* figure 3.13). The volume of sediment thus entrained is calculated as (figure 3.25):

$$V_h = H_{cb}\left|\frac{\partial n_B}{\partial t}\right| + \frac{1}{2}\left|\frac{\partial n_B}{\partial t}\right|^2 \tan\beta_b \qquad (3.121)$$

in which V_h is the volume of sediment supplied per unit length of bank, corresponding to a retreat of the bank toe over a distance n_B, while H_{cb} and β_b denote the height of the cutbank and upper bank slope, respectively. The second term on the right hand side is only relevant if the flow depth exceeds the height of the cutbank.

Bank sediment entrained by hydraulic lateral erosion is added to the sediment load of the channel. The entrained bank material is considered to consist of a fraction, ω_{h1}, of fine, cohesive material ($D < 0.062$ mm) and a fraction, ω_{h2}, of granular material ($D \geq 0.062$ mm), where:

$$\omega_{h1} + \omega_{h2} = 1 \qquad (3.122)$$

The fine material is assumed to be removed from the system as wash load. The granular material is presumed to have similar properties to the bed material, and is added to the sediment load of the channel. This assumption is required as MRIPA's sediment transport submodel is based on a single representative grainsize. The supply of sediment thus delivered to the sediment load of the channel equals:

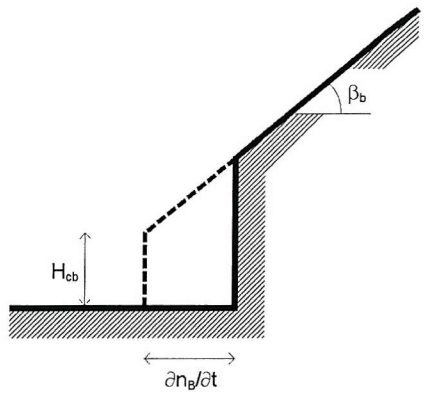

Figure 3.25: Definition sketch for calculating near-toe lateral erosion. The bank geometry is represented by height of the vertical cutbank, H_{cb}, and the angle of the bank slope, β_b.

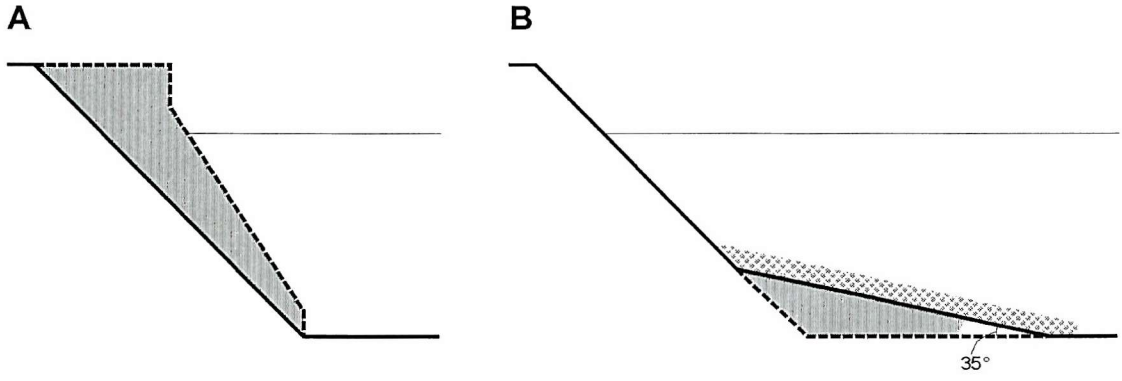

Figure 3.26: Distribution of failed material. **A**: Situation just before failure, with the failure block indicated as shaded area. **B**: Situation after failure. A fraction ω_{f3} of the failed material, indicated as shaded area, is deposited on the channel bed, at an angle of 35 degrees. A fraction ω_{f2}, indicated with small dots, is added to the channel bed load. A final fraction ω_{f1}, not depicted, is removed from the system as washload.

$$V_{h2} = \omega_{h2} V_h = \omega_{h2} \left(H_{cb} \left| \frac{\partial n_B}{\partial t} \right| + \frac{1}{2} \left| \frac{\partial n_B}{\partial t} \right|^2 \tan \beta_b \right) \tag{3.123}$$

where V_{h2} is the volume of entrained sediment consisting of granular material.

Lateral toe erosion steepens the bank. Vertical erosion near the bank toe, resulting from bed topography changes, both steepens and heightens the bank. This change in bank geometry may lead to bank instability (*cf.* section 3.5). When geotechnical bank failure occurs, the failed sediment is delivered to the channel. The failed bank material is considered to consist of a fraction ω_{f1} of fine, cohesive material ($D < 0.062$ mm), a fraction ω_{f2} of small granular material (0.062 mm $\leq$ D < 2.0 mm), and a fraction ω_{f3} of coarse granular material (D $\geq$ 2.0 mm) , where:

$$\omega_{f1} + \omega_{f2} + \omega_{f3} = 1 \tag{3.124}$$

The volumes of each of these fractions can be obtained from:

$$V_{f1} = \omega_{f1} V_f \tag{3.125a}$$

$$V_{f2} = \omega_{f2} V_f \tag{3.125b}$$

$$V_{f3} = \omega_{f3} V_f \tag{3.125c}$$

where V_f is the total volume of the failed block, as obtained from equation 3.71, and V_{f1}, V_{f2}, and V_{f3} are the volumes of the fine cohesive, small granular and coarse granular fractions, respectively. This partitioning is similar, but not identical, to the partitioning of bank sediment fractions with respect to lateral toe erosion. As is the case for entrained sediments, the fractions ω_{f1} and ω_{f2} are removed as wash load or added to the bed load of the system, respectively. A key difference, however, is the consideration the fraction ω_{f3}, which is too coarse to be entrained by the flow, but which can enter the channel through mass failure. This fraction is deposited on the channel bed and transforms the bed topography (figure 3.26). The extent of the deposition is such that the deposition angle equals 35°, and that the deposition volume equals V_{f3}. This method is similar to other depositional models (Pizzuto, 1990; Nagata *et al.*, 2000). In natural rivers, a block of deposited material may remain in position for a long time, until it is weathered into smaller particles or until it is entrained by larger floods (Simon and Darby, 1997). In the model, however, the deposited material

immediately takes the characteristics of the bed material and can be entrained by the flow. Any vegetation present on the failed block is assumed to be instantly removed by the flow (*i.e.* woody debris and other forms of relic riparian vegetation are not considered herein).

The sediment supplied from the banks to the channel bed load has to be accounted for in the sediment continuity equation (equation 3.65). The total volume that is added to the sediment load is:

$$V_2 = V_{h2} + V_{f2} \tag{3.126}$$

where V_2 denotes the total bank sediment contribution to the bed load, V_{h2} is the volume of the contribution by lateral toe erosion (equation 3.123) and V_{f2} is the volume of the contribution by bank failure (equation 3.125b). The sediment added to the sediment load is distributed over the near bank zone, using a distribution function $\delta(n)$, which satisfies the condition:

$$\int_{n_{RB}}^{n_{LB}} \delta(n)\,\mathrm{d}n = 1 \tag{3.127}$$

where n_{RB} and n_{LB} respectively denote the n-coordinates of right and left bank. In the model, the distribution function is chosen such that the sediment is distributed evenly over a lateral distance equal to the bank height. Bank material added to the sediment load acts as a source term in the sediment continuity equation. Using the above relations, equation 3.64 can be expanded to:

$$\varepsilon^* \frac{\partial z_b}{\partial t} + \frac{\partial(\varepsilon^* S_s)}{\partial s} + \frac{\partial(\varepsilon^* S_n)}{\partial n} + \frac{\varepsilon^* S_s}{R_n} + \frac{\varepsilon^* S_n}{R_s} = V_{2,R}\delta_R(n) + V_{2,L}\delta_L(n) \tag{3.128}$$

where the terms on the right hand side denote the bed load supply from the right bank and left bank, respectively denoted with subscripts $_R$ and $_L$.

Lateral erosion near the bank toe and geotechnical bank failure change the channel planform shape. Hence, the flow field calculations are also affected by bank erosion. Migration of bank points is perpendicular to the local bank line. The model does not contain

a lateral sedimentation routine, *i.e.* all deposition is vertical deposition on the channel bed. Therefore, the channel can only widen, not narrow. As the channel widens, flow depth will decrease. Migration of bank points will stop when the shear strength on the banks is too small to cause further entrainment of sediments (*cf.* equation 3.66).

3.6.3. Assumptions and limitations

Many assumptions have been made in the development of the model. Knowledge of the assumptions, is necessary for understanding the limitations and applicability of the model. Mostly, these assumptions constrain the complexity of the problem and simplify the computational procedure; other assumptions are necessitated by lack of empirical data. The most important assumptions have been explicitly noted in the text. However, occasionally some presumptions have been made without being explicitly stated. Hence, for purposes of clarity, an overview of all assumptions made in the model is listed in table 3.1. Most of these are justifiable in terms of the channels under consideration, *i.e.* lowland meandering alluvial channels with riparian vegetation.

3.7. Conclusion

In the preceding sections the development of a two-dimensional numerical model has been described. The model captures the essential physical processes needed to evaluate the evolution of bed topography and channel planform geometry: river flow, sediment transport and bank erosion. Some of the effects of riparian vegetation on each of these groups of processes have been incorporated into the model. Many assumptions (table 3.1) have been made in representing the physical processes in mathematical form. This puts some restrictions on the applicability of the model. However, most of the assumptions can be justified for a wide range of lowland meandering, alluvial rivers with riparian vegetation. In the following chapters, the model will be tested for accuracy and applied to investigate the effects of vegetation on channel migration and bed topography in meandering rivers.

Table 3.1: Assumptions made in the mRIPA model.

assumptions for flow field	flow is incompressible
	flow is subcritical
	flow is quasi-steady
	water pressure is hydrostatic
	no external forces (e.g. wind or Coriolis force) act on the flow
	there is no lateral friction along the side walls
	vertical scale is much smaller than horizontal scale in flow calculation
	the flow field may be approximated as being two-dimensional
	vertical velocity profiles of primary and secondary flow are self-similar
	development of secondary flow may be applied along streamwise coordinate lines
	secondary flow adapts immediately to channel topography and geometry
	secondary flow is zero along the banks
	flow velocity and shear stress are much less for secondary flow than for primary flow
	there is no return flow
	there is no overbank flow
assumptions for sediment transport	longitudinal slope has negligible effect on sediment transport
	sediment transport rate depends on local flow field only
	suspended load transport may be ignored
	bed material is homogenous
	there is no bedlevel change along the inflow boundary
	shear stress applied on the bank is proportional to near-bank bed shear stress
	bank particles are entrained only near the toe of the bank
	entrained bank particles are distributed evenly over the near-bank zone
assumptions for bank erosion	the floodplain is horizontal
	there is no external loading, except from vegetation
	bank can be described with a simple cutbank-slope-cliff profile
	bank material is homogeneous
	banks fail along planar slip surfaces
	the failure surface passes through the toe of the bank
	the soil aquifer is horizontal
	confining pressure is hydrostatic
	banks fail at fully mobilized shear stress
	a fraction of bank material is evacuated as wash load
	upon deposition, bank material assumes the characteristics of bed material
assumptions for vegetation	vegetation elements on failure blocks are instantly removed by the flow
	vegetation is static and does not colonize, grow, die or otherwise change
	roots are randomly oriented, but distributed symmetrically underneath the plant
	root density distribution can be described by an exponential decline
	there is a root density below which the effect of roots may be ignored
	the presence of roots does not affect friction angle of the soil
	roots are linearly elastic and mobilize full tensile strain
	during failure, roots break and are not pulled out
	root biomass can be ignored with respect to above ground biomass
	vegetation suction is proportional to matric suction
	plant stems can be treated as flexible cylinders
	the effects of leaves and branches can be ignored
	species-dependent vegetation parameters can be derived from academic literature
	wake-effects of vegetation can be ignored
	critical shear stress for bank sediment entrainment is altered by vegetation
other	computations of flow, sediment transport and bank erosion may be decoupled
	transverse spacing of grid points is roughly equidistant

Chapter 4
Model Calibration and Validation

4.1. Introduction

This chapter discusses the performance of the MRIPA model in terms of its ability to predict changes in channel bed topography and bank morphology. A lack of experimental data for vegetated channels constrains this assessment to non-vegetated channels. The effects of vegetation are examined in chapter 5, using a different methodology. Here, the process of assessing the model's performance is split in three distinct components: sensitivity analysis, calibration and validation. In the first stage, sensitivity analysis (section 4.2), each of the model parameters is systematically varied over a given range and the resulting model outputs are compared for quantitative and qualitative differences. This allows identification of the most responsive model parameters. In the second stage, model calibration (section 4.3), the model is used to replicate laboratory experiments for which high quality data (detailed information on initial and final morphology as well as discharge conditions) is available. The model parameters are adjusted to generate optimal correspondence between the experimentally observed data and the model's output. This adjustment process focuses on the most responsive parameters, as identified in the sensitivity analysis. In the third stage, model validation (section 4.4), the model is run on a different experimental data set, using the calibrated parameters without further adjustments. Comparison of modelled and observed topography facilitates assessment of the model's accuracy and limitations.

4.2. Parameter sensitivity analysis

To be capable of running a simulation, the MRIPA model requires a certain amount of data to be specified. Most of this input data is concerned with describing the boundary conditions, *i.e.* initial topography and discharge conditions, but it also includes physical, empirical and numerical parameters. For some of these parameters the values can be derived easily and accurately from field measurements; others can only be estimated within a certain

bound; others yet can be chosen freely, albeit within theoretical or empirical constraints. The values chosen for these parameters influence the calculations in the model. Hence, any choice of parameter values, or any inaccuracies in their determination, will affect the outcome of a simulation. It is, therefore, useful to investigate how sensitive the model is to changes in these parameters. To this end, a series of simulations is conducted in a sample channel (section 4.2.2), where some of the more important empirical and numerical parameters (section 4.2.1) are changed between each simulation. The effect of changing the parameters is quantified by means of a 'sensitivity index' (section 4.2.3). The results and limitations of this analysis are discussed in sections 4.2.4 and 4.2.5. The sensitivity analysis conducted here is restricted to model parameters only. Sensitivity to grid resolution is a separate issue, which is considered in appendix A3, for each of the grids used in this study.

4.2.1. Parameters

Nine parameters are included in the sensitivity analysis (table 4.1). Most of these are empirical or numerical parameters. However, the Chezy roughness coefficient, C, is also included, as there often is considerable uncertainty in its estimation. The impact of each parameter is analysed separately, *i.e.* all but one of the parameters are kept constant during the simulations. In each simulation, the values for the "constant" parameters are taken from a set of reference parameter values (table 4.1). These reference values are taken from recommendations from other authors (Mosselman, 1992; Olesen, 1987) or picked arbitrarily within the theoretical range. Note that, although MRIPA allows for spatially variable roughness coefficients, C, for simplicity a constant value is applied over the entire reach for each simulation in this analysis.

Table 4.1: Parameters used in the sensitivity analysis.

parameter (P)	symbol	reference value
Chezy roughness coefficient [-]	C	37.6
weighting coefficient for streamwise bed-slope [-]	k_{ls}	4.0
coefficient for model for k_{ts} [-]	k_{tm}	1.78
exponent in model for k_{ts} [-]	p_{tm}	1.0
weighting coefficient for secondary flow intensity [-]	k_{si}	9.89
secondary flow convection factor [-]	k_{sn}	0.94
adaptation length of secondary flow [m]	λ_r	0.7
coefficient in power law for sediment transport [-]	k_s	0.0002
exponent in power law for sediment transport [-]	p_s	5.0

4.2.2. Sample channel

The sample channel, used for testing the sensitivity of the model parameters, describes a simple 180 degree bend with a flat bed (figure 4.1). It is a slightly simplified version, using vertical sidewalls, of the laboratory flume at the Iowa Institute for Hydraulic Research (Odgaard, 1984), which is used for the calibration process, as discussed in the next section. The channel is represented numerically on a grid of 1029 points: 49 cross-sections, consisting of 21 points each (figure 4.2). The initial flow depth is set equal to 0.102 m at every point and a discharge of 0.154 m^3/s is maintained throughout the simulation. The bed is free to adjust to the simulated flow conditions, while the banks are fixed. The simulation continues until equilibrium bed topography and flow conditions have developed.

Figures 4.3 and 4.4 illustrate the flow field and the equilibrium bed topography as predicted using the reference parameter values. Note that MRIPA does not predict bed topography directly, instead it predicts flow depths. However, as the model is a rigid lid model, it is easy to convert flow depths to bed elevations relative to an arbitrary datum. The terms "equilibrium bed topography" and "equilibrium flow depth" are, therefore, used interchangeably throughout this text. Similarly, all figures of bed topographies actually illustrate flow depths, although they are colored according to topographic convention for ease of interpretation.

4.2.3. Definition of the sensitivity index

For each parameter P included in the sensitivity analysis, a series of N_P simulations is run, with different values P_i for the parameter, where the subscript i takes a value between 1 and N_P. From these simulations, the local impact of a change in parameter value, ΔP_i, is quantified, for each point on the grid, through its resulting change in predicted equilibrium flow depth, ΔH_i:

$$impact = \frac{\Delta H_i}{\Delta P_i} \tag{4.1}$$

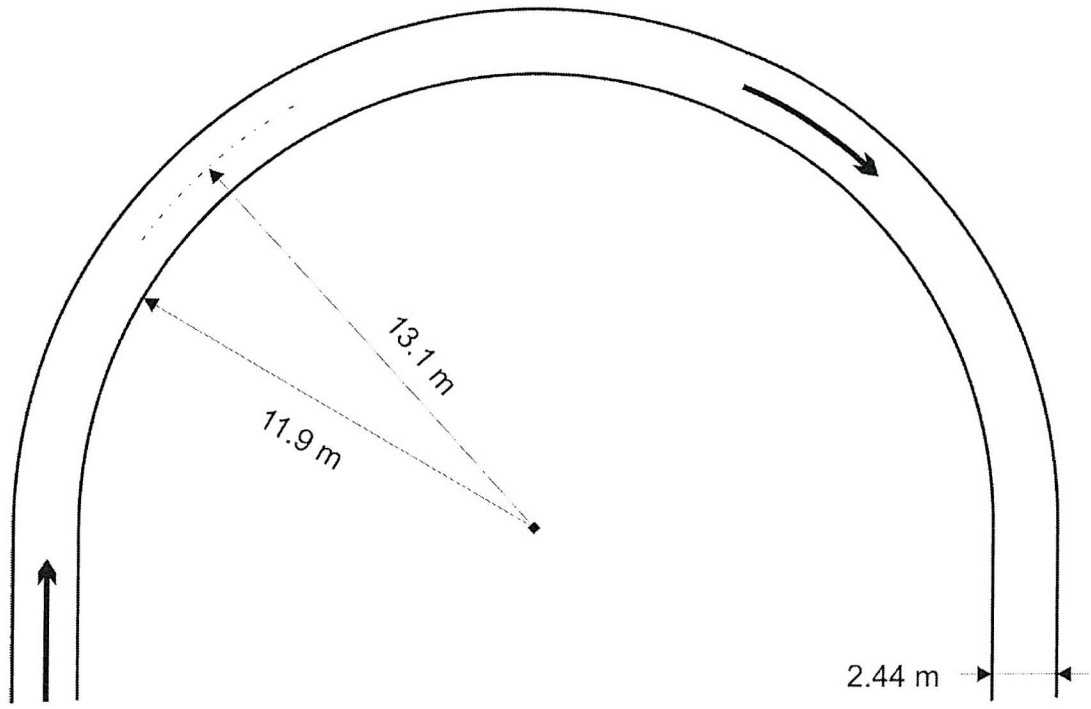

Figure 4.1: Layout-sketch of the sample channel.

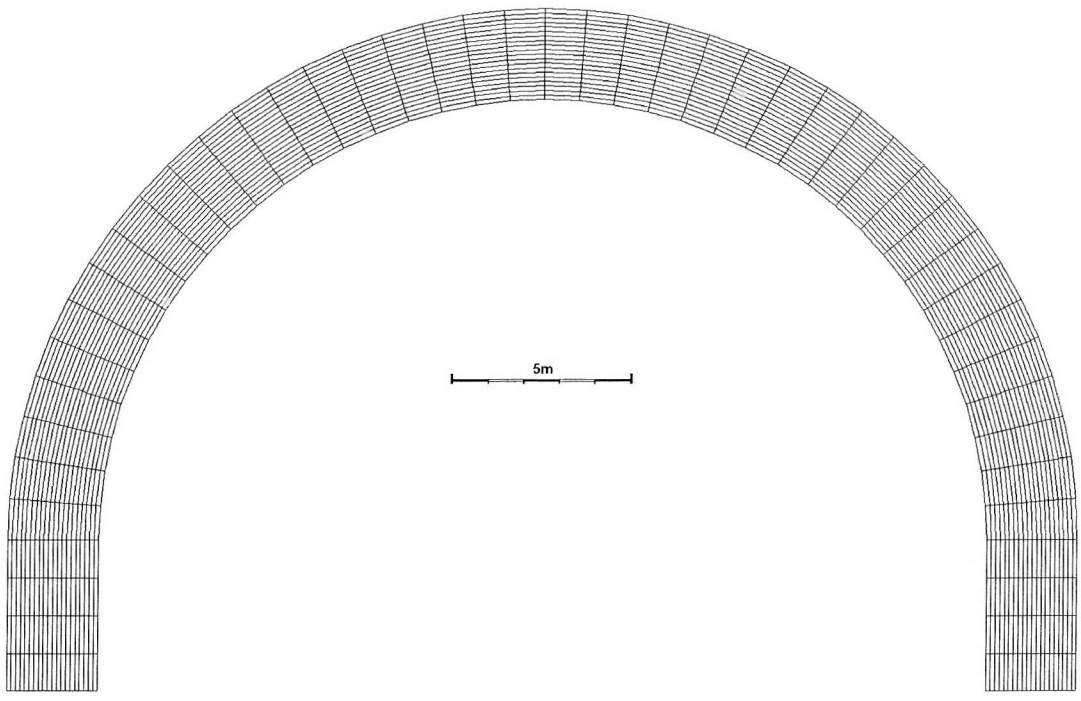

Figure 4.2: Numerical grid for the sample channel.

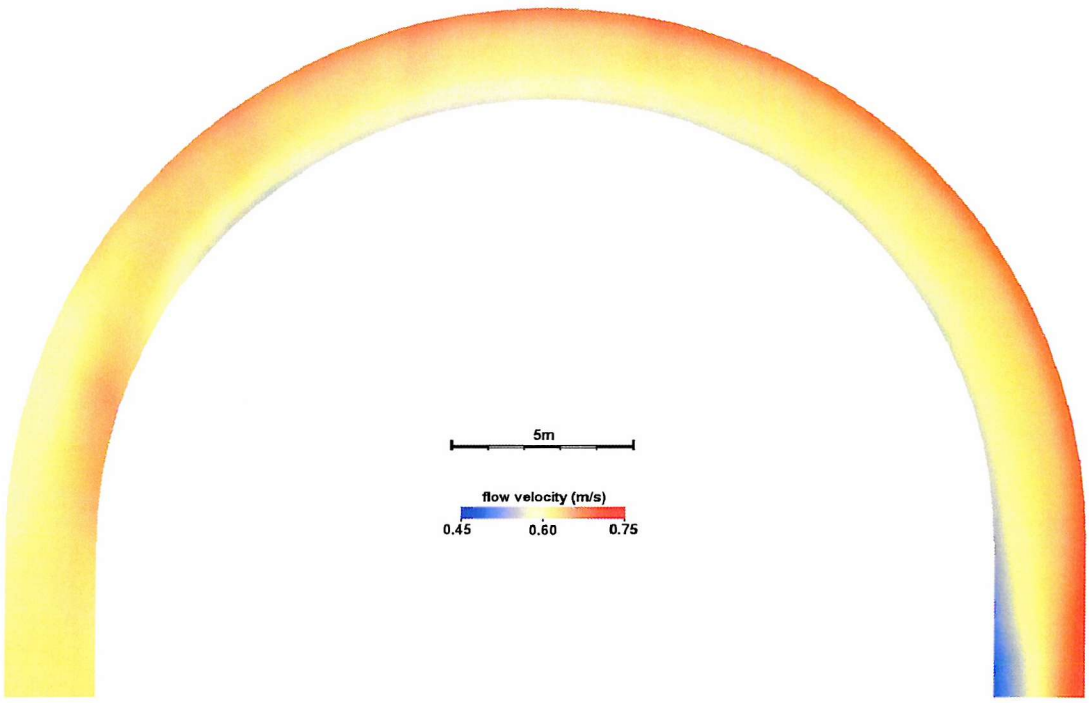

Figure 4.3: Predicted flow velocity in the sample channel, using reference parameter values.

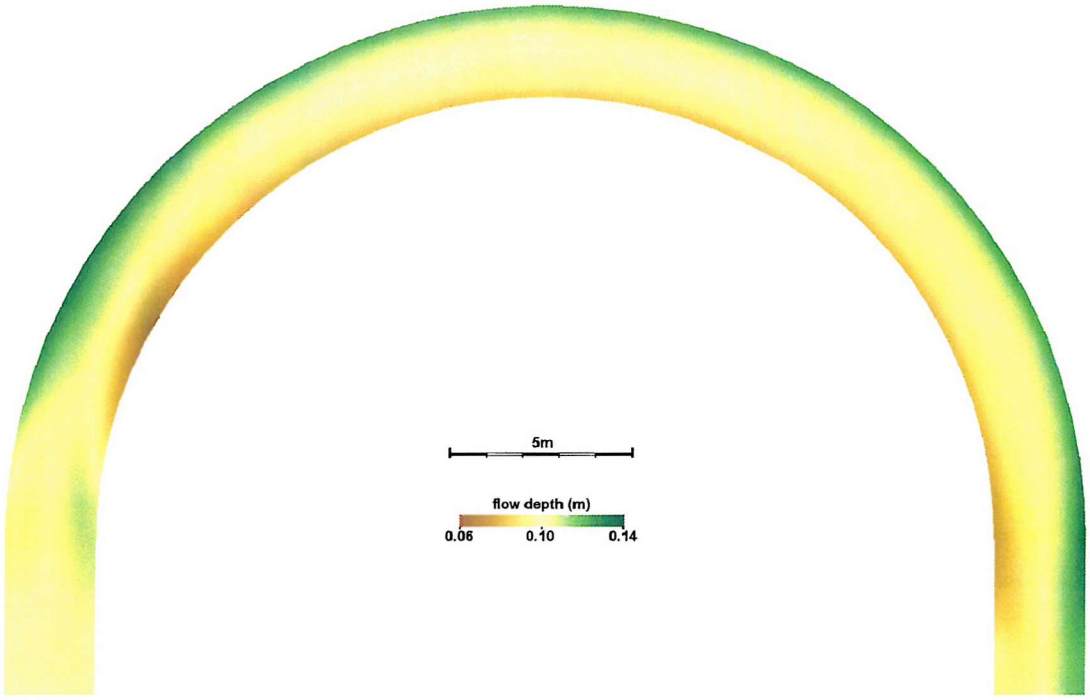

Figure 4.4: Predicted bed topography in the sample channel, using reference parameter values.

The various parameters in the model are likely to have different impacts on the outcome of the model. To allow comparison between the impacts of different parameters, the change in parameter is normalised:

$$\Delta P^* = \frac{\Delta P}{P_{avg}} = \frac{P_{\max} - P_{\min}}{P_{avg}} \tag{4.2}$$

where ΔP^* denotes the normalised parameter change and P_{avg}, P_{min} and P_{max} refer to the average, minimal and maximal value of the parameter, respectively. Likewise, the change in predicted equilibrium topography can also be normalised:

$$\Delta H^* = \frac{\Delta H}{H_{avg}} = \frac{H_{\max} - H_{\min}}{H_{avg}} \tag{4.3}$$

where ΔH^* denotes the normalised change in flow depth, and H_{avg}, H_{min} and H_{max} respectively represent the average, minimal and maximal predicted flow depth at the point under consideration. Note that the values for H_{avg}, H_{min} and H_{max} themselves are spatially variable over the entire grid and that the averaging and the taking of extreme values is not spatial, but rather that it occurs over the variation in flow depths predicted, at a specific point, using the different values of P_i. Hence, the value for ΔH^* is also spatially variable. Following the idea from equation 4.1, a local sensitivity index, $N_{SI,loc}$, is now defined as:

$$N_{SI,loc} = k_{NSI} \frac{\Delta H^*}{\Delta P^*} \tag{4.4}$$

in which the coefficient $k_{NSI} = 1$ if $H_{Pmin} > H_{Pmax}$ and $k_{NSI} = -1$ if $H_{Pmin} < H_{Pmax}$, where H_{Pmax} and H_{Pmin} denote the flow depths for P_{max} and P_{min} respectively. This index takes a negative value when an increase in the parameter value results in an increase in flow depth, and a positive value when an increase in the parameter value results in a decrease in flow depth. Following this procedure, a local sensitivity index, $N_{SI,loc}$, is obtained for each grid point, which can subsequently be visualized on planform graphs. Such graphs are a useful tool, as they provide insight in the spatial effects of changes in a parameter's value. However, for ease of summarising and comparing the impacts of different parameters, a single global sensitivity index, N_{SI}, for each parameter is more helpful. There are several possible methods to derive a global sensitivity index from the local ones. The two most obvious methods are to take the

overall root-mean-square (RMS) of all the local sensitivity indices, or, alternatively, to look at the range of all the local sensitivity indices. Here the first option is chosen, as this indicator is less affected by outliers and better represents the overall, reach-scale impacts of parameter change, which is considered to be of more interest, especially for comparison between parameters. Hence, the global sensitivity index, N_{SI}, is defined as:

$$N_{SI} = \sqrt{\frac{\sum_{grid} N_{SI,loc}^2}{n_{grid}}} \tag{4.5}$$

in which n_{grid} denotes the number of points in the grid (n_{grid} = 1029 for the sample channel). Thus, N_{SI} describes the RMS, taken over the entire channel, of normalised changes in predicted equilibrium topography relative to the normalised change in parameter value, for the parameter under consideration.

4.2.4. Parameter sensitivity

For each of the nine parameters P included in the sensitivity analysis, a series of N_P simulations is run. In these simulations the value of P is varied over a certain range (table 4.2), while the values of the other parameters is kept equal to the reference value.

Table 4.2: Setup of the parameter sensitivity analysis.

parameter P	number of simulations N_P	minimal value P_{min}	maximal value P_{max}	normalised range ΔP^*
C	5	27.6	47.6	0.53
k_{ls}	4	2.0	8.0	1.20
k_{tm}	6	0.59	2.08	1.12
p_{tm}	4	0.5	2.0	1.20
k_{si}	5	3.30	9.89	1.00
k_{sn}	6	0.31	1.09	1.11
λ_r	4	0.5	1.1	0.75
k_s	6	0.0001	0.0006[1]	1.43
p_s	4	3.0	6.0	0.67

note: [1] values larger than 0.0006 resulted in numerical instabilities for the sample channel

The global sensitivity indices, N_{SI}, are calculated for each of the parameters and ranked from high to low (table 4.3; figure 4.5). Higher values of N_{SI} for a parameter, P, indicate that the model is more sensitive to changes in the values of this parameter. Thus, it is clear that MRIPA is very sensitive to the transport formula parameters, k_s and p_s, and to the weighting coefficient for the influence of the secondary flow intensity, k_{si}. It can also be seen, that the coefficient in the transverse slope model, k_{tm}, is much more influential than the exponent, p_{tm}, and that the model is not very sensitive in changes to the convection factor, k_{sn}, the adaptation length of the secondary flow, λ_r, or the weighting coefficient k_{ls}. The results also indicate that the model is fairly sensitive to the Chezy roughness coefficient, C, highlighting the need for accurate determination of the roughness values.

Although the global sensitivity indices allow to compare the different parameters in terms of their sensitivity to change, they do not give any insight on how a change in parameter value affects the simulated equilibrium flow depth. However, the local sensitivity indices, $N_{SI,loc}$, for each parameter do provide this information. When plotted spatially, they not only show how a change in parameter value affects simulated flow depth at each point, but also how this impact is distributed throughout the reach. This information is very helpful in the calibration process (section 4.3). Figures 4.6 to 4.10 illustrate the patterns of the local sensitivity indices, $N_{SI,loc}$, for the five most influential parameters. Blue colouring indicates that increasing the parameter value increases the equilibrium flow depth, *i.e.* lowers the equilibrium bed topography, while red colouring indicates that equilibrium flow depth decreases with increasing parameter values. For example, an increase in p_s reduces the flow depth along the outer bank and increases it along the inner bank (figure 4.6A). This results in a shallower transverse bed slope (figure 4.6D). It can be seen that nearly all the parameters have little impact in the centre of the channel, whilst they significantly affect the equilibrium topography near the banks. Some patterns are consistent throughout the bend, like that of p_s, k_{si} and k_{tm} (figures 4.6A, 4.8A and 4.10A), while the impact of a change in k_s or C alternates near the pointbar (figures 4.7A and 4.9A). The spatial distribution of $N_{SI,loc}$ for the Chezy roughness coefficient (figure 4.9A) appears to be related to the spatial distribution of the flow velocity (*cf.* figure 4.3). Most parameters have a more pronounced impact in the beginning of the bend, *i.e.* over the point bar or upstream of it. This is especially true for the four less important parameters (not depicted here), which hardly have any impact beyond the point bar ($N_{SI,loc} \approx 0$).

Table 4.3: Global sensitivity index of MRIPA parameters.

parameter P	symbol	sensitivity index N_{SI}
exponent in power law for sediment transport	p_s	0.377
coefficient in power law for sediment transport	k_s	0.237
weighting coefficient for secondary flow intensity	k_{si}	0.226
Chezy roughness coefficient	C	0.128
coefficient in model for k_{ts}	k_{tm}	0.101
secondary flow convection factor	k_{sn}	0.063
adaptation length for secondary flow	λ_r	0.044
weighting coefficient for streamwise bed-slope	k_{ls}	0.044
exponent in model for k_{ts}	p_{tm}	0.010

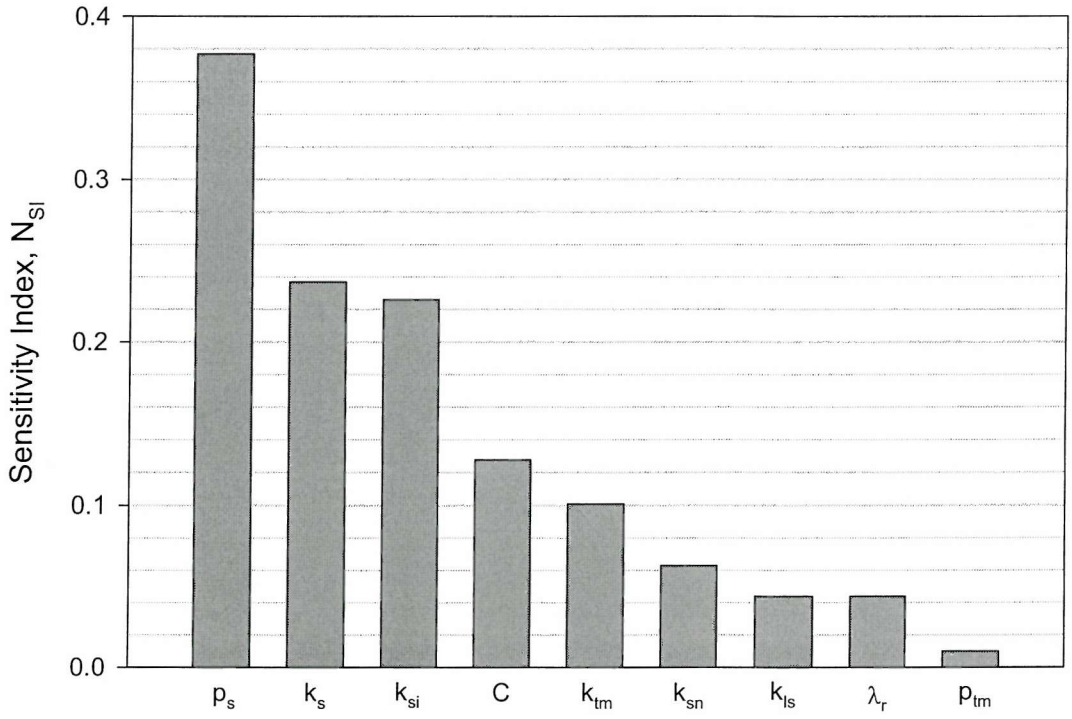

Figure 4.5: Global sensitivity index, N_{SI}, for the tested parameters.

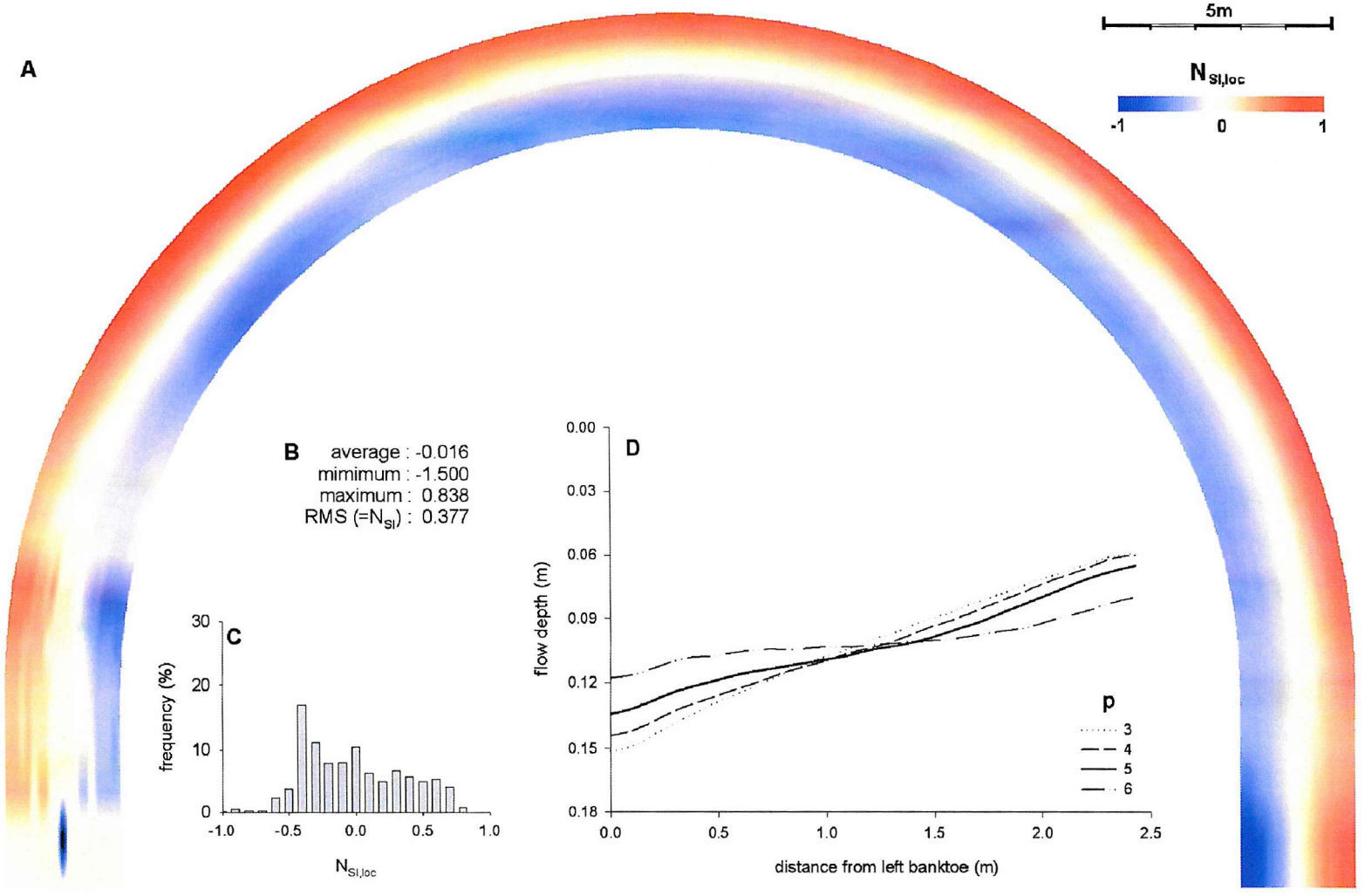

Figure 4.6: Sensitivity plot of the exponent in the power law for sediment transport, p_s. **A**: Spatial distribution of $N_{SI,loc}$. **B**: Basic descriptive statistics of the global distribution of $N_{SI,loc}$. **C**: Histogram of the distribution of $N_{SI,loc}$. **D**: Cross-sections over the pointbar for the range of tested parameter values.

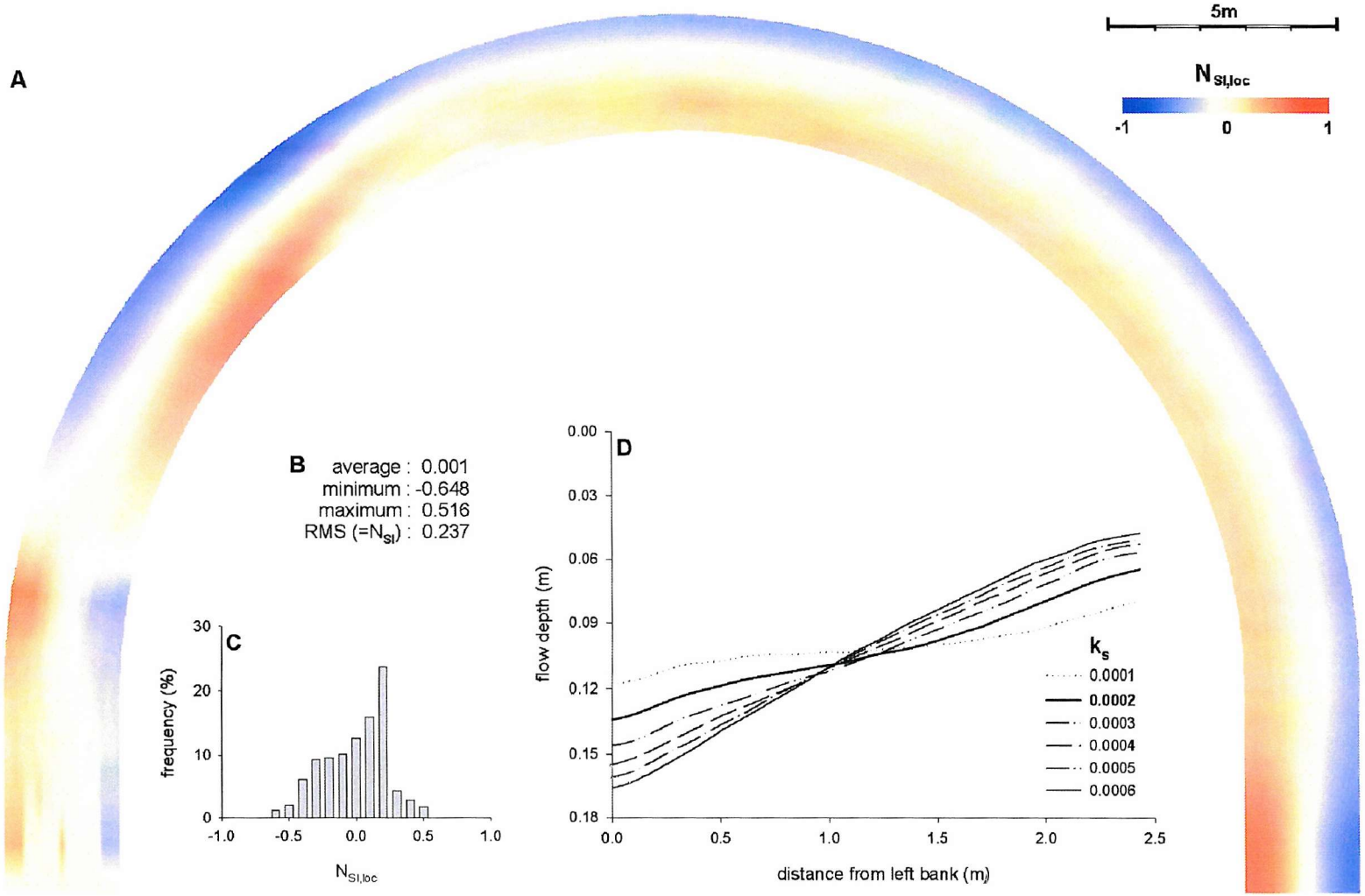

Figure 4.7: Sensitivity plot of the coefficient in the power law for sediment transport, k_s. **A**: Spatial distribution of $N_{SI,loc}$. **B**: Basic descriptive statistics of the global distribution of $N_{SI,loc}$. **C**: Histogram of the distribution of $N_{SI,loc}$. **D**: Cross-sections over the pointbar for the range of tested parameter values.

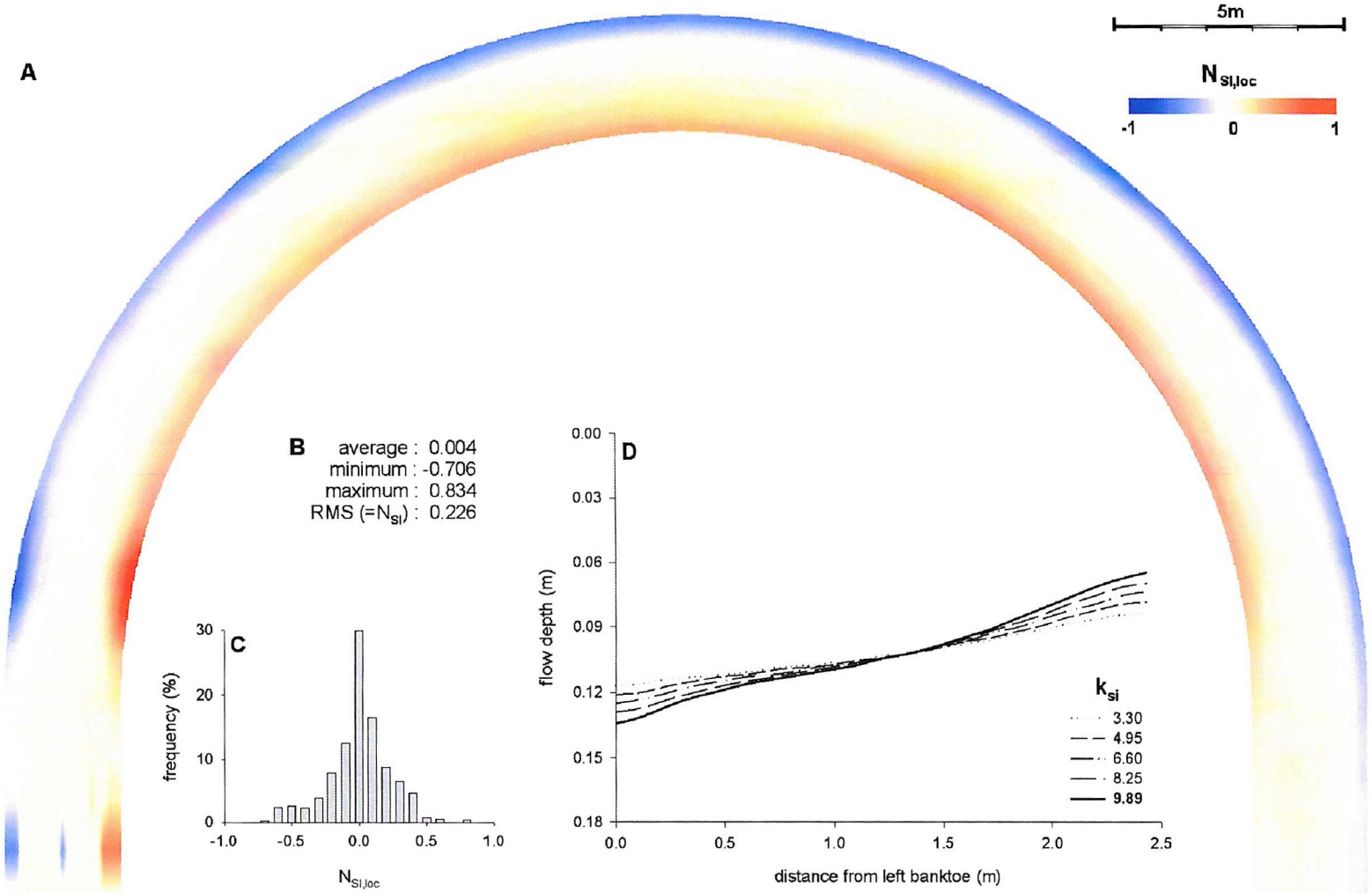

Figure 4.8: Sensitivity plot of the weighting coefficient for secondary flow intensity, k_{si}. **A**: Spatial distribution of $N_{SI,loc}$. **B**: Basic descriptive statistics of the global distribution of $N_{SI,loc}$. **C**: Histogram of the distribution of $N_{SI,loc}$. **D**: Cross-sections over the pointbar for the range of tested parameter values.

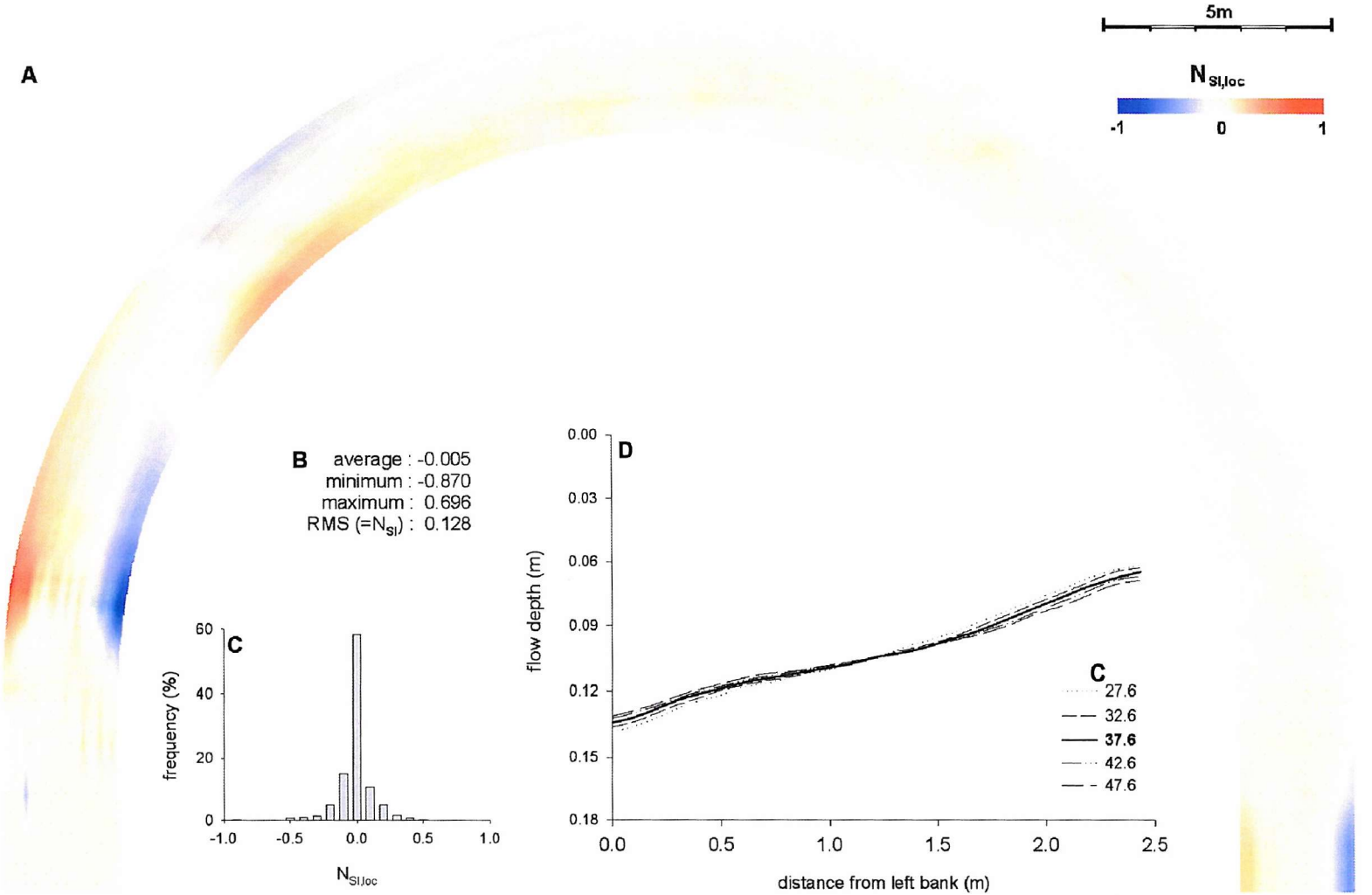

Figure 4.9: Sensitivity plot of the Chezy roughness coefficient, *C*. **A**: Spatial distribution of $N_{Sl,loc}$. **B**: Basic descriptive statistics of the global distribution of $N_{Sl,loc}$. **C**: Histogram of the distribution of $N_{Sl,loc}$. **D**: Cross-sections over the pointbar for the range of tested parameter values.

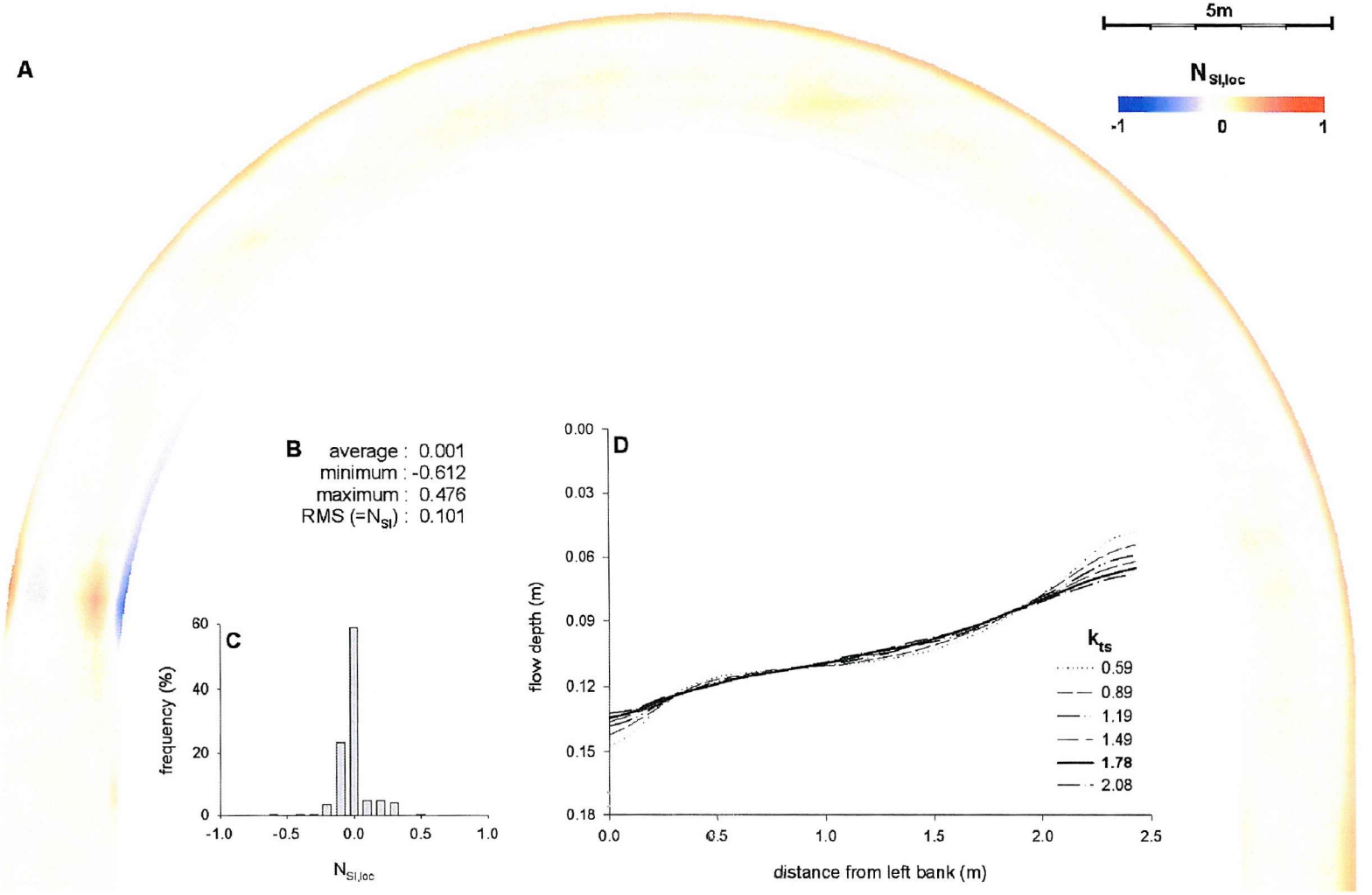

Figure 4.10: Sensitivity plot of the coefficient in the transverse slope model, k_{tm}. **A**: Spatial distribution of $N_{Sl,loc}$. **B**: Basic descriptive statistics of the global distribution of $N_{Sl,loc}$. **C**: Histogram of the distribution of $N_{Sl,loc}$. **D**: Cross-sections over the pointbar for the range of tested parameter values.

4.2.5. Limitations of the sensitivity analysis

The method of sensitivity analysis, as outlined and performed in the preceding sections, suffers from two limitations. First, the results apply to the sample channel only, and may well be different for channels with other geometries. The response to a change in a parameter may depend on width-depth ratios, channel curvature and bank angle. Ideally, a sensitivity analysis would be performed for each channel geometry to which the model is applied. Practically, however, this is not always possible. It is thought that although the values of N_{SI} may not be applicable to every channel, they are sufficiently indicative of the responsiveness of the model to allow identification of the most important parameters.

The second limitation is that parameter space is poorly sampled when parameters are changed individually (hereafter referred to as the IS-method). By keeping all but one of the parameters constant, interactions between parameters are not considered. However, the model's response to a change in a parameter P can depend on the values of the other parameters, which may have significant consequences for the obtained sensitivity indices. For example, the effect of changing k_{tm} from 0.59 to 2.08 is likely to be different at $k_{sn} = 0.31$ than at $k_{sn} = 1.09$. Such inter-parameter effects are not accounted for in the IS-method. Effectively, each of the nine parameter analyses represents a line through parameter space, with all lines intersecting at the same point. An alternative method of analysis could be suggested, where the parameter space is sampled more exhaustively, for example by allowing all possible combinations of the values P_i (figure 4.11). The main advantage of exhaustive sampling (referred to as the ES-method) is that it would help to identify parameter interaction. The main disadvantages are the prohibitively high number of simulations required as the number of parameters increases, and the subsequent difficulty of analysing and summarizing the results. Covering the parameter space of the nine parameters listed in table 4.1 requires only 36 simulations with the IS-method, but it takes almost 1400000 simulations to cover the same range of parameter values at the same intervals with the ES-method.

Variant methods of sampling parameter space, using sparser point sampling and hence requiring fewer simulations, can be suggested, although the total will still be considerably higher than when analysing the parameters individually. Even though the IS-method is not as comprehensive as the alternative(s), and does not allow for inter-parameter effects, it still allows some basic insights in the responsiveness of the model to

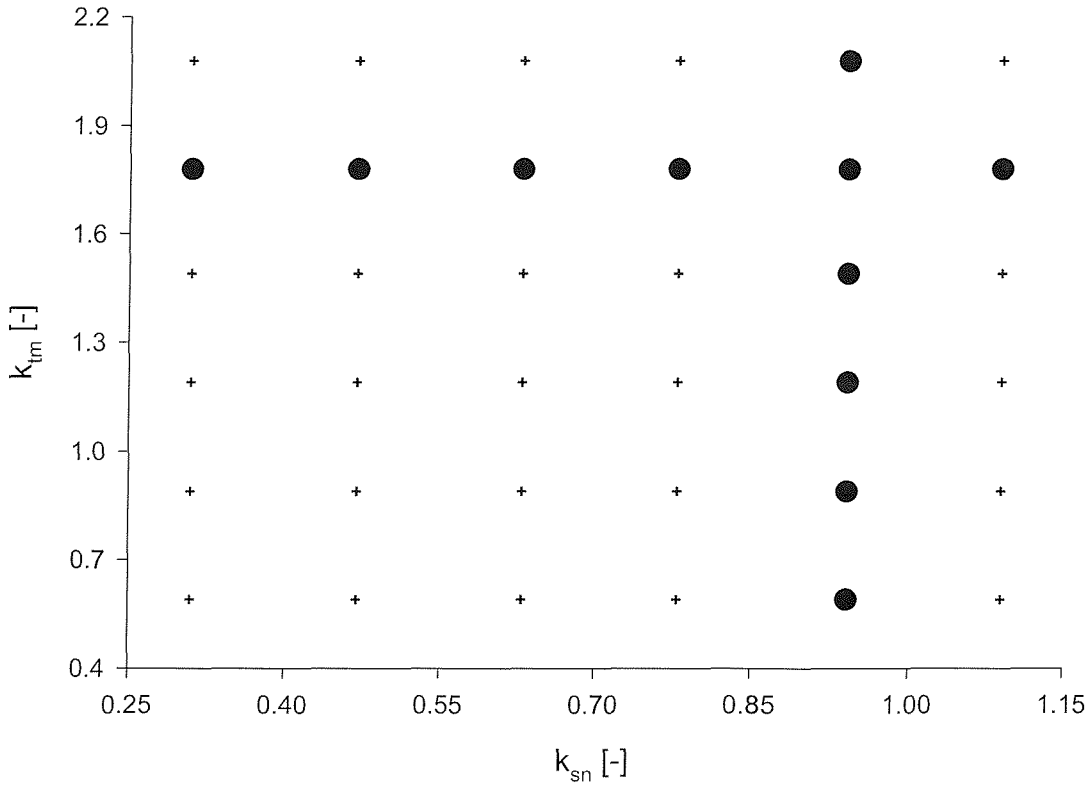

Figure 4.11: Example of parameter space sampling strategies, using only 2 parameters. Points sampled using the IS-method are indicated by large dots; points sampled with the ES-method are indicated with small crosses. The IS-method traces two lines through parameter space which intersect at the reference values. Parameter space is clearly better covered with the ES-method. Each of the two parameters is sampled over 6 values, leading to 36 (6x6) sample points for the ES-method and 11 (6+6-2+1) sample points for the IS-method. Extending the graph to all nine parameters included in the sensitivity analysis would show a similar pattern with the ES-method fully covering a 9 dimensional parameter space, and IS-method tracing nine lines through the parameter space, all intersecting in the same point. The difference in number of points sampled diverges rapidly as more parameters are added. For all nine parameters included in the sensitivity analysis, the IS-method only samples 36 (= ΣN_p - 9 + 1) points, while using the ES-method would result in 1382400 (= ΠN_p) sampled points. As each sampled point requires a run of the model, the improved covering of parameter space clearly comes at a heavy computational price.

changes in the parameter values. Since the idea of the sensitivity analysis is to provide an indicative measure of parameter sensitivity, it is believed that the disadvantages of the ES-method outweigh its advantages, and that the choice for adopting the simpler IS-method is justified.

4.3. Calibration

The model contains several parameters which cannot readily be obtained from physical measurement, yet for which a value still needs to be supplied. If this is the case, a value for these parameters may be obtained through calibration. Where possible, the model should be calibrated for every new channel reach to which it is applied. However, as the calibration process is very data intensive, this will frequently be impractical. In this section, some recommended values for the parameters will be derived through calibration on two laboratory flume datasets. Parts of this section have been reported elsewhere (Darby, Alabyan and Van De Wiel, 2002). The calibrated values are subsequently applied on yet another dataset to validate the model (section 4.4).

4.3.1. Calibration method

Calibration is the process by which values are obtained for uncertain parameters, by forcing optimal agreement between observed and modelled data. Although this initially appears a simple and straightforward task, the process of calibrating parameters actually is quite a contentious topic in the field of numerical modelling. Several calibration methods exist, none of which is universally accepted. One problem is knowing when the 'optimal agreement' has been found, which depends not only on how the agreement is quantified, but also on the definition of 'optimal' in this context. Usually the agreement is some measure of correspondence between the observed dataset and the modelled results, which should, ideally, be maximized. Unfortunately, it may not always be straightforward - or indeed possible - to locate the parameter value at which maximal agreement occurs. In these cases 'optimal agreement' is frequently replaced by 'acceptable agreement', in which a certain divergence between modelled and observed data is tolerated. However, this is not the main problem with the calibration process. A more serious concern is that when there is more than

one parameter to be calibrated, there might be several sets of parameter combinations, which all give acceptable results although the values for the individual parameters are markedly different (Hankin and Beven, 1998; Odoni and Darby, 2002). This has profound implications for the model, especially where the parameters have a physical interpretation: if there are several sets of acceptable parameter values, how do you know which one of them, if any, corresponds to 'the real world'? And also, although the different sets of calibrated parameter values produce similar outputs for the calibrated dataset, it does not necessarily follow that this will apply to any other datasets as well.

Hankin and Beven (1998) argue that, if multiple parameters need calibrating, a Monte Carlo type calibration should be employed, where the parameter space of the calibration parameters is explored. It would then be possible to obtain likelihoods of parameter values, rather than single values that would inspire a false sense of security. This method, although conceptually attractive, is very computationally intensive and time-consuming. Hence, it is not used here. The calibration method, as applied in this work, is an extension of the method applied by Erik Mosselman for the original RIPA model (Mosselman, 1992). Calibration is achieved in four phases, the first three of which focus on bed topography and calibrates the parameters in the sub-models for flow and sediment transport, while the last phase concerns the bank erosion parameters. First, the longitudinal positioning of point bars is calibrated, *i.e.* the wavelength between the bed-topography undulations is optimized. Second, the amplitude of the undulation is optimized. These two steps are performed by adjusting the parameters to which the model shows the highest sensitivity. Next, the less responsive parameters are adjusted to 'fine-tune' the agreement between observed and modelled equilibrium bed topographies. Finally, in a separate series of simulations, in which the model is run with the calibrated flow and sediment transport parameters, the bank erosion parameters are calibrated.

This simple calibration method will lead to a single set of calibrated parameter values for a given dataset. Even though it follows a very systematic procedure to find this set, it is impossible to preclude the existence of other sets of parameter values which would achieve similar agreement between observed and modelled data. For the flow and sediment transport parameters, this problem is partially intercepted by calibrating two different datasets. Comparison of the two resulting sets of calibrated parameter values, both with each other and with other published values, might give some indication of the reliability of the obtained parameter values.

4.3.2. Calibration of flow and sediment transport parameters

Calibration parameters

From section 4.2 the most important calibration parameters for flow and sediment transport can be identified (*cf.* figure 4.5). The exponent in the transverse slope model, p_{tm}, has no discernible impact on the model, and is excluded from the calibration process. The Chezy roughness factor, C, is considered to be a measurable physical property of the channel. Hence, it is considered to be an input variable rather than a calibration parameter. This leaves seven parameters for calibration. The most important of these are the exponent, p_s, and coefficient, k_s, in the sediment transport power-law, and the weighting coefficient for spiral flow intensity, k_{si}. Less relevant, yet exerting some influence, are the coefficient in the transverse bed-slope model, k_{tm}, the secondary flow convection factor, k_{sn}, the weighting coefficient for the influence of the longitudinal bed-slope, k_{ls}, and the adaptation length of the secondary flow. Using a specific sediment transport equation, such as the Engelund-Hansen equation (equation 3.51) or the Meyer-Peter-Müller equation (equation 3.48), would eliminate the need for calibrating k_s and p_s. However, since such transport equations are empirically derived, under hydraulic and geometric conditions which may not be valid to all channels, it is considered more sound to apply the general power-law for sediment transport in the calibration exercise.

The parameters, k_{si}, λ_r, k_{ls} and k_{sn}, are all in some way related to the Chezy roughness coefficient, C. For the first three parameters the dependency on the Chezy roughness coefficient is evident from the following relations (Olesen, 1987; Mosselman, 1992):

$$k_{si} = \frac{2k_1}{\kappa^2}\left(1 - \frac{\sqrt{g}}{\kappa C}\right) \tag{4.6a}$$

$$\lambda_r = k_2 \frac{H\,C}{\sqrt{g}} \tag{4.6b}$$

$$k_{ls} = k_3 \frac{C^2}{g} \tag{4.6c}$$

in which κ is the Von Kárman constant, D_{50} denotes the median grain size, g is the gravitational acceleration, ρ_{rel} is the relative sediment density, H is the flow depth and k_1, k_2 and k_3 are coefficients. Theoretically, these are the coefficients that need calibrating, rather than k_{si}, k_{ls} and λ_r. However, since the MRIPA model allows the Chezy roughness coefficient to vary spatially, this would imply spatially variable values for k_{si}, k_{ls} and λ_r. Hence, the parameters k_{si}, k_{ls} and λ_r are calibrated directly. By applying a global roughness coefficient, the results obtained can be back-calculated to estimate global values for k_1, k_2, and k_4, using equations 4.6a to 4.6c. The secondary flow convection factor, k_{sn}, is also a function of Chezy roughness (figure 4.12). It is possible to derive a value for k_{sn} from figure 4.12, again by using a global roughness value to avoid spatially varied values for k_{sn}. However, as there is considerable uncertainty in the depicted relationship between k_{sn} and C, the secondary flow convection factor is here treated as a calibration parameter in its own right.

Datasets

The first of the two laboratory flume experiments considered for the calibration procedure, was conducted in a semi-circular flume representing a single 180-degree bend. This experiment was undertaken by Jacob Odgaard at the Iowa Institute of Hydraulic Research (Odgaard, 1984), and will henceforth be referred to as the IIHR-experiment. The IIHR-flume describes a 180-degree bend with straight inlet and outlet reaches (figure 4.13). The channel has a trapezoidal cross-section profile with a constant width throughout the flume. The flume has fixed banks and an erodible bed. The initially flat bed was allowed to erode or accumulate under constant discharge until a steady-state flow had been reached. Removed sediment was recirculated in the system, so that upstream sediment input matches downstream sediment output. Table 4.4 summarizes all the relevant geometrical and physical properties of the experiment. Further details are described by Odgaard and Kennedy (1983) and Odgaard (1984).

The second experiment was performed by Peter Whiting and William Dietrich at the University of California, Berkeley (Whiting and Dietrich, 1993b). It will be referred to as the UCB-experiment in this text. The UCB-flume describes a series of three elongated sinusoidal bends with short straight inlet and outlet reaches (figure 4.14). The channel initially has a rectangular cross-section profile. The width is held constant throughout the flume and the vertical banks are fixed. The erodible bed was allowed to

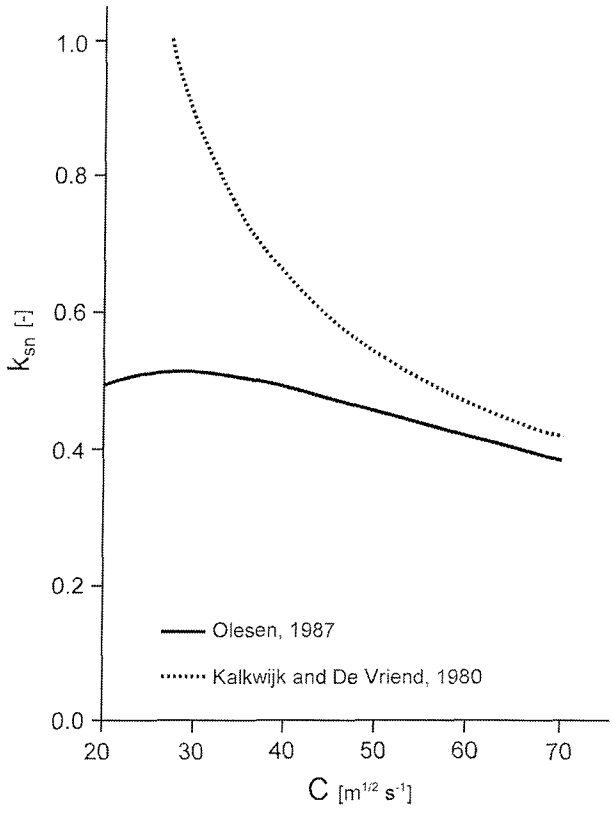

Figure 4.12: Relation between the secondary flow convection factor, k_{sn}, and the Chezy roughness coefficient (after Olesen, 1987). A theoretical relation, derived by Kalkwijk and De Vriend (1980), deviates substantially from Olesen's proposed relation, especially for lower Chezy values (higher roughness). This is caused by different assumptions on the shape of the vertical velocity profile. In the MRIPA model, it is recommended to use Olesen's relation, or to treat k_{sn} as a calibration parameter.

Table 4.4: Flume experiment details.

property	symbol	IIHR	UCB
shape		circular	sinusoidal
length [m]	L	80.8	18.0
width [m]	W	2.13	0.25
radius of curvature [m]	R_c	13.1	0.81
flow depth [m]	h	0.154	0.016
discharge [m^3 s^{-1}]	Q	0.147	0.001
sediment size [mm]	D_{50}	0.3	0.62
roughness [$m^{0.5}$ s^{-1}]	C	43.23	29.14
width/depth ratio [-]	W/h	13.8	15.6
curvature ratio [-]	R_c/W	6.15	3.24

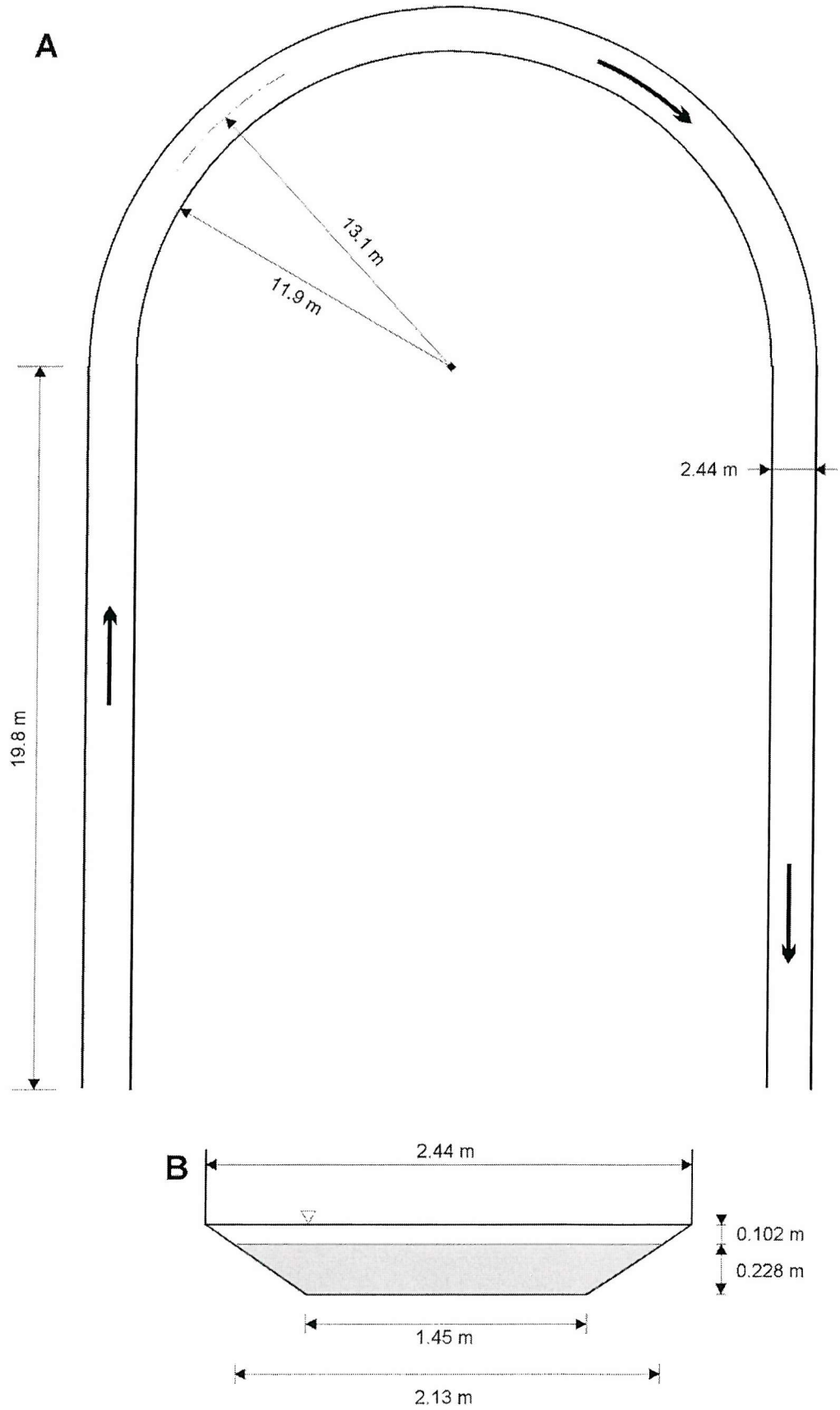

Figure 4.13: IIHR laboratory flume layout (after Odgaard and Kennedy, 1983).
A: planform (arrows indicate flow direction)
B: cross-section (shading indicates initial sediment layer)

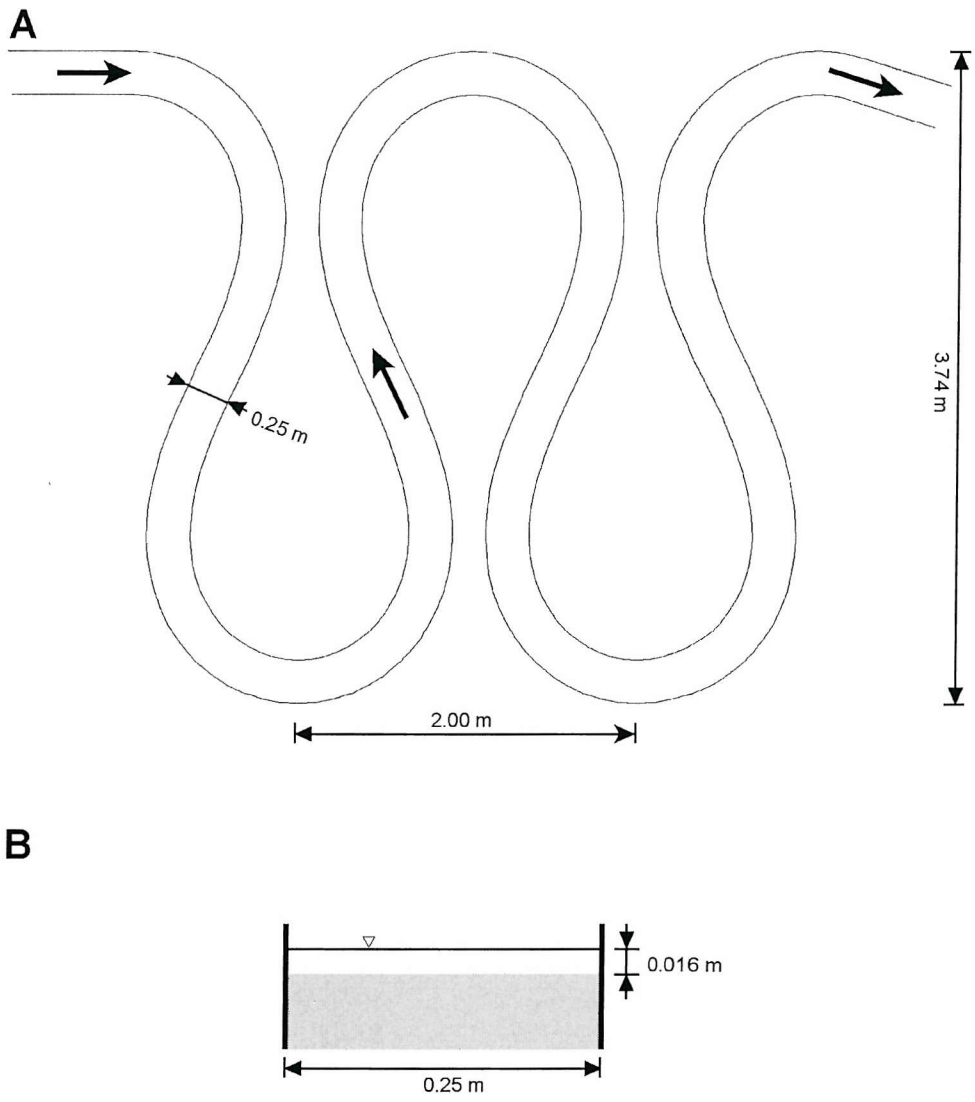

Figure 4.14: UCB flume layout (after Whiting and Dietrich, 1993b).
A: planform (arrows indicate flow direction)
B: cross-section (shading indicates initial sediment layer)

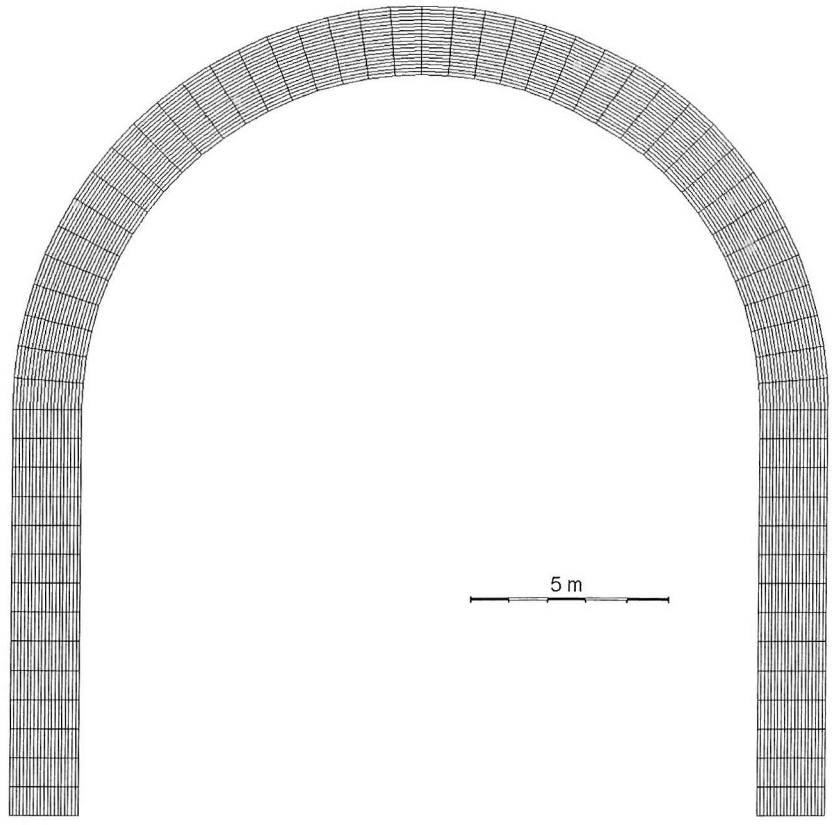

Figure 4.15: Grid used for IIHR simulations.

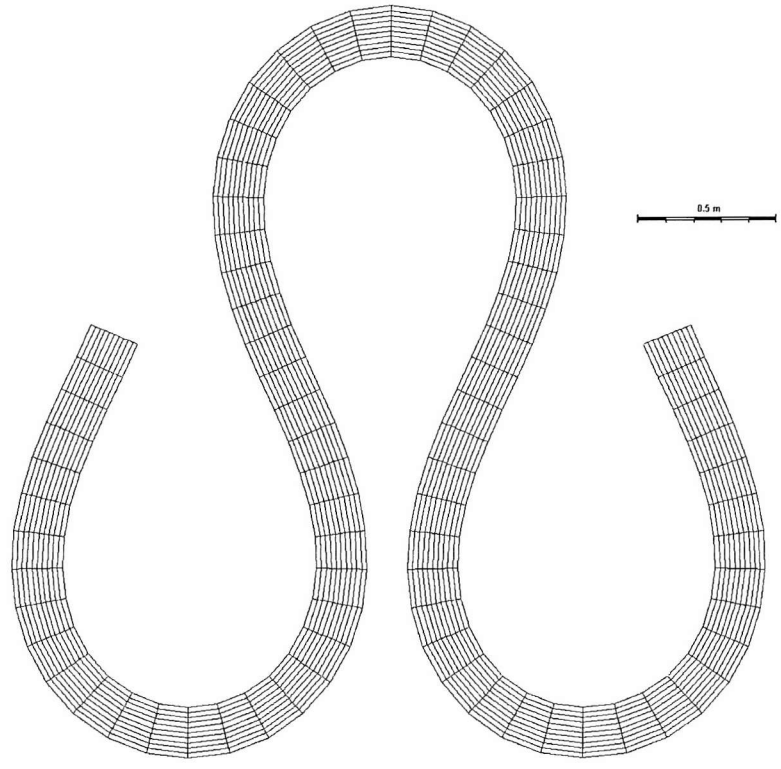

Figure 4.16: Grid used for UCB simulations.

adjust under constant discharge, while removed sediments were reinjected upstream. The UCB-flume differs from the IIHR-flume not only in shape, but also in scale. Channel width and flow depth are about an order of magnitude lower each, while discharge is roughly two orders of magnitude smaller (table 4.4). Further details are described by Whiting and Dietrich (1988; 1993b).

Numerical representation

Figure 4.15 shows the grid which was used in the IIHR-simulations. Channel width is taken to be equal to 2.134 metres, which is the width of the bed at the beginning of the experiment. The longitudinal dimensions of the grid differ from the IIHR laboratory experiment in that the straight inlet and outlet reaches are shortened to improve computational efficiency. Figure 4.16 shows the grid used for the UCB-simulations. As the simulation focuses on the three central bends, the inlet and outlet reaches are omitted. An overview of the grid properties for both simulations is given in table 4.5. Details of a grid sensitivity analysis and mass conservation check, performed for each grid, are described in appendices A3 and A4.

The fixed, sloping sidewall of the IIHR-flume poses problems in the modelling of bed-level changes (figure 4.17). The trapezoidal shape of the flume inhibits vertical incision at the boundaries. Any erosion of the channel bed at the boundary will necessarily be accompanied by a horizontal displacement of the boundary point. In effect, the channel bed becomes narrower as the boundary point "slides" down the sidewall to its new position. This effect is not represented by the model, which assumes a fixed width for this simulation. Bed-level erosion is thus modelled as vertical incision at all points. The lack of horizontal displacement in the numerical simulations may have some consequences near the outer bank where the incision is expected to be greatest.

Table 4.5: Grid details.

	gridpoints	longitudinal sections	transverse sections	longitudinal spacing[1]	transverse spacing
IIHR	1449	69	21	1.018 m	0.122 m
UCB	869	79	11	0.176 m	0.025 m

note: [1] average value on centerline

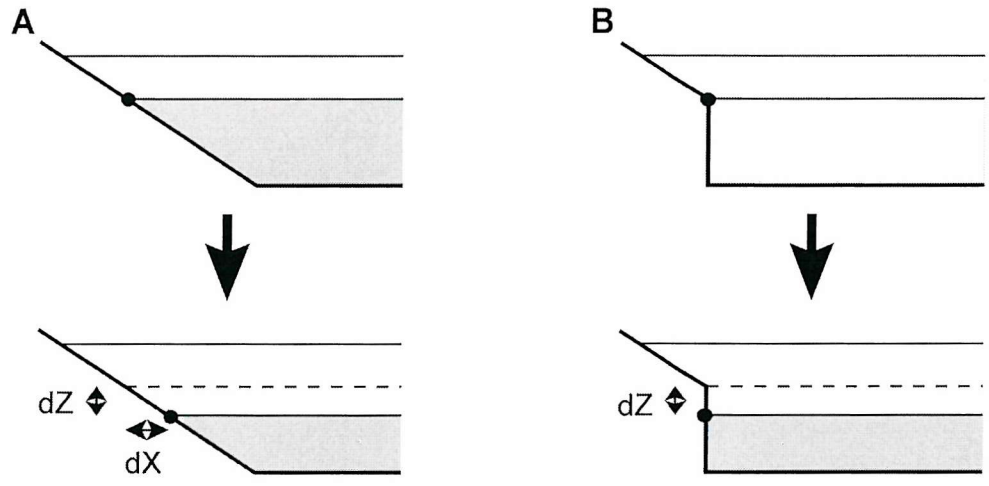

Figure 4.17: Differences in bed-level erosion at a boundary point in the IIHR laboratory experiment (**A**) and in the numerical model (**B**). The shaded area denotes the bed sediment. In the laboratory flume, any bed-level erosion (*dZ*) at the boundary will force an inward horizontal movement (*dX*) of the boundary point, due to the physical constraints of the flume itself. In the model such a constraint is not incorporated. Thus, the horizontal displacement is not accounted for.

Results for semi-circular channel (IIHR-flume)

Performance of the model is evaluated by comparing the simulated flow depths with the observed laboratory flume flow depths. Since MRIPA is a rigid lid model, this is equivalent to comparing simulated and observed equilibrium bed topographies. The comparison with the IIHR-experiment focuses on the bend itself, and largely ignores the inlet and outlet reaches. Odgaard (1984) gives 20 cross-sectional profiles of flow depth, of 19 measurements each. In order to create a sufficiently detailed comparison surface these data were longitudinally interpolated (cubic spline method; Press *et al.*, 1992) to obtain 45 cross-sections, with equal longitudinal spacing as the numerical grid. Thus a mesh of 855 comparison points was generated. The simulated channel is wider than the real channel due to the "sliding boundary point"-phenomenon. The simulated flow depths were interpolated (cubic spline method) in the transverse direction to match the position of the flume measurement points. This option was chosen in favour of extrapolation of observed data in order to suppress extrapolation errors.

Figures 4.18A and 4.18B illustrate the observed and modelled equilibrium flow depths. It is clear that the model is capable of representing the main features of the observed bed topography: a thalweg along the entire outer bend, and a point bar along the inner bend. Both the spatial positioning and the magnitude of the erosion and deposition are correctly predicted for these features. Overall, there is a good agreement between modelled and observed flow depths (figures 4.18C, 4.19A-H and 4.20). The overall good performance of the model is confirmed through a quantitative analysis of the results (table 4.6; figure 4.21). On average, the model overpredicts flow depths by 2 millimetres. Circa 64% of simulated flow depths are within ± 2.0 cm of the observed values, while over 96% of all grid points are within ± 5.0 cm, compared to an observed bed relief of 24 cm. Although the agreement is good, it is not perfect and three systematic errors can be observed. First of all, the model predicts a rather smooth bed topography and fails to pick out the irregularities which can be observed in laboratory experiments (figures 4.18A and 4.19A-H). Second, there is a marked overprediction of flow depth at the outer bend (indicated by a thin blue line along the outer bend in figure 4.18C, and also easily picked out on each of the cross-sections in figure 4.19). The third systematic error is the slight underprediction of flow depth along the observed thalweg (indicated by the reddish region close to the outer bend in figure 4.18C, and also noticeable in figures 4.19D,E,H,J,K), which results in an underprediction of the transverse slopes. These three errors explain the variance in figure 4.21. Much of the variance can be

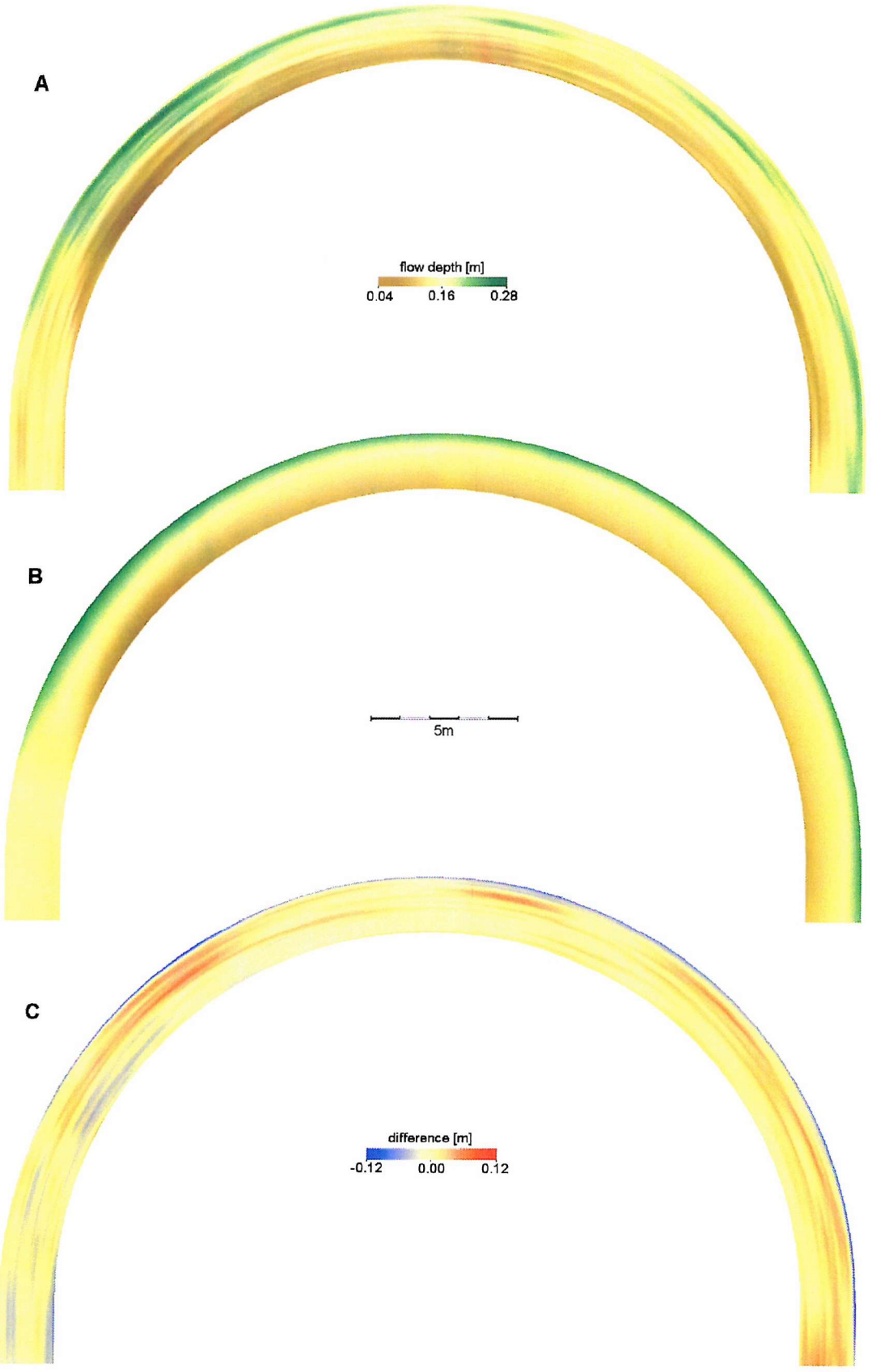

Figure 4.18: Comparison between observed and modelled bed-topography.
A: observed flow depth (interpolated from Odgaard, 1984)
B: modelled flow depth
C: differences in flow depth (observed - modelled)

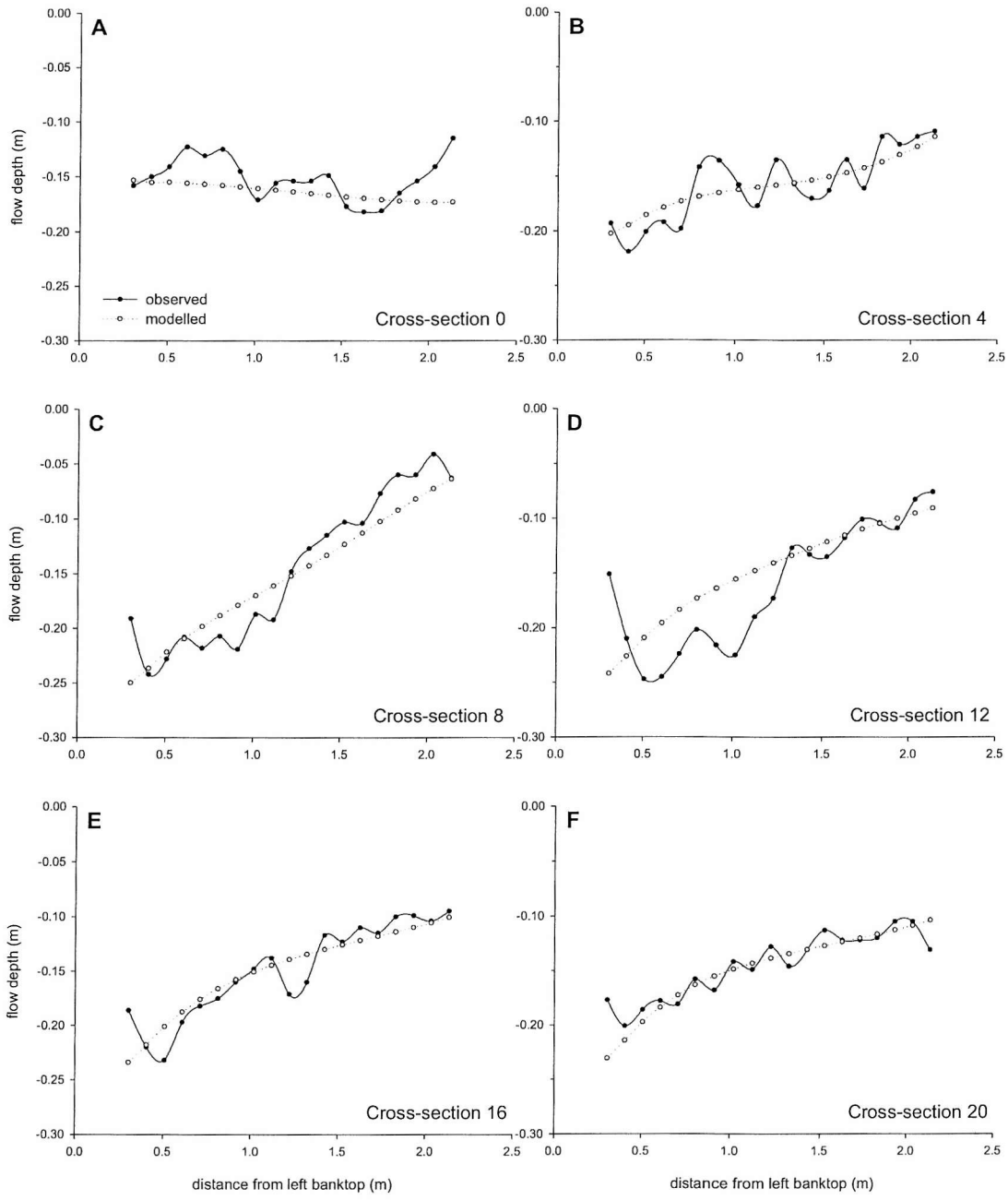

Figure 4.19: Observed and modelled flow depths at selected cross-sections (continued on next page).

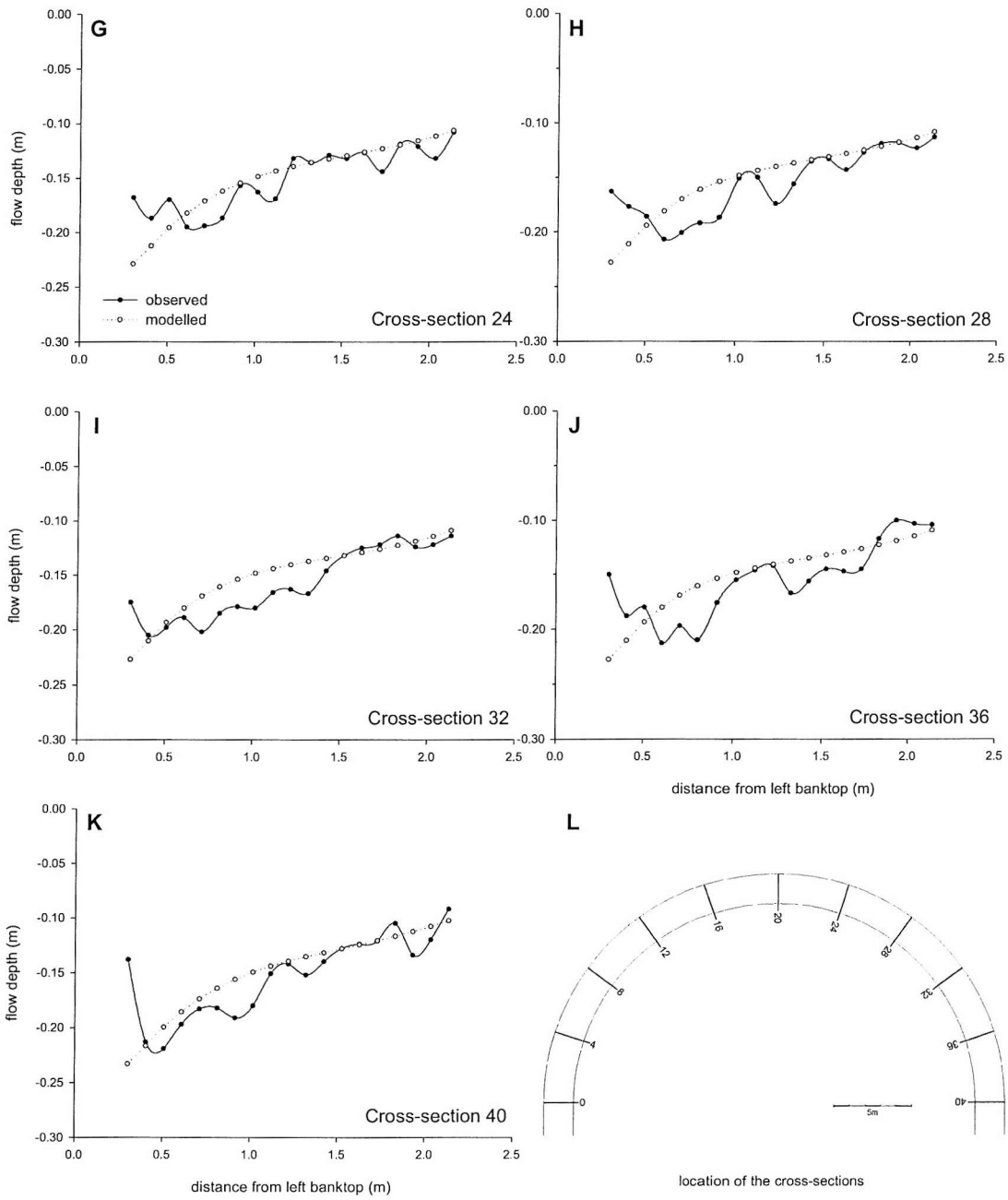

Figure 4.19 (continued): Observed and modelled flow depths at selected cross-sections.

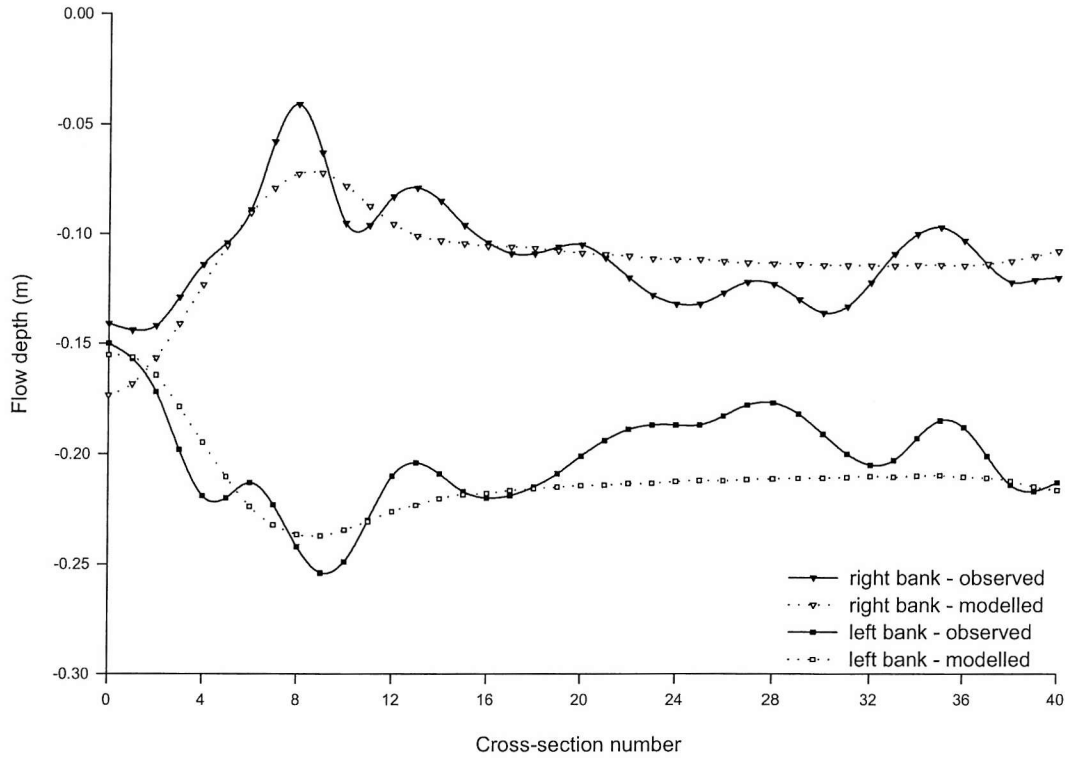

Figure 4.20: Observed and modelled flow depths at longitudinal profiles near channel banks. Profiles were taken at 1/6th channel widths inside from the top of the banks, due to the sloping side wall (see figure 4.19L for location of cross-sections).

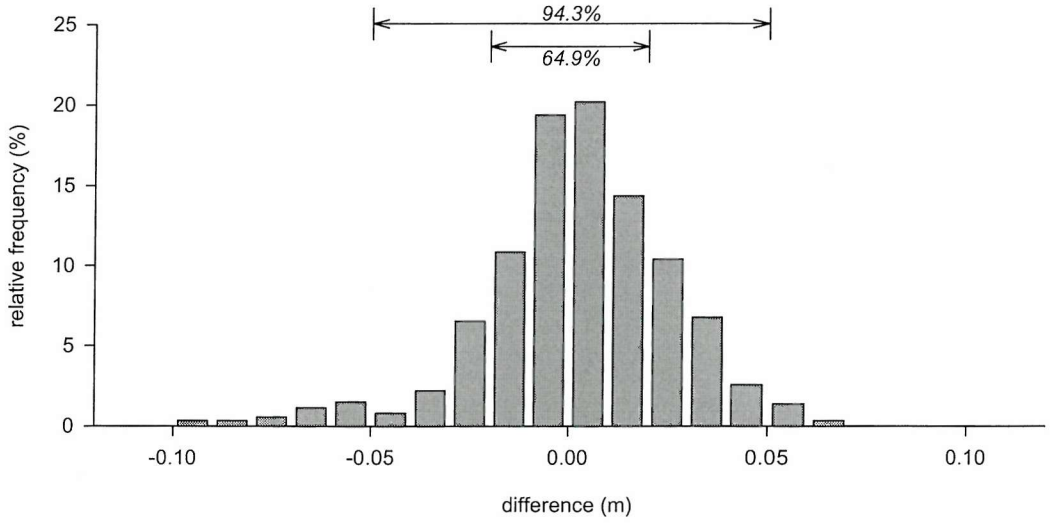

Figure 4.21: Distribution of differences in flow depth (observed - modelled).

Table 4.6: Descriptive statistics of differences in flow depth (observed - modelled).

number of points	855
minimal value [m]	-0.095
maximal value [m]	0.069
median [m]	0
average value [m]	0.002
standard deviation [m]	0.024
variance [m^2]	0.001
skewness	-0.701

ascribed to smoothening of the micro-topography, but part of it must be attributed to the systematic under-prediction of flow depths in the thalweg and to the over-prediction along the outside bend boundary. These last two errors explain the slightly skewed distribution of errors. The systematic underprediction of the flow depths along the observed thalweg causes a slightly higher frequency of positive differences, while the overprediction of flow depths near the outer boundary causes the tailing off to the negative side.

Results in a sinusoidal bend

The evaluation of the UCB-experiment focuses on the central bend, due to constraints on data availability for the two other bends (figures 4.22). Whiting and Dietrich (1988) provides flow depth measurements for 25 cross-sections irregularly spread along the central bend. Each of the cross-sections consists of 11 measurements. The observed flow depths were interpolated longitudinally (cubic spline method) to obtain a sufficiently detailed mesh, consisting of 37 evenly spaced cross-sections. The resulting mesh matches the numerical grid, and provides 407 data points for comparison.

Figures 4.22A and 4.22B illustrate the observed and modelled equilibrium flow depths. As is the case with the IIHR-experiment, the model seems to reproduce the main morphological features: a pointbar along the inside bend, and a pattern of scour along the outside bend. However, the equilibrium topography flume- experiment model shows three separate pools along the outside bend, while the model is not capable to resolve these individual pools within the context of the overall pattern of scour along the outside bend. This is clear from the difference plot (figure 4.22C), the cross-sectional graphs (figures 4.23A

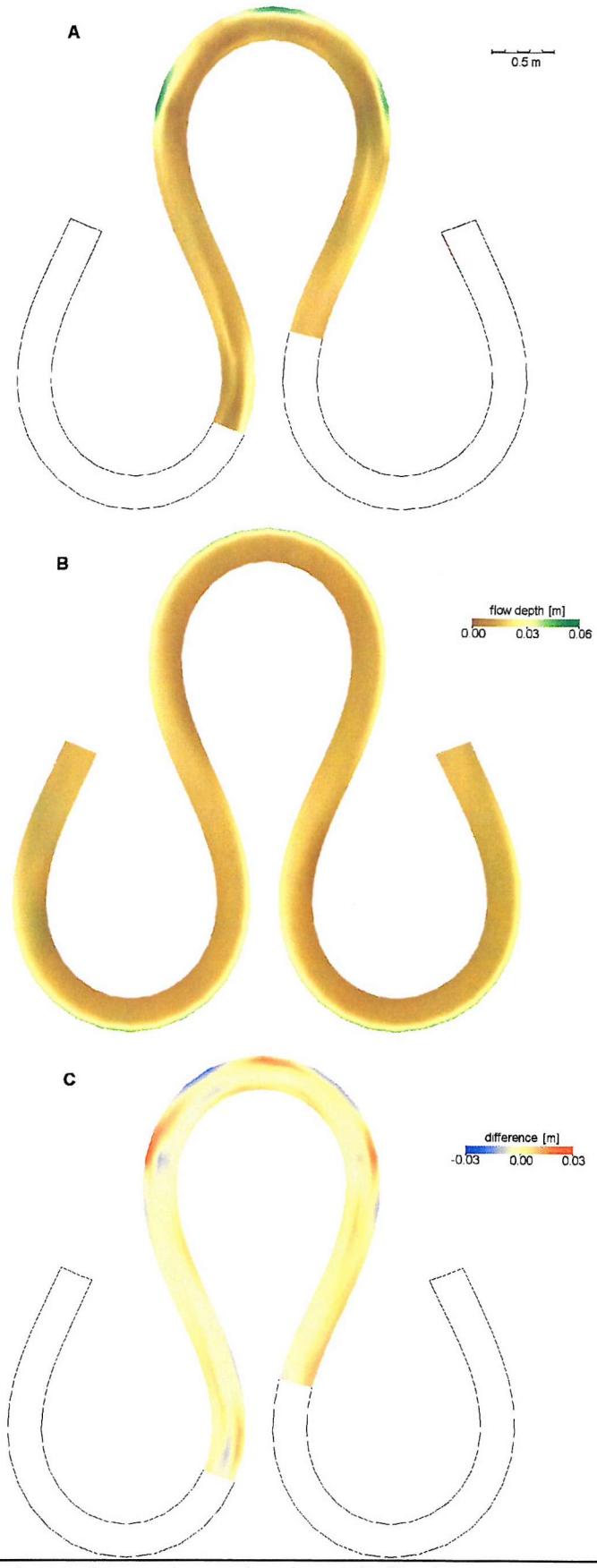

Figure 4.22: Comparison between observed and modelled bed-topography.
A: observed flow depth (interpolated from Whiting and Dietrich, 1993b)
B: modelled flow depth
C: differences in flow depth (observed - modelled)

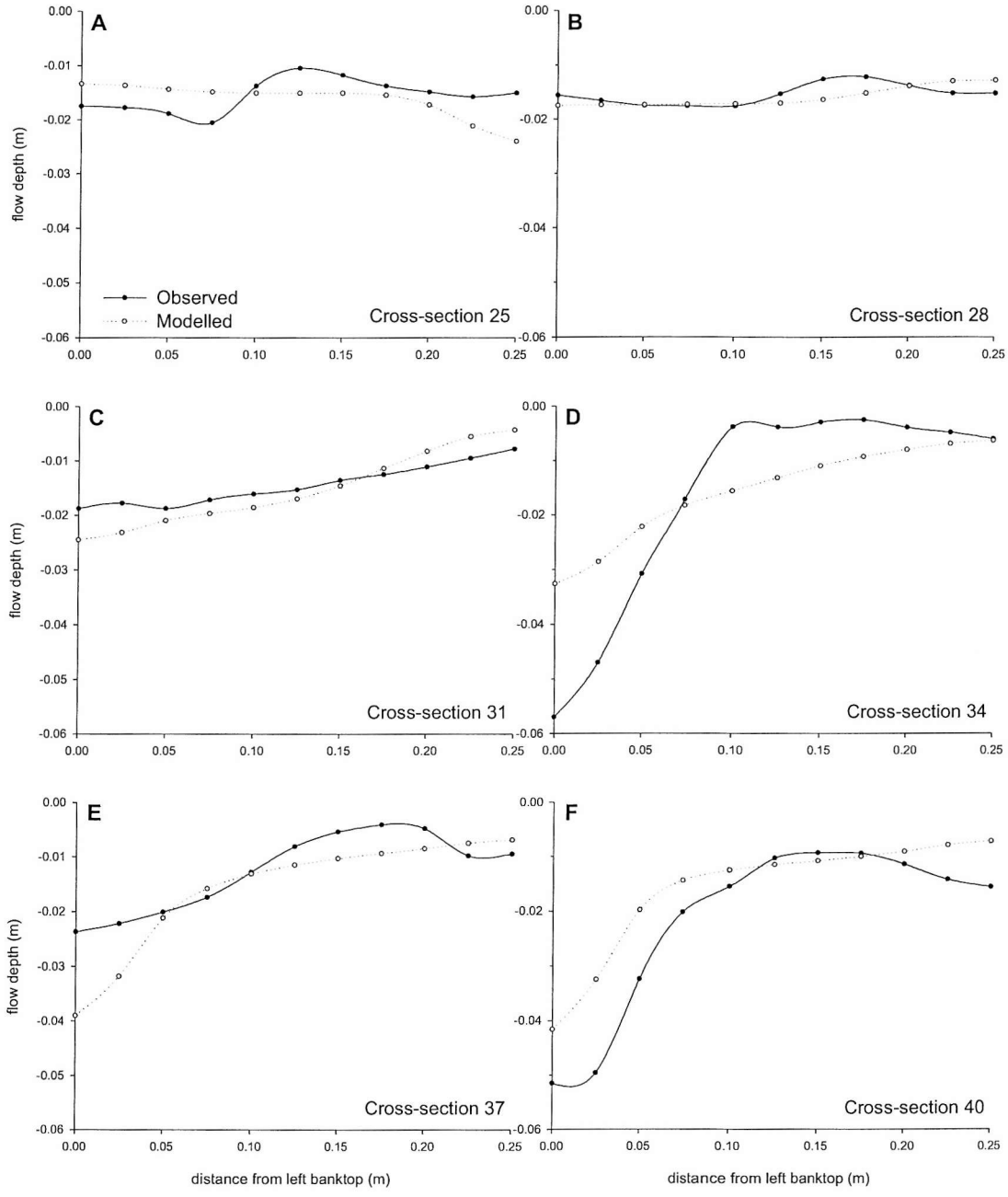

Figure 4.23: Observed and modelled flow depths at selected cross-sections (continued on next page).

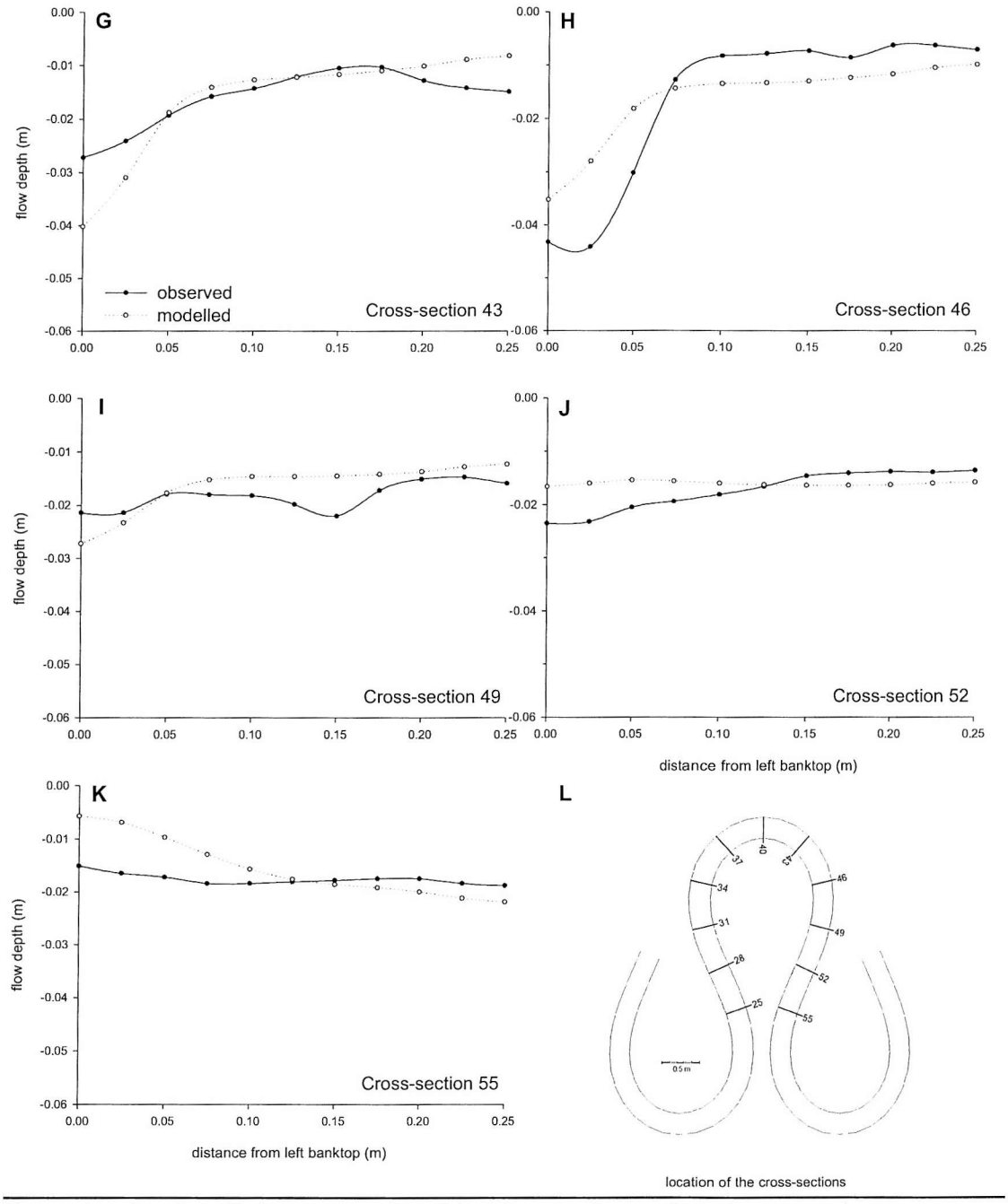

Figure 4.23 (continued): Observed and modelled flow depths at selected cross-sections.

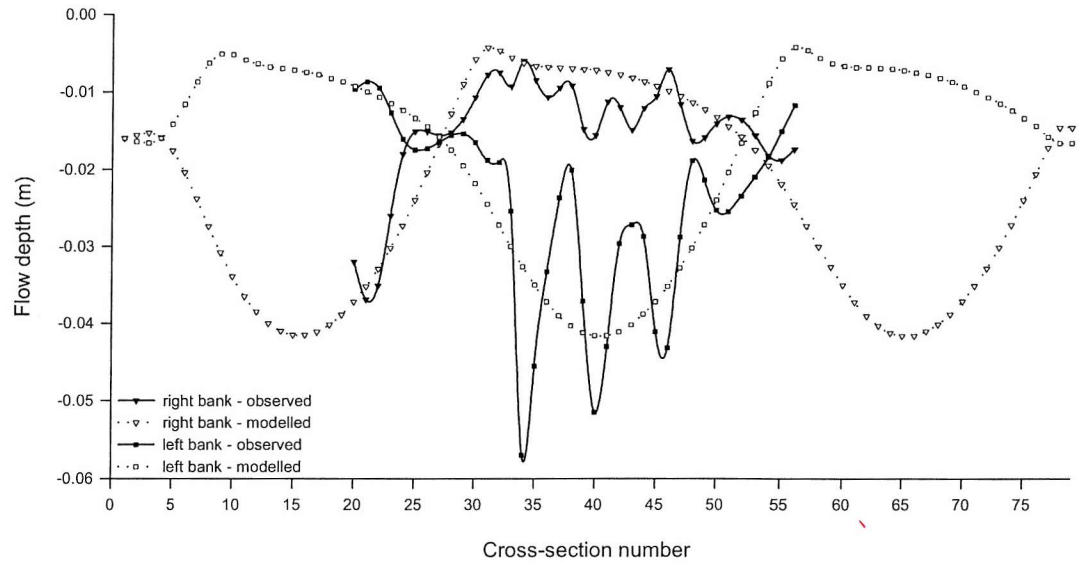

Figure 4.24: Observed and modelled flow depths at longitudinal profiles along the channel banks. (see figure 4.23L for location of cross-sections)

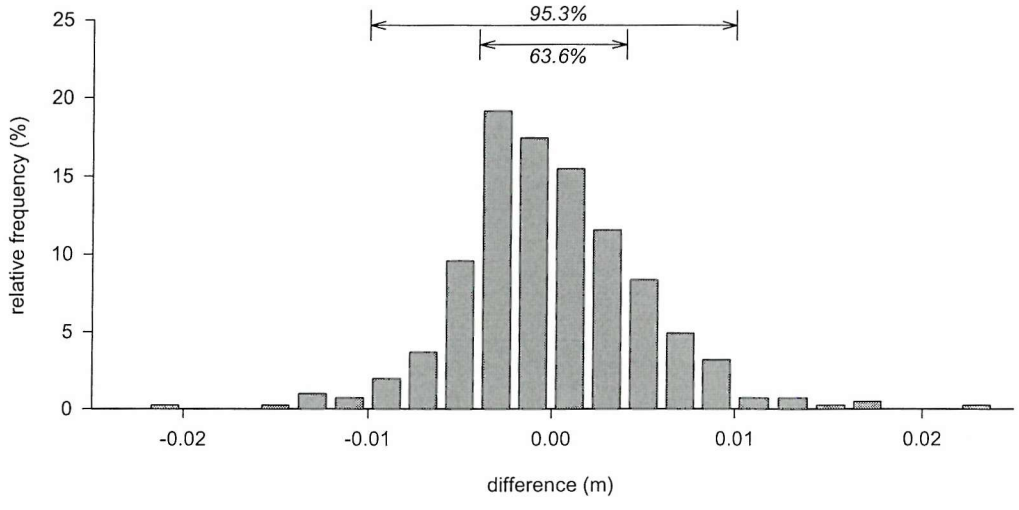

Figure 4.25: Distribution of differences in flow depth (observed - modelled).

to 4.23H) and the longitudinal plot (figure 4.24). The statistical agreement between observed and predicted flow depths is, again, quite good (table 4.7; figure 4.25). About 63% of grid points have simulated depths within ± 0.2 cm of the observed value, while over 95% are within ± 1.0 cm, compared to an observed bed relief of 6 cm. The variance in differences between observed and modelled flow depths can again be explained through the model's smoothening of micro-topography and also by its inability to resolve the multiple pools.

Table 4.7: Descriptive statistics of differences in flow depth (observed - modelled).

number of points	407
minimal value [m]	-0.02
maximal value [m]	0.024
median [m]	0
average value [m]	0
standard deviation [m]	0.005
variance [m^2]	0
skewness	0.366

Discussion

The model appears to be capable of adequately simulating the spatial positioning and magnitude of major bed features such as point bars and pools. This ability to represent macro-scale morphological features provides tentative evidence that the flow and sediment transport submodels are physically realistic. However, the good statistical agreement between observed and modelled equilibrium bed topographies should not be surprising, as this is exactly what the calibration process is trying to achieve. Indeed, it merely indicates that the model is calibrated appropriately. In terms of assessing the model's performance, it is more instructive to examine how the predicted and observed topographies deviate, as this may lead to insight into where, and under what circumstances, the model has poor process representation (Lane and Bates, 1998).

From the calibration experiments it seems that the model has four shortcomings: smoothing of micro-morphological features, overprediction of flow depths along the outer bank, under prediction of transverse slopes and inability to model multiple pools. The first of

these shortcomings is the least problematic. The smoothing of micro-morphological features is thought to have only a minor impact on the performance of the model, in terms of predicting flow and sediment transport patterns. Furthermore, it appears from the description of the laboratory experiments that this micro-topography is not static, but rather that the equilibrium micro-morphology is dynamic, at least for the IIHR-experiment (Odgaard, 1984; Olesen, 1987, p.183).

The second shortcoming, overprediction of flow depths along the outer bank, is most pronounced in the IIHR-flume simulations. It might be due to an incorrect representation of the flow field in the near-bank zone, which results in an overestimation of the sediment flux. However, as the error is nearly absent in the UCB-simulations, it is tempting to shift the blame on the "sliding boundary point"-phenomenon associated with the IIHR-simulations as described above (*cf.* figure 4.17). Although this certainly explains at least part of the observed differences, it does not exclude the possibility that the near-bank flow field is poorly represented.

The underprediction of transverse slopes, and the associated underprediction of flow depths in the thalweg, appears to result from an unrealistically high cross-stream sediment flux across the point bar near the inner bank. The cause of this inability to accurately represent the sediment flux vector is not immediately clear. It might be either an inherent problem with the sediment transport model, or an inability to solve the flow field driving sediment motion, or both. Consideration of the possible reasons why the model fails to predict the multiple pools in the UCB-experiment might provide further clues as to the true explanation.

The occurrence of multiple pools along the outer bank of certain high-amplitude meander bends is thought to be a depth-oscillation resulting from an alternate-bar like response to a sudden change in curvature at the bend entrance (Whiting and Dietrich, 1993c; Parker and Johanneson, 1989) and an inherent instability in the flow that results from the lateral transport of streamwise momentum by the secondary flow (Whiting and Dietrich, 1993c; Johanneson and Parker, 1989; Dietrich *et al.*, 1979). It is likely that the secondary flow convection model in MRIPA is too simple to capture the details of these processes. Specifically, the MRIPA model seems to be unable to distinguish between free bars (alternating or migrating) and fixed bars (point bars). This might be due to an unrealistically high stress-divergence over the bar face, sufficient to evacuate the sediment delivered there

and hence prevent bar migration (Kinoshita and Miwa, 1974). This explanation is consistent with the model's failure to predict the depth-oscillation along the outer bend in high-amplitude meander bends, and also seems to suggest that the underprediction of transverse slopes is likely to be caused by an inability to solve the flow field accurately, rather than by an inherent problem with the sediment transport model itself. It might be that the inability to solve the flow field is particular to the physical design of the UCB-flume experiment. In developing the numerical procedure for solving the flow equations, the assumption of mild channel curvature ($r_c/W > 5.0$) was made, both in applying the self-similarity hypothesis and representing the transverse exchange of momentum as an additional acceleration or friction (*cf.* section 3.3.1). However, the highly sinuous shape of the flume channel has a curvature ratio, R_c/W, equal to 3.24 at the bend apex (table 4.4). It is possible that flow prediction near the bend apex is erroneous because the assumptions underlying the flow model do not hold in this region. Alternatively, the inability to predict free bars might stem from a uniform distribution of sediment inflow along the upstream boundary, as numerical models require a small perturbance in the transverse distribution of the sediment inflow in order to be able to simulate migrating or alternating bars (Mosselman, pers. comm. 2001; Seminara, pers. comm. 2002). The current version of MRIPA does not allow for this option. Whatever the cause, mRIPA's inability to simulate free bars is a significant limitation of the model in its current form, since the distinctive nature and interaction of the free and forced bars is important in the evolution of bank migration and meander forms (Blondeaux and Seminara, 1985; Colombini *et al.*, 1987; Tubino and Seminara, 1990).

Having established that the calibrated model is able to reproduce the spatial positioning and magnitude of the macro-morphological features of the laboratory experiments adequately, albeit with some restrictions, the next question relates to the extent to which the calibrated parameter values are realistic. This is done through comparison with other published values, which were either physically measured or derived through similar calibration exercises. Table 4.8 lists the calibrated parameter values for the two datasets, as well as an overview of values published in the literature. It can be seen that all the calibrated parameters are within the range of values as reported previously. However, this is not the case for the sub-parameters k_1, k_2 and k_3, which were calibrated indirectly from k_{si}, λ_r and k_{ls}, using equations 4.6a to 4.6c. The values for the sub-parameters obtained for the UCB-simulations exceed the range of the previously published values. This does not necessarily imply that these calibrated values are incorrect, only that they are different. As the obtained values are of the same order of magnitude as the previously reported values, there is no

reason to assume that they are incorrect. The differences can be attributed to the channel shape, which is notably different from the channel shape of the other experiments for which values for these sub-parameters were reported. The high-amplitude meandering affects the secondary flow pattern and the sediment flux. Thus, the higher values of k_1, k_2 and k_3 appear to reflect the high amplitude of the meanders in the UCB-experiments. It is reasonable to assume that the sub-parameters are in some way related to bend curvature, R_c. Currently, there is not enough data to elucidate what this relationship might be, apart from that high curvature seems to imply high values of k_1, k_2 and k_3.

Table 4.8: Comparison of calibrated parameter values with published values.

parameter	symbol	IIHR	UCB	range[1]
coefficient in power law for sediment transport	k_s	0	0	
exponent in power law for sediment transport	p_s	4	5	4 - 6
coefficient in transverse slope model	k_{tm}	1.05	0.69	0.50 - 1.78
exponent in transverse slope model	p_{tm}	1.0 [2]	1.0 [2]	0.0 - 2.0
secondary flow convection factor	k_{sn}	0.47	0.45	0.38 - 1.18
weighting coefficient for secondary flow intensity	k_{si}	10.23	9.89	3.0 - 12.0 [4]
adaptation length for secondary flow	λ_r	0.7 [3]	0.7 [3]	0.5 - 0.9 [4]
weighting coefficient for streamwise bed-slope	k_{ls}	4	8	0.0 - 9.5 [4]
sub-parameter for k_{si} in equation 4.6a	k_1	1.04 [5]	1.12 [5]	0.33 - 1.04
sub-parameter for λ_r in equation 4.6b	k_2	0.33 [5]	4.70 [5]	0.25 - 1.3
sub-parameter for k_{ls} in equation 4.6c	k_3	0.02 [5]	0.09 [5]	0.00 - 0.05

notes: [1] Range of values previously reported (Olesen, 1987; Mosselman, 1992; Struiksma and Crosato, 1989; De Vriend, 1981; Van Bendegom, 1947; Kalkwijk and Booij, 1986).

[2] p_{tm} was not actually calibrated, as the sensitivity analysis illustrated it had very little influence. A value of 1.0 was chosen because it was the most frequently occurring of previously reported values.

[3] Variation in λ_r produced very minor spatial differences in the final output. However, these differences were too small to unequivocally select an optimal parameter value. Therefore, a value of 0.7 was used here, which was previously reported as an optimal value (Mosselman, 1992).

[4] Some of the reported values for k_{si}, λ_r and k_{ls}, were transformed from related parameters k_1, k_2 and k_3.

[5] Values for k_1, k_2 and k_3 were not actually calibrated, but back-calculated from the parameters k_{si}, λ_r and k_{ls}.

4.3.3. Calibration of bank erosion parameters

Calibration parameters

Several parameters in the model affect the bank erosion computations. Where possible, these should be determined from *in-situ* measurements, such as for the physical properties of the bank sediments: soil cohesion, c, bank material friction angle, ϕ, unit weight, W_0, and grainsize fractions ω_{h1}, ω_{h2}, ω_{f1}, ω_{f2} and ω_{f3}. However, some parameters are more difficult to determine in the field, most notably the parameters k_τ, $\tau_{B,c}$, k_B and p_B related to hydraulic bank erosion as expressed in equations 3.66 and 3.67. These three parameters respectively denote the bank shear proportionality coefficient, the critical shear stress and the erodibility of the bank material, and the excess shear exponent. Although the value of k_τ is theoretically dependent on the bank angle, it is usually taken to be equal to 0.75 (*cf.* section 3.4.4; figure 3.11). This value will also be adopted here, although it could conceptually be treated as a calibration parameter. The critical shear stress, $\tau_{B,c}$, is often difficult to measure *in-situ*, although recent technological advances might overcome this problem (Hanson and Simon, 2001). However, guidelines to critical shear stress value do exist (Julien, 1995; Vanoni, 1946; Shields, 1936). Thus, only k_B and p_B remain as bank erosion parameters that require calibration.

Dataset

The dataset used here is similar to that of the UCB-experiment above. Whiting and Dietrich (1993b) performed a variant experiment, where part of the outer bank in one of the bends was allowed to erode and migrate freely. This experiment, hereafter referred to as the UCB2-experiment, was conducted in the same high-amplitude meandering flume (*cf.* figure 4.14), under slightly different hydraulic conditions. Like the UCB-experiment, the bed was initially flat. However, discharge, slope, flow depth and roughness all were slightly different in the UCB2-experiment (table 4.9). The bank material parameters c, ϕ and γ_s are not specified for this dataset. Here, their values are estimated as typical for cohesionless material. However, Whiting and Dietrich (1993b) do provide a value for $\tau_{B,c}$. Bank erosion parameters are only set along the erodible part of the bank. The values for the calibration parameters for flow and sediment transport are identical to those derived in the preceding section (table 4.9).

Table 4.9: Physical characteristics of the UCB and UCB2 experiments.

property	symbol	UCB	UCB2
reach length [m]	L	± 18.0	± 18.0
channel width [m]	W	0.25	0.25
radius of curvature [m]	R_c	0.81	0.81
discharge [m^3/s]	Q	1.00×10^{-6}	1.04×10^{-6}
flow depth [m]	h	0.016	0.011
width depth ratio [-]	W/h	15.6	22.7
curvature ratio [-]	R_c/W	3.24	3.24
Chezy flow resistance [-]	C	29.14	26.5
bed material grain size [mm]	D_{50}	0.62	0.62
bank material unit weight [N/m^3]	γ_s	n/a	20000
bank material cohesion [Pa]	c	n/a	100
bank material friction angle [deg]	ϕ	n/a	20
bank material critical shear stress [Pa]	$\tau_{b,c}$	n/a	0.32
fine cohesive fraction (failed) [-]	ω_{f1}	n/a	0.5
small granular fraction (failed) [-]	ω_{f2}	n/a	0.5
coarse granular fraction (failed) [-]	ω_{f3}	n/a	0
fine cohesive fraction (intact) [-]	ω_{h1}	n/a	0.5
granular fraction (intact) [-]	ω_{h2}	n/a	0.5
coefficient in power law for sediment transport [-]	k_s	5	5
exponent in power law for sediment transport [-]	p_s	0.00064	0.00064
coefficient in transverse slope model [-]	k_{tm}	0.67	0.67
exponent in transverse slope model [-]	p_{tm}	1	1
secondary flow convection factor [-]	k_{sn}	0.45	0.45
weighting coefficient for secondary flow intensity [-]	k_{si}	9.89	9.89
adaptation length for secondary flow [m]	λ_r	0.7	0.7
weighting coefficient for streamwise bed-slope [-]	k_{ls}	8	8

Results and discussion

Whiting and Dietrich (1988) measured bank erosion at several points in time. Here, two of the time-slices are considered: after 36 and 62 minutes. Best results were obtained with $k_B = 0.0001$ and $p_B = 1.0$. The model predicts erosion along the entire erodible section, as is observed in the laboratory flume (figure 4.26). Although the simulated bank erosion is of the same order of magnitude as the observations, there are some differences to be noted. In the laboratory experiment there are two distinct maxima of bank retreat, while the model predicts only one maximum, corresponding to the first of the observed maxima. The second maximum is not picked up in the model, even though it is more extreme than the first one. Hence, the model is fairly accurate for the first part of the bend, before the apex, but underpredicts the bank erosion along the second part of the bend. Furthermore, the model also slightly overpredicts bank retreat at the beginning and the end of the erodible section. Thus, the simulated bank erosion appears to be in rough agreement with the observations. However, considering that the model is calibrated to give optimal correspondence, the actual level of agreement is relatively disappointing; at some points along the second part of the bend, the model predicts less than half of the observed erosion. This problem is most likely related to the model's inability to represent the secondary flow field and the sediment flux accurately, as discussed above (section 4.3.2). Whiting and Dietrich (1993b) noted that the pattern of bank erosion was associated with the movement of bars through the channel, which confirms the theory that the interaction of free and forced bars is an important element in the evolution of bank migration and meander forms (Blondeaux and Seminara, 1985; Colombini *et al.*, 1987; Tubino and Seminara, 1990). The MRIPA model is not capable of representing free bars and multiple pools. Consequently, it misrepresents the shear stresses exerted on the bank. Thus, since the model only predicts the presence of one pool along the outer bend, it also predicts only one maximum in bank retreat. Furthermore, the model tends to underpredict pools and transverse slopes. Since channel incision near the toe of the bank is one of the driving mechanisms for bank failure, it is likely that the calibration of the parameters compensates for this underprediction by overestimating the values for the erodibility coefficient, k_B. Thus, the relatively poor prediction of bank erosion accentuates the problem of the flow and sediment transport submodels. However, the shortcomings of these submodels need not be the only influencing factors. The underprediction of bank retreat rates may also be partially contributed to a general inadequacy of the bank failure model. A tendency to underpredict bank erosion rates and overpredict bank stability was already observed in an earlier numerical model, where a similar mass-wasting analysis was applied on straight channels (Darby *et al.*, 1996).

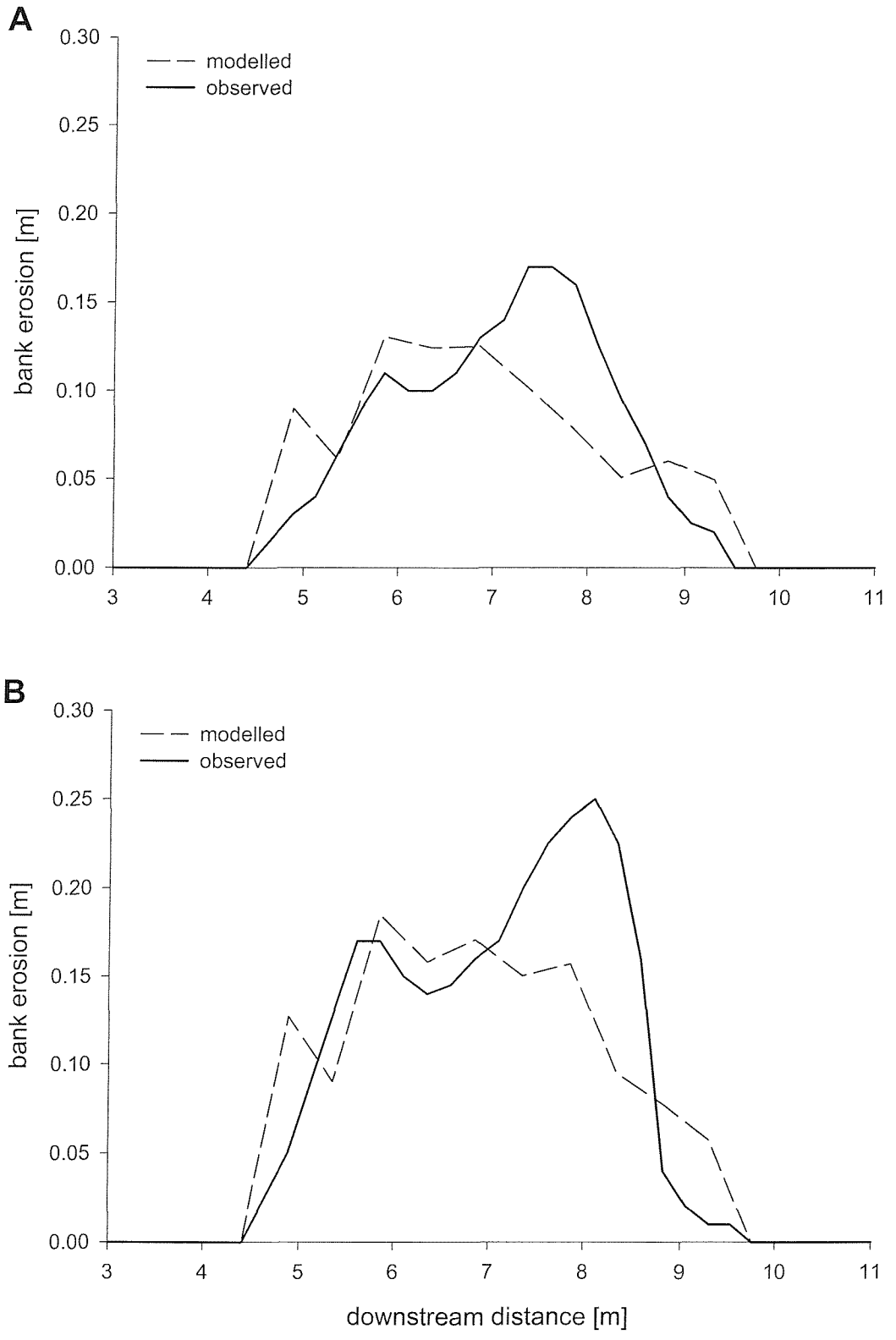

Figure 4.26: Modelled and observed bank erosion in the UCB2-flume. **A**: after 36 minutes. **B**: after 62 minutes.

4.4. Validation

In order to evaluate the performance of the model, the MRIPA model is used to simulate changes in a natural river reach over an extended period of time. For this simulation, the values of calibration parameters are not adjusted to force agreement between simulated and observed data. Instead, the values chosen are based on the results from the previous calibration exercise. This unforced running of the model allows an unbiased evaluation of its overall performance.

4.4.1. Site description

The model was tested on a reach of Goodwin Creek, Mississippi, USA (figure 4.27). This channel was selected as a case study for three reasons. First, it is a natural river. As such, it differs substantially from the laboratory experiments that were used in the calibration process. As the MRIPA model is aimed to be applied on natural rivers, it seems reasonable to select a natural river for the validation process. Second, it is a dynamic river with actively eroding banks such that changes are observable. The changes have been monitored over suitably long spatial and temporal scales to allow modelling and to be relevant to river engineering and river management. Finally, it is one of the few sites where data on flow, sediment transport, channel morphology, as well as bed and bank material properties are available in sufficient detail to meet the model's extensive input data requirements. Appropriate parameterization of the river, although often difficult to achieve, is essential for testing the numerical model (ASCE Task Committee, 1998b).

The study-reach is 707 metres long (figure 4.28A). The banks along this reach are cohesive and relatively resistant to fluvial entrainment. Hence, the predominant erosion mechanism is mass-wasting (Murphy and Grissinger, 1985). The channel width varies between 15.8 and 23.3 metres. The simulation period of channel change spans five and a half years, from November 1982 to May 1988. A full description of the nature of the study reach and the monitoring studies undertaken there have been reported elsewhere (Blackmarr, 1995; Kuhlne *et al.*, 1996).

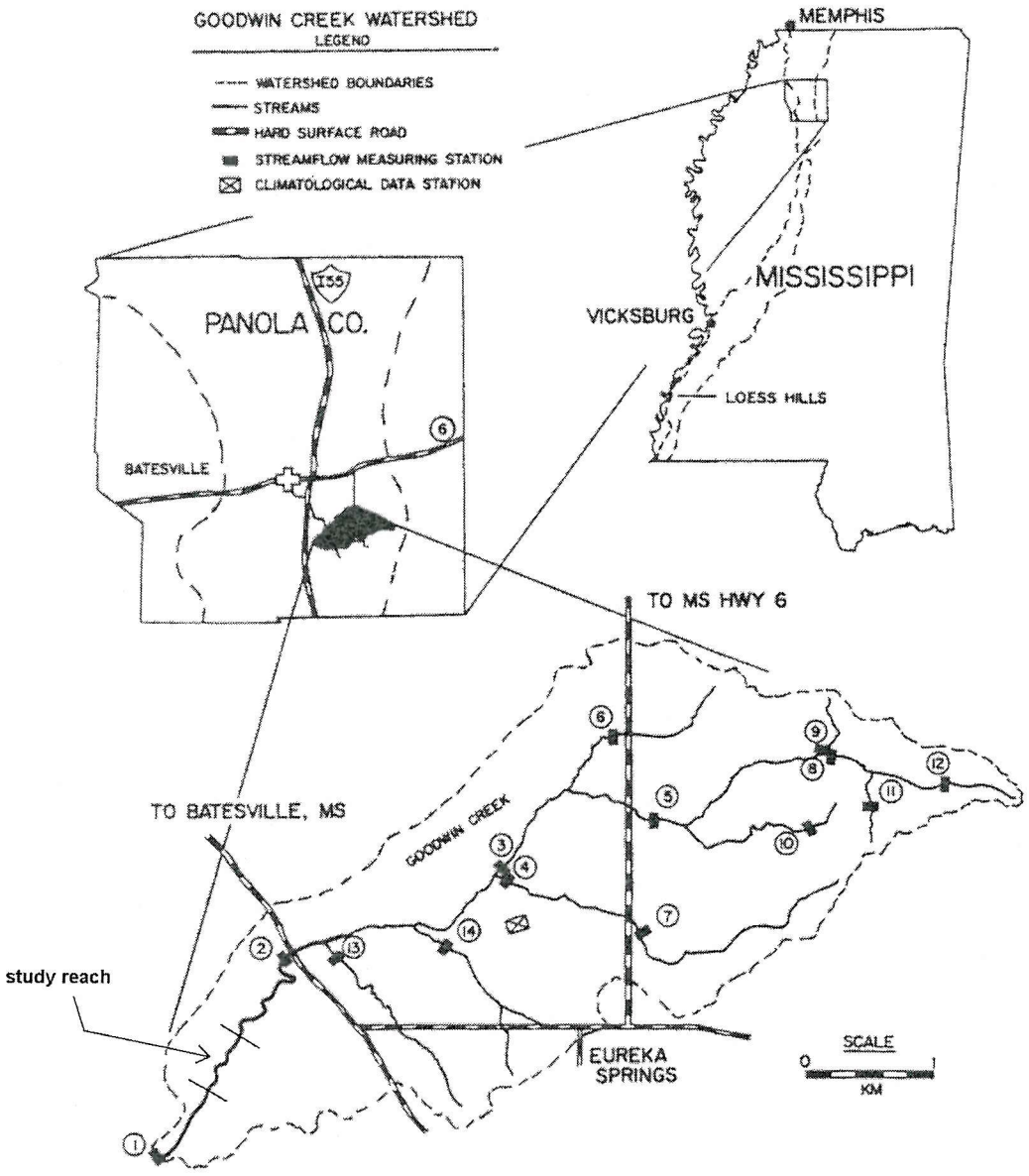

Figure 4.27: Location of the Goodwin Creek basin (from Murphey and Grissinger, 1985; with minor modifications). The study reach is located at the bottom of the basin, between flow gauges #1 and #2.

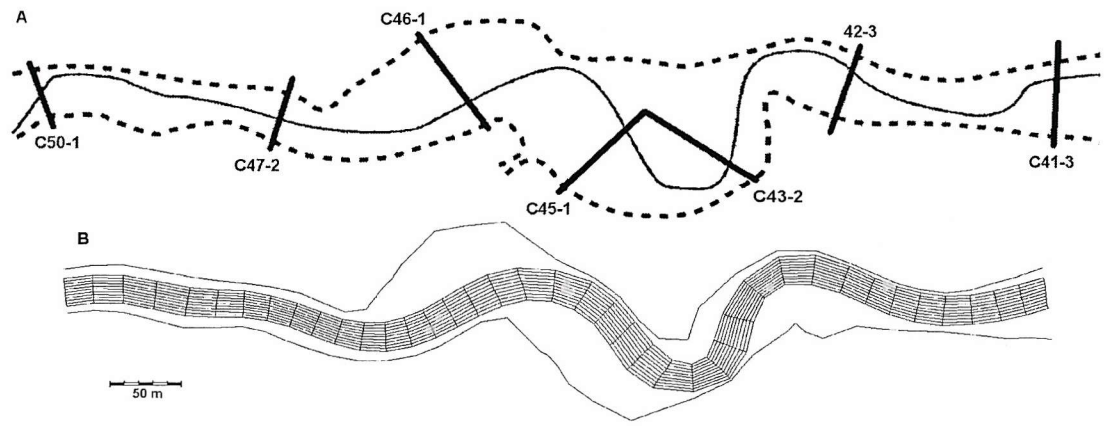

Figure 4.28: Goodwin Creek study reach. **A**: Schematic planform, using an established numbering system for cross-sections (Murphey and Grissinger, 1985; Blackmarr, 1995). **B**: Numerical grid. The bank tops are indicated as a thin line on either side of the bed. Flow direction is from left to right.

Table 4.10: Grid details.

gridpoints	longitudinal sections	transverse sections	longitudinal spacing[1]	transverse spacing[1]
451	41	11	17.6 m	1.9 m

note: [1] average value over entire reach

4.4.2. Numerical representation

The channel is reproduced numerically on a grid of 451 points (figure 4.28B). Transverse and longitudinal spacing of grid points is variable over the reach, due to its irregular shape. Some of the essential characteristics of the grid are summarized in table 4.10. Details of numerical mass conservation on this grid are given in appendix A4.

The descriptive variables of the study reach are summarized in table 4.11. Although the MRIPA model is capable of simulating quasi-steady flow, with stepped hydrographs, it has been observed that stability is improved when steady discharge is used. In this case study, a steady representative discharge is used, which is equivalent to the estimated dominant discharge value, Q = 7.5 m^3/s (Darby, Alabyan and Van De Wiel, 2002). Based on flow duration data from a nearby gauging station (Station #2 on figure 4.27), a simulation time of 358 days is equivalent to the real time lapse during the November 1982 to May 1988 study period. Using a steady equivalent discharge thus not only improves numerical stability, but also reduces simulation times by a factor 5.5. The disadvantage, however, is that extreme flow events, which are frequently associated with extensive bank mass-failure, are not explicitly modelled. The critical shear stress for entrainment of bank sediments is unknown. However, it is known that the banks are relatively resistant to fluvial attack (Murphey and Grissinger, 1985). Thus, a relatively high value for $\tau_{B,c}$ is chosen here. Other bank material properties are set in accordance with published data for the study reach (Murphey and Grissinger, 1985; Kuhlne *et al.*, 1996). The values of the calibration parameters are derived from the calibration exercise in section 4.3, and are listed in table 4.12. The parameters λ_r, k_{sn}, p_s, k_{tm} and p_{tm} are set in accordance with the values obtained in section 4.3.2. The values for k_{si} is derived from the sub-parameters k_l, using equation 4.6a with a uniform Chezy-coefficient, C = 10.0, where k_l is set to the value calculated in the calibration exercise. As sediment transport rates in Goodwin Creek are known to be high (Murphey and Grissinger, 1985), the coefficient for the sediment transport equation, k_s, was set to an arbitrarily chosen high value. The value for k_{ls} is more problematic. The model is numerically unstable when the values obtained for k_{ls} in section 4.3.2 are applied to the Goodwin Creek reach. Its value is, therefore, increased until stability is achieved. In a sense, k_{ls} is the only 'calibrated' parameter in the model, although it is adjusted only to assure numerical stability, and not to force any agreement of the simulated output with observed data. Indeed, it may not be an optimal value at all. The calibration parameters related to bank erosion were set identical to the ones observed in the calibration process (section 4.3.3).

Table 4.11: Characteristics of the Goodwin Creek reach.

property	symbol	value
reach length [m]	L	705.4
channel width [m]	W	19.2 [1]
maximal radius of curvature [m]	R_c	34.8 [2]
discharge [m^3/s]	Q	7.5 [3]
flow depth [m]	h	0.90 [4]
width/depth ratio [-]	W/h	21.3
curvature ratio [-]	R_c/W	1.81
Chezy flow resistance [-]	C	10
bed material grain size [mm]	D_{50}	1.2
bank material unit weight [N/m^3]	γ_b	18.9
bank material cohesion [Pa]	c_b	12000
bank material friction angle [deg]	ϕ	20
bank material critical shear stress [Pa]	$\tau_{B,c}$	20.0 [5]
fine cohesive fraction (failed) [-]	ω_{f1}	0.87
small granular fraction (failed) [-]	ω_{f2}	0
coarse granular fraction (failed) [-]	ω_{f3}	0.13
fine, cohesive fraction (intact) [-]	ω_{b1}	0.87
granular fraction (intact) [-]	ω_{b2}	0.13

note: [1] reach average, the model uses actual widths

[2] maximal value along the reach

[3] steady representative discharge (see text)

[4] reach averaged flow depth, corresponding to the steady representative discharge

[5] estimated value, chosen to reflect the bank material's resistance to fluvial attack

Table 4.12: Values for the calibration parameters.

parameter	symbol	value
coefficient in power law for sediment transport	k_s	0.01
exponent in power law for sediment transport	p_s	5
coefficient in transverse slope model	k_{tm}	0.67
exponent in transverse slope model	p_{tm}	1
secondary flow convection factor	k_{sn}	0.46
weighting coefficient for secondary flow intensity	k_{si}	2.93
adaptation length for secondary flow	λ_r	0.7
weighting coefficient for streamwise bed-slope	k_{ls}	12
sub-parameter for k_{si} in equation 4.6a	k_1	1.04
sub-parameter for k_{ls} in equation 4.6c	k_3	1.17
coefficient in fluvial bank erosion equation	k_b	1.0×10^{-4}
exponent in fluvial bank erosion equation	p_b	1

4.4.3. Results

Direct comparison between modelled and observed data is restricted in scope, due to the limited availability of observed data. There are only seven cross-sections within the reach for which observed bed topography data are available, two of which define the upstream and downstream boundary (*cf.* figure 4.28A). Evaluation of the model will focus on bed morphology and bank erosion predictions for the remaining five cross-sections (cross-sections C47-2, C46-1, C45-1, C43-2 and C42-3).

The simulated bed topography at the end of the simulation period is shown in figure 4.29. The main features of the bed morphology are the well-defined point bar in the bend between cross-sections C43-2 and C42-3 and the associated thalweg along the outer bank of the same bend. This point bar is also the dominant feature on a 1985 aerial photograph of the study reach (Darby, Alabyan and Van De Wiel, 2002). When comparing individual cross-sections (figure 4.30), it can be seen that there is reasonable agreement between modelled and observed bed data, although the simulated transverse slopes are too shallow, especially at cross-sections C46-1, C45-1 and C43-2.

Figure 4.31 illustrates the spatial pattern of simulated bank retreat over the study period, as well as observed values. The simulation results are broadly consistent with the observed data in that the model correctly predicts that most bank erosion is located along the left bank, with a maximum close to the bend apex between cross-sections C43-2 and C42-3. However, the model is inaccurate in that it underpredicts the amount of bank retreat, as well as the spatial extent of it. The maximal observed bank retreat over the study period is 17.67 metres at cross-section C43-2, while the maximal retreat predicted by the model is only 13.54 metres. Bank retreat is observed along the left bank at sections C45-1, C43-2, C42-3 and C41-3, while the model only predicts bank retreat along part of this reach, mainly around the apex of the bend between sections C42-3 and C41-3. The model also fails to reproduce a minor change on the right bank at cross-section C46-1. Instead, it incorrectly predicts bank retreat along the right bank near cross-section C43-2. The absence of modelled bank retreat at cross-section C50-1, where 5.55 metres was observed, can be attributed to this being the inlet boundary cross-section.

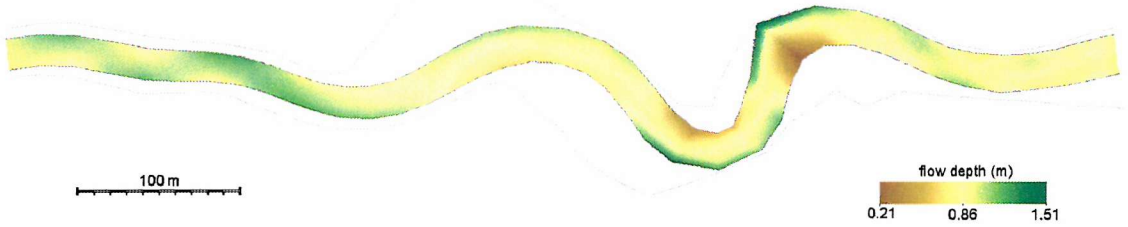

Figure 4.29: Final (May 1988) simulated planform and flow depth for the study reach.

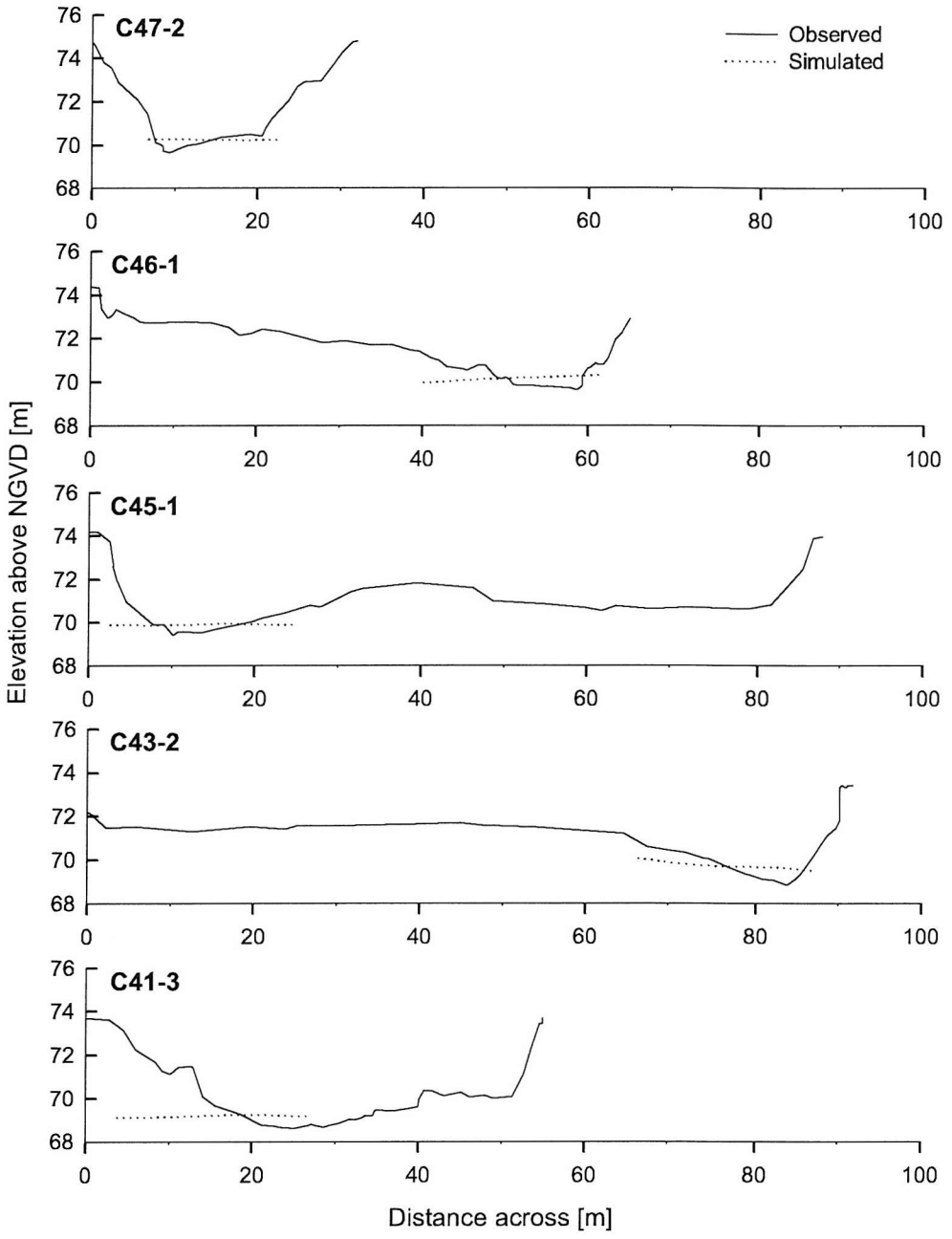

Figure 4.30: Observed and simulated cross-section topography for May 1988. Cross-section C42-3 is not depicted, as this was not included in the 1988 survey.

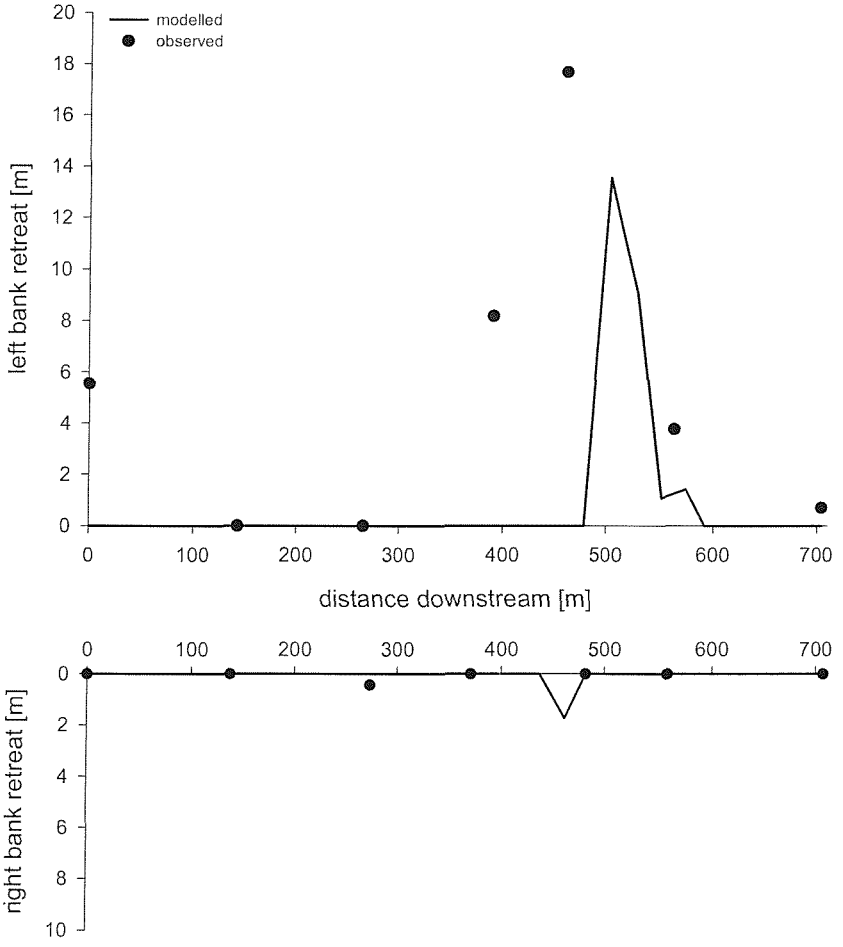

Figure 4.31: Modelled and observed bank retreat in the study reach for May 1988.

4.4.4. Discussion

In general, the model performs reasonably well, especially when considering that the calibration parameters are not adjusted for this particular channel. The purpose of the validation exercise is, after all, to evaluate the performance of the MRIPA model on a natural channel, where the calibration parameters are set to arbitrary, but rational and representative values.

The predicted bed morphology is broadly in agreement with the observed bed topography, and the dominant morphological features are represented in the model. However, smaller-scale morphological elements are less successfully reproduced, and particularly the predicted transverse slopes are too shallow. This is consistent with the systematic underprediction of pool depths and transverse slopes in the fixed-width laboratory flumes (section 4.3), and is a further indication that the model's representation of the flow field may need improving.

Occurrence and location of bank retreat are mostly predicted correctly, although both the spatial extent and the rate of bank erosion are underpredicted. This is, undoubtedly, at least partially related to the underprediction of pool depths in the near-bank zone. Another partial explanation might be the tendency of the bank failure model to underpredict bank erosion rates and overpredict bank stability (Darby *et al.*, 1996). Another possible explanation still is the inability of a steady-flow simulation to represent peak flows. In particular the observed bank retreat along the left bank at cross-sections C45-1 and C43-2, might well be related to individual high flow events, as their left bank is situated on the convex part of a bend which is in a very prone position for attack during extreme flows (*cf.* figure 4.28). By using an equivalent steady discharge, the model does not represent any of these high flows, and hence also not their increased hydraulic power, nor any draw-down effects that might effect bank stability. Finally, the underprediction of bank erosion rates might be due to a poor calibration of the bank erosion parameters. Although this is less tenable as a single cause, since the banks are relatively resistant to fluvial attack, it might enhance the shortcomings of any or all of the other factors mentioned above.

4.5. Conclusion

Overall, the integration of a geotechnical bank erosion algorithm with the two-dimensional flow and sediment transport model seems to have been successful. The MRIPA model is capable of predicting macro-scale changes in the bed and bank morphology of both laboratory flumes and natural river channels. This conclusion was recently backed up by an independent validation of the model, performed by Nigel Wright and Afshin Honarbakhsh at the University of Nottingham (Wright *et al.*, 2002). They applied the model to predict flow structure, sediment transport and bank erosion on the Fall River, Rocky Mountain National Park, Colorado. Predictions of flow and sediment transport were also compared with prediction obtained from a 3D CFD model, SSIIM-3D (Olsen, 2003). They conclude that the MRIPA model may be applied to predict flow structure and patterns of bank erosion in natural rivers (Wright *et al.*, 2002).

It must be noted, however, that there appear to be some shortcomings in the representation of the flow field, particularly in the near-bank zone of the outer bend. This subsequently affects estimation of sediment fluxes, which results in a tendency to underpredict pool depths and transverse slopes. The bank erosion component of the model seems to be capable of predicting overall patterns in bank retreat and channel migration. However, it tends to underestimate actual rates of bank erosion, possibly as a result of the inaccurate representation of the near-bank flow field. Thus, the performance of MRIPA may be too crude to be applied in river engineering, river management or other commercial activities, although this drawback was already anticipated by limiting the processes to be modelled to the essentials (*cf.* section 2.7). However, the model seems well suited for exploring differences in various what-if scenarios where patterns and trends are more relevant than specific values. In this sense, it appears that the model can indeed be applied for the investigative purpose for which it was designed: studying the effects of riparian vegetation on the morphological evolution of meandering, alluvial channels, as discussed in the next chapter.

Chapter 5
Analysis of Vegetation Effects

5.1. Introduction

It was noted in the previous chapter that, due to a lack of suitable datasets, the performance of the vegetation components of the mRIPA model cannot be verified in the same way as the flow, sediment transport or bank erosion components. Instead, in this chapter a more qualitative approach will be adopted to analyse the impact of vegetation on model results. First, the biophysical properties of vegetation are parameterized for use in the model (section 5.2). Subsequently, the effects of vegetation on channel morphology are studied, with the emphasis progressively shifting from verification of model behaviour to investigation of unknown or contentious issues in biogeomorphology. In section 5.3 the effects of vegetation on the geotechnical bank stability model are analysed in isolation, *i.e.* without linking it to the flow and sediment transport submodels. In section 5.4 all the submodels are coupled, enabling the influence of vegetation to be studied at the reach scale. Different simulations are performed in a hypothetical river reach, focussing on channel response to variations in vegetation species and density. Implications and limitations are discussed in section 5.5.

5.2. Parameterization of vegetation properties

Within the model, vegetation is characterized through parameterization of the relevant biophysical properties (table 5.1). The parameterization is deterministic in the sense that each biophysical property of the simulated vegetation is quantified as a single, unchanging value. This implies that, within the model, the plants of a particular species are considered to be identical and their properties do not change over time. Real vegetation, however, is diverse, complex and dynamic, even for homogeneous stands, as the properties of individual trees will vary as a function of age, health, season and local conditions such as soil material, pH and microclimate. This natural variability is not represented in the model

for two reasons. First, it is impractical, in that the numerical implementation would be both computationally demanding and subject to considerable uncertainty in view of the available empirical data. Second, and equally important in terms of the current study, representing vegetation species via a set of unvariable characteristics facilitates interpretation of the results in terms of identifying the vegetation properties that exert most influence on channel morphology. Thus, each modelled species must be considered as a collection of specific biophysical properties rather than a genuine species. Nonetheless, the vegetation data used for the parameterization in the simulations is broadly based on real riparian species to ensure that the parameters are at least pseudo-realistic.

Table 5.1: Biophysical properties selected for parameterization.

parameter	symbol
stem height [m]	H_v
stem diameter at base [m]	d_{vb}
stem diameter at top [m]	d_{vt}
wood mass density [kg/m^3]	ρ_v
vertical root depth [m]	L_{rV}
horizontal root extent [m]	L_{rH}
maximal root density [-]	A_{rmax}
root tensile strength [kPa]	T_r
critical shear modifier [kPa]	k_T
modus of elasticity [N/m^2]	E
drag coefficient [-]	C_d

5.2.1. Selection of species

The hypothetical vegetation species analysed herein are selected according to three criteria. First, they must be common riparian species. Second, they must be structurally different, in order to cover a broad range of the spectrum of possible biophysical properties. Finally, there must be sufficient published data available to allow parameterization of these biophysical properties. Based on these criteria, four species are selected for the numerical simulations, consisting of three woody and one herbaceous species: *"Betula"* (birch), *"Populus"* (poplar), *"Salix"* (willow) and *"Convolvulvus"* (bindweed). The names of the species are in quotation marks to highlight the fact that they represent virtual species, *i.e.* a collection of parameter values, not a genuine species. For a similar reason, the subspecies

name is neglected, although, wherever possible, each species is modelled on one particular subspecies (table 5.2). For example, the virtual species *"Betula"* is largely based on *Betula pendula* (silver birch), although it is considered to be representative of a wide range of birch species in general. However, none of the subspecies of *Betula*, including *Betula pendula*, is likely to conform precisely to all the properties of the virtual *"Betula"* simulated herein.

Table 5.2: The origin of species.

modelled species	based on
"Betula"	*Betula pendula* (silver birch)
"Populus"	*Populus nigra* (black poplar)
"Salix"	*Salix fragilis* (crack willow)
"Convolvulvus"	*Convolvulvus arvensis* (bindweed)

Where possible, parameterization of vegetation properties is based on published data. For some parameters, however, values can only be estimated, due to the limited availability of empirical data. In the following paragraphs, the parameterization for each of the biophysical properties is detailed. While the focus is on the selected species, data for other species, including some non-riparian species, is also presented to provide a context for some of the more ambiguous parts of the parameterization.

5.2.2. Parameterization

Parameterization of above-ground plant dimensions

The above-ground physical dimensions of woody vegetation are defined by the stem diameter and tree height. Tree stems are represented as tapering cylinders, identified through the diameter at the base of the stem, which is normally measured at breast height, and the diameter at the top. While values for the stem height and the diameter at the base of the stem are commonly reported in flora or other compendia (table 5.3), there is little data available for the stem diameter near the top. The published values are "typical" values for mature trees. Maximal values are frequently up to 50 % higher for stem height, and up to 200 % higher for stem diameter (Rehder, 1947; Forest Products Research Laboratory, 1956).

Table 5.3: Typical above-ground dimensions for mature trees of various species.

vegetation species		height	base diameter
Latin name	common name	[m]	[m]
Acer saccharinum	soft maple	25	1.1
Alnus glutinosa	black alder	30	0.8
Betula nigra	river birch	20	0.7
Betula pendula	silver birch	15	0.8
Fagus sylvatica	European beech	25	1.5
Fraxinus excelsior	European ash	30	1.1
Picea abies	European spruce	35	1.4
Pinus sylvestris	Scots pine	30	1.0
Populus alba	white poplar	22	1.0
Populus deltoides	cottonwood	27	1.1
Populus nigra	black poplar	30	1.1
Pseudotsuga menziesii	Douglas fir	65	1.4
Quercus robur	oak	30	1.7
Salix alba	white willow	25	1.3
Salix fragilis	crack willow	25	0.7
Salix nigra	black willow	10	0.5
Tilia americana	basswood	20	0.8
Ulmus americana	white elm	27	1.0

sources: Rehder, 1947; Forest Products Research Laboratory, 1956; Nicholson and Clapham, 1975

Table 5.4 lists the parameter values selected for the virtual species modelled herein. Parameterization of tree height and stem diameter at base is based on table 5.3. The stem diameter at the top has been estimated, arbitrarily, as being 10 cm for "*Betula*" and "*Salix*" and 15 cm for "*Populus*". For grasses, the above-ground dimensions are also defined by the height and stem diameter. However, for grasses the stem diameter is assumed to be constant over the entire height. The height of the grasses refers to the erect height, *i.e.* unaffected by the flow. No values are published for the grass species used in this study. The values for "*Convolvulvus*" presented in table 5.4 are estimates, based on observations of other species of grasses and reeds.

Table 5.4: Parameterization of above-ground properties.

modelled species	height [m]	diameter at base [m]	diameter at top [m]
"Betula"	15	0.5	0.10
"Populus"	25	1.0	0.15
"Salix"	15	0.6	0.10
"Convolvulvus"	0.3	0.01	0.01

Parameterization of root dimensions

Subsurface root structure is known to be very dependent on soil properties and soil hydrology in particular, to the extent that these external factors dominate over species characteristics (Kozlowski, 1971). This makes a parameterization of root dimensions as a function of species highly questionable. Furthermore, empirical data on root properties of vegetation is generally more scarce than data on stem or canopy properties, due to the practical difficulties associated with below-ground measurements. Although maximal reported values for vertical root depth extend well beyond 20 metres, the roots are usually confined to the top three metres of the soil (Kozlowski, 1971; Greenway, 1987). Recent analyses of the root structure of seven common riparian species in Australia and North America show that roots commonly develop up to about a metre depth, with some deep rooted species (e.g. *Eucalyptus camaldulensis*) reaching down to about two metres and some species (e.g. *Betula nigra*) developing more shallow root networks (Abernethy and Rutherfurd, 2001; Simon and Collison, 2002). Lateral extent of roots is often related to rules of thumb like "twice as far as the width of the crown" or "equal to the height of the tree". For two Australian riparian species, Abernethy and Rutherford (2001) report the root extent to be greater than 2.5 m and 17.2 m, while Simon and Collison (2002) estimated the average root plate radius for five common riparian tree species to be about 2.1 metres. Binns (1980) provides a qualitative overview of rooting habits in clay soils for different species (table 5.5). The parameterization of vertical root depth and horizontal root extent used in simulations herein (table 5.6) is largely based on this qualitative description. The qualitative terms for rooting depth were parameterized as follows: "shallow" = 0.5 m, "moderately deep" = 1.0 m, and "deep" = 2.0 m. Horizontal root extent is taken to be 2.5 m, unless it was specified as being "widespread", in which case it is parameterized as 5.0 m. This is roughly in keeping with the experimental values reported by Simon and Collison (2002) and Abernethy and Rutherfurd (2001). The grass species is assumed to have very shallow roots, relative to the roots of the tree species (Coppin and Richards, 1990; Jackson *et al.*, 1996). The maximal root density is arbitrarily set equal to 0.8 for all species. Although this is much higher than reported root-area-ratio values (e.g. Abernethy and Rutherfurd, 2001; Simon and Collison, 2002), a value of 0.8 is chosen to represent the transition of stem to root, where most of the soil will be occupied by the roots. The exponentially declining root-area-ratio model (section 3.5.4) ensures that the average root-area-ratio will be considerably lower (typically around 10^{-4} to 10^{-3}) and more consistent with published values of this parameter.

Table 5.5: Qualitative description of the root structure for various plant species.

vegetation species		vertical root depth	horizontal root extent
Latin name	common name		
Aesculus hippocastanum	horse chestnut	moderately deep	normal
Alnus firma v. multinervis	alder	moderately deep	normal
Alnus firma v. yasha	alder	moderately deep	normal
Alnus incana	alder	moderately deep	normal
Betula pendula	silver birch	shallow	normal
Chameocyparis lawsoniana	Lawson cypress	moderately deep	normal
Cupressus macrocaipa	Monterey cypress	moderately deep	normal
Fagus sylvatica	beech	shallow	normal
Fraxinus excelsior	ash	moderately deep	normal
Picea abies	European spruce	shallow	normal
Picea sitchensis	Sitka spruce	shallow	normal
Pinus nigra	Corsican pine	moderately deep	normal
Pinus sylvestris	Scots pine	shallow	normal
Populus nigra	black poplar	deep	widespread
Populus deltoides	poplar	deep	widespread
Populus euramericana	American poplar	deep	widespread
Populus yunnanensis	Yunnan poplar	deep	widespread
Pseudotsuga menziesii	Douglas fi	shallow	normal
Quercus robur	oak	deep	normal
Salix cinerea	willow	moderately deep	normal
Salix dasyclados	willow	moderately deep	normal
Salix elaeagnos	willow	moderately deep	normal
Salix fragilis	willow	moderately deep	normal
Salix hastata	willow	moderately deep	normal
Salix hegetschweileri	willow	moderately deep	normal
Salix helvetica	willow	moderately deep	normal
Salix matsudana	willow	moderately deep	normal
Salix purpurea	willow	moderately deep	normal
Salix starkeana	willow	moderately deep	normal

sources: Binns, 1980 (cited in Greenway, 1987)

Table 5.6: Parameterization of root geometry.

modelled species	vertical root depth [m]	lateral root extent [m]	maximal root density [-]
"Betula"	0.5	2.5	0.8
"Populus"	2.0	5.0	0.8
"Salix"	1.0	2.5	0.8
"Convolvulvus"	0.15	0.10	0.8

Parameterization of root tensile strength

The tensile strengths of roots vary not only with species, but also with growing environment, age, season, root diameter and root orientation (Greenway, 1987; Coppin and Richards, 1990; Abernethy and Rutherfurd, 2001; Simon and Collison, 2002). The dependence of root tensile strength on root diameter is illustrated in figure 5.1. Differences in tensile strength for the same species can be up to two orders of magnitude (Simon and Collison, 2002). Any averaged value is, therefore, likely to be subject to a considerable degree of uncertainty and should be used with caution. Nonetheless, many averaged values have been published (table 5.7), and these at least provide a rough guide to the root tensile strengths of various species of grasses, herbs, shrubs and trees. The parameterization for the selected species is given in table 5.8.

Parameterization of mass density

The plant mass density is used to determine the vegetation's surcharge on the banks. The surcharge of grasses is considered negligible relative to the weight of an incipient failure block. Hence, only the surcharge induced by shrubs and trees is considered here. The mass density for living trees depends on the dry wood mass density and the amount of water within the tree. The dry wood mass density depends on species only, but water content is variable and can contribute between 10% and 80% of the tree weight (Husch, 1963; Forest Products Research Laboratory, 1956). Nevertheless, the representative mass densities for live trees listed in table 5.9 are considered to be an adequate approximation for the parameterization of the virtual species (table 5.10)

Parameterization of modus of elasticity

The modus of elasticity is not a parameter in the strict sense. It is related empirically to plant height and stem diameter via equation 3.43. Hence, the modi of elasticity of the modelled species can be derived from the above parameterization of the stem properties. The values thus obtained (table 5.11) are of the same order of magnitude as published values (table 5.12).

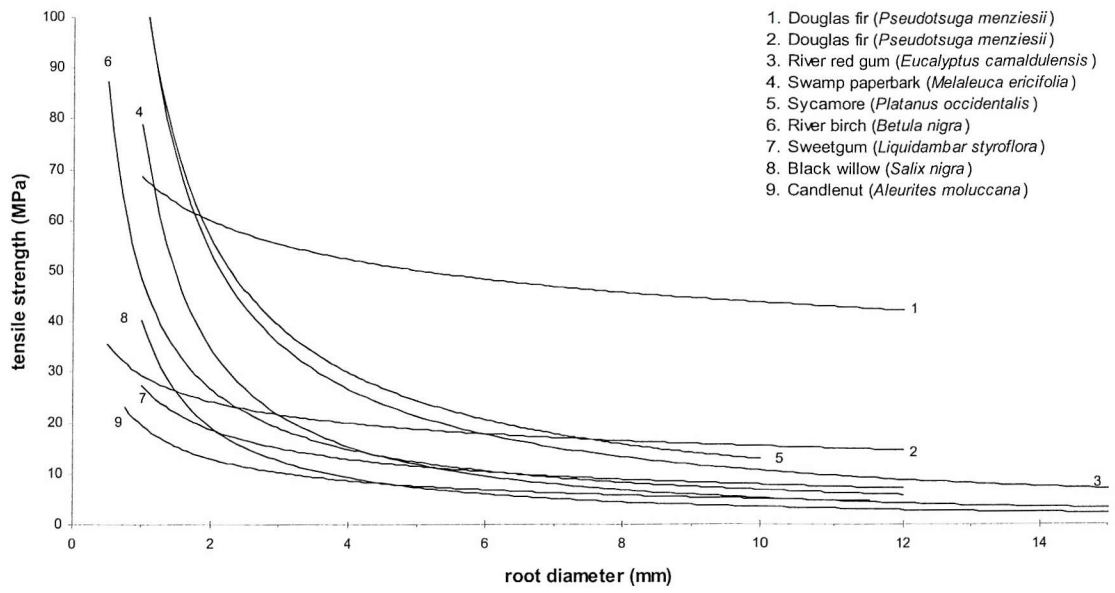

Figure 5.1: Root tensile strength as function of root diameter for different tree species. Root tensile strength declines with increasing root diameter. Within one species, tensile strength can vary by up to two orders of magnitude, depending on root diameter. The rate of decline is species dependent. For a given root diameter, tensile strength can vary by up to an order of magnitude between species. Even when considering two specimens of the same species, the relation between tensile strength and root diameter can vary significantly (e.g. graphs 1 and 2). Note: Part of the variance shown here might be due to differences in measurement techniques, as there is no standardized method for measuring root tensile strength. Sources: 1,2,9: Greenway, 1987; 3,4: Abernethy, 1999; 5-8: Simon and Collison, 2002.

Table 5.7: Root tensile strength for various plant species.

vegetation type	vegetation species		tensile strength [MPa]
	Latin name	common name	
grasses and herbs	*Campanula trachelium*	bellflower	2
	Convolvulus arvensis	bindweed	13
	Elymus repens	couch grass	16
	Medicago sativa	alfalfa	25-87
	Panicum virgatum 'Alamo'	Alamo switch grass	19 (2-128)
	Plantago lanceolata	plantain	6
	Taraxacum officinale	dandelion	2
	Trifolium pratense	red clover	15
	Tripsacum dactyloides	eastern gamma grass	28 (4-98)
shrubs and trees	*Acacia confusa*	acacia	11
	Aleurites moluccana	candlenut	6
	Alnus firma v. multinervis	alder	51
	Alnus firma v. yasha	alder	4-74
	Alnus incana	alder	32
	Alnus japonica	Japanese alder	41
	Betula nigra	river birch; black birch	16 (2-70)
	Betula pendula	silver birch	37
	Cyticus scoparius	Scotch broom	32
	Eucalyptus calamdulensis	river red gum	25 (2-214)
	Ficus microcarpa	Chinese banyan	16
	Lespedeza bicolor	shrub lespedeza	69
	Meterosideros umbellata	rata	53
	Liquidambar styroflora	sweetgum	12 (2-57)
	Melaleuca ericiflora	swamp paperbark	25 (1-105)
	Nothofagus fusca/truncata	beech	36
	Picea abies	European spruce	27
	Picea sitchensis	Sitka spruce	23
	Pinus densiflora	Japanese red pine	32
	Pinus radiata	radiata pine	18
	Platanus occidentalis	sycamore	23 (2-125)
	Populus nigra	black poplar	5-12
	Populus deltoides	poplar	36; 38
	Populus euramericana	American poplar	32; 46
	Populus yunnanensis	Yunnan poplar	38
	Pseudotsuga menziesii	Douglas fir	19; 50; 61
	Quercus robur	oak	32
	Robinia pseudoacacia	black locust	68
	Salix cinerea	willow	11
	Salix dasyclados	willow	17
	Salix elaeagnos	willow	15
	Salix fragilis	willow	18
	Salix hastata	willow	14
	Salix hegetschweileri	willow	9
	Salix helvetica	willow	13
	Salix matsudana	willow	36
	Salix nigra	black willow	12 (1-70)
	Salix purpurea	willow	36
	Salix starkeana	willow	12
	Thuja plicata	western red cedar	56
	Tilia cordata	linden	26
	Tsuga heterophylla	western hemlock	27
	Vaccinium	huckleberry	16

sources: Greenway, 1987; Coppin and Richards, 1990; Abernethy and Rutherford, 2001; Simon and Collison, 2002

Table 5.8: Parameterization of tensile strength.

modelled species	tensile strength [kPa]
"Betula"	37000
"Populus"	10000
"Salix"	18000
"Convolvulvus"	13000

Table 5.9: Wood mass densities for various tree species.

vegetation species		mass density [kg/m^3]
Latin name	common name	
Acer pseudoplatanus	great maple (sycamore)	817
Aesculus hippocastanum	horse chestnut	929
Alnus glutinosa	black alder	865
Betula pendula	silver birch	961
Fagus sylvatica	European beech	961
Fraxinus excelsior	European ash	833
Populus alba	white poplar	881
Populus nigra	black poplar	881
Quercus robur	oak	1073
Salix alba	white willow	705
Salix fragilis	crack willow	705

source: Forest Products Research Laboratory, 1956

Table 5.10: Wood mass density for the modelled species.

modelled species	mass density [kg/m^3]
"Betula"	960
"Populus"	880
"Salix"	705
"Convolvulvus"	not applicable

Table 5.11: Parameterization of modus of elasticity.

modelled species	modus of elasticity [N/m^2]
"Betula"	2.98×10^8
"Populus"	2.33×10^8
"Salix"	3.46×10^8
"Convolvulvus"	2.98×10^8

Table 5.12: Modi of elasticity for various species.

vegetation species		modus of elasticity
Latin name	common name	[N/m²]
Allium sativum	garlic	3.2×10^8 - 3.9×10^8
Alnus incana	alder	1.7×10^9
Cornus ssp.	dogwood	2.1×10^8 - 3.0×10^9
Euonymus		4.1×10^8
Platanus acercifolia	sycamore	2.7×10^9
Populus deltoides	poplar(cottonwood)	1.8×10^7 - 1.1×10^8
Rosa ssp.	rose bush	1.7×10^7 - 9.5×10^8
Salix exigua	pacific willow	3.5×10^7 - 8.0×10^9
Salix lasiandra	sandbar willow	3.2×10^7 - 1.0×10^9
Salix lemonii	lemon's willow	3.8×10^7 - 6.5×10^8
Salix nigra	black willlow	1.5×10^9
Sambucus ssp.	elderberry	2.6×10^7 - 1.7×10^9

sources: Rahmeyer *et al.* 1998; Freeman *et al.*, 2000; Niklas and Moon, 1988

Parameterization of roughness

As yet, no theoretical model exists for evaluating the drag coefficient, C_d, for different vegetation species and configurations. While Wu *et al.* (1999) suggest a generic formula to calculate the combined effect of the drag coefficient and vegetation blocking area, it is more common to evaluate the drag coefficient separately. For a single vertical cylinder C_d, is estimated as 1.2 (Li and Shen, 1973), while for low trees it is approximated as 1.5 (Klaassen and Van der Zwaard, 1973). Based on empirical data from various sources Petryk and Bosmajian (1975) state that, for vegetation, the drag coefficient is *"of the order of 1.0"*. In subsequent studies this claim is often simplified to C_d equals 1.0 (e.g. Graeme and Dunkerley, 1993; McKenney *et al.,* 1995). However, depending on the flow velocity and the spatial pattern of vegetation elements, the drag coefficient may range from 0.2 to 3.0 (Petryk, 1969; Li and Shen, 1973; Klaassen and Van der Zwaard, 1973). The true value of C_d is likely to show an additional dependency on the shape and structure of the vegetation (Fathi-Moghadam and Kouwen, 1997). Furthermore, the drag force is also dependent on the Reynolds-number, R_e, of the flow, having a near constant value in the turbulent region, but with notably higher values in laminar flow (Kadlec, 1990).

There are currently no specific data for the species selected in this study. The parameterization is, therefore, based on estimates. Trees are modelled as rigid cylinders, and the drag coefficient values adopted here are taken to be close to unity (table 5.13). Minor deviations are superimposed, to account for skin roughness: an 'average' skin for

"Populus", a slightly smoother skin for *"Betula"* and a rough skin for *"Salix"*. The grass species "*Convolvulvus*" has been assigned a value in the same range, although there is no specific justification for this.

Table 5.13: Parameterization of drag coefficient

modelled species	drag coefficient [-]
"Betula"	0.9
"Populus"	1.0
"Salix"	1.2
"Convolvulvus"	1.2

Parameterization of shear strength modifier

Vegetation protects sediments against fluvial entrainment by reducing sediment exposure and binding soil material with their roots. It seems reasonable to assume that the critical shear stress for vegetated banks would be higher than for unvegetated banks. However, there is very little data to quantify the increase in shear strength. Millar and Quick (1998) report that the shear strengths of tree-covered cohesive soils is about three times higher than those of comparable unvegetated or lightly vegetated cohesive soils, while grass-covered soils have roughly the same shear strengths as unvegetated or lightly vegetated soils. On the other hand, Micheli and Kirchner (2002) report that the shear strength of soil colonized by rush or sedge can be up to 15 times higher than a comparable unvegetated soil, depending on the density of the vegetation stand. It has also been observed that the removal of vegetation from grassland can reduce the critical shear stress for gully initiation by overland flow by an order of magnitude (Prosser *et al.*, 1995). Recent technological advances allow for *in situ* measurements of shear strengths of bank material (Hanson and Simon, 2001; Hanson and Temple, 2002). Application of this technology to vegetated banks might provide improved measurements of the bank material's shear strength.

In the model, the increased shear stress due to the vegetation is represented through a shear strength modifier, $k_{\tau,veg}$ (equation 3.68). In view of the limited available data, the parameterization hereof is necessarily arbitrary (table 5.14). The shear strength modifier for the simulated trees is presumed to be equal to three, in accordance with the observations of Millar and Quick (1998). In contrast, the shear strength modifier of grasses is assumed to be

much higher ($k_{\tau,veg} = 20$), partly in accordance with the observations of Micheli and Kirchner (2002) and partly reflecting the higher density of the near-surface root network of grasses and herbaceous species (Jackson *et al.*, 1996; Liquori and Jackson, 2001).

Table 5.14: Parameterization of the shear strength modifier.

modelled species	shear strength modifier [-]
"Betula"	3
"Populus"	3
"Salix"	3
"Convolvulvus"	20

5.2.3. Overview

Four representative species have been selected and their biophysical properties have been parameterized. Table 5.15 summarizes the results of the parameterization procedure. It is clear from the above discussion that many assumptions and approximations have been made in the parameterization. Nonetheless, the parameterization of the four hypothetical species covers a range of representative biophysical properties and is considered to be adequate for the current study. The model's sensitivity to the changes in vegetation parameters will be analysed in section 5.3.4.

Table 5.15: Vegetation parameters used in the mRIPA model.

parameter	symbol	*"Betula"*	*"Populus"*	*"Salix"*	*"Convolvulvus"*
stem height [m]	H_v	20	30	25	0.3
stem diameter at base [m]	d_{vb}	0.80	1.10	0.70	0.01
stem diameter at top [m]	d_{vt}	0.10	0.15	0.10	not applicable
wood mass density [kg/m^3]	ρ_v	960	880	705	not applicable
vertical root depth [m]	L_{rV}	0.5	2.0	1.0	0.15
horizontal root extent [m]	L_{rH}	2.5	5.0	2.5	0.10
maximal root density [-]	A_{rmax}	0.8	0.8	0.8	0.8
root tensile strength [kPa]	T_r	37000	10000	18000	13000
critical shear modifier [kPa]	k_r	3	3	3	20
modus of elasticity [N/m^2]	E	2.98×10^8	2.33×10^8	3.46×10^8	2.98×10^8
drag coefficient [-]	C_d	0.9	1.0	1.2	1.2

5.3. Geotechnical bank stability analysis with vegetation

In section 3.5.4 an improved method for analysing bank stability with respect to mass failure, incorporating vegetation effects, was introduced. Here, this new approach will be illustrated and evaluated. Only the geotechnical module is applied in the analyses in this section. Nonetheless, it will be extensively discussed, as the incorporation of vegetation effects constitutes a significant conceptual improvement over many existing bank stability models. The stand-alone application of the bank stability module facilitates its interpretation, as it avoids the complexities of interaction between hydraulic processes and bank failure processes. However, the interactions with hydraulic processes are an important aspect of the morphologic evolution of river channels and of the MRIPA model. As such, they will be addressed in a later section (section 5.4)

5.3.1. Setup of the analysis

As the analyses are site-based, rather than reach-based, it suffices to specify the geometry and physical simulated properties of the bank. Unless specifically stated otherwise, a "standard" riverbank is used in each of the analyses (table 5.16; figure 5.2; also *cf.* figure 3.14). In unvegetated circumstances, the standard bank is just stable, with a factor of safety slightly above unity (N_{FS} = 1.013; table 5.17). Throughout this section, this value will be used as a reference for studying the impact of vegetation on bank stability. It is worth reiterating that although vegetation might influence the factor of safety, and, hence, whether or not a bank fails, it does not affect the failure geometry (*cf.* section 3.5.4). Thus, the variables describing the failure geometry are valid also for the analyses with vegetation (table 5.17).

Vegetation can be represented in one of two ways. First, as one or more individual plants, in which case the horizontal distance, x_v, from the toe of the bank to the plant stems needs to be specified (figure 5.3A; also *cf.* figure 3.21). However, specifying the position of each plant can be cumbersome, especially for grasses or dense stands of trees. Therefore, stands of vegetation can also be specified. In this case, the spacing of the vegetation, σ_v, needs to be specified, as well as the starting and ending coordinates, x_{v1} and x_{v2}, of the vegetation strip (figure 5.3B). These two ways of representing vegetation will be discussed separately.

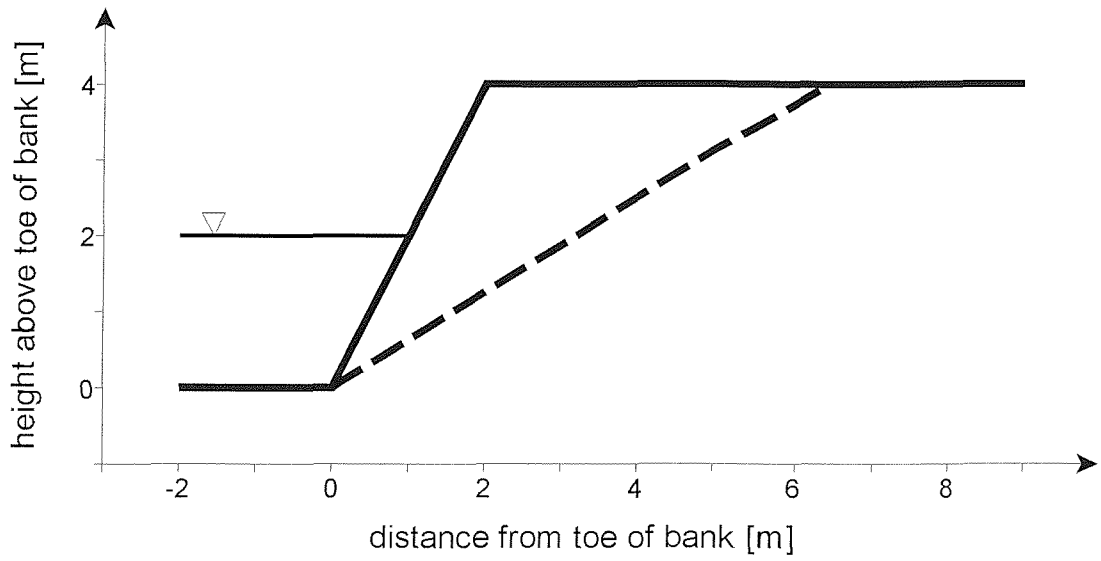

Figure 5.2: The "standard" river bank for geotechnical analyses. The bank profile is shown in bold, with the incipient failure plane as a dashed line.

Table 5.16: Properties of the "standard" riverbank.

parameter	symbol	value
bank height [m]	H_b	4.0
cutbank [m]	H_{cb}	0
vertical cliff [m]	H_c	0
tension crack [m]	H_t	0
bank slope [deg]	β_b	60.0
flow depth [m]	H_w	2.0
groundwater level [m]	H_g	2.0
bank material cohesion [Pa]	c	3000
unit soil weight [N/m^3]	γ_s	20000
friction angle [deg]	ϕ	20
matric suction angle [deg]	ϕ^b	15

Table 5.17: Failure variables of the "standard" riverbank.

variable	symbol	value
factor of safety [-]	N_{FS}	1.013 [1]
slope of incipient failure plane [deg]	β_f	38.9
length of incipient failure plane [m]	L_f	6.37
horizontal length of incipient failure [m]	$L_f \cos(\beta_f)$	4.96

Note: [1] Valid for unvegetated conditions only

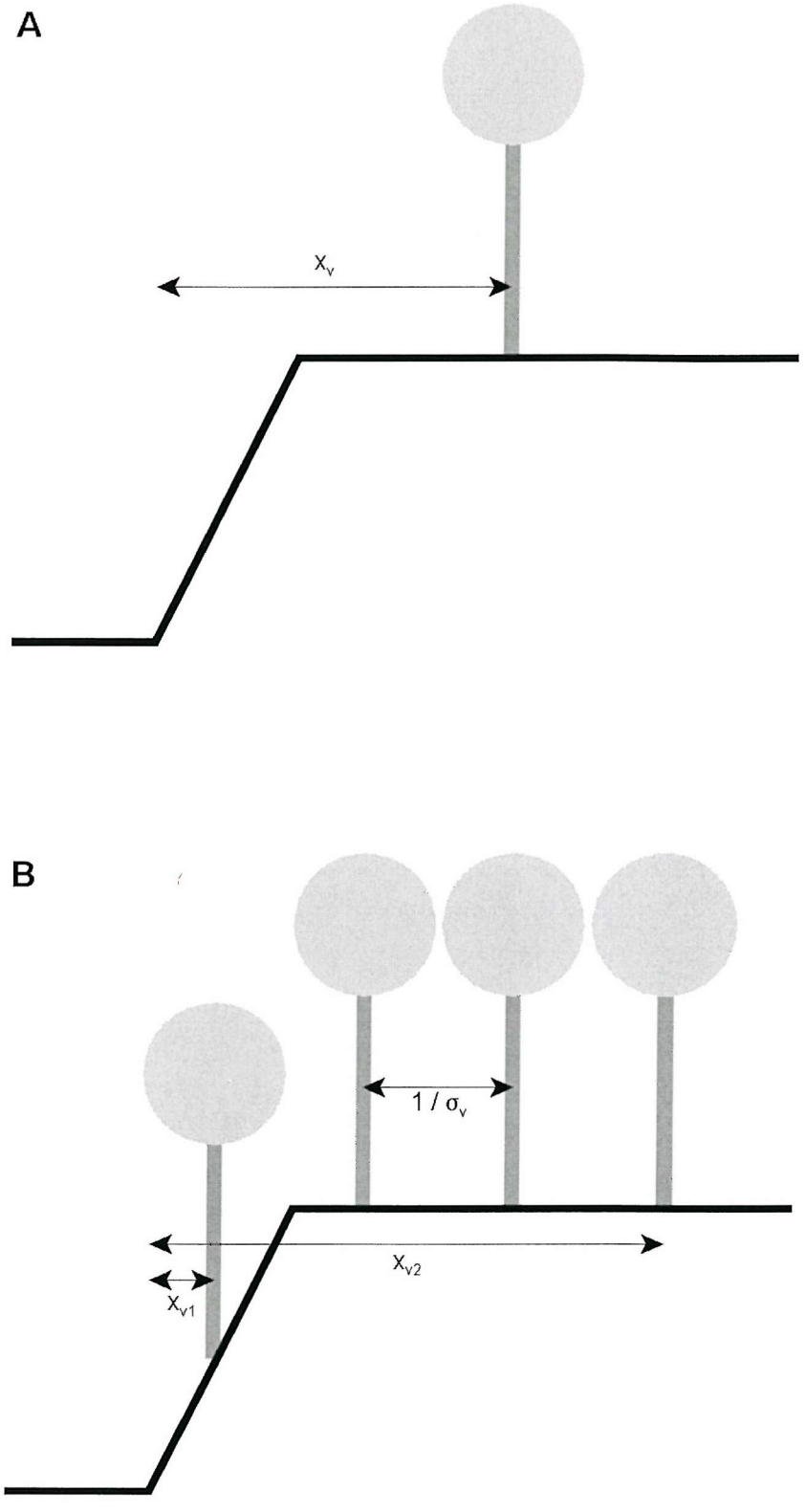

Figure 5.3: Vegetation positioning. **A**. individual plants. **B**: stands of vegetation.

5.3.2. Results with a single vegetation element

Distribution of root cohesion

The distribution of root cohesion or root shear strength, s_R, through the soil is closely related to the distribution of root-area-ratio, A_R. Figure 5.4A illustrates the spatial distribution of root-area-ratio through the soil, for a single "*Populus*" plant. The exponential decline of root-area-ratio in both the horizontal and vertical directions can clearly be observed. The distribution of apparent root cohesion (figure 5.4B) also shows an exponential decline, due to the simple relation between root-area-ratio and apparent root cohesion (equation 3.106). Although the calculations are slightly different and applied to different species, these graphs are very similar to results obtained by Abernethy and Rutherfurd (2001).

The maximal value for apparent root cohesion depends on the tensile strength of the roots and is, therefore, species dependent. Likewise, the rates of decline, which are defined by the maximal rooting depth and the maximal horizontal root extent of the species, are also species dependent. This dependency is illustrated in figure 5.5 for the three tree species. It is obvious that the roots of "*Populus*", having both deep and widespread roots, provide additional cohesion to a large area of the bank. In contrast, "*Betula*" only affects a small area, having a shallow and less wide root network. Nonetheless, as "*Betula*" roots have the highest tensile strength, these roots also provide the highest maxima root cohesion value (35.5 kPa, compared with 9.6 kPa for "*Populus*" and 17.3 kPa for "*Salix*"), albeit restricted to a very small area directly beneath the stem of the tree.

Rather than the distribution of root cohesion throughout the soil, a geotechnical stability analysis requires knowledge of the distribution of root cohesion along the incipient failure plane. This is illustrated in figure 5.6 for the case of an individual tree located four metres away from the toe of the bank. Clearly the results are species dependent, but the exponential nature of the root cohesion distribution can be observed for each of the species. The root cohesion is suddenly reduced to zero where the failure plane ends (at 4.96 m from the toe of the bank). The exact shape of the curve depends on the physical properties of the roots, in particular the ratio of maximal root depth to maximal horizontal extent, and on the lateral position of the vegetation on the bank. The former of these two aspects will be discussed in the parameter sensitivity analysis (section 5.3.4), the latter will be discussed next.

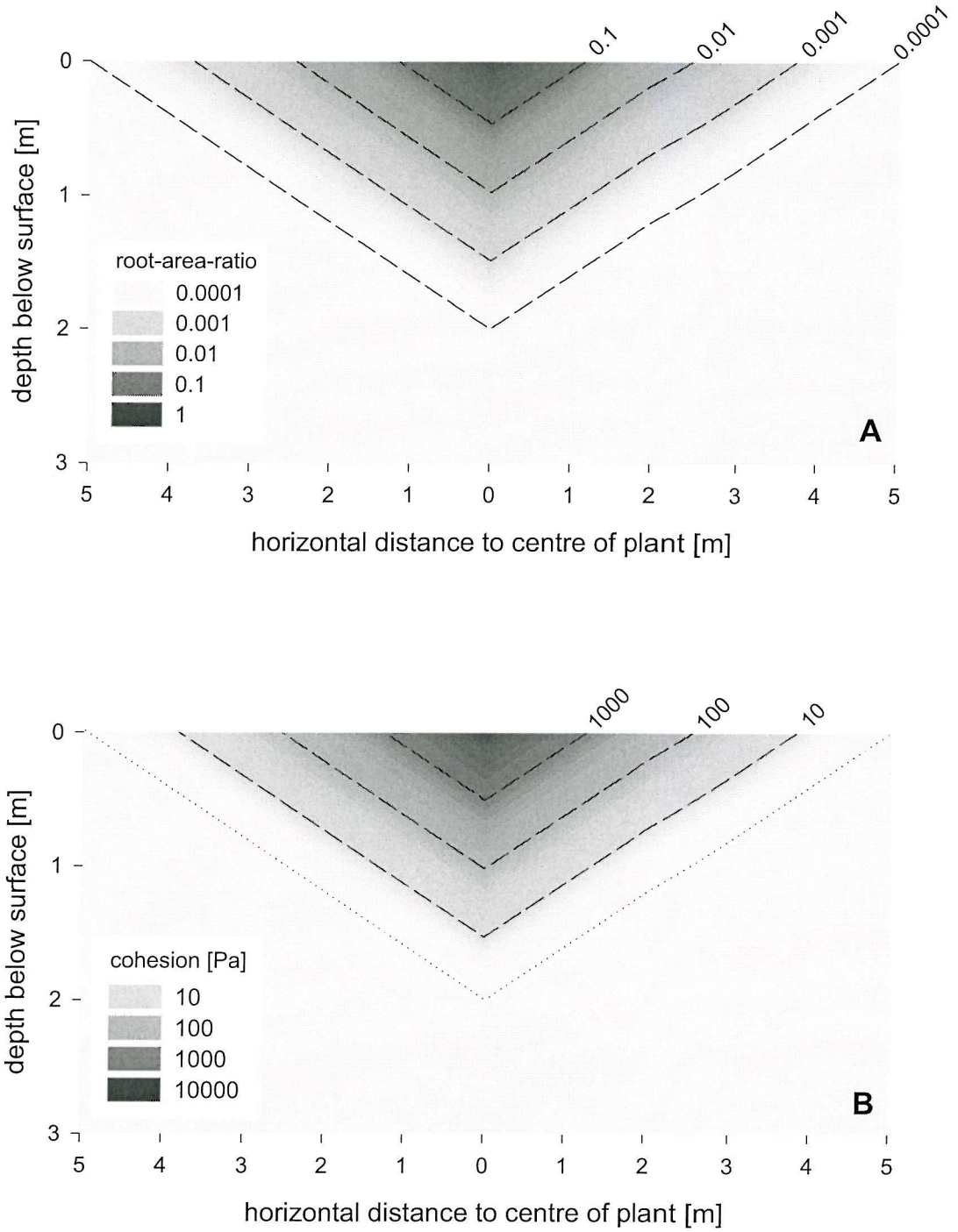

Figure 5.4: Spatial distribution of root-area-ratio (**A**) and root cohesion (**B**) for a single "*Populus*" tree (τ_r = 10 MPa).

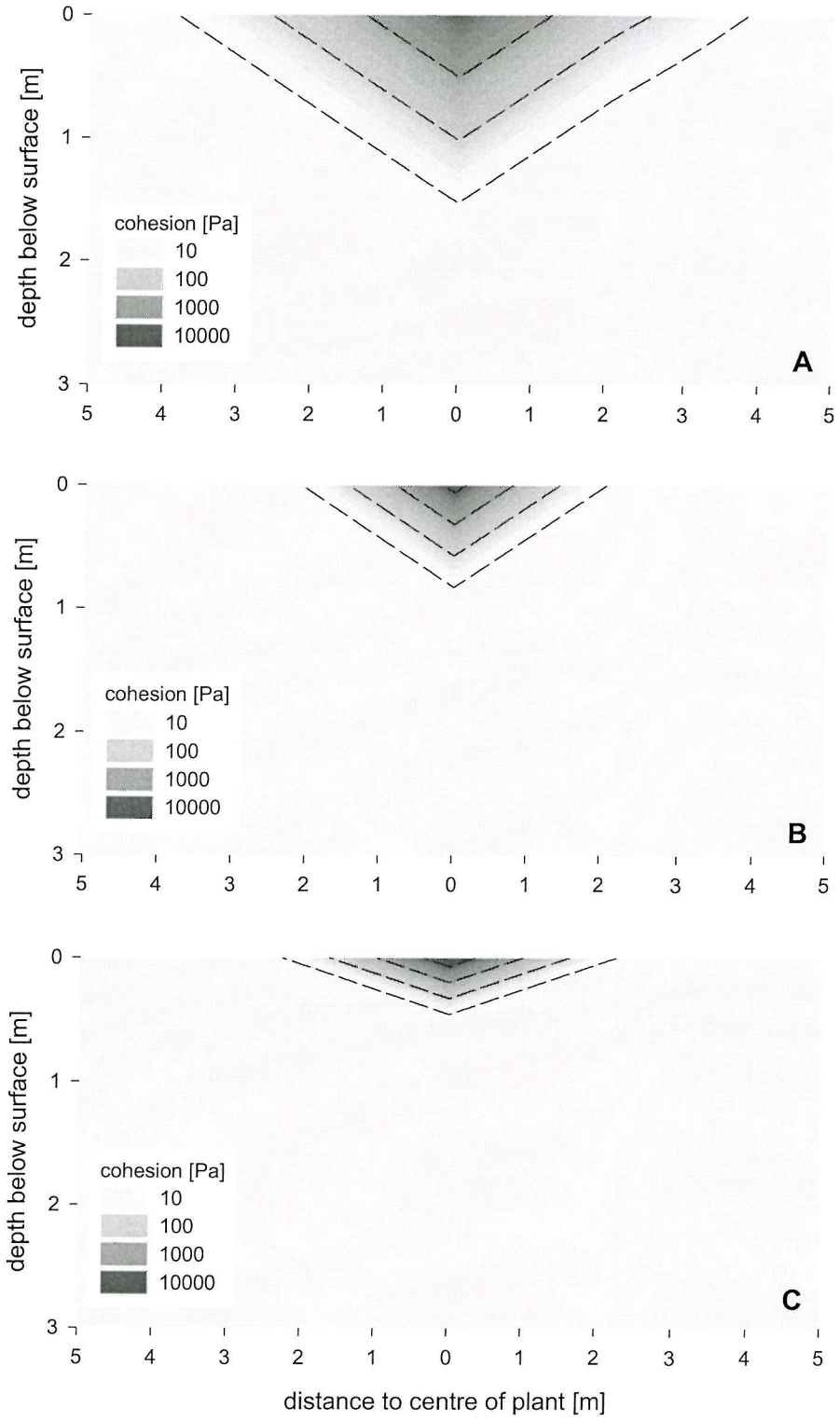

Figure 5.5: Spatial distribution of root cohesion for different tree species. **A** "*Populus*" (τ_r = 10Mpa). **B** "*Salix*" (τ_r = 18 MPa). **C** "*Betula*" (τ_r = 37 MPa).

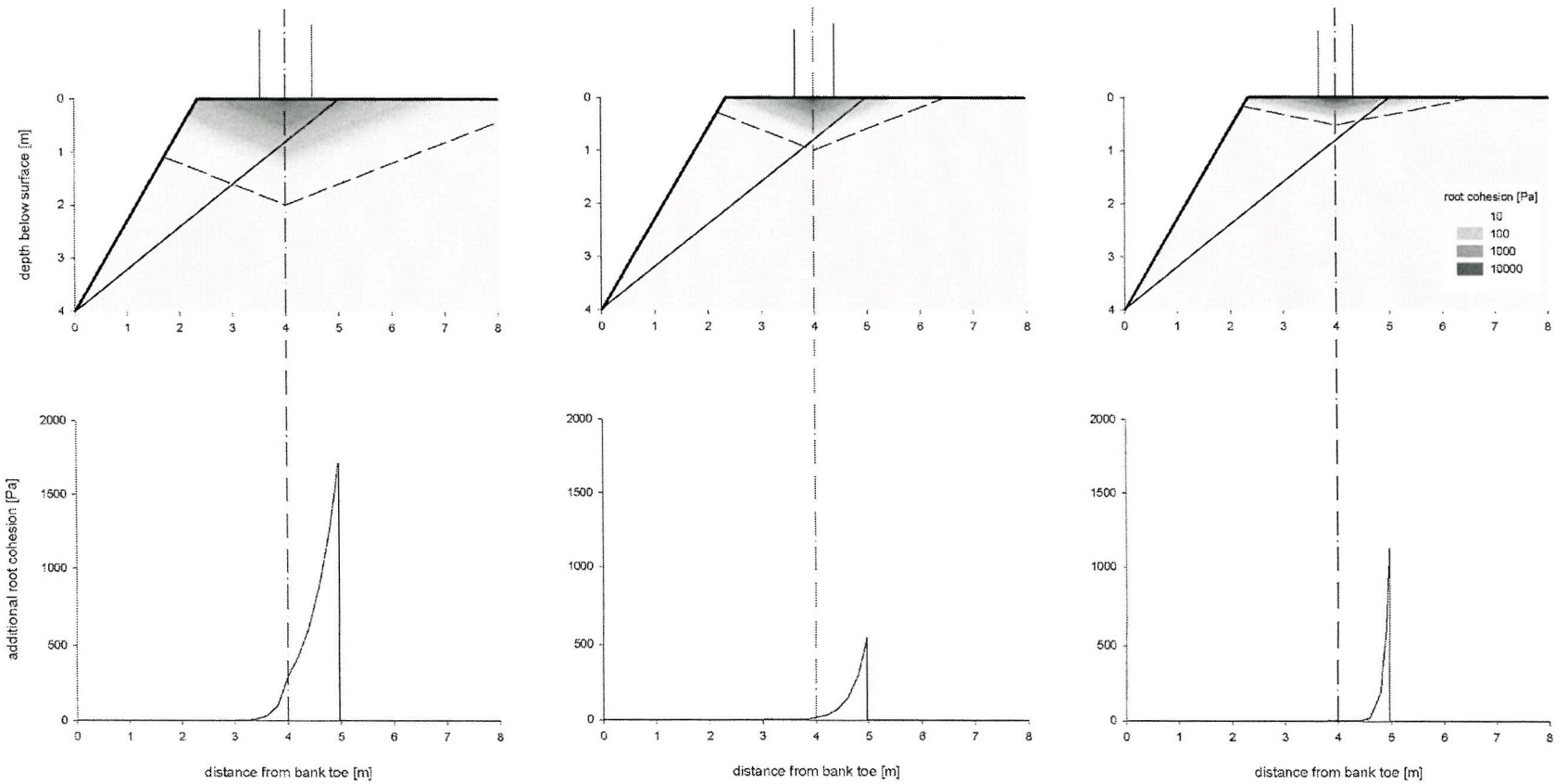

Figure 5.6: Distribution of root cohesion along the incipient failure plane for individual trees. Left: "*Populus*". Middle: "*Salix*". Right: "*Betula*". Trees are placed 4 metres from the toe of the bank (locations indicted by the vertical dashed line).

Effects of vegetation positioning

Although vegetation positioning is generally recognized as an element of key importance in the literature, only few studies (Collison and Anderson, 1996; Abernethy and Rutherford, 1998) have addressed this issue specifically. However, repeated application of the extended bank stability analysis provides insight into the effect of vegetation positioning on bank stability. Different lateral positions, x_v, of the tree significantly affect the root cohesion distribution within the bank and along the failure plane (figures 5.7, 5.8 and 5.9). Clearly, the peak root cohesion values are affected by the position of the vegetation, but also by the length of the intersection between the failure plane and the root wad. Therefore, the average root cohesion over the failure plane, *i.e.* the additional cohesion that the tree actually provides, will also be affected.

A series of simulations was performed in which tree position was progressively varied in the range from x_v = 0 m to x_v = 10 m, at 5 cm intervals. This was done for each of the three woody species (figure 5.10). The average root cohesion reaches two maxima over this range: the first near the toe of the bank and the other near the point where the failure plane intersects the floodplain. In other words, average root cohesion is maximized when the failure plane passes close to the stem of the tree. In spite of the previously noted differences in maximal root cohesion between species, the peaks in average root cohesion are less differentiated (table 5.18). This is caused by a trade-off between the size of the root wad and the tensile strength of the roots. The more extensive root network of "*Populus*" means that the intersection with the failure plane is generally longer compared with the other species, thereby compensating for its lower tensile strength. The peak values are of the same order of magnitude (~2.5 kPa) as the soil cohesion (3 kPa). In between the two peaks the average root cohesion is markedly reduced. For "*Betula*" and "*Salix*", it drops below 0.1 kPa between x_v = 1.0 m and x_v = 3.8 m. This means that trees positioned within this distance fail to significantly contribute to bank stability, as the root wad in this area does not intersect the incipient failure plane. Alternatively, if it does intersect, then it is only for a short length and with very small root-area-ratios. It is worth noting that trees positioned beyond the end of the failure plane can still contribute to the average root cohesion over the incipient failure plane, because of the lateral extent of their roots. This is most pronounced in "*Populus*" as it has widespread roots, but can also be observed for the other species.

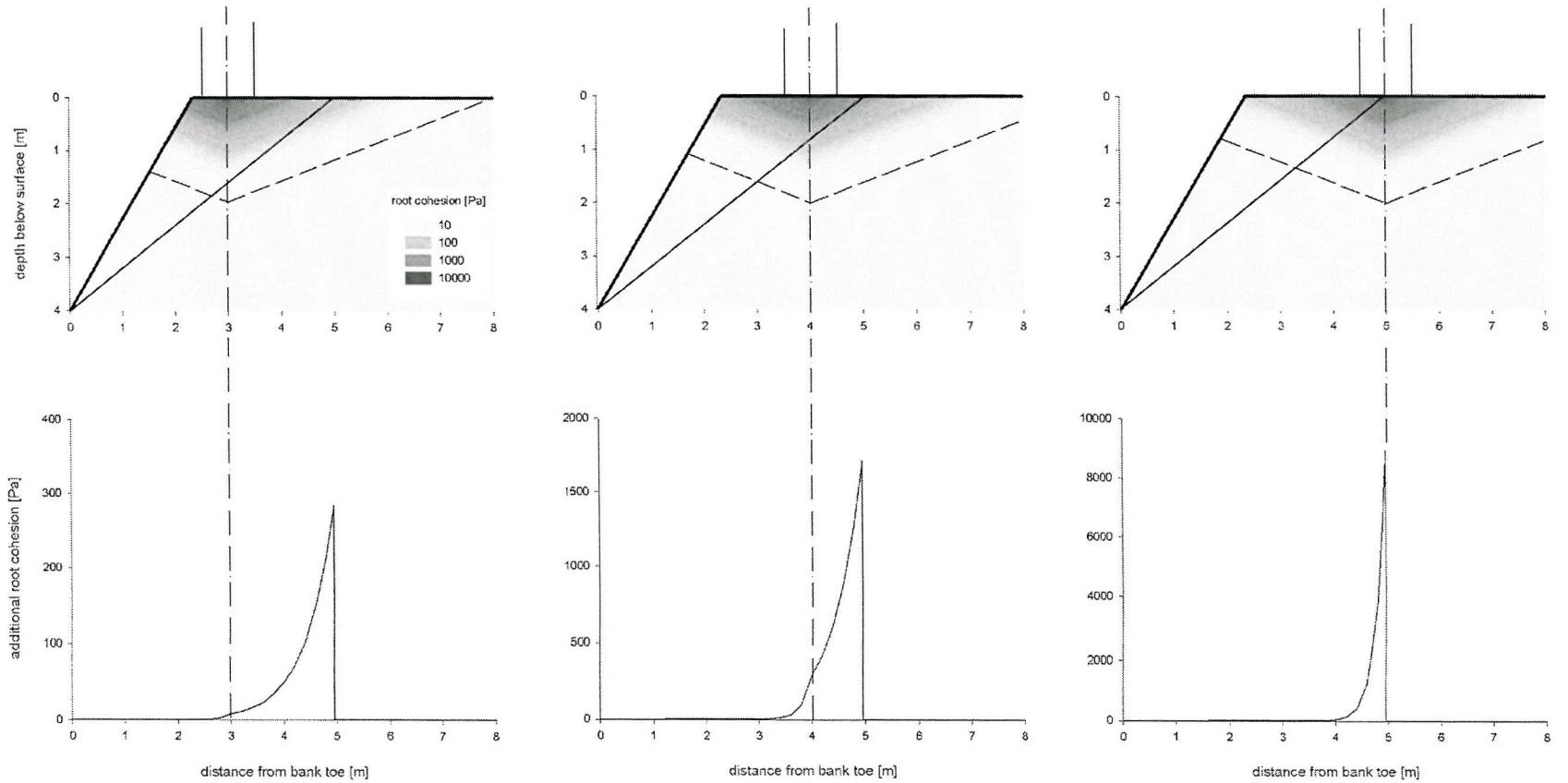

Figure 5.7: Distribution of root cohesion along the incipient failure plane for individual "*Populus*" trees located at different lateral positions. Tree positions, x_v, are indicated by the dashed line. Left: x_v = 3 m. Middle: x_v = 4 m. Right: x_v = 5 m. Note the fivefold differences in the scale on the Y-axes of each figure.

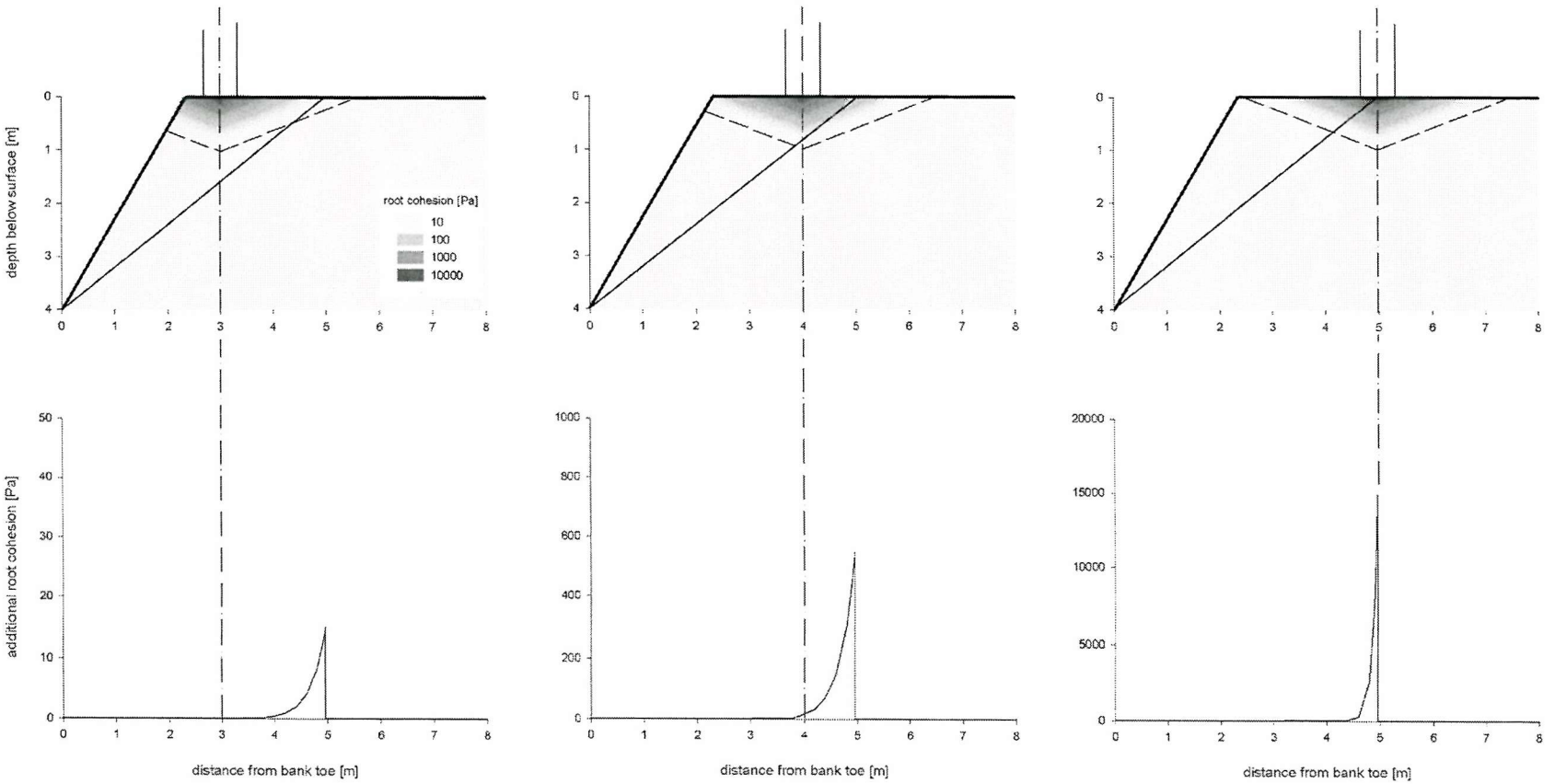

Figure 5.8: Distribution of root cohesion along the incipient failure plane for individual "*Salix*" trees located at different lateral positions. Tree positions, x_v, are indicated by the dashed line. Left: x_v = 3 m. Middle: x_v = 4 m. Right: x_v = 5 m. Note the twentyfold differences in the scale on the Y-axes of each figure.

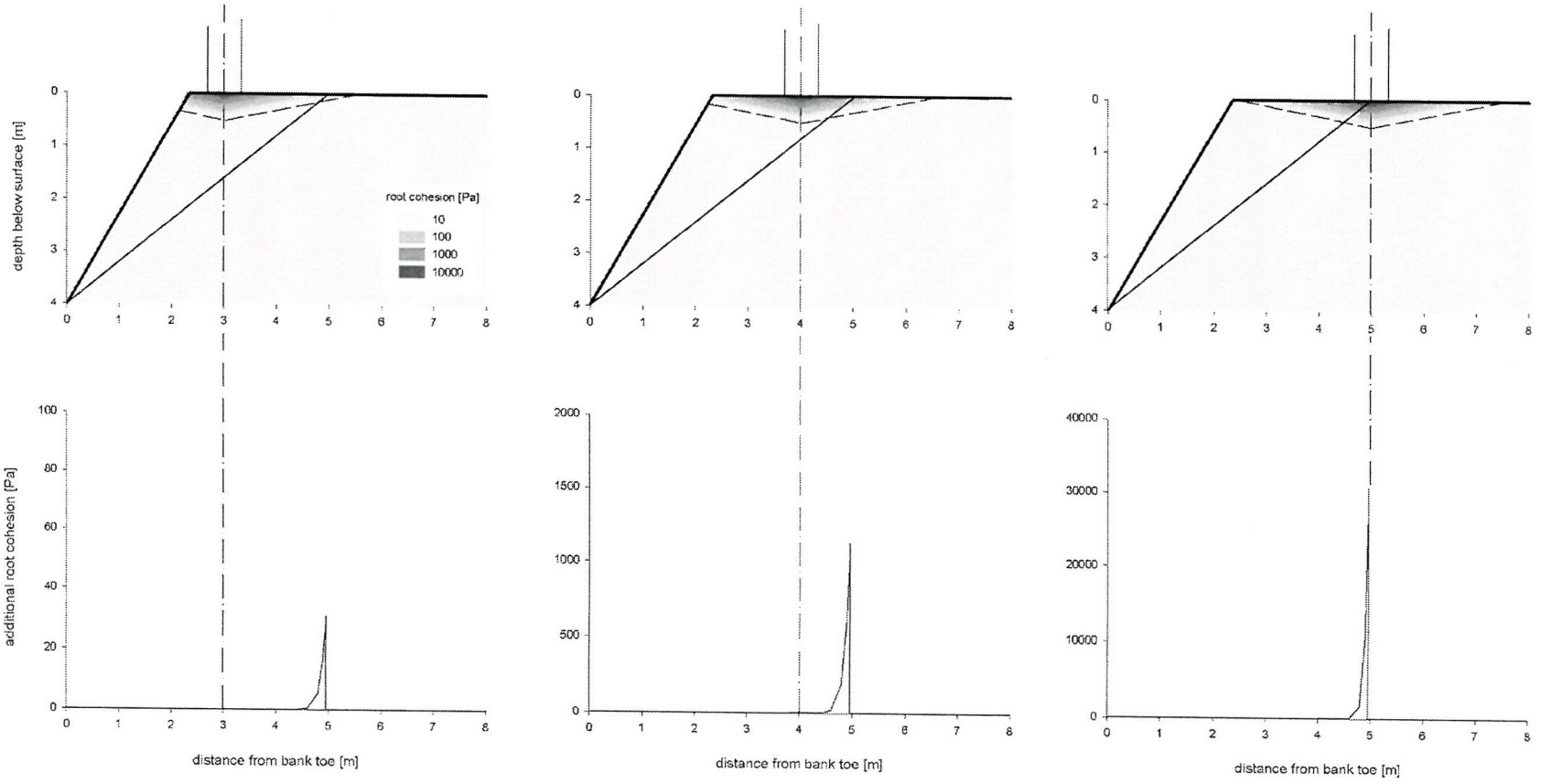

Figure 5.9: Distribution of root cohesion along the incipient failure plane for individual "*Betula*" trees located at different lateral positions. Tree positions, x_v, are indicated by the dashed line. Left: x_v = 3 m. Middle: x_v = 4 m. Right: x_v = 5 m. Note the twentyfold differences in the scale on the Y-axes for each figure.

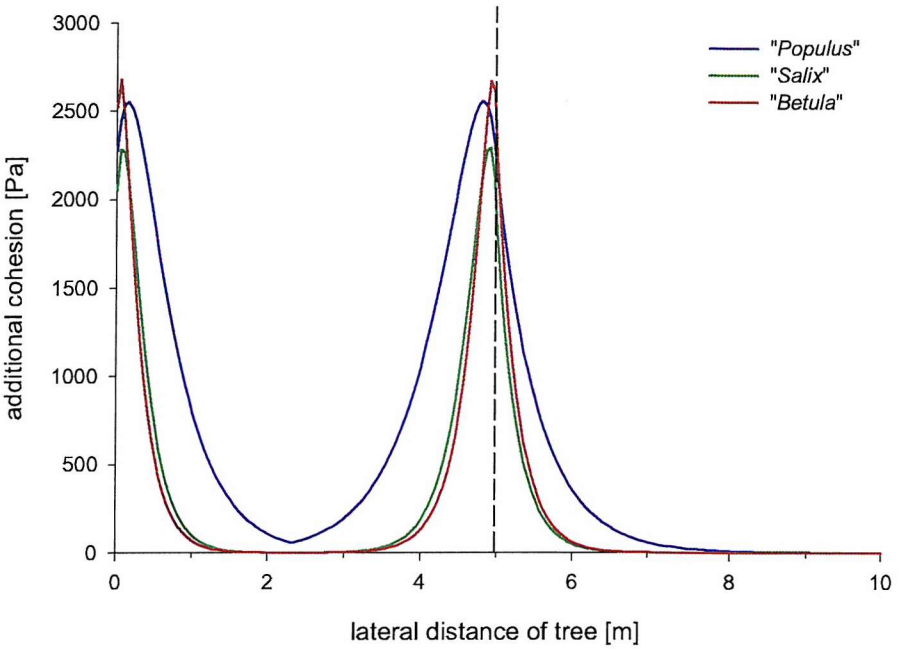

Figure 5.10: Average root cohesion as a function of tree position. The end of the failure plane is indicated by the vertical dashed line.

Table 5.18: Maximal values of local and average root cohesion.

species	maximal local root cohesion [Pa]	maximal average root cohesion [Pa]
"*Salix*"	17280	2293
"*Betula*"	35520	2682
"*Populus*"	9600	2557

Note: 'Maximal average root cohesion' refers to the average root cohesion along the failure plane, when the tree is placed in its optimal position. 'Maximal local root cohesion' refers to the maximal root cohesion added to the soil at any particular location, and is irrespective of the positioning of the tree.

Vegetation surcharge

Until now the discussion has focused on the contribution of roots to bank cohesion. However, additional cohesion provided by roots is only one of two ways in which vegetation influences the geotechnical stability of a riverbank, vegetation surcharge being the other. Like root cohesion, the effect of vegetation surcharge depends on the lateral position of the tree, although the relation is more straightforward (figure 5.11). The weight of the tree itself is constant for each species and does not rely on its position. However, whether it exerts a surcharge or not, does depend on the tree's position. Only when the tree is positioned on the incipient failure block, *i.e.* before the end of the incipient failure plane, does its weight affect the factor of safety.

Factor of safety

Both the additional cohesion, c_v, and vegetation surcharge, W_v, appear in the relation for the factor of safety (equation 3.120). However, unlike root cohesion, which only adds to the forces resisting bank failure, the surcharge of trees adds to both the resisting forces and the driving forces (equation 3.120). Whether or not the additional surcharge leads to an increase in stability depends on the other forces acting on the bank and on the slope of the failure plane. However, for the bank profile modelled in these examples (and for most other steep banks where stability might be an issue), the effect is such that an increase in surcharge decreases the factor of safety. Thus, the two effects of vegetation on bank stability work in different directions. Root cohesion tends to increase bank stability, while surcharge tends to decrease it. Their combined effect on the factor of safety depends on the relation between the two.

Since both root cohesion and surcharge are dependent on vegetation species and lateral positioning, it is to be expected that the same holds true for the factor of safety (figure 5.12). The effects of root cohesion can clearly be seen in the overall shape of the curves (*cf.* figure 5.10). Like the average root cohesion, the factor of safety is also maximized when vegetation is positioned near the toe of the bank or near the end of the failure plane. As the position of a tree is increased beyond the end of the failure plane, the factor of safety rapidly decreases to the reference value for an unvegetated bank. This is because the bank effectively becomes unvegetated if the only tree on the floodplain is too far away. In

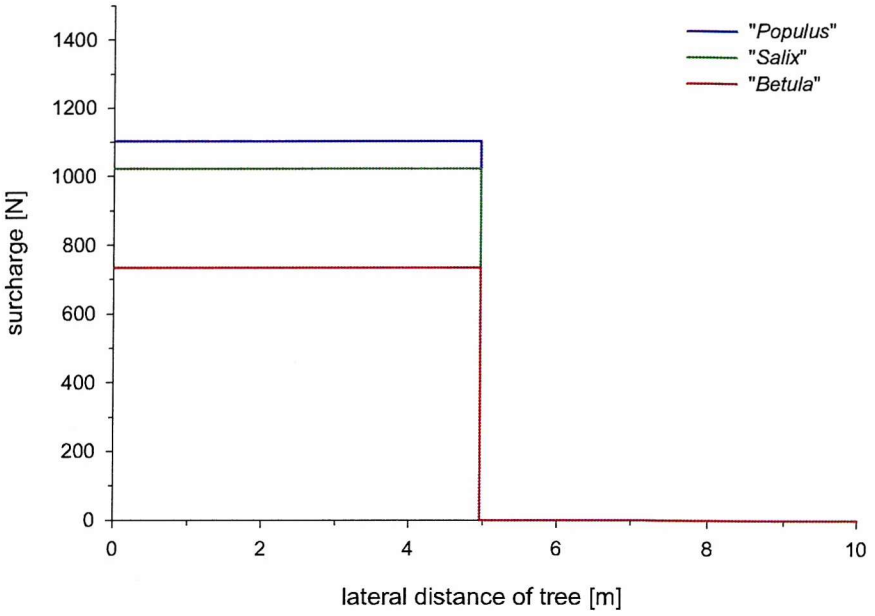

Figure 5.11: Vegetation surcharge as function of tree position.

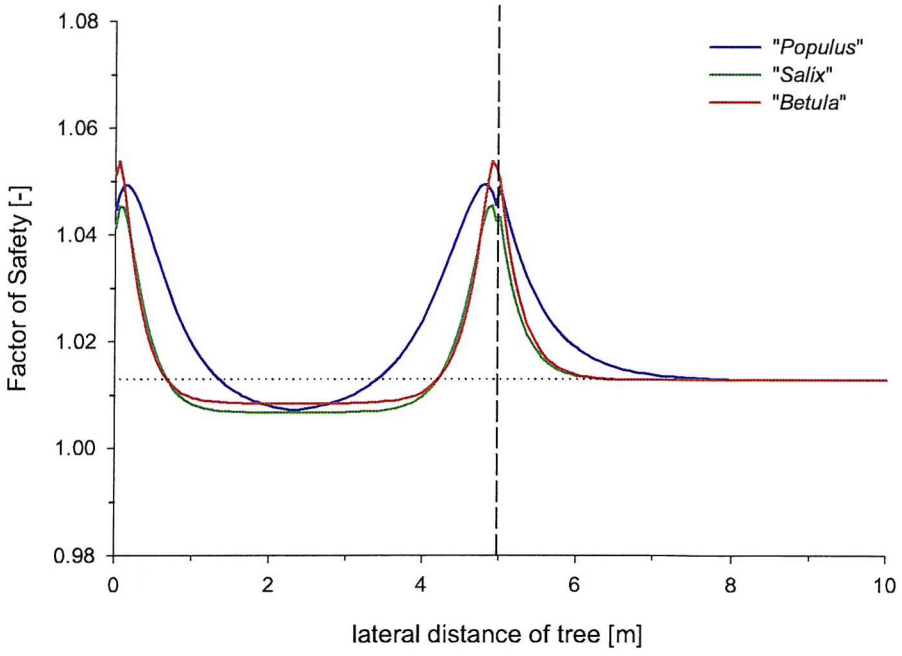

Figure 5.12: Factor of safety as function of tree position. The end of the failure plane is indicated by the vertical dashed line. The horizontal dotted line marks the value of the factor of safety in the absence of vegetation (N_{FS} = 1.013). Note that the Y scale does not start at zero.

between the two peaks, however, the factor of safety not only decreases, but also falls below the reference value. This indicates an area along the bank profile, where the presence of vegetation decreases the overall bank stability, as the surcharge effects outweigh the root cohesion effects, because the roots do not sufficiently penetrate the failure plane. This area centres around a point about 2.5 metres from the toe of the bank. It is nearly 4 metres wide in the case of "*Betula*" and "*Salix*", and about 2 metres for "*Populus*", indicating the beneficial effects of "*Populus*" with respect to mass failure.

Figure 5.12 has some relevance in terms of bank erosion management. Although the results are valid only for the "standard" bank used in this analysis and the exact nature of the impact of vegetation on bank stability is likely to show additional dependence on bank geometry and bank material properties, the implications can be generalized. Individual trees on a river bank are most likely to improve bank stability when they are placed near the extremes of the incipient failure plane, a result also obtained by Collison and Anderson (1996). Trees which are placed in between these two optimal locations are likely to have a less beneficial impact on bank stability, and potentially the impact may even be adverse. Trees which are placed too far away do not have any impact at all. Practically, however, there are some difficulties with these generalized implications. Although the bank toe has been identified as one of the two optimal positions, it might not always be feasible to get trees to grow near the bank toe due to the adverse effects of prolonged inundation and flow shear on saplings (Hosner, 1960; Friedman and Auble, 1999; Amlin and Rood, 2001). The second optimal placements for trees is near the point where the incipient failure plane intersects the floodplain. However, it is not always easy to predict this position, as the location of the incipient failure plane is generally not known. Even if it is, the bank geometry might change over time, due to interactions with the flow or to repeated bank failure, which would result in a different optimal position for the trees. A possible alternative might be to place several trees over the entire bank profile, or part thereof. This would both remove the uncertainty in locating the optimal position of an individual tree and anticipate potential changes in this optimal position over time. However, this would also involve placing trees in less advantageous positions, possibly detrimental to the bank stability, which might put the overall benefit in doubt. This, and other issues related to stands of vegetation, will be addressed next.

5.3.3. Results with multiple vegetation elements

The geotechnical bank stability routine in MRIPA allows two different ways of specifying the location of multiple vegetation elements. First, there is the logical extension of the individual vegetation positioning, where each of the multiple vegetation elements is individually placed. This method might be useful for situations where only a few plants are located on the banks and their exact position is known. It is, however, cumbersome for larger numbers of vegetation elements, like grasses or dense stands of trees. An alternative method is provided, in which strips of vegetation can be placed. In the following analyses it is this latter method that is applied.

Effects of vegetation density

The vegetation strips are identified by their lateral start and end points, x_{v1} and x_{v2}, and by the density of the vegetation within the strip (*cf.* figure 5.3B). Vegetation density is represented by the average distance, σ_v, between the centres of the stems of two neighbouring plants within the vegetation strip. However, it is difficult to compare differences in density effects between species using this indicator, because the average spacing between two grass plants is likely to be several times lower than the average spacing between tree stems. Hence, vegetation ground cover, A_{gv}, is used as an alterative indicator for vegetation density. It is defined as the total width of stems occupying a unit length of bank soil and is related to the average spacing, σ_v, and the stem diameter, d_{vb}:

$$A_{gv} = \frac{d_{vb}}{\sigma_v} \tag{5.1}$$

Effectively, as the average spacing between stems decreases, the ground cover increases. Stem diameter was included to avoid the physically impossible overlapping of vegetation stems. Thus, the ground cover equals unity when the average spacing between the centres of neighbouring stems equals the diameter of the stems. Although ground cover values close to unity are not realistic for mature trees, they are realistic for grasses. For completeness and ease of comparison, these unrealistically dense stands of trees are included in the simulations below.

A series of simulations is undertaken in which the ground cover is gradually increased from zero (no vegetation) to unity (full cover), over the entire profile of the standard bank (section 5.3.1). All four virtual species are included in the simulations. Figure 5.13 shows the effects of changing vegetation density on the additional root cohesion along the failure plane, c_v, vegetation surcharge, W_v, and on the factor of safety, N_{FS}, for each of the four species. The most striking feature of this graph is the linear relation between ground cover and the dependent variables, N_{FS}, c_v, *and* W_v. Hence, it is possible to derive simple, linear equations relating each of the dependent variables to vegetation ground cover, A_{gv}:

$$c_v = k_{cv} A_{gv} \tag{5.2a}$$

$$W_v = k_{Wv} A_{gv} \tag{5.2b}$$

$$N_{FS} = N_{FS,bare} + k_{FS} A_{gv} \tag{5.2c}$$

where $N_{FS,bare}$ indicates the factor of safety in the absence of vegetation ($N_{FS,bare} = 1.013$), and k_{FS}, k_{cv} and k_{Wv} are coefficients depending on vegetation species, bank geometry and bank material properties. In practice, equations 5.2a to 5.2c are not particularly useful, since the coefficients k_{FS}, k_{cv} and k_{Wv} are not universal, but depend on a range of variables related to species parameterization, bank geometry and geotechnical bank properties. Nonetheless, they can help in the interpretation of figure 5.13. It is worth noting that the coefficients k_{FS}, k_{cv} and k_{Wv} are positive for each species – at least for the standard bank. It can be seen that, for most species, but not "*Populus*", vegetation surcharge increases more rapidly with increasing ground cover than root cohesion ($k_{Wv} > k_{cv}$). This might lead to the conclusion that factor of safety should decrease with increasing vegetation density. However, it is clear from figure 5.13B that this is not the case. The reason for this apparent inconsistency is that although vegetation surcharge is detrimental to bank stability overall, it does contribute to both resisting and driving forces (equation 3.120). Together with the root cohesion, the total increase in resisting forces is still greater than the increase in driving forces, for any given vegetation density, and for all species. Thus, bank stability improves with increasing vegetation density. The improvement in stability is not high: only 6% increase in N_{FS} at best, and that is for an unrealistically dense stand of "*Populus*". More realistic vegetation densities for patches of mature trees ($A_{gv} \approx 0.3$) result in stability improvements between 1 % and 2 %. Although the stability improvement provided by the tree species are relatively small, they are still a lot higher than those of the grass species. "*Convolvulvus*" does not improve

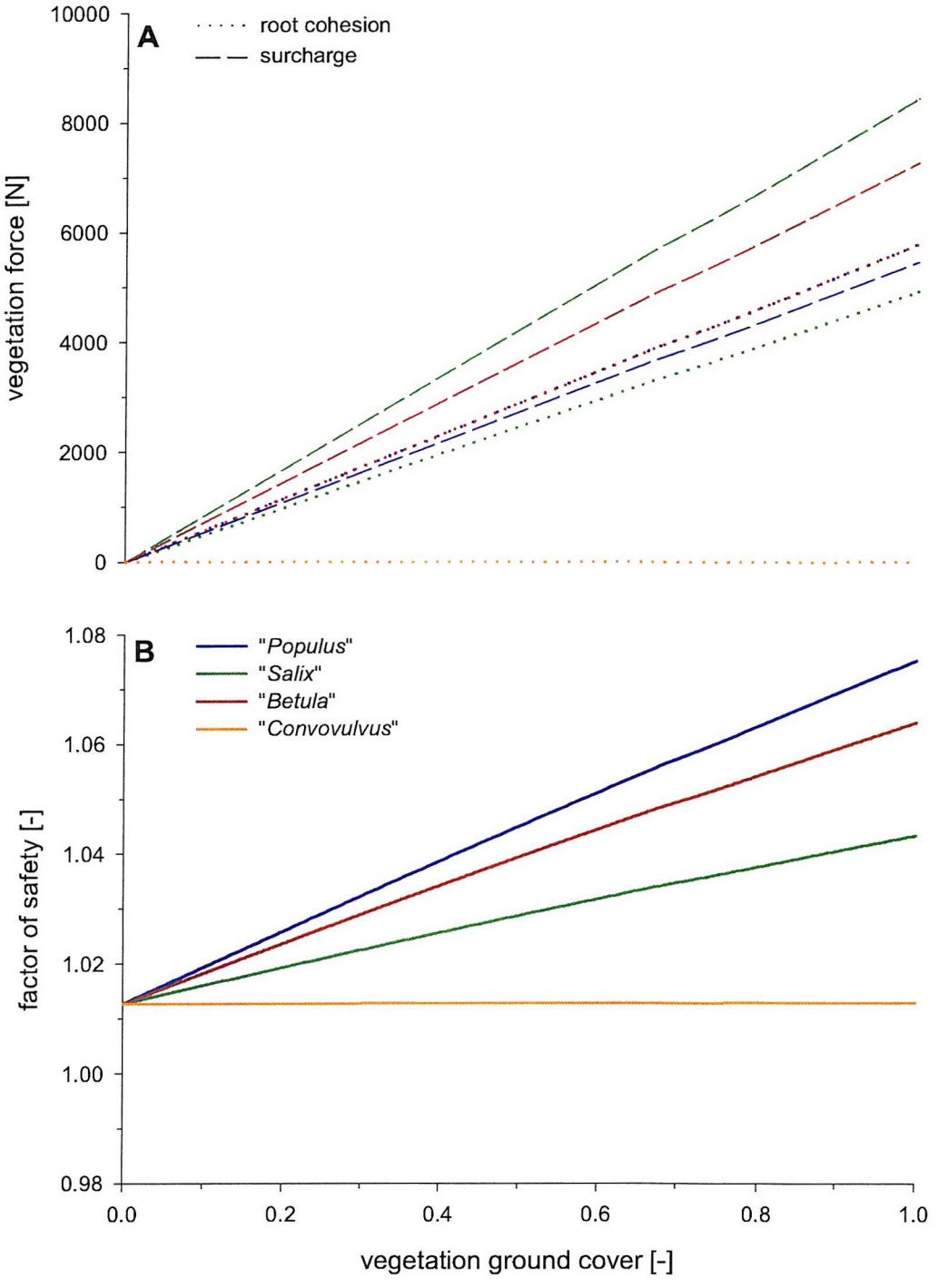

Figure 5.13: Effect of vegetation ground cover on vegetation forces (**A**) and factor of safety (**B**).

stability at all, even at very dense ground coverage (actually it does, but only by 0.02 %). This is because of the shallowness of its rootmat, which does not intersect the incipient failure plane over a sufficient length to exert any significant influence. A final, surprising, observation is that the increases in total root cohesion for "*Populus*" and "*Betula*" are identical ($k_{cv,Populus} = k_{cv,Betula}$). This, however, is nothing but a remarkable coincidence, resulting from the parameterization of these two virtual species as well as from the particular geometrical and geotechnical properties of the standard bank.

It has already been stressed that the insights derived from figure 5.13 only apply to the standard bank, due to the dependency on the geometry and geotechnical properties of the bank. In the following paragraphs the analysis will be expanded to evaluate the extent of this dependency and, where possible, to generalize any of the findings. A series of simulations is conducted in which one geometrical or geotechnical bank parameter is allowed to deviate from the definition of the standard bank (*cf.* section 5.3.1). All other aspects of the bank geometry, bank hydrology or bank material are kept constant, as are the bank material properties. The simulations are run for unvegetated conditions, and for five ground coverages (0.1 to 0.5) for each of the three tree species. Grass is deemed to have no discernible impact and is not included in any of the remaining analyses in this section.

Effects of bank geometry

The most obvious variables defining bank geometry are the bank height and bank slope. In a first series of experiments the bank slope is gradually varied from shallow ($\beta_b = 30°$) to near vertical, at 5° increments. All other bank parameters are kept the same as for the standard bank. Figure 5.14A shows the effect on factor of safety for both unvegetated banks (black) and for each of the tree species (colour) at 30% ground cover ($A_{gv} = 0.3$). It can be seen that bank slope has a considerable impact on bank stability, with factors of safety ranging from 0.6 to 2.7. Predictably, the bank is most stable with shallow slopes and becomes less stable as the banks get steeper. It can also be seen that there is not much difference between vegetated and unvegetated banks, although the vegetated banks appear slightly more stable for any given bank angle. This is further illustrated in figure 5.14B, which shows the change in factor of safety of a vegetated bank relative to the factor of safety of an unvegetated bank, for each of the three species (top: "*Populus*"; middle: "*Salix*"; bottom: "*Betula*"), and for 5 different vegetation densities. The relative change is positive in

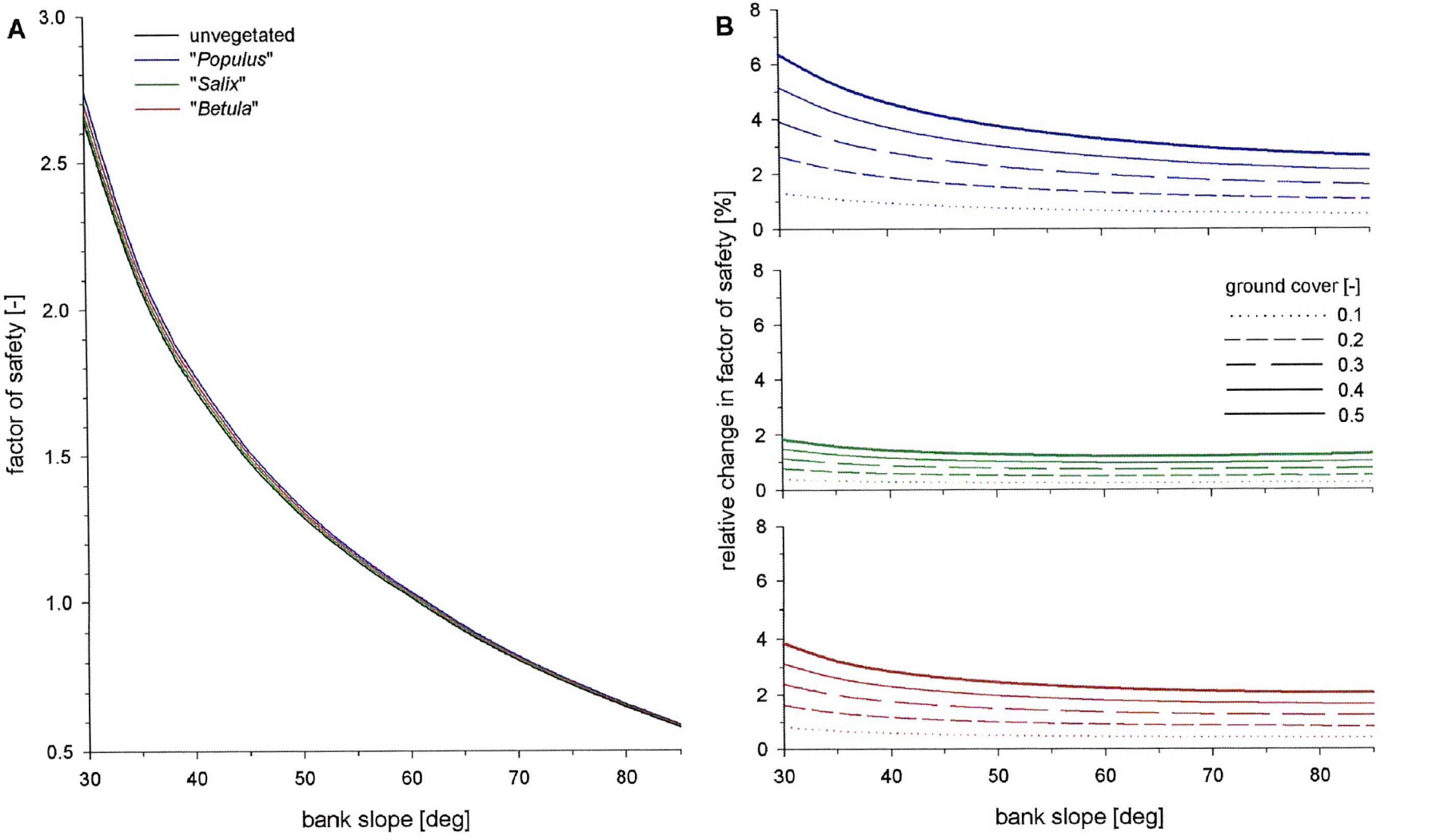

Figure 5.14: Effect of bank slope on bank stability (**A**) and vegetation impact (**B**). See text for explanation.

all cases, which implies that vegetation will always tend to stabilize the bank, irrespective of bank angle or vegetation cover. The amount by which the stability is improved varies with species and vegetation cover, but is generally less than 4 %. Densely vegetated banks have a higher stability than sparsely vegetated banks, which in turn have a higher stability than unvegetated banks. Vegetation has the highest relative impact on shallow sloping banks ($\beta_b < 45°$), which already are relatively stable ($N_{FS,bare} > 1.5$). It is worth noting though that the impact of a given vegetation cover becomes nearly constant as the bank angle increases. For example, a stand of "*Betula*" at $A_{gv} = 0.4$ increases bank stability by 1.9% at 55° and by 1.7% at 85°. Thus, although the factor of safety itself is highly dependent on bank slope, the impact that vegetation has on this factor of safety is relatively independent of the bank slope – except for shallow slopes where vegetation is slightly more effective (because the contribution of surcharge to resisting forces, rather than driving forces, dominates at low bank angles).

A similar series of simulations is conducted where bank height, H_b, is varied from 1 m to 10 m, at 0.1 m intervals (figure 5.15). Again all other bank parameters are kept as defined for the standard bank, with the exception of flow depth, H_w, and groundwater level, H_g. These are allowed to vary together with bank height and are specified as being half of the bank height. So, although the absolute value of H_w and H_g is variable, their relative value with respect to H_b remains constant. This adjustment in the setup of the experiments is necessary to avoid issues relating to bank hydrology (such as pore pressures and confining pressures) interfering with the interpretation of the variation of bank height. The influence of bank hydrology is discussed separately in a later paragraph.

Unsurprisingly, the factor of safety is strongly dependent on the total bank height (figure 5.15A). As with bank slope, the relation is inverse. Shallow banks are very stable, but the stability reduces rapidly as bank height increases. It can be seen that, for shallow banks, vegetation has a significant impact on the factor of safety, although the impact diminishes for higher banks. Figure 5.15B illustrates this further. Shallow banks have a high relative change in factor of safety for each of the species. The improvement of the factor of safety can be as much as 18 %, for high density stands of "*Betula*". However, as bank height increases, the impact of vegetation becomes less. This results from the fact that it is less likely that the roots will intercept the failure plane. Hence, their contribution to the total cohesion is gradually reduced, while the vegetation surcharge remains. It is possible that the difference between root cohesion and surcharge effects is such that their effect on the driving

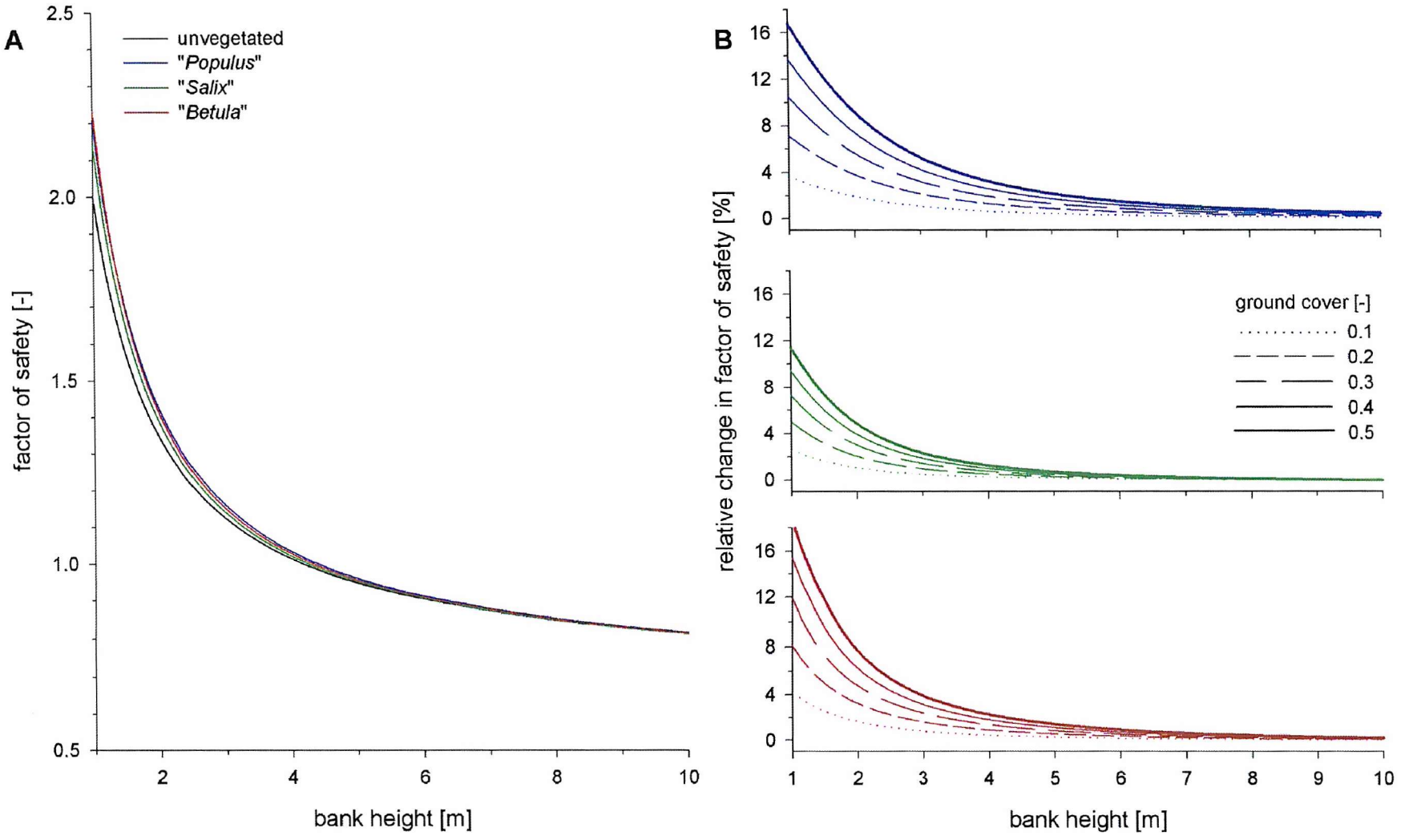

Figure 5.15: Effect of bank height on bank stability (**A**) and vegetation impact (**B**). See text for explanation.

forces outweighs their effect on the resisting forces and that the relative change in factor of safety becomes negative, *i.e.* destabilizing. This is the case, for example, with "*Salix*", the presence of which reduces the factor of safety on very high banks ($H_b > 9$ m). Thus, the factor of safety is inversely related to bank height, and so is the impact of vegetation on this factor of safety. It is possible for the vegetation to be destabilizing, on very high banks.

Another defining aspect of bank geometry is the tension crack. In the standard bank it is presumed that there is no tension crack ($H_t = 0$ m). Here, a series of simulations is run to see how the results would differ if there were to be one. The depth of the crack gradually increases from 0 m to 2 m, at 0.05 m intervals. The results show a slight dependency of bank stability on the size of the tension crack (figure 5.16A) with factors of safety for unvegetated conditions ranging from 1.01 down to 0.88. Although this range is small, compared with the ranges observed when varying the bank height or bank slope, it is sufficient to cause a failure in the otherwise stable standard bank. Surprisingly, there is a 'worst' crack depth size, of about 1.2 m, at which the factor of safety is minimal. The exact reason for this is not entirely clear, but is undoubtedly related to the fact that the depth of the tension crack also determines the shape of the incipient failure block, in particular the length of the incipient failure plane, and hence the length over which the forces acting on the failure plane can exert their influence. Presumably, there is a non-linear interaction between the hydrological forces, pore pressure and matric suction, both of which depend on the shape of the failure block. The impact of vegetation on the factor of safety is relatively complex. Each of the graphs in figure 5.16B also shows a hollow, where the effects of vegetation on the factor of safety are minimal and, in the case of "*Salix*" and "*Betula*", negative. The effects of vegetation are maximal in the absence of a tension crack and for very small tension cracks ($H_t < 0.1$ m). The minimum occurs at crack depths between 0.25 m and 0.75 m, after which the impact initially rises again, but then levels off at $H_t > 1.5$ m.

Effects of bank material

Another way to alter the standard bank is to keep the geometry the same but change the parameters related to bank material. Here, the effects of two parameters are examined: soil cohesion and friction angle. Again, only one of these parameters is varied at a time, while all other bank parameters are kept as specified for the standard bank. In a first series of simulations the soil cohesion, c, is gradually varied from 1.0 kPa to 12.0 kPa, in increments

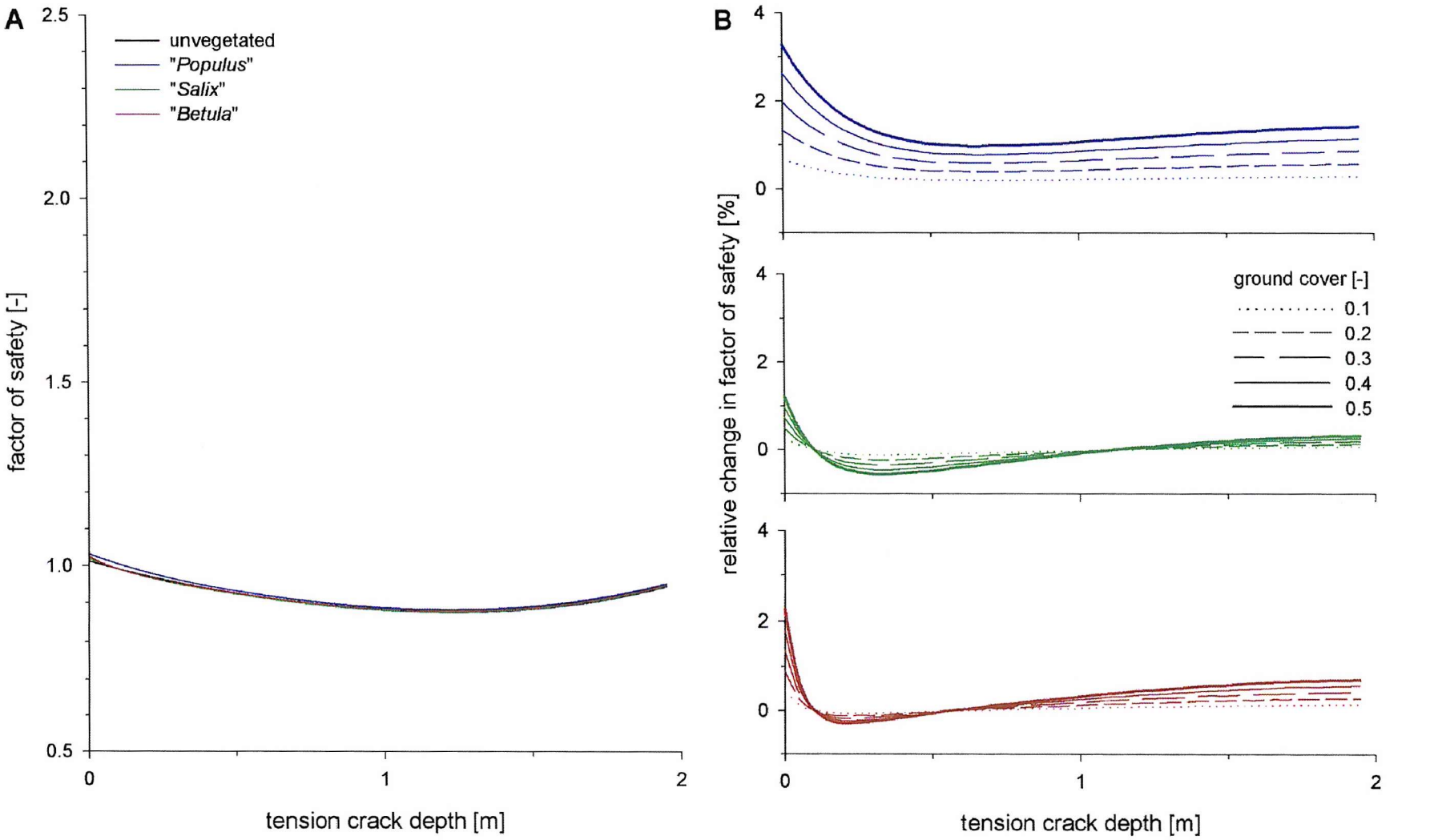

Figure 5.16: Effect of tension crack depth on bank stability (**A**) and vegetation impact (**B**). See text for explanation.

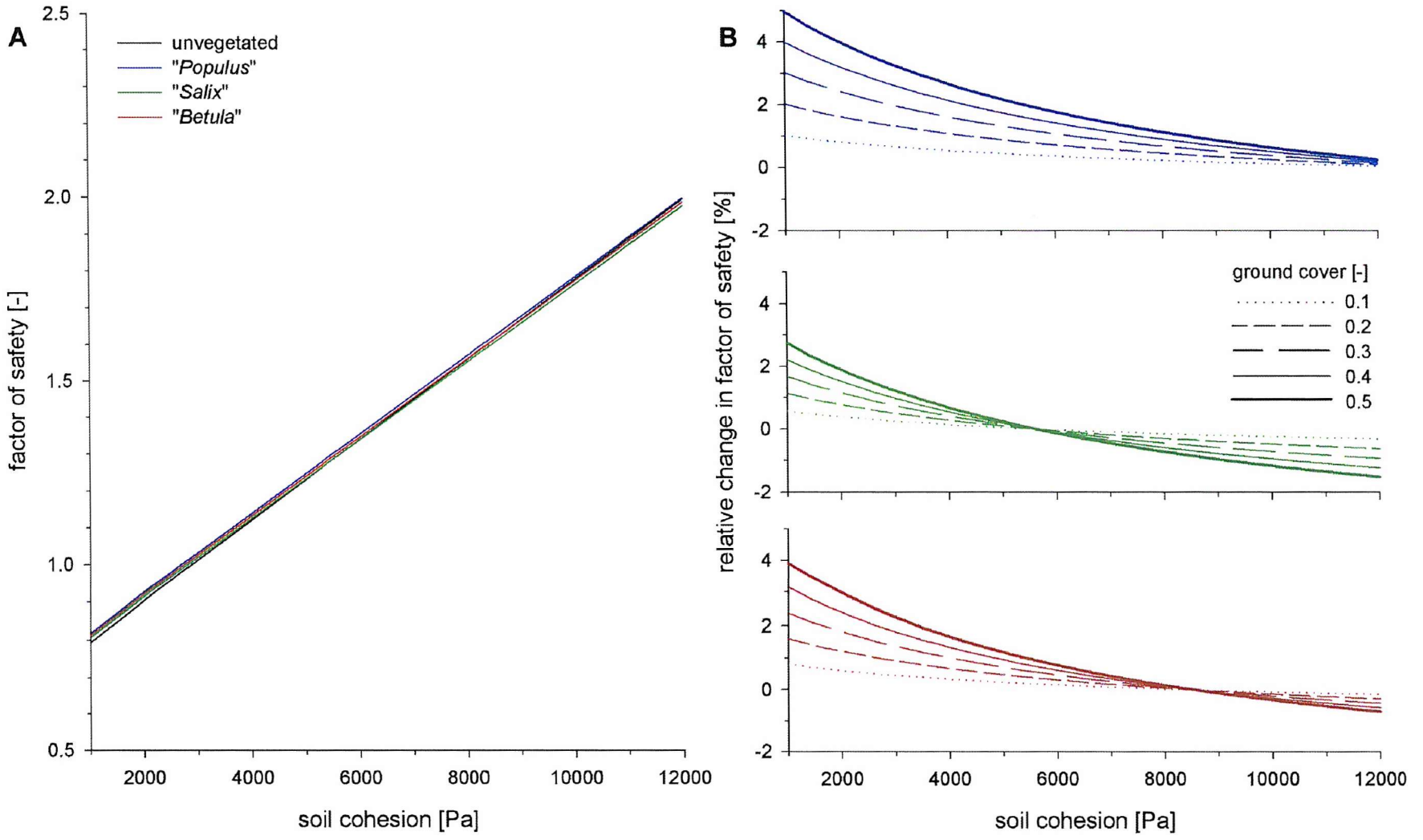

Figure 5.17: Effect of soil cohesion on bank stability (**A**) and vegetation impact (**B**). See text for explanation.

of 0.2 kPa. The relation with the factor of safety is linear (figure 5.17A) and, as expected, banks with cohesive soils are found to be more stable than banks with less cohesive soils. More interesting is the impact of vegetation on the factor of safety (figure 5.17B). The relation is inverse. The presence of vegetation is positive for weakly cohesive bank materials, and can increase the factor of safety by up to 5 %, as is the case for high density stands of "*Populus*". However, as the cohesion of the soil increases, the relative impact of the vegetation is reduced and eventually becomes negative. This is due to the fact that the relative contribution of root cohesion to the total cohesion becomes smaller and smaller as the soil cohesion increases (*cf.* equation 3.107). The contribution of vegetation surcharge to the driving forces remains the same and at some critical point outweighs the relative effect of the root cohesion. At this point the effect of the vegetation becomes negative. It must be noted that it is only the relative change in factor of safety, compared with an unvegetated bank, which becomes negative at some threshold value of soil cohesion. The actual increase in soil cohesion is such that very cohesive soils are still more stable than weakly cohesive soils, even with a vegetation cover (figure 5.17A). However, figure 5.17 does provide some useful theoretical insights. In the previous paragraphs it was shown that vegetation is most effective in stabilizing banks that are not very high and that have a shallow bank slope, *i.e.* banks which tend to be stable. Here, however, the presence of vegetation has a maximal positive impact when it is most likely to be needed, *i.e.* for weakly cohesive banks. The beneficial effect of riparian vegetation on such soils has also been observed along natural rivers (Shields and Gray, 1992).

Similar trends can be observed when the impact of friction angle, ϕ, is considered (figure 5.18). The friction angle was varied from 15° to 45°, at 1° increments. As is the case for soil cohesion, the factor of safety increases as the friction angle increases, although the relation is not linear (figure 5.18A). As is the case with soil cohesion, there is also a negative relation between the impact of vegetation and friction angle. Thus, vegetation is again seen to be most beneficial for the least stable soils, *i.e.* those with low internal friction angles, and is less beneficial when the bank is likely to be more stable, *i.e.* for high friction angles.

Hydrological effects

In a final series of simulations the hydrology of the bank is considered. Here, the near-bank flow depth, H_w, and the groundwater level, H_g, are varied, while the other bank

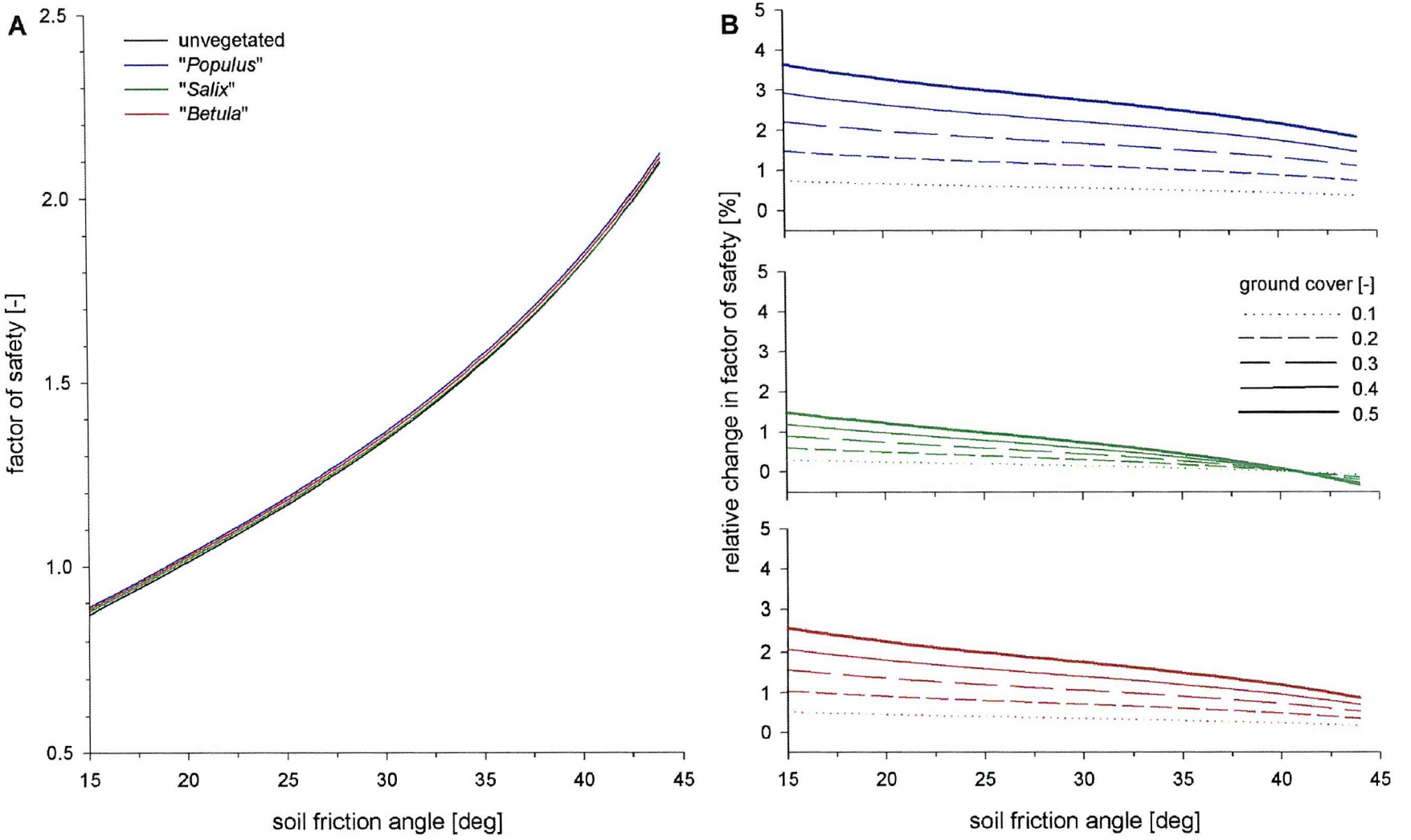

Figure 5.18: Effect of internal friction angle on bank stability (**A**) and vegetation impact (**B**). See text for explanation.

parameters are kept the same. However, in this analysis both variables are changed at the same time, in such a way that the equilibrium is maintained ($H_g = H_w$). In the current series of simulations the water level (in-channel and in-bank) is varied in cases ranging from a dry bed ($H_w = H_g = 0.0$ m) to bankfull flow ($H_w = H_g = 4.0$ m), in 10 cm increments. The factor of safety over this range of water levels varies from 1.0 to 1.5 (figure 5.19A), where the minimum value is reached at an intermediate water level ($H_w = H_g = 1.8$ m). The shape of the relation is explained by the interaction of the hydro-geotechnical forces: matric suction, pore pressure and confining pressure. Matric suction is maximal at low water levels, while pore pressures and confining pressures are minimal at this point. For high water levels the reverse is true. Their rates of change as a function of water level, and their combined interactions in determining the forces driving and resisting a bank failure, are such that a minimum factor of safety occurs at $H_w = H_g = 1.8$ m. The impact of vegetation follows an inverse pattern to that of the factor of safety itself (figure 5.19B). Thus, vegetation tends to improve the factor of safety by up to 2 % or 3 % at intermediate water levels. The explanation must, again, be sought in the relative contributions of root cohesion and of vegetation surcharge to the driving and resisting forces of bank failure, and how that relative contribution is maximized when contributions of the hydro-geotechnical forces are lowest, *i.e.* at intermediate water levels.

Summary

In the preceding paragraphs the geotechnical module's dependency on bank parameters has been analysed, both in terms of the direct influence of the bank parameters themselves, and in terms of the impact that vegetation may have on bank stability. When considering bank geometry, it appears that vegetation is most effective in improving bank stability on low banks, *i.e.* those that already are relatively stable. Bank slope does not seem to have a big influence on how vegetation affects bank stability. When considering bank material or bank hydrology, it appears that vegetation is most effective in improving bank stability on banks that are relatively unstable, *i.e.* banks with low cohesion or low friction angle, or at intermediate water levels.

In terms of the vegetation densities and the species themselves, it is found that grasses do not exert any noteworthy influence on bank stability with respect to mass failure. Trees seem capable of influencing the factor of safety by a couple of percent, depending on

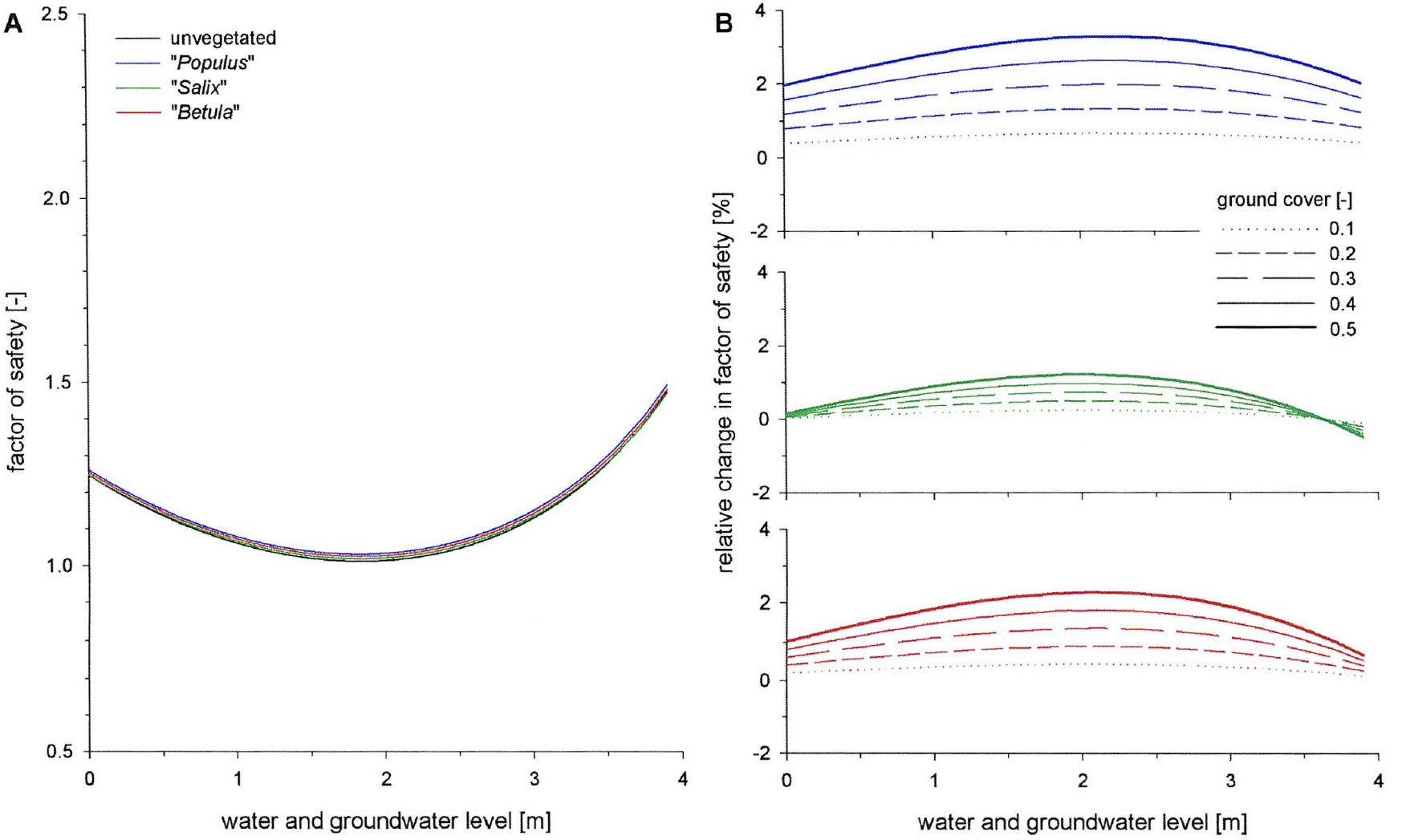

Figure 5.19: Effect of bank hydrology on bank stability (**A**) and vegetation impact (**B**). See text for explanation.

the bank geometry and geotechnical bank properties. The net effect is usually positive, but can, in some circumstances, be negative. Whether positive or negative, the effects are always more pronounced for dense stands of vegetation. In general, "*Populus*" provides the most significant changes in factor of safety, followed by "*Betula*", while "*Salix*" is the least influential of the tree species simulated here. This is, of course, due to the particular parameterization of these species (*cf.* table 5.15), in particular root geometry and root tensile strength. The sensitivity of the species parameterization, in terms of the geotechnical module, is discussed next.

5.3.4. Sensitivity of species parameterization

It has already been stressed that this parameterization, although based upon real world data, is subject to large degrees of uncertainty (section 5.2). It is helpful to have an indication of how this uncertainty might affect the results of the analyses undertaken herein and, hence, the conclusions drawn from them. This is achieved by undertaking a sensitivity analysis of the vegetation parameterization. Seven of the vegetation parameters are used in the geotechnical module: rooting depth, lateral root extent, root tensile strength, stem diameter at the base and at the top, stem height and wood mass density. As such there is a seven-dimensional parameter space to explore. Similar to the sensitivity tests of the flow and sediment transport modules this will be done by exploring lines through the parameter space (*cf.* figure 4.11). The lines are created by gradually varying one vegetation parameter, while the others are kept constant. The effect of the change in vegetation parameter is measured by the change it brings to the factor of safety of the unvegetated standard bank ($N_{FS} = 1.013$), when vegetation is present with a ground cover of 30% ($A_{gv} = 0.3$). However, unlike the sensitivity analysis of section 4.2, not one, but three lines will be drawn for each parameter, as the effect of the parameter change will be considered for all three tree species. This method of sensitivity analysis has similar drawbacks and advantages to those mentioned in section 4.2.4. The main advantage is that the method gives a quick indication of parameter behaviour, while avoiding the complexities and practical difficulties of sampling the full seven-dimensional parameter space. The main disadvantage of looking at individual lines is that the interaction between parameters is not considered. However, in the current analysis this disadvantage is partially removed because three lines are drawn for each parameter (one line for each species). Different behaviour of these lines can be interpreted, at least qualitatively, in terms of the other parameters, which may differ between species.

Root parameters

Rooting depth sensitivity tests are conducted for root depths ranging from 0.1 m to 5.0 m, in 0.1 m increments. This covers the range of commonly accepted rooting depths (section 5.2.2). Within this range, the relation to the relative change in factor of safety is almost linear and positive (figure 5.20). As rooting depth increases, so does its impact on bank stability. This implies that, all other things being equal, deep-rooted species will have the biggest impact on bank stability. This is because deeper roots have a better chance of intersecting the incipient failure plane. Larger intersection areas generally result in larger root-area-ratios (equation 3.116) and, hence, higher root cohesion. The effect is the greatest (steepest gradient) for "*Betula*", because of the high tensile strength of this species. The results imply that if, for example, during the parameterization, root depth of "Betula" were increased by as little as 0.1 m (L_{rV} = 0.6 m, instead of L_{rV} = 0.5 m), the relative change in factor of safety would increase from its current value of 1.37% to 1.93% (figure 5.20), a relative increase of 40%. Likewise, if the rooting depths for "*Salix*" and "*Populus*" were increased by 0.1 m, then the respective relative increases in the relative change in factor of safety would be 32% and 8%. Conversely, decreasing the parameterize rooting depth would reduce the vegetation impact. For small rooting depths the overall impact becomes negative. This does not mean that the root cohesion is negative. It simply implies that the relative contribution of root cohesion to the forces resisting bank failure is outweighed by the contribution of surcharge to the driving forces. A crude measure of a parameter's sensitivity can be provided by the range of vegetation impacts that is generated, *i.e.* the range of values along the Y-axis in figure 5.20. Vegetation impacts vary from -1 % to +28 % for the range of root depths included in this simulations series, resulting in a vegetation parameter sensitivity, N_{Slv}, of 29. This number is obviously dependent on the range of root depth values that are included in the analysis. Nonetheless, it provides a rough indication of how sensitive the model is to change in a particular parameter, provided that the range of parameter values is plausible (*cf.* section 5.5.2).

Lateral root extent is varied from 1 m to 10 m, in 0.1 m increments. This range covers the reported values for lateral root extent (section 5.2.2). The effect on the relative change in factor of safety is distinctly non-linear (figure 5.21), which is caused by the fact that root extent serves a dual purpose within the module. It is a factor in the determination of the root-area-ratio (equation 3.116) and, therefore, of root cohesion. But it also is a factor in the determination of vegetation surcharge, which is inversely proportional to the square of

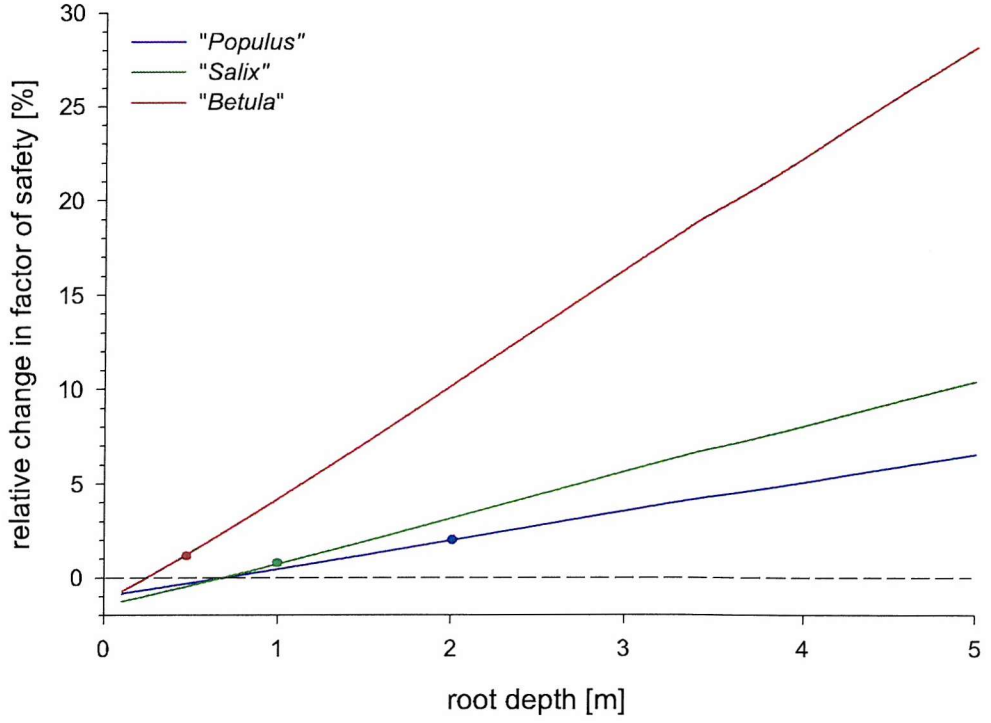

Figure 5.20: Sensitivity of root depth parameterization. Actual parameter values are indicated by a dot.

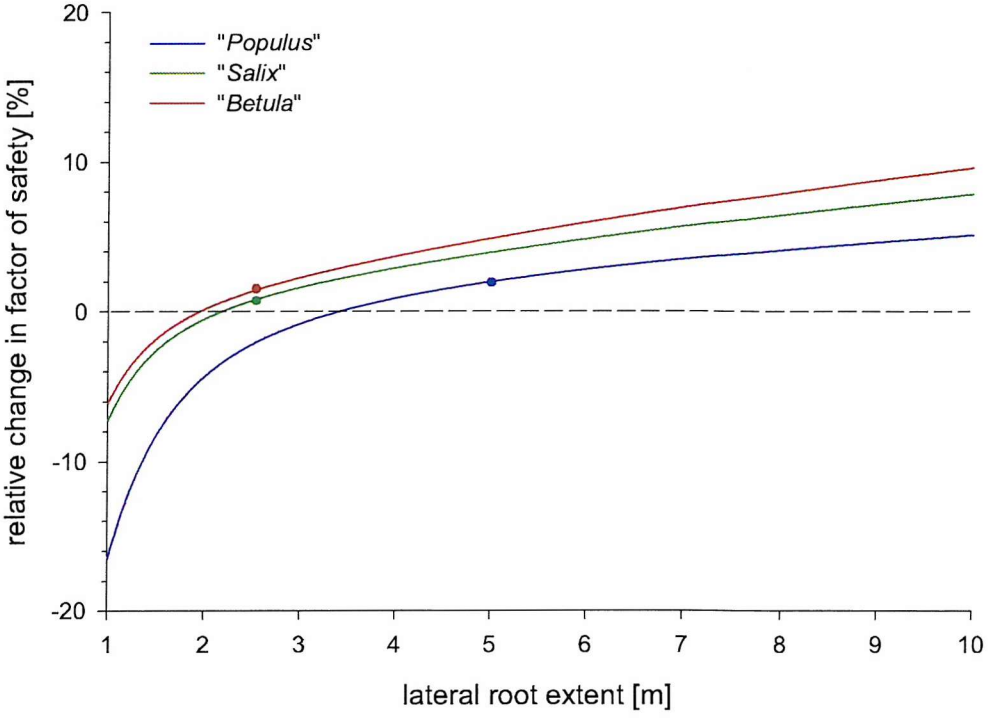

Figure 5.21: Sensitivity of root extent parameterization. Actual parameter values for each species are indicated by a dot.

the root extent (equation 3.119). The combined effect of these forces is such that the dependency of the factor of safety is non-linear. Vegetation impacts vary from -16% to +10% for the range of root extents included in this simulations series, or $N_{SIv} = 26$. The graphs have a positive gradient. Thus, an increase in the lateral root extent will enhance the impact of the vegetation on bank stability. It can also be seen that the parameterization of "*Salix*" is precarious. If the root extent of this species were to be parameterized as 2.0 m (rather than the current value of 2.5 m), then it would have a net negative impact on the stability of the standard bank, rather than the positive impact identified previously.

Root tensile strengths are varied over the range of published average values (section 5.2.2), *i.e.* from 5 MPa to 50 MPa, at 1 MPa intervals. As for the other root parameters, the gradient of the relation is positive (figure 5.22), so that an increase in tensile strength enhances the impact of the vegetation stand on bank stability. The effect is most pronounced for "*Populus*", as this is the species with the most extensive root network. For example, if the parameterization of the root tensile strength of "*Populus*" were to be increased by 1 MPa (i.e. from 10 MPa to 11 MPa), then the relative change in factor of safety would increase from its current value of 1.98% to 2.28% (figure 5.22), a relative increase of 15%. Overall, the vegetation impact on relative change in factor of safety varied from -1% to 14%, over the range of parameter values included in the analysis (figure 5.22), resulting in $N_{SIv} = 15$ for tensile strength. This lower value of N_{SIv}, compared to the values of the two other root parameters, indicates that the parameterization of the tensile strength is relatively robust, at least when compared to the parameterization of the extent of the root network.

Above-ground parameters

Tree heights are varied from 10 m to 40 m, at 1 m intervals. This range covers the maximal tree heights of most riparian species (section 5.2.2). The vegetation impact is seen to be inversely proportional to the tree height (figure 5.23). Thus, an increase in simulated tree height will reduce the stabilizing effect of vegetation. It is noteworthy that the vegetation impact varies over a much smaller range than the root parameters: from -1% to +2.6 % for the tree heights sampled ($N_{SIv} = 3.6$). "*Populus*" is least affected by a change in tree height, presumably because its widespread root network allows the surcharge to be spread over a larger area than the other species (*cf.* equation 3.119). The low N_{SIv} value indicates that the parameterization of tree height is very robust.

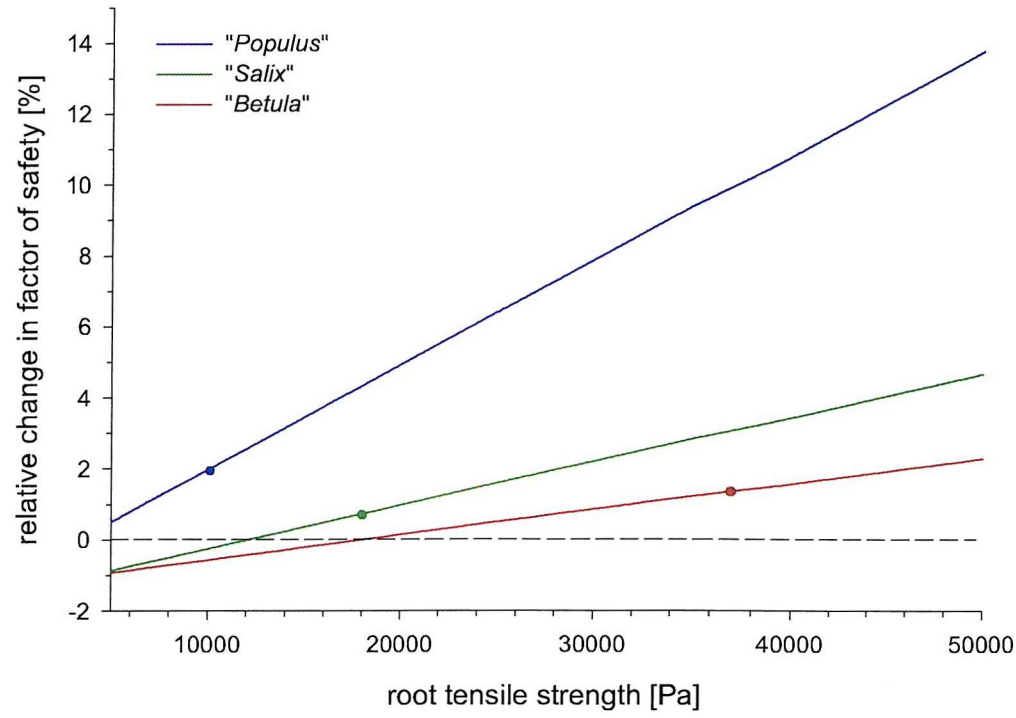

Figure 5.22: Sensitivity of root tensile strength parameterization. Actual parameter values of each species are indicated by a dot.

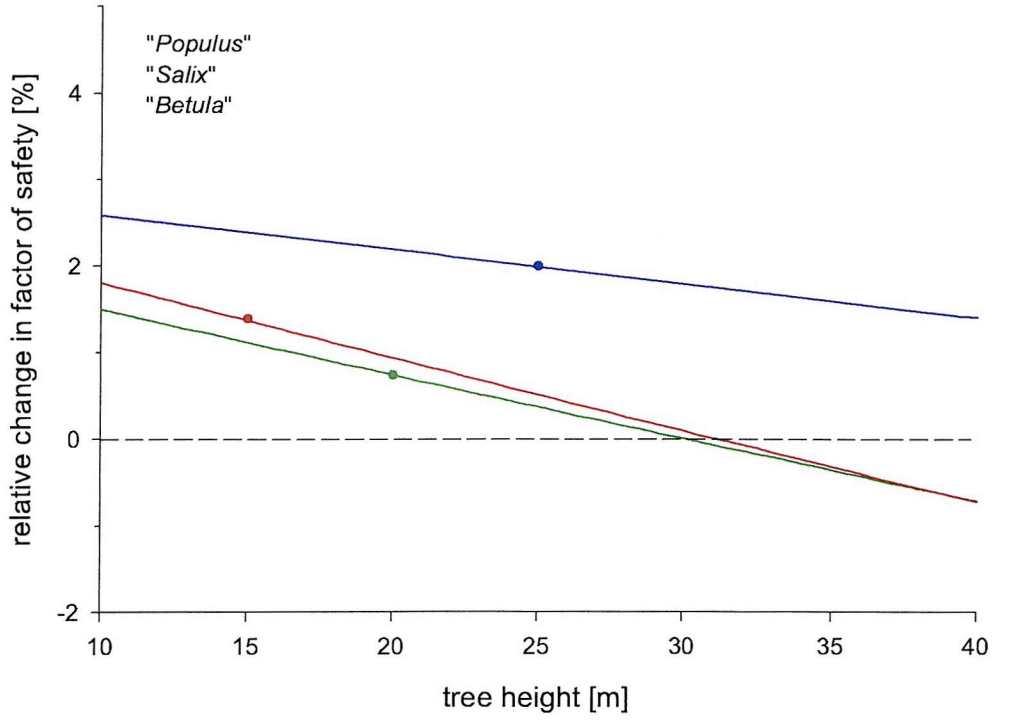

Figure 5.23: Sensitivity of tree height parameterization. Actual parameter values of each species are indicated by a dot.

The effect of changing the stem diameter at the base is illustrated in figure 5.24. The stem diameter at the top is kept constant in these simulations. Base stem diameters are varied from 0.20 m to 1.20 m, at 5 cm increments, which covers most of the reported maximum stem diameters (section 5.2.2). Here again, the relation has a negative gradient, implying that an increase in stem diameter will adversely affect the impact of vegetation on bank stability. The non-linearity in this relation results from the fact that the square of the stem diameter is used to calculate the tree surcharge (equation 3.119) and from the influence it has on ground cover (equation 5.1). The vegetation impact ranges from -1.6 % to +14.6 % for the given range of base diameters. Hence, N_{SI_V} is approximately equal to 16, for the range of stem diameters included in the analysis. The large N_{SI_V}-value is probably due to the stem diameter's effect on vegetation density, since the sensitivity analysis for tree height has already shown that vegetation volume does not exert a big influence over vegetation impact. However, it does indicate that the parameterization of tree height might be precarious for some species.

In a separate series of simulations the stem diameter at the top is varied, from 0.0 m to 0.3 m, at 0.01 m increments. The effect on bank stability is minimal over this span of parameter values, as indicated by the near horizontal graphs in figure 5.25. In this case the parameter sensitivity, although small (N_{SI_V} = 1.6), overestimates the actual influence of the stem diameter at the top, as it is more indicative of the difference between species than of the change in stem diameter itself. This highlights a conceptual problem with the crude sensitivity index that is used here, although it is not of much relevance in the context of the current analysis.

Wood mass density is varied over the range of reported values (section 5.2.2), *i.e.* from 600 kg/m^3 to 1200 kg/m^3, in increments of 50 kg/m^3. This parameter also appears to have little influence on vegetation impact (figure 5.26). Insofar as it does affect the impact of vegetation on bank stability, it tends to become more destabilizing as the density increases. The low N_{SI_V}-value (N_{SI_V} = 2.6) is partially due to the range of mass densities included in the test, which is relatively small compared to those other variables included. However, this is a result of the fact that there is less uncertainty involved in the parameterization of mass density (*cf.* section 5.5.2; table 5.10). Hence, the range of plausible values is smaller than those of parameters which are more uncertain.

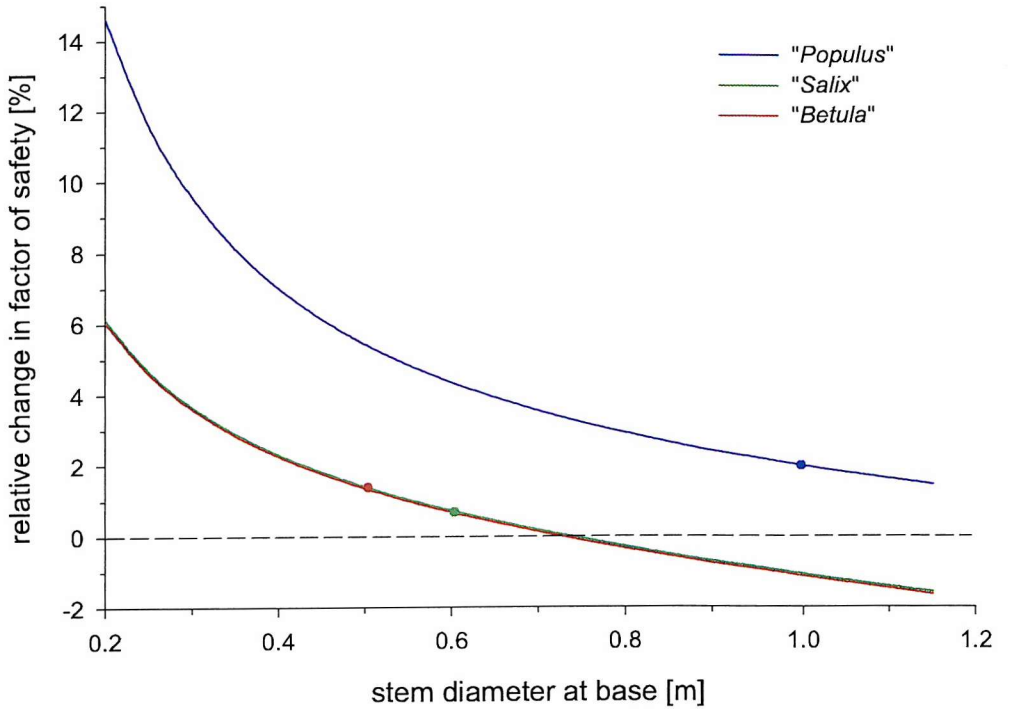

Figure 5.24: Sensitivity of stem base diameter parameterization. Actual parameter values for each species are indicted by a dot.

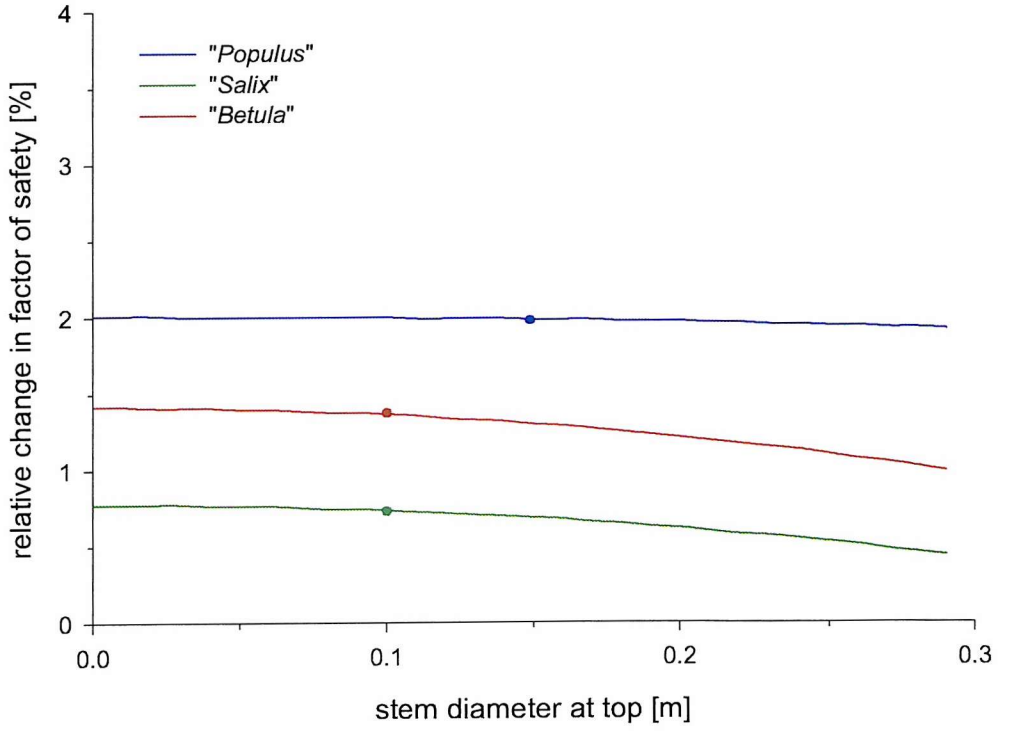

Figure 5.25: Sensitivity of stem top diameter parameterization. Actual parameter values of each species are indicated by a dot.

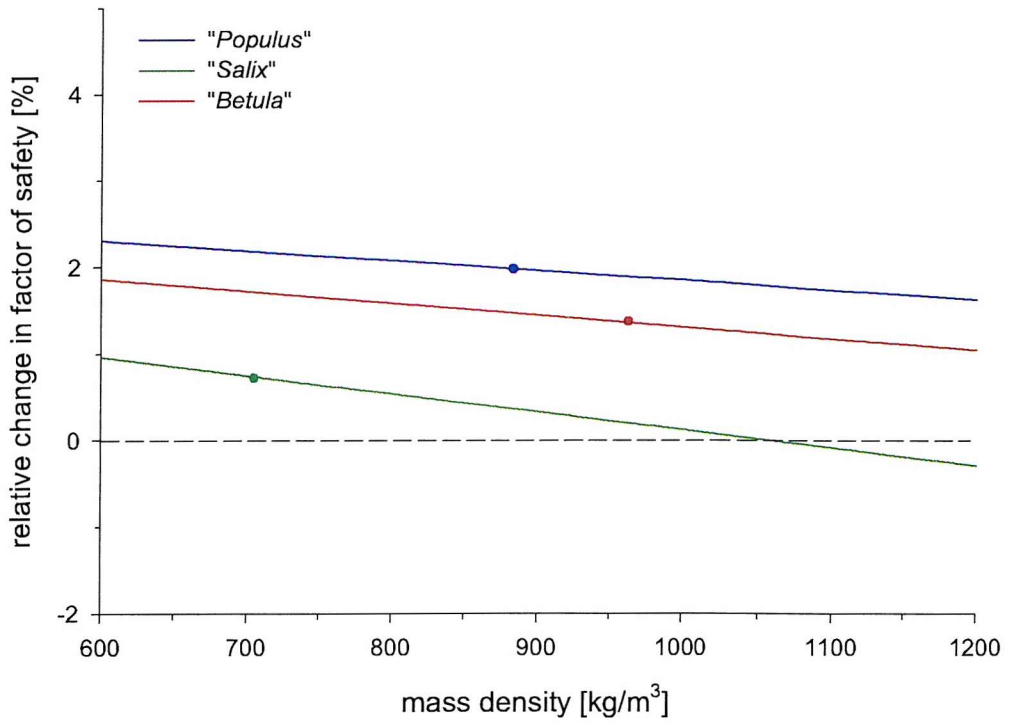

Figure 5.26: Sensitivity of mass density parameterization. Actual parameter values are indicated by a dot.

Table 5.19: Sensitivity of vegetation parameters.

parameter	direction	N_{Slv}
root depth	+	29
lateral root extent	+	26
root tensile strength	+	15
stem height	-	3.6
stem diameter at base	-	16
stem diameter at top	-	1.6
wood mass density	-	2.6

Summary

The results of the sensitivity analysis are summarized in table 5.19. There is a clear distinction between the below-ground and the above-ground parameters. First, all the root parameters act in a positive direction, indicating that an increase in the parameter value will enhance the impact of vegetation on bank stability. Conversely, the above-ground parameters, which are all related to surcharge, act in a negative direction. Second, the sensitivity index is about an order of magnitude smaller for most of the stem parameters, than it is for the below-ground parameters. An exception to this is the stem diameter. However, this is likely to be due to the effect this parameter has on the calculation of vegetation cover, A_{gv}. Nonetheless, it is clear, even with this crude sensitivity analysis, that the geotechnical module is fairly sensitive to the vegetation parameterization, and to the root parameterization in particular. The latter is both significant and unfortunate, in that parameterization of below-ground properties is very difficult from a practical viewpoint. However, the sensitivity analysis does indicate that there is an urgent need to enhance the knowledge of rooting networks, and improve parameterization of vegetation effects on mass wasting. Recent techniques like ground-penetrating radar (Stokes *et al.*, 2002; Butnor *et al.*, 2001; Hruska *et al.*, 1999) and X-ray tomography (Stuppy *et al.*, 2003; Moran *et al.*, 2000; Pierret *et al.*, 1999; Sustek *et al.*, 1999) offer some potential and further exploration of their applicability to root geometry analysis could provide the much needed improvement.

5.3.5. Discussion

The performance of the additional vegetation routines, which form the core improvements to the geotechnical module, should, ideally, be evaluated qualitatively, as there is little quantitative data available for comparison. Even so, the quantitative results can not be neglected, and one of the most striking results of the simulations is the relatively minor impact that vegetation appears to have on the simulated factor of safety. In most cases, the observed increases in factor of safety due to the presence of vegetation is less than 5%. This is very small, considering the generally held view that vegetation has a significant impact on geotechnical bank stability. Three possible explanations for this discrepancy can be forwarded. These three explanations are not mutually exclusive, and it is possible that the discrepancy between modelled and expected vegetation impact stems from the combined effect of all three of them. First, there might be a general tendency to overestimate the

anticipated geotechnical impact of vegetation. Second, the parameterization of the vegetation properties might be incorrect. Finally, the model might not correctly represent the effects of vegetation on bank stability. Although the first two of these explanations certainly have some credibility, it is the latter that deserves further elaboration, especially in the context of the current study. The model incorporates two major effects of vegetation: soil reinforcement and surcharge. The results obtained suggest that these two aspects are represented correctly (see below). However, the model does not include a third effect of vegetation, namely the hydrological impact on bank drainage (hereafter referred to as 'vegetation suction'), although this has been shown to have a considerable impact on bank stability in some circumstances (Simon and Collison, 2001). It is expected that the incorporation of vegetation suction, F_{vs}, in the geotechnical model would result in augmented estimates of the factor of safety for vegetated banks. A separate series of simulations, using a simple -though unverified- mathematical formulation of vegetation suction, confirms that this indeed is the case (figure 5.27). However, the parameterization of the suction coefficient, k_{vs}, is both subjective and spurious. Moreover, the mathematical expression of F_{vs}, as used in figure 5.27, lacks physical foundation and is likely to be too simplistic (Andrew Collison, 2001, pers. comm.). It was therefore decided to exclude vegetation suction effects from the model (*i.e.* $F_{vs} = 0$). Thus, as far as vegetation suction is concerned, the banks herein are effectively assumed to be fully saturated. Under such conditions, the overall impact of vegetation on bank stability is minimal (Simon and Collison, 2001) and is of the same order of magnitude as the results obtained herein. Hence, the model can be expected to produce reasonable predictions of the factor of safety in worst case scenarios, such as rapid drawdown or prolonged bankfull flow, when the banks indeed are fully saturated; and to significantly underpredict the factor of safety in more favourable conditions.

In other aspects, however, the model developed herein appears to work acceptably well. The root cohesion distributions through the soil are similar to those obtained by Abernethy and Rutherfurd (2001). Likewise, the prediction that the optimal vegetation position is near the extreme ends of the incipient failure plane matches the observations of Collison and Anderson (1996). The model's behaviour in terms of vegetation parameters is also realistic: more extensive root networks and stronger roots tend to improve bank stability, while excessive vegetation weight tends to be destabilizing. Thus, in situations where we can realistically have expectations about how the model should behave, it is confirmed that the model does indeed behave in accordance with these expectations. This gives some confidence in the capabilities of the model, including those cases when it is used for simulations where there is no *a priori* expectation of the outcome.

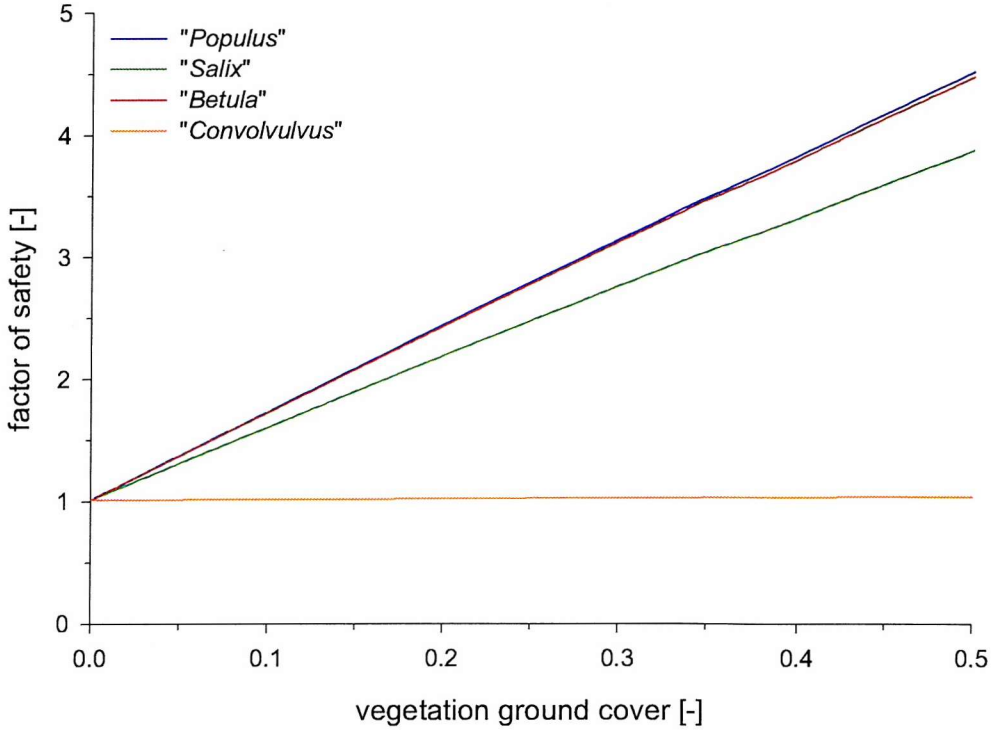

Figure 5.27: Impact of vegetation cover on the factor of safety of the standard bank, using an extended stability model. The extended model incorporates vegetation suction: $F_{vs} = k_{vs} F_{ms}$, which is added to the matric suction, F_{ms}: $F_{ms} = F_{ms} + F_{vs}$. Thus, vegetation suction is assumed to be a simple, linear function of matric suction, where the proportionality is given by a suction coefficient, k_{vs}. Here, a value of $k_{vs} = 5$ is used, based on limited data in Simon and Collison (2001). Using this extended stability model, the factor of safety shows a strong dependency on vegetation cover, at least for woody species. For a given vegetation density, the change in factor of safety is about two orders of magnitude higher if vegetation suction is included in the model. E.g. the N_{FS} for *"Betula"* at $A_{gv} = 0.3$ increases by 1.6 % without F_{sv} modelling, and by about 210% with F_{sv} modelling. Such high changes in factor of safety are also reported by Simon and Collison (2001). The herbaceous species has a higher impact on factor of safety if vegetation suction is included in the model, but it is still negligible compared to the woody species.

One such observation is that "*Convolvulvus*" has little impact on geotechnical bank stability, because the roots do not penetrate deep enough. This can be generalized to apply to all shallow rooted grasses. Another observation is that individual trees can destabilize a river bank, when they are not placed in the optimal location near the extremes of the incipient failure plane. However, the stabilizing effect of trees placed at the optimal position is such that the overall effect of stands of trees that cover the entire bank profile is generally still positive. Of the three virtual species included in this analysis, "*Populus*" generally provides the largest increase in bank stability, followed by "*Betula*", while "*Salix*" has the least impact. However, much of the impact of vegetation on the stability of a bank depends on the exact geometry of the bank, and on the bank material. Vegetation is more likely to stabilize lower banks than higher banks, and indeed might be destabilizing on very high banks. The presence of vegetation is more effective in banks consisting of weakly cohesive material or with low internal friction angles. A final observation, and perhaps the most surprising, is that bank angle, although itself very influential in the determination of the bank stability, does not have a big impact on the way in which vegetation influences the factor of safety. However, there is one major caveat to all these generalized observations: the results of the model are significantly dependent on the parameterization of the biophysical vegetation properties. Of particular significance is that rooting properties, the values of which are usually associated with large uncertainties, have a big influence on the predicted factor of safety.

All of the above is valid for stand-alone geotechnical analyses, where interactions with flow hydraulics and sediment transport are excluded. One of the main strengths of the MRIPA model is that it takes these interactions into account. The remainder of this chapter focuses on the way vegetation influences simulations within the fully coupled model, *i.e.* simulations where flow, sediment transport and geotechnical mass failure are allowed to interact, at the scale of the river reach.

5.4. Effects of vegetation in MRIPA

Vegetation not only affects bank stability, but also hydraulic roughness, flow pattern and sediment transport. In this section the interactions between these elements of vegetation impact are discussed. First, the fully coupled model is applied to a hypothetical unvegetated

reach, which establishes a reference case for further simulations. Next, a series of simulations is undertaken to analyse the effects of vegetation species and vegetation density with respect to channel bed morphology and bank migration. The simulations are performed in a reach of an idealized meandering river, to facilitate interpretation of the results. In the next chapter the model will be applied to a natural river.

5.4.1. Setup of the analysis

The hypothetical reach used in this series of simulations consists of four consecutive bends in a sinuous channel (figure 5.28A; table 5.20). The channel reach is about 900 m long. The initial cross-sectional shape is trapezoidal, with a flat, 20 m wide channel bed and 4 m high banks (figure 5.28B). The initial flow depth is specified as 1.0 m over the entire reach. The groundwater level is assumed to be in equilibrium with the in-channel flow ($H_g = H_w$). The initial bank geometry is similar to the geometry of the standard bank of section 5.5.3, although a small vertical cliff and a tension crack are added for the current analysis. For this combination of flow depth, groundwater, bank geometry and bank material, the unvegetated banks are initially stable, at $N_{FS} = 1.01$. Further details of the channel configuration are listed in table 5.20. A steady discharge of 20 cumecs is applied. Neither the planform shape of the channel nor the bed topography are in equilibrium with this flow, and it is expected that the channel morphology will try to adapt to the flow. Both channel planform and bed morphology are allowed to develop over the simulation duration. Simulations are run for a 60-day period only to avoid manual adjustment of the bank point spacing, due to the deformation of the grid (*cf.* section 3.3.3). However, the 60-day period is not long enough to establish an equilibrium channel morphology, and as such puts some limitations on the interpretation of the results. Nonetheless, the simulations allow one to gain insight in to the rates at which processes operate under different vegetation conditions.

The channel bed is discretized on a 200 x 11 curvilinear grid (figure 5.29). This amounts to an average cell size of 4.5 m by 1.8 m. A grid sensitivity analysis and a numerical mass conservation check for this grid are presented in appendices A3 and A4.The values of the calibration parameters used for this simulation series (table 5.21) are similar to those obtained in the calibration process of chapter 4.

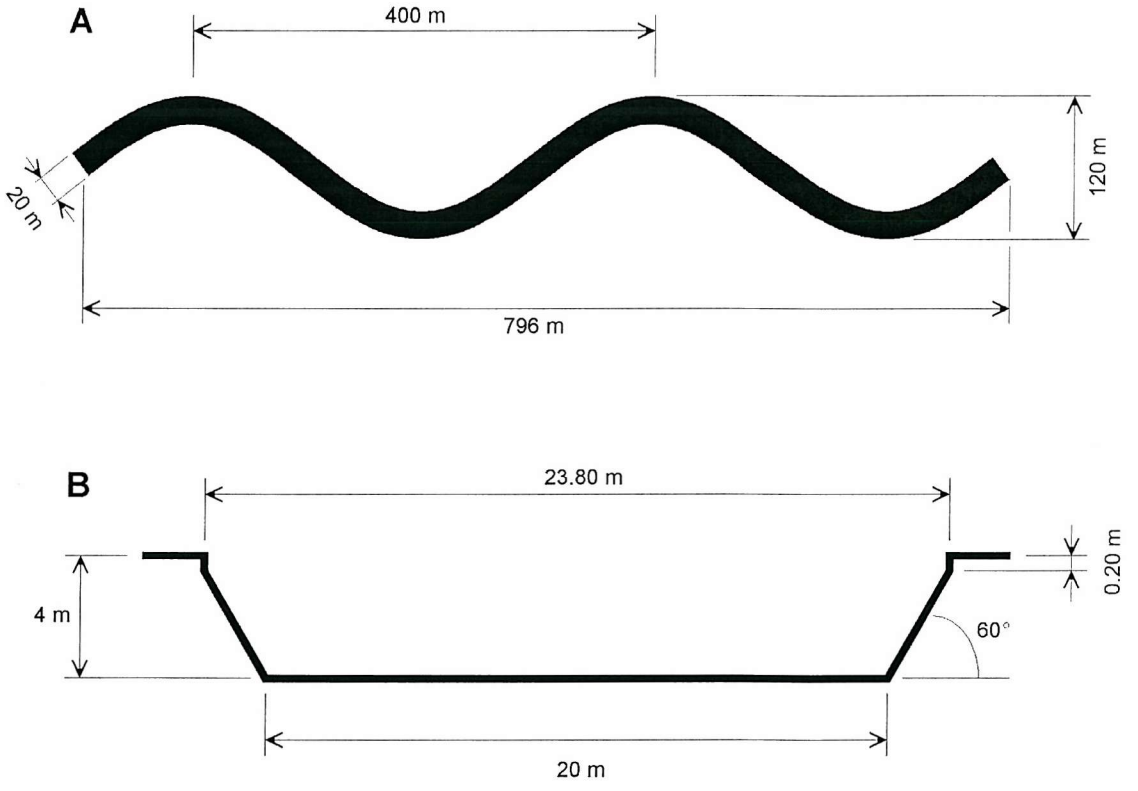

Figure 5.28: Channel geometry of idealized reach. **A**: Planform. **B**: Cross-sectional profile.

Table 5.20: Properties of the idealized channel.

group	property	symbol	value
channel planform	channel width (bed) [m]	W	20.0
	channel width (top) [m]	W_{top}	23.8
	channel length [m]	L_c	906
	valley length [m]	L_v	796
	sinuosity [-]	S_m	1.14
	radius of curvature at apex	r_c	81.3
	curvature ratio	r_c / W	4.07
	meander wavelength [m]	λ_m	400
	meander belt width [m]	W_m	120
	meander amplitude [m]	A_m	50
bank geometry	bank height [m]	H	4.0
	bank angle [deg]	β_b	60
	cliff height [m]	H_c	0.2
	cutbank height [m]	H_{cb}	0.0
	tension crack depth [m]	H_t	0.2
bank material	cohesion [Pa]	c_b	3000
	unit weight [N/m^3]	γ_s	20000
	friction angle [deg]	ϕ	20
	matric suction angle [deg]	ϕ^b	15
	critical shear stress [Pa]	$\tau_{B,c}$	0.7
	fine cohesive fraction (intact) [-]	ω_{h1}	0.8
	granular fraction (intact) [-]	ω_{h2}	0.2
	fine, cohesive fraction (failed) [-]	ω_{f1}	0.8
	small granular fraction (failed) [-]	ω_{f2}	0.2
	coarse granular fraction (failed) [-]	ω_{f3}	0.0
bed material	median grain size [m]	D_{50}	0.001
	90-percentile grain size [m]	D_{90}	0.002
	relative density [-]	ρ_{rel}	1.65
hydraulic	discharge [m^3/s]	Q	20.0
	initial flow depth [m]	h	1.0
	roughness [-]	C	64.84

Table 5.21: Values for the calibration parameters.

parameter	symbol	value
coefficient in power law for sediment transport [-]	k_s	0.0001
exponent in power law for sediment transport [-]	p_s	4
coefficient in transverse slope model [-]	k_{tm}	1.78
exponent in transverse slope model [-]	p_{tm}	1.0
secondary flow convection factor [-]	k_{sn}	0.45
weighing coefficient for secondary flow intensity [-]	k_{si}	3.3
adaptation length for secondary flow [m]	λ_r	0.7
weighing coefficient for streamwise bed-slope [-]	k_{ls}	12.0
coefficient in fluvial bank erosion equation [-]	k_b	1.0×10^{-7}
exponent in fluvial bank erosion equation [-]	p_b	1.0

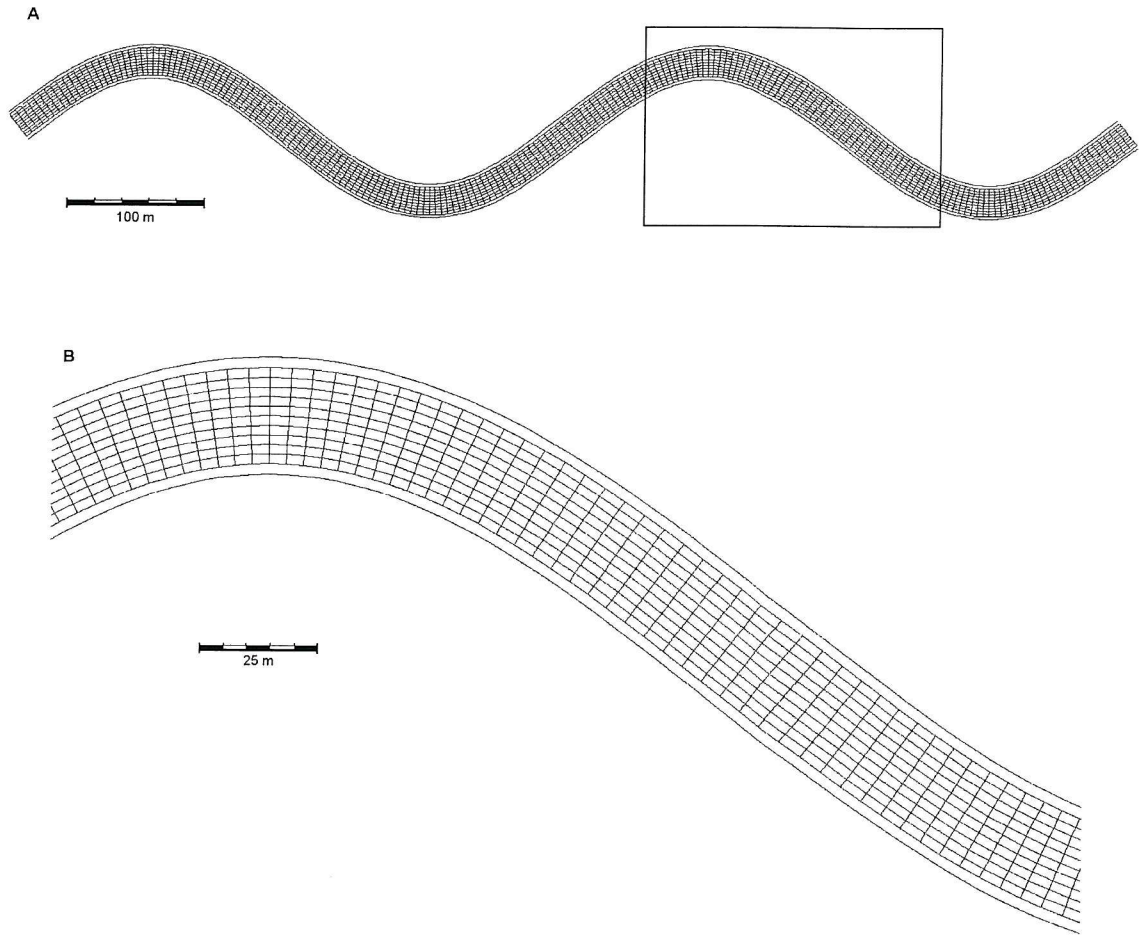

Figure 5.29: Numerical grid for the idealized reach. **A**. Entire reach. **B**. Zoom on highlighted area.

5.4.2. Quantitative indicators

One of the main strengths of mRIPA is its ability to perform spatial analyses. Most of the discussion of the results is, therefore, focussed on spatial distributions of vegetation-induced morphological change. However, it is sometimes useful to quantify these changes on the reach scale, for ease of comparison, even though doing so necessarily implies a loss of spatial information. In the following sections ten indicators are used to quantify the morphological changes of the channel: eight for changes in bed morphology, and two for bank retreat.

The magnitude of bed erosion and deposition can be quantified in different ways. Eight different indicators are used to quantify changes in bed morphology, four each for both deposition and erosion: maximal change in bed elevation, average change in bed elevation, spatial extent of occurrence, and total volume of sediment affected. As mRIPA is a rigid lid model, differences in bed elevation are equivalent to differences in flow depth. Let ΔH denote the difference between the initial and the final flow depth at a grid cell ($\Delta H = H_{initial} - H_{final}$), then a positive value for ΔH indicates deposition over the simulation period. Likewise, a negative value for ΔH indicates erosion. The maximal erosion, ΔZ^*_{ero}, maximal deposition, ΔZ^*_{dep}, average erosion, $\Delta \overline{Z}_{ero}$, and average deposition, $\Delta \overline{Z}_{dep}$, are defined as:

$$\Delta Z^*_{ero} = \max\left(\left|\Delta H_i\right| \right) \qquad \forall i : \Delta H_i < 0 \tag{5.3}$$

$$\Delta Z^*_{dep} = \max\left(\left|\Delta H_i\right| \right) \qquad \forall i : \Delta H_i > 0 \tag{5.4}$$

$$\Delta \overline{Z}_{ero} = \frac{1}{n_{ero}} \sum \left|\Delta H_i\right| \qquad \forall i : \Delta H_i < 0 \tag{5.5}$$

$$\Delta \overline{Z}_{dep} = \frac{1}{n_{dep}} \sum \left|\Delta H_i\right| \qquad \forall i : \Delta H_i > 0 \tag{5.6}$$

where n_{ero} and n_{dep} respectively are the number of cells where erosion occurs ($\Delta H < 0$) and the number of cells where deposition occurs ($\Delta H > 0$). Note that $\Delta \overline{Z}_{ero}$ and $\Delta \overline{Z}_{dep}$ are defined as the average change in bed elevation, not over the entire reach, but over the eroding or

depositing cells only. Note also that no adjustment is made for the variable size of the grid cells in the calculation of these averages. Nonetheless, both values give a quick indication of the average magnitude of change in bed elevation, where such change occurs. The spatial extent of erosion, A_{ero}, and deposition, A_{dep}, are defined as:

$$A_{ero} = \frac{n_{ero}}{n_{tot}} \tag{5.7}$$

$$A_{dep} = \frac{n_{dep}}{n_{tot}} \tag{5.8}$$

where n_{tot} denotes the total number of grid cells ($n_{tot} = 2200$). Both indicators are taken relative to n_{tot} to allow comparison between scenarios, as the total surface area might differ between scenarios, due to lateral bank erosion. Between n_{dep}, n_{ero} and n_{tot} the following relation holds: $n_{dep} + n_{ero} \leq n_{tot}$. The inequality is due to the possibility that there is no change in bed elevation for a small number of cells ($\Delta H = 0$). Generally, however, $n_{dep} + n_{ero} \approx n_{tot}$, and hence: $A_{dep} + A_{ero} \approx 1$. Again, no adjustment is made for the variable size of the grid cells. As such, these two indicators are only approximations of the actual extents of erosion and deposition. The last two indicators of bed morphology change are the total volumes of eroded and deposited sediment, V_{ero} and V_{dep}, which are defined as:

$$V_{ero} = \sum \left(A_i \left| \Delta H_i \right| \right) \qquad \forall i : \Delta H_i < 0 \tag{5.9}$$

$$V_{dep} = \sum \left(A_i \left| \Delta H_i \right| \right) \qquad \forall i : \Delta H_i > 0 \tag{5.10}$$

where A_i denotes the size of the grid cell at node i. Thus, V_{ero} and V_{dep}, represent actual total simulated volumes of erosion and deposition, as their calculations do account for the size of the grid cells.

Bank erosion is quantified with two parameters: maximal bank retreat and total floodplain area loss. The first is simply the maximal simulated retreat of the bank tops, ΔW_{max}, reported along either bank of the reach. It is a point-specific value and serves only to give a feel for the magnitude of the bank erosion. Total floodplain area loss, A_{fpl}, is a reach-

averaged indicator. It is defined as:

$$A_{fpl} = \frac{1}{n_b} \sum_{1}^{n_b} \left(\Delta W_i \, L_{b,i} \right) \tag{5.11}$$

where n_b denotes the number of grid points along the bank, ΔW_i is the simulated banktop retreat at point i and $L_{b,i}$ is the length of the cell at point i. Assuming that the variability in cell lengths is small, the total floodplain area loss can be approximated as:

$$A_{flp} \approx \left(\frac{1}{n_b} \sum_{1}^{n_b} \Delta W_i \right) \sum_{1}^{n_b} L_{b,i} \approx 2 \, L_c \, \Delta \overline{W} \tag{5.12}$$

where $\Delta \overline{W}$ represents the average bank retreat along the reach and L_c denotes the channel length. This approximation will slightly underestimate the true simulated total floodplain area loss because local bank retreat, ΔW_i, and local cell length, $L_{b,i}$, are not independent of each other. Bank retreat is likely to be higher along the outer bend, and in such regions the grid cells are more elongated as well. However, the right hand part of equation 5.12 provides a fast and easy, albeit slightly underestimated, evaluation of total floodplain area loss.

5.4.3. Reference scenario without vegetation

Figure 5.30 shows the flow pattern through the channel at the end of the simulation. High flow velocities (> 1.0 m/s) are marked in red, while low flow velocities (< 0.75 m/s) are shown in blue. At the entrance of each bend, the highest velocities are along the inner bank. As the flow passes though the bend, the core of high flow velocities is gradually pushed toward the outer bank. The core of high flow velocities connects with the outer bank approximately 50 m (or 0.12 wavelengths) beyond the apex of the bend, and subsequently persists along this bank until the next bend. The bed topography of the unvegetated reference scenario at the end of the simulation is illustrated in figure 5.31, although it is emphasized that this is not an equilibrium morphology (*cf.* section 5.4.1). Figure 5.31 clearly shows the development of a sequence of point bars along the inside bends and thalwegs along the outside bends. The points of maximal observed point bar deposition and maximal bed erosion are located slightly beyond the bend apices, and coincide with the locations where

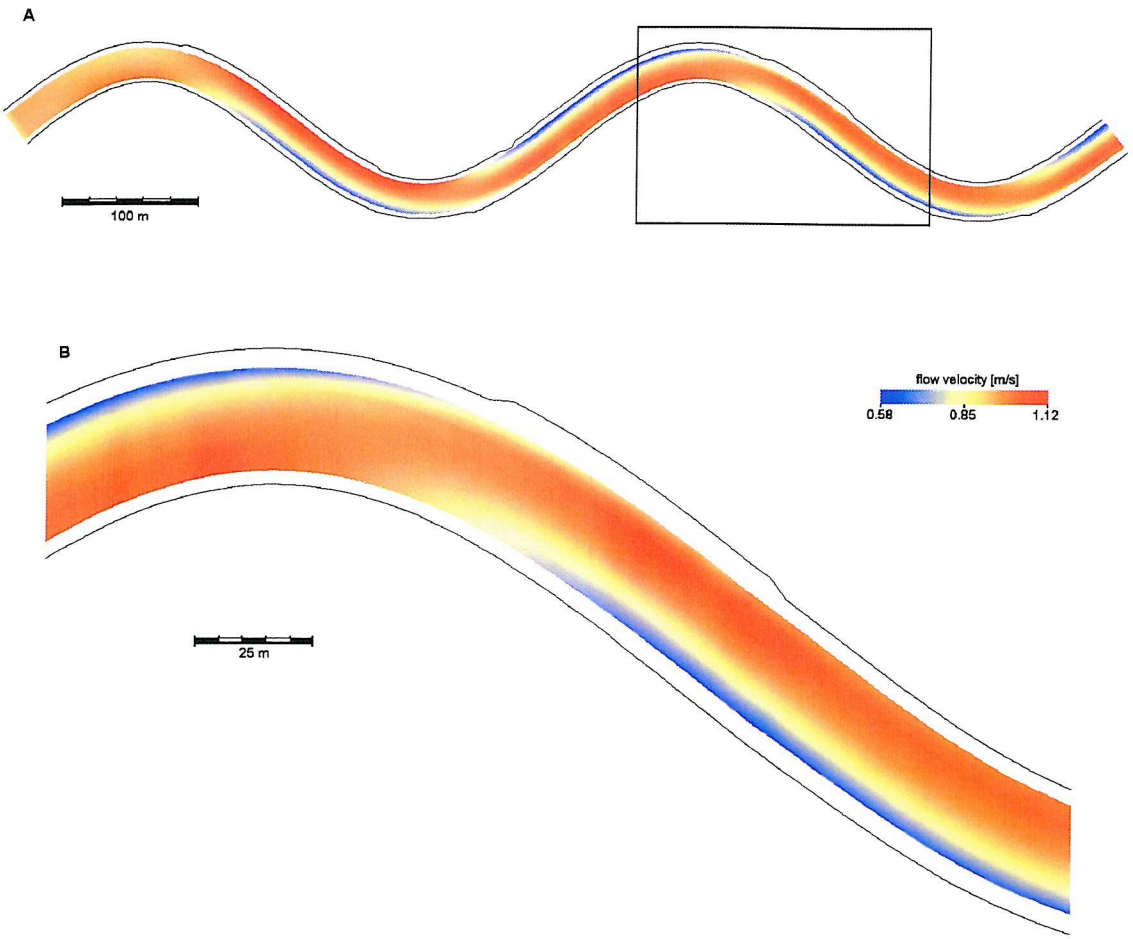

Figure 5.30: Flow pattern for the unvegetated reference scenario, at the end of the simulation (t = 60 days). **A**. Entire reach. **B**. Zoom on highlighted area. The single lines on either site of the channel mark the top of the channel bank. Flow is from left to right.

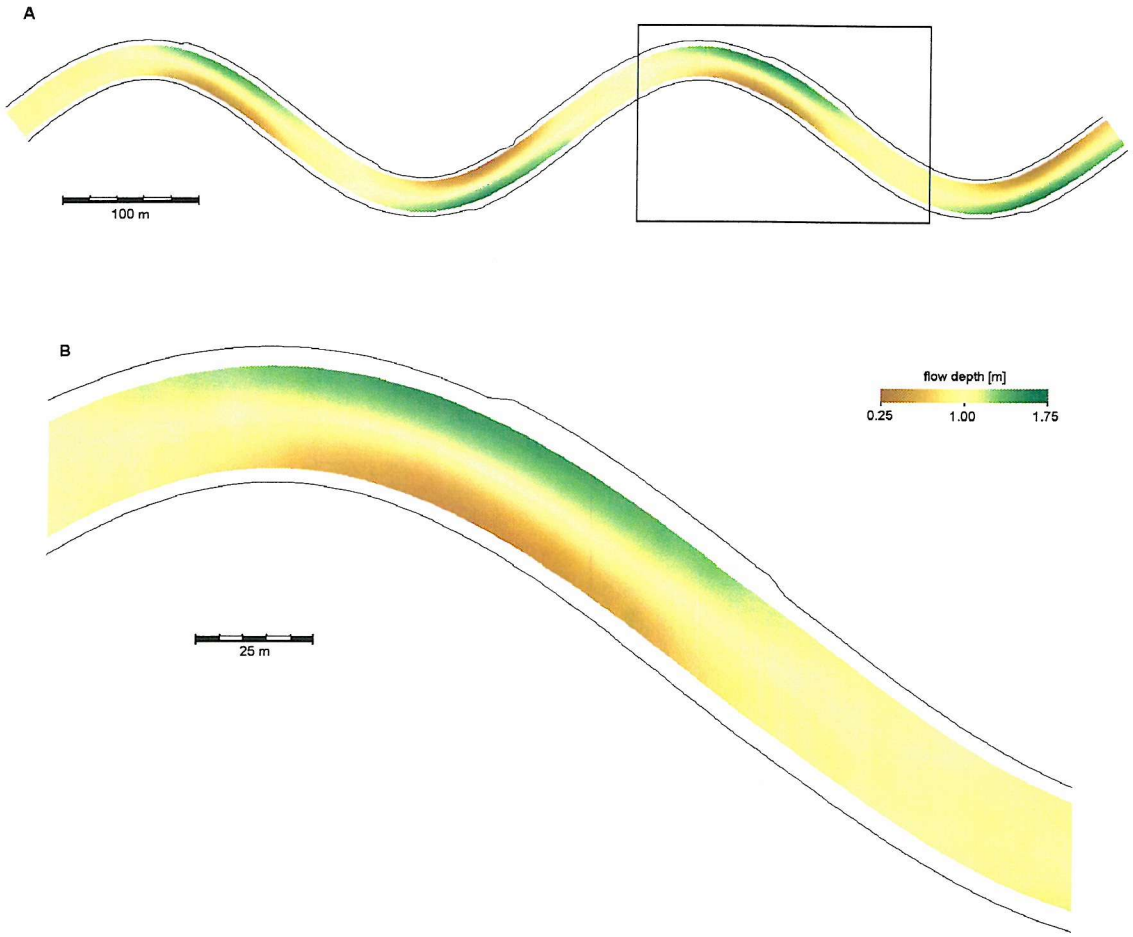

Figure 5.31: Final bed topography for the unvegetated reference scenario. **A**. Entire reach. **B**. Zoom on highlighted area. Flow is from left to right.

the core of high flow velocities reaches the outer bank (*cf.* figure 5.30). Furthermore, these locations also coincide with the parts of the channel where the bank retreat is the greatest (figures 5.30B and 5.31B). Hence, there is a phase-shift between bed morphology and channel planform shape (figure 5.32). The phase displacement of bank migration follows a similar pattern, albeit more staggered due to the episodic nature of bank failures. The extent of the phase shift between bank migration and channel planform shape is of the same order as that for bed topography and planform shape, which is another indication of the interactions between flow hydraulics and the morphological processes of bed and banks. As the banks are initially stable ($N_{FS} = 1.01$), the occurrence of bank failure can only be due to changes in bank geometry, as induced by fluvial entrainment, both lateral and vertical, near the toe of the bank. Hence, the occurrence of maximal bank retreat is likely to coincide with the occurrence of maximal scour of the bed. The phase-shift between channel planform shape and bank migration is a key feature in terms of the evolution of meandering channels. It implies that the maximal bank retreat is not located at the apex of the bend, but downstream thereof, thus allowing for the channel to migrate in a general downvalley direction. However, there still is some bank retreat at the bend apex as well, which leads to an increasing meander amplitude. Hence, for the reference case, the model replicates the two main modes of meander evolution: downvalley migration or "translation", and increasing amplitude or "extension" (Hooke, 1977; 1984).

Although the spatial pattern of bank retreat is periodic, with the maxima along the outer bend and downstream of the bend apex (*cf.* figure 5.32), it is also distinctly discontinuous (figure 5.33), due to the episodic nature of bank failure. While fluvial entrainment of sediments from the bank and from the near-bank channel bed is a continuous process, mass failure of the river bank occurs only when a critical threshold is exceeded ($N_{FS} < 1$). Following mass failure, the bank is stable until enough sediments have been evacuated at the toe of the bank to exceed the threshold once again. Hence, the occurrence of mass failure is episodic rather than continuous (figure 5.34). This temporal discontinuity is also expressed spatially, as not all points along the reach are subjected to the same number of bank failures during the simulation (figure 5.35). Most of the channel banks experience a single failure throughout the simulated period. However, in the part of the channel where the core of high flow velocities connects the outer bank, two failures occur. This is illustrated in figures 5.34 and 5.35B for the right bank of section XS092 and the left bank of section XS142 (see figure 5.35A for location of cross-sections mentioned in this paragraph). On the other hand, the left bank of XS092 does not fail at all, although the fact that its factor of safety is

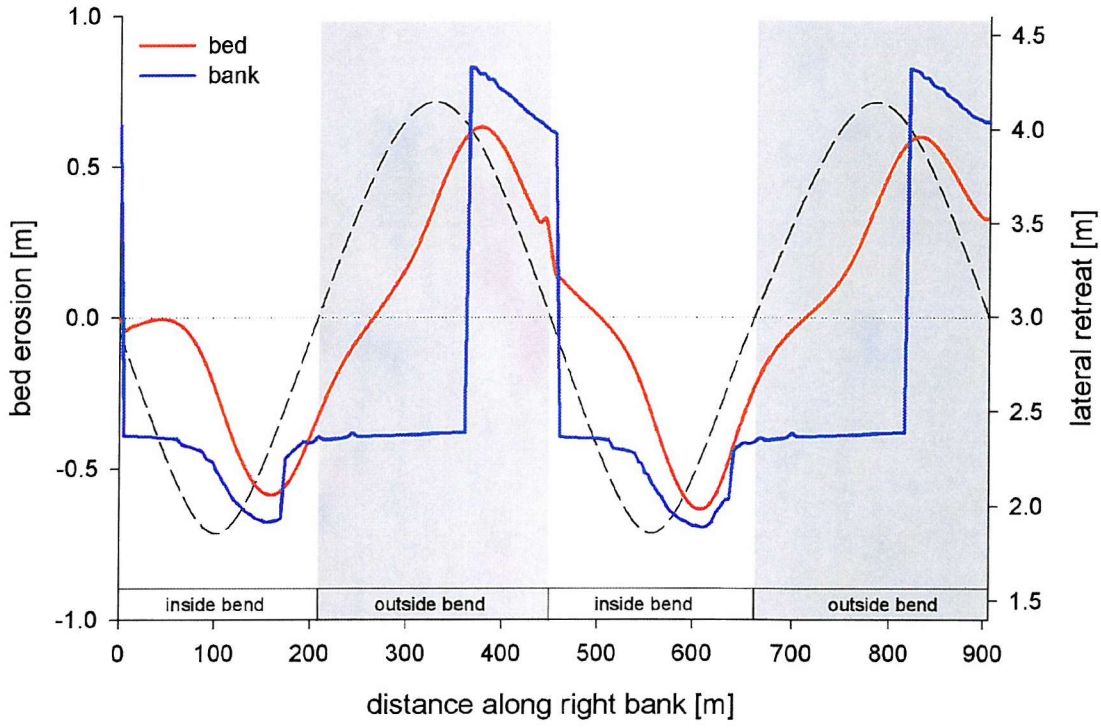

Figure 5.32: Phase shift between planform shape and magnitude of morphological change. The dashed line represents the amplitude of the channel along the right bank (no values on Y-axis; peaks indicate outside bend, lows indicate inside bend). Bed erosion and lateral bank retreat are respectively indicated by the red and blue line. Negative values for bed erosion denote net deposition. Both maximal bed erosion and maximal deposition lag behind planform shape by about 50 m (approximately 0.12 wavelengths). A similar effect is observed for lateral bank retreat. Only the patterns along the right bank is depicted. The phase-shift along the left bank follows a similar pattern.

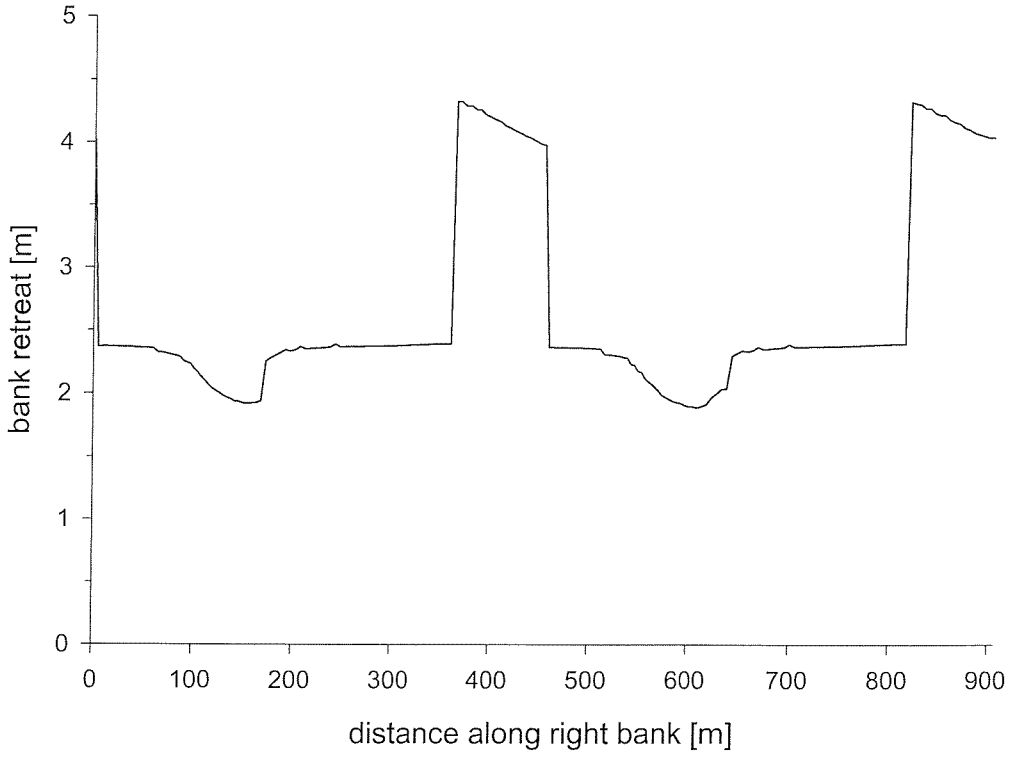

Figure 5.33: Spatial occurrence of bank retreat in the unvegetated scenario. Only retreat along the right bank is depicted. Retreat along the left bank follows a similar pattern, although displaced by half a wavelength.

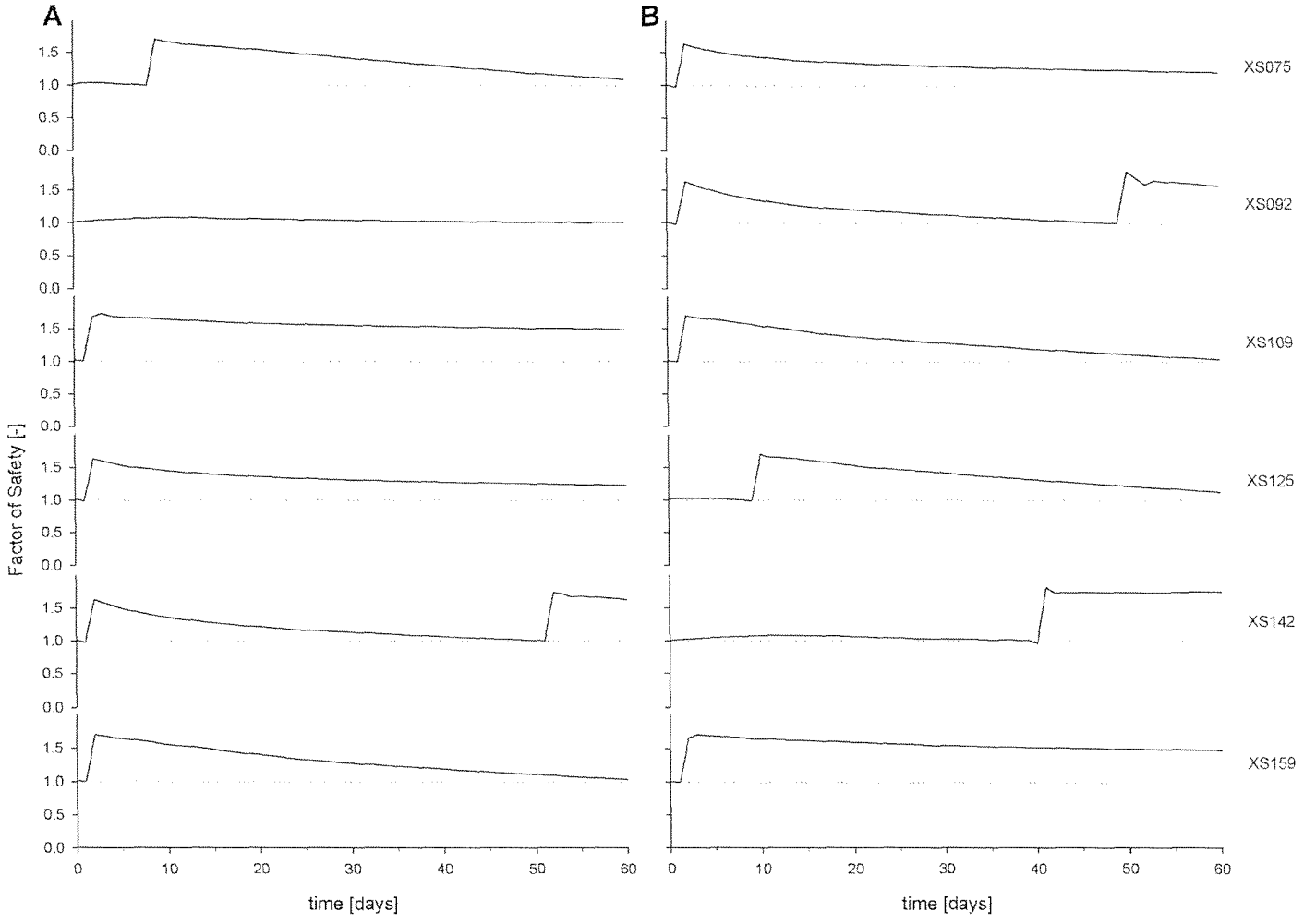

Figure 5.34: Temporal evolution of factor of safety for six selected cross-sections along the unvegetated reference scenario. **A.** Left bank. **B.** Right bank. See figure 5.35A for cross-section locations.

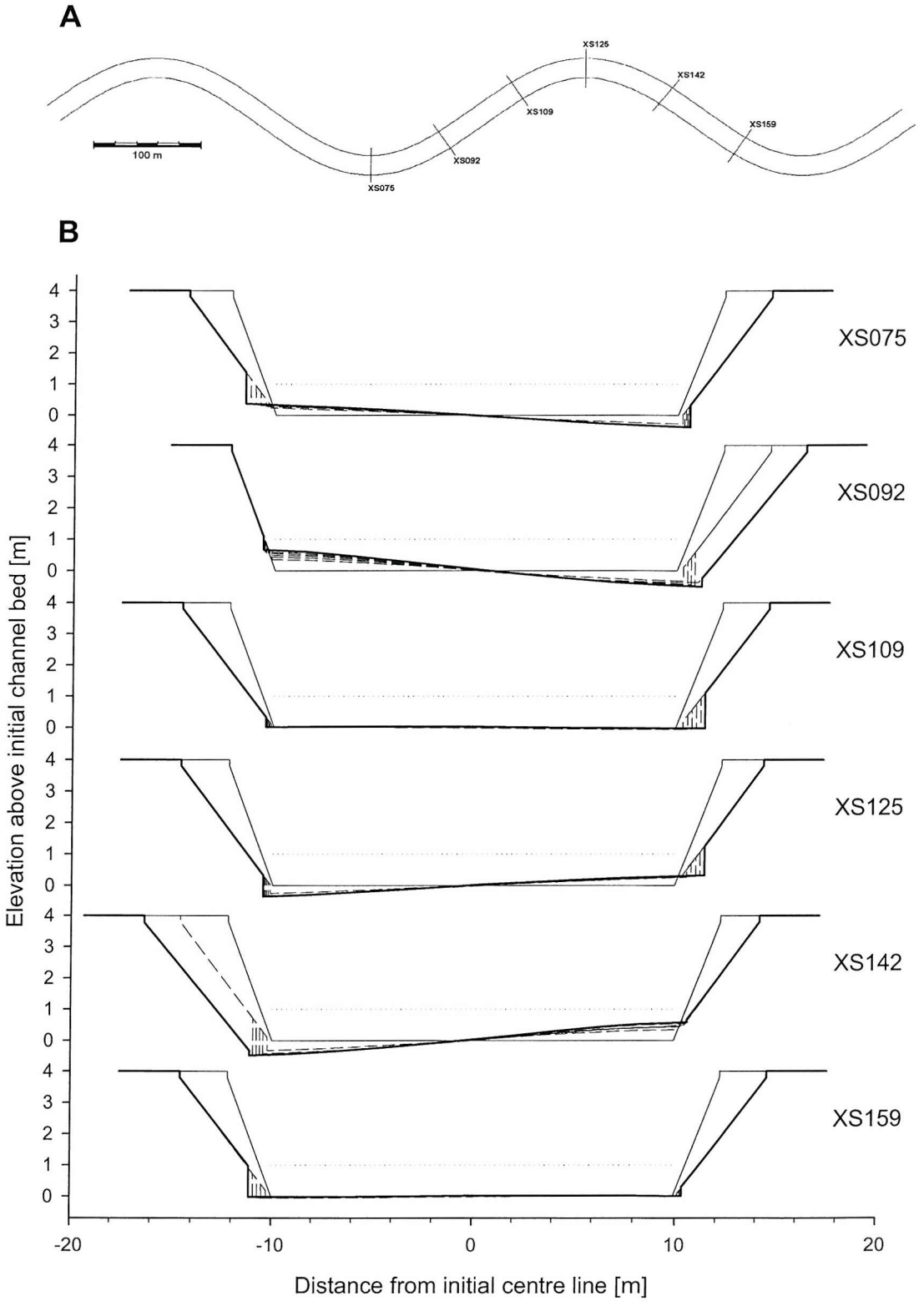

Figure 5.35: Cross-sectional change over the simulation period, for six selected cross-sections. **A.** Location of the cross-sections. **B.** Cross-sectional profiles. The initial profile (t = 0 days) is shown as a tin line; the final profile (t = 60 days) is shown as a thick solid line; intermediate stages(in 10-day intervals) are shown as thin dashed lines. The thin dotted line marks the water-level. Elevations are measured relative to the initial elevation of the channel bed for each cross-section. Distances across the channel are measured relative to the centre-line of the initial channel planform. Negative distances indicate a position left of the initial centre-line.

very close to unity and slowly decreasing (figure 5.34), suggests that it would have been likely to fail if the simulation continued beyond 60 days. The failures are triggered by lateral erosion and/or vertical incision near the toe of the bank. As the initial banks are only barely stable (N_{FS} = 1.01), a slight change in channel morphology near the bank toe can be sufficient to induce a mass failure. Both the left and right banks of all the cross-sections shown in figure 5.35 are subjected to lateral erosion, while vertical adjustment (incision or aggradation) only occurs at cross-sections XS075, XS092, XS125 and XS142 (*i.e.* at or slightly beyond the bend apex). For all depicted banks, except the left bank at XS092, the lateral change alone is sufficient to trigger the first bank failure, although vertical incision near the toe of both the right bank at XS092 and the left bank at XS142 also contributed to the first failure of these banks. The main reason why the left bank at XS092 has not failed yet, is because the destabilizing effect of the lateral erosion has been compensated by a stabilizing effect of vertical aggradation near the bank toe. The same phenomenon explains why the right bank at XS142 fails on day 40 of the simulation (figure 5.34), more than 30 days later than banks of the other depicted sections have failed. At the points where a second failure occurs (right bank of section XS092 and left bank of section XS142), this is almost entirely driven by lateral erosion of the bank toe (figure 5.35). In fact, in the cross-sections where vertical channel adjustment is observed, most of it occurs during the first 10 days of the simulation. In contrast, lateral erosion of the bank toe continues throughout the entire simulation period, for all sections, although the its rate is gradually diminishing. There is a marked difference between the amounts of lateral erosion for the left and right bank for each cross-section. For sections XS092, XS109 and XS125, lateral toe erosion of the right bank exceeds that of the left bank; and vice versa for the other cross-sections (figure 5.35). This is especially noteworthy for the left bank of XS075 and the right bank of XS125, both of which experience more lateral erosion than their opposites, even though they are located along the inner banks at the apices of the meander bends. However, this apparent inconsistency is explained by the earlier observation that the core of high flow velocities does not connect with the outer bank until beyond the bend apex (*cf.* figure 5.30). Lateral erosion near the bank toe is driven by fluvial entrainment, and is thus related to the flow velocity (*cf.* equation 3.66). Figure 5.36 displays the cross-sectional flow velocities for each of the sections shown in figure 5.35A. It can be seen that the highest flow velocities do not necessarily coincide with the deepest parts of the channel cross-section. In particular, for XS075 and XS125, the flow velocity appears inversely related to the flow depth (*i.e.* the core of high velocities near the inner bank), which explains the higher rates of lateral toe erosion at the inside of the bend in these sections.

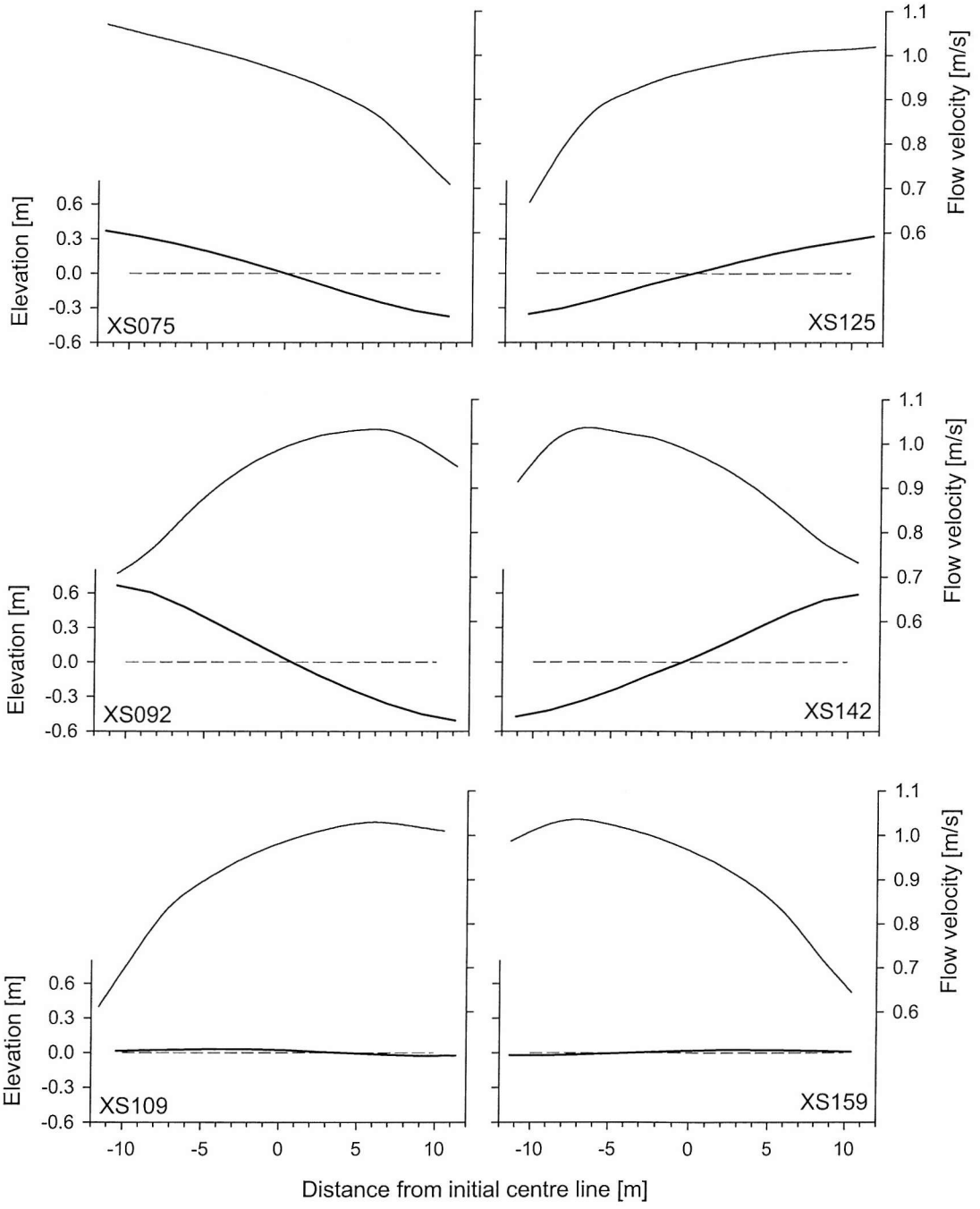

Figure 5.36: Cross-sectional velocity profiles for the unvegetated reference scenario at the end of the simulation (t = 60 days). The lower part of each graph shows the initial (dashed) and final (solid) bed topographies. Distances are measured relative to the initial centre-line of the channel, with negative numbers indicating positions to the left thereof. Elevations are measured relative to the initial channel bed for each cross-section. See figure 5.35A for cross-section locations.

Table 5.22: Summary of channel change for the unvegetated scenario.

group	variable	value
bed change	relative eroding area [%] [1]	38.9
	maximal bed erosion [m]	0.63
	average bed erosion [m]	0.21
	total bed erosion [m^3]	9439
	relative deposition area [%] [1]	60.5
	maximal bed deposition [m]	0.72
	average bed deposition [m]	0.18
	total bed deposition [m^3]	11049
bank change	maximal bank retreat [m]	4.33
	average bank retreat [m]	2.64
	floodplain area loss [m^2]	4783

Note: [1] Relative eroding area and relative deposition area indicate the spatial extents of the occurrence of erosion and deposition, expressed as a percentage of total bed surface area.

Table 5.22 describes the morphological change of the channel in terms of the quantitative indicators. It can be seen that pool scour and point bar deposition are of the same order of magnitude. The maximal deposition on the point bar is 0.72 m (flow depth = 0.28 m), while maximal bed erosion is about 0.63 m (flow depth = 1.63 m). However, the total volumes of bed erosion and bed deposition are not equal, because part of the entrained and failed bank sediments are deposited on the channel bed within the reach. The total floodplain loss due to bank retreat approximately equals 4783 m^2.

5.4.4. Effects of species variation

In the first group of simulations, uniform stands of different simulated species are placed along the banks. To allow inter-species comparison, the ground cover is set to 30% (A_{gv} = 0.3) for each vegetation stand. The following paragraphs describe the impact of this simulated vegetation presence, in terms of effects on bank migration and bed topography in relation to the reference scenario. In this section, only the results of the simulations are presented. Discussion and interpretation of these results is delayed until section 5.4.6.

The total floodplain area loss is, in each of the vegetation scenarios, reduced relative to the reference case (table 5.23). The three woody species reduce floodplain area loss by between 26% to 32%, while the herbaceous species achieves a decrease of about 5%. Similar to the bank stability analysis, the woody species appear to have a bigger impact than the herbaceous species, although it is noteworthy that the impact of the latter can not be neglected in the full mRIPA analysis.

Table 5.23: Floodplain area loss for the vegetation scenarios.

scenario	area loss [m^2]	reduction in area loss[1] [%]
unvegetated	4783	-
"*Convolvulvus*"	4531	5.3
"*Betula*"	3534	26.1
"*Salix*"	3509	26.7
"*Populus*"	3281	31.4

note: [1] relative to the unvegetated scenario

The reduction in total floodplain area loss is spatially variable for each species (figure 5.37). Again, the effect is more pronounced for the woody species (figures 5.37BCD), whose influences range from -12% to 100% reduction, *i.e.* from a small increase in bank retreat to complete prevention of bank retreat, depending on position along the channel. Complete reduction is achieved along the point bars at the inside bends, where a single failure occurs in the unvegetated scenario, but none in the scenarios with woody vegetation. More importantly, however, is the fact that in each of these scenarios the double failure along the outside bends is reduced to a singe failure. In the cross-over reach between the inside and outside bends, the vegetation has no discernible impact on the number of failures occurring, although it is important to note that the magnitude of the failure is sometimes slightly higher, which results in locally increased lateral retreat. This is particularly notable for the first failure after the point bars along the inside bends, where bank retreat is increased by up to 12%. The presence of herbaceous vegetation does not influence the bank retreat along most of the channel, although it does narrow the spatial extent of the double failure along the outside bends (figure 5.37A).

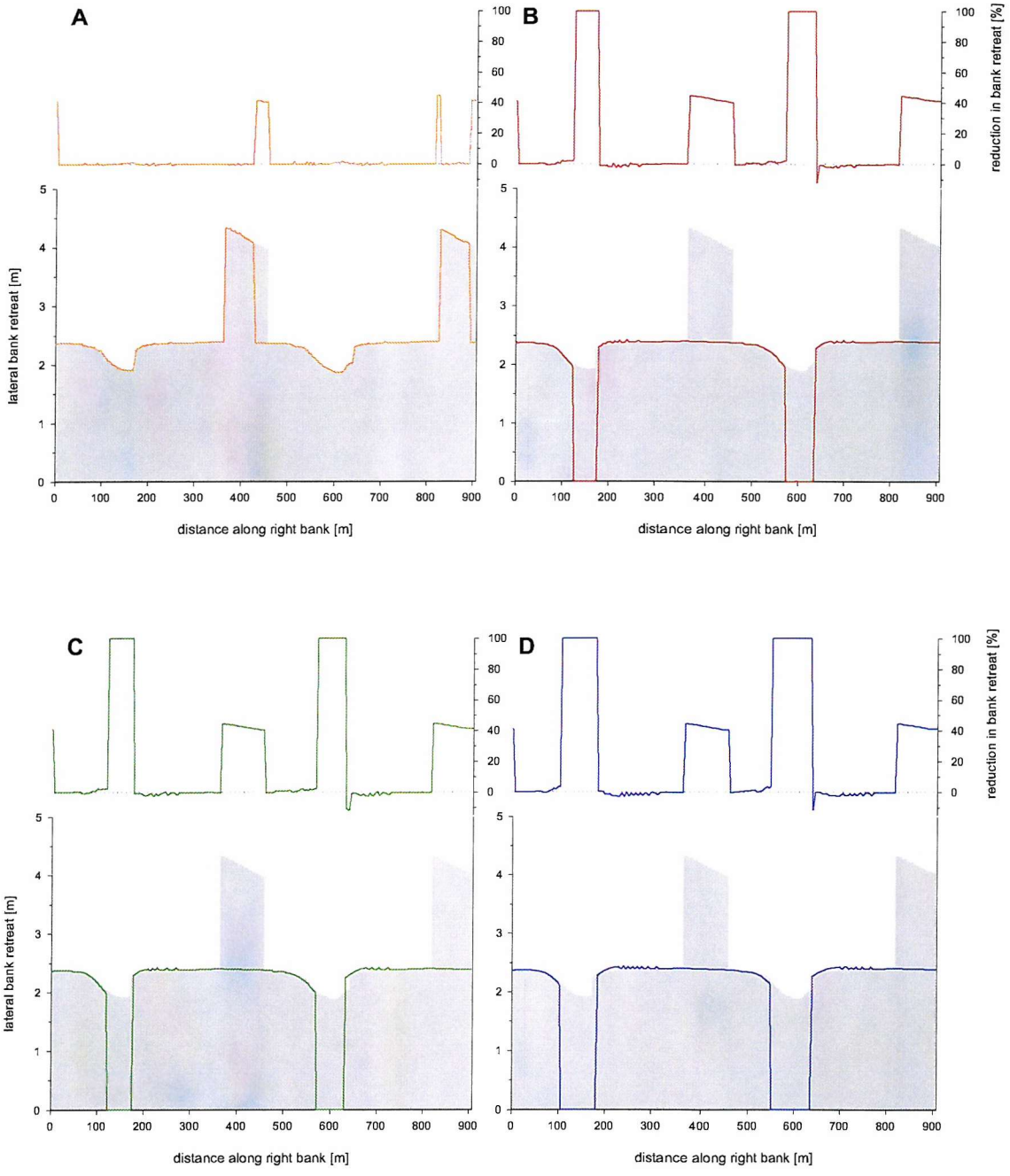

Figure 5.37: Spatial distribution of bank retreat for different simulated vegetation species. **A**: "*Convolvulvus*", **B**: "*Betula*", **C**: "*Salix*", **D**: "*Populus*". The lower part of each graph shows the spatial distribution of bank retreat for both the vegetated scenario (line) and the unvegetated scenario (gray background; *cf.* figure 5.33). The upper part of each graph shows the reduction in lateral bank retreat, relative to the unvegetated scenario. The dotted grey line denotes 0% change. Only the right bank is depicted; bank retreat along the left bank follows a similar pattern, although displaced over half a wavelength.

The distinction between the impacts of woody and herbaceous species also extends to changes in simulated bed topography. Under a herbaceous riparian cover, the spatial occurrence of erosional and depositional processes are nearly the same as for the unvegetated reference scenario: about 40% of the channel bed is eroding , while about 60% of the bed is depositing (table 5.24). However, when the banks are covered with woody species, roughly 60% of the bed surface is eroding, and deposition occurs only on about 40% of the bed. At the same time, both maximal and average deposition and erosion are smaller when compared to the unvegetated reference case (table 5.24). The increase in eroding bed surface area appears to counter the decrease in erosion magnitude, so that the total eroded volume is approximately the same as for the unvegetated reference scenario (up to 3% less). On the other hand, the decrease in the spatial extent of sediment deposition, coupled with its decreased magnitude, results in a markedly lower overall deposition in the channel (between 40 and 50% less).

Table 5.24: Bed topography change in the vegetation scenarios.

variable	unvegetated	"*Convolvulvus*"	"*Betula*"	"*Salix*"	"*Populus*"
relative eroding area [%]	38.9	39.9	56.0	57.8	61.2
maximal bed erosion [m]	0.63	0.73	0.56	0.55	0.55
average bed erosion [m]	0.21	0.19	0.15	0.15	0.14
total bed erosion [m^3]	9439	9272	9138	9164	9215
relative deposition area [%]	60.5	59.6	43.4	41.5	38.3
maximal bed deposition [m]	0.72	0.70	0.53	0.51	0.49
average bed deposition [m]	0.18	0.17	0.16	0.16	0.16
total bed deposition [m^3]	11049	10283	6534	6244	6083

Figure 5.38 shows the final bed topography for the "*Populus*" scenario. On first glance this appears similar to the final bed topography simulated for the unvegetated reference scenario (*cf.* figure 5.31), which implies that the main features of the channel, *i.e.* point bars and thalweg, are still being formed. However, the differences between the two scenarios become clear in the difference model shown in figure 5.39. The red and blue colouring indicates areas where the final bed elevation of the "*Populus*" scenario is respectively higher and lower, compared to the bed topography of the unvegetated scenario. Yellow shading denotes areas of little or no difference. It is evident that the effect of "*Populus*" is to induce bed lowering on the point bars, while bed raising is induced in the thalwegs (figure 5.39A and 5.39B). Hence, the transverse bed slopes become shallower in the "*Populus*" scenario. The frequency distribution of changes in final bed topography

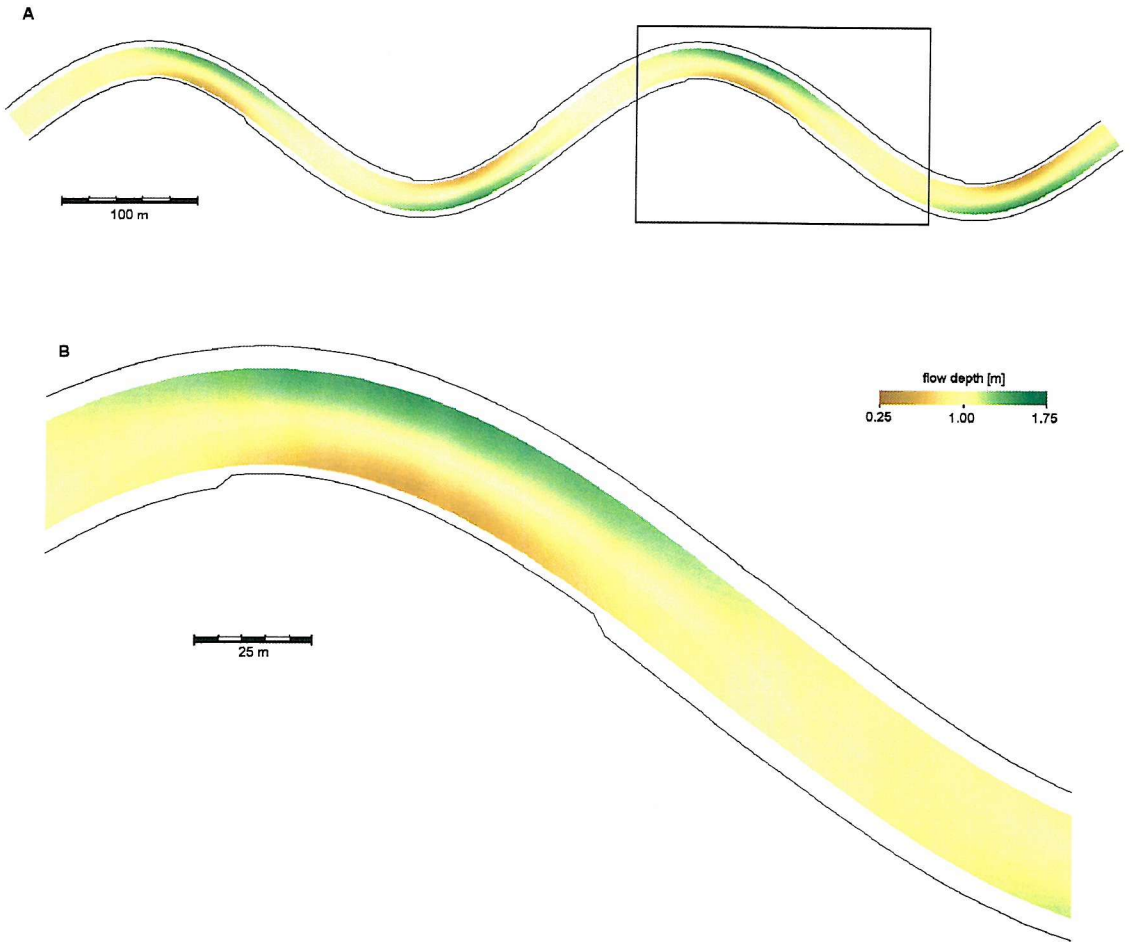

Figure 5.38: Final bed topography for a stand of "*Populus*", at 30% ground cover. **A**. Entire reach. **B**. Zoom on highlighted area. Flow is from left to right.

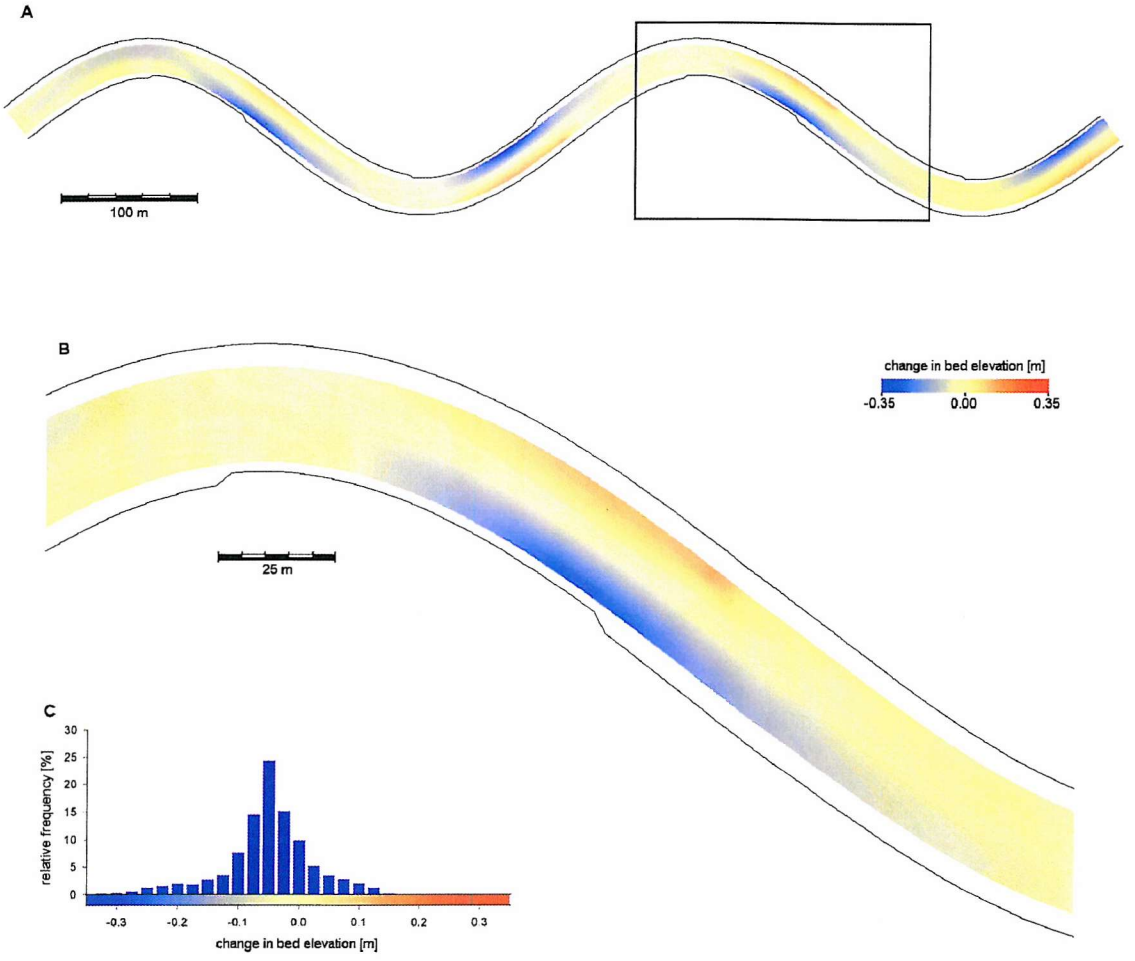

Figure 5.39: Difference in final bed topography between unvegetated scenario and a stand of "*Populus*" at 30% ground cover. **A**. Entire reach. **B**. Zoom on highlighted area. **C**. Relative frequency of magnitude of change over the entire reach. Flow is from left to right.

(figure 5.39C) indicates a systematic shift in favour of a lower bed (*i.e.* increased flow depths). The frequency distribution of changes in final bed topography of all vegetation scenarios is illustrated in figure 5.40. The distributions for the two other woody vegetation scenarios are similar to that of the "*Populus*" scenario. Their spatial distribution is similar as well and is, therefore, not illustrated here. However, the frequency distribution of "*Convolvulvus*" is clearly different, with 72% of the bed elevations within 25 mm of the bed elevations of the unvegetated scenario. The spatial difference plot (figure 5.41) shows that although the same pattern of differences exists between the "*Convolvulvus*" scenario and the unvegetated scenario, it is clearly less pronounced than that of the "*Populus*" (*cf.* figure 5.39). This, again, implies that the "*Convolvulvus*" scenario is more similar to the unvegetated scenario than to any of the woody vegetation scenarios. The same information is represented in an alternative form in figure 5.42B, which shows ten cross-sections of the bed at the end of simulations, about 45 metres apart and covering a full meander wavelength (figure 5.42A). In most of these graphs, the cross-sections of the unvegetated reference scenario and the "*Convolvulvus*" scenario nearly coincide, while the cross-sections of the woody vegetation scenarios form a separate cluster. These cross-sections also confirm the earlier finding that the simulated transverse bed slope is less steep in simulation scenarios involving the woody species.

5.4.5. Effects of density variation

In a second group of simulations, the density of the vegetation stands is varied. For each of the woody species, the ground cover is varied from 1% to 50% ($0.01 \leq A_{gv} \leq 0.50$), while the ground cover of the "*Convolvulvus*" ranges from 2% to 80% ($0.02 \leq A_{gv} \leq 0.80$). The difference in the simulated ranges of woody and herbaceous species reflects the fact that the density of vegetation reaches a lower upper limit for woody species, as discussed previously (section 5.3.3). Several simulations are run for each species to cover the range within these boundaries (table 5.25). In total, 46 simulations are performed. As in the previous section, only the results of the simulations are presented here. Discussion and interpretation of the results is delayed until section 5.4.6.

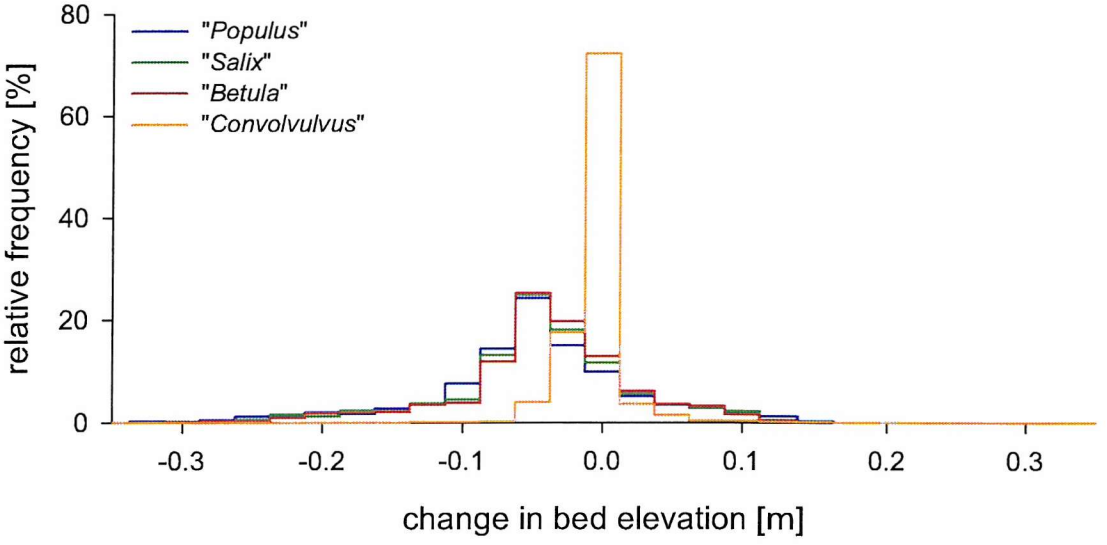

Figure 5.40: Frequency distribution of change in channel bed elevation for each of the vegetation scenarios. The changes in bed elevation are relative to the unvegetated scenario, and are grouped in classes of 2.5 cm.

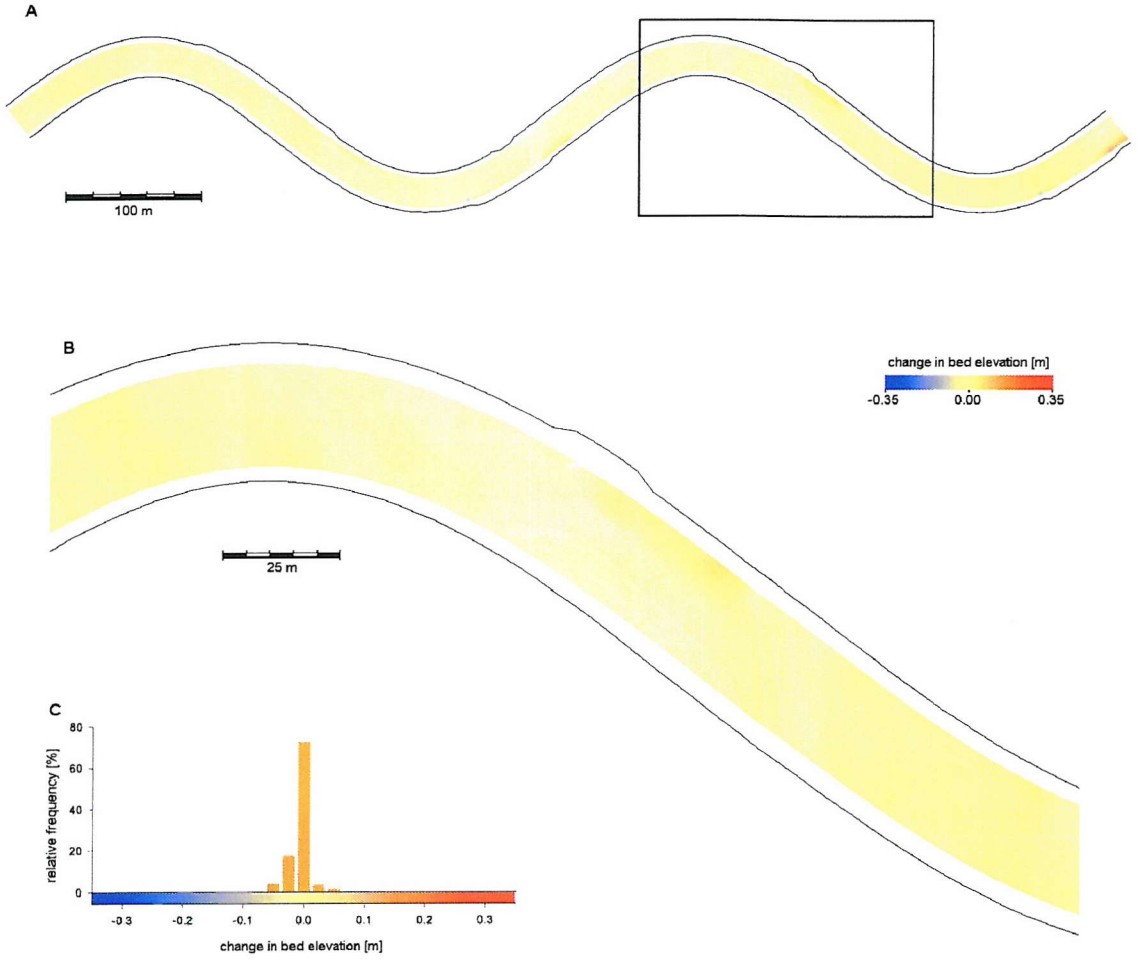

Figure 5.41: Difference in final bed topography between unvegetated scenario and a stand of "*Convolvulvus*" at 30% ground cover. **A**. Entire reach. **B**. Zoom on highlighted area. **C**. Relative frequency of magnitude of change over the entire reach. Flow is from left to right.

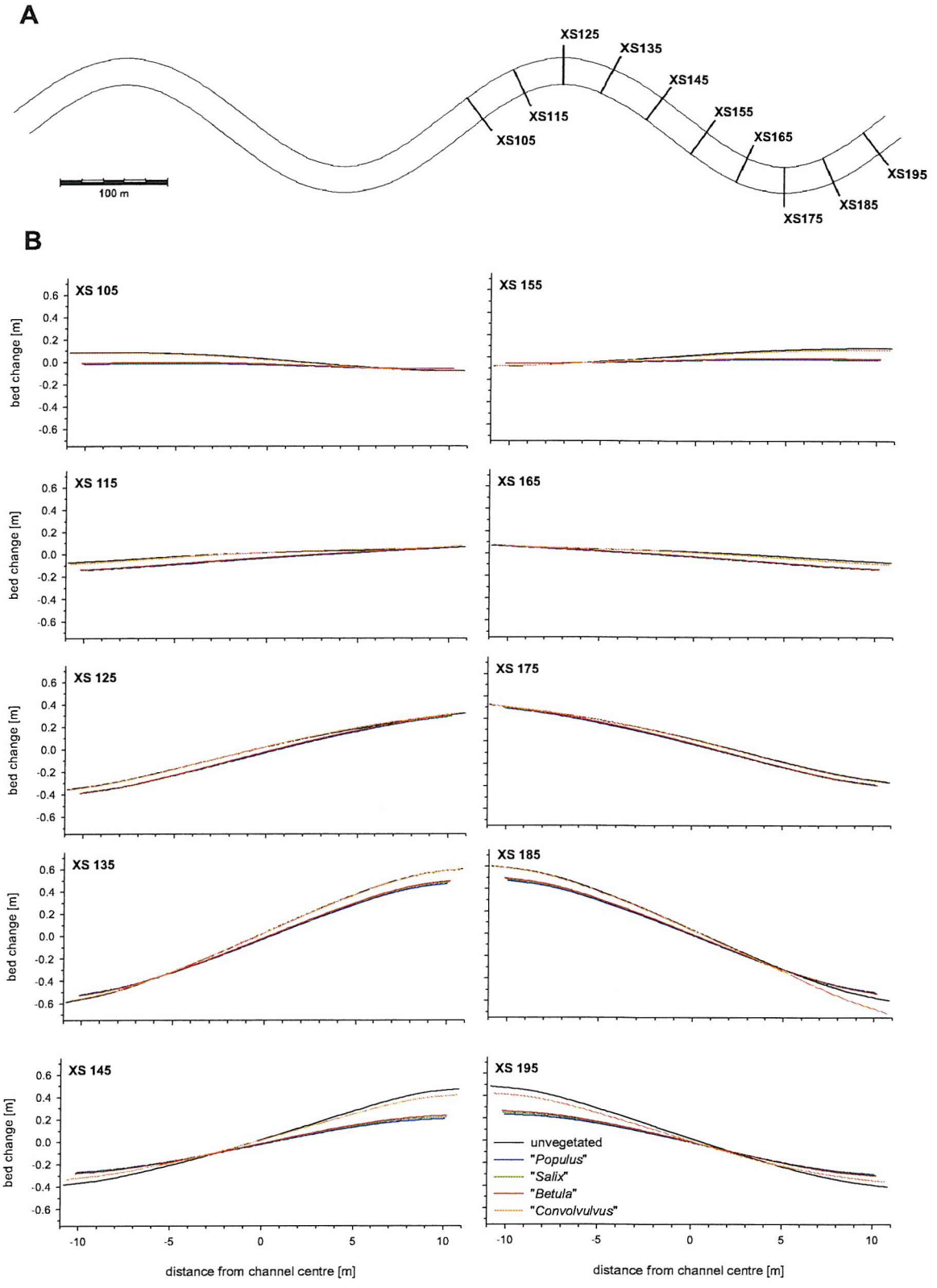

Figure 5.42: Selected cross-sectional profiles along the reach. The cross-sections span two consecutive bends or one meander wavelength (**A**). In each of the cross-sections (**B**), bed topography at the end of the simulation is shown, for each of the vegetation scenarios, as well as for the unvegetated reference scenario.

Table 5.25: Setup of vegetation density scenarios.

ground cover [-]	"*Populus*"	"*Salix*"	"*Betula*"	"*Convolvulvus*"
0.01	✓	✓	✓	
0.02	✓	✓	✓	✓
0.03	✓	✓	✓	
0.04	✓	✓	✓	
0.05	✓	✓	✓	
0.10	✓	✓	✓	
0.15	✓			
0.20	✓	✓	✓	✓
0.25	✓			
0.30	✓	✓	✓	✓
0.35	✓			
0.39	✓			
0.40	✓	✓	✓	✓
0.41	✓			
0.42	✓			
0.43	✓			
0.44	✓			
0.45	✓			
0.50	✓	✓	✓	✓
0.80				✓

Modelled lateral bank retreat along the reach tends to decrease as the simulated vegetation density increases. Put another way, the reductions in floodplain area lost to bank erosion, relative to the floodplain area loss in the unvegetated scenario, increase with higher ground cover (figure 5.43). For the woody vegetation species, there is a steep reduction in floodplain area loss at small vegetation densities ($A_{gv} < 0.10$). Above this threshold, the impact of additional vegetation is less influential. It appears that there is a second density threshold above which the vegetation becomes more influential again, at least in the "*Populus*" scenario, at $A_{gv} = 0.40$. In the case of "*Convolvulvus*", the relation between ground cover and reduction in floodplain area loss is more gradual. In fact, it is nearly linear. However, this does not imply that the reduction in bank retreat is more uniformly spread over the reach. In the preceding sections it was already observed that both the distribution of lateral retreat and the change therein due to the presence of vegetation are spatially variable. Figure 5.43 illustrates how this spatial variability is affected by vegetation density. For each of the simulated species, the spatial distribution of lateral retreat along the right bank is shown for a low density scenario ($A_{gv} = 0.10$) and a high density scenario ($A_{gv} = 0.50$). An intermediate density scenario ($A_{gv} = 0.30$) was discussed previously (*cf.* figure 5.37). At low

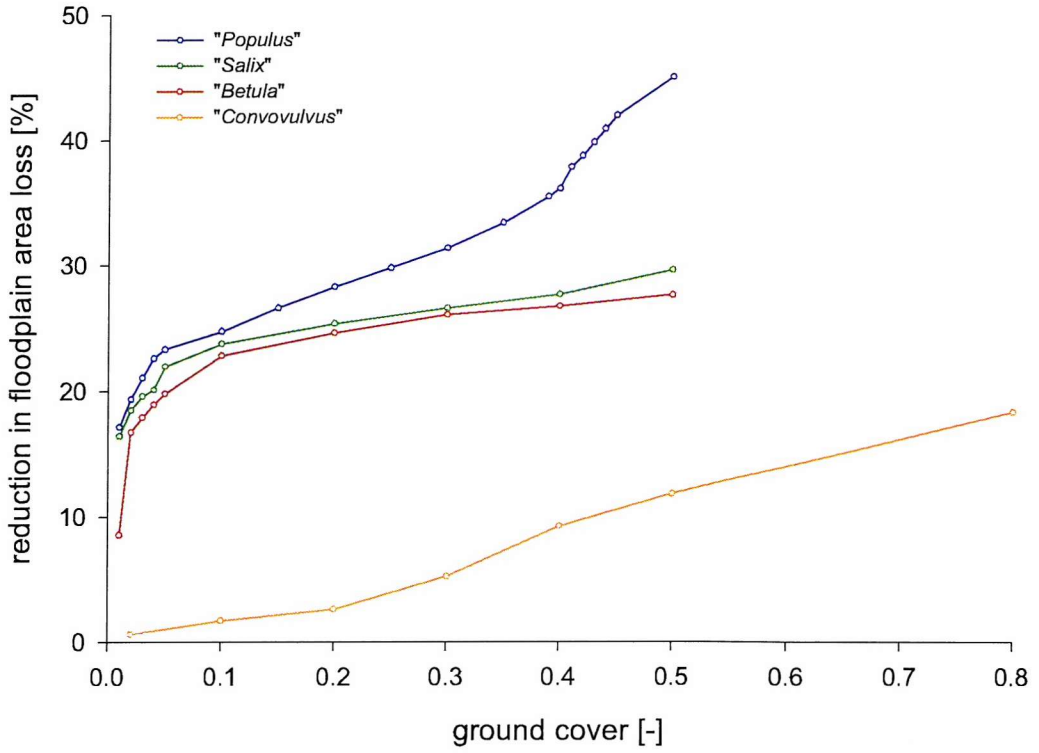

Figure 43: Effect of species density on floodplain area loss. The indicated reduction in floodplain area loss is taken relative to the floodplain area loss for unvegetated conditions.

density, "*Convolvulvus*" has a negligible impact along most of the reach, apart from a small area along the outside bends, where the double failure from the unvegetated reference case is reduced to a single one (figure 5.43A). At intermediate densities, the spatial extent of this area of reduced failure is further increased (*cf.* figure 5.37A). At high density the area is extended further still, covering most of the zone of double failures along the outside bends (figure 5.43B), while part of the bank along the inside bends is prevented from failing as well. In the scenarios with woody vegetation, all of the double failures along the outside bends simulated in the unvegetated reference case are reduced to a single failure, even at low density (figures 5.43C, 5.43E, 5.43G). The main effect of an increase in ground cover of woody species, above $A_{gv} = 0.10$, is that failures are prevented along a larger area along the inside bends (figures 5.43D, 5.43F, 5.43H), particularly for "*Populus*" (figure 5.43H).

The effects of vegetation density on the morphological evolution of the channel bed also show a clear distinction between the woody and herbaceous species. In the unvegetated reference scenario, about 40% of the bed surface is eroding, while about 60% is depositional. This ratio changes only very slightly with increasing density of "*Convolvulvus*" (figure 5.45). For woody species, however, the balance reverses into an erosion dominated channel, at least in terms of affected bed surface area, with 60% eroding and 40% deposition (figure 5.45). Nonetheless, the net erosion volume is roughly independent of both vegetation species and vegetation density (figure 5.45A). For "*Convolvulvus*" there is a slight gradual decrease in total net channel erosion, while the woody species incur a small initial decline in net erosion at low densities, followed by a stabilization at higher densities. These changes in net erosion volume are very small (up to 4% of the net eroded volume in relation to the unvegetated reference case), especially when contrasted against the changes in net deposition volume (figure 5.45B). Under a riparian cover of "*Convolvulvus*" the net deposition decreases slowly, but linearly, with increasing vegetation density, and can be reduced by values of nearly 1600 m^3 at high densities. The decline is approximately logarithmic for the woody species, where the net deposition volume can be reduced by over 5000 m^3 at high densities. The high density "*Populus*" scenario incurs the highest reduction at 5684 m^3, which is 51% less than the net deposition in the unvegetated reference scenario. As before, differences within the woody species are less pronounced than the differences between woody and herbaceous species.

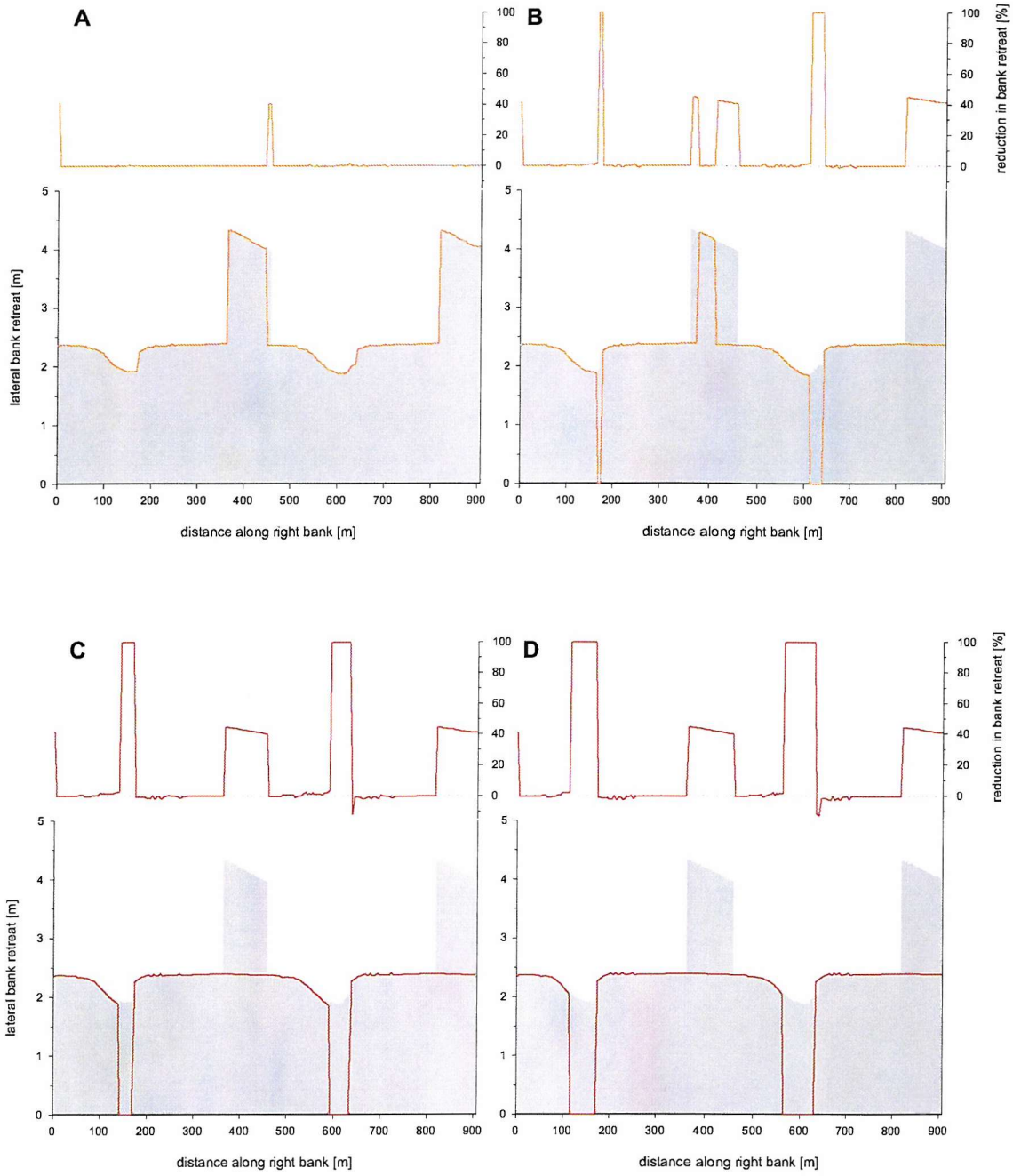

Figure 5.44: Spatial distribution of bank retreat for different species and densities (continued on next page). **A**: "*Convolvulvus*" at 10% ground cover, **B**: "*Convolvulvus*" at 50%, **C**: "*Betula*" at 10%, **D**: "*Betula*" at 50%, **E**: "*Salix*" at 10%, **F**: "*Salix*" at 50%, **G**: "*Populus*" at 10%, **H**: "*Populus*" at 50%. The lower part of each graph shows the spatial distribution of bank retreat in the vegetation scenario (line) and in the unvegetated reference scenario (gray background; *cf.* figure 5.33). The upper part of each graph shows the reduction in lateral bank retreat, relative to the unvegetated scenario. The dotted grey line denotes 0% change. Only the right bank is depicted; bank retreat along the left bank follows a similar pattern, although displaced over half a wavelength.

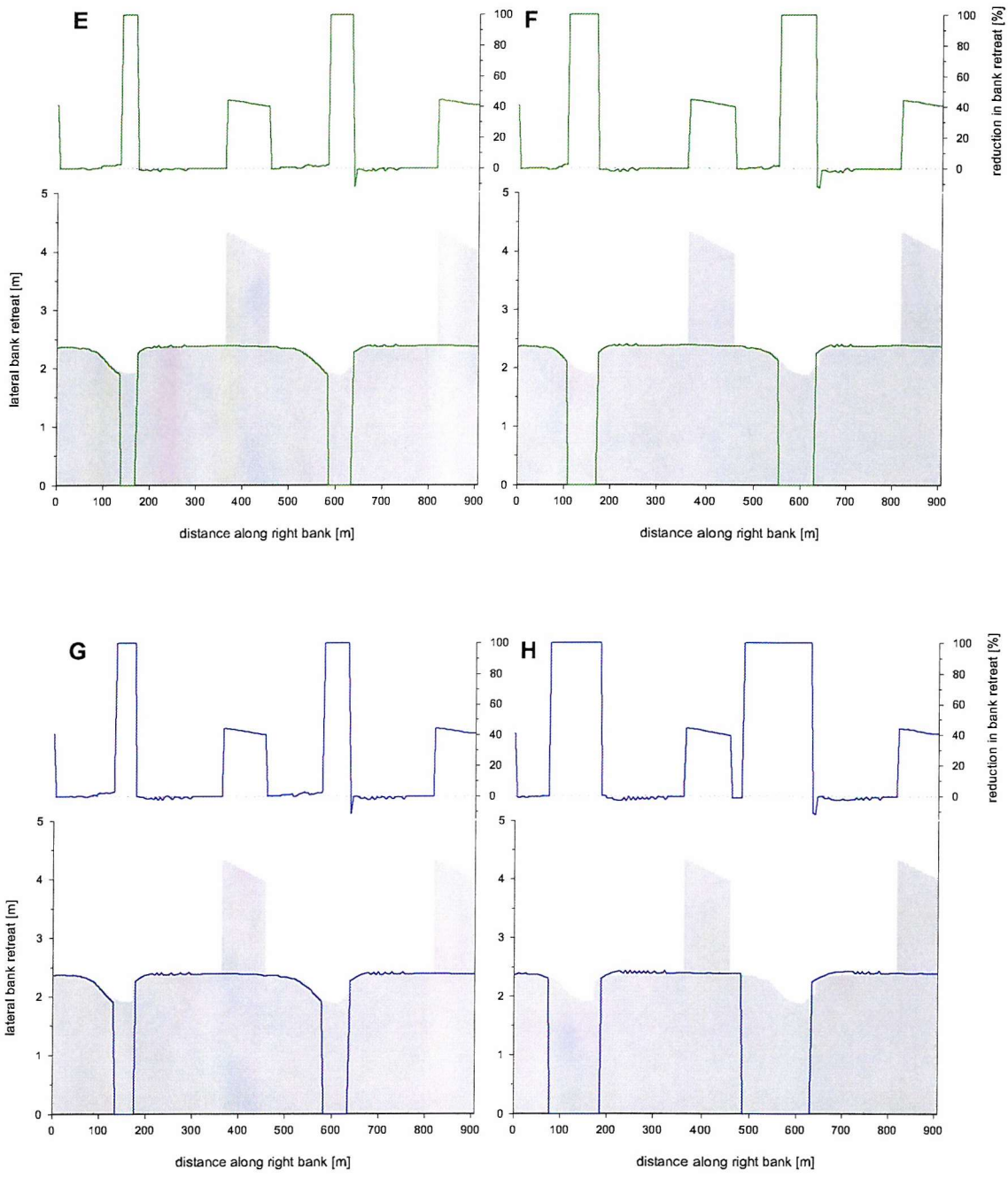

Figure 5.43 (continued): Spatial distribution of bank retreat for different species and densities.

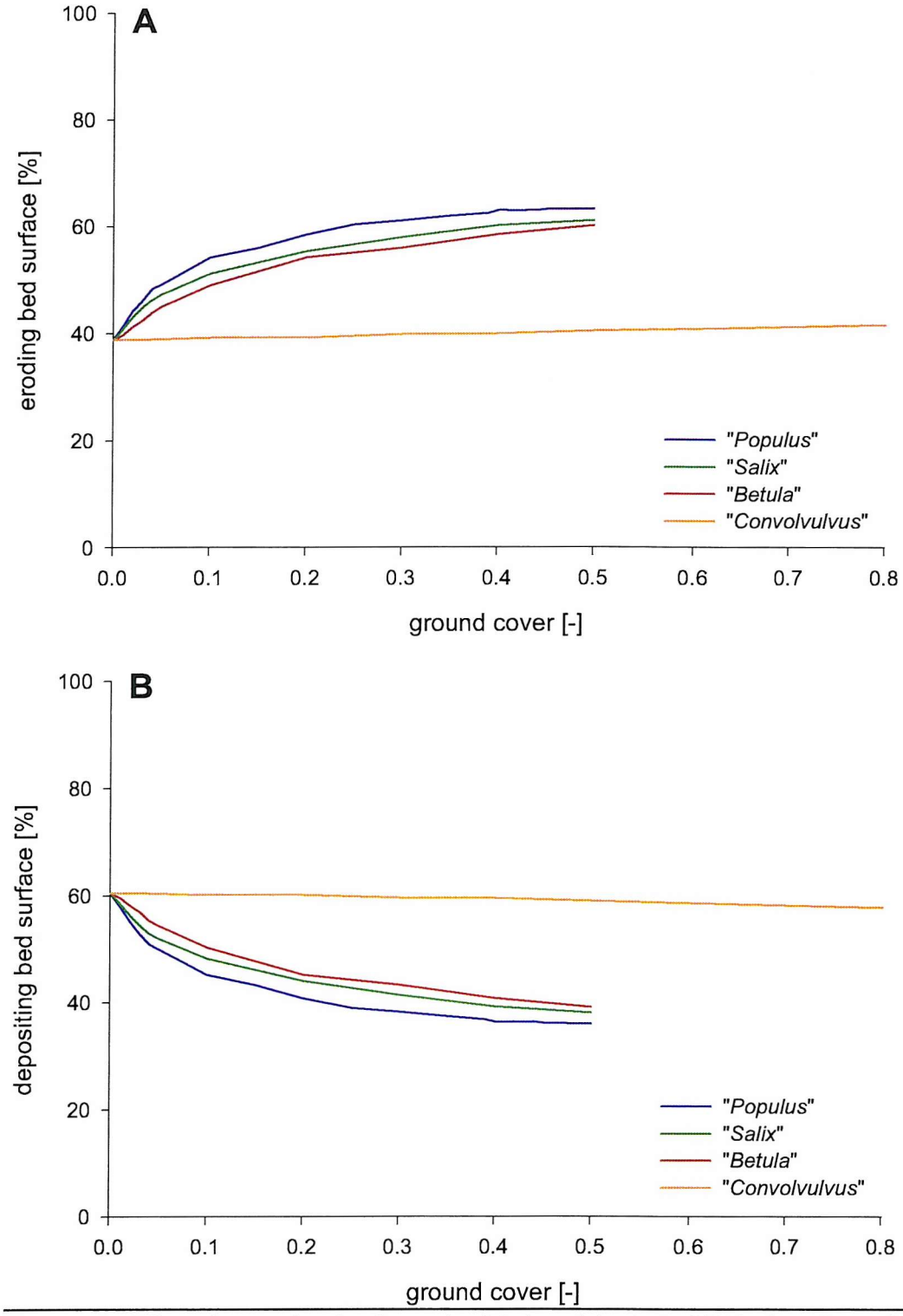

Figure 5.45: Effect of vegetation density on simulated spatial extent of (**A**) bed erosion and (**B**) bed deposition. The indicators on the Y-axes denote the relative bed surface area with net erosion (**A**) or net deposition (**B**) at the end of the simulations. This is represented as a percentage of total bed surface area. Note: the total bed surface area is slightly different in each simulation, due to the changes in lateral erosion.

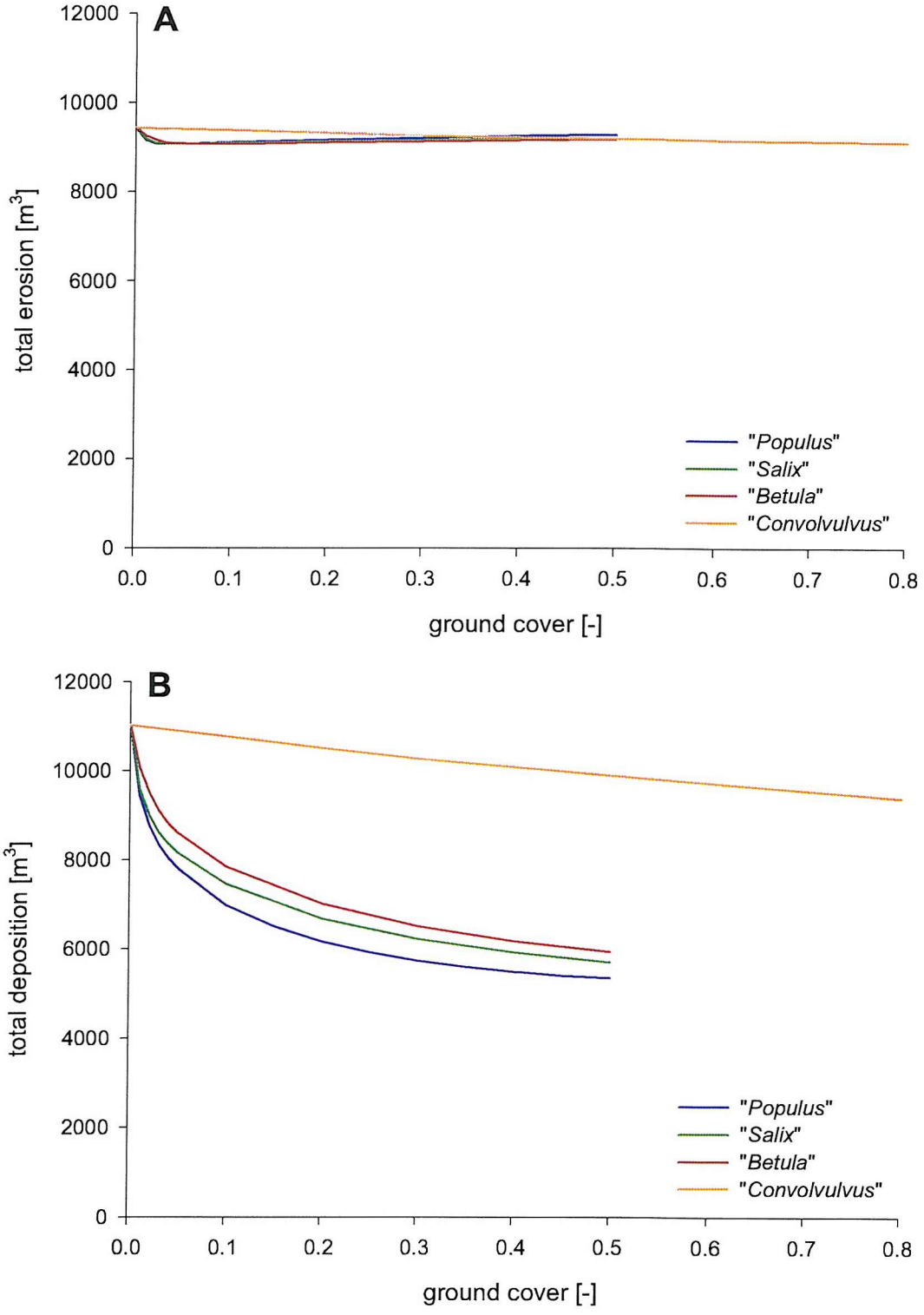

Figure 5.46: Effect of vegetation density on (**A**) total erosion and (**B**) total deposition volumes.

The differences in volumes of eroded and deposited sediments, and the differences in channel bed area affected by them, also manifest themselves in the at-a-point incision and deposition. The maximal depth of bed scour decreases slightly for the woody species as the vegetation density increases (figure 5.47A). At high density the incision is reduced by between 10% to 15% for the woody species "*Betula*", "*Populus*" and "*Salix*". The relation between density and maximal incision is more irregular for the "*Convolvulvus*" scenarios (figure 5.47A). This irregularity is, in fact, caused by anomalous behaviour at a single outer bend grid point, slightly beyond the bend apex, where the bed scour is increased with respect to bed scour in the unvegetated scenario. It is possible that this reflects a true physical change of the channel bed, *i.e.* a relatively deep, local scouring of the bed. However, the fact that the erratic behaviour occurs at a single grid point suggests an isolated instance of numerical instability as a more likely explanation. Moreover, the average erosion over the eroding surface area also decreases gradually with increasing vegetation density, as for the other species (not depicted). The maximal bed aggradation is less inconsistent, with both the herbaceous and woody species showing an inverse relation with vegetation density (figure 5.47B). The relation is similar to that between the deposited sediment volume and vegetation density (*cf.* figure 5.45B), *i.e.* linear for "*Convolvulvus*" and inverse logarithmic for the woody species. The total reduction in maximal aggradation height, relative to the maximal aggradation height under unvegetated conditions, reaches 30% to 33% for the high density scenarios of "*Betula*", "*Populus*" and "*Salix*", and up to 8% for "*Convolvulvus*".

Finally, the presence of vegetation has an important impact on the spatial positioning of the bed's topographical features. Specifically, the location of the point bars and thalweg are affected. Although these features still occur in roughly the same place as in the unvegetated reach, *i.e.* slightly beyond the apex of the bend, their exact positions depend on the vegetation species and density. This is illustrated in figure 5.48, which shows a longitudinal profile of the channel's undulating bed topography near the right bank for the unvegetated reference scenario and for two densities of "*Populus*". Clearly, the bed topography extrema of the two vegetated scenarios are displaced with respect to the extrema of the unvegetated scenario. Effectively, the phase-shift between the channel planform shape and the bed topography features becomes smaller with a stand of "*Populus*" on the channel banks. However, there is little difference between a low density cover ($A_{gv} = 0.1$) and a high density cover ($A_{gv} = 0.5$). Note also that the amplitude of the bed undulation decreases with increasing vegetation density, as observed in the preceding section. The relation between vegetation density and the magnitude of the phase-shift is shown in figure 5.49, for each of

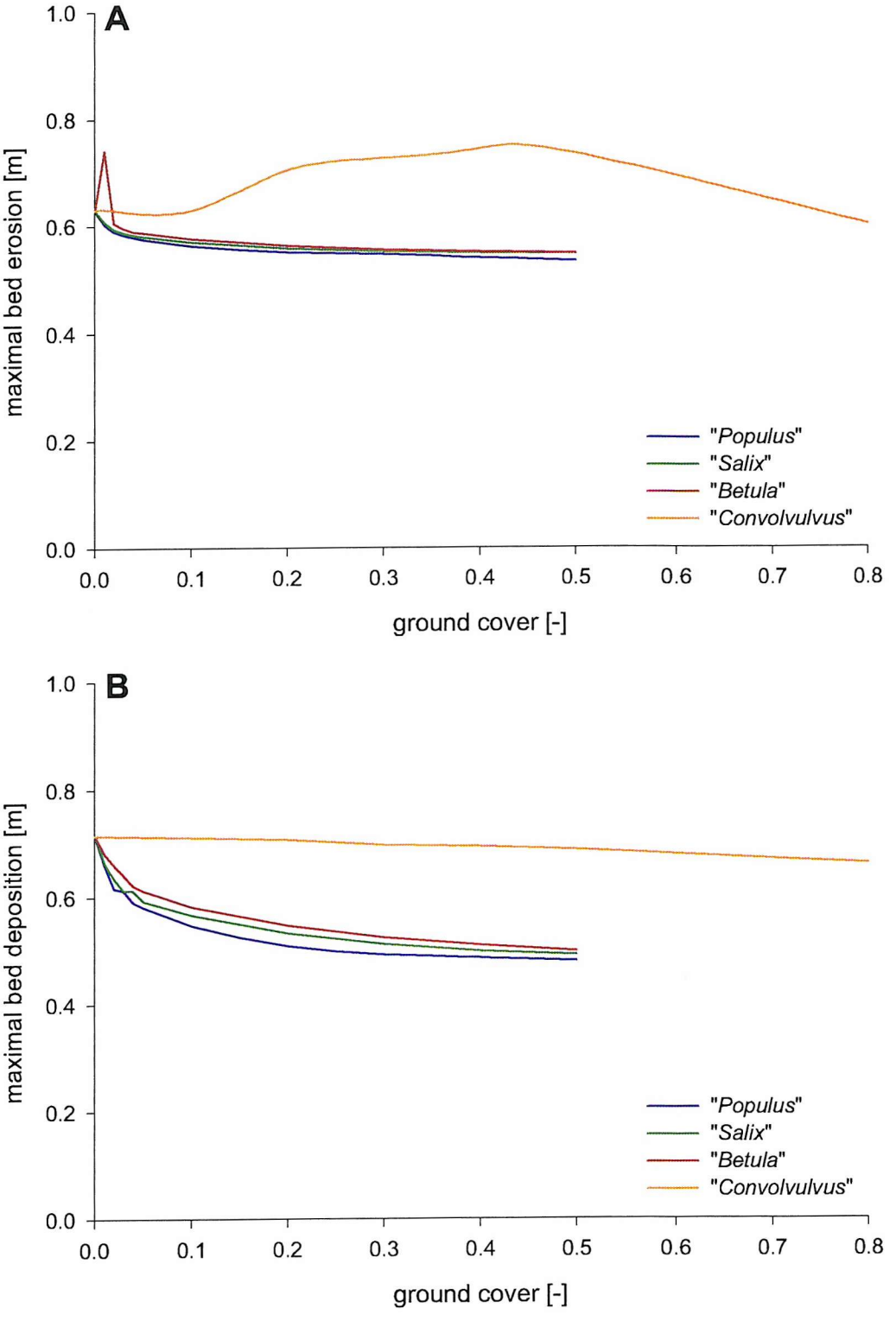

Figure 5.47: Effect of vegetation density on (**A**) maximal channel incision and (**B**) maximal channel aggradation.

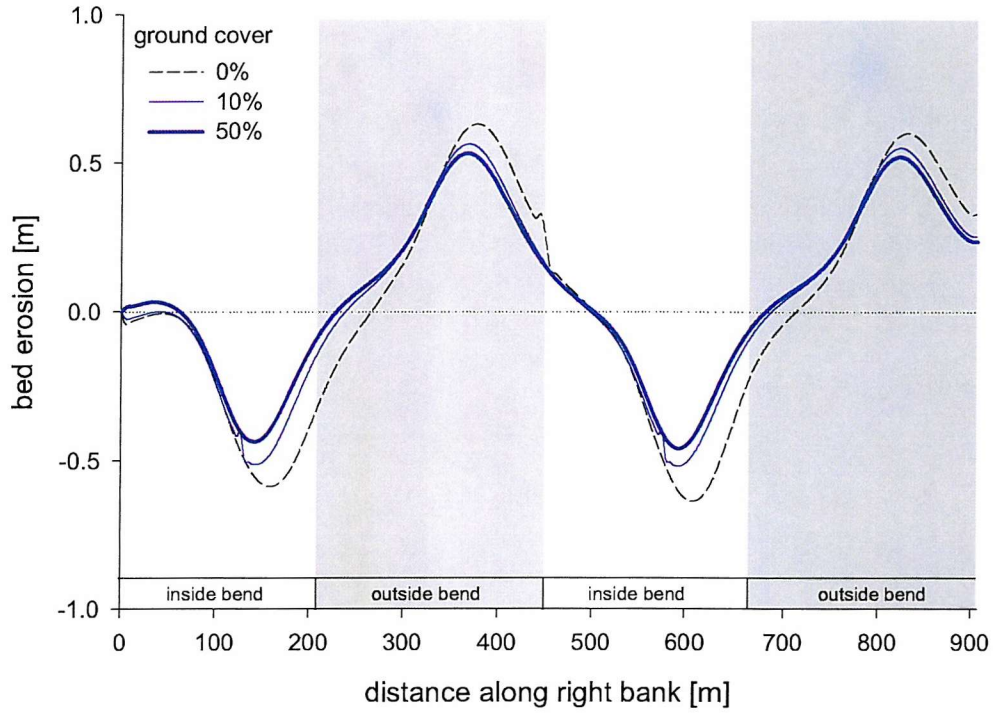

Figure 5.48: Changes in bed undulation for three different vegetation densities: high density (50% ground cover), low density (10% ground cover), unvegetated (0% ground cover). The graph shown here depicts data from the "*Populus*" scenarios. Similar results are obtained for "*Betula*" and "*Salix*".

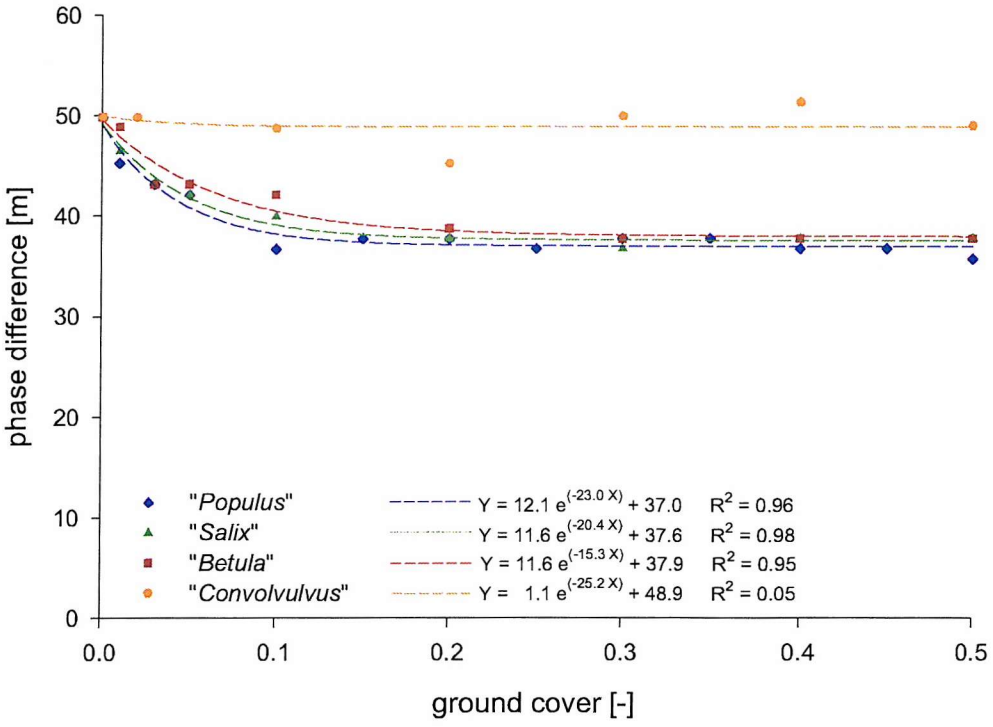

Figure 5.49: Effect of vegetation density on the magnitude of the phase shift between channel planform shape and bed topography undulation. Values from the modelled scenarios are indicated through dots. An exponential regression, shown as a dashed line, is fitted through the data points for each species.

the species simulated. For the woody species there is a strong initial decline in the phase shift, at low vegetation densities ($A_{gv} < 0.10$), after which a phase-shift equilibrium is established. "*Convolvulvus*", on the other hand, does not have a consistent impact on the phase-shift. This is not entirely surprising, as "*Convolvulvus*" also has a much lower impact on the quantitative indices of sediment erosion and deposition. Nonetheless, there is some variability in phase shift at different densities, although this does not appear to be consistent and is mostly due to the irregular occurrence of localized scour at a single grid point (see above).

5.4.6. Discussion

The application of the fully coupled MRIPA model to idealized scenarios with different vegetation covers, both in terms of species and density, allows the inference of some generalized conclusions about the impact of specific types of riparian vegetation on channel morphology. Some of these generalizations are predictable and in accordance with expected behaviour, while other aspects are more surprising.

First, it can be seen that the presence of riparian vegetation may have a large impact on river bank erosion and channel migration. In terms of reducing bank retreat, the most striking result is the magnitude of the impact of the simulated vegetation in the scenarios investigated here. Floodplain area loss is significantly reduced in most of the scenarios, depending on vegetation density. At high vegetation density ($A_{gv} > 0.5$) a reduction of up to 50% is observed for "*Populus*", and even at low vegetation density ($A_{gv} = 0.05$) each of the simulated woody species achieves a 20% reduction in floodplain area loss (*cf.* figure 5.43). This is in stark contrast to the results obtained from the stand-alone geotechnical analysis (section 5.3), where the impact of simulated vegetation on the factor of safety was generally found to be less than 5%, even in high density scenarios. Thus, for the idealized meandering channel used in these simulations, bank stability appears to benefit significantly from the role of vegetation in enhancing hydraulic roughness and increasing the critical shear stress for fluvial entrainment of bank material.

Another aspect of the impact of riparian vegetation on bank retreat is its spatial variability. Although the channel bank geometry is uniform throughout the channel at the start of each simulation, a spatially variable pattern of bank retreat emerges as a consequence

of interactions between geotechnical mass failures and near-bank hydraulic processes in the sequence of simulated bends. The effects of vegetation upon these processes are, themselves, also spatially variable. More specifically, three zones of vegetation impact can be identified: the inner bend, the outer bend, and the cross-over reaches in between. In the cross-over sections, the vegetation does not appear to have any significant impact on bank retreat. Along the inner bend, the presence of simulated vegetation evidently limits the occurrence of erosion, at least in the simulations undertaken herein. In the absence of vegetation, the sections along the inner bend fail because of the lateral erosion of the bank toe (*cf.* section 5.4.3; figure 5.35). In all of the woody vegetation scenarios, as well as in the high density "*Convolvulvus*" scenario, this lateral retreat is reduced and bank failure can, therefore, be avoided (*cf.* figures 5.37 and 5.43). More important, however, is the impact of vegetation along the outer bend, where lateral retreat is maximal under unvegetated conditions. Here, the bank retreat can be significantly reduced, by up to 50% (*cf.* figures 5.37 and 5.43). It appears that the woody species simulated herein are much more effective in limiting bank retreat than the simulated herbaceous species. This is not entirely surprising since the woody species also have the largest geotechnical impact (section 5.3). However, it is worth noting that the reduction in lateral erosion along the outer bend is achieved at relatively low densities ($A_{gv} = 0.10$) of woody vegetation, and that additional increases in vegetation density do not result in significant further reduction of bank failures along the outer bank. Finally, it should be noted that in some localized parts of the channel, the bank retreat actually increases when riparian vegetation is present. This occurs mostly at the upstream end of the cross-over reaches, just downstream of the point bar in the preceding bend (*cf.* figures 5.37 and 5.43). As such, it is most likely a consequence of alterations in the patterns of flow and shear stress as a result of the non-failure of the bank along the inner bend. Although this is only a minor effect in quantitative terms, it has two important implications. First, it demonstrates that vegetation, as a tool for channel stabilization, is not uniquely beneficial. Second, it highlights the importance of interactions between bank and flow processes, as the local effects of vegetation at one point are determined not only by the vegetation and channel properties at that point, but also by the impact of vegetation-induced changes in sediment delivery and flow alteration upstream.

It should be noted that the effect of the simulated vegetation on bank retreat is likely to under-estimate the vegetation's true impact, due to the non-dynamic nature of the vegetation model. Although MRIPA does remove vegetation on banks subjected to mass failure, it does not model vegetation dynamics such as colonization or plant growth. When a

bank fails along part of the reach, the vegetation on the failed block is removed; and although the floodplain vegetation beyond the failure plane remains in place, the bank surface is unvegetated for the remainder of the simulation. Thus, subsequent to a failure, the impact of vegetation is restricted to the geotechnical aspects of the remaining vegetation on the floodplain, since there is no new vegetation colonizing the bank face to interact with the flow or the soil. It is, therefore, likely that a more advanced model, which incorporates dynamic vegetation would show a higher geomorphological impact. Although this affects all vegetation species, it particularly relevant for herbaceous species, whose morphological impact is largely dependent on interaction with the flow.

The second major conclusion derived from the simulations undertaken herein is that riparian vegetation can affect the channel bed morphology. In general, the effect of vegetation on bed topography is such that the channel morphology becomes more uniform throughout the reach, *i.e.* with less undulation and shallower transverse slopes. This is a significant observation, in that it is frequently argued that riparian vegetation can enhance in-channel habitat diversity (e.g. Newson and Newson, 2000; Montgomery, 1997). However, the results from the simulations performed herein suggest that at least some aspects of physical habitat diversity on the channel bed may be reduced when riparian vegetation is introduced. Of course, the simulations reveal nothing about the impact of vegetation-induced shading, nor about the effects of large woody debris sourced from the riparian vegetation, both of which are important controls on in-channel habitat diversity (Schlosser, 1991). Nonetheless, in the simulated scenarios, riparian vegetation evidently causes a spatial redistribution of sediment erosion and deposition over the channel bed, which tends to homogenize the bed topography. The magnitude of this redistribution is dependent on the density of the cover and specific biophysical parameters. In general, more parts of the bed are subjected to erosion and fewer parts to deposition, particularly for the woody species simulated herein. However, the amplitude of bed forms, *i.e.* point bar height and pool depth, decreases. The total volumetric erosion over the entire reach appears to be independent of riparian vegetation (*cf.* figure 5.45A). The net volumetric deposition, however, is markedly reduced as vegetation density increases (*cf.* figure 5.45B). At first glance, this result seems counter-intuitive in that vegetation is generally considered to promote sediment deposition through its effect on hydraulic roughness. However, the reduced deposition is not a direct consequence of vegetation effects on flow and sediment transport. Rather, it results from a smaller lateral input of sediments due to the impact of vegetation on bank mass wasting. As the banks fail less frequently and less floodplain is eroded, fewer bank-derived sediments are

delivered into the channel to be transported and/or deposited on the bed. Although this may reflect the specific circumstances of the reach simulated here, it highlights, once again, the importance of interactions between bank and flow processes. Flow hydraulics and sediment transport do not only influence bank erosion processes (see above), but are influenced by them as well. Thus, riparian vegetation is seen to affect the morphological evolution of the channel bed in meandering alluvial channels in two ways: directly, through the roughness effects on flow hydraulics and sediment transport; and indirectly, through its impact on bank failure processes. Likewise, vegetation also affects channel planform evolution directly, through its impacts on geotechnical mass wasting; and indirectly, through its impact on flow hydraulics and sediment transport.

The third major conclusion derived from the preceding analysis, is that the impacts on bank erosion and bed morphology are observed, to a greater or lesser extent, for all the species simulated herein, including the herbaceous "*Convolvulvus*". This is in contrast with results derived from the stand-alone geotechnical bank stability analysis (section 5.3), where the impact of "*Convolvulvus*" is negligible due to the limited interaction of its root system with the failure plane. Hence, any impacts on channel morphology of this species must be attributed to the effects of its hydraulic roughness and its influence on critical shear stress for fluvial entrainment of bank material. Nonetheless, there is a distinct difference between the impacts associated with the woody and herbaceous species simulated herein, with the former having a much larger influence on morphological processes than the latter. As the values of both the critical shear modifier, k_τ, and the drag coefficient, C_d, are highest for the herbaceous species (*cf.* table 5.15), this must be attributed to either the increased roughness of emergent vegetation, or the effects of woody vegetation on bank stability. It should be noted that the low overall impact of herbaceous species is partly due to the non-dynamic nature of the simulated vegetation (see above).

For the idealized channel simulated herein, the differences between the simulated woody species are less pronounced than their difference with simulated herbaceous species. Nonetheless, "*Populus*" consistently has a higher impact on channel morphology, while "*Betula*" and "*Salix*" have almost identical impacts. The slightly higher impact of "*Populus*" is related to its significant effect on geotechnical bank stability as a result of its extensive root network (*cf.* table 5.15 and section 5.3). It is notable that although "*Betula*" has the highest tensile strength of the species simulated herein, its impact on floodplain area loss is less than that of "*Populus*", which has a lower tensile strength, but which has a deeper and

more extensive root network with higher average root-area-ratios. Hence, it seems that root structure is more important than root tensile strength. This is in agreement with empirical observations that most of the reinforcement comes from species with high root-area-ratios (Simon and Collinson, 2002). Nonetheless, the differences between the impacts of the woody species are small. Although no sensitivity analysis of vegetation parameterization is performed for the coupled simulations undertaken here, it is notable that the overall impact of woody vegetation is relatively independent of the species, regardless of differences in their parameterization. Thus, the geotechnical stability analysis' sensitivity to vegetation parameterization, which was highlighted in section 5.3, appears to be attenuated by the impact of vegetation on flow hydraulics.

Lastly, from the three preceding conclusions, it is clear that no single aspect of vegetation influence can be identified as being "the most important", either in reducing bank retreat or in affecting bed morphology in meandering, alluvial rivers. In some respects, the hydraulic impact of vegetation appears to have a great influence, particularly in the homogenization of the morphological impact of the woody species and in the limited impact of "*Convolvulvus*". On the other hand, the fact that the simulated woody species are dominant over "*Convolvulvus*", in spite of their lower parameters for the drag coefficient and critical shear stress (*cf.* table 5.15), emphasises the importance of the geotechnical properties of the vegetation. Thus, neither geotechnical stabilization, nor hydraulic flow diversion, nor roughness, nor soil binding can, by themselves, explain the variety and extent of morphological change incurred when vegetation is introduced into the idealized test channel. Instead, it is their combined effect that determines the evolution of the channel's planform shape as well as of its bed topography. This holistic view of vegetation functioning as a morphological agent also has implications for the interpretation of field and laboratory experiments on the impact of vegetation in fluvial systems. Virtually all preceding research has adopted an approach in which efforts have been made to isolate individual aspects or processes of the vegetation-channel interaction. The results of this study would suggest that the conclusions derived from those preceding analyses must be treated with caution when attempting to generalize the findings to geomorphological response at the reach-scale. This is another consequence of the inter-dependency of morphological processes and their interaction with riparian vegetation.

5.5. Conclusion

In this chapter the vegetation submodel has been analysed; first, as part of a stand-alone geotechnical stability analysis and, second, as part of the coupled MRIPA model. Representation of vegetation in the model requires parameterization of the biophysical properties of the modelled species. Due to a lack of adequate data this parameterization is necessarily crude. Although the results of the geotechnical sub-model are quite sensitive to changes in the parameterization, this dependency appears to be diminished in the fully coupled model. Nonetheless, it is not recommended to interpret the results of the simulations in terms of their absolute values, because of the inaccuracies involved in parameterizing the biophysical vegetation properties. However, it is possible to infer the nature of the vegetation impact on channel morphology by making qualitative comparisons between different scenarios.

The extended geotechnical analysis provides a significant improvement over most existing analyses, through the incorporation of a physically-based vegetation component. Although the modelled extent of vegetation influence on geotechnical bank stability is below expectation in quantitative terms, this can, at least partly, be attributed to the absence of vegetation suction modelling (*cf.* section 5.3.5). The adequacy of the geotechnical model is illustrated through its capacity to represent the distribution of root cohesion through the soil and its ability to correctly predict the optimal locations of vegetation along the bank profile. The ability of the fully coupled mRIPA model to simulate the interactions between flow, sediment transport, bank stability and vegetation submodels provides an additional important improvement over existing models. The mRIPA model is able to replicate realistic modes of lateral channel change and bed morphology evolution, such as migration and extension of meanders and the development of thalwegs and point bars, and the effects of vegetation thereon.

Overall, the model appears to be capable of representing the morphological effects of riparian vegetation, at least in qualitative terms. The potential of the model to study vegetation-channel interactions was illustrated in a series of simulations representing a range of different vegetation scenarios. This exercise provided insights into the role of vegetation as a geomorphological agent and in the applicability of vegetation as a management tool in erosion control projects.

The central conclusion from a geomorphological point of view is that, for the idealized meandering, alluvial channel considered herein, the impact of riparian vegetation on bank erosion and bed morphology change cannot be isolated. In any channel where riparian vegetation interacts with the flow and the banks, it influences both processes simultaneously. Moreover, both morphological processes influence each other as well. That is, bank erosion processes affect the evolution of the channel bed and, vice versa, bed morphology affects the bank erosion processes. These interactions result in a complex spatial and temporal variability of the morphological evolution of a river channel. This complexity cannot be captured in stand-alone geotechnical stability analyses, nor in channel evolution models that do not account for discontinuous bank erosion processes. This, again, highlights one of the key features of MRIPA, namely the ability to couple a two-dimensional flow and sediment transport model with a physically-based geotechnical bank stability analysis. Closely related is a second observation that no single aspect of vegetation influence can be identified as being "the most important" in reducing bank retreat nor in affecting bed morphology of alluvial, meandering channels. Instead, a holistic view of the morphological impact of vegetation emerges, where geotechnical, hydraulic and sedimentological effects of vegetation cannot easily be isolated.

From a river management perspective, it appears that woody species are more efficient than herbaceous species in reducing lateral erosion in meandering alluvial rivers. Although the differences between the woody species simulated herein are relative small, "*Populus*" consistently has the greatest beneficial impact on bank stability, because of its extensive root network. The simulations also show that the impact of vegetation is greatest on shallow banks consisting of weakly cohesive material. It must be noted that the lower failure rate of the banks will result in a reduced input of sediments into the channel, which can significantly alter the distribution of erosion and deposition of the channel bed and which will thereby affect the morphological evolution of the channel. Thus, reduced lateral retreat at one point along the reach may cause additional bank erosion at another. Therefore, although the overall impact of vegetation on bank retreat is beneficial when viewed over the entire reach, it may be detrimental at localized areas along the reach.

These observations and conclusions are based on simulations in an idealized, mathematical channel. In the next chapter, the model will be applied to a natural river reach, to check if the generalized conclusions are still valid in a natural environment.

Chapter 6
Model Application

6.1. Introduction

In this chapter, parts of which are also presented in Van de Wiel and Darby (in press), the model is applied to a natural, meandering, river. The channel selected for this exercise is a reach of Goodwin Creek, Mississippi. This is the same reach as used previously in the validation of the model (section 4.4). Here, the fully coupled MRIPA model is used to investigate how the introduction of vegetation would affect the morphological evolution of this reach. To achieve this aim, a series of numerical experiments is performed. In total, 28 scenarios are simulated: 27 vegetation scenarios, and a control scenario without vegetation. The control scenario serves as a base reference with which the other simulations can be compared. Both the question and the approach are similar to the analysis of section 5.4, where the impact of vegetation on an idealized sinuous channel was studied. However, there are three major differences. First, the geometry of the natural channel is more irregular, both in planform and bed topography. Second, the physical properties of the banks are different, particularly the cohesion of the bank sediment. Finally, the duration of the simulated events is much longer in the current analysis. As a consequence of these differences, the analysis described in this chapter provides an opportunity to check – and potentially generalize – the conclusions of section 5.4.

6.2. Experiment setup

All simulations reported in this chapter are undertaken on a short reach of Goodwin Creek, Mississippi, USA (figure 6.1A; also see section 4.4.1 and figure 4.27 for a description of the reach and its location). Many elements of the simulation setup are identical to those of the validation exercise (section 4.4). The same 451-node grid is used to represent the initial channel (figure 6.1B), which, as before, corresponds to the November 1982 channel topography (figure 6.1C). Simulations are run for a 5.5 year period, ending in May 1988.

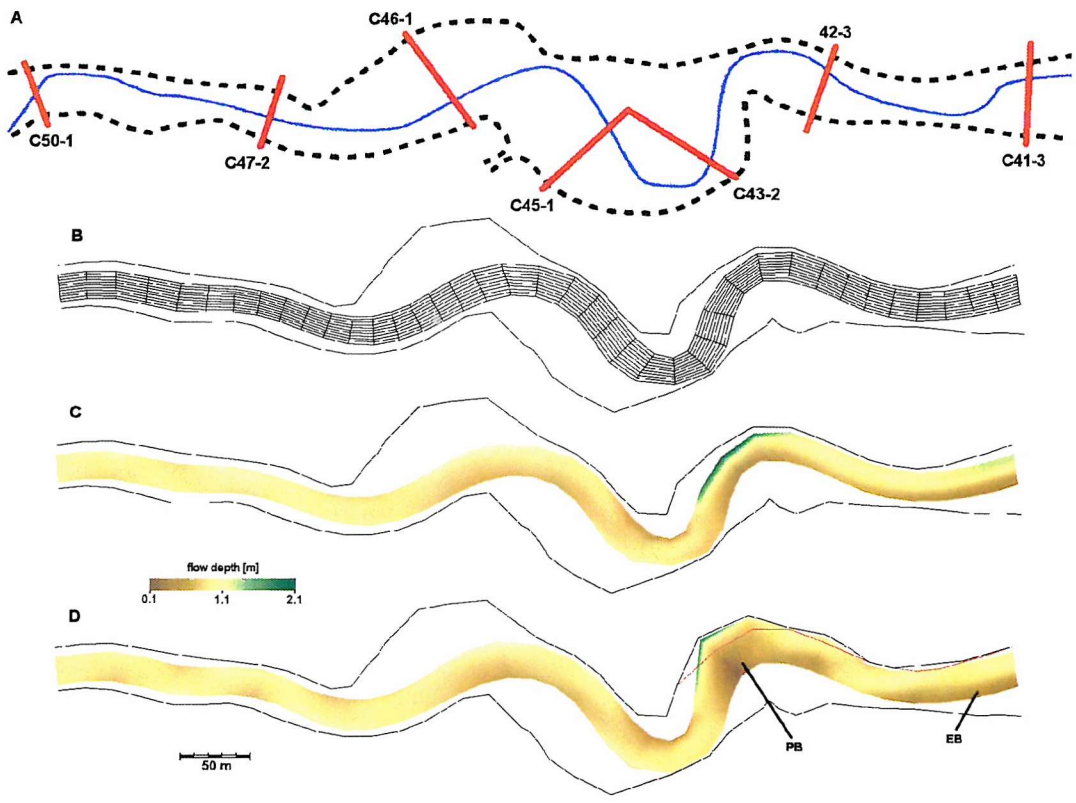

Figure 6.1: Goodwin Creek study reach. **A**: Schematic representation of the channel planform (Murphey and Grissinger, 1985), using an established numbering system to identify the monitored cross-sections (marked in red). **B**: Numerical grid of the channel bed at the start of the simulations; the black lines on either side of the channel indicate the location of the bank tops. **C**: Initial bed topography, based on the 1982 channel survey (Murphey and Grissinger, 1985). **D**: Simulated final bed topography (1988) for the unvegetated control scenario. The initial bank position is superimposed (thin red line) for reference. The markings **PB** and **EB** respectively indicate the position of the large point bar and the elongated bar, as referred to in the text. Flow direction is from left to right.

The values of the physical, numerical and calibrated parameters are also the same as in the validation exercise (*cf.* tables 4.10, 4.11 and 4.12), with two exceptions: the critical shear stress of the bank material, $\tau_{B,c}$, and the erodibility coefficient, k_B (table 6.1). For the purpose of model validation, these parameters were set in accordance with the calibrated values from the laboratory experiments (*cf.* section 4.4.2). However, this does not necessarily generate optimal agreement with observed channel changes. Indeed, it is found that by altering these two parameters, the modelled channel change provides a slightly better agreement with observed data (see below).

A control scenario, without riparian vegetation, is run to provide a base reference for the vegetation scenarios. The simulated final morphology (1988) of this reference scenario is depicted in figure 6.1D. Although there are some small point bars in the upper parts of the reach, the major topographical features are located in the lower part of the reach. Most striking of these are a well-defined point bar (PB) along the right bank, between cross-section C43-2 and C42-3 (*cf.* figure 6.1A for cross-section locations), the associated thalweg along the left bank, and an elongated bar (EB) near the right bank between cross-sections C42-3 and C41-3.

As a consequence of changing the two bank erosion parameters, the simulated bank erosion in the control scenario corresponds better to the observed data, particularly towards the downstream end of the reach (figure 6.2). It is possible that further improvement could be made by calibrating the flow parameters as well. However, a full calibration of the model is not attempted here, and the setup used herein only differs from the validation exercise in the two mentioned parameters. Although it is recognized that there are still some deficiencies in the model simulation relative to the observed data, it is believed that the general pattern of simulated bed topography and bank erosion is broadly consistent with observations (also *cf.* section 4.4). It is, therefore, appropriate to use the Goodwin Creek simulation as a base reference for qualitative comparisons of different vegetation scenarios.

From a river management perspective, two aspects of vegetation are readily available for consideration in any bioengineering design: species and density. These two aspects of vegetation have, therefore, been selected as the variable parameters for the numerical simulations undertaken herein.

Table 6.1: Redefined setup parameters.

parameter	symbol	value in validation	current value
critical shear stress of bank material [Pa]	$\tau_{B,c}$	20.0	17.5
coefficient in fluvial bank erosion equation [-]	k_b	1×10^{-4}	1×10^{-6}

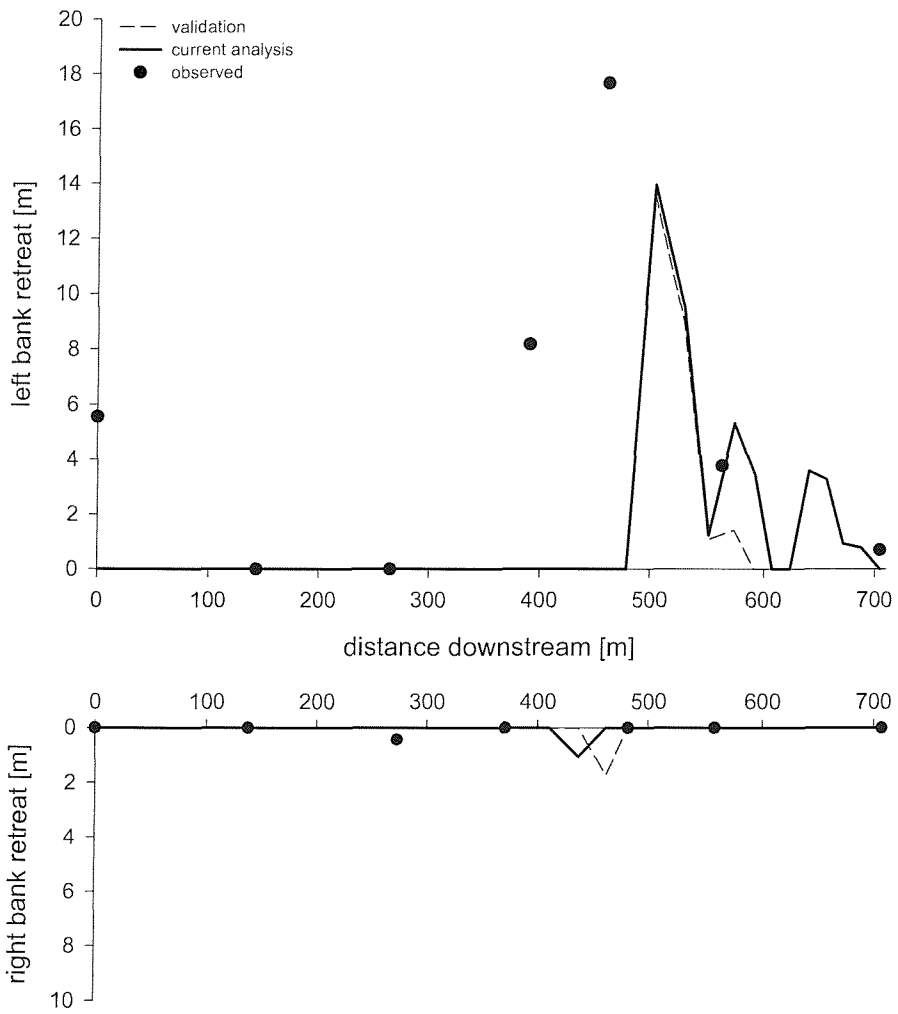

Figure 6.2: Modelled bank retreat in the unvegetated control scenario and the validation exercise (*cf.* figure 4.31), compared with observed bank retreat, along the left bank (top) and right bank (bottom).

A total of 27 vegetation scenarios are simulated (table 6.2), comprising four hypothetical species ("*Populus*", "*Salix*", "*Betula*" and "*Convolvulvus*"; *cf.* section 5.2 for details of their biophysical properties) and a range of densities, representing sparse ($A_{gv} = 0.05$) to very dense ground covers. For woody species a very dense cover is specified as 50% ground cover ($A_{gv} = 0.50$), which is an effective upper limit; for the herbaceous species, "*Convolvulvus*", the maximal simulated density is 80% ground cover ($A_{gv} = 0.80$). The fact that there is a difference between the various densities is more relevant than their actual values. This reinforces the idea that the numerical experiments presented in this study do not attempt to represent real simulations of vegetation in Goodwin Creek, but rather are a series of hypothetical scenarios to investigate the impact of vegetation parameters on bed topography and planform change in a meandering river with riparian trees. It is worth repeating that when part of the riverbank fails, the vegetation on the failure block is removed instantly, leaving the bank face bare for the remainder of the simulation (*cf.* section 5.4.6).

Table 6.2: setup of vegetation density scenarios.

ground cover [-]	*"Populus"*	*"Salix"*	*"Betula"*	*"Convolvulvus"*
0.05	✓	✓	✓	✓
0.10	✓	✓	✓	✓
0.20	✓	✓	✓	✓
0.30	✓	✓	✓	✓
0.40	✓	✓	✓	✓
0.50	✓	✓	✓	✓
0.60				✓
0.70				✓
0.80				✓

6.3. Results

Table 6.3 summarizes the morphological characteristics of the channel at the end of the simulation, for all the scenarios investigated herein. The following sub-sections describe the results in more detail, in terms of both evolution of bed topography and channel planform change. The connections between these two morphological characteristics of the channel, and their relation to parameters of the simulated vegetation, are discussed in section 6.4, as are the similarities and differences with the analysis of section 5.4.

Table 6.3: Overview of results.

vegetation		bed change		planform change	
species	ground cover [-]	maximal scour [m]	maximal deposition [m]	maximal bank retreat [m]	floodplain area loss [m^2]
none	n/a	0.30	0.66	13.9	745
"Betula"	0.05	0.49	0.78	12.2	715
	0.10	0.37	0.67	12.2	646
	0.20	0.31	0.61	12.1	609
	0.30	0.38	0.56	8.8	458
	0.40	0.40	0.55	8.7	406
	0.50	0.42	0.52	7.8	345
"Salix"	0.05	0.37	0.68	12.2	681
	0.10	0.35	0.62	12.2	611
	0.20	0.43	0.58	8.8	410
	0.30	0.43	0.51	7.8	348
	0.40	0.44	0.47	7.0	316
	0.50	0.46	0.44	6.0	248
"Populus"	0.05	0.35	0.65	12.3	680
	0.10	0.27	0.63	12.2	613
	0.20	0.38	0.58	8.9	380
	0.30	0.43	0.47	7.2	320
	0.40	0.46	0.46	6.2	253
	0.50	0.48	0.41	5.4	222
"Convolvulus"	0.05	0.30	0.66	13.9	745
	0.10	0.29	0.66	13.9	745
	0.20	0.30	0.66	13.9	745
	0.30	0.30	0.66	13.9	745
	0.40	0.30	0.66	13.9	744
	0.50	0.28	0.67	13.9	745
	0.60	0.29	0.66	12.3	717
	0.70	0.29	0.66	12.3	683
	0.80	0.30	0.66	12.3	683

6.3.1. Bed topography change

From table 6.3 it appears that the maximal erosion and deposition of the channel bed is most affected in the scenarios with woody species, particularly at high ground-cover densities. This is further illustrated in figures 6.3 to 6.6, not only for maximal erosion and deposition of the bed (figure 6.3), but also for the average erosion and deposition (figure 6.4), the spatial extent of erosion and deposition (figure 6.5), and the total volume of sediment eroded and deposited (figure 6.6). The definitions of these indicators are given in section 5.4.2 (equations 5.3 to 5.10).

From figures 6.3 to 6.6, it is evident that the simulated herbaceous species has little impact on the morphological evolution of the bed. The values of each of the indicators is constant for "*Convolvulvus*", irrespective of the density of the cover. The simulated woody species, on the other hand, do induce change in the channel bed topography. Generally, maximal erosion depth increases and maximal deposition height decreases with increasing ground cover density (figure 6.3). However, this trend is disrupted at low vegetation densities ($A_{gv} < 0.15$), particularly for "*Betula*", where the maximal erosion depth and maximal deposition height are greatest at $A_{gv} = 0.05$. The reason for the increased amplitude of the bed forms in this scenario is not immediately obvious, and is likely related to complex spatial interactions between flow pattern, sediment transport and riparian vegetation (section 6.4). Average erosion and deposition follow similar overall trends, respectively increasing and decreasing with vegetation density, albeit less pronounced and with more irregularities (figure 6.4). The spatial extent of the erosion and deposition, however, is significantly affected by the presence of vegetation (figure 6.5). As the vegetation density increases, the relative bed surface area over which erosion occurs, increases from 45% in the unvegetated reference scenario, to over 70% at medium to high vegetation densities ($A_{gv} > 0.3$). As a consequence, the relative bed surface area over which deposition occurs, decreases, from 52% in the unvegetated reference scenario to less than 30% at medium to high vegetation densities. Since the average erosion depth and the spatial extent of the erosion increase with ground cover density, it is expected that the total volume of eroded sediment also increases. Likewise, it is expected that the total volume of deposited sediment decreases. Figure 6.6 shows that this indeed is the case. The volume of eroded sediment is nearly doubled in the high density woody vegetation scenarios ($A_{gv} = 0.5$): 842 m^3, 928 m^3 and 947 m^3 respectively for "*Betula*", "*Salix*" and "*Populus*", compared with 447 m^3 in the unvegetated reference scenario (figure 6.6A). The volume of deposited sediment, on the other hand, is reduced by

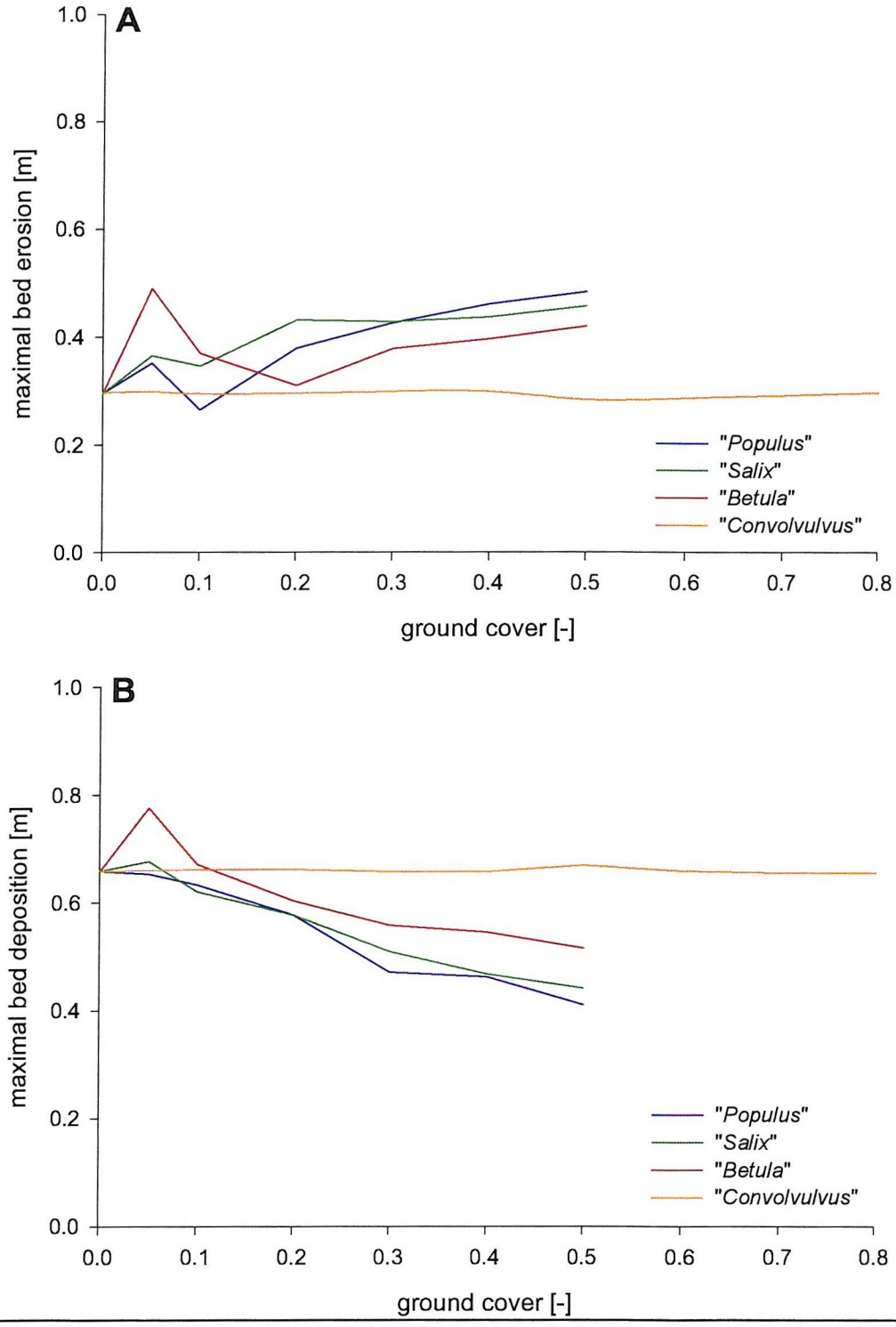

Figure 6.3: Effect of vegetation density on (**A**) maximal bed erosion and (**B**) maximal bed deposition.

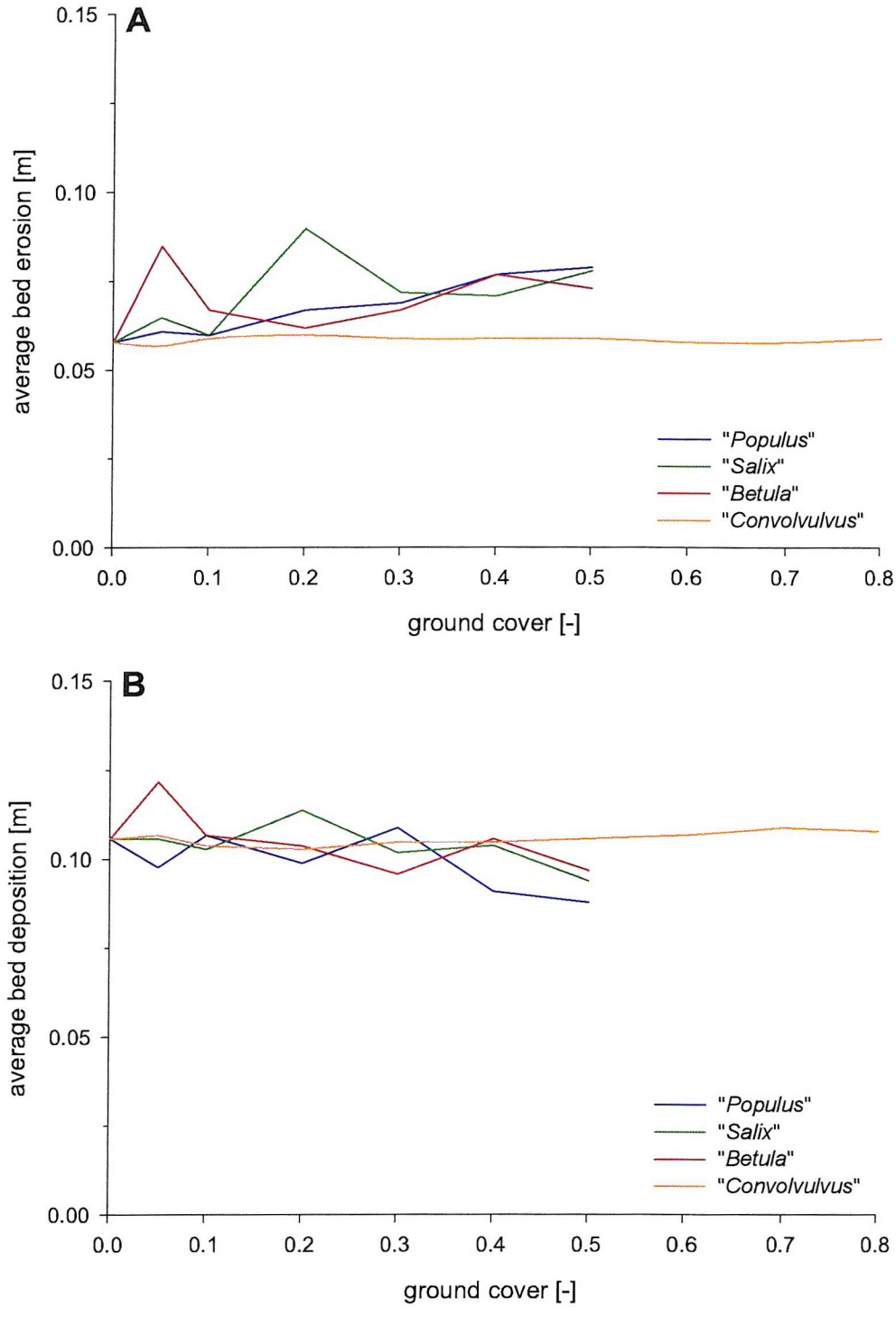

Figure 6.4: Effect of vegetation density on (**A**) average bed erosion and (**B**) average bed deposition.

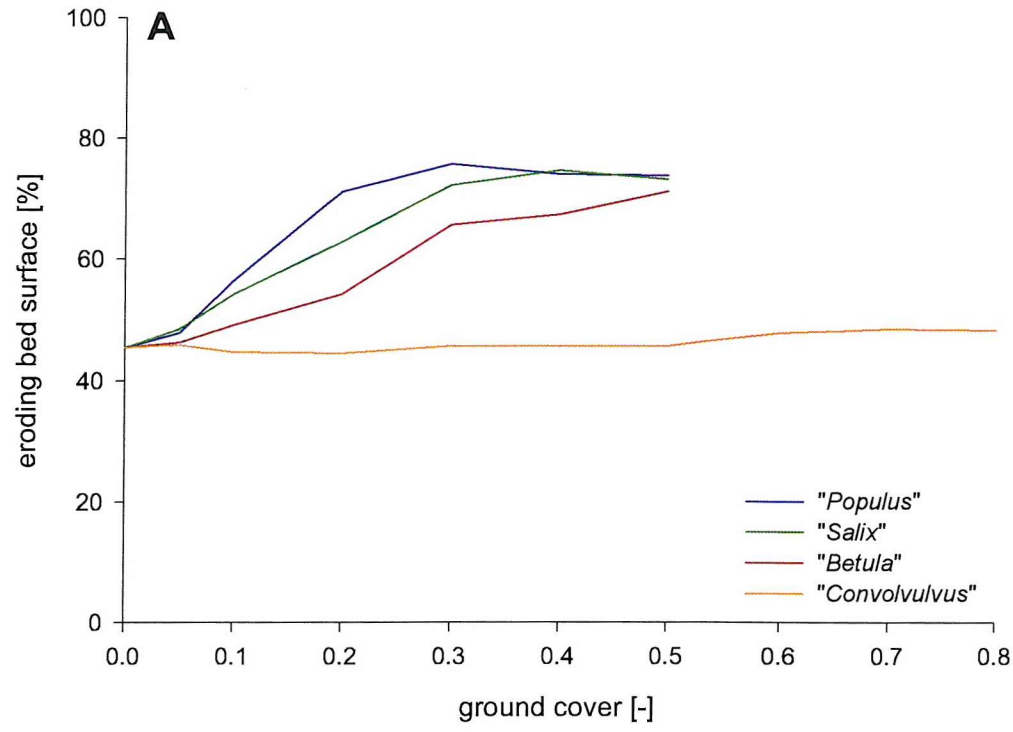

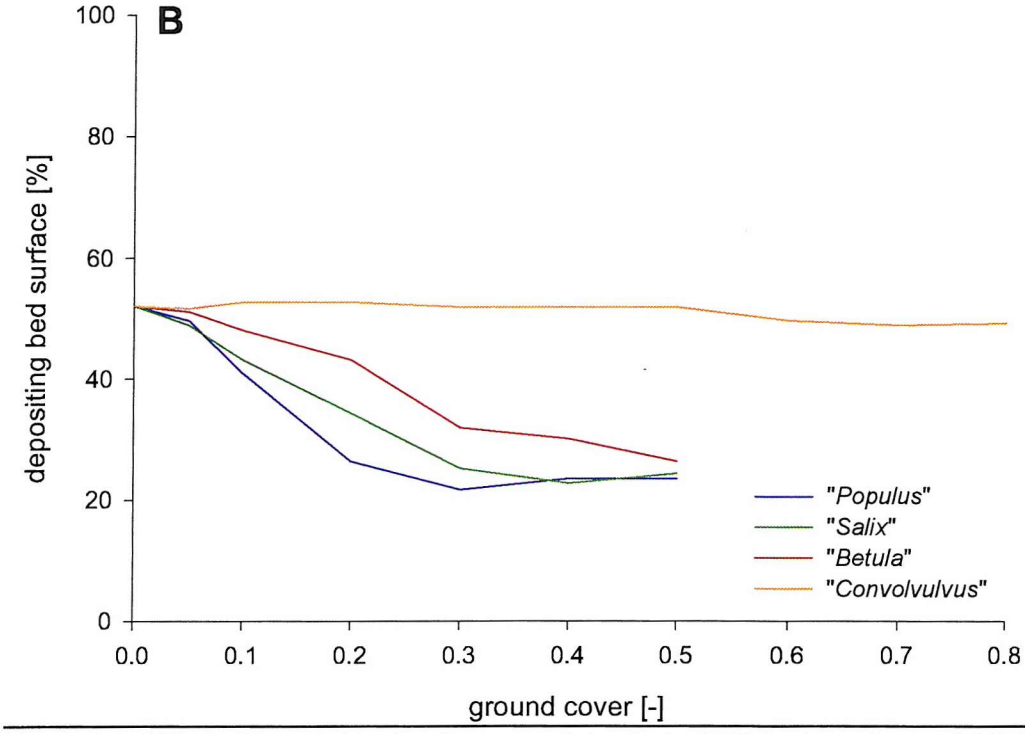

Figure 6.5: Effect of vegetation density on spatial extent of (**A**) bed erosion and (**B**) bed deposition. The indicators on the Y-axes denote the relative bed surface area with net erosion (**A**) or net deposition (**B**) at the end of the simulations. This is represented as a percentage of total bed surface area.

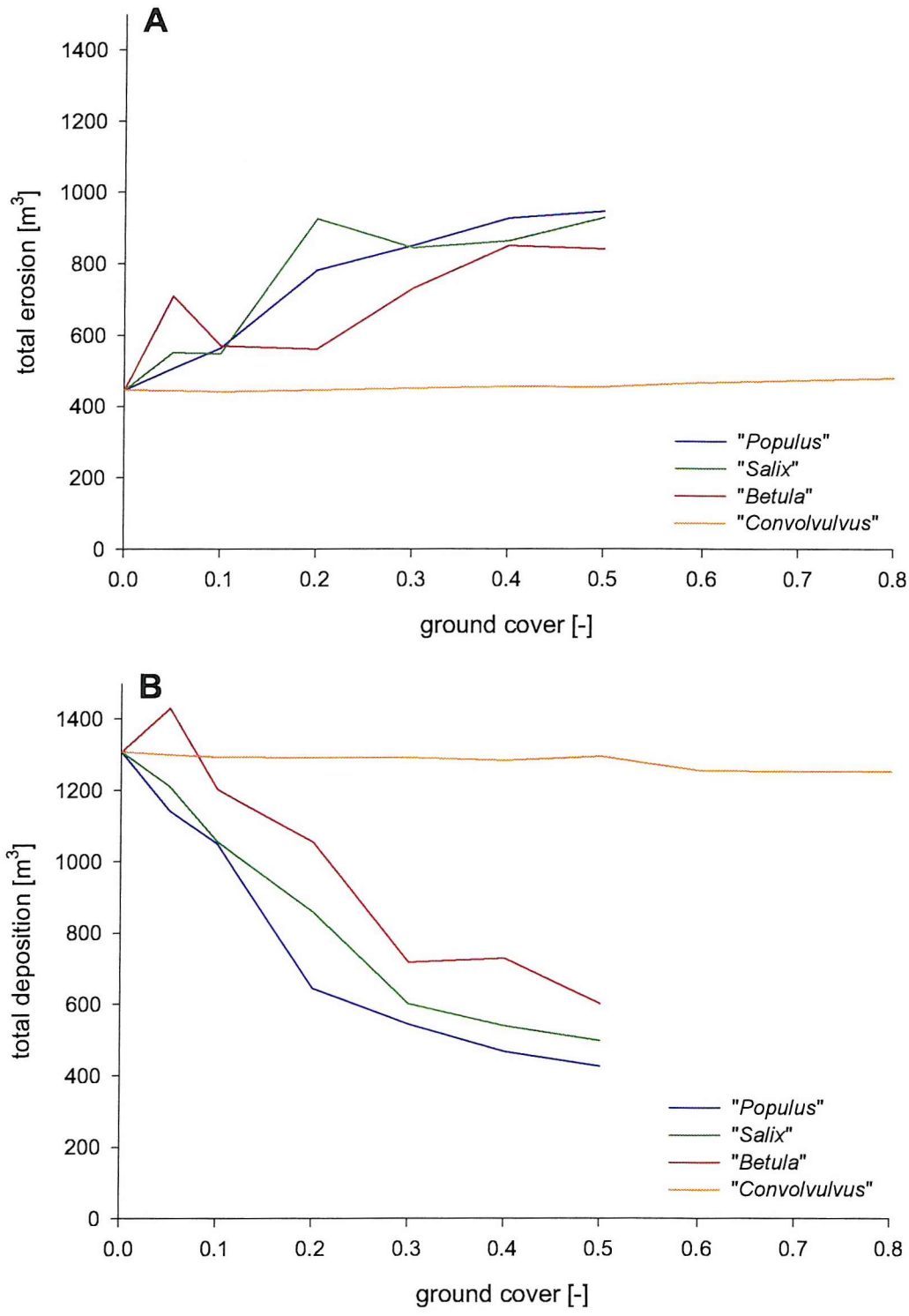

Figure 6.6: Effect of vegetation density on (**A**) total erosion and (**B**) total deposition volumes.

between 700 m^3 and 900 m^3. In the unvegetated control scenario 1308 m^3 of sediment is deposited in the channel, but this is reduced to 602 m^3, 499 m^3 and 426 m^3 respectively in the high density "*Betula*", "*Salix*" and "*Populus*" scenarios (figure 6.6B). Thus, in summary, the impact of the simulated woody vegetation tends towards more bed erosion, and less bed deposition, as the density of the ground cover increases, while "*Convolvulvus*" has little impact on the morphological evolution of the bed. These general trends hold for each of the quantitative indicators, albeit with some irregularities at low vegetation densities.

However, summarizing the results using a single maximal or averaged indicator gives an indication of what processes are occurring within the reach as a whole, but gives no insight into the spatial distribution of those processes. Nonetheless, such insight is important for understanding the relation between bed morphology, bank erosion and channel migration, and the effects of riparian vegetation upon all of these processes. Hence, six scenarios are described in more detail to analyse the spatial aspect of vegetation-induced morphological change of the channel bed. These six scenarios comprise a low and high density scenario for each of the woody species (table 6.4). As the bed morphology changes for the "*Convolvulvus*" scenarios are very small, their spatial variations are not included in this part of the discussion.

Table 6.4: Scenarios selected for spatial analysis.

scenario	species	ground cover density
B1	"*Betula*"	low
B2	"*Betula*"	high
S1	"*Salix*"	low
S2	"*Salix*"	high
P1	"*Populus*"	low
P2	"*Populus*"	high

Note: low density covers are A_{gv} =0.1; high density covers are A_{gv} = 0.5

Figures 6.7 to 6.12 illustrate the simulated bed topographies for the selected scenarios. The top graphs show the modelled bed topographies, while the lower graphs show the differences in bed morphology relative to the control scenario, with blue indicating more erosion (increase in flow depth) and red indicating more deposition (decrease in flow depth). In terms of interpreting these graphs, it is helpful to make a distinction between the upper and lower parts of the reach, where the upper part stretches from cross-section C50-1 to C43-2, and the lower part from C43-2 to C41-3 (*cf.* figure 6.1A for cross-section locations).

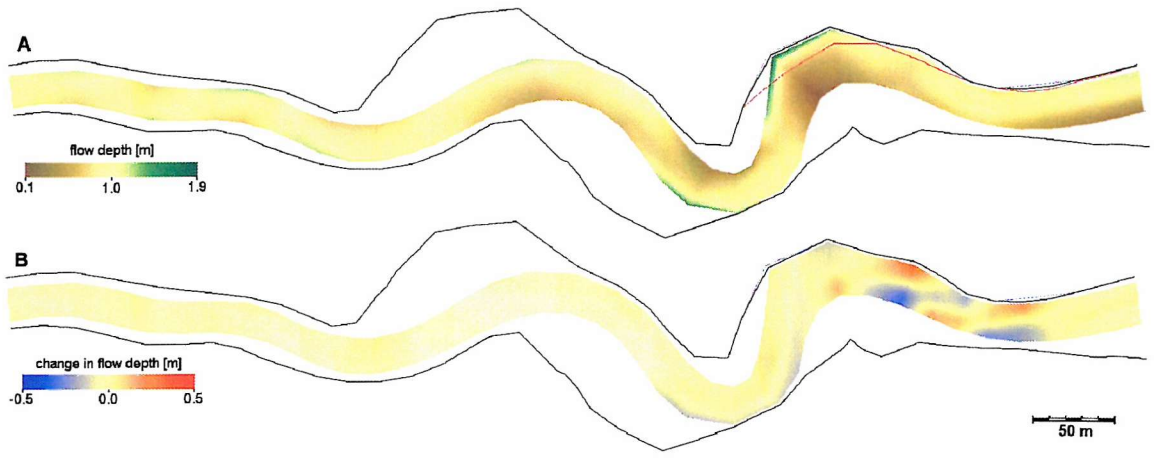

Figure 6.7: Modelled channel morphology for scenario B1 (low density "*Betula*"). **A**: Final (1988) bed topography, represented as flow depths. **B**: Change in flow depths (initial - final). The black lines indicate the simulated final (1988) position of the bank tops. As a reference, the simulated final (1988) position of the bank tops for the unvegetated control scenario (blue line) and the initial (1982) position of the bank tops (red line, graph **A** only) are shown as well. Flow direction is from left to right.

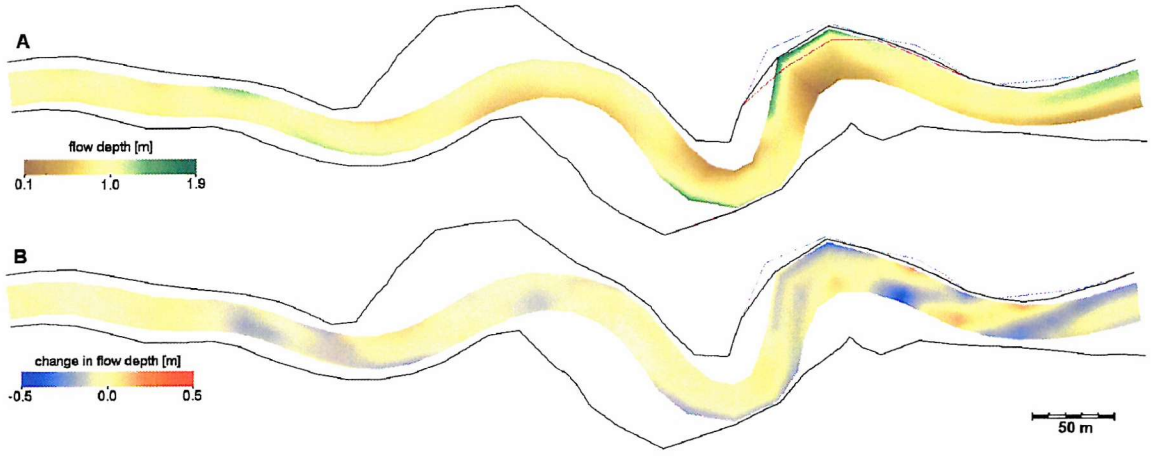

Figure 6.8: Modelled channel morphology for scenario B2 (high density "*Betula*"). **A**: Final (1988) bed topography, represented as flow depths. **B**: Change in flow depths (initial - final). The black lines indicate the simulated final (1988) position of the bank tops. As a reference, the simulated final (1988) position of the bank tops for the unvegetated control scenario (blue line) and the initial (1982) position of the bank tops (red line, graph **A** only) are shown as well. Flow direction is from left to right.

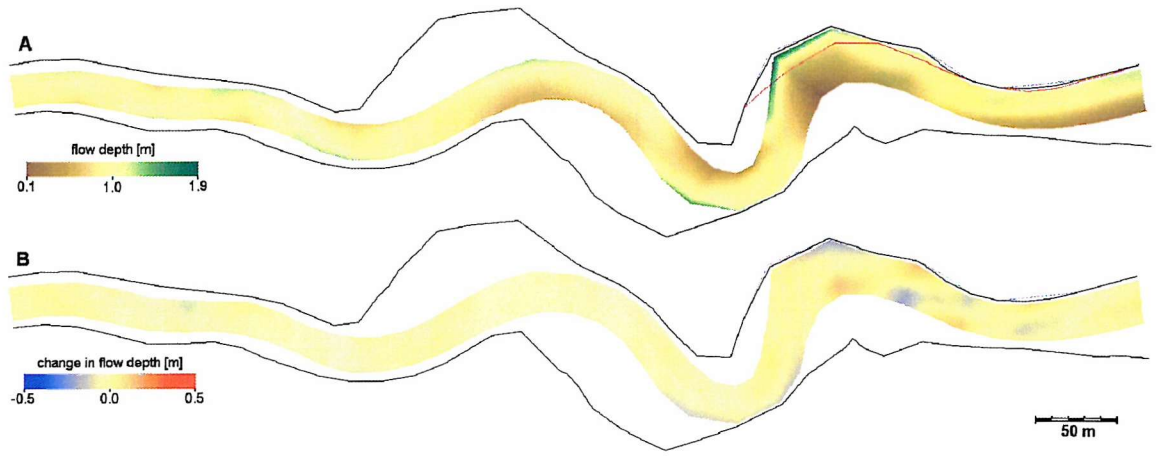

Figure 6.9: Modelled channel morphology for scenario S1 (low density "*Salix*"). **A**: Final (1988) bed topography, represented as flow depths. **B**: Change in flow depths (initial - final). The black lines indicate the simulated final (1988) position of the bank tops. As a reference, the simulated final (1988) position of the bank tops for the unvegetated control scenario (blue line) and the initial (1982) position of the bank tops (red line, graph **A** only) are shown as well. Flow direction is from left to right.

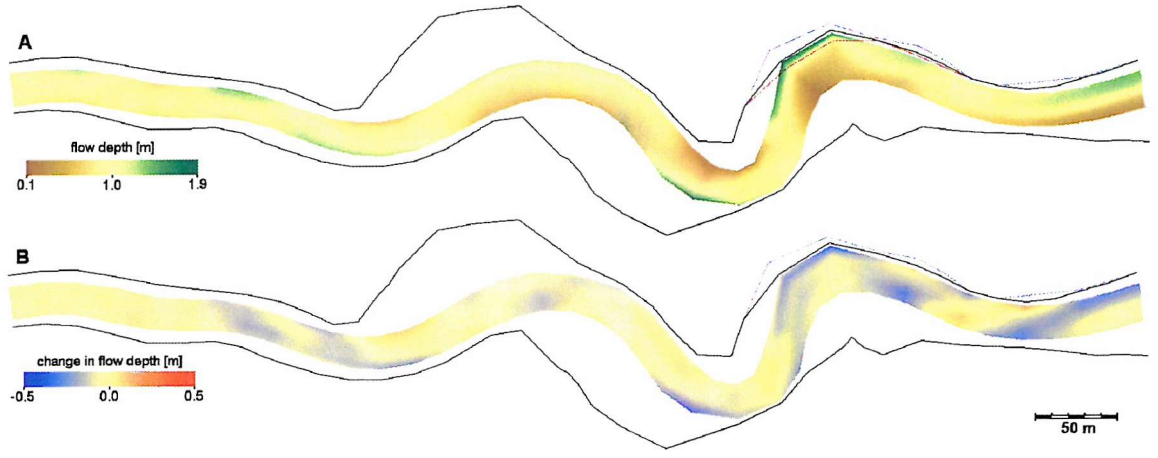

Figure 6.10: Modelled channel morphology for scenario S2 (high density "*Salix*"). **A**: Final (1988) bed topography, represented as flow depths. **B**: Change in flow depths (initial - final). The black lines indicate the simulated final (1988) position of the bank tops. As a reference, the simulated final (1988) position of the bank tops for the unvegetated control scenario (blue line) and the initial (1982) position of the bank tops (red line, graph **A** only) are shown as well. Flow direction is from left to right.

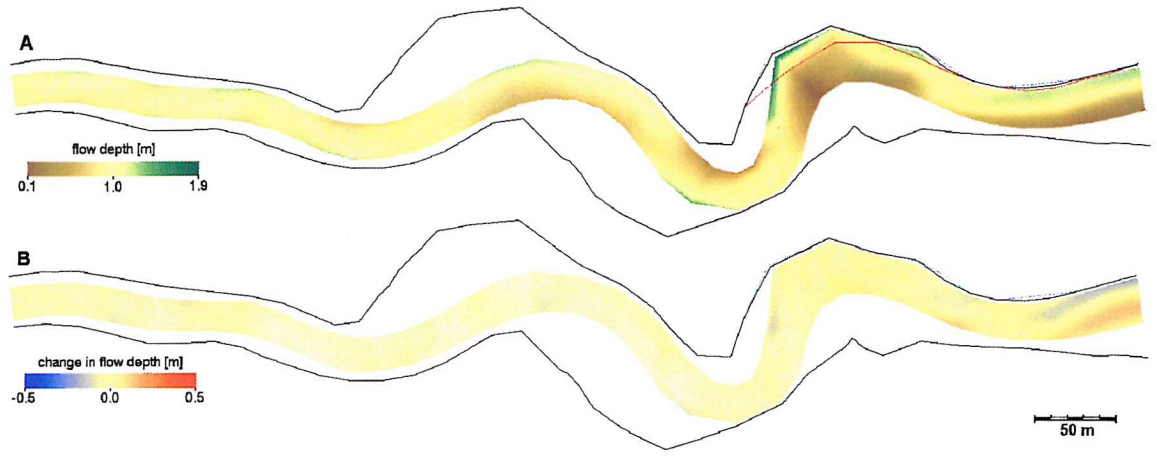

Figure 6.11: Modelled channel morphology for scenario P1 (low density "*Populus*"). **A**: Final (1988) bed topography, represented as flow depths. **B**: Change in flow depths (initial - final). The black lines indicate the simulated final (1988) position of the bank tops. As a reference, the simulated final (1988) position of the bank tops for the unvegetated control scenario (blue line) and the initial (1982) position of the bank tops (red line, graph **A** only) are shown as well. Flow direction is from left to right.

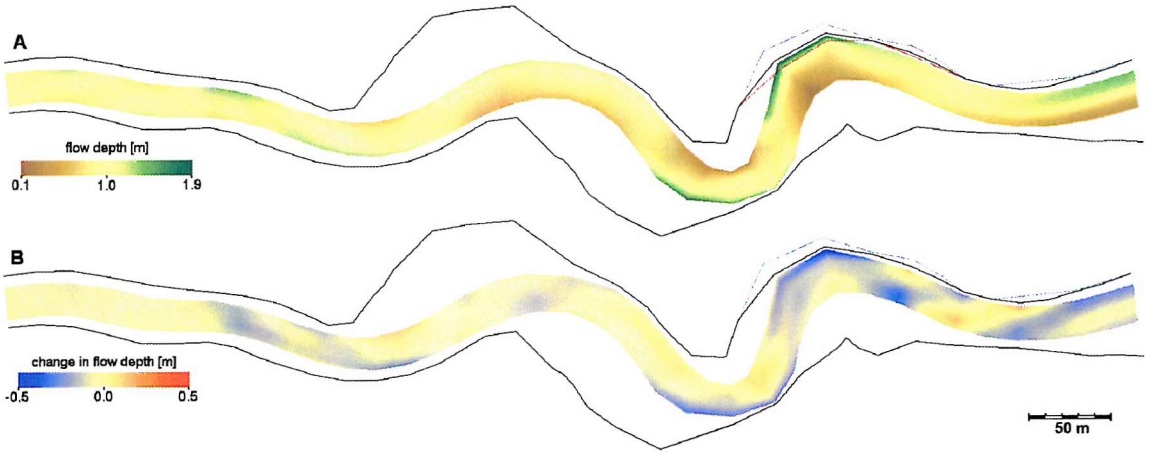

Figure 6.12: Modelled channel morphology for scenario P2 (low density "*Populus*"). **A**: Final (1988) bed topography, represented as flow depths. **B**: Change in flow depths (initial - final). The black lines indicate the simulated final (1988) position of the bank tops. As a reference, the simulated final (1988) position of the bank tops for the unvegetated control scenario (blue line) and the initial (1982) position of the bank tops (red line, graph **A** only) are shown as well. Flow direction is from left to right.

The reason for this distinction will be discussed in section 6.4, but is related to the large bend just downstream of cross-section C43-2. For the low density scenarios (B1, S1 and P1), there is little change in bed topography in the upper part of the reach, compared to the unvegetated control scenario (figures 6.7, 6.9, and 6.11).

For the high density scenarios (B2, S2 and P2), the presence of vegetation accentuates the bed forms in the upper part of the reach (figures 6.8, 6.10, and 6.12). In these scenarios the point bars are up to 0.15 m higher than in the control scenario, and the deepest parts of the thalwegs are between 0.10 m and 0.25 m deeper. However, for all woody vegetation scenarios, the most significant changes in bed topography, compared to the reference case, mainly occur in the lower part of the reach (figures 6.7 to 6.12). Here, the morphological impact of vegetation is more pronounced and more complex, largely due to the change in lateral sediment inputs induced by the vegetation covers (see below). The morphology of the large point bar (PB; *cf.* figure 6.1D) is affected in all of the selected scenarios. In contrast with the point bars in the upper part of the reach, there is generally less deposition on PB, although a distinction can be made between its upstream and downstream side. In each of the scenarios, there is less deposition on the upstream side of PB, compared with the unvegetated control case. More specifically, the deposition is between 0.02 m and 0.07 m less in the low density scenarios and between 0.07 m and 0.15 m less in the high density scenarios. In scenarios S2 and P2, there also is about 0.05 m less deposition on the downstream side of PB (figures 6.10 and 6.12). Together with the decreased deposition on the upstream side, this implies an overall shallower point bar PB, compared to the unvegetated control case. However, in scenarios B1, B2, S1 and P1 there is between 0.04 m and 0.14 m more deposition on the downstream side of PB (figures 6.7, 6.8, 6.9 and 6.11). This combination of less deposition on the upstream side and more deposition on the lee side of PB results in an overall downstream displacement of the bar, relative to its position in the unvegetated control scenario.

In scenarios B2, S2 and P2, the thalweg opposite the large point bar PB is respectively 0.34 m, 0.36 m and 0.49 m deeper than in the unvegetated control scenario (figures 6.8, 6.10 and 6.12). For the scenarios involving low density vegetation covers (B1, S1 and P1), there only is between 0.08 m and 0.20 m more erosion in the simulated depth of the thalweg at this point (figures 6.7, 6.9 and 6.11). Downstream of the pointbar PB and thalweg a streamwise alteration of increased scour and increased deposition can be observed in all scenarios, except P1 (figures 6.7 to 6.12). The magnitude of this undulation varies for each of the

scenarios. It is most pronounced in B1, where there is up to 0.34 m more scour and up to 0.33 m more deposition than in the control scenario (figure 6.7). In the final part of the reach, on and opposite the elongated bar (EB, *cf.* figure 6.1D), there is no consistent pattern of erosion or scour in the selected scenarios. In the high density scenarios (B2, S2 and P2), there is about 0.25 m less deposition on the upstream part of the bar EB, no significant change on the downstream end of it, and about 0.20 more scour in the opposite thalweg (figures 6.8, 6.10, and 6.12). In the P1 scenario, there is significant deposition on the downstream part of the bar EB, which is about 0.15 m higher than in the unvegetated control scenario (figure 6.11). In the B1 scenario, however, the deposition occurs in the thalweg opposite EB, and on the downstream part of the bar EB itself there is about 0.05 m less deposition than in the unvegetated control case (figure 6.7). Finally, in the S1 scenario, the bar EB differs only slightly from the same bar in the unvegetated control case, with up to 0.09 m less deposition on its upstream end and up to 0.04 m more deposition on its downstream end (figure 6.9).

The above description of changes in bed evolution illustrates that the effect of vegetation on erosion and aggradation of the channel bed is not just one of magnitude. The spatial pattern of bed topography change is also altered, in particular at the lower end of the reach. The possible causes and implications hereof are discussed in detail in section 6.4. First, however, results of the simulations are described in terms of the vegetation's impact on planform change.

6.3.2. Planform change

Planform change is quantified in terms of both maximal bank retreat and total floodplain area loss (*cf.* section 5.4.2). The values of both these indicators decrease with increasing vegetation density (table 6.3; figure 6.13A and 6.13B). Again, the effect is strongest for the woody species, with maximal bank retreat reduced from 13.9 m in the unvegetated control scenario, down to 5.4 m, 6.0 m and 7.8 m respectively for "*Populus*", "*Salix*" and "*Betula*" at high density stands ($A_{gv} = 0.5$; figure 6.13A). Likewise, floodplain area loss is reduced by more than 50 % under high density vegetation covers ($A_{gv} = 0.5$; figure 6.13C). However, although the impact of the herbaceous species, "*Convolvulvus*", is negligible at low densities ($A_{gv} < 0.3$), it cannot be neglected at high densities ($A_{gv} > 0.5$). As in chapter 5, it is noted that the model is likely to under-estimate the magnitude of the bank retreat, due to the non-dynamic nature of the simulated vegetation (*cf.* section 5.4.6).

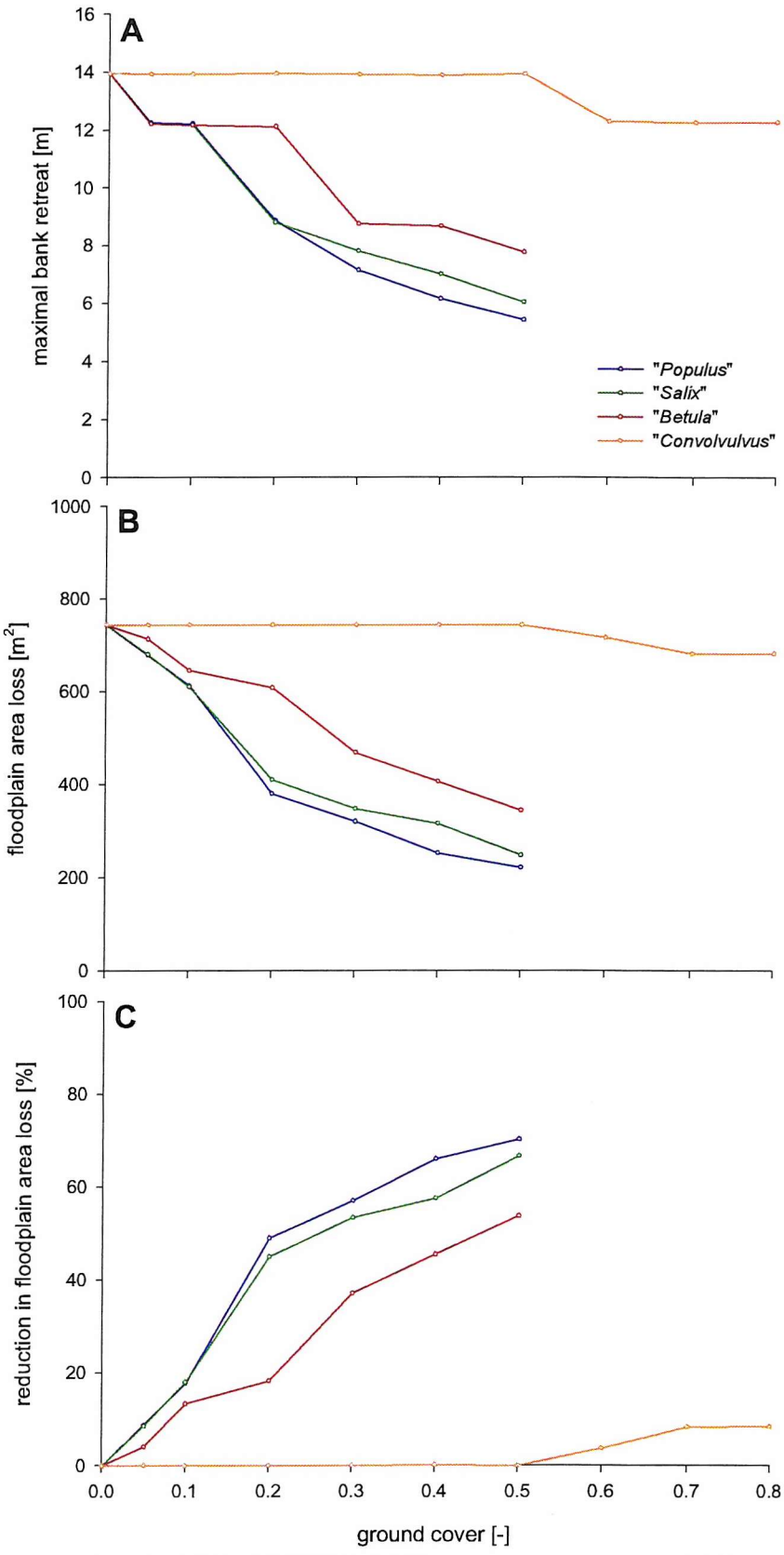

Figure 6.13: Influence of vegetation density on bank retreat. **A**: maximal bank retreat. **B**: total floodplain area loss. **C**: reduction in floodplain area loss, relative to the unvegetated control scenario.

Spatially, the bank retreat in the unvegetated control scenario does not occur over the entire reach. Rather, nearly all bank retreat occurs along the left bank of the lower part of the reach (*cf.* figure 6.2), with two peaks of bank retreat at 515 m and 575 m along the bank, *i.e.* opposite the point bar (LPB), and a smaller one about 650 m along the bank, *i.e.* opposite the elongated bar (EB). The lateral retreat of the riverbanks does not result from a single failure, but rather from a series of failures. For example, at the point of maximal bank retreat, about 500 m along the channel, nine discrete failures are modelled throughout the simulation period (figure 6.14). The incorrect prediction of bank retreat along the right bank near cross-section C43-2 is due to the a single failure of 1.05 m, which occurred about three years into the simulation (November 1985).

The impact of the vegetation on bank retreat is also spatially variable and is described here in more detailed for eight selected scenarios: a low and high density scenario for each of the simulated species (table 6.5). The differences between modelled bank retreat in the selected scenarios and the unvegetated control scenario are illustrated in figure 6.15. In the C1 scenario, the bank retreat is the same as in the unvegetated control case. In the C2 scenario, however, there is a reduction in bank retreat along two of the peaks along the left bank (figure 6.15A). At these peaks the bank retreat is reduced by 1.7 m and 2.0 m, which amounts to respectively 12 % and 57 % of the modelled bank retreat in the unvegetated scenario. In the low density woody vegetation scenarios, B1, S1 and P1, the effects of the trees on bank retreat are similar to those of the high density herbaceous stand (scenario C2), *i.e.* a reduction of nearly 2 m in bank retreat. In the B1 scenario this occurs at the first and last erosion peak (figures 6.15B), similar to C2, while in the P1 and S1 scenarios the second of the three erosion peaks is also affected (figures 6.15C and 6.15D). For high ground cover density values, each of the woody species affect all three erosion peaks. At the first two peaks, opposite the large point bar (PB), bank retreat is reduced by about 40 % in the B2 scenario and about 60 % in the S2 and P2 scenarios. The third peak, opposite the elongated bar (EB), is removed entirely in all three high density, woody species scenarios (B2, S2 and P2). Furthermore, in the S2 and P2 scenarios, the single failure along the right bank is also prevented (not depicted), although it is not affected in any of the six other scenarios.

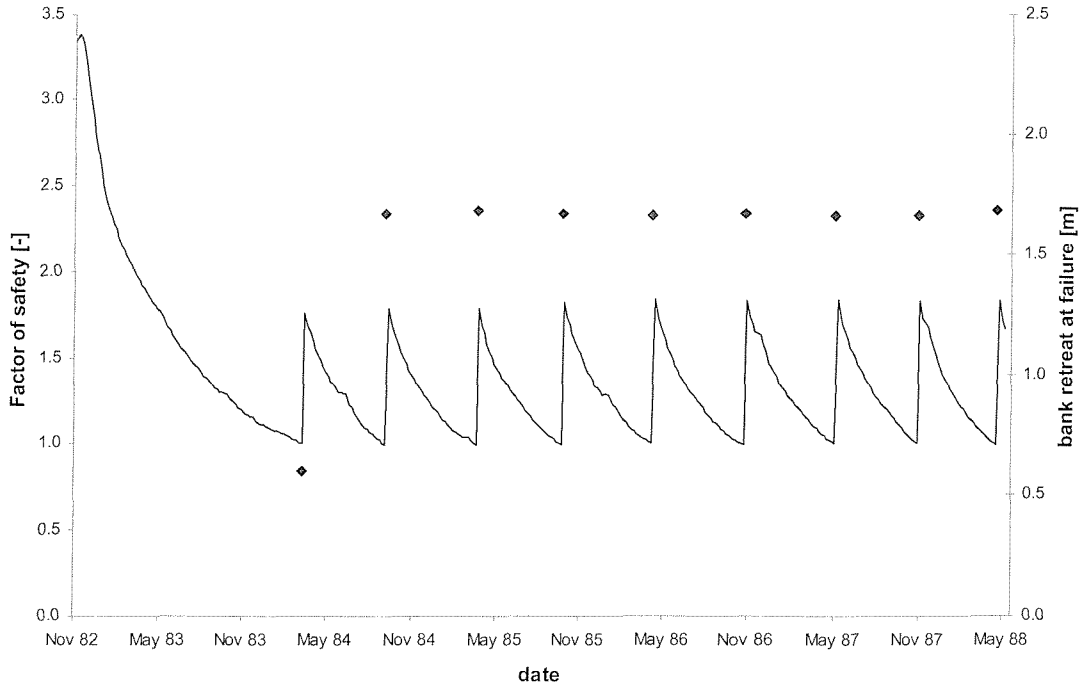

Figure 6.14: Temporal change in the simulated factor of safety at the point of maximal bank retreat (515 m along the left bank). The graph shows both the factor of safety (line) and the magnitude of the failure (dots). During the simulation, the factor of safety declines (due to hydraulic entrainment of bank and bed sediments; *cf.* figure 3.25) until it becomes less than unity, at which point the bank fails. The post-failure bank geometry is stable again, which results in a sudden increase in the factor of safety (N_{FS} after failure = 1.8). Because of its shallow initial profile, the bank's first failure only occurs after about 17 months of simulation and is relatively small (0.6 m retreat). Subsequent failures occur more rapidly, as the bank geometry after a failure is less stable than the initial geometry. Both the frequency of subsequent failures and their magnitude (1.7 m retreat) is very regular, due to the fact that the simulation is run with a steady, equivalent discharge, rather than a natural, variable hydrograph.

Table 6.5: Scenarios selected for spatial analysis.

scenario	species	ground cover density
C1	"*Convolvulvus*"	low
C2	"*Convolvulvus*"	high
B1	"*Betula*"	low
B2	"*Betula*"	high
S1	"*Salix*"	low
S2	"*Salix*"	high
P1	"*Populus*"	low
P2	"*Populus*"	high

Note: low density covers are A_{gv} =0.1; high density covers are A_{gv} = 0.5 for woody species and A_{gv} = 0.8 for herbaceous species

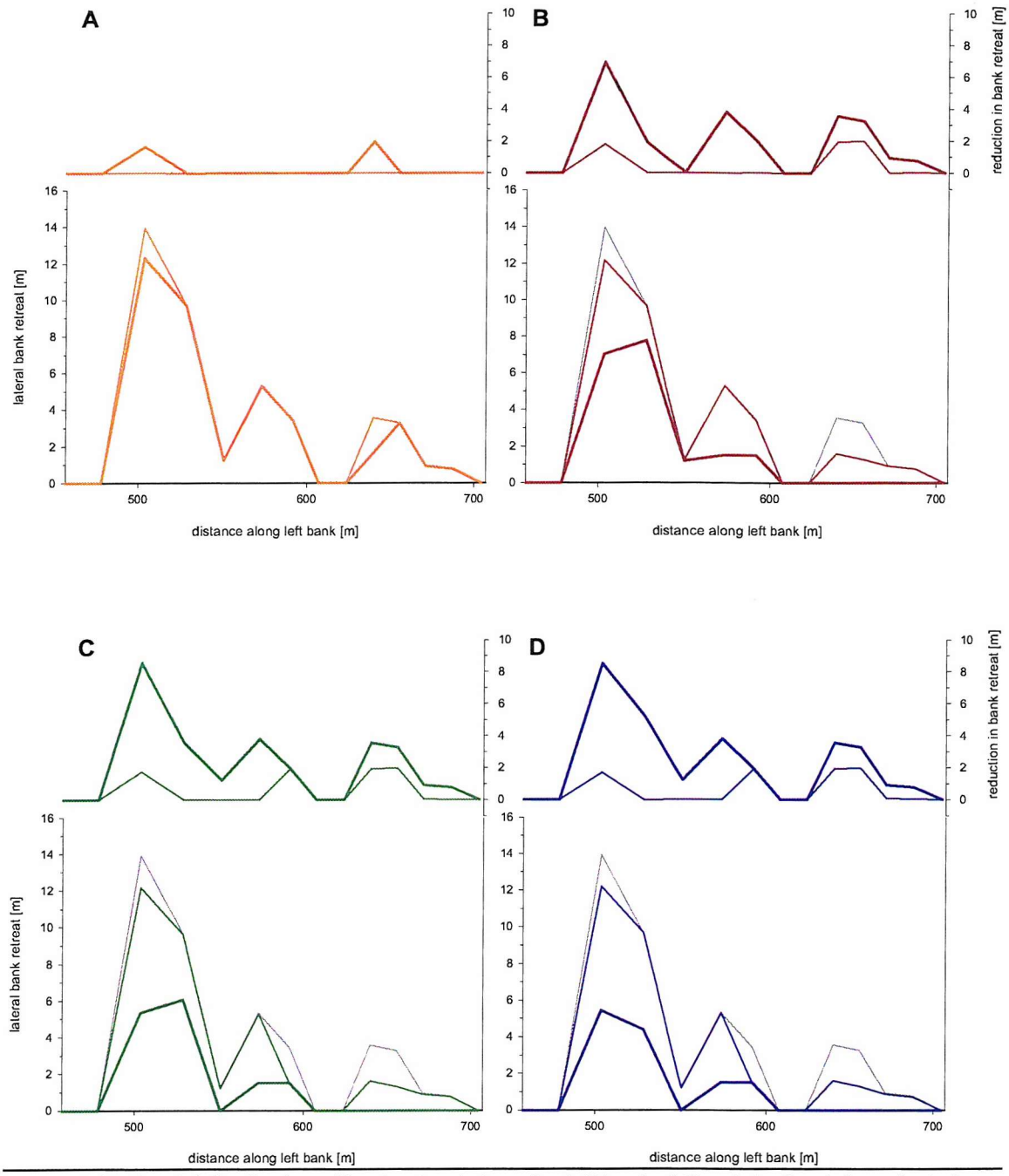

Figure 6.15: Spatial distribution of bank retreat along the left bank of Goodwin Creek for selected vegetation scenarios. **A**: "*Convolvulvus*". **B**: "*Betula*". **C**: "*Salix*". **D**: "*Populus*". The lower part of each graph shows the modelled lateral retreat for the unvegetated control scenario (thin grey line), a low density vegetation scenario (thin coloured line; A_{gv} = 0.1) and a high density vegetation scenario (bold coloured line; A_{gv} = 0.5 for the woody species and A_{gv} = 0.8 for "*Convolvulvus*"). The upper part of the graph shows the reduction in bank retreat in the vegetation scenarios, relative to the unvegetated control scenario, for the same low density (thin coloured line) and high density (bold coloured line) vegetation stands. Note: Only the lower part of the Goodwin Creek reach is shown here, as no bank retreat was modelled in the upper reaches of any of the scenarios.

6.4. Discussion

It is clear, from the results of the various scenarios simulated herein, that vegetation can significantly influence bank retreat and bed morphology along Goodwin Creek. Moreover, the impact of simulated riparian vegetation on bed topography is closely related to the effects it has on bank retreat, and *vice versa*. A significant change in bed morphology is notable only in those scenarios where bank retreat is also significantly affected. Most of the change in bed topography occurs in the lower 150 m of the reach, downstream of the bend with the highest rates of bank retreat, while only minor changes in bed topography are observed upstream of this bend. Thus it appears that the bed topography change in Goodwin Creek is directly linked to the upstream bank retreat, either due to the different sediment supply from the banks, or to the change in channel curvature and its effect on the flow field. Likely, it is a combination of both, although the effects cannot be isolated from each other in the current setup of the simulations. This subsequently affects the transverse bed slope, secondary flow, flow pattern, sediment transport and the distribution of scour and deposition further downstream.

The smaller changes in bed topography in the upper parts of the reach can only be explained in terms of vegetative roughness and resistance against fluvial entrainment, as there are no bank failures in this part of the channel. The roughness of the riparian vegetation reduces the near bank flow velocity, which in turn affects the secondary flow pattern and, hence, the distribution of scour and deposition across the channel. Furthermore, the increased critical shear stress for fluvial entrainment of bank sediments, due to the soil binding of the near-surface roots, decreases the sediment supply to the channel. Again, the impact is spatially distributed, as interaction with the flow causes the effects of vegetation to propagate downstream.

The results of the simulations performed herein imply that Goodwin Creek's morphological evolution depends not only on the local vegetation conditions, but also on the changes in flow pattern, hydraulic activity and sediment transport, due to the influence of vegetation stands located upstream along the reach. Particularly, the large point bar and the elongated bar (PB and EB on figure 6.1D) appear to be affected by changes in flow pattern and sediment supply. Traditional, at-a-site analyses of bank stability do not account for flow pattern, leave alone any changes therein due to upstream vegetation conditions. This, once

more, emphasizes the benefit of spatial modelling in representing the complexity and spatial variability of the impact of riparian vegetation on channel morphology.

The spatial variability of the impact of riparian vegetation also complicates the identification of relevant vegetation parameters in terms of their influence on bed topography, bank stability and channel planform change. The influence of vegetation not only depends on the vegetation properties themselves, but also on how the local bed topography has been affected by processes upstream. However, a few general trends can be observed. First, for each of the four simulated "species", the overall effect of vegetation on bed topography and floodplain area loss is greater in the high density scenarios. This highlights vegetation density as an obvious key parameter. Second, herbaceous species appear to have less impact than woody species. And third, the differences between the effects of the woody species are relatively small, with "*Populus*" slightly more efficient in reducing bank retreat than either "*Salix*" or "*Betula*".

These generalizations are similar to the ones made in section 5.4, where a similar analysis was performed on an idealized channel with a perfectly sinuous planform. However, it is interesting to compare the trends in the results of both analyses in more detail (table 6.6).

Table 6.6: Comparison of vegetation effects in an idealized meandering channel (IM) and a natural channel (Goodwin Creek; GC).

morphological indicator	"*Populus*"		"*Salix*"		"*Betula*"		"*Convolvulvus*"	
	IM	GC	IM	GC	IM	GC	IM	GC
maximal bed erosion	o	+	o	+	o	+	+/-	o
maximal bed deposition	-	-	-	-	-	-	o	o
average bed erosion	-	+	-	+	-	+	o	o
average bed deposition	-	-	-	-	-	-	-	o
bed erosion area	++	++	++	++	++	++	o	o
bed deposition area	--	--	--	--	--	--	o	o
volume eroded sediment	o	++	o	++	o	++	o	o
volume deposited sediment	--	--	--	--	--	--	-	o
maximal bank retreat	--	--	--	--	--	--	o	-
floodplain area loss	--	--	--	--	--	--	-	-

Note: The symbols denote how the morphological indicator changes with increasing vegetation density. A positive correlation is denoted as '+', a negative correlation as '-', while 'o' denotes little correlation between the indicator and vegetation density. Double symbols indicate that the vegetation has a strong impact on that morphological indicator.

In many aspects the idealized meandering channel and the natural channel behave similarly, when their banks are populated by the same species. Woody riparian vegetation strongly reduces bank retreat, which affects sediment supply to the channel and, hence, also the deposition of sediment within the channel. However, some differences can be noted as well, particularly regarding the effect of woody vegetation on the erosion pattern. In the idealized channel, vegetation does not appear to affect scour depth nor the total volume of eroded sediment. In Goodwin Creek, on the other hand, bed erosion increases with the density of the woody vegetation cover. The latter is consistent with empirical evidence. Several authors have observed that tree-lined rivers are generally narrower and deeper than comparable grass-lined channels (Andrews, 1984; Hey and Thorne, 1986; Thorne *et al.*, 1988; Rowntree, 1991), except in headwaters where the tree-lined channels tend to be wider and shallower than grass-lined channels (Zimmerman *et al.*, 1967; Murgatroyd and Ternan, 1983; Davies-Colley, 1997). The apparently anomalous relation between bed erosion and riparian vegetation in the idealized channel (section 5.4) might, therefore, be due to the setup of the experiment, since the initial flat-bed does not represent a natural bed form. Alternatively, it might be yet another indication of the complexity of the spatial interaction between bed morphology processes, bank erosion processes and riparian vegetation.

Table 6.6 also confirms that the morphological impact of the simulated herbaceous species is small relative to the impact of the woody species, at least for the meandering, alluvial channels simulated herein. This relative performance is, again, in agreement with the empirical observation that grass-lined channels are, generally, wider and shallower than comparable tree-lined channels (Andrews, 1984; Hey and Thorne, 1986; Thorne *et al.*, 1988; Rowntree, 1991). However, it is worth repeating that the relatively minor impact of herbaceous vegetation might be due to the non-dynamic nature of the vegetation within the model. MRIPA does not incorporate any mechanism for the re-establishment of vegetation on the bank slope after a mass-failure, which particularly affects "*Convolvulvus*", since this species mainly relies on interaction with the flow to exert its morphological influence (*cf.* section 5.4.6).

6.5. Conclusion

The application of MRIPA to a natural river reach, *i.e.* Goodwin Creek, confirms the potential of riparian vegetation as a tool to reduce rates of bank retreat in alluvial meandering channel reaches. The simulation results indicate that, depending on the biophysical properties of the simulated species and spatial density, riparian trees can have a considerable impact on vegetative roughness, bank stability, and thus channel planform evolution, floodplain area loss and, to a lesser extent, bed topography of the Goodwin Creek channel. Higher density stands of vegetation are, as expected, more effective in stabilizing river banks, and woody vegetation is more efficient than herbaceous vegetation.

Similar to the analysis in the previous chapter, it is found that the bed morphology in the Goodwin Creek simulations is also affected by the vegetation. Reaches lined with woody vegetation tend to be not only narrower than unvegetated or grass-lined channels, but are also deeper. Again, high density vegetation stands have a more pronounced impact than low density ones. The increase in flow depth appears to be partly related to a decrease in sediment supply from the eroding banks. It is, therefore, possible that the impact of riparian vegetation on bed morphology will differ between reaches with high and low upstream sediment supplies. Thus, although its exact nature depends on channel-specific conditions, it can be concluded that the impact of riparian vegetation on bed morphology is spatially variable throughout the reach.

Finally, the interaction between flow and bank processes means that the local effects of vegetation can propagate downstream. Hence, bed morphology and planform shape of the modelled Goodwin Creek reach are not only influenced by the local vegetation, but also by the impacts of upstream vegetation. The resulting spatial variability emphasizes both the complex nature of fluvial biomorphological systems, and the need for adequate, spatial models to represent their morphological evolution.

Chapter 7
Conclusion

7.1. Introduction

Over the preceding chapters a new numerical model of river morphology, MRIPA, has been developed, evaluated and applied. The new model aims to simulate the morphological evolution of meandering alluvial channels with riparian vegetation. Section 7.2 summarizes the essential properties, capabilities and limitations of MRIPA, and illustrates that it achieves this aim. Section 7.3 describes the main findings of the simulations, undertaken in chapters 5 and 6, designed to elucidate impact of riparian vegetation on bed topography and bank migration. Finally, section 7.4 discusses the scope for further research in this area.

7.2. The MRIPA model

MRIPA was developed with the specific aim of simulating, in a simplified numerical environment, the reach-scale morphological evolution of meandering alluvial channels with riparian vegetation over medium temporal scales (section 1.1). Specifically, it provides two new elements relative to existing morphological models. First, MRIPA uses a physically-based geotechnical bank stability algorithm (section 3.5), which is integrated within a two-dimensional computational fluid dynamics model of flow and sediment transport (sections 3.3 and 3.4). This coupling allows for simulation of episodic bank failures, rather than the continuous bank retreat observed in existing models. Furthermore, the integration with a flow model also provides an improvement over traditional at-a-site bank analyses, in that mRIPA is able to simulate spatially variable bank retreat. Second, a vegetation component has been incorporated, to represent the salient features of riparian vegetation which might affect the processes of morphological channel change. Although some existing flow models account for the hydraulic impacts of riparian vegetation, mRIPA is the first model to explicitly address the impacts of vegetation on geotechnical bank erosion processes as well (section 3.5.4).

Despite these additions, it must always be remembered that models are abstract approximations of reality. Representation of the real world within a model is based on several simplifying assumptions, which can be grouped in one of two categories: those that arise from "what" is being modelled, and those that arise from "how" it is being modelled. The former reflect the identification of the salient physical processes that are to be modelled (section 2.7); the latter relate to the mathematical abstractions of the selected processes (chapter 3). The simplifying assumptions define the limitations of the model. An understanding of a model's assumptions, and the implications thereof, is therefore essential for making a balanced interpretation of the results obtained from the model. The most pertinent assumptions which underlie the MRIPA model are, therefore, summarized here. The first major assumption is that the morphological evolution of meandering alluvial river channels mainly results from the interactions between in-channel flow, fluvial entrainment and transport of bank and bed sediment and geotechnical mass wasting along planar failures (*cf.* table 2.4). The second major assumption is that the vertical scales in the flow calculations are much smaller than the horizontal scales. This implies that the flow field is adequately represented by the two-dimensional depth-averaged flow vectors (section 3.3). Although attempts are made to estimate the near-bed flow vectors, MRIPA is inherently unable to represent the full three-dimensional flow structure, and may be subject to inaccuracies over complex bed topographies and planforms. The third major assumption is that the three major submodels – calculation of flow field, bed change and bank retreat – can be decoupled in time (section 3.6.1). This is based on the idea that the relevant processes operate on largely different timescales. These three assumptions, which are justifiable for a wide range of meandering lowland rivers, lie at the core of the model and define its mathematical and computational structure. Other assumptions help constrain the model's complexity, but also reduce its predictive ability: the channel bends are mildly curved; there is no overbank flow; all bank failures are assumed to be planar and to pass through the bank toe; bed material is assumed homogeneous; suspended sediment transport is ignored; all vegetation is mature and static; vegetation is removed upon failure; and several others (*cf.* table 3.1). These assumptions simplify the structure of the model, albeit at the cost of limiting its practical application range.

In spite of the many simplifying assumptions, or possibly because of them, the model is capable of simulating the morphology of meandering, alluvial river channels in a realistic manner, at least for the simulations undertaken herein. Particularly, the position and amplitude of large-scale bed features, such as point bars, pools and lateral bars, are predicted

acceptably well (sections 4.3 and 4.4). Likewise, the spatial occurrence and rates of bank retreat are replicated within reasonable agreement, even though the latter are slightly under-estimated (sections 4.3 and 4.4). Finally, MRIPA is capable of reproducing the two major modes of meander evolution: extension and downstream migration (section 5.4.3). However, the model does tend to underpredict transverse bed slopes and cannot correctly simulate the occurrence of multiple pools in high amplitude meanders (section 4.3.2). Although the newly developed stability analysis of vegetated riverbanks is evaluated in qualitative terms only, it does appear to behave in agreement with empirical observations: the distribution of root cohesion through the soil, optimal lateral positioning of trees and relative impact of surcharge and root reinforcement are all predicted in accordance with published observations (section 5.3.5).

Thus, having established that the vegetation stability analysis is robust and that MRIPA as a whole is capable of reproducing the salient reach-scale morphological features of meandering alluvial rivers, it is reasonable to apply the model as a research tool to investigate the effects of riparian vegetation on the morphological evolution of such channels.

7.3. Impact of vegetation on channel morphology

A series of simulations to investigate the impact of riparian vegetation on channel morphology was carried out for two specific cases: an idealized channel, consisting of a sequence of sinuous bends (section 5.4), and a reach of a natural river, Goodwin Creek, Mississippi (chapter 6). These simulations, the essential results of which are summarized here from geomorphological and river management perspectives, illustrate how MRIPA can be applied to improve our understanding of interactions between channel morphology and riparian vegetation in meandering alluvial rivers.

Channel morphology is spatially and temporally complex, as a result of interactions between flow hydraulics and processes of bed formation and bank erosion. As riparian vegetation may influence all of these, the impact of vegetation is also spatially complex. Unfortunately, it is precisely this complex interaction between flow, sediment transport and bank erosion processes, and the extent to which vegetation influences each of those, that prohibits a single, simple answer as to how vegetation will affect channel morphology.

However, it is clear from the simulations conducted herein, that vegetation is capable of significantly affecting river morphology in alluvial meandering channels; especially when considering that the model's predictions are likely to underestimate the geomorphological impact of natural vegetation, because the simulated vegetation is not allowed to re-establish after bank failure (*cf.* section 5.4.6).

In the numerical experiments undertaken herein, the riparian vegetation's most pronounced geomorphological effect is on the river bank's stability with respect to geotechnical mass wasting along planar failures. The simulations show that the presence of riparian vegetation can significantly reduce rates of lateral retreat and total floodplain area loss in meandering alluvial river reaches. In some scenarios, involving high density stands of woody vegetation, the total floodplain area loss is reduced by up to 60% (*cf.* section 6.3.2). It should be noted that this conclusion only concerns the rates of the erosional process; no claims are made towards any potential differences in a final equilibrium state, as none of the simulations conducted herein are run until equilibrium is achieved. In general, vegetation appears most effective in reducing bank retreat on shallow banks, consisting of weakly cohesive material.

Even though the reach-averaged erosion rates are generally reduced in vegetated conditions, compared to unvegetated conditions in the same reach, localized parts of the channel experienced an increase in simulated bank retreat. This mainly occurs just downstream of sections which experienced a significant decrease in bank retreat (section 5.5), and is likely the result of the upstream alteration in the flow pattern. Additionally, inappropriate positioning of woody vegetation, *i.e.* such that the roots cannot interact with the incipient failure plane (for example near the top of a high, near-vertical bank), can also be detrimental to the bank's stability (section 5.3). Thus, the presence of riparian vegetation is usually, but not exclusively, beneficial to the lateral stability of the channel banks.

Riparian vegetation not only affects lateral migration of meandering rivers, but also the morphological evolution of the channel bed. In the simulations undertaken herein, the effect of vegetation on bed topography is generally such that the channel morphology becomes more uniform throughout the reach, *i.e.* with less undulation and shallower transverse slopes. The presence of simulated riparian vegetation causes a spatial redistribution of sediment erosion and deposition over the channel bed, which tends to homogenize the bed topography. The magnitude of this redistribution depends on the density of the cover and specific

biophysical parameters of he simulated vegetation. In general, more parts of the bed are subjected to erosion and fewer parts to deposition, particularly for the woody species simulated herein. However, the amplitude of bed forms, *i.e.* bar height and pool depth, decreases. The effect of riparian vegetation on the bed is both direct, through the effect of vegetation on the flow pattern, and indirect, through its effects on bank retreat. The latter not only affects the channel cross-sectional geometry and, hence, the structure of the flow field, but also the supply of sediment to the channel bed and, hence, the morphological evolution thereof. The alteration of the flow field and sediment supply is a key effect of the vegetation, as it indicates that the geomorphological influences of riparian vegetation can propagate downstream, and thereby affect the bed and bank in other parts of the channel.

In nearly all the simulations undertaken herein, the impact of simulated grass on bank retreat and bed topography change is much lower than the impact of simulated woody species. The latter can affect bank retreat along meandering alluvial channels, even at low ground cover densities, while the simulated herbaceous species only has an impact at very high ground cover densities. The differences between the simulated woody species are relatively small, although the species with the most extensive root network, *i.e.* "*Populus*", tends to be most effective in reducing bank retreat, and, hence, also has the largest impact on bed morphology. However, it is difficult to isolate individual biophysical properties of the vegetation as being more important than others. In stand-alone stability analyses, the impact of vegetation on geotechnical bank stability is surprisingly low (section 5.4). However, when hydraulic aspects are considered, the geomorphological impact of vegetation is considerably higher. Although this might suggest that the impact of vegetation on flow hydraulics and sediment transport is more important than its effect on geotechnical processes, this simple conclusion is contradicted by the observation that the simulated woody species incur the most pronounced changes in the channel's morphology. This can only be attributed to their geotechnical impact, since the parameterization of the woody species' parameters that affect flow hydraulics is generally lower than that of herbaceous species (section 5.2). Thus, neither geotechnical stabilization, nor alteration of the hydraulic flow pattern, nor soil binding, can, by themselves, explain the variability and extent of the morphological change incurred in the river channel. Instead it is their combined effect that determines the morphological evolution of the channel. This holistic view of vegetation's impact suggests that generalizations about the reach-scale influence of individual biophysical properties of a vegetation species should be treated with caution, not just in this study, but in all empirical and numerical studies.

Finally, and critically, it is evident from the simulations conducted herein that the impact of riparian vegetation on meandering alluvial rivers is spatially variable. Riparian vegetation is seen to affect the morphological evolution of the channel bed in two ways: directly, through the effects on flow hydraulics and sediment transport; and indirectly, through its impact on bank failure processes. Likewise, vegetation also affects channel planform evolution directly, through its impacts on geotechnical mass wasting; and indirectly, through its impact on flow hydraulics and sediment transport. The fact that local effects can propagate downstream and affect other parts of the channel, implies that at-a-site analysis by itself is not enough to determine the net impact of riparian vegetation on channel morphology, even in terms of bank stability. Instead, the spatial variability of the effects of vegetation highlights the complexity and intricacy of fluvial systems. Empirical research, numerical studies and river management studies all need to consider the interactions between bank mechanisms, flow processes and riparian vegetation, in order to represent the spatial diversity of fluvial morphology and processes in alluvial, meandering rivers.

7.4. Scope for further research

mRIPA's ability to combine physically-based bank stability analyses with modelling of hydraulics and sediment transport marks an advance in the simulation of vegetated river channels. As such, it can be a useful tool to improve our understanding of the impact of riparian vegetation on channel morphological change. Nonetheless, mRIPA does not answer all questions on this issue, nor is it capable of doing so.

There are questions remaining. Some focus on geomorphological insight and understanding: Does riparian vegetation have an effect on the final equilibrium form (if any) of a river channel, or does it only affect the rates of erosion processes? To what extent does discharge regime affect the way in which vegetation influences channel geomorphology? How does upstream sediment supply affect the vegetation's impact? Other questions are more relevant to river management: Can assemblages of different species provide additional protection against bank retreat? Does the presence of riparian vegetation affect the risk or frequency of flooding? Does riparian vegetation contribute to in-channel habitat diversity? Although MRIPA, in its current form, might be able to provide tentative answers to some of these questions, others require alteration or improvement of the model.

Many improvements can be made to the model itself, mainly by addressing some of the limitations that result from the assumptions made during the model development (sections 2.7 and 3.6.3). For example, other failure processes (rotational, cantilever, complex) should be included; adjustments can be made to the sediment transport model to account for multiple sediment grain sizes; suspended sediment transport could be included; sediment trapping by vegetation can be incorporated; flow could be modelled using a three-dimensional flow model. All these advances are likely to improve the model's realism, albeit at the cost of increased complexity and possibly introducing additional uncertainty in the parameterization of the model. Furthermore, it is not clear to what extent the additional realism would contribute to enhanced understanding, although the improved predictive ability might be desirable from a river management perspective. Possibly the most interesting question that arises from the suggested improvements, and having the widest range of implications, concerns the three-dimensional flow model: Does the predicted channel morphology, on a reach scale, differ significantly between simulations based on a two- and a three-dimensional flow model?

An entirely different area of improvement concerns the availability of data, particularly regarding the vegetation component of the model. The first issue in this context is the lack of suitable reference datasets to quantitatively calibrate and validate MRIPA's vegetation routines. The second issue, highlighted throughout this study, is the lack of adequate data for vegetation parameterization, which is currently subject to large uncertainties (section 5.2). As such, there is an urgent need for empirical research to establish a comprehensive database of biophysical properties of a wide range of riparian species. Finally, there is a need to develop a dynamic vegetation model, in which the simulated plants can grow, spread and colonize new deposits. The ability to simulate dynamic vegetation would, undoubtedly, be the largest single conceptual improvement to the current model, affording a greater degree of realism in terms of modelling the effects of vegetation on geomorphology, but also offering the potential to investigate how geomorphological processes influence the evolution of riparian flora.

Appendix 1

Rates of Bank Adjustment

A1.1. Bank erosion rates

The overview in the table A1.1 is an expansion of similar lists published in the past (Hooke, 1980; Lawler 1990). Some erroneous entries in these lists have been corrected, and new entries been added to account for information available in the last decade. Although the overview is relatively comprehensive, it is unlikely to be exhaustive. Figure 2.14 is compiled from those entries in table A1.1 for which both 'Erosion Rate' and 'Drainage Basin Area' are specified. However, the dataset also contains additional entries for which the 'Drainage Basin Area' could not be obtained.

Most of the cited erosion rates are long term averages of observations made over several years. Erosion rates extrapolated from single events are not included in the dataset. Some of the cited erosion rates are spatially averaged. In some instances, where numerical data are not provided in the original publication, the drainage basin area has been estimated from graphical data in the original publication or from an external source. Some erosion rates were also estimated from graphical data in the original publication.

A1.2. Bank accretion rates

Table A1.2 provides a short overview of published bank accretion rates. In the context of the current study, lateral accretion rates are most relevant. However, a few vertical accretion rates (*i.e.* floodplain sedimentation) have been included for reference. More comprehensive reviews of floodplain sedimentation rates can be found in Walling and He, 1999 and Rumsby, 2000.

Table A1.1: Overview of published erosion rates.

Reference	River	Erosion Rate m/yr	Drainage Basin Area km²	Mean Annual Discharge m³/s	Bankfulll Width m	Timespan of Measurement yr
Abam, 1993	Niger, Nigeria	4.75	2071105			3
Abbe and Montgomery, 1996	Queets River, Washington State, USA	10	1164			54
Alexander and Nunally, 1972	Ohio River, Kentucky, USA	0.357				14000
Andrews, 1982	East Fork River, Wyoming, USA	0.6	502			6
Ashbridge, 1995	River Culm, Devon, UK	0.278	276	4.15		2
Bartholdy and Billy, 2002	Cecina, Italy	3.125	900		50	32
Bartholdy and Billy, 2002	Cecina, Italy	7	900		50	1.5
Blacknell, 1981	Afon Crewi, Wales	2	35.5		9.3	3
Bluck, 1971	Endrick, Scotland	0.55[2]	252.8	6.96	25[2]	
Bray, 1987	Nashwaaksis, Canada	1.5	26.9	0.54	11	10
Brice, 1973	White River, Indiana, USA	0.67	6040	66.4	60	31
Brice, 1977	Middle Sacramento, California, USA	4.6				
Brierley and Fitchett, 2000	Waiau River, New Zealand	17.5	8200	560		12
Bull, 1996	Severn, Wales	0.0129	3.5			
Bull, 1996	Severn, Wales	0.0156	4			
Bull, 1996	Severn, Wales	0.0488	4			
Bull, 1996	Severn, Wales	0.0591	8			
Bull, 1996	Severn, Wales	0.0648	3.5			
Bull, 1996	Severn, Wales	0.2341	170			
Bull, 1997	Severn, Wales	0.013	3.5		3.99	2
Bull, 1997	Severn, Wales	0.059	8.7		6	2
Bull, 1997	Severn, Wales	0.461	380		29.45	2
Burckhardt and Todd, 1998	Bridge Creek, Missouri, USA	0.27	118.4		8.8	
Burckhardt and Todd, 1998	Bridge Creek, Missouri, USA	0.70	118.4		8.8	
Burckhardt and Todd, 1998	Bridge Creek, Missouri, USA	1.70	118.4		8.8	
Burckhardt and Todd, 1998	Bridge Creek, Missouri, USA	3.19	118.4		8.8	
Burckhardt and Todd, 1998	Cottonwood Creek tributary, Missouri, USA	0.18	6.15		3.6	
Burckhardt and Todd, 1998	Cottonwood Creek tributary, Missouri, USA	0.27	6.15		3.6	
Burckhardt and Todd, 1998	Locust Creek, Missouri, USA	0.20	647.5		36.5	
Burckhardt and Todd, 1998	Locust Creek, Missouri, USA	1.60	647.5		36.5	
Burckhardt and Todd, 1998	Middle Fabius, Missouri, USA	0.43	162.1		14	
Burckhardt and Todd, 1998	Middle Fabius, Missouri, USA	0.94	162.1		14	
Burckhardt and Todd, 1998	Mussel Fork, Missouri, USA	0.58	296.5		14.9	
Burckhardt and Todd, 1998	Mussel Fork, Missouri, USA	1.70	296.5		14.9	
Burckhardt and Todd, 1998	South Fabius, Missouri, USA	0.09	125		9.1	
Burckhardt and Todd, 1998	South Fabius, Missouri, USA	0.52	125		9.1	
Burckhardt and Todd, 1998	Spring Creek, Missouri, USA	0.70	140.1		20.4	
Burckhardt and Todd, 1998	Spring Creek, Missouri, USA	1.37	117.2		17.3	

Table A1.1: Overview of published erosion rates (continued).

Reference	River	Erosion Rate m/yr	Drainage Basin Area km²	Mean Annual Discharge m³/s	Bankfull Width m	Timespan of Measurement yr
Burckhardt and Todd, 1998	Spring Creek, Missouri, USA	2.13	140.1		20.4	
Burckhardt and Todd, 1998	Spring Creek, Missouri, USA	2.61	117.2		17.3	
Carey, 1969	Mississippi, Louisiana, USA	23	3450978	16860		
Castaldini and Piacente, 1995	Po, Italy	1	46000	1470		10
Church and Slaymaker, 1989	Beatton, British Columbia, Canada	0.5	4070			
Church and Slaymaker, 1989	Upper Fraser, British Columbia, Canada	0.7	1385			
Church and Slaymaker, 1989	Upper Fraser, British Columbia, Canada	1.3	150			
Church and Slaymaker, 1989	Liard and Peach River, BC, Canada	2.3	6765			
Church and Slaymaker, 1989	Liard and Peach River, BC, Canada	2.7	1510			
Church and Slaymaker, 1989	Liard and Peach River, BC, Canada	2.9	10530			
Church and Slaymaker, 1989	Liard and Peach River, BC, Canada	2.9	8110			
Church and Slaymaker, 1989	Liard and Peach River, BC, Canada	4.4	47815			
Coldwell, 1957	Washita, Oklahoma, USA	3.04				15
Coleman, 1969	Brahmaputra, Bangladesh	165	600000	19048	3000	19
Coleman, 1969	Brahmaputra, Bangladesh	243	600000	19048	3000	8
Cooper and Hollingshead, 1973	Porcupine River, Alaska, USA	0.88	54108	351		11
Crickmay, 1960	Pembina, Canada	3		19.3	64	35
Crouch, 1990	gully bank	0.03	1.2			
Crouch and Blong, 1989	gully bank	0.04	2.9			
Cummins and Potter, 1972	Bradgate Brook, Leicestershire, UK	0.2[2]	15[2]			2
Davis and Gregory, 1994	Highland Water, New Forest, UK	0.063	11.4			0.75
Demlow and Edgeworth, 1984	Cottonwood River, British Columbia, Canada	1920	279			6
Demlow and Edgeworth, 1984	Skeena River, British Columbia, Canada	42200	919			13
Demlow and Edgeworth, 1984	Skeena River, British Columbia, Canada	42200	919			22
Dryer and Davis, 1911	Normal Brook, Indiana, USA	1.06	2.59			
Duijsings, 1987	Schrondweilerbaach, Luxembourg	0.35	0.61			2
Emmett, 1974	Watts Branch, Maryland, USA	0.45	9.6	0.09	5.8	8
Erskine *et al.*, 1993	River Murray, New South Wales, Australia	0.1		250		
Everitt, 1968	Little Missouri, North Dakota, USA	4.56[2]	21980	16	91.2	100
Fisk, 1951	Mississippi, USA	48.2				
Friedman *et al.*, 1996	Plum Creek, Colorado, USA	9	728			10
Galay, 1980	Ganges, Bangladesh	67				42
Galay, 1980	Meghna, Bangladesh	91				10
Galay, 1980	Meghna, Bangladesh	426				10
Gardiner, 1983	Lagan, North Ireland	0.103	20[2]			1
Gardiner, 1983	Lagan, North Ireland	0.139	85			
Gatto, 1984	Tanana River, Alaska, USA	3.34	51800	532		26
Gatto, 1984	Tanana River, Alaska, USA	3.65	51800	532		6

Table A1.1: Overview of published erosion rates (continued).

Reference	River	Erosion Rate m/yr	Drainage Basin Area km²	Mean Annual Discharge m³/s	Bankfull Width m	Timespan of Measurement yr
Gatto, 1984	Tanana River, Alaska, USA	5.47	51800	532		2
Gatto, 1984	Tanana River, Alaska, USA	8.20	51800	532		8
Gatto, 1984	Tanana River, Alaska, USA	9.12	51800	532		6
Gilvaer *et al.*, 2000	Luangwa River, Zambia	8	73433	128	150	8
Gilvaer *et al.*, 2000	Luangwa River, Zambia	30	73433	128	150	30
Gole and Chitale, 1966	Kosi, India	0.16				86
Gole and Chitale, 1966	Kosi, India	0.32				34
Gole and Chitale, 1966	Kosi, India	0.48				27
Gole and Chitale, 1966	Kosi, India	0.72				15
Gole and Chitale, 1966	Kosi, India	0.8				34
Gole and Chitale, 1966	Kosi, India	1.04				17
Gole and Chitale, 1966	Kosi, India	2.57				11
Goswami *et al.*, 1999	Subansiri, Assam, India	19.7	37000	1388		50
Goswami *et al.*, 1999	Subansiri, Assam, India	32.2	37000	1388		20
Graf, 1981	Gila River, Arizona, USA	13.39[2]	128700	2.8	60	112
Graf, 1983	Salt River, Arizona, USA	14.3	38400		125	112
Graf, 1983	Salt River, Arizona, USA	25.9	38400		125	58
Green *et al.*, 1999	Warrah Creek, NSW, Australia	0.84	150			1
Green *et al.*, 1999	Warrah Creek, NSW, Australia	0.33	150			19
Grove, 2000	Swale, UK	0.07	4.2			
Grove, 2000	Swale, UK	0.09	141			
Grove, 2000	Swale, UK	0.13	1282			
Grove, 2000	Swale, UK	0.14	52.4			
Grove, 2000	Swale, UK	0.26	82.6			
Grove, 2000	Swale, UK	0.35	593			
Grove, 2000	Swale, UK	0.41	748			
Grove, 2000	Swale, UK	0.62	183			
Grove, 2000	Swale, UK	3.58	399			
Gurnell *et al.*, 1994	Dee, Wales	0.11[2]	1100[2]	37	30	73
Hagerty *et al.*, 1981	Ohio River, Illinois, USA	2.28				89
Hagerty *et al.*, 1981	Ohio River, Illinois, USA	10	10000			
Handy, 1972	Des Moines, Iowa, USA	11.6				
Handy, 1972	Des Moines, Iowa, USA	7.6				
Harmel *et al.*, 1999	Illinois River, Oklahoma, USA	1.4	2483	26.5		12
Harmel *et al.*, 1999	Illinois River, Oklahoma, USA	1.4	2483	32		1
Hickin and Nanson, 1975	Beatton, BC, Canada	0.616	700[2]	186	70	250
Hickin and Nanson, 1975	Beatton, BC, Canada	0.475	900[2]	186	70	250
Hickin and Nanson, 1975	Beatton, BC, Canada	0.463	1400[2]	186	70	250

Table A1.1: Overview of published erosion rates (continued).

Reference	River	Erosion Rate m/yr	Drainage Basin Area km²	Mean Annual Discharge m³/s	Bankfull Width m	Timespan of Measurement yr
Hieb, 1954	Laramie, Wyoming, USA	0.3				
Hill, 1973	Clady, North Ireland	0.054	4			2
Hill, 1973	Crawfordsburn, North Ireland	0.03	3			2
Hill, 1973	Crawfordsburn, North Ireland	0.008	3			1.5
Hooke, 1977	Axe, Devon, UK	0.54	295		9	60
Hooke, 1977	Axe, Devon, UK	0.37	295		9	2
Hooke, 1980	Axe, Devon, UK	0.33	288		94	1.5
Hooke, 1980	Axe, Devon, UK	0.568	288		94	17
Hooke, 1980	Coly, Devon, UK	0.08	74			1.5
Hooke, 1980	Creedy, Devon, UK	0.26	235			1.5
Hooke, 1980	Exe, Devon, UK	0.865	620		254	1.5
Hooke, 1980	Exe, Devon, UK	1.234	620		254	7
Hooke, 1980	Hookamoor Brook, Devon, UK	0.08	9.2			1.5
Hooke, 1980	Lower Culm, Devon, UK	0.46	268			7
Hooke, 1980	Lower Culm, Devon, UK	0.24	268			1.5
Hooke, 1980	Upper Culm, Devon, UK	1.07	270			7
Hooke, 1980	Upper Culm, Devon, UK	0.18	270			1.5
Hooke, 1980	Yarty, Devon, UK	0.67	51			17
Hooke, 1980	Yarty, Devon, UK	0.7	51			1.5
Hughes, 1977	Cound, Shropshire, UK	0.62	100			2.5
Imeson and Jungerius, 1974	Birbaach, Luxembourg	0.008	1.57			
Jackson, 1975, 1976a	Wabash River, Illinois, USA	10	74070	746		
Kalliola and Puhakka, 1988	Kamjokha, Finland	0.3	60		7.5	17
Keller and Melhorn, 1973	Dry Creek, California, USA	0.76		22.1	10	2
Kelsey, 1980	Van Duzen, California, USA	0.27[2]	575		70	53
Kesel and Baumann, 1981	Mississippi, Louisiana, USA	18.9	3450978	12000	1050	5
Kesel and Baumann, 1981	Mississippi, Louisiana, USA	18	3450978	12000	1050	6
Kesel and Baumann, 1981	Mississippi, Louisiana, USA	6.8	3450978	12000	1050	5
Kesel and Baumann, 1981	Mississippi, Louisiana, USA	14.8	3450978	12000	1050	16
Klimek, 1974	Wisloka, Poland	8	4245			
Knighton, 1973	Bollin, Cheshire, UK	0.9	56[2]			1.5
Knighton, 1973	Bollin, Cheshire, UK	0.09	120[2]		12.87	1.5
Knighton, 1973	Dean, Cheshire, UK	0.71	33[2]			1.5
Kondolf and Curry, 1986	Lower Carmel River, USA	0.6	660			
Laczay, 1977	Hernad, Hungary	7.5	5400			
Lajczak, 1995	Vistula, Poland	2.4	50000	470		60
Lajczak, 1995	Vistula, Poland	1.23	50000	470		92
Lajczak, 1995	Vistula, Poland	7.08	50000	470		60

Table A1.1: Overview of published erosion rates (continued).

Reference	River	Erosion Rate m/yr	Drainage Basin Area km²	Mean Annual Discharge m³/s	Bankfull Width m	Timespan of Measurement yr
Lapointe and Carson, 1986	Rouge, Canada	1.5	2800	57		50
Lawler, 1978	Ilston, Wales	0.05	6.41			
Lawler, 1986	Ilston, Wales	0.238[2]	13.18			1.5
Lawler, 1993	Ilston, Wales	0.064	6.75		5	2.25
Lawler and Bull, 1977	Pennard Pill, Wales	1.25	30			
Leeks *et al.*, 1988	Trannon, Wales	0.49	72			
Leopold, 1973	Watts Branch, Maryland, USA	0.43	9.6	0.09	7.6	
Leopold *et al.*, 1966	Slopewash Tributary, New Mexico, USA	0.006	0.13			
Leopold *et al.*, 1966	gully bank	0.006	9.7			
Lewin, 1972	Rheidol, Wales	1.92[2]	1794			
Lewin, 1972	Tyfi, Wales	1.41[2]	6334			
Lewin *et al.*, 1974	Maesnant, Wales	0.03	0.54			
Lewin *et al.*, 1977	Alwen, Wales	0.035			7.6	71
Lewin *et al.*, 1977	Amman, Wales	0.348			14.9	79
Lewin *et al.*, 1977	Banwy, Wales	0.67			24.8	46
Lewin *et al.*, 1977	Ceiriog, Wales	0.373			11.9	47
Lewin *et al.*, 1977	Ceirw, Wales	0.105			7.8	66
Lewin *et al.*, 1977	Clun, Wales	0.146			5	47
Lewin *et al.*, 1977	Clywd, Wales	0.051			4.3	72
Lewin *et al.*, 1977	Cych, Wales	0.107			6.6	60
Lewin *et al.*, 1977	Daron, Wales	0.073			1.3	58
Lewin *et al.*, 1977	Dee, Wales	0.114			31	72
Lewin *et al.*, 1977	Dee, Wales	0.057			35	72
Lewin *et al.*, 1977	Elan, Wales	0.145			19.8	62
Lewin *et al.*, 1977	Rheidol, Wales	0.462			23.5	64
Lewin *et al.*, 1977	Rhiw Saeson, Wales	0.108			5.2	60
Lewin *et al.*, 1977	Severn, Wales	0.234			26.8	62
Lewin *et al.*, 1977	Severn, Wales	0.162			16.1	62
Lewin *et al.*, 1977	Tawe, Wales	0.098			26.3	78
Lewin *et al.*, 1977	Tawe, Wales	0.286			22.4	78
Lewin *et al.*, 1977	Teme, Wales	0.327			9.6	61
Lewin *et al.*, 1977	Teme, Wales	0.334			9	62
Lewin *et al.*, 1977	Teme, Wales	0.328			10.7	61
Lewin *et al.*, 1977	Tywi, Wales	0.877			30.9	61
Lewin *et al.*, 1977	Usk, Wales	0.615			37	68
Lewin *et al.*, 1977	Usk, Wales	0.74			31.7	67
Lewin *et al.*, 1977	Wye, Wales	0.258			53.5	44
Leys and Werrity, 1999	Cleekhimin Burn, Scotland	0.998	25.2			126

Table A1.1: Overview of published erosion rates (continued).

Reference	River	Erosion Rate m/yr	Drainage Basin Area km²	Mean Annual Discharge m³/s	Bankfull Width m	Timespan of Measurement yr
McGreal and Gardiner, 1977	Lagan, Northern Ireland	0.08	85			
McKenney *et al.*, 1995	???, Arkansas, USA	1.5	380			
McKenney *et al.*, 1995	Jack's Fork, Missouri, USA	4.7	789		75	3
Micheli and Kirchner, 2002	South Fork Kern River, California, USA	0.24	380	11	30	40
Micheli and Kirchner, 2002	South Fork Kern River, California, USA	1.4	380	11	30	40
Mosley, 1975	Bollin, Cheshire, UK	1.66	120²		7.66	18
Mosley, 1975	Bollin, Cheshire, UK	3.6	120²		12.87	6
Mosley, 1975	Bollin, Cheshire, UK	0.16	120²		8.27	63
Murgatroyd and Ternan, 1983	Narrator Brook, Devon, UK	0.025	4.75		3.4	50
Nadler and Schumm, 1981	Arkansas, Colorado, USA	6.75²	30900²	6.8	45	51
Nanson and Hean, 1985	Illawara, New South Wales, Australia	16.4	37.8			
Nanson *et al.*, 1994	Gordon, Tasmania	0.06	5500²			1
Nanson *et al.*, 1994	Gordon, Tasmania	1	5500²			4
Nelson, 1966	Chemung, New York, USA	3.05				
Nicholas *et al.*, 1999	Alfios, Greece	3.3	3400²	55		30
Nicholas *et al.*, 1999	Alfios, Greece	3.5	3400²	55		3
Odgaard, 1987	Des Moines, Iowa, USA	2.4	32320			37
Odgaard, 1987	Des Moines, Iowa, USA	3.7	34640			37
Odgaard, 1987	Des Moines, Iowa, USA	3.2	36360			37
Odgaard, 1987	East Nishnabotna, Iowa, USA	2.1	1129			35
Odgaard, 1987	East Nishnabotna, Iowa, USA	3.2	2314			35
Okagbue and Abam, 1986	Ekole Creek, Nigeria	0.36	1560			1
Piégay and Marston, 1998	Ain, France	9	3762	130	67.5	18
Piégay and Marston, 1998	Ain, France	15	3762	130	67.5	28
Piest and Bowie, 1974	Pigeon Roost, Mississippi, USA	0.02	4			
Piest and Bowie, 1974	Pigeon Roost, Mississippi, USA	0.5	303			
Pizutto, 1994	Powder, Montana, USA	11	16875²	13	53.2	1
Pizutto, 1994	Powder, Montana, USA	1.01	16875²	13	53.2	14
Prosser *et al.*, 2000	Ripple Creek canal, Australia	0.013	46		2	1
Salo *et al.*, 1986	Rio Manú, Peru	12				13
Schmidt *et al.*, 1995	Snake River, Idaho, USA	3		531		3
Schmidt *et al.*, 1995	Snake River, Idaho, USA	6		531		3
Scott, 1982	Kenai, Alaska, USA	0.3	5700			
Simon and Hupp, 1992	Cane Creek, Tennessee, USA	2.35	225			2.5
Simon and Hupp, 1992	North Fork Deer River, Tennessee, USA	1.16	2465			2.5
Simon and Hupp, 1992	North Fork Obion River, Tennessee, USA	0.95	1496			2.5
Simon and Hupp, 1992	Rutherford Fork Obion River, Tennessee, USA	0.55	717			2.5
Simon and Hupp, 1992	South Fork Deer River, Tennessee, USA	1.26	2747			2.5

Table A1.1: Overview of published erosion rates (continued).

Reference	River	Erosion Rate m/yr	Drainage Basin Area km²	Mean Annual Discharge m³/s	Bankfull Width m	Timespan of Measurement yr
Simon and Hupp, 1992	South Fork Obion River, Tennessee, USA	0.9	1103			2.5
Smith *et al.*, 1993	Bambi Creek, Alaska, USA	0.5	1.55		3.9	4
Soufi, 1997	gully bank	0.0114	0.1			
Stanley *et al.*, 1966	Mississippi, Louisiana, USA	2.6	3450978	16860		17
Stott, 1997	Kirkton, Scotland	0.047	6.85			10
Stott, 1997	Monachyle, Scotland	0.059	7.7			10
Stott, 1999	Cyff, Wales	0.05	3.1			1.5
Stott, 1999	Tanllwyth, Wales	0.035	0.89	0.06		2.5
Stott, 1999	Tanllwyth, Wales	0.095	0.89	0.06		2.5
Sundborg, 1956	Klaralven, Sweden	1.6				
Thomson and Townsend, 1979	North Saskatchewan, Canada	0.6		570		70
Thomson and Townsend, 1979	North Saskatchewan, Canada	1.5		570		5
Thomson and Townsend, 1979	North Saskatchewan, Canada	0.3		570		23
Thorne and Lewin, 1979	Severn, Wales	0.45	375		30	1
Thorne and Lewin, 1979	Severn, Wales	0.7	375		30	27
Thorne and Tovey, 1981	Severn, Wales	0.37				2
Trimble, 1994	Jenkins Creek, Tennessee, USA	0.056	14.4		0.8	6
Twidale, 1964	Torrens, Australia	0.58	77			3
Vertessey, 1990	Daly, Australia	20				14
Walker *et al.*, 1987	Colville, Alaska, USA	1.6	53000	500		3
Warner, 1987	Bellinger River, New South Wales, Australia	0.8	1200			
Watson *et al.*, 1997	Harland Creek, Mississippi, USA	4.27			21.6	36
Werrity and Ferguson, 1980	Feshie, Scotland	4	235	8.1		1
Williams *et al.*, 1979	Ottawa River, Canada	0.6	148000		1300[2]	56
Wolman, 1959	Watts Branch, Maryland, USA	0.43	10.24		6	5
Wolman and Leopold, 1957	Colorado River, California, USA	243	441663			25
Wolman and Leopold, 1957	Larami River, Wyoming, USA	0.3	11909			103
Wolman and Leopold, 1957	Mississippi River, Mississippi, USA	48	2847769			15
Wolman and Leopold, 1957	Missouri River, Nebraska, USA	76	906108			20
Wolman and Leopold, 1957	North River, Virginia, USA	2.43	129.4			
Wolman and Leopold, 1957	Ramanga River, India	3.95	258888			62
Wolman and Leopold, 1957	Ramanga River, India	4.25	258888			77
Wolman and Leopold, 1957	Ramanga River, India	80	258888			21
Wolman and Leopold, 1957	Seneca Creek, Maryland, USA	0.06	264.5			50
Woodyer *et al.*, 1979	Barwon River, Australia	0.3	139000			10

Table A1.2: Overview of published accretion rates.

Reference	River	accretion type	accretion rate (m/yr)
Hupp, 1992	Cub Creek, Tennessee, USA	lateral	0.05
Hupp, 1992	Hatchie, Tennessee, USA	lateral	0.01
Hupp, 1992	Obion, Tennessee, USA	lateral	0.05
Hupp, 1992	Pond Creek, Tennessee, USA	lateral	0.05
Hupp, 1992	Porters Creek, Tennessee, USA	lateral	0.05
Hupp, 1992	Wolf, Tennessee, USA	lateral	0.03
Nanson and Beach, 1977	Beatton, BC, Canada	lateral	0.5
Ritter *et al.*, 1973	Delaware, Pennsylvania, USA	vertical	0.001
Moody *et al.*, 1999	Powder, Montana, USA	vertical	0.005
Nanson and Beach, 1977	Beatton, BC, Canada	vertical	0.008
Nanson and Beach, 1977	Beatton, BC, Canada	vertical	0.6
Macklin *et al.*, 1992	Tyne, United Kingdom	vertical	0.07
Macklin *et al.*, 1992	Tyne, United Kingdom	vertical	0.004
Walling *et al.*, 1992	Culm, United Kingdom	vertical	0.007
Walling *et al.*, 1992	Severn, United Kingdom	vertical	0.005
Gomez *et al.*, 1999	New Waipaoa, Zealand	vertical	0.5

Appendix 2

Expression for Failure Plane Angle under Simplified Conditions

Equation 3.92 can be solved analytically under simplified conditions, where the hydrostatic confining pressure, F_{cp}, and the pore pressures, F_{cp} and F_{ms}, are considered negligible. In this case equation 3.93 is reduced to:

$$c = \frac{W_f}{L_f}\left(\sin\beta_f - \cos\beta_f \tan\phi\right)$$

Using equations 3.70 to 3.72 to expand W_f and L_f, this can be rewritten as:

$$c = \frac{\sin\beta_f}{\left(H_b - H_t\right)}\frac{\gamma}{2}\left[\frac{H_b^2 - H_t^2}{\tan\beta_f} - \frac{\left(H_b - H_{cb}\right)^2 - H_c^2}{\tan\beta_b}\right]\left(\sin\beta_f - \cos\beta_f \tan\phi\right)$$

or, when regrouped in terms of β_f:

$$c = \frac{\gamma}{2}\frac{1}{\left(H_b - H_t\right)}\left[\frac{A_1}{\tan\beta_b}\left(\sin\beta_f \cos\beta_f \tan\phi - \sin^2\beta_f\right) - A_2\left(\cos^2\beta_f \tan\phi - \sin\beta_f \cos\beta_f\right)\right]$$

where

$$A_1 = \left(H_b - H_{cb}\right)^2 - H_c^2$$

$$A_2 = H_b^2 - H_t^2$$

Using this expression for c, equation 3.92 is solved as follows

$$\frac{\partial c}{\partial \beta_f} = 0$$

$$\Leftrightarrow \quad \frac{A_1}{\tan\beta_b}\left[\tan\phi\,\frac{\partial\left(\sin\beta_f\cos\beta_f\right)}{\partial\beta_f} - \frac{\partial\sin^2\beta_f}{\partial\beta_f}\right] - A_2\left[\tan\phi\,\frac{\partial\cos^2\beta_f}{\partial\beta_f} - \frac{\partial\left(\sin\beta_f\cos\beta_f\right)}{\partial\beta_f}\right] = 0$$

$$\Leftrightarrow \quad \frac{A_1}{\tan\beta_b}\left[\tan\phi\cos\left(2\beta_f\right) - \sin\left(2\beta_f\right)\right] - A_2\left[-\tan\phi\sin\left(2\beta_f\right) - \cos\left(2\beta_f\right)\right] = 0$$

$$\Leftrightarrow \quad \cos\left(2\beta_f\right)\tan\phi - \sin\left(2\beta_f\right) + \frac{A_2\tan\beta_b}{A_1}\left[\sin\left(2\beta_f\right)\tan\phi + \cos\left(2\beta_f\right)\right] = 0$$

$$\Leftrightarrow \quad \tan\phi - \tan\left(2\beta_f\right) + \frac{A_2}{A_1}\tan\left(2\beta_f\right)\tan\beta_b\tan\phi + \frac{A_2}{A_1}\tan\beta_b = 0$$

$$\Leftrightarrow \quad \tan\left(2\beta_f\right)\left[1 - \frac{A_2}{A_1}\tan\beta_b\tan\phi\right] = \frac{A_2}{A_1}\tan\beta_b + \tan\phi$$

$$\Leftrightarrow \quad \tan\left(2\beta_f\right) = \frac{\frac{A_2}{A_1}\tan\beta_b + \tan\phi}{1 - \frac{A_2}{A_1}\tan\beta_b\tan\phi}$$

Using the trigonometric relation $\tan\left(x+y\right) = \dfrac{\tan x + \tan y}{1 - \tan x\tan y}$, this can be solved for β_f:

$$\beta_f = \frac{1}{2}\left[\arctan\left(\frac{A_2}{A_1}\tan\beta_b\right) + \phi\right]$$

which is the solution presented in chapter 3 (equation 3.100).

Appendix 3
Grid Sensitivity Analysis

The dependency of the MRIPA model to grid parameterization is tested through a series of simulations in which the grid resolutions, and hence the grid cell dimensions, are varied, while other parameters and boundary conditions are kept constant. The effect of the changes in grid resolution are measured as changes in simulated values for five indicators: maximal flow velocity, U_{max}; average change in bed elevation in eroding cells, $\Delta\overline{Z}_{ero}$ (equation 5.5); average change in bed elevation in depositional cells, $\Delta\overline{Z}_{dep}$ (equation 5.6); total volumetric change in eroding cells, V_{ero} (equation 5.9); and total volumetric change in depositional cells, V_{dep} (equation 5.10).

Simulations are run for the IIHR and UCB flume experiments (*cf.* section 4.3), and for the idealized meandering (IM) channel (*cf.* section 5.4). For each of these channels, the simulations start with a flat bed, thereby guaranteeing an identical initial morphological setup for each of the grids used in the sensitivity analysis. No grid sensitivity analysis was performed for the Goodwin Creek scenario (*cf.* section 4.4), as the initial bed morphology is non-uniform throughout the channel. Applying different grid resolutions to this channel, involves interpolation the bed topography to correspond to the new grid cell dimensions. Interpretation of such simulations is skewed, as any differences in the simulated output would reflect not only the grid-dependency of the model, but also the model's response to the differences in bed morphology.

The grid properties of the simulations included in the sensitivity analysis are listed in table A3.1, as are the modelled values of the selected indicators. The impact of the grid size on the indicators is analysed by looking at the variations in simulated indicator. To facilitate comparison between indicators and channels, these variations are considered relative to the averages of the simulated indicator values for each channel. Ideally, these deviations would be equal to 0.0%, indicating that the model output is completely independent of the grid parameterization. In practice, however, small deviations of up to 5% are observed (table A3.2). These deviations show a slight relation to the cell dimension ratio, *dS/dN*, defined as average cell length over average cell width (figures A3.1 - A3.5).

Table A3.1: Overview of grid sensitivity simulations.

simulation series	grid properties					simulation results				
	# cells longitudinal [-]	# cells transverse [-]	average cell length [m]	average cell width [m]	length/width ratio [-]	maximum flow velocity [m/s]	average erosion [m]	average deposition [m]	erosion volume [m^3]	deposition volume [m^3]
IIHR	35	21	2.06	0.12	16.87	0.508	3.94×10^{-2}	3.20×10^{-2}	7.46	6.66
	35	15	2.06	0.17	11.83	0.505	4.01×10^{-2}	3.23×10^{-2}	7.41	6.62
	35	11	2.06	0.24	8.43	0.501	4.18×10^{-2}	3.15×10^{-2}	7.31	6.53
	35	9	2.06	0.31	6.75	0.498	4.25×10^{-2}	3.09×10^{-2}	7.22	6.47
	69	21	1.03	0.12	8.43	0.509	3.91×10^{-2}	3.23×10^{-2}	7.35	6.74
	69	15	1.03	0.17	5.91	0.506	3.98×10^{-2}	3.24×10^{-2}	7.30	6.70
	69	11	1.03	0.24	4.22	0.502	4.19×10^{-2}	3.17×10^{-2}	7.20	6.61
	69	9	1.03	0.31	3.37	0.499	4.25×10^{-2}	3.12×10^{-2}	7.12	6.54
UCB	48	7	0.29	0.04	6.98	0.344	7.49×10^{-3}	4.25×10^{-3}	3.34×10^{-2}	3.27×10^{-2}
	48	9	0.29	0.03	9.45	0.351	6.81×10^{-3}	4.39×10^{-3}	3.46×10^{-2}	3.37×10^{-2}
	48	11	0.29	0.03	11.72	0.356	7.04×10^{-3}	4.28×10^{-3}	3.52×10^{-2}	3.42×10^{-2}
	48	15	0.29	0.02	16.28	0.363	6.92×10^{-3}	4.29×10^{-3}	3.61×10^{-2}	3.48×10^{-2}
	79	7	0.18	0.04	4.19	0.344	7.33×10^{-3}	4.14×10^{-3}	3.35×10^{-2}	3.28×10^{-2}
	79	9	0.18	0.03	5.68	0.351	6.96×10^{-3}	4.28×10^{-3}	3.47×10^{-2}	3.38×10^{-2}
	79	11	0.18	0.03	7.04	0.357	7.23×10^{-3}	4.22×10^{-3}	3.54×10^{-2}	3.43×10^{-2}
	79	15	0.18	0.02	9.78	0.363	7.07×10^{-3}	4.22×10^{-3}	3.63×10^{-2}	3.49×10^{-2}
	79	21	0.18	0.01	13.54	0.369	7.00×10^{-3}	4.19×10^{-3}	3.65×10^{-2}	3.53×10^{-2}
	110	7	0.13	0.04	3.00	0.344	7.39×10^{-3}	4.16×10^{-3}	3.37×10^{-2}	3.30×10^{-2}
	110	11	0.13	0.03	5.04	0.357	7.26×10^{-3}	4.26×10^{-3}	3.55×10^{-2}	3.45×10^{-2}
	110	21	0.13	0.01	9.69	0.369	7.11×10^{-3}	4.25×10^{-3}	3.68×10^{-2}	3.54×10^{-2}
IM	80	9	11.39	2.50	4.56	1.243	2.12×10^{-1}	1.82×10^{-1}	9475	11018
	80	13	11.39	1.67	6.82	1.239	2.02×10^{-1}	1.82×10^{-1}	9517	11092
	80	17	11.39	1.25	9.11	1.243	1.98×10^{-1}	1.80×10^{-1}	9561	11106
	80	21	11.39	1.00	11.39	1.245	1.96×10^{-1}	1.79×10^{-1}	9577	11107
	200	9	4.52	2.50	1.81	1.230	2.12×10^{-1}	1.77×10^{-1}	9439	11018
	200	11	4.52	2.00	2.26	1.239	2.05×10^{-1}	1.77×10^{-1}	9439	11049
	200	15	4.52	1.43	3.16	1.225	1.99×10^{-1}	1.75×10^{-1}	9478	11112
	200	19	4.52	1.11	4.07	1.228	1.96×10^{-1}	1.74×10^{-1}	9485	11125
	200	21	4.52	1.00	4.52	1.230	1.95×10^{-1}	1.73×10^{-1}	9499	11139
	320	11	2.82	2.00	1.41	1.230	2.07×10^{-1}	1.75×10^{-1}	9460	11070
	320	17	2.82	1.25	2.26	1.225	1.97×10^{-1}	1.73×10^{-1}	9452	11104
	320	21	2.82	1.00	2.82	1.225	1.94×10^{-1}	1.72×10^{-1}	9458	11119

Table A3.2: Descriptive statistics of grid sensitivity simulations.

		IIHR	UCB	IM
simulation properties	number of simulations	8	12	12
	range of cell lengths	1.03 - 2.06	0.13 - 0.29	2.82 - 11.39
	range of cell widths	0.12 - 0.31	0.01 - 0.04	1.00 - 2.50
	range of dS / dN ratios	3.4 - 16.9	3.0 - 16.3	1.4 - 11.4
maximum flow velocity	average [m/s]	0.504	0.356	1.234
	standard deviation [m/s]	0.004	0.009	0.008
	maximal relative deviation [%]	1.10	3.75	0.96
average erosion	average [m]	4.09×10^{-2}	7.13×10^{-3}	2.01×10^{-2}
	standard deviation [m]	1.44×10^{-3}	2.06×10^{-4}	6.61×10^{-3}
	maximal relative deviation [%]	4.40	4.99	5.65
average deposition	average [m]	3.18×10^{-2}	4.24×10^{-3}	1.77×10^{-1}
	standard deviation [m]	5.63×10^{-4}	6.63×10^{-5}	3.43×10^{-3}
	maximal relative deviation [%]	2.71	3.44	3.26
total erosion volume	average [m^3]	7.29	3.52×10^{-2}	9487
	standard deviation [m^3]	0.113	1.19×10^{-3}	44.9
	maximal relative deviation [%]	2.45	4.92	0.95
total deposition volume	average [m^3]	6.61	3.41×10^{-2}	11088
	standard deviation [m^3]	0.091	9.29×10^{-4}	40.6
	maximal relative deviation [%]	2.13	4.04	0.64

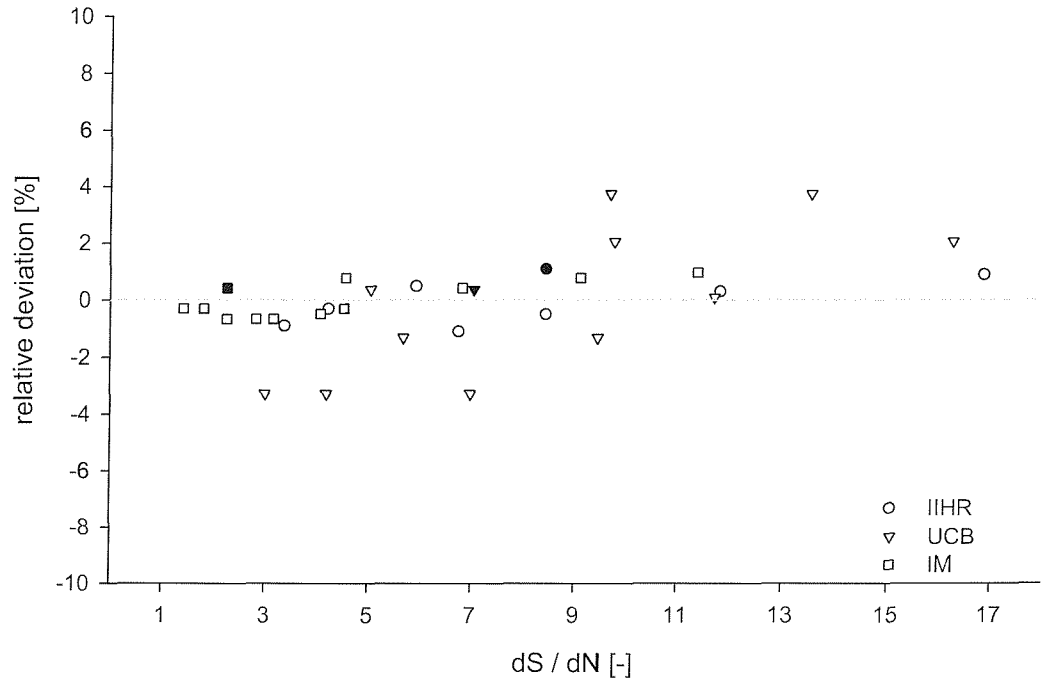

Figure A3.1: Sensitivity of maximum flow velocity to grid cell dimensions. Filled symbols mark the grids used for the simulations in the main text.

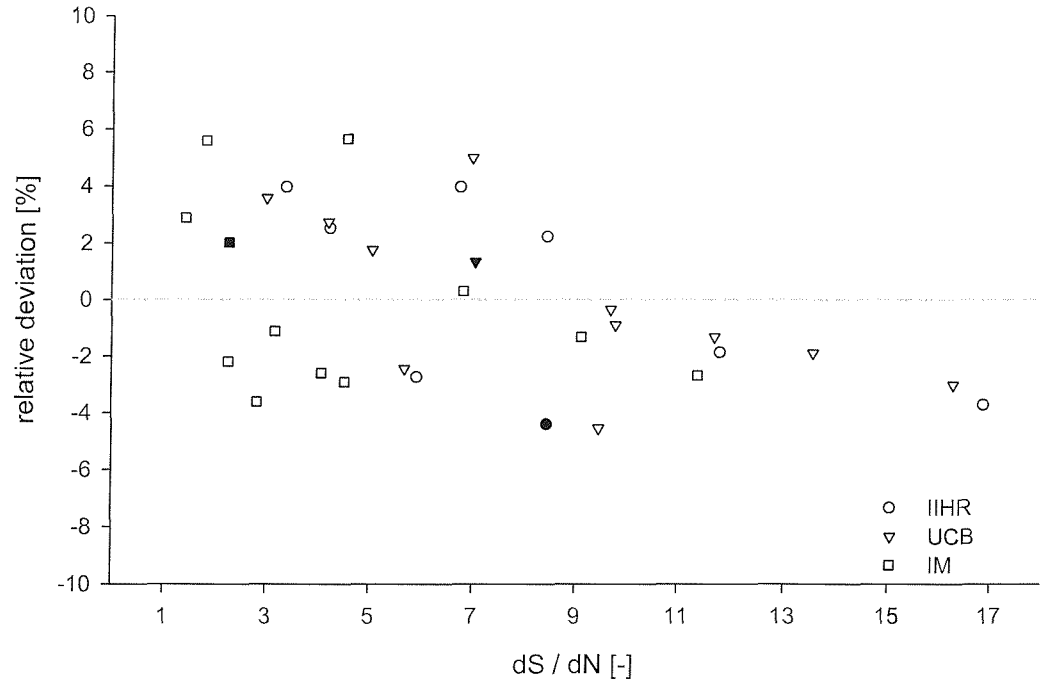

Figure A3.2: Sensitivity of average bed erosion to grid cell dimensions. Filled symbols mark the grids used for the simulations in the main text.

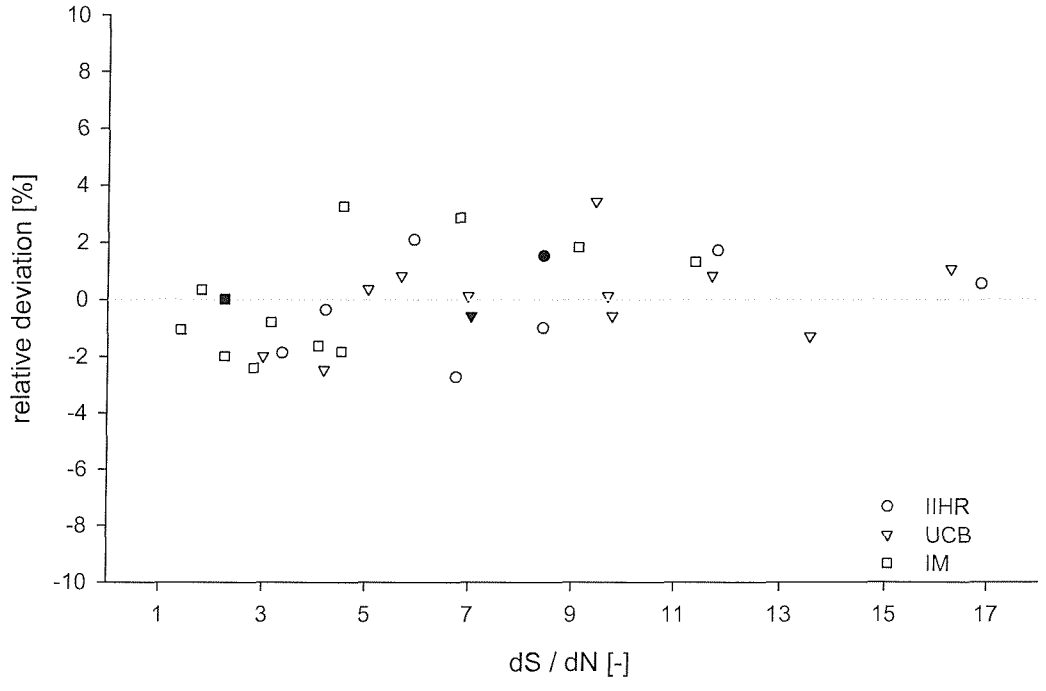

Figure A3.3: Sensitivity of average bed deposition to grid cell dimensions. Filled symbols mark the grids used for the simulations in the main text.

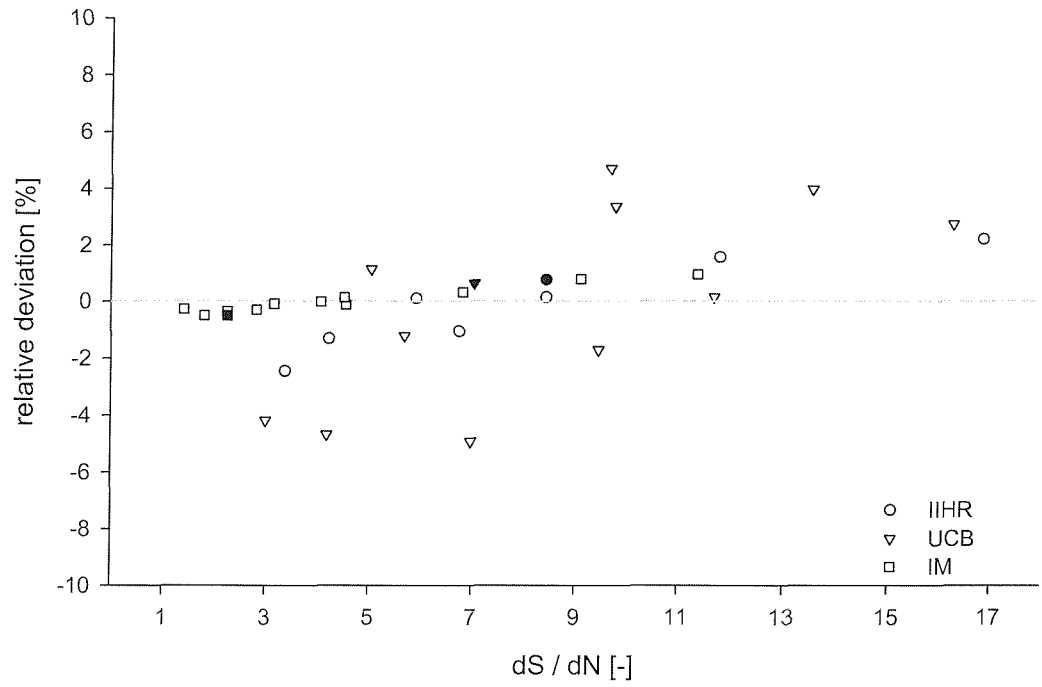

Figure A3.4: Sensitivity of total erosion volume to grid cell dimensions. Filled symbols mark the grids used for the simulations in the main text.

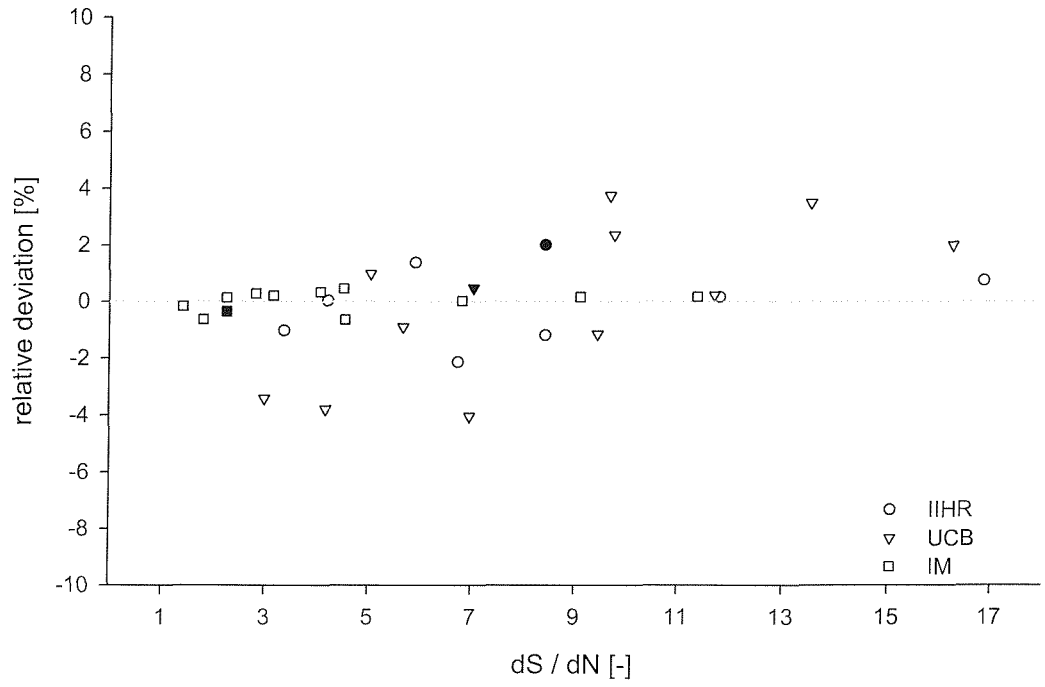

Figure A3.5: Sensitivity of total deposition volume to grid cell dimensions. Filled symbols mark the grids used for the simulations in the main text.

Grid resolution has the strongest impact on $\Delta\overline{Z}_{ero}$ and $\Delta\overline{Z}_{dep}$ (table A.3.2; figures A3.2 and A4.3.3). However, these indicators do not account for the surface area of the grid cells (*cf.* section 5.4.2). The volumetric indicators, V_{ero} and V_{dep}, which do account for cell surface area, are less affected by grid resolution. Both V_{ero} and V_{dep}, as well as U_{max}, tend to increase with increasing cell dimension ratio (figures A3.4, A3.4 and A3.5). With the exception of $\Delta\overline{Z}_{ero}$, the sensitivity of the indicators to grid parameterization is greater in the UCB channel, which might be indicative of the low r_c/w ratio of this channel ($r_c/w = 3.24$). MRIPA is designed for use in mildly curved channels ($r_c/w > 5.0$), where deviation of orthogonality and grid point spacing gradients are small. Although adjustments are made to the flow equations to account for non-orthogonality of the grids (Mosselman, 1991; 1992), the model appears to be more sensitive to changes in grid parameterization in sharply curved channels. In mildly curved channels, such as the IIHR and IM channels included here, the grid discretization has a lesser impact on U_{max}, V_{ero} and V_{dep}.

Appendix 4

Mass Conservation

A4.1. Conservation of water

The mass conservation of flow is measured here by calculating the cross-sectional discharge after the flow field has established. This is done for each of the grids used in the main text: the IIHR and UCB flume experiments (*cf.* section 4.3), the Goodwin Creek (GC) reach (*cf.* section 4.4), and the idealized meandering (IM) channel (*cf.* section 5.4). The prescribed inflow-discharges for these channels vary over 5 orders of magnitude.

Ideally, the calculated cross-sectional discharge should be equal to the prescribed inflow-discharge, for each of the cross-sections on the grid. In practice, small deviations are observed. The deviations are very small (< 0.25 %) for the IIHR and UCB flumes and for the IM channel, but are more pronounced (up to 2.5%) for the Goodwin Creek channel (table A4.1). There is no systematic trend in the deviations (figure A4.1). For the IIHR channel the average deviation is less than 0.01%; the UCB and GC channel slightly over-predict discharge (respectively by 0.08% and 0.29% on average), while the IM channel tends to underpredict the cross-sectional discharge (by 0.06%). It is clear from the spatial distribution in the GC channel the errors are not cumulative. Instead the deviations appear to be arbitrary for each cross-section. The undulating pattern of deviations observed on the UCB channel might suggest a relation between the deviation channel curvature. However, this hypothesis is refuted by absence of such undulations in the IM channel.

Table A4.1: Water conservation data

	IIHR	UCB	IM	GC
number of cross-sections	41	79	200	41
prescribed discharge [m^3/s]	0.147	0.001	20.0	7.50
mean modelled discharge [m^3/s]	0.147	0.001	20.0	7.52
maximal difference [%]	0.038	0.211	0.057	2.532
median difference [%]	0.008	0.072	-0.064	0.089
mean difference [%]	0.009	0.083	-0.056	0.292
standard deviation [%]	0.006	0.073	0.057	0.528

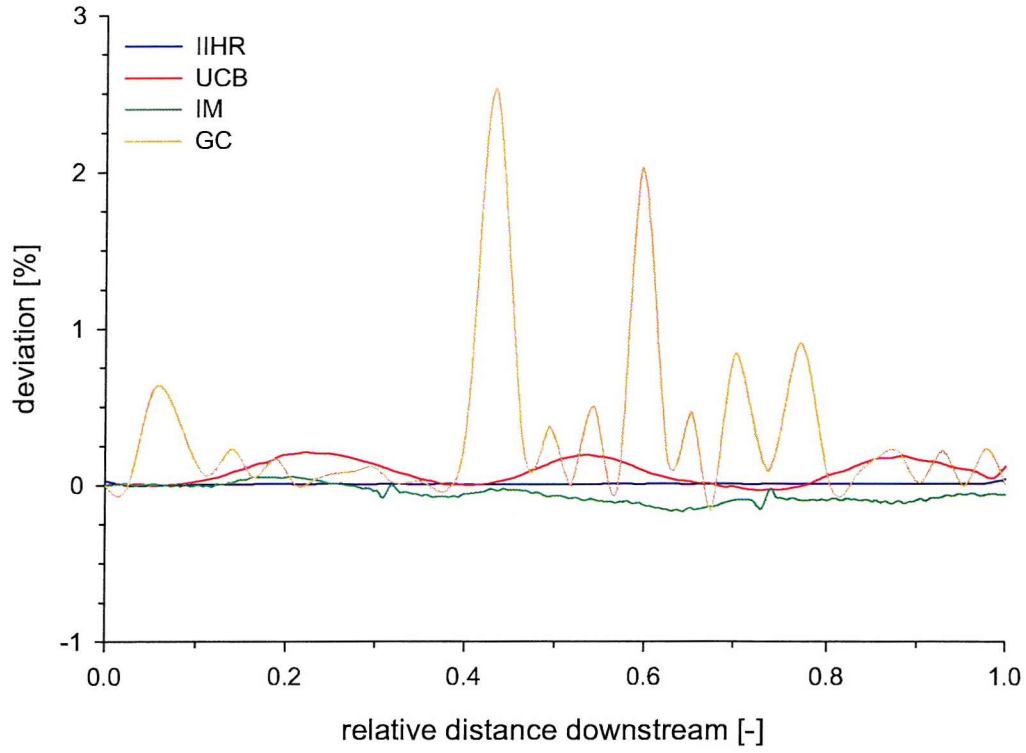

Figure A4.1: Deviation in cross-sectional discharge throughout the channel. The distance along the channel is scaled to the total channel length for each channel.

A4.2. Conservation of sediment

The conservation of sediment is explicitly programmed into the model. For each grid point, the adjust of the bed elevation, dz_b/dt, is calculated from equation 3.126. However, repeated application in time and space might introduce errors. On a reach scale, the total sediment volume of the sources, V_{src}, should equal the total sediment volume of the sinks, V_{snk}; where V_{src} = sediment inflow + sediment eroded from the bed + sediment eroded from the banks (without washload), and V_{snk} = sediment outflow + sediment deposited on the bed. The difference, $\Delta V = V_{src} - V_{snk}$, can be considered a measure of the conservativeness of the model. However, it is dependent on the spatial scale of the model and on the duration of the simulation. Therefore a normalized relative difference, $\Delta V_{rel} = \Delta V / V_{src}$, is used. Table A4.2 lists the reach-scale totalled contributions to the sediment equation, at the end of each simulation. The small values of ΔV_{rel} (between 0.0004% and 0.0460 %) indicate that MRIPA can be considered to be mass conservative for sediment.

Table A4.2: Sediment conservation data

	IIHR	UCB	IM	GC
sediment inflow [m^3]	3.15×10^{0}	6.86×10^{-3}	3.82×10^{4}	2.32×10^{5}
bed erosion [m^3]	1.14×10^{1}	3.35×10^{-2}	9.44×10^{3}	4.47×10^{2}
bank erosion [m^3]	-	-	5.63×10^{2}	1.58×10^{3}
sediment outflow [m^3]	7.14×10^{0}	7.56×10^{-3}	3.71×10^{4}	2.33×10^{5}
bed deposition [m^3]	7.44×10^{0}	3.28×10^{-2}	1.10×10^{4}	1.31×10^{3}
difference [m^3]	-9.68×10^{-5}	-1.86×10^{-5}	-2.09×10^{-1}	-1.05×10^{1}
relative difference [%]	-0.0007	-0.0460	-0.0004	-0.0045

Bibliography

Abam, T.K., 1993. "Factors affecting distribution of instability of river banks in the Niger Delta", Engineering Geology, 35, pp.123-133.

Abam, T.K.S., 1997. "Genesis of bank channel overhangs in the Niger Delta and analysis of failure", Geomorphology, 18, pp.151-164.

Abbe, T.B., and Montgomery, D.R., 1996. "Large woody debris jams, channel hydraulics and habitat formation in large rivers", Regulated Rivers Research and Management, 12, pp.201-221.

Abernethy, B., 1999. On the Role of Woody Vegetation in Riverbank Stability. PhD Thesis, Monash University, Clayton, Victoria, Australia.

Abernethy, B., and Rutherfurd, I.D., 1998. "Where along a river's length will vegetation most effectively stabilise stream banks", Geomorphology, 23, pp.55-75.

Abernethy, B., and Rutherfurd, I.D., 2000a. "The effect of riparian tree roots on the mass-stability of riverbanks", Earth Surface Processes and Landforms, 25, pp.921-937.

Abernethy, B., and Rutherfurd, I.D., 2000b. "Does the weight of trees destabilize riverbanks?", Regulated Rivers Research and Management, 16, pp.565-576.

Abernethy, B., and Rutherfurd, I.D., 2001. "The distribution and strength of riparian tree roots in relation to riverbank reinforcement", Hydrological Processes, 15, pp.63-79.

Abt, S.R., Clary, W.P., and Thornton, C.I., 1994. "Sediment deposition and entrapment in vegetated streambeds", Journal of Irrigation and Drainage Engineering, ASCE, 120, pp.1098-1111.

Ackers, P., and Charlton, F.G., 1970. "Meander geometry aring from varying flows", Journal of Hydrology, 11, pp.230-252.

Ackers, P., and White, W.R., 1973. "Sediment transport: a new approach and analysis", Journal of the Hydraulics Division, ASCE, 99, pp.2041-2060.

Alabyan, A., and Chalov, R.S., 1998. "Types of river channel patterns and their natural controls", Earth Surface Processes and Landforms, 23, pp.467-474.

Alexander, C.S., and Nunnally, N.R., 1972. "Channel stability on the lower Ohio River", Annals of the Association of American Geographers, 62, pp.411-417.

Allen, J.R.L., 1965. "A review of the origin and characteristics of recent alluvial sediments", Sedimentology, 5, pp.89-191.

Allen, J.R.L., 1970. "A quantitative model of grain size and sedimentary structures in lateral deposits", Journal of Geology, 7, pp.129-146.

Allen, J.R.L., 1984. Sedimentary Structures: Their Character and Physical Basis, Elsevier, Amsterdam, The Netherlands

Amlin, N.A., and Rood, S.B., 2001. "Inundation tolerances of riparian willows and cottonwoods", Journal of the American Water Resources Association, 37, pp.1709-1720.

Ananyan, A.K., 1957. Fluid Flow in Bends of Conduits, (In Russian; English translation: Israel Program for Scientific Translations,1965)

Anderson, J.D., 1995. Computational Fluid Dynamics, McGraw-Hill, Singapore. 547 p.

Andrews, E.D., 1982. "Bank stability and river width adjustment, East Fork River, Wyoming", Water Resources Research, 18, pp.1184-1192.

Andrews, E.D., 1984. "Bed-material entrainment and hydraulic geometry of gravel-bed rivers in Colorado", Geological Society of America Bulletin, 95, pp.371-378.

Arcement, G.J.J., and Schneider, V.R., 1989. Guide for selecting Manning's roughness coefficients for natural channels and floodplains. FHWA-TS-84-204, US Dept. of Transport, Federal

Highway Administration.

Ariathurai, R., and Arulanandan, K., 1978. "Erosion rates of cohesive soils", Journal of the Hydraulics Division, ASCE, 104, pp.279-283.

ASCE Task Committee on Hydraulics Bank Mechanics and Modeling of River Width Adjustment, 1998a. "River width adjustment. I: Processes and mechanisms", Journal of Hydraulic Engineering, ASCE, 124, pp.881-902.

ASCE Task Committee on Hydraulics Bank Mechanics and Modeling of River Width Adjustment, 1998b. "River width adjustment. II: Modeling", Journal of Hydraulic Engineering, ASCE, 124, pp.903-917.

Axelsson, V., 1967. "The Laitaure delta. A study of deltaic morphology and processes", Geografiska Annaler, 49A, pp.1-127.

Barnes, H.H.J., 1967. "Roughness characteristics of natural channels", USGS Water Resources Investigations, 1849, pp.213.

Bartholdy, J., and Billi, P., 2002. "Morphodynamics of a pseudomeandering gravel bar reach", Geomorphology, 42, pp.293-310.

Bates, P.D., Anderson, M.G., Baird, L., Walling, D.E., and Simm, D., 1992. "Modelling floodplain flow with a two dimensional finite element scheme", Earth Surface Processes and Landforms, 17, pp.575-588.

Bates, P.D., Anderson, M.G., Price, D.A., Hardy, R.J., and Smith, C.N., 1996. "Analysis and development of hydraulic models for floodplain flows", In: Floodplain Processes, M.G. Anderson, D.E. Walling, and P.D. Bates (eds.), John Wiley, Chichester, U.K., pp.215-254.

Bates, P.D., and De Roo, A.P.J., 2000. "A simple raster-based model for flood inundation simulation", Journal of Hydrology, 236, pp.54-77.

Bates, P.D., Horritt, M., and Hervouet, J.-M., 1998. "Investigating two-dimensional, finite element predictions of floodplain inundation using fractal generated topography", Hydrological Processes, 12, pp.1257-1277.

Bates, P.D., Horritt, M.S., Smith, C.N., and Mason, D., 1997. "Integrating remote sensing observations of flood hydrology and hydraulic modelling", Hydrological Processes, 11, pp.1777-1795.

Bathurst, J.C., 1979. "Distribution of boundary shear stress in rivers", In: Adjustment of the Fluvial System, D.D. Rhodes and G.P. Williams (eds.), Kendall/Hunt, Dubuque, Iowa, pp.95-116.

Bathurst, J.C., Thorne, C.R., and Hey, R.D., 1977. "Direct measurements of secondary currents in river bends", Nature, 269, pp.504-506.

Bathurst, J.C., Thorne, C.R., and Hey, R.D., 1979. "Secondary flow and shear stress at river bends", Journal of the Hydraulics Division, ASCE, 105, pp.1277-1295.

Bayley, P.B., 1995. "Understanding large river-floodplain ecosystems", BioScience, pp.45.

Beffa, C., and Connell, R.J., 2001. "Two-dimensional flood plain flow. II: Model validation", Journal of Hydrologic Engineering, ASCE, 6, pp.406-415.

Bendix, J., 1998. "Impact of a flood on southern California riparian vegetation", Physical Geography, 19, pp.162-174.

Berlamont, J., Ockenden, M., Toorman, E., and Winterwerp, J., 1993. "The characterisation of cohesive sediment properties", Coastal Engineering, 21, pp.105-128.

Best, J.L., 1996. "The fluid dynamics of small-scale alluvial bedforms", In: Advances in Fluvial Dynamics and Stratigraphy, P.A. Carling and M.R. Dawson (eds.), John Wiley, Chichester, UK, pp.67-125.

Beven, K., 1996. "Equifinality and uncertainty in geomorphological modelling", In: The Scientific Nature of Geomorphology, B.L. Rhoads and C.E. Thorne (eds.), John Wiley, Chichester, UK, pp.289-313.

Beven, K., and Binley, A., 1992. "The future of distributed models: Model calibration and uncertainty prediction", Hydrological Processes, 6, pp.279-298.

Biedenham, D.S., Combs, P.G., Hill, G.J., Pinkard, C.F., and Pinkston, C.B., 1989. "Relationship between channel migration and radius of curvature on the Red River", In: Sediment Transport Modelling, S.S. Wong (ed.), American Society of Civil Engineers.

Biggs, B.J.F., 1996. "Hydraulic habitat of plants in streams", Regulated Rivers Research and Management, 12, pp.131-144.

Binns, W.O., 1980. Trees and Water, Forestry Commision Research Station, Farnham, UK.

Bishop, A.W., 1955. "The use of the slip circle in the stability analysis of slopes", Geotechnique, 5, pp.7-17.

Blackmarr, W.A., 1995. Documentation of hydrologic, geomorphic and sediment transport measurements on the Goodwin Creek Experimental Watershed, Northern Mississippi, for the period 1982 to 1993. Research Report 3, National Sedimentation Laboratory, US Department of Agriculture, Oxford, Mississippi.

Blacknell, C., 1981. "River erosion in an upland catchment", Area, 13, pp.39-44.

Blondeaux, P., and Seminara, G., 1985. "A unified bar-bend theory of river meanders", Journal of Fluid Mechanics, 157, pp.449-470.

Bluck, B.J., 1971. "Sedimentation in the meandering River Endrick", Scottish Journal of Geology, 7, pp.93-138.

Booker, D.J., Sear, D.A., and Payne, A.J., 2001. "Modelling three-dimensional flow structures and patterns of boundary shear stress in a natural pool-riffle sequence", Earth Surface Processes and Landforms, 26, pp.553-576.

Bradbrook, K.F., Biron, P.M., Lane, S.N., Richards, K.S., and Roy, A.G., 1998. "Investigation of controls on secondary circulation in a simple confluence geometry using a three-dimensional numerical model", Hydrological Processes, 12, pp.1371-1396.

Brandt, C.J., and Thornes, J.B., 1987. "Erosional energetics", In: Energetics of Physical Environment, K.J. Gregory (ed.), John Wiley, Chichester, UK, pp.50-87.

Bray, D.I., 1987. "A study of channel changes in a reach of the North Nashwaaksis stream, New Brunswick, Canada", Earth Surface Processes and Landforms, 12, pp.151-165.

Brice, J., 1977. Lateral migration of the Middle Sacramento River, California. 77/052, NTIS Rep. PB-271 662, US Geological Survey.

Brice, J.C., 1973. "Meandering patterns of the White River in Indiana - an analysis", In: Fluvial Geomorphology, M. Morisawa (ed.), State University New York, Binghamton, N.Y., pp.178-200.

Bridge, J.S., "Flow and sedimentary processes in river bends: comparison of field observation and theory", In: River Meandering, 24-26 October, 1983, New Orleans, Louisiana, C.M. Elliot (ed.), ASCE, New Orleans, Louisiana, pp.857-872.

Bridge, J.S., and Jarvis, S., 1982. "The dynamics of a river bend: a study in flow and sedimentary processes", Sedimentology, 29, pp.499-541.

Brierley, G.J., and Fitchett, K., 2000. "Channel planform adjustments along the Waiau River, 1946-1992: Assessment of the impacts of flow regulation", In: River Management: The Australian Experience, S. Brizga and B. Fnlayson (eds.), John Wiley, Chichester, UK, pp.51-71.

Bull, L.J., 1996. Dynamics of Fluvial Suspended Sediment Transport from Bank Erosion Sediment Supply. PhD Thesis, University of Birmingham, Birmingham, UK.

Bull, L.J., 1997. "Magnitude and variation in the contribution of bank erosion to the suspended load to the Riven Severn, UK", Earth Surface Processes and Landforms, 22, pp.1109-1124.

Burckhart, J.C., and Todd, B.L., 1998. "Riparian forest effect on lateral stream channel migration in the glacial till plains", Journal of the American Water Resources Association, 34, pp.179-184.

Butnor, J.R., Doolittle, J.A., Kress, L., Cohen, S., and Johnsen, K.H., 2001. "Use of ground-penetrating radar to study tree roots in the southeastern United States", Tree Physiology, 21, pp.1269-1278.

Callander, R.A., 1969. "Instability and river channels", Journal of Fluid Mechanics, 36, pp.464-480.

Campbell, E.P., Fox, D.R., and Bates, B.C., 1999. "A Bayesian approach to parameter estimation and pooling in non-linear flood event models", Water Resources Research, 35, pp.211-220.

Carey, W.C., 1969. "Formation of floodplain lands", Journal of the Hydraulics Division, ASCE, 95, pp.981-994.

Carlston, C.W., 1965. "The relation of free meander geometry to stream discharge and its geomorphic implications", American Journal of Science, 263, pp.864-885.

Carson, M., and Kirkby, M.J., 1972. Hillslope Form and Process, Cambridge University Press, Cambridge, UK.

Carson, M.A., 1986. "Characteristics of high-energy "meandering" rivers: The Canterbury Plains, New Zealand", Geological Society of America Bulletin, 97, pp.886-895.

Carson, M.A., and Lapointe, M.F., 1983. "The inherent asymmetry of river meander planform", Journal of Geology, 91, pp.41-55.

Casagli, N., Rinaldi, M., Gargini, A., and Curini, A., 1999. "Pore water pressure and streambank stability: results from a monitoring site on the Sieve River, Italy", Earth Surface Processes and Landforms, 24, pp.1095-1114.

Castaldini, D., and Piacente, S., 1995. "Channel changes on the Po river, Mantova Province, northern Italy", In: River Geomorphology, E.J. Hickin (ed.), John Wiley, Chichester, UK, pp.193-207.

Chang, H.H., 1984. "Regular meander path model", Journal of Hydraulic Engineering, ASCE, 110, pp.1398-1411.

Chang, T.P., and Toebes, G.H., 1970. "A statistical comparison of meander planforms in the Wabash basin", Water Resources Research, 6, pp.557-577.

Changxing, S., Petts, G., and Gurnell, A., 1999. "Bench development along the regulated, lower River Dee, U.K", Earth Surface Processes and Landforms, 24, pp.135-149.

Chen, Z.Y., and Morgenstern, N.R., 1983. "Extensions to the generalized method of slices for stability analysis", Canadian Geotechnical Journal, 20, pp.104-119.

Chitale, S.K., 1970. "River channel patterns", Journal of the Hydraulics Division, ASCE, 96, pp.201-221.

Chitale, S.V., 1973. "Theories and relationships of river channel patterns", Journal of Hydrology, 19, pp.285-308.

Chow, V.T., 1959. Open Channel Hydraulics, McGraw-Hill

Church, M., and Slaymaker, O., 1989. "Holocene disequilibrium of sediment yield in British Columbia", Nature, 327, pp.452-454.

Clark, J.D., Kenyon, N.H., and Pickering, K.T., 1992. "Quantitative analysis of the geometry of submarine channels: implications for the classification of submarine fans", Geology, 20, pp.633-636.

Clarke, S., and Elliot, A.J., 1998. "Modelling suspended sediment concentrations in the Firth of Forth", Estuarine, Coastal and Shelf Science, 47, pp.235-250.

Coldwell, A.E., 1957. "Importance of channel erosion as a source of sediment", Transactions of the American Geophysical Union, 38, pp.908-912.

Coleman, J.M., 1969. "Brahmaputra River: Channel processes and sedimentation", Sedimentary Geology, 3, pp.129-239.

Coleman, N.L., 1986. "Effects of suspended sediment on the open-channel velocity distribution", Water Resources Research, 22, pp.1377-1384.

Collins, D.B., Bras, R.L., and Tucker, G.E., 2001. "Modeling the influence of vegetation dynamics

on landscape erosion", EOS Transactions, AGU, Spring Meeting Supplement, 82, pp.H52A-01.

Collison, A.J.C., and Anderson, M.G., 1996. "Using a combined slope hydrology/stability model to identify suitable conditions for landslide prevention by vegetation in the humid tropics", Earth Surface Processes and Landforms, 21, pp.737-747.

Collison, A.J.C., Pollen, N.L., and Simon, A., "Mechanical reinforcement and enhanced strength of streambanks: contribution of common riparian species", In: AGU Fall Meeting, December 2001, San Francisco, California, San Francisco, California.

Colombini, M., Seminara, G., and Tubino, M., 1987. "Finite-amplitude alternate bars", Journal of Fluid Mechanics, 181, pp.213-232.

Colombini, M., Seminara, G., and Tubino, M., 1987. "Finite-amplitude alternate bars", Journal of Fluid Mechanics, 181, pp.213-232.

Cooper, R.H., and Hollingshead, A.B., "River bank erosion in regions of permafrost", In: Fluvial Processes and Sedimentation, Ottawa, Canada, Information Canada, Ottawa, Canada, pp.272-283.

Coppin, N.J., and Richards, I.G., 1990. Use of Vegetation in Civil Engineering, Butterworths, London, UK.

Coulthard, T.J., Macklin, M.G., and Kirkby, M.J., 2002. "A cellular model of Holocene upland river basin and alluvial fan evolution", Earth Surface Processes and Landforms, 27, pp.269-288.

Cowan, W.L., 1956. "Estimating hydraulic roughness coefficients", Agricultural Engineering, 37, pp.473-475.

Cox, M.B., and Palmer, V.J., 1948. Results of tests on vegetated waterways and method of field application. MP-12, Oklahoma Agricultural Experiment Station, Stillwater, Oklahoma.

Crickmay, G.H., 1960. "Lateral activity of a river in northwestern Canada", Journal of Geology, 68, pp.377-391.

Crosato, A., 1990. Simulation of meandering river processes. Report No. 90-3, T.U. Delft, Delft, Netherlands.

Crouch, R.J., 1990. "Rates and mechanisms of discontinuous gully erosion in a red-brown earth catchment, New South Wales, Australia", Earth Surface Processes and Landforms, 15, pp.277-282.

Crouch, R.J., and Blong, R.J., 1989. "Gully sidewall classification: methods and applications", Zeitschrift fur Geomorphologie, 33, pp.291-305.

Culmann, C., 1866. Grafische Statik, Zurich, Switzerland

Cummins, W.A., and Potter, H.R., 1972. "Rates of erosion in the catchment area of Cropston Resevoir, Charnwood Forest, Leicestershire", Mercian Geologist, 4, pp.149-157.

Darby, S.E., 1994. A Physically-Based Numerical Model of River Channel Widening. PhD Thesis, University of Nottingham, Nottingham, UK.

Darby, S.E., 1999. "Modeling the effect of riparian vegetation on flow resistance and flood potential", Journal of Hydraulic Engineering, ASCE, 125, pp.443-454.

Darby, S.E., Alabyan, A.M., and Van De Wiel, M.J., 2002. "Numerical simulation of bank erosion and channel migration in meandering rivers", Water Resources Research, 38, pp.1163, doi:10.1029/2001WR000602.

Darby, S.E., Rinaldi, M., and Pistolesi, I., 1997. "Effects of flexible riparian vegetation growth on discharge capacity", In: Environmental and Coastal Hydraulics, F.M. Holly and A. Alsaffar (eds.), ASCE, New York, N.Y., pp.394-399.

Darby, S.E., and Thorne, C.R., 1994. "Prediction of tension crack location and riverbank erosion hazards along destabilised channels", Earth Surface Processes and Landforms, 19, pp.233-245.

Darby, S.E., and Thorne, C.R., 1996a. "Numerical simulation of widening and bed deformation of

straight sand-bed rivers. I: Model development", Journal of Hydraulic Engineering, ASCE, 122, pp.184-193.

Darby, S.E., and Thorne, C.R., 1996b. "Development and testing of riverbank-stability analysis", Journal of Hydraulic Engineering, ASCE, 122, pp.443-454.

Darby, S.E., and Thorne, C.R., 1996c. "Predicting stage-discharge curves in channels with bank vegetation", Journal of Hydraulic Engineering, ASCE, 122, pp.583-586.

Darby, S.E., Thorne, C.R., and Simon, A., 1996. "Numerical simulation of widening and bed deformation of straight sand-bed rivers. II: Model evaluation", Journal of Hydraulic Engineering, ASCE, 122, pp.194-202.

Darby, S.E., and Van De Wiel, M.J., 2003. "Models in Fluvial Geomorphology", In: Tools in Fluvial Geomorphology, G.M. Kondolf and H. Piégay (eds.), John Wiley, Chichester, UK, pp.503-537.

Davies, T.R., and Sutherland, A.J., 1980. "Resistance to flow past deformable boundaries", Earth Surface Processes, 5, pp.175-179.

Davies, T.R.H., and Tinker, C., 1984. "Fundamental characteristics of stream meanders", Geological Society of America Bulletin, 95, pp.505-512.

Davies-Colley, R.J., 1997. "Stream channels are narrower in pasture than in forest", New Zealand Journal of Marine and Freshwater Research, 31, pp.599-608.

Davis, R.J., and Gregory, K.J., 1994. "A new distinct mechanism of riverbank erosion in a forested catchment", Journal of Hydrology, 157, pp.1-11.

De Bruin, H.A.R., and Moore, C.J., 1985. "Zero-plane displacement and roughess length for tall vegetation, derived from a simple mass conservation hypothesis", Boundary Layer Meteorology, 31, pp.39-49.

De Vriend, H.J., 1976. A mathematical model of steady flow in curved shallow channels. Report No. 76-1, T.U. Delft, Delft, Netherlands.

De Vriend, H.J., 1977. "A mathematical model of steady flow in curved shallow channels", Journal of Hydraulic Research, 15, pp.37-54.

De Vriend, H.J., 1981. "Velocity redistribution in curved rectangular channels", Journal of Fluid Mechanics, 107, pp.423-439.

De Vriend, H.J., and Geldof, H.J., 1983. "Main flow velocity in short river bends", Journal of Hydraulic Engineering, ASCE, 109, pp.991-1011.

De Vriend, H.J., and Struiksma, N., "Flow and bed deformation in river bends", In: River Meandering, 24-26 October, 1983, New Orleans, Louisiana, C.M. Elliot (ed.), ASCE, New Orleans, Louisiana, pp.810-839.

De Vries, D.G., 1974. "Multi-stage line intersect sampling", Forestry Science, 20, pp.129-133.

Demlow, T.C., and Edgeworth, A.L., "The effects of river migration on pipelines in Western Canada", In: River Meandering, 24-26 October, 1983, New Orleans, Louisiana, C.M. Elliot (ed.), ASCE, New Orleans, Louisiana, pp.240-249.

Dietrich, W.E., and Smith, J.D., 1983. "Influence of the point bar on flow through curved channels", Water Resources Research, 19, pp.1173-1192.

Dietrich, W.E., and Smith, J.D., 1984. "Bed load transport in a river meander", Water Resources Research, 20, pp.1355-1380.

Dietrich, W.E., Smith, J.D., and Dunne, T., 1979. "Flow and sediment transport in a sand bedded meander", Journal of Geology, 87, pp.305-315.

Dietrich, W.E., and Whiting, P., 1989. "Boundary shear stress and sediment transport in river meanders of sand and gravel", In: River Meandering, S. Ikeda and G. Parker (eds.), American Geophysical Union, Washington, D.C., pp.1-50.

Dryer, C.R., and Davis, M.K., 1911. "The work done by Normal Brook in 13 years", Indiana

Academy of Science Proceedings 1910, pp.147-152.
Duijsings, J.J.H.M., 1987. "A sediment budget for a forested catchment in Luxembourg and its implications for channel development", Earth Surface Processes and Landforms, 12, pp.173-184.
Dury, G.H., 1965. "General theory of meandering valleys", USGS Professional Paper, 452C, pp.1-43.
Eakin, H.M., 1911. "The influence of the earth's rotation upon the lateral erosion of streams", Journal of Geology, 18, pp.435-447.
Einstein, A., 1926. "Die Ursache der Meanderbildung der Flusslaufe und des sogenanten Baerschen Gesetzes", Naturwissenchaften, 11.
Einstein, H.A., 1950. "The bed load function for sediment transportation in open channel flows", USDA Technical Bulletin, 1026.
Einstein, H.A., and Harder, J.A., 1954. "Velocity distribution and the boundary layer at channel bends", Transactions of the American Geophysical Union, 35, pp.114-120.
Einstein, H.A., and Li, H., 1958. "Secondary currents in straight channels", Transactions of the American Geophysical Union, 39, pp.1085-1088.
Einstein, H.A., and Shen, H.W., 1964. "A study of meandering in straight alluvial channels", Journal of Geophysical Research, 69, pp.5239-5247.
Emmett, W.W., 1974. "Channel changes", Geology, 2, pp.271-272.
Engelund, F., 1974. "Flow and bed topography in channel bends", Journal of the Hydraulics Division, ASCE, 100, pp.1631-1648.
Engelund, F., and Hansen, E., 1967. A Monograph on Sediment Transport in Alluvial Streams, Technical University of Denmark, Copenhagen, Denmark
Espinoza, R.D., Repetto, P.C., and Muhunthan, B., 1992. "A general framework for slope stability analysis", Geotechnique, 42, pp.603-615.
Everitt, B.L., 1968. "Use of cottonwood in an investigation of the recent history of a flood plain", American Journal of Science, 266, pp.417-439.
Falinski, J.B., 1978. "Uprooted trees, their distribution and influence in the primeval forest biotope", Vegetatio, 38, pp.175-183.
Farajalla, N.S., and Vieux, B.E., 1995. "Capturing the essential spatial variability in distributed hydrological modelling: Infiltration parameters", Hydrological Processes, 9, pp.55-68.
Fathi-Moghadam, M., and Kouwen, N., 1997. "Non-rigid, non-submerged vegetative roughness on floodplains", Journal of Hydraulic Engineering, ASCE, 123, pp.51-57.
Fellenius, W., 1927. Erdstatische Berechnungen, Ernst, Berlin, Germany
Ferguson, R.I., 1973. "Regular meander path models", Water Resources Research, 9, pp.1079-1086.
Fetherston, K.L., Naiman, R.J., and Bilby, R.E., 1995. "Large woody debris, physical process, and riparian forest development in montane river networks of the Pacific Northwest", Geomorphology, 13, pp.133-144.
Fischer-Antze, T., Stoesser, T., Bates, P., and Olsen, N.R.B., 2001. "3D numerical modelling of open-channel flow with submerged vegetation", Journal of Hydraulic Research, 39, pp.303-310.
Fisk, H., 1951. "Mississippi River valley geology relation to river regime", Transactions of the American Society of Civil Engineers, 117, pp.667-689.
Flood, R.D., and Damuth, J.E., 1987. "Quantitative characteristics of sinuous distributary channel on the Amazon deep-sea fan", Geological Society of America Bulletin, 98, pp.728-738.
Fonda, R.W., 1974. "Forest succession in relation to river terrace development in Olympic National Park, Washington", Ecology, 55, pp.927-942.
Forest Products Reseach Laboratory, 1956. A Handbook of Hardwoods, Forest Products Research

Laboratory, UK
Fredlund, D.G., and Rahardjo, H., 1993. Soil Mechanics for Unsaturated Soils, John Wiley, New York, N.Y., 517 p.
Fredsøe, J., 1978. "Meandering and braiding of rivers", Journal of Fluid Mechanics, 84, pp.607-624.
Freeman, G.E., Rahmeyer, W.J., and Copeland, R.R., 2000. Determination of Resistance Due to Shrubs and Woody Vegetation. TR-00-25, US Army Corps of Engineers, Engineer Research and Development Center, Coastal and Hydraulics Laboratory, Vicksburg, Mississippi.
Friedkin, J.F., 1945. A Laboratory Study of the Meandering of Alluvial Rivers, US Army Corps of Engineers, Vicksburg, Mississippi
Friedman, J.M., and Auble, G.T., 1999. "Mortality of riparian box elder from sediment mobilization and extended inundation", Regulated Rivers Research and Management, 15, pp.463-476.
Friedman, J.M., Osterkamp, W.R., and Lewis, W.M., 1996. "The role of vegetation and bed-level fluctuations in the process of channel narrowing", Geomorphology, 14, pp.341-351.
Galay, V.J., "River channel shifting on large rivers in Bangladesh", In: International Symposium on River Sedimenation, March 1980, Bejing, China, Guunghua Press, Bejing, China, pp.543-562.
Garde, R.J., and Ranga Raju, K.G., 1985. Mechanics of Sediment Transportation and Alluvial Stream Problems, Wiley Eastern, New Delhi, India.
Gardiner, T., 1983. "Some factors promoting channel bank erosion, River Lagan, County Down", Journal of Earth Sciences, Royal Dublin Society, 5, pp.231-239.
Gatto, L.W., "Bank and channel changes near dikes, Tanana River, Alaska", In: River Meandering, 24-26 October, 1983, New Orleans, Louisiana, C.M. Elliot (ed.), ASCE, New Orleans, Louisiana, pp.212-222.
Gee, D.M., Anderson, M.G., and Baird, L., 1990. "Large scale floodplain modelling", Earth Surface Processes and Landforms, 15, pp.513-523.
Gibling, M.R., and Rust, B.R., 1993. "Alluvial ridge-and-swale topography: a case study from the Morien Group of Atlantic Canada", In: Alluvial Sedimentation, M. Marzo and C. Puigdefábregas (eds.), Blackwell Scientific, Oxford, UK, pp.133-150.
Gilbert, G.K., 1884. "The sufficiency of terrestrial rotation for the deflection of streams", American Journal of Science, 27, pp.427-432.
Gilvear, D., Winterbottom, S., and Sichingabula, H., 2000. "Character of channel planform change and meander development: Luangwa River, Zambia", Earth Surface Processes and Landforms, 25, pp.421-436.
Gole, C.V., and Chitale, S.V., 1966. "Inland delta building activity of Kosi River", Journal of the Hydraulics Division, ASCE, 92, pp.111-126.
Gomez, B., and Church, M., 1989. "An assessment of bed load sediment transport formulae for gravel bed rivers", Water Resources Research, 25, pp.1161-1186.
Gomez, B., Eden, D.N., Hicks, D.M., Trustrum, N.A., Peacock, D.H., and Wilmshurst, J., 1999. "Contribution of floodplain sequestration to the sediment budget of the Waipaoa River, New Zealand", In: Floodplains: Interdisciplinary Approaches, S.B. Marriott and J. Alexander (eds.), Geological Society, London, UK, pp.69-88.
Gorycki, M.A., 1973. "Hydraulic drag - A meandering initiating mechanism", Geological Society of America Bulletin, 84, pp.175-186.
Goswami, U., Sarma, J.N., and Patgiri, A.D., 1999. "River channel changes of the Subansari in Assam, India", Geomorphology, 30, pp.227-244.
Gourlay, M.R., 1970. "Discussion on 'Flow retardance in vegetated channels' (Kouwen et al., 1969)", Journal of the Irrigation and Drainage Division, ASCE, 96, pp.351-357.
Graeme, D., and Dunkerley, D.L., 1993. "Hydraulic resistance by river red gum, *Eucalyptus Camaldulensis*, in ephemeral desert streams", Australian Geographical Studies, 31, pp.141-

154.
Graf, W.H., and Warlick, D.G., 1971. "Some 'fluvio'-morphologic features on the moon", In: Sedimentation, H.W. Shen (ed.), Fort Collins, Colorado.
Gray, D.H., 1995. "The influence of vegetation on the stability of slopes", In: Vegetation and Slopes, D.H. Barker (ed.), Thomas Telford, London, UK, pp.2-25.
Gray, D.H., and Leiser, A.T., 1982. Biotechnical Slope Protection and Erosion Control, Van Nostrand Rheinhold, New York, New York.
Gray, D.H., and Megahan, W.F., 1981. Forest vegetation removal and slope stability in the Idaho batholith. INT-271, Intermountain Forest and Range Experiment Station, Ogden, Utah.
Gray, D.H., and Ohashi, H., 1983. "Mechanics of fibre reinforcement in sand", Journal of Geotechnical Engineering, ASCE, 109(3), pp.335-353.
Greenway, D.R., 1987. "Vegetation and slope stability", In: Slope Stability, M.G. Anderson and K.S. Richards (eds.), John Wiley, Chichester, UK, pp.187-230.
Gregory, K.J., and Gurnell, A.M., 1988. "Vegetation and river channel form and process", In: Biogeomorphology, H.A. Viles (ed.), Basil Blackwell, Oxford, UK, pp.11-42.
Gregory, S.V., Swanson, F.J., McKee, W.A., and Cummins, K.W., 1991. "An ecosystem perspective of riparian zones", BioScience, 41, pp.540-551.
Grissinger, E.H., 1982. "Bank erosion of cohesive materials", In: Gravel-Bed Rivers, R.D. Hey, J.C. Bathurst, and C.R. Thorne (eds.), John Wiley, Chichester, UK, pp.273-287.
Grove, J.R., 2000. Downstream change in the processes of riverbank erosion along the River Swale, UK. PhD Thesis, University of Birmingham, Birmingham, UK.
Guccione, M.J., 1993. "Grain-size distribution of overbank sediment and its use to locate channel positions", In: Alluvial Sedimentation, M. Marzo and C. Puigdefábregas (eds.), Blackwell Scientific, Oxford, UK, pp.185-194.
Gurnell, A., 1995. "Vegetation along river corridors: Hydrogeomorphological interactions", In: Changing River Channels, A. Gurnell and G. Petts (eds.), John Wiley, Chichester, UK, pp.237-260.
Gurnell, A.M., Downward, S.R., and Jones, R., 1994. "Channel planform change on the River Dee meanders, 1876-1992", Regulated Rivers Research and Management, 9, pp.187-204.
Gurnell, A.M., and Gregory, K.J., 1995. "Interactions between semi-natural vegetation and hydrogeomorphological processes", Geomorphology, 13, pp.49-69.
Gurnell, A.M., Petts, G.E., Harris, N., Ward, J.V., Tockner, K., Edwards, P.J., and Kollman, J., 2000. "Large wood retention in river channels: the case of the flume Tagliamento, Italy", Earth Surface Processes and Landforms, 25, pp.255-275.
Gwinn, W.R., and Ree, W.O., 1980. "Maintenance effects on the hydraulic properties of a vegetation-lined channel", Transactions of the American Society of Agricultural Engineers, 23, pp.636-642.
Hagerty, D.J., 1991. "Piping/sapping erosion I: Basic considerations", Journal of Hydraulic Engineering, ASCE, 117, pp.991-1008.
Hagerty, D.J., Spoor, M.F., and Parola, A.C., 1995. "Near-bank impacts of river stage control", Journal of Hydraulic Engineering, ASCE, 121, pp.196-207.
Hagerty, D.J., Spoor, M.F., and Ullrich, C.R., 1981. "Bank failure and erosion on the Ohio River", Engineering Geology, 17, pp.141-158.
Handy, R.L., 1972. "Alluvial cut-off dating from subsequent growth of a meander", Geological Society of America Bulletin, 83, pp.475-480.
Hankin, B.C., and Beven, K., 1998. "Modelling dispersion in complex open channel flows: Equifinality of model structure", Stochastic Hydrology and Hydraulics, 12, pp.377-396.
Hansen, E., 1967. On the formation of meanders as a stability problem. 13, Technical University of

Denmark, Lyngby, Denmark.

Hanson, G.J., and Simon, A., 2001. "Erodibility of cohesive streambeds in the loeass area of the midwestern USA", Hydrological Processes, 15, pp.23-38.

Hanson, G.J., and Temple, D.M., 2002. "Performance of bare-earth and vegetated steep channels under long-duration flows", Transactions of the American Society of Agricultural Engineers, 45, pp.695-701.

Hardy, R.J., Bates, P.D., and Anderson, M.G., 1999. "The importance of spatial resolution in hydraulic models for floodplain environments", Journal of Hydrology, 216, pp.124-136.

Hardy, R.J., Bates, P.D., and Anderson, M.G., 2000. "Modelling suspended sediment deposition on a fluvial floodplain using a two-dimensional dynamic finite element model", Journal of Hydrology, 229, pp.202-218.

Harmel, R.D., Haan, C.T., and Dutnell, R., 1999. "Bank erosion and riparian vegetation influences: Upper Illinois River, Oklahoma", Transactions of the American Society of Agricultural Engineers, 42, pp.1321-1329.

Hasegawa, K., 1981. "Bank-erosion discharge based on a nonequilibrium theory", Transactions of the Japanese Society of Civil Engineers, 13, pp.202-204.

Hasegawa, K., 1989. "Universal bank erosion coefficient for meandering rivers", Journal of Hydraulic Engineering, ASCE, 115, pp.744-765.

Haslam, S.M., 1978. River Plants, Cambridge University Press, London, UK.

Hemphill, R.W., and Bramley, M.E., 1989. Protection of River and Canal Banks, Butterworths, London, UK.

Henkel, D.J., 1967. "Local geology and the stability of natural slopes", Journal of the Soil Mechanics and Foundations Division, ASCE, 93, pp.437-446.

Hereford, R., 1984. "Climate and ephemeral-stream processes: Twentieth century geomorphology and alluvial stratigraphy of the Little Colorado River, Arizona", Geological Society of America Bulletin, 95, pp.654-668.

Hervouet, J.-M., and Van Haren, L., 1996. "Recent advances in numerical methods for fluid flows", In: Floodplain Processes, M.G. Anderson, D.E. Walling, and P.D. Bates (eds.), John Wiley, Chichester, U.K., pp.183-214.

Hey, R.D., and Thorne, C.R., 1975. "Secondary flow in river channels", Area, 7, pp.191-195.

Hey, R.D., and Thorne, C.R., 1986. "Stable channels with mobile gravel beds", Journal of Hydraulic Engineering, ASCE, 112, pp.671-689.

Hickin, E.J., 1979. "Concave-bank benches on the Squamish River, British Columbia", Canadian Journal of Earth Sciences, 16, pp.200-203.

Hickin, E.J., 1984. "Vegetation and river channel dynamics", Canadian Geographer, 28, pp.111-126.

Hickin, E.J., and Nanson, G.C., 1975. "The character of channel migration on the Beatton River, Northeast British Columbia, Canada", Geological Society of America Bulletin, 86, pp.487-494.

Hickin, E.J., and Nanson, G.C., 1984. "Lateral migration of river bends", Journal of Hydraulic Engineering, ASCE, 110, pp.1557-1567.

Hieb, D.L., 1954. Fort Laramie National Monument, Wyoming, US Department of the Interior, National Park Service, 43 p.

Hill, A.R., 1973. "Erosion of river banks composed of glacial till near Belfast, Northern Ireland", Zeitschrift fur Geomorphologie, 17, pp.428-442.

Hodskinson, A., and Ferguson, R.I., 1998. "Numerical modelling of separated flow in river bends: Model testing and experimental investigation of geometric controls on the extend of flow separation at the concave bank", Hydrological Processes, 12, pp.1323-1338.

Hooke, J., 2003. "River meander behaviour and instability: a framework for analysis", Transactions

of the Institute of British Geographers, 28, pp.238-253.
Hooke, J.M., 1977. "The distribution and nature of changes in river channel patterns: the example of Devon", In: Channel Changes, K.J. Gregory (ed.), John Wiley, Chichester, UK, pp.265-280.
Hooke, J.M., 1979. "An analysis of the processes of bank erosion", Journal of Hydrology, 42, pp.39-62.
Hooke, J.M., 1980. "Magnitude and distribution of rates of river bank erosion", Earth Surface Processes and Landforms, 5, pp.143-157.
Hooke, J.M., 1984. "Changes in river meanders: a review of techniques and results of analysis", Progress in Physical Geography, 8, pp.473-508.
Hooke, J.M., 1987. "Discussion on 'Lateral migration rates of river bends' (Hickin and Nanson, 1984)", Journal of Hydraulic Engineering, ASCE, 113, pp.915-918.
Hooke, J.M., 1995. "River channel adjustment to meander cutoffs on the River Bollin and River Dane, northwest England", Geomorphology, 14, pp.235-253.
Hooke, J.M., 1997. "Styles of channel change", In: Applied Fluvial Geomorphology for River Engineering and Management, C.R. Thorne, R.D. Hey, and M.D. Newson (eds.), John Wiley, Chichester, UK, pp.236-268.
Hooke, J.M., and Redmond, C.E., 1992. "Causes and nature of river planform change", In: Dynamics of Gravel-bed Rivers, P. Billi, R.D. Hey, C.R. Thorne, and P. Taconi (eds.), John Wiley, Chichester, UK, pp.557-571.
Hooke, R.L.B., 1975. "Distribution of sediment transport and shear stress in a meander bend", Journal of Geology, 83, pp.543-565.
Hooper, D.I., 1992. Relationships between vegetation and hydrogeomorphic characteristics of British riverine environments: a remotely sensed perspective. PhD Thesis, University of Southampton, Southampton.
Hosner, J.F., 1960. "Relative tolerance to complete inundation of fourteen bottomland tree species", Forest Science, 8, pp.180-186.
Howard, A.D., "Simulation model of meandering", In: River Meandering, 24-26 October, 1983, New Orleans, Louisiana, C.M. Elliot (ed.), ASCE, New Orleans, Louisiana, pp.952-963.
Howard, A.D., 1992. "Modelling channel migration and floodplain sedimentation in meandering streams", In: Lowland Floodplain Rivers: Geomorphological Perspectives, P.A. Carling and G.E. Petts (eds.), John Wiley, Chichester, UK, pp.1-41.
Howard, A.D., 1996. "Modelling channel evolution and floodplain morphology", In: Floodplain Processes, M.G. Anderson, D.E. Walling, and P.D. Bates (eds.), John Wiley, Chichester, UK, pp.15-62.
Howard, A.D., and Hemberger, A., 1991. "Multivariate characterization of meandering", Geomorphology, 4, pp.161-186.
Howard, A.D., and Knutson, T.R., 1984. "Sufficient conditions for river meandering: A simulation approach", Water Resources Research, 20, pp.1659-1667.
Howard, G.W., 1941. "Discussion on 'Basic aspects of stream-meanders' (Matthes, 1941)", Transactions of the American Geophysical Union, 22, pp.636.
Hruska, J., Cermak, J., and Sustek, S., 1999. "Mapping of tree root systems by means of the ground penetrating radar", Tree Physiology, 19, pp.125-130.
Hsü, K.J., 1989. Physical Principles of Sedimentology, Springer Verlag, Berlin, Germany
Hughes, D.J., 1977. "Rates of erosion on meander arcs", In: River Channel Changes, K.J. Gregory (ed.), John Wiley, Chichester, UK, pp.193-205.
Hupp, C.R., 1988. "Plant ecological aspects of flood geomorphology and paleoflood history", In: Flood Geomorphology, V.R. Baker, R.C. Kochel, and P.C. Patton (eds.), John Wiley, New York, N.Y., pp.335-356.

Hupp, C.R., 1990. "Vegetation patterns in relation to basin hydrogeomorphology", In: Vegetation and Erosion, J.B. Thornes (ed.), John Wiley, Chichester, UK, pp.217-237.

Hupp, C.R., 1992. "Riparian vegetation recovery patterns following stream channelization: A geomorphic perspective", Ecology, 73, pp.1209-1226.

Hupp, C.R., and Osterkamp, W.R., 1985. "Bottomland vegetation distribution along Passage Creek, Virginia, in relation to fluvial landforms", Ecology, 66, pp.670-681.

Hupp, C.R., and Osterkamp, W.R., 1996. "Riparian vegetation and fluvial geomorphic processes", Geomorphology, 14, pp.277-295.

Hupp, C.R., and Simon, A., 1991. "Bank accretion and the development of vegetated depositional surfaces along modified alluvial channels", Geomorphology, 4, pp.111-124.

Husch, B., 1963. Forest Mensuration and Statistics, Ronald Press, New York, NY

Ikeda, H., 1989a. "Sedimentary controls on channel migration and origin of point bars in sand-bedded meandering rivers", In: River Meandering, S. Ikeda and G. Parker (eds.), American Geophysical Union, Washington, D.C., pp.51-68.

Ikeda, S., 1989b. "Sediment transport and sorting at bends", In: River Meandering, S. Ikeda and G. Parker (eds.), American Geophysical Union, Washington, D.C., pp.103-125.

Ikeda, S., Parker, G., and Sawai, K., 1981. "Bend theory of river meanders: I. Linear development", Journal of Fluid Mechanics, 112, pp.363-377.

Imeson, A.C., and Jugerius, P.D., 1977. "The widening of valley incisions by soil fall in a forested keuper area, Luxembourg", Earth Surface Processes, 2, pp.141-152.

Inglis, C.C., 1949. The Behaviour and Control of Rivers and Canals, Central Water-Power-Irrigation and Navigation Research Station, Poona, India

Ippen, A.T., and Drinker, P.A., 1962. "Boundary shear stress in curved trapezoidal channels", Journal of the Hydraulics Division, ASCE, 88, pp.143-179.

Jackson, R.B., Canadell, J., Ehleringer, J.R., Mooney, H.A., Sala, O.E., and Schulze, E.-D., 1996. "A global analysis of root distribution for terrestrial biomes", Oecologia, 108, pp.389-411.

Jackson, R.G., 1975. "Velocity-bedform-texture patterns of meander bends in the lower Wabush River of Illinois and Indiana", Geological Society of America Bulletin, 86, pp.1511-1522.

Jackson, R.G., 1976a. "Depositional model of point bars in the lower Wabash River", Journal of Sediment Petrology, 46, pp.579-594.

Jackson, R.G., 1976b. "Sedimentological and fluid-dynamic implications of the turbulent bursting phenomenon in geophysical flows", Journal of Fluid Dynamics, 77, pp.531-560.

Jefferson, M., 1902. "Limiting width of meander belts", National Geographic Magazine, 13, pp.373-384.

Johanneson, H., and Parker, G., 1989. "A linear theory of meanders", In: River Meandering, S. Ikeda and G. Parker (eds.), American Geophysical Union, Washington, D.C., pp.181-213.

Julien, P.Y., 1995. Erosion and Sedimentation, Cambridge University Press, Cambridge, UK.

Kadlec, R.H., 1990. "Overland flow in wetlands: Vegetation resistance", Journal of Hydraulic Engineering, ASCE, 116, pp.691-706.

Kalkwijk, J.P.T., and Booij, R., 1986. "Adaptation of secondary flow in nearly-horizontal flow", Journal of Hydraulic Research, 24, pp.19-37.

Kalkwijk, J.P.T., and De Vriend, H.J., 1980. "Computation of the flow in shallow river bends", Journal of Hydraulic Research, 18, pp.327-342.

Kalliola, R., and Puhakka, M., 1988. "River dynamics and vegetation mosaicism: a case study of the River Kamajohka, northernmost Finland", Journal of Biogeography, 15, pp.703-719.

Keller, E.A., 1972. "Development of alluvial stream channels: a five-stage model", Geological Society of America Bulletin, 83, pp.1531-1536.

Keller, E.A., and Swanson, F.J., 1979. "Effect of large organic material on channel form and fluvial

processes", Earth Surface Processes and Landforms, 4, pp.361-380.
Keller, E.A., and Melhorn, W.N., 1973. "Bedforms and fluvial processes in alluvial stream channels: selected observations", In: Fluvial Geomorphology, M. Morisawa (ed.), State University New York, Binghamton, N.Y., pp.178-200.
Kesel, R.H., and Baumann, R.H., 1981. "Bluff erosion of a Mississippi meander at Port Hudson, Louisiana", Physical Geography, 2, pp.62-82.
Kim, J., Salgado, R., and Lee, J., 2002. "Stability analysis of complex soil slopes using limit analysis", Journal of Geotechnical and Geoenvironmental Engineering, ASCE, 128, pp.546-557.
Kinoshita, R., and Miwa, H., 1974. "River channel formation which prevents downstream translation of transverse bars", Journal of the Erosion Control Engineering Society Japan, 94, pp.12-17.
Kisling-Møller, J., 1993. "Bedform migration and related sediment transport in a meander bend", In: Alluvial Sedimentation, M. Marzo and C. Puigdefábregas (eds.), Blackwell Scientific, Oxford, UK, pp.51-61.
Klaassen, G.J., and Van der Zwaard, J.J., 1974. "Roughness coefficients of vegetated flood plains", Journal of Hydraulic Research, 12, pp.43-63.
Klimek, K., 1974. "Retreat of alluvial banks", Geographica Polonica, 28, pp.59-76.
Knighton, A.D., 1973. "Riverbank erosion in relation to streamflow conditions, River Bollin-Dean, Cheshire", East Midlands Geographer, 5, pp.416-426.
Komar, P.D., 1996. "Entrainment of sediment from deposits of mixed grain sizes and densities", In: Advances in Fluvial Dynamics and Stratigraphy, P.A. Carling and M.R. Dawson (eds.), John Wiley, Chichester, UK, pp.127-181.
Komatsu, G., and Baker, V.R., 1994. "Meander properties of Venusian channels", Geology, 22, pp.67-70.
Kondolf, G.M., and Curry, R.R., 1986. "Channel erosion along the Carmel River, Monterey County, California", Earth Surface Processes and Landforms, 11, pp.307-319.
Kouwen, N., 1988. "Field estimation of the biomechanical properties of grass", Journal of Hydraulic Research, 26, pp.559-568.
Kouwen, N., and Fathi-Moghadam, M., 2000. "Friction factors for coniferous trees along rivers", Journal of Hydraulic Engineering, ASCE, 126, pp.732-740.
Kouwen, N., and Li, R.-M., 1980. "Biomechanics of vegetative channel linings", Journal of the Hydraulics Division, ASCE, 106, pp.1085-1103.
Kouwen, N., Li, R.-M., and Simons, D.B., 1981. "Flow resistance in vegetated waterways", Transactions of the American Society of Agricultural Engineers, 24, pp.684-698.
Kouwen, N., and Unny, T.E., 1973. "Flexible roughness in open channels", Journal of the Hydraulics Division, ASCE, 99, pp.713-728.
Kouwen, N., Unny, T.E., and Hill, H.M., 1969. "Flow retardance in vegetated channels", Journal of the Irrigation and Drainage Division, ASCE, 95, pp.pp.329-342.
Kozlowski, T.T., 1971. Growth and Development of Trees, Academic Press, New York, N.Y.
Laczay, I.A., 1977. "Channel pattern changes of Hungarian rivers: the example of the Hernad River", In: River Channel Changes, K.J. Gregory (ed.), John Wiley, Chichester, UK, pp.185-192.
Lajczak, A., 1995. "The impact of river regulation, 1850-1990, on the channel and floodplain of the Upper Vistula river, southern Poland", In: River Geomorphology, E.J. Hickin (ed.), John Wiley, Chichester, UK, pp.209-233.
Lane, E.W., 1955. "Design of stable channels", Transactions of the American Society of Civil Engineers, 120, pp.1234-1260.
Lane, S.N., 1998. "Hydraulic modelling in hydrology and geomorphology: A review of high resolution approaches", Hydrological Processes, 12, pp.1131-1150.

Lane, S.N., and Bates, P.D., 1998. "Introduction", In: High Resolution Flow Modelling in Hydrology and Geomorphology, S.N. Lane and P.D. Bates (eds.), John Wiley, Chichester, UK, pp.1-12.

Lane, S.N., and Richards, K.S., 1998. "High resolution two-dimensional spatial modelling of flow processes in a multi-threaded channel", Hydrological Processes, 12, pp.1279-1298.

Langbein, W.B., and Leopold, L.B., 1966. "River meanders : Theory of minimum variance", USGS Professional Paper, 422H, pp.1-15.

Lapointe, M.F., and Carson, M.A., 1986. "Migration patterns of an asymmetric meandering river: The Rouge River, Quebeq", Water Resources Research, 22, pp.731-743.

Larsson, R., 1986. "Coriolis generated secondary currents in channels", Journal of Hydraulic Engineering, ASCE, 112, pp.750-767.

Lavelle, W.J., and Mofjeld, H.O., 1987. "Do critical shear stresses for incipient motion really exist?", Journal of Hydraulic Engineering, ASCE, 113, pp.370-388.

Lawler, D.M., 1978. "The use of erosion pins in river banks", Swansea Geographer, 16, pp.9-18.

Lawler, D.M., 1986. "River bank erosion and the influence of frost: A statistical examination", Transactions of the Institute of British Geographers, 11, pp.227-242.

Lawler, D.M., 1992. "Process dominance in bank erosion systems", In: Lowland Floodplain Rivers: Geomorphological Perspectives, P.A. Carling and G.E. Petts (eds.), John Wiley, Chichester, UK, pp.117-143.

Lawler, D.M., 1993. "Needle ice processes and sediment mobilization on river banks: the River Ilston, West Glamorgan, U.K", Journal of Hydrology, 150.

Lawler, D.M., and Bull, P.A., 1977. "Erosion in the valley of Pennard Pill", Journal of the Gower Society, 28, pp.46-54.

Lee, I.W.Y., 1985. "A review of vegetative slope stabilisation", Hong Kong Engineer, 13, pp.9-21.

Leeks, G.J., Lewin, J., and Newson, M.D., 1988. "Channel change, fluvial geomorphology and river engineering: the case of the Afon Trannon, mid-Wales", Earth Surface Processes and Landforms, 13, pp.207-223.

Leliavsky, S., 1955. An introduction to Fluvial Hydraulics, Constable & Co., London, UK.

Leopold, L.B., 1973. "River channel change with time: an example", Geological Society of America Bulletin, 84, pp.1845-1860.

Leopold, L.B., Emmett, W.W., and Myrick, R.H., 1966. "Channel and hillslope processes in a semi arid area, New Mexico", USGS Professional Paper, 352-G.

Leopold, L.B., and Wolman, M.G., 1957. "River channel patterns: Braided, meandering and straight", USGS Professional Paper, 282B, pp.39-85.

Leopold, L.B., Wolman, M.G., and Miller, J.P., 1964. Fluvial Processes in Geomorphology, W.H. Freeman Co., San Francisco, California

Leshchinsky, D., 1990. "Slope stability analysis generalized appraoch", Journal of Geotechnical Engineering, ASCE, 116, pp.851-867.

Lewin, J., 1972. "Late-stage meander growth", Nature Physical Science, 240, pp.116.

Lewin, J., and Brewer, P.A., 2001. "Predicting channel patterns", Geomorphology, 40, pp.329-339.

Lewin, J., Hughes, D., and Blacknell, C., 1977. "Incidence of river erosion", Area, 9, pp.177-180.

Leys, K.F., and Werritty, A., 1999. "River channel planform change: software for historical analysis", Geomorphology, 29, pp.107-120.

Li, R.-M., and Shen, H.W., 1973. "Effect of tall vegetation on flow and sediment", Journal of the Hydraulics Division, ASCE, 99, pp.793-814.

Lien, H.C., Hsieh, T.Y., Yang, J.C., and Yeh, K.C., 1999. "Bend-flow simulation using 2D depth-averaged model", Journal of Hydraulic Engineering, ASCE, 125, pp.1097-1108.

Lindner, K., 1982. Der Strömungswiderstand von Pflanzenbeständen, Leichtweiss-Institut für Wasserbau der Technischen Universität Braunschweig, Braunschweig, Germany

Lindsey, A.A., Pettey, R.O., Sterling, D.K., and Van Asdall, W., 1961. "Vegetation and environment along the Wabash and Tippecanoe rivers", Ecological Monographs, 31, pp.105-156.

Liquori, M., and Jackson, C.R., 2001. "Channel response from shrub dominated riparian communities and associated effects on salmonid habitat", Journal of the American Water Resources Association, 37, pp.1639-1651.

Lopez, F., and Garcia, M., 1997. Open channel flow through simulated vegetation: Turbulence modelling and sediment transport, Hydrosystems Laboratory, Department of Civil Engineering, University of Illinois, Campaign, Illinois

Ludin, A., 1926. "Influence of the rotation of the earth on rivers", Die Wasserkraft, 21, pp.216.

Lyell, C., 1830. Principles of Geology, John Murray, London, Uk

Macklin, M.G., Rumsby, B.T., and Newson, M.D., 1992. "Historical floods and vertical accretion of fine-grained alluvium in the lower Tyne valley, northeast England", In: Dynamics of Gravel-bed Rivers, P. Billi, R.D. Hey, C.R. Thorne, and P. Taconi (eds.), John Wiley, Chichester, UK, pp.573-589.

Malanson, G.P., 1993. Riparian Landscapes, Cambridge University Press, Cambridge, UK.

Markham, A.J., 1990. Flow and Sediment Processes in Gravel-bed River Bends, PhD Thesis, Department of Geography, Queen Mary and Westfield College, University of London, London, UK.

Masterman, R., and Thorne, C.R., 1992. "Predicting influence of bank vegetation on channel capacity", Journal of Hydraulic Engineering, ASCE, 118, pp.1052-1058.

Matthes, G.H., 1941. "Basic aspects of stream meanders", Transactions of the American Geophysical Union, 22, pp.632-636.

McGreal, W.S., and Gardiner, T., 1977. "Short-term measurements of erosion from a marine and fluvial environment in County Down, Northern Ireland", Area, 9, pp.282-289.

McKenney, R., Jacobson, R.B., and Wertheimer, R.C., 1995. "Woody vegetation and channel morphogenesis in low-gradient gravel-bed streams in the Ozrak Plateaus, Missouri and Arkansas", Geomorphology, 13, pp.175-198.

Meehan, W.R., and Platts, W.S., 1978. "Livestock grazing and the aquatic environment", Journal of Soil and Water Conservation, 33, pp.274-278.

Meentemeyer, R.K., Vogler, J.B., and Butler, D.R., 1998. "The geomorphic influences of burrowing beavers on streambanks, Bolin Creek, North Carolina", Zeitschrift fur Geomorphologie, 42, pp.453-468.

Meyer-Peter, E., and Müller, R., "Formulas for bedload transport", In: International Association for Hydraulic Structure Research, 2nd Meeting, Stockholm, pp.39-64.

Miall, A.D., 1996. The Geology of Fluvial Deposits, Springer Verlag, Berlin, Germany

Michalowski, R.L., 1995. "Slope stability analysis: a kinematical approach", Geotechnique, 45, pp.283-293.

Micheli, E.R., and Kirchner, J.W., 2002. "Effects of wet meadow riparian vegetation on streambank erosion. 2. Measurements of vegetated bank strength and consequences for failure mechanics", Earth Surface Processes and Landforms, 27, pp.687-697.

Millar, R.G., 2000. "Influence of bank vegetation on channel patterns", Water Resources Research, 36, pp.1109-1118.

Millar, R.G., and Quick, M.C., 1998. "Stable width and depth of gravel-bed rivers with cohesive banks", Journal of Hydraulic Engineering, ASCE, 124, pp.1005-1013.

Mitchell, P.B., 1988. "The influence of vegetation, animals and microorganisms on soil processes", In: Biogeomorphology, H.A. Viles (ed.), Basil Blackwell, Oxford, UK, pp.43-82.

Montgomery, D.R., 1997. "What's best on the banks?", Nature, 388, pp.328-329.

Moody, J.A., Pizutto, J.E., and Meade, R.H., 1999. "Ontogeny of a flood plain", Geological Society

of America Bulletin, 111, pp.291-303.
Moran, C.J., Pierret, A., and Stevenson, A.W., 2000. "X-ray absorption and phase contrast imaging to study the interplay between plant roots and soil structure", Plant and Soil, 233, pp.99-115.
Morgenstern, N.R., and Price, V.E., 1965. "The analysis of the stability of general slip surfaces", Geotechnique, 15, pp.79-93.
Morisawa, M., 1985. Rivers: Form and Process, Longman, London, UK.
Mosley, M.P., 1975. "Channel changes on the River Bollin, Cheshire, 1872-1973", East Midlands Geographer, 6, pp.185-199.
Mosselman, E., 1991. Modelling of river morphology with non-orthogonal horizontal curvilinear coordinates. Report No. 91-1, T.U. Delft, Delft, Netherlands.
Mosselman, E., 1992. Mathematical Modelling of Morphological Processes in Rivers with Erodible Cohesive Banks. PhD Thesis, Technische Universiteit Delft, Delft, Netherlands.
Moulin, C., and Slama, E.B., 1998. "The two-dimensional transport module SUBIEF. Applications to sediment transport and water quality processes", Hydrological Processes, 12, pp.1183-1195.
Murgatroyd, A.L., and Ternan, J.L., 1983. "The impact of afforestation on stream bank erosion and channel form", Earth Surface Processes and Landforms, 8, pp.357-369.
Murphey, J.B., and Grissinger, E.H., 1985. "Channel cross-section changes in Mississippi's Goodwin Creek", Journal of Soil and Water Conservation, 40, pp.148-153.
Murray, A.B., and Paola, C., 1997. "Properties of a cellular braided stream model", Earth Surface Processes and Landforms, 22, pp.1001-1025.
Nadler, C.T., and Schumm, S.A., 1981. "Metamorphosis of South Platte and Arkansas Rivers, eastern Colorado", Physical Geography, 2, pp.95-115.
Nagata, N., Hosoda, T., and Muramato, Y., 2000. "Numerical analysis of river channel processes with bank erosion", Journal of Hydraulic Engineering, ASCE, 126, pp.243-252.
Naiman, R.J., and Décamps, H., 1997. "The ecology of interfaces: Riparian zones", Annual Review of Ecology and Systematics, 28, pp.621-658.
Nakamura, F., and Swanson, F.J., 1993. "Effects of coarse woody debris on morphology and sediment storage of a mountain stream system in western Oregon", Earth Surface Processes and Landforms, 18, pp.43-61.
Nanson, G.C., 1981. "New evidence of scroll bar formation on Beatton River", Sedimentology, 28, pp.889-891.
Nanson, G.C., 1986. "Episodes of vertical accretion and catastrophic stripping: A model of disequilibrium flood-plain development", Geological Society of America Bulletin, 97, pp.1467-1475.
Nanson, G.C., and Beach, H.F., 1977. "Forest succession and sedimenation on a meandering-river floodplain, northeast British Columbia, Canada", Journal of Biogeography, 4, pp.229-251.
Nanson, G.C., and Croke, J.C., 1992. "A genetic classification of floodplains", Geomorphology, 4, pp.459-486.
Nanson, G.C., and Hean, D., 1985. "The West Dapo flood of February 1984: rainfall characteristics and channel changes", Australian Geographer, 16, pp.249-258.
Nanson, G.C., Von Krusenstierna, A., Bryant, E., and Renilson, M., 1994. "Experimental measurements of river-bank erosion caused by boat-generated waves on the Gordon River, Tasmania", Regulated Rivers Research and Management, 9, pp.1-14.
Nanson, G.C., and Young, R.W., 1981. "Overbank deposition and floodplain formation on small coastal strreams of New South Wales", Zeitschrift fur Geomorphologie, 25, pp.332-347.
Naot, D., Nezu, I., and Nakagawa, H., 1996. "Hydrodynamic behavior of partly vegetated open channels", Journal of Hydraulic Engineering, ASCE, 122, pp.625-633.
Nash, D., 1987. "A comparative review of limit equilibrium methods of stability analysis", In: Slope

Stability, M.G. Anderson and K.S. Richards (eds.), John Wiley, Chichester, UK, pp.11-75.

Neill, C.R., and Mollard, J.D., "Examples of erosion and sedimentation processes along some northern Canadian rivers", In: International Symposium on River Sedimenation, March 1980, Bejing, China, Guunghua Press, Bejing, China, pp.565-597.

Nelson, J.G., 1966. "Man and geomorphic processes in the Chemung River valley, New York and Pennsylvania", Annals of the Association of American Geographers, 56, pp.24-32.

Nelson, J.M., and Smith, J.D., 1989a. "Flow in meandering channels with natural topography", In: River Meandering, S. Ikeda and G. Parker (eds.), American Geophysical Union, Washington, D.C., pp.69-102.

Nelson, J.M., and Smith, J.D., 1989b. "Evolution and stability of erodible channel beds", In: River Meandering, S. Ikeda and G. Parker (eds.), American Geophysical Union, Washington, D.C., pp.321-378.

Neu, H.A., 1967. "Transverse flow in a river due to the earth's rotation", Journal of the Hydraulics Division, ASCE, 93, pp.149-165.

Newson, M.D., and Newson, C.L., 2000. "Geomorphology, ecology and river channel habitat: mesoscale approaches to basin-scale challenges", Progress in Physical Geography, 24, pp.195-217.

Nicholas, A.P., and Mitchell, C.A., 2003. "Numerical simulation of overbank processes in topographically complex floodplain environments", Hydrological Processes, 17, pp.727-746.

Nicholas, A.P., Woodward, J.C., Christopoulos, G., and Macklin, M.G., 1999. "Modelling and monitoring river responce to environmental change: The impact of dam construction and gravel extraction on bank erosion rates in the Lower Alfios Basin, Greece", In: Fluvial Processes and Environmental Change, A.G. Brown and T.A. Quine (eds.), John Wiley, Chichester, UK, pp.117-137.

Nicholson, B.E., and Clapham, A.R., 1975. The Oxford Book of Trees, Oxford University Press, Oxford, UK, 216 p.

Niklas, K.J., and Moon, F.C., 1988. "Flexural stiffness and modulus of elasticity of flower stalks from *Allium stivum* as measured by multiple resonance frequency spectra", American Journal of Botany, 75, pp.1517-1525.

Niño, Y., Atala, A., Barahona, M., and Aracena, D., 2002. "Discrete particle model for analyzing bedform development", Journal of Hydraulic Engineering, ASCE, 128, pp.381-389.

Nuding, A., "Hydraulic resistance of river banks covered with trees and brushwood", In: 2nd International Conference of River Flood Hydraulics, W.R. White and J. Watts (eds.), John Wiley, Chichester, UK, pp.427-437.

Odgaard, A.J., 1984. "Flow and bed topography in an alluvial channel bend", Journal of Hydraulic Engineering, ASCE, 110, pp.521-536.

Odgaard, A.J., 1987. "Streambank erosion along two rivers in Iowa", Water Resources Research, 23, pp.1225-1236.

Odgaard, A.J., and Kennedy, J.F., 1983. "River-bend bank protection by submerged vanes", Journal of Hydraulic Engineering, ASCE, 109, pp.1161-1173.

Odoni, N., and Darby, S.E., 2002. "Exploring equifinality in a numerical landscape evolution model", EOS Transactions, AGU, Fall Meeting Supplement, 83, pp.H12B-0923.

Okagbue, C.O., and Abam, T.K.S., 1986. "An analysis of stratigraphic control on riverbank failure", Engineering Geology, 22, pp.231-245.

Olesen, K.W., 1987. Bed topography in shallow river bends. Report No. 87-1, T.U. Delft, Delft, Netherlands.

Olsen, N.R.B., 2003. "Three-dimensional CFD modeling of self-forming meandering channel", Journal of Hydraulic Engineering, ASCE, 129, pp.366-372.

Olsen, N.R.B., and Kjellesvig, H.M., 1998. "Three-dimensional numerical flow modeling for estimation of maximum local scour depth", Journal of Hydraulic Research, 36, pp.579-590.

Osman, A.M., and Thorne, C.R., 1988. "Riverbank stability analysis. I: Theory", Journal of Hydraulic Engineering, ASCE, 124, pp.134-150.

Page, K., and Nanson, G., 1982. "Concave bank benches an associated flood plain formation", Earth Surface Processes and Landforms, 7, pp.529-543.

Parker, G., 1976. "On the causes and characteristic scales of meandering and braiding in rivers", Journal of Fluid Mechanics, 76, pp.457-480.

Parker, G., "Theory of meander bend deformation", In: River Meandering, 24-26 October, 1983, New Orleans, Louisiana, C.M. Elliot (ed.), ASCE, New Orleans, Louisiana, pp.722-731.

Parker, G., and Andrews, E.D., 1985. "Sorting of bed load sediment by flow in meander bends", Water Resources Research, 21, pp.1361-1373.

Parker, G., and Andrews, E.D., 1986. "On the time development of meander bends", Journal of Fluid Mechanics, 162, pp.139-156.

Parker, G., and Johannesson, H., 1989. "Observations on several recent theories of resonance and overdeepening in meandering channels", In: River Meandering, S. Ikeda and G. Parker (eds.), American Geophysical Union, Washington, D.C., pp.379-415.

Parker, G., Sawai, K., and Ikeda, S., 1982. "Bend theory of river meanders: II. Non-linear deformation of finite-amplitude bends", Journal of Fluid Mechanics, 115, pp.303-314.

Parsons, D.A., 1960. "Effects of flood flows on channel boundaries", Journal of the Hydraulics Division, ASCE, 86, pp.21-34.

Pasche, E., and Rouvé, G., 1985. "Overbank flow with vegetatively roughened flood plains", Journal of Hydraulic Engineering, ASCE, 111, pp.1262-1278.

Perkins, H.J., 1970. "The formation of streamwise vorticity in turbulent flow", Journal of Fluid Mechanics, 44, pp.721-740.

Pethick, J., Leggett, D., and Husain, L., 1990. "Boundary layers under salt marsh vegetation developed in tidal currents", In: Vegetation and Erosion, J.B. Thornes (ed.), John Wiley, Chichester, UK, pp.114-124.

Petryk, S., 1969. Drag on Cylinders in Open Channel Flow. Ph.D. Thesis, Colorado State University, Fort Collins, Colorado.

Petryk, S., and Bosmajian, G., 1975. "Analysis of flow through vegetation", Journal of Hydraulic Engineering, ASCE, 101, pp.871-884.

Pickup, G., and Warner, R.F., 1976. "Effects of hydrologic regime on magnitude and frequency of dominant discharge", Journal of Hydrology, 29, pp.51-75.

Piégay, H., and Marston, R.A., 1998. "Distributions of large woody debris along the outer bend of meanders in the Ain River, France", Physical Geography, 19, pp.318-340.

Pierret, A., Capowiez, Y., Moran, C.J., and Kretzschmar, A., 1999. "X-ray computed tomography to quantify tree rooting spatial distributions", Geoderma, 90, pp.307-326.

Pierson, T.C., 1983. "Soil pipes and slope stability", Quarterly Journal of Engineering Geology, 16, pp.1-11.

Piest, R.F., and Bowie, A.J., "Gully and streambank erosion", In: Proceedings of 29th Annual Meeting of the Soil Conservation Society of America, pp.188-196.

Pitlo, R.H., "Flow resistance of aquatic vegetation", In: Proceedings of the European Weed Research Society 6th Symposium on Aquatic Weeds, pp.225-234.

Pizzuto, J.E., 1990. "Numerical simulation of gravel river widening", Water Resources Research, 26, pp.1971-1980.

Pizzuto, J.E., 1994. "Channel adjustments to changing discharges, Powder River, Montana", Geological Society of America Bulletin, 106, pp.1494-1501.

Power, M.E., Parker, G., Dietrich, W.E., and Sun, A., 1995. "How does floodplain width affect floodplain river ecology? A preliminary exploration using simulations", Geomorphology, 13, pp.301-317.

Power, M.E., Sun, A., Parker, G., Dietrich, W.E., and Wootton, J.T., 1995. "Hydraulic food chain models: An approach to the study of food web dynamics in large rivers", BioScience, 45, pp.159-167.

Prandtl, L., 1952. Essentials of Fluid Dynamics, Blackie and Sons, London, UK.

Press, W.H., Vetterling, W.T., Teukolsky, S.A., and Flannery, B.P., 1992. Numerical Recipes in Fortran 77, Cambridge University Press, Cambridge, UK.

Prosser, I.P., Dietrich, W.E., and Stevenson, J., 1995. "Flow resistance and sediment transport by concentrated overland flow in a grassland valley", Geomorphology, 13, pp.71-86.

Prosser, I.P., Hughes, A.O., and Rutherford, I.D., 2000. "Bank erosion of an incised upland channel by subaerial processes: Tasmania, Australia", Earth Surface Processes and Landforms, 25, pp.1085-1101.

Rahmeyer, W., Werth, D., and Freeman, G.E., 1999. Flow resistance to vegetation in compound channels and floodplains. Report No. DACW39-94-K-0009, US Army Waterways.

Raudkivi, A.J., 1990. Lose Boundary Hydraulics (3rd edition), Pergamon Press, Oxford, UK.

Raupach, M.R., and Shaw, R.H., 1982. "Averaging procedures for flow within vegetation canopies", Boundary Layer Meteorology, 22, pp.79-90.

Raupach, M.R., Thom, A.S., and Edwards, I., 1980. "A wind-tunnel study of turbulent flow close to regularly arrayed rough surfaces", Boundary Layer Meteorology, 18, pp.373-397.

Ree, W.O., and Palmer, V.J., 1949. "Flow of water in channels protected by vegetative linings", US Department of Agriculture Technical Bulletin, 967.

Rehder, A., 1947. Manual of Cultivated Trees and Shrubs, MacMillan, New York, NY

Reid, I., Bathurst, J.C., Carling, P.A., Walling, D.E., and Webb, B.W., 1997. "Sediment erosion, transport and deposition", In: Applied Fluvial Geomorphology for River Engineering and Management, C.R. Thorne, R.D. Hey, and M.D. Newson (eds.), John Wiley, Chichester, UK, pp.95-135.

Rhoads, B.L., and Welford, M.R., 1991. "Initiation of meandering", Progress in Physical Geography, 15(2), pp.127-156.

Rice, J.R., 1983. Numerical Methods, Software and Analysis: ISML Reference Edition, McGraw Hill, New York, N.Y.

Richards, K.S., 1982. Rivers: Form and Process in Alluvial Channels, Methuen, London, UK.

Richards, K.S., and Lorriman, N.R., 1987. "Basal erosion and mass movement", In: Slope Stability, M.G. Anderson and K.S. Richards (eds.), John Wiley, Chichester, UK, pp.331-357.

Rinaldi, M., and Casagli, N., 1999. "Stability of streambanks formed in partially saturated soils and effects of negative pore water pressures: the Sieve River, Italy", Geomorphology, 26, pp.253-277.

Ritter, D.F., Kinsey, W.F., and Kauffman, M.E., 1973. "Overbank sedimentation in the Delaware River valley during the last 6000 years", Science, 179, pp.374-375.

Robertson, J.M., Johnson, J.W., Selim, M.A., Nelidov, I., Woodward, S.M., Howe, J.W., Posey, C.J., and Mockmore, C.A., 1944. "Discussion on 'Flow around bends in stable channels' (Mockmore, 1944)", Transactions of the American Society of Civil Engineers, 109, pp.619-628.

Rowntree, K.M., 1991. "An assessment of the potential impact of alien invasive vegetation on the geomorphology of river channels in South Africa", South African Journal of Aquatic Science, 17, pp.28-43.

Rozovskii, I.L., 1957. Flow of Water in Bends of Open Channels, Academy of Sciences of the

Ukranian SSR, Institute of Hydrology and Hydraulic Engineering, Kiev, Ukrainian SSR. (In Russian; English translation: Israel Program for Scientific Translations,1961).

Rumsby, B., 2000. "Vertical accretion rates in fluvial systems: A comparison of volumetric and depth-based estimates", Earth Surface Processes and Landforms, 25, pp.647-631.

Salo, J., Kalliola, R., Hakkinen, I., Makinen, Y., Niemala, P., Puhakka, M., and Coley, P.D., 1986. "River dynamics and the diversity of Amazon lowland forest", Nature, 322, pp.254-258.

Sand-Jensen, K., 1998. "Influence of submerged macrophytes on sediment composition and near-bed flow in lowland streams", Freshwater Biology, 39, pp.663-379.

Sand-Jensen, K., and Mebus, J.R., 1996. "Fine-scale patterns of water velocity within macrophyte patches in streams", Oikos, 76, pp.169-180.

Sarma, S.K., 1973. "Stability analysis of embankments and slopes", Geotechnique, 23, pp.423-433.

Sarma, S.K., 1979. "Stability analysis of embankments and slopes", Journal of the Geotechnical Division, ASCE, 105, pp.1511-1524.

Schauberger, V., 1930. "Fundamentals principles of river regulation", Die Wasserwirtschaft, 24, pp.498-502 (in German).

Schlosser, I.J., 1991. "Stream fish ecology: a landscape perspective", BioScience, 41, pp.704-712.

Schmidt, J.C., Grams, P.E., and Webb, R.H., 1995. "Comparison of the magnitude of erosion along two large regulated rivers", Water Resources Bulletin, 31, pp.617-631.

Schumm, S.A., 1960. "The shape of alluvial channels in relation to sediment type", USGS Professional Paper, 352-B, pp.17-30.

Schumm, S.A., 1963. "Sinuosity of alluvial rivers on the great plains", Geological Society of America Bulletin, 74, pp.1089-1099.

Schumm, S.A., 1969. "River metamorphosis", Journal of the Hydraulics Division, ASCE, 95, pp.255-273.

Schumm, S.A., 1985. "Patterns of alluvial rivers", Annual Review of Earth and Planetary Sciences, 13, pp.5-27.

Schumm, S.A., 1993. "River response to baselevel change: Implications for sequence stratigraphy", Journal of Geology, 101, pp.279-294.

Schumm, S.A., and Khan, H.R., 1972. "Experimental study of channel patterns", Geological Society of America Bulletin, 83, pp.1755-1770.

Scott, K.M., 1982. "Erosion and sedimentation in the Kenai River, Alaska", USGS Professional Paper, 1235, pp.1-35.

Selby, M.J., 1993. Hillslope materials and processes, Oxford University Press, Oxford, UK.

Sellin, R.H.J., Ervine, D.A., and Willetts, B.B., 1993. "Behaviour of meandering two-stage channels", Proceedings of the Institution of Civil Engineers - Water, Maritime and Energy, 101, pp.99-111.

Seminara, G., and Tubino, M., 1989. "Alternate bars and meandering: free, forced and mixed interactions", In: River Meandering, S. Ikeda and G. Parker (eds.), American Geophysical Union, Washington, D.C., pp.267-320.

Severn, F.R., 1982. The Conflict between Land Drainage and Habitat Conversion: The Effects of Watercourse vegetation on Channel Capacity. M.Sc. Thesis, Imperial College of Science, University of London, London, UK.

Sewell, G., 1988. The Numerical Solution of Ordinary and Partial Differential Equations, Academic Press, Boston, Massachussetts

Shen, H.W., and Komura, S., 1968. "Meandering tendencies in straight alluvial channels", Journal of the Hydraulics Division, ASCE, 94, pp.997-1015.

Shields, A., 1936. "Anwendung der Aehnlichkeitsmechanik und der Turbulenz Forschung auf die Geschibebewegung", Mitteilungen der Preussiche Versuchanstalt fur Wasserbau und

Schiffbau.
Shields, F.D., and Abt, S.R., 1989. "Sediment deposition in cutoff meander bends and implications for effective management", Regulated Rivers Research and Management, 4, pp.381-396.
Sidle, R.C., Pearce, A.J., and O'Loughlin, C.L., 1985. Hillslope stability and land use, AGU, Washington D.C.
Simon, A., and Collison, A.J.C., 2001. "Pore-water pressure effects on the detachment of cohesive streambeds: seepage forces and matric suction", Earth Surface Processes and Landforms, 26, pp.1421-1442.
Simon, A., and Collison, A.J.C., 2002. "Quantifying the mechanical and hydrological effects of riparian vegetation on streambank stability", Earth Surface Processes and Landforms, 27, pp.527-546.
Simon, A., Curini, A., Darby, S., and Langendoen, E., 1999. "Streambank mechanics and the role of bank and near-bank processes in incised channels", In: Incised River Channels, S.E. Darby and A. Simon (eds.), John Wiley, Chichester, UK, pp.123-152.
Simon, A., Curini, A., Darby, S.E., and Langendoen, E.J., 2000. "Bank and near-bank processes in an incised channel", Geomorphology, 35, pp.193-217.
Simon, A., and Darby, S.E., 1997. "Process-form interactions in unstable sand-bed river channels: A numerical modeling approach", Geomorphology, 21, pp.85-106.
Simon, A., and Hupp, C.R., 1992. Geomorphic and vegetative recovery processes along modified stream channels of West- Tennessee. 91-502, US Geological Survey, Nashville, Tennessee.
Simon, A., Wolfe, W.J., and Molinas, A., "Mass wasting algorithms in an alluvial channel model", In: 5th Federal Interagency Sedimentation Conference, sep 22 - sep 29, Las Vegas, Nevada.
Smith, J.C., 1990. "Recirculating flow and sedimentation in the Colorado River in Grand Canyon, Arizona", Journal of Geology, 98, pp.709-724.
Smith, J.D., and McLean, A., 1984. "A model for flow in meandering streams", Water Resources Research, 20, pp.1301-1315.
Smith, R.D., Sidle, R.C., and Porter, P.E., 1993. "Effects on bedload transport of experimental removal of woody debris from a forest gravel-bed stream", Earth Surface Processes and Landforms, 18, pp.455-468.
Sotir, R.B., 1995. "Soil bioengineering experiences in North America", In: Vegetation and Slopes, D.H. Barker (ed.), Thomas Telford, London, UK, pp.190-201.
Soufi, M., 1997. Processes and Rates of Gully Development in Pine Plantations, Southeastern New South Wales. University of New South Wales, Sydney, Australia.
Speight, J.G., 1965. "Meander spectra of the Angabunga River", Journal of Hydrology, 3, pp.1-15.
Spencer, E., 1967. "A method of analysis of the stability of embankments assuming parallel inter-slice forces", Geotechnique, 15, pp.11-26.
Spencer, T., Douglas, I., Greer, T., and Suhun, W., 1990. "Vegetation and fluvial geomorphological processes in South East Asian tropical rainforest", In: Vegetation and Erosion, J.B. Thornes (ed.), John Wiley, Chichester, UK, pp.451-469.
Springer, F.M., Ullrich, C.R., and Hagerty, D.J., 1985. "An analysis of streambank stability", Journal of Geotechnical Engineering, ASCE, 111, pp.624-640.
Stanley, D., Krinitzsky, E.L., and Compton, J.R., 1966. "Mississippi River bank failure, Fort Jackson, Louisiana", Geological Society of America Bulletin, 77, pp.859-866.
Stephens, J.C., Blackburn, R.D., Seaman, P.E., and Weldon, L.W., 1963. "Flow retardance by channel weeds and their control", Journal of the Irrigation and Drainage Division, ASCE, 89, pp.31-53.
Steward, M.D., Bates, P.D., Price, D.A., and Burt, T.P., 1998. "Modelling the spatial variability in floodplain soil contamination during flood events to improve chemical mass balance

estimates", Hydrological Processes, 12, pp.1233-1255.

Stokes, A., Fourcaud, T., Hruska, J., Cermak, J., Nadyezdhina, N., Nadyezdhin, V., and Praus, L., 2002. "An evaluation of different methods to investigate root system architecture of urban trees *in situ*: I. ground-penetrating radar", Journal of Arboriculture, 28, pp.2-10.

Stølum, H.-H., 1998. "Planform geometry and dynamics of meandering rivers", Geological Society of America Bulletin, 110, pp.1485-1498.

Stott, T., 1997. "A comparison of stream bank erosion processes on forested and moorland streams in the Balquhidder catchments, central Scotland", Earth Surface Processes and Landforms, 22, pp.383-399.

Stott, T., 1999. "Stream bank and forest ditch erosion: preliminary responses to timber harvesting in Mid- Wales", In: Fluvial Processes and Environmental Change, A.G. Brown and T.A. Quine (eds.), John Wiley, Chichester, UK, pp.47-70.

Struiksma, N., 1985. "Prediction of 2-D bed topography in rivers", Journal of Hydraulic Engineering, ASCE, 111, pp.1169-1182.

Struiksma, N., and Crosato, A., 1989. "Analysis of a 2-D bed topography model for rivers", In: River Meandering, S. Ikeda and G. Parker (eds.), American Geophysical Union, Washington, D.C., pp.153-180.

Struiksma, N., Olesen, K.W., Flokstra, C., and De Vriend, H.J., 1985. "Bed deformation in curved alluvial channels", Journal of Hydraulic Research, 23, pp.57-79.

Stuppy, W.H., Maisano, J.A., Colbert, M.W., Rudall, P.J., and Rowe, T.B., 2003. "Three-dimensional analysis of plant structure using high- resolution X-ray computed tomography", Trends in Plant Science, 8, pp.2-6.

Sun, T., Meakin, P., J ssang, T., and Schwarz, K., 1996. "A simulation model for meandering rivers", Water Resources Research, 32, pp.2937-2954.

Sun, T., Meakin, P., and Jossang, T., 2001. "A computer model for meandering rivers with multiple bedload sediment sizes. 2. Computer simulations", Water Resources Research, 37, pp.2243-2258.

Sundborg, A., 1956. "The River Klaralven, a study of fluvial processes", Geografiska Annaler, 38, pp.127-316.

Sustek, S., Hruska, J., Druckmuller, M., and Michalek, T., 1999. "Root surfaces in the large oak tree estimated by image analysis of the map obtained by the ground penetrating radar", Journal of Forest Science, 45, pp.139-143.

Talmon, A.M., 1992. Bed Topography of River Bends with Suspended Sediment Transport. PhD Thesis, Technische Universiteit Delft, Delft, Netherlands.

Tanner, F.W., 1960. "Helicoidal flow: a possible cause of meandering", Journal of Geophysical Research, 65, pp.993-995.

Tattersall, G.R., Elliot, A.H., and Lynn, N.M., 2003. "Suspended sediment concentrations in the Tamar estuary", Estuarine, Coastal and Shelf Science, 57, pp.679-688.

Taylor, D.W., 1948. Fundamentals of Soil Mechanics, John Wiley, New York, N.Y.

Temple, D.M., 1980. "Tractive force design of vegetated channels", Transactions of the American Society of Agricultural Engineers, 23, pp.884-890.

Temple, D.M., 1982. "Flow retardance of submerged grass channel linings", Transactions of the American Society of Agricultural Engineers, 25, pp.1300-1303.

Temple, D.M., 1986. "Velocity distribution coefficients for grasslined channels", Journal of Hydraulic Engineering, ASCE, 112, pp.193-205.

Thomas, R., and Nicholas, A.P., 2002. "Simulation of braided flow using a new cellular routing scheme", Geomorphology, 43, pp.179-195.

Thomas, T.G., and Williams, J.J.R., 1995. "Large eddy simulation of a symmetrical trapezoidal

channel at a Reynolds number of 430000", Journal of Hydraulic Research, 33, pp.825-842.

Thompson, A., 1986. "Secondary flow and the pool-riffle unit: A case study of the processes of meander development", Earth Surface Processes and Landforms, 11, pp.631-641.

Thompson, G.T., and Roberson, J.A., 1976. "A theory of flow resistance for vegetated channels", Transactions of the American Society of Agricultural Engineers, 19, pp.288-293.

Thompson, J.F., Warsi, Z.U.A., and Mastin, C.W., 1985. Numerical Grid Generation, Foundations and Applications, North-Holland, Amsterdam, Netherlands

Thomson, J., 1876. "On the origins and winding of rivers in alluvial plains", Proceedings of the Royal Society, 25, pp.5-8.

Thomson, S., and Townsend, D.L., 1979. "River erosion and bank stabilisation - north Saskatchewan River, Edmonton, Alberta", Canadian Geotechnical Journal, 16, pp.567-576.

Thorne, C.R., 1978. Processes of Bank Erosion in River Channels. Ph.D. Thesis, University of East-Anglia, Norwich, UK.

Thorne, C.R., 1982. "Processes and mechanisms of river bank erosion", In: Gravel-Bed Rivers, R.D. Hey, J.C. Bathurst, and C.R. Thorne (eds.), John Wiley, Chichester, UK, pp.227-271.

Thorne, C.R., 1990. "Effect of vegetation on riverbank erosion and stability", In: Vegetation and Erosion, J.B. Thornes (ed.), John Wiley, Chichester, UK, pp.125-144.

Thorne, C.R., Chang, H.H., and Hey, R.D., "Prediction of hydraulic geometry of gravel-bed streams using the minimum stream power concept", In: Proceedings of the International Conference on River Regime, 18-20 May 1988, Wallingford, England, W.R. White (ed.), John Wiley, Chichester, UK, pp.29-40.

Thorne, C.R., and Hey, R.D., 1979. "Direct measurements of secondary currents at a river inflection point", Nature, 280, pp.226-228.

Thorne, C.R., and Lewin, J., 1979. "Bank erosion, bed material movement and planform development in a meandering river",, In: Adjustment of the Fluvial System, D.D. Rhodes and G.P. Williams (eds.), Kendall/Hunt, Dubuque, Iowa, pp.117-137.

Thorne, C.R., and Osman, A.M., "The influence of bank stability on regime geometry of natural channels", In: Proceedings of the International Conference on River Regime, 18-20 May 1988, Wallingford, England, W.R. White (ed.), John Wiley, Chichester, UK, pp.135-147.

Thorne, C.R., and Tovey, K., 1981. "Stability of composite river banks", Earth Surface Processes and Landforms, 6, pp.469-484.

Thorne, C.R., Zevenbergen, L.W., Rais, S., Bradley, J.B., and Julien, P.Y., 1985. "Direct measurements of secondary currents in a meandering sand-bed river", Nature, 315, pp.746-747.

Thorne, S.D., and Furbish, D.J., 1995. "Influences of course bank roughness on flow within a sharply curved river bend", Geomorphology, 12, pp.241-257.

Thornton, C.I., Abt, S.R., and Clary, W.P., 1997. "Vegetation influence on small stream siltation", Journal of the American Water Resources Association, 33, pp.1279-1288.

Tobias, S., 1995. "Shear strength of the soil root bond system", In: Vegetation and Slopes, D.H. Barker (ed.), Thomas Telford, London, UK, pp.280-286.

Trimble, S.W., 1994. "Erosional effects of cattle on streambanks in Tennessee, U.S.A", Earth Surface Processes and Landforms, 19, pp.451-464.

Trimble, S.W., and Mendel, A.C., 1995. "The cow as a geomorphic agent - a critical review", Geomorphology, 13, pp.233-253.

Tritton, D.J., 1988. Physical Fluid Dynamics, Oxford Science Publications, Oxford, U.K.

Tsujimoto, T., 1996. "Coherent fluctuations in a vegetated zone of open-channel flow: Causes of bedload lateral transport and sorting", In: Coherent Flow Structures, P.J. Ashworth, S.J. Bennett, J.L. Best, and S.J. McLelland (eds.), John Wiley, Chichester, UK, pp.375-396.

Tsujimoto, T., 1999. "Fluvial processes in streams with vegetation", Journal of Hydraulic Research, 37, pp.789-803.

Tsujimoto, T., Shimizu, T., and Okada, T., 1991. Turbulent structure of flow over rigid vegetation-covered bed in open channels, Hydraulic Laboratory, Kanazawa University, Japan

Tubino, M., Repetto, R., and Zolezzi, G., 1999. "Free bars in rivers", Journal of Hydraulic Research, 37, pp.759-775.

Tubino, M., and Seminara, G., 1990. "Free-forced interactions in developing meanders and supopression of free bars", Journal of Fluid Mechanics, 214, pp.131-159.

Twidale, C.R., 1964. "Erosion of an alluvial bank at Birkwood, South Australia", Zeitschrift fur Geomorphologie, 8, pp.189-211.

Ullrich, C.R., Hagerty, D.J., and Holmberg, R.W., 1986. "Surficial failures of alluvial stream banks", Canadian Geotechnical Journal, 23, pp.304-316.

Van Alphen, J.S.L.J., Bloks, P.M., and Hoekstra, P., 1984. "Flow and grainsize pattern in a sharply curved river bend", Earth Surface Processes and Landforms, 9, pp.513-522.

Van Bendegom, L., 1947. "Eenige beschouwingen over riviermorphologie en rivierverbetering", De Ingenieur, 59, pp.1-11.

Van De Wiel, M.J., and Darby, S.E., in press. "Numerical modeling of bed topography and bank erosion along tree-lined meandering rivers", In: Riparian Vegetation and Fluvial Geomorphology: Hydraulic, Hydrologic, and Geotechnical Interactions, S.J. Bennett and A. Simon (eds.), American Geophysical Union, Washington, DC.

Van den Berg, J.H., 1995. "Prediction of alluvial channel patterns of perennial rivers", Geomorphology, 12, pp.259-279.

Van Rijn, L.C., 1984. "Sediment transport. Part I: Bed load transport", Journal of Hydraulic Engineering, ASCE, 110, pp.1431-1456.

Vanapalli, S.K., "A simple experimental procedure for determining the fitting parameter, *K*, for predicting the shear strength of an unsaturated soil", In: Proceedings of the 54th Canadian Geotechnical Conference,Calgary, Canada, pp.622-629.

Vanapalli, S.K., and Fredlund, D.G., 2000. "Comparison of different procedures to predict unsaturated soil shear strength", In: Advances in Unsaturated Soils, C. Shackleford, S.L. Houston, and N.-Y. Chang (eds.), American Society of Civil Engineers, Reston, VA, pp.195-209.

Vandekerckhove, L., Poesen, J., Oostwoud Wijdenes, D., Gyssels, G., Beuselinck, L., and de Lune, E., 2000. "Characteristics and controlling factors of bank gullies in two semi-arid mediterranean environments", Geomorphology, 33, pp.37-58.

Vanoni, V.A., 1946. "Transportation of suspended sediment by water", Transactions of the American Society of Civil Engineers, 111, pp.67-102.

Vanoni, V.A., and Nomicos, G.N., 1959. "Resistance properties of sediment laden streams", Journal of the Hydraulics Division, ASCE, 85, pp.77-107.

Versteeg, H.K., and Malalasekera, W., 1995. An Introduction to Computational Fluid Dynamics: The Finite Volume Method, Pearson Prentice Hall, Harlow, UK. 257 p.

Vertessey, R., 1990. Morphodynamics of macrotidal rivers in Far Northern Australia. Departent of Geography, Australian National University, Canberra, Australia.

Von Schelling, H., 1951. "Most frequent particle paths in a plane", Transactions of the American Geophysical Union, 22, pp.222-226.

Walker, H.J., Arnborg, L., and Peippo, J., 1987. "Riverbank erosion in the Colville delta, Alaska", Geografiska Annaler, 69A, pp.61-70.

Walker, H.J., and Morgan, H.M., 1964. "Unusual weather and river bank erosion in the delta of the Colville river, Alaska", Arctic, 17, pp.41-47.

Walling, D.E., Quine, T.A., and He, Q., 1992. "Investigating contemporary rates of floodplain sedimentation", In: Lowland Floodplain Rivers: Geomorphological Perspectives, P.A. Carling and G.E. Petts (eds.), John Wiley, Chichester, UK, pp.165-184.

Walling, D.E., and He, Q., 1999. "Changing rates of overbank sedimentation on the floodplains of British rivers during the past 100 years", In: Fluvial Processes and Environmental Change, A.G. Brown and T.A. Quine (eds.), John Wiley, Chichester, UK, pp.207-222.

Warner, R.F., 1987. "Bank erosion in the Bellinger Valley, New South Wales: definition and management", Australian Geographical Studies, 25, pp.3-14.

Watson, C.C., Abt, S.R., and Derrick, D., 1997. "Willow posts bank stabilization", Journal of the American Water Resources Association, 33.

Watson, D., 1987. "Hydraulic effects of aquatic weeds in U.K. rivers", Regulated Rivers Research and Management, 1, pp.211-227.

Weigel, T.A., and Hagerty, D.J., 1983. "Riverbank change - Sixmile Island, Ohio River, USA", Engineering Geology, 19, pp.119-132.

Werner, P.W., 1951. "On the origin of river meanders", Transactions of the American Geophysical Union, 32, pp.898-902.

Werritty, A., and Ferguson, R.I., 1980. "Pattern changes in a Scottish braided river over 1, 30 and 200 years", In: Timescales in Geomorphology, R.A. Cullingford, D.A. Davidson, and J. Lewin (eds.), John Wiley, Chichester, UK, pp.53-68.

Whiting, P.J., and Dietrich, W.E., 1988. Experimental river meander data. Unpublished laboratory notes for 'Experimental studies of bed topography and flow patterns in large-amplitude meanders' (Whiting and Dietrich, 1993b).

Whiting, P.J., and Dietrich, W.E., 1993a. "Experimental constraints on bar migration through bends: Implications for meander wavelength selection", Water Resources Research, 29, pp.1091-1102.

Whiting, P.J., and Dietrich, W.E., 1993b. "Experimental studies of bed topography and flow patterns in large-amplitude meanders: 1. Observations", Water Resources Research, 29, pp.3605-3614.

Whiting, P.J., and Dietrich, W.E., 1993c. "Experimental studies of bed topography and flow patterns in large-amplitude meanders: 2. Mechanisms", Water Resources Research, 29, pp.3615-3622.

Williams, D.R., Romeril, P.M., and Mitchell, R.J., 1979. "Riverbank erosion and recession in the Ottawa area", Canadian Geotechnical Journal, 16, pp.641-650.

Williams, G.P., 1986. "River meanders and channel size", Journal of Hydrology, 88, pp.147-164.

Wilson, N.R., and Shaw, R.H., 1977. "A higher order closure model for canopy flow", Journal of Applied Meteorology, 16, pp.1197-1205.

Wolfe, S.A., and Nickling, W.G., 1993. "The protective role of sparse vegetation in wind erosion", Progress in Physical Geography, 17, pp.50-68.

Wolman, M.G., 1959. "Factors influencing erosion of a cohesive riverbank", American Journal of Science, 257, pp.204-216.

Wolman, M.G., 1967. "A cycle of sedimentation and erosion in urban river channels", Geografiska Annaler, 49A, pp.385-395.

Wolman, M.G., and Leopold, L.B., 1957. "River flood plains: some observations on their formation", USGS Professional Paper, 282-C, pp.87-107.

Woodyer, K.D., 1975. "Concave-bank benches on the Barwon River, New South Wales", Australian Geographer, 13, pp.36-40.

Woodyer, K.D., Taylor, G., and Crook, K.A.W., 1979. "Depositional processes along a very low gradient suspended load stream: the Barwon River, New South Wales", Sedimentary Geology, 22, pp.97-120.

Wright, N.G., Honarbakhsh, A., and Thorne, C., "Numerical modelling of bank erosion in

meandering river channels", In: River Flow 2002 - Proceedings of the International Conference on Fluvial Hydraulics, Louvain-La-Neuve, Belgium, September 2002, D. Bousmar and Y. Zech (eds.), Lisse, the Netherlands, Swets & Weitlinger, Lisse, the Netherlands.

Wu, F.-C., Shen, H.W., and Chou, Y.-J., 1999. "Variation of roughness coefficients for unsubmerged and submerged vegetation", Journal of Hydraulic Engineering, ASCE, 125, pp.934-942.

Wu, J., and Tsanis, I.K., 1994. "Pollutant transport and residence time in a distorted model and a numerical model", Journal of Hydraulic Research, 32, pp.583-598.

Wu, T.H., 1976. Investigation of Landslides on Prince of Wales Island. Geotechnical Engineering Report 5, Civil Engineering Department, Ohio State University, Columbus, Ohio.

Wu, T.H., McKinnell, W.P., and Swanton, D.N., 1979. "Strength of tree roots and landslides on Price of Wales Island, Alaska", Canadian Geotechnical Journal, 16, pp.19-33.

Wu, W., Rodi, W., and Wenka, T., 2000. "3D numerical modeling of flow and sediment transport in open channels", Journal of Hydraulic Engineering, ASCE, 126, pp.4-15.

Yalin, M.S., 1963. "An expression for bed-load transportation", Journal of the Hydraulics Division, ASCE, 89, pp.221-250.

Yang, C.T., 1973. "Incipient motion and sediment transport", Journal of the Hydraulics Division, ASCE, 99, pp.1679-1704.

Yang, C.T., and Wan, S., 1991. "Comparison of selected bed-material formulas", Journal of Hydraulic Engineering, ASCE, 117, pp.973-989.

Yanoski, T.M., 1982. "Effects of flooding upon woody vegetation along parts of the Potomac River flood plain", USGS Professional Paper, 1206, pp.1-21.

Zeller, J., 1967. "Flussmorphologische Studie zum Meanderproblem", Geographica Helvetica, 22.

Zimmerman, C., 1977. "Roughness effects on the flow direction near curved stream beds", Journal of Hydraulic Research, 15, pp.73-85.

Zimmerman, R.C., Goodlett, J.C., and Comer, G.H., 1967. "The influence of vegetation on channel form of small streams", International Association of Scientific Hydrology Publication, 75, pp.255-275.